Royal Netherlands Academy of Arts and Sciences
P.O. Box 19121, 1000 GC Amsterdam, the Netherlands

Proceedings of the colloquium,
'Transitional Boundary Layers in Aeronautics',
Amsterdam, 6-8 December 1995

ISBN 0-444-85812-1

Koninklijke Nederlandse Akademie van Wetenschappen
Verhandelingen, Afd. Natuurkunde, Eerste Reeks, deel 46

Transitional Boundary Layers in Aeronautics

Edited by R.A.W.M. Henkes and J.L. van Ingen

North-Holland, Amsterdam / Oxford / New York / Tokyo, 1996

Preface

In the thin boundary layer of air along aircraft surfaces, somewhere transition from the laminar to the turbulent state will occur. As the transition marks a significant increase in viscous drag, the transition location is an important design parameter. But the physics of stability and transition of fluid flows are quite complex. A better knowledge of what is going on will enable to implement the concept of *Laminar Flow Control* in future generations of aircraft.

Since the pioneering experiments of Reynolds, more than a century ago, for the transition of the flow in a pipe, much progress has been made in transition research. Over the past 4 decades, the e^n method for the prediction of the transition location has been very popular in the aerodynamic design of airfoils and wings. In the past few years some new ideas and concepts have come up, which are very promising, and are expected to have an influence on design methods in the next decade. For example, there is now considerable interest in receptivity, which describes how environmental disturbances enter the boundary layer and are transformed into unstable waves. Also the Parabolized Stability Equations (PSE) have been introduced. The nonlinear PSE contain much more physics than the e^n method (which is fully based on linear theory), but still much needs to be done to make it available for designers. The availability of supercomputers enables to perform Direct Numerical Simulations (DNS) for all stages of the transition process. The resulting data bases contribute to the fundamental understanding of the transition process. Although the capabilities of PSE and DNS are quite impressive, accurate experimental data remain required for their validation. The experiments are particularly important for the receptivity process. The experiments can also reveal new (primary and higher order) instability mechanisms, not yet captured by the physical models. A remarkable improvement of the experimental techniques over the last years is the use of sophisticated disturbance generators, which can introduce two-dimensional or oblique waves of a prefixed frequency and wavelength.

In view of the fast scientific progress, on the one hand, and the strong need for improved prediction methods by industries, on the other hand, a 3-day Colloquium (6-8 December 1995) on *Transitional Boundary Layers in Aeronautics* was organized in the historical building of the Royal Netherlands Academy of Arts and Sciences in Amsterdam, The Netherlands. The Colloquium had the subtitle *State-of-the-art and Future Directions of Research.* The state-of-the-art was covered by 14 invited speakers, coming from universities, research institutes, and industries. In fact all speakers of our first choice did accept the invitation. Following a call-for-papers, 23 technical presentations were selected (out of double the number of submitted abstracts). These presentations give a valuable overview of current and future research on transition with aeronautical applications. The Colloquium was attended by 50 invited participants, coming from 12 countries: Australia (1), Belgium (1), France (1), Germany (13), India (1), The Netherlands (9), Portugal (1), Russia (5), UK (7), Sweden (1), Switzerland (1), and USA (9).

The Colloquium was concluded with a general discussion on the future directions of research. It became very clear that the collaboration between the developers of transition theory ('the scientists') and the end users of transition-prediction tools in aircraft industries ('the engineers') should be further strengthened. Industries want tools that can be used by an engineer, without the need to have a thorough knowledge of all the details of transition theory. Therefore industries very much like the simple e^n method, though the limitations for extension to 3D are realized. The scientists emphasize that the physics of transition are not simple, and therefore hard to capture in engineering methods. We think that the present Colloquium will help to bridge the gap between the engineering and the scientific world.

All papers included in this volume of the 'Verhandelingen' of the Royal Netherlands Academy of Arts and Sciences were double reviewed. All authors are acknowledged for the time they spent in delivering these high-quality papers. Thanks are also due to the members of the Scientific Committee of the Colloquium: Prof. P.H. Alfredsson (Royal Institute of Technology, Stockholm); Prof. T. Cebeci (McDonnell Douglas Aerospace, USA); Prof. Y.S. Kachanov (Russian Academy of Sciences, Novosibirsk); Prof. Th. Herbert (The Ohio State University, USA) and Dr H.W. Stock (Dornier Luftfahrt). The Scientific Committee selected the presentations and did most of the review of the written papers. Thanks are also due to Bas Flipsen, student of our Faculty of Aerospace Engineering, who helped to bring the papers in their final uniform format.

R.A.W.M. Henkes & J.L. van Ingen
Faculty of Aerospace Engineering, Delft University of Technology
Delft, July 1996

The Colloquium on *Transitional Boundary Layers in Aeronautics* was organized under the auspices of the Royal Netherlands Academy of Arts and Sciences, which also provided financial support.
Additional financial support was obtained from the J.M. Burgers Centre for Fluid Mechanics.

List of Participants

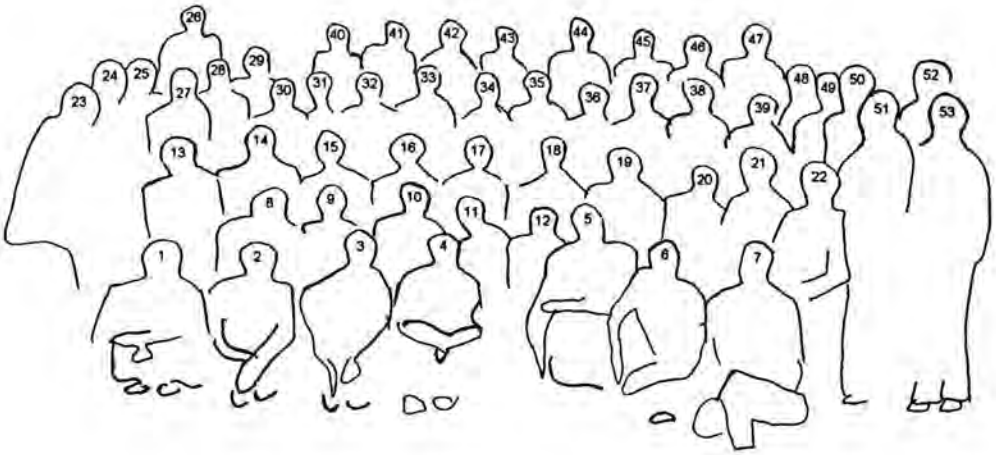

1. U. Dallman
2. T. Lerche
3. U. Rist
4. V. Theofilis
5. H.L. Boerrigter
6. A.R. Starke
7. B.F.A. van Hest
8. T. Wintergerste
9. S. Bake
10. W. Eissler
11. M.A. Zanchetta
12. V. Wendt
13. G. Simeonides
14. R.A.W.M. Henkes
15. P.H. Alfredsson
16. Y.S. Kachanov
17. J.L. van Ingen
18. Th. Herbert
19. H.W. Stock
20. H.H. Chen
21. T. Cebeci
22. B. van den Berg
23. J.M.M. Sousa
24. A. Bertelrud
25. N.V. Semionov
26. K. Chapman
27. W.S. Saric
28. T. Corke
29. H. Bestek
30. D.I.A. Poll
31. P.W. Duck
32. P.R. Ashill
33. F.T. Smith
34. W. Nitsche
35. V.A. Gushchin
36. V.V. Kozlov
37. V.A. Kazakov
38. K. Hanjalić
39. H. Bippes
40. A.D. Kosinov
41. M. Baumann
42. E. Laurien
43. G.J. Walker
44. C.J. Atkin
45. A.M. Savill
46. J.P. Gostelow
47. D. Arnal
48. P.R. Spalart
49. N. Voogt
50. I. Hadžić
51. S. Graves
52. B. Oskam
53. R. Narasimha

Contents

Session 2: Cross-Flow Instabilities

Session 3: Attachment-Line Instabilities

Session 4: Applied Transition Analysis

Session 7: Disturbance Sources and Receptivity

Session 8: High-Speed Flows

Background, Summary, and Discussion

R.A.W.M. Henkes

Colloquium on Transitional Boundary Layers in Aeronautics; Background, Summary and Discussion

Abstract

This paper gives background information on the specific aspects of *Transitional Boundary Layers in Aeronautics* that were handled in the 8 sessions at the colloquium that was held on 6-8 December 1995 at the Royal Netherlands Academy of Arts and Sciences in Amsterdam. Invited and technical presentations in each of the sessions are summarized. The general discussion on future directions of research, with which the colloquium was closed, is also included.

Introduction

In the external aerodynamics of aircraft, the thin boundary layer along the surface plays an important role. To a large extent, the boundary layer determines the drag of the aircraft. A better knowledge of the laminar-turbulent transition process within the boundary layer may provide technical possibilities for transition control. In this way transition can be postponed, leading to a reduction of the total drag and consequently of the fuel consumption.

It is generally recognized that transition belongs to the most difficult problems in fluid mechanics. Due to the fast development of computational capabilities and of new measuring techniques, in recent years our knowledge of transition has been greatly improved. Therefore the Royal Netherlands Academy of Arts and Sciences (KNAW) has organized, in collaboration with the J.M. Burgers Centre for Fluid Mechanics, a three-day Colloquium (6-8 December 1995) on *Transitional Boundary Layers in Aeronautics*. The Colloquium was meant to bring together leading researchers in this field.

Fourteen invited speakers have given an overview on what has been reached up to now. These lectures formed the basis for discussions, which will contribute to establishing the research directions that can be taken in the coming years. The emphasis in the Colloquium was on the scientific aspects of transition. Some speakers from the aircraft industry were also invited; their problems and wishes are of particular importance for directing future research. Next to the invited lectures also 23 technical papers were presented, which were selected by the scientific committee following a call-for-papers.

The present paper gives the general background for the different sessions that were part of the colloquium, it summarizes the invited and technical presentations, and it ends with some remarks on possible future directions of the transition research with applications in aeronautics.

Past and future

From detailed experiments by Schubauer & Skramstad (1947) on a smooth plate in a wind tunnel with a degree of turbulence less than 0.1% it is known that the flow is completely laminar when the local Reynolds number is below 2.8×10^6 and fully turbulent for Reynolds numbers above 3.9×10^6. For intermediate values of the Reynolds number, a transition region occurs where the flow passes from the laminar to the turbulent state. A similar behaviour is found for the boundary-layer flow along the aircraft surfaces (such as the fuselage and wings). Although the phenomenon of transition has been known already since the famous experiments for pipe flows by Reynolds in 1883, all aspects of the mechanisms leading to transition are still not yet completely understood.

The colloquium was opened with a presentation by Fernholz (Technical University of Berlin), who made a historical excursion and revisited one of the earliest experimental data sets for laminar-turbulent transition of boundary layers, namely the experiments for the zero-pressure gradient boundary layer performed by Burgers & Van der Hegge Zijnen in 1924 at Delft University of Technology [1]. The hot-wire measurements show maximum fluctuations in the transition regime. Fernholz rescaled the data in the turbulent regime by the now well-known inner scalings, which shows that the old data are in very good agreement with more recent experiments.

This paper, pointing to the value of the past, was immediately followed by a paper pointing to future applications of transition research: the invited presentation by Voogt (Fokker Aircraft, The Netherlands) describes the results from a test flight with a special laminar flow glove on a Fokker 100 wing, which was developed within the collaborative program ELFIN (European Laminar Flow INvestigation). Transition was measured in flight by an infrared camera at different transonic Mach numbers and for different sweep angles of the wing (simulated by side slipping of the aircraft). The transition location turns out to be considerably affected by environmental conditions, such as ice crystals on the wing and insect impact. This may pose a serious problem for maintaining Natural Laminar Flow (NLF). The obtained flight data can be used for the validation of transition prediction methods. First comparisons show considerable differences between the methods, which give predictions ranging from 30 to 50% of the chord.

Before addressing the methods for transition prediction for such applications, first three sessions were devoted to the basic physical mechanisms of stability and transition.

[1] Prof. J.M. Burgers gave his name to the later Dutch research school for fluid mechanics, that co-organizes the present colloquium

Session 1: Tollmien-Schlichting waves and subsequent instabilities

Rayleigh (1880), Tollmien (1929), and Schlichting (1933) have developed a linear theory that describes the onset of transition. In this theory it is shown that small harmonic disturbances in the boundary layer may become unstable and amplify. These linear instabilities become visible as so-called travelling Tollmien-Schlichting (TS) waves in the boundary layer. These waves were discovered in wind-tunnel experiments for a flat-plate boundary layer by Schubauer & Skramstad (1947). It was found that the linear stability theory is valid only if the turbulence level in the free stream outside the boundary layer is less than about 0.1%. In the free atmosphere and in modern low-speed wind tunnels the turbulence degree is indeed considerably less than 0.1%, and under such circumstances transition on smooth bodies is, at least initially, governed by linear stability theory.

As this linear theory assumes the perturbations to be sufficiently small, it cannot describe the whole transition process. Further downstream, nonlinear interaction leads to subsequent higher-order instabilities (such as secondary and tertiary instabilities). From experiments it is known that once the perturbations have become sufficiently large, suddenly turbulent spots are generated in the flow. These spots grow and merge as they move downstream, until finally they cause the breakdown into a fully turbulent flow.

For the Blasius boundary layer the subsequent instabilities have been investigated in different experiments using *controlled* disturbances. Sophisticated devices have been developed to introduce disturbances with some well defined frequency, and streamwise and spanwise wave lengths. Examples of such devices are the vibrating ribbon, heating elements, suction/blowing elements, and series of loudspeakers. Transition introduced by controlled disturbances should be distinguished from *natural* transition, in which the disturbance level naturally present in the wind tunnel introduces the transition.

For the subsequent instabilities, following the 2D Tollmien-Schlichting type of primary instability in the Blasius boundary layer, one of the next (at least) two regimes may occur:

(i) *fundamental regime*; This regime was experimentally found by Klebanoff *et al.* (1962), and is therefore also referred to as the K-type breakdown of the primary instability. With the help of a vibrating ribbon 2D Tollmien-Schlichting waves were introduced with superimposed 3D waves, *i.e.* so-called oblique modes. Further downstream this leads to a spanwise wave modulation of the Tollmien-Schlichting waves, showing alternating regions of high and low shear in spanwise direction, denoted as the splitting in *peaks* and *valleys*, respectively. The resulting three-dimensional structures are denoted as Λ *vortices*, and they appear in an aligned pattern with the same fundamental streamwise wavelength as the original Tollmien-Schlichting waves.

Further downstream a tertiary instability enters the flow, which is characterized by additional discrete frequencies in the frequency spectrum, which are referred to as *spikes*.

(ii) *subharmonic regime*; This regime of breakdown is also referred to as C-

type or H-type (after Craik, 1971, and Herbert, 1988, respectively, who did some theoretical work on the subject), or also as N-type (after Novosibirsk, the name of the Russian city in which Kachanov *c.s.* performed the stability experiments). Kachanov & Levchenko (1984) have used a vibrating ribbon to introduce the disturbances. Now the secondary instability manifests itself by a *staggered* pattern of lambda vortices, implying that the streamwise wavelength is double the value of the Tollmien-Schlichting wave. For unaltered phase speed this implies that the frequency has become twice as small, which explains the name *subharmonic* breakdown.
In contrast to the fundamental regime, where the tertiary instability set in as spikes, for the subharmonic regime the tertiary instability seems to manifest itself as a gradual broadening of the frequency spectrum.

The prevailing type of secondary instability depends on the amplitude, frequency, and phase of the external disturbances. Herbert (1988) has analytically studied the linear, secondary instability of Tollmien-Schlichting waves by superimposing linear disturbances on periodic waves, using so-called Floquet theory. This is actually an eigenvalue problem for periodic base flows. Direct Numerical Simulations (DNS) are also a valuable approach to analyse the higher-order stability of boundary layers. For example the temporal approach with DNS has been followed by Kleiser *c.s.* (see also Wintergerste & Kleiser in the next session), and the spatial approach with DNS has been considered by Rist *c.s.* (see this session).

At the colloquium, the invited paper by Kachanov (Institute for Theoretical and Applied Mechanics, Novosibirsk, Russia) gave an overview of recent experimental studies for the *linear* stability of 2D and 3D boundary layers with respect to Tollmien-Schlichting waves and Cross-Flow Vortices (see also next session). The linear theory is of importance for engineering transition prediction methods, such as the e^n method (see Session 4). The paper also includes experiments for the 3D instability of the 2D boundary layer along airfoils, and for the swept wing boundary layer. In contrast to the 2D instability, non-parallel effects are important in the 3D instability. There is qualitative agreement between available experiments and the linear theory, but more needs to be done for the quantitative verification.

The paper by Van Hest, Groenen, & Passchier (Delft University of Technology, The Netherlands) presents hot-wire measurements for the transitional boundary layer under an adverse streamwise pressure gradient. Here the transition is not triggered by controlled disturbances, but instead the *natural* transition is examined. The energy in the dominant Tollmien-Schlichting waves shows a double near-wall maximum. Further downstream a secondary instability sets in; one maximum shows the characteristics of a fundamental resonance whereas the other maximum shows the characteristics of a subharmonic resonance. Finally turbulent spots appear and the resulting intermittency distribution was also measured.

The paper by Bake, Kachanov & Fernholz (Technical University of Berlin) describes experiments for the subsequent instabilities in the Blasius boundary

layer. Controlled perturbations, consisting of 2D waves or oblique waves, are introduced with a new technique, utilizing loud-speaker pulses. In earlier experiments the occurrence of spikes was only found in the K-regime (fundamental regime) of breakdown (with the aligned pattern of Λ structures), but the present experiments also reveal the spikes in subharmonic regime of breakdown (with the staggered pattern of Λ structures); this explains the apparently conflicting title of the paper *subharmonic K-regime of breakdown.*

Baumann & Nitsche (Technical University of Berlin) have developed an experimental device to test the possibility of active control of TS waves in the boundary layer of an airfoil. 2D instabilities are detected by a surface hot-film sensor, after which an anti-wave is introduced through a downstream positioned actuator, that consists of a suction/blowing slot. The system was found to work well for wave cancellation in the boundary layer along a NACA 0012 airfoil. Whether the concept of active control also works for 3D or nonlinear instabilities remains a challenging topic for future research.

The invited paper by Rist gives an overview of the work on Direct Numerical Simulations for transitional boundary layers as performed in the group at the University of Stuttgart, Germany. DNS are presented for spatially evolving boundary layers with zero and adverse streamwise pressure gradient, undergoing a K-type transition. The considered adverse pressure gradient cases are the Falkner-Skan base flow with Hartree parameter $\beta_H = -0.18$ and the flow along the NACA 64_2-A-215 airfoil with suction. The computed breakdown for the zero pressure gradient case closely resembles Kachanov's experiments. The breakdown of the $\beta_H = -0.18$ case shows roughly the same characteristics as the breakdown of the Blasius flow, but also some differences are reported. The integral boundary layer parameters for the airfoil also agree with Van Ingen's experiments. Future DNS in the Stuttgart group will concern flow control, receptivity, and the late-stage structures of transition.

The last paper of this session is due to Gushchin (Institute for Computer Aided Design, Moscow), and is devoted to DNS for unsteady structures in the near wake of a circular cylinder. This topic is a bit on the side of the main focus of the colloquium. The numerical results were obtained on somewhat coarse grids, but accurate DNS for separating flows, including transitional separation bubbles in boundary layers and unsteady features in wakes of streamlined or bluff bodies, seem to be feasible in the near future.

Session 2: Cross-flow instabilities

The cross-flow instability can occur in the three-dimensional boundary layer that develops along a wing with nonzero sweep angle Λ. On the leading edge of the wing an inviscid streamline can be identified which marks the distinction between fluid that will follow the suction side of the wing and fluid that will follow the pressure side of the wing: this is the so-called attachment line. For the two-dimensional flow along unswept wings ($\Lambda = 0$) the attachment line also contains the stagnant points (that is all three velocity components are zero at this line),

but for swept wings a nonzero velocity component along the attachment line remains. Due to the resulting nonzero spanwise pressure gradient, the inviscid streamline (which describes the flow outside the boundary layer) coming from the leading edge will be bent inwards to the wing root (for $\Lambda > 0$), and outwards when reaching the trailing edge. As the streamwise velocity, and hence the momentum, is smaller inside the boundary layer than at the outer edge, the effect of the spanwise pressure gradient is largest inside the boundary layer causing a cross flow, which is directed towards the wing root at the leading edge and towards the wing tip at the trailing edge.

The cross flow profile has zero velocity at the wall and at the outer edge, and reaches a maximum inside the boundary layer. As a result, the cross flow profile always has a point of inflection which is known to give rise to inviscid (Kelvin-Helmholtz-like) instabilities. The typical maximum cross flow is only a few percent of the oncoming velocity (Gregory *et al.*, 1955).

Different groups have performed experiments for cross-flow instabilities. Poll (1985) has measured the flow along a swept cylinder (with Λ varied between 55^o and 71^o), which gives stationary co-rotating vortices, or so-called *cross-flow vortices*, which are practically aligned with the inviscid streamwise direction. Saric *c.s.* at Arizona State University (see *e.g.* Dagenhart *et al.*, 1989) also found such stationary cross-flow vortices in experiments for a swept wing with $\Lambda = 45^o$. Müller & Bippes (1988) found, besides stationary vortices, also travelling waves in the flow along a 45^o swept flat plate (with a displacement body above it to generate a negative streamwise pressure gradient). It seems that, depending on the external disturbance level, both stationary vortices and travelling waves appear as the primary cross-flow instability (Saric, 1994). If the free-stream turbulence level is very low, the receptivity mechanism is by surface inhomogeneities and small roughness, which gives stationary vortices. If the free-stream level is somewhat larger, travelling waves are generated.

Most stability computations for the swept wing have concentrated on the region close to the blunt leading edge. Close to the leading edge the configuration can be replaced by a flat plate that is perpendicular to the oncoming flow if $\Lambda = 0$, and which is swept for nonzero Λ. Similarity solutions of the three-dimensional boundary-layer equations are described by the Falkner-Skan-Cooke equations. One of the similarity solutions holds for the here considered yawed plate, giving the so-called (swept) Hiemenz flow.

The velocity at the outer edge of the boundary layer close to the attachment line has two components: $U = \Phi_\infty \cos\Lambda$ in the x direction, which is along the surface, but perpendicular to the attachment line, and $W = \Phi_\infty \sin\Lambda$ in z direction, which is along the attachment line (here Φ_∞ is the undisturbed velocity). Close to the leading edge the potential solution gives

$$U = C^* x, \tag{1}$$

where C^* is a constant that depends on the configuration; for example for the

potential flow along a cylinder it follows that

$$C^* = 2\Phi_\infty \frac{\cos\Lambda}{r}, \tag{2}$$

with r being the cylinder radius. Using the Hiemenz base flow, it can be shown that the stability problem close to the blunt leading edge is covered by two Reynolds numbers:

$$R = \frac{Ul}{\nu}, \quad \text{and} \quad \overline{R} = \frac{Wl}{\nu}, \tag{3}$$

with $l = \sqrt{\frac{\nu}{C^*}}$ being a typical boundary-layer thickness. $\overline{R}$ is fixed for a given flow, but R depends on the local x coordinate according to

$$R = x\sqrt{\frac{C^*}{\nu}}. \tag{4}$$

Malik *et al.* (1994) have computed the stability of the swept Hiemenz flow, using different approaches, including the parallel, linear analysis, linear and non-linear PSE, and linearized Navier-Stokes equations. For some selected $\overline{R}$ values, the critical x position (*i.e.* $R_{\rm cr}$) was determined for the onset of the cross-flow instability. All considered approaches give more or less the same $R_{\rm cr}$ and growth rates. Inclusion of non-parallel effects is found to slightly destabilize the flow. Travelling disturbances are amplified more than stationary disturbances.

The first paper in this session was delivered by the invited speaker Saric (Arizona State University, USA). Hot-wire measurements, performed in his wind tunnel, are described for the cross-flow instability developing on a 45° swept airfoil. Uniform stationary cross-flow vortices are generated on an NLF(2)-0415 airfoil through arrays of 6 μm roughness elements near the leading edge. The experiments are in very good agreement with nonlinear PSE computations. Without the array of roughness elements, it was found that the natural surface roughness, though polished up to 0.25 μm, was sufficient to generate nonuniform cross-flow vortices.

Lerche & Bippes (DLR, Göttingen, Germany) present an experimental hot-wire study for cross-flow instabilities on a 45° swept flat plate with imposed pressure gradient. In addition to Saric's roughness elements, also unsteady oblique perturbations were introduced by a new disturbance generator, consisting of an array of 40 membranes, flush mounted parallel to the leading edge, and driven by loud speakers connected via tubes. In this way the interaction between stationary and travelling cross-flow modes can be measured. The characteristics of the travelling waves agree with predictions from local linear stability theory. The nonlinear interaction of stationary and travelling modes can lead to the high-frequency secondary instability, as was also found in the experiments of Kohama *et al.* (1991).

The DNS as presented by Wintergerste & Kleiser (Swiss Federal Institute of Technology, Zürich) are adapted to the swept-wing experiment of Lerche &

Bippes. The local base flow is assumed to be parallel and is described by a Falkner-Skan-Cooke similarity profile. The transition and breakdown to turbulence are simulated by the temporal approach using Fourier modes parallel to the wall, and Chebyshev modes normal to the wall; the spatial discretization applies a total of $240 \times 192 \times 160$ grid points. The introduced initial disturbance consists of a stationary cross flow mode and a travelling 3D wave. The modes grow exponentially in time as predicted by linear theory. Once they saturate new 3D vortices emerge which initiate the full breakdown to turbulence.

Atkin & Poll (DRA and Cranfield University, UK) have applied the e^n transition prediction method to the swept cylinder with cross-flow instabilities, for which experiments were obtained by Poll (1985). The envelope integration strategy is used in the e^n approach to account for the three-dimensionality, which gives a constant n value of about 15 at the position of transition introduced by the unsteady cross flow vortices.

The last paper in this session is presented by Chapman, Glauser, Reibert, and Saric (Clarkson University and Arizona State University, USA) and applies the Proper Orthogonal Decomposition to detect wave structures in the experimental data for a 45° swept wing. Stationary cross flow vortices are introduced with an array of roughness elements, as described in the invited paper by Saric. The data were obtained with surface-mounted multi-element hot films, which were positioned both in streamwise and spanwise direction. Furthermore two-point correlations were obtained with cross-wire anemometry. The POD analysis shows that 98% of the total energy is contained in the first three spanwise modes, whereas 69% is contained in the first three streamwise modes.

Session 3: Attachment-line instabilities

Depending on the value of the Reynolds number $\overline{R}$, which does not depend on x (see equation (3)), the boundary layer at swept wings can become directly unstable at the attachment line. At the attachment line there is no cross flow but only a streamwise velocity profile in the direction of the attachment line. Therefore the first instability is a viscous, streamwise instability giving Tollmien-Schlichting waves which travel along the attachment line.

Hall *et al.* (1984) have solved the linear stability problem for the attachment line. The swept-Hiemenz flow is used as the base flow, which is not only an exact solution of the similarity equations, but also of the steady Navier-Stokes equations. To examine the stability, Hall *et al.* have introduced so-called Görtler-Hämmerlin modes, which are exact solutions of the linearized Navier-Stokes equations. In contrast to the normal modes, used to derive the Orr-Sommerfeld equation, the Görtler-Hämmerlin modes also account for nonparallel effects. The nonparallel approach gives $\overline{R}_{cr} = 583$, whereas the parallel approach using the Orr-Sommerfeld equation gives a significantly larger value $\overline{R}_{cr} = 662$. Hence nonparallel effects destabilize the flow.

Another instability mechanism that can occur along the attachment (or: the leading edge) is the so-called leading-edge contamination. This term is used

to describe that the turbulence which is formed in the boundary layer along the fuselage of aircraft can easily be convected along the leading edge, causing the direct transition of the whole boundary layer on the wing. It turns out that the contamination can occur at Reynolds numbers above about $\overline{R} = 250$, which is more than twice smaller than the linear stability limit $\overline{R} = 583$. The occurrence of this so-called *subcritical* instability mechanism, emphasizes that the linear theory only holds for very small disturbances. Leading-edge contamination might be interpreted as a type of by-pass transition, in which disturbances are so large that linear instability mechanisms are by-passed.

If one wants to design a wing with (partly) laminar flow, first the occurrence of leading edge-contamination has to be prevented. Gaster (1965) has developed a special device, a so-called *Gaster bump*, that can be used for that purpose: a small bump is placed on the leading edge close to the wing root, which stops the propagation of the turbulence along the attachment line, and creates a new laminar boundary layer instead. Another solution to stop the turbulence is the use of boundary-layer suction at the leading edge.

The session was opened by the invited lecture of Arnal (Onera, Toulouse, France). A typical value for $\overline{R}$ at the root of the wing of large transport aircraft is $800 - 1000$, which means that first the leading edge contamination needs to be removed before systems like NLF (Natural Laminar Flow), LFC (Laminar Flow Control) or HLFC (Hybrid Laminar Flow Control) can become meaningful. To prevent leading-edge contamination two devices were tested for a 40^o and 50^o swept wing in the transonic wind tunnel of Onera: the Gaster bump and suction along the attachment line. Without such means contamination occurs at $\overline{R} = 250$; the Gaster bump gives $\overline{R} = 320$; and the maximum obtainable suction rate further delays the contamination to $\overline{R} = 550$. If leading-edge contamination is avoided, the attachment-line is the next problem that needs to be considered. Arnal's experiments show that even weak suction is sufficient to suppress the attachment-line instability. e^n and nonlinear PSE computations were performed also for such instabilities. The e^n method is able to predict the trends, but a unique n value does not seem to exist. The nonlinear PSE poses the new problem of finding proper initial conditions.

Poll, Danks & Yardley (Cranfield University and University of Manchester, UK) present experiments for the attachment-line flow along a 60^o swept cylinder. Hot-wire measurements were performed for different blowing and suction rates. Blowing reduces the Reynolds number at transition onset by a factor 3, whereas a minimum suction seems to exist above which the turbulent attachment-line flow is always re-laminarized.

Theofilis (DLR, Göttingen) closes the session with a presentation on the computation of the secondary instability of the attachment-line instability. For incompressible flow this is done by applying linear stability theory, utilizing Floquet secondary theory, to the Görtler-Hämmerlin primary modes of the Hiemenz stagnation flow at the attachment-line region. For compressible flow the secondary stability analysis becomes much more complex as something similar to the GH modes does not seem to exist. Therefore a method using DNS is being

developed for the compressible attachment-line flow. As a first step, the method has been validated for inflection-point instabilities in the compressible free shear layer.

Session 4: Applied transition analysis

A well-known method to predict the streamwise growth of disturbances and the resulting transition position is the e^n method, which was developed independently by Smith & Gamberoni (1956) and by Van Ingen (1956). The e^n method can be summarized as follows. First the undisturbed laminar flow is computed by solving, for instance, the boundary-layer equations. For the computed velocity profiles at different streamwise positions the corresponding stability diagrams are determined. If the boundary layer is similar, only one diagram is needed. In the diagram a curve for a constant physical frequency is followed. For increasing x position, a typical frequency is first in the stable region, it crosses the neutral curve and enters the unstable region, and finally it crosses the neutral curve again and returns to the stable region. From this trajectory the amplification factor for the considered frequency can be determined as $\sigma = \ln A/A_0$. For each frequency the amplitude development can be determined and collected in a $\sigma - Re_x$ diagram. In that diagram one can determine for each Re_x station the maximum amplification ratio, denoted by n, that occurs for all possible frequencies. In this way a n-envelope is constructed as a function of Re_x.

By comparison with experiments for 2D boundary layers it was found that transition occurs when n has reached a more or less universal value, being about 9. This method is called the e^n method, or sometimes also the e^9 method. It is based on the finding that independent on the details of the boundary layer, and independent on the precise amplitude level A_0 at the neutral curve, transition takes place when the amplitude ratio A/A_0 exceeds a critical value. Through the years experiments have shown that n is not really a universal constant, but depends on, for instance, the free-stream turbulence level of the wind tunnel.

Linear instabilities such as Tollmien-Schlichting waves grow on a relatively slow viscous time scale, whereas secondary and subsequent instabilities grow on a much faster convective time scale. Hence a relatively large region of linear growth is followed by a short region of nonlinear growth quickly leading to transition. This seems to be the main reason why the e^n method, which is based on linear theory, can be adequate to predict transition onset. Disadvantages of the method are that it does not account for nonlinear effects, it neglects non-parallel effects, and its extension to 3D boundary layers and instabilities requires a choice on the proper integration strategy in the wave plane. Receptivity is also only indirectly included by properly tuning the n value. Despite this, the e^n method has proven to be a very practical tool for engineering transition predictions.

A very efficient stability formulation that has the potentials to overcome the shortcomings of the e^n method been proposed by Herbert & Bertolotti (1987), and is named the Parabolized Stability Equations (PSE). Disturbance modes for

the base flow are introduced with a stream function of the form

$$\psi(x,y,t) = \phi(x,y) \exp\,(i(\alpha x - \beta t)). \tag{5}$$

In contrast to the normal-mode formulation, used to derive the Orr-Sommerfeld equation, now the amplitude function ϕ does not only depend on the y coordinate, but also on the x coordinate. Furthermore the wave number α can be a function of x as well. It is assumed that the streamwise dependence of ϕ and α is only weak, which justifies the neglect of the terms ϕ_{xx}, α_{xx}, and $\alpha_x\phi_x$. Substitution of equation (5) into the Navier-Stokes equations and neglecting the mentioned terms gives the Parabolized Stability Equations.

If the PSE are linearized the linear PSE method is obtained, which is similar to the Orr-Sommerfeld equation in case the flow is assumed to be parallel. Both linear and nonlinear PSE have become popular approaches. Bertolotti *et al.* (1992) have applied the linear and nonlinear PSE to the stability of the Blasius boundary layer. The linear PSE gives only a very small modification of the neural curve resulting from the Orr-Sommerfeld equation. This shows that non-parallel effects cannot explain the difference between theory and experiments. Nonlinear PSE gives only a small modification also. During the discussions at the colloquium Alfredsson has shown new experiments as obtained in his group at KTH Stockholm. These new data are in very good agreement with the theory. Great care was taken in the experimental set-up to obtain a very good zero zero streamwise pressure gradient. Therefore it seems probable that a small nonzero pressure gradient was present at the leading edge of the plate used in the classical experiments by Schubauer and Skramstad (1947).

Van Ingen opened the session with some remarks on the 40 years history of the e^n method. Despite the physical limitations of the method, the e^n approach is still very popular in airfoil design. This is partly due to the complexity of the full transition process, which makes it difficult to come with a better design method, containing more physics. The success is also due to the fact that a large part of the transition is dominated by linear physics. The e^n method has shown to be useful to predict the distance to transition in 2D incompressible flows. Apparently the linear stability theory has also enough physics to account for the effects of pressure gradient, suction and heating or cooling.

Stock (Dornier Luftfahrt, Germany) has presented an invited paper on the application of the e^n method in industrial aircraft design. A data base has been set up in which the linear stability characteristics are stored for a series of self-similar velocity and temperature profiles. For real (non-similar) boundary layers the stability limits according to the data-base method agrees very well with the limits computed by numerically solving the stability problem. Of course the data base method is much faster, which makes it suitable for design purposes.

The invited paper by Cebeci (McDonnell Douglas Aerospace, and California State University) reviews the envelope, or 'Zarf', strategy in applying the e^n method to 3D boundary layers. The choice for the strategy, *i.e.* the chosen relation between the two spatial wave numbers and the frequency, has a large influence on the performance of the e^n method. The envelope method

was checked to give good predictions for the critical frequencies and transition location for different experimental test cases, including the ONERA-D airfoil (at different sweep and incidence angles), a 15° swept Aérospatiale wing, and a prolate spheroid at 10° incidence angle.

Herbert (DynaFlow Inc. and Ohio State University) was invited to give the last presentation of this session. He gave a comprehensive review on the status of applied transition analysis, that is the e^n method and the linear or nonlinear PSE approach. Industries want methods that are fast and can be used by their engineers without requiring much knowledge on transition. Different existing codes utilizing the e^n method with the same 3D strategy were found to lead to different transition predictions. Possible causes for these differences are discussed, one of them being insufficiently accurate numerics for the base flow. The e^n method is a local stability analysis, implying that some strategy is needed to reconnect the local solutions to provide amplitude growth curves. Only for 2D and swept-wing boundary layers a rigorous proof on the correct strategy exists, which is violated by, for example, the envelope method. Different strategies lead to different n factors. For fully 3D boundary layers no theory for the best strategy is available, and a single n value for such cases does not seem to exist. The PSE method is able to track the evolution of disturbances without any heuristic strategy, but needs a considerable higher computational effort than the e^n method. Nonlinear PSE needs proper initial and boundary conditions; at least the most dangerous ingredients of the disturbance environment and the receptivity mechanism should be included, such as the free-stream turbulence level and the average surface roughness. Most parameters for the input model are derived from primary and secondary stability characteristics, and receptivity coefficients are derived from experiments. The nonlinear PSE method was applied to various flows were experimental data are available, such as the turbine blade with 0.5 to 2.4% free-stream turbulence level and the swept wing, using the ATTAS flight-test database. It is remarkable that the input model for the swept wing gives transition at a location that corresponds with an n factor of about 9 in the e^n method. More understanding of receptivity and detailed documentation of the actual disturbance environment is needed for further improvement of the transition analysis for engineering design.

Session 5: Transition modelling

Quite soon after secondary and tertiary instabilities have entered the flow, the first so-called turbulent spots appear. These spots are also referred to as Emmons spots, after Emmons (1951), who first observed them in a boundary layer of water.

The first appearance of turbulent spots in transitional boundary layer occurs quite randomly in space and time. Further downstream the spots overlap, and interact, and more and more spots are being generated. As a measure of the actual turbulent-spot activity at a certain location the level of *intermittency* can be used. The intermittency γ is defined as the fraction of time that the flow

is turbulent: hence $\gamma = 0$ just before transition when turbulent spots are still absent, and $\gamma = 1$ when the transition is complete, and the flow has become fully turbulent. The intermittency first reaches the value of one close to the x position where the wall-shear stress reaches a local maximum. This marks the end of the transition regime. The length of the transition regime might be defined as the x distance between the positions where the wall-shear stress obtains its local maximum and minimum, respectively.

The intermittency is in fact a function of both x and y. Approaching the outer-edge of the boundary layer, γ decays to zero, whereas close to the wall the maximum intermittency is found. Narasimha (see Dhawan & Narasimha, 1958) detected, from experiments for a constant pressure boundary layer, a more or less universal streamwise distribution of the intermittency close to the wall in the transitional regime:

$$\gamma(x) = 1 - \exp\left[-0.411\frac{(x - x_{tr})^2}{\lambda^2}\right], \tag{6}$$

where λ is the distance between the x positions where $\gamma = 0.75$ and 0.25, respectively.

It is clear that transition does not occur in a single *point*, but rather over a certain *length*. Hence in prediction methods for transition a model for the transition length is needed. The transition length is of particular importance for the prediction of the flow on gas-turbine blades. Here the transition is due to free-stream turbulence, induced by the turbulent wake of the previous row of blades. The operational conditions of the blades (Reynolds number and streamwise pressure gradients) of the blades are such that extensive regions of transitional flow can be found. For the transition on aircraft wings the overall Reynolds number is so high that the transition length is only a very small portion of the chord; here the representation of the transition length by a transition point might be sufficiently accurate. In particular the transition length is short when transition occurs in a region with adverse pressure gradients.

For instance, the e^n method can be used for the prediction of the position of transition onset x_{tr}. Using experimental data, Van Ingen (1977) has also derived a simple relation, based on the e^n approach to denote the end of the transition regime. For free-stream induced by-pass transition, Abu-Ghannam & Shaw (1980) have used experimental data for boundary layers with different streamwise pressure gradients to derive empirical relations for the start and end of transition.

More sophisticated models for the transition region try to connect the laminar flow with the fully turbulent flow (as described by a turbulence model) by using some model for the streamwise intermittency function γ. Different types of models can be used in the turbulent regime, such as algebraic models, two-equation models, and Differential Stress Models. A simple method to connect the laminar velocity profile (denoted by $\overline{u_l}$) and the turbulent velocity profile (denoted by $\overline{u_t}$) is taking a linear combination with the help of the intermittency

function

$$\overline{u} = (1 - \gamma)\overline{u_l} + \gamma\overline{u_t}. \tag{7}$$

Narasimha's relation (6) can be applied for the intermittency.

Another approach of modelling transition is by simply ignoring the direct effect of intermittency, and applying turbulence models, originally developed for fully turbulent flow, in the laminar and transitional regimes as well. No stability analysis is performed. Hence the turbulence model is used to predict both the instability position and the start and end of the transition regime. This approach can only be expected to work, if it works at all, in cases where transition is introduced through a sufficient amount of turbulence at the outer edge of the boundary layer (say for free-stream turbulence levels above 1% or so). In those cases it might work if proper so-called low-Reynolds-number terms are included in the turbulence model. Those terms were originally added in the description of fully turbulent boundary layers to account for the damping of turbulence when a fixed wall is approached. With respect to the turbulence activity, the subsequent regions in normal direction of a fully turbulent boundary layer (namely the viscous sublayer, the buffer layer, and the inertial sublayer) show an analogy with the subsequent streamwise regions of a boundary layer (namely, the laminar state, transitional state, and fully turbulent state, respectively). Based on this analogy, the low-Reynolds-number terms developed for near-wall turbulence, might also predict streamwise transition.

There is no doubt that DNS and LES (Large Eddy Simulations) can give much better predictions of the transition regime than the above mentioned models and empirical correlations. For practical applications in engineering design, however, such methods are much too costly, and there is still a strong need to further improve the simpler models.

The invited paper by Spalart (Boeing Commercial Aircraft Group, USA) focusses on industrial viscous flows with transition. Boeing wants a single model that can compute a variety of viscous flows. High-lift configurations and LFC require detailed control of turbulence in the computational solution. Calculations are performed with the Reynolds-Averaged Navier-Stokes equations (RANS) with the one-equation Spalart-Allmaras model for the turbulence. It is investigated how the transition from a laminar to a turbulent region can be established. Zonal methods are avoided, as they become unmanageable in complex high-lift systems, especially when computed with multi-block and unstructured-grid numerics. Two transition methods are considered: a method with and without triggering strip respectively. At the strip some turbulence is introduced which directly triggers the transition to occur over a length of about 8 boundary-layer thicknesses, which is considerably shorter than found in Narasimha's experiments. However, for wing applications the transition length is of less importance and considered as higher-order effect; it is reminded that perfection is not expected from the turbulence model. Examples of transition with and without triggering are given for different cases, such as for the leading edge flow over a flap (where the upper boundary layer is naturally triggered to turbulence by diffusion of turbulence from the cove below the main airfoil trailing edge) and the

flow behind a cylinder (where the transition and turbulence are self-sustained through the unstable free shear layers and the turbulence back transport in the recirculation zone). Future CFD challenges are the effects of turbulence generators and relaminarization in favourable pressure gradient.

The invited paper by Hanjalić (Delft University of Technology, The Netherlands) explores how single-point closure models for turbulence can be used to predict certain types of transition, such as by-pass transition introduced in the boundary layer by a relatively high free-stream turbulence level. Such models are not expected to be able to predict the natural transition along aircraft wings, which encounter only extremely low free stream turbulence levels, but they might be suitable for the transition prediction along, for example, turbine blades. A new Differential-Stress Model (second-moment closure), which includes low-Reynolds-number effects and near-wall effects, is used to demonstrate the capabilities for different test cases. Concerning the transition location, the model closely reproduces the experiment for by-pass transition in the flat-plate boundary layer with 6% free-stream turbulence level, but agreement for the 3% test case can only be found after modifying the initial level of the dissipation rate. The prediction for the transition and relaminarization for a boundary layer with a streamwise edge velocity oscillating around a zero mean is in very good agreement with experiments and Direct Numerical Simulations.

The invited paper by Narasimha (Indian Institute of Science, Bangalore) discusses recent developments in the linear combination model. There is a remarkable difference between workers studying the pre-onset of transition (instability regime) and those studying the finite-length transition region itself. Concerning the prediction of the position of transition onset, Narasimha *c.s.* has shown with asymptotic analysis that non-parallel effects can be neglected in the linear stability problem, unless the adverse pressure gradient is strong. Therefore it is sufficient to base the e^n method on the Orr-Sommerfeld equation. The linear combination model of Dey and Narasimha has been extended for application in cases with nonzero pressure gradients and compressibility by taking new experimental data on the spot shape and formation rate into account.

An overview of the efforts with RANS-based statistical turbulence models applied to by-pass transition (with free-stream turbulence levels up to 10%) has been given by Savill (Cambridge University, UK). A comparison study is made by different groups, all collaborating within the European organization ERCOFTAC. A variety of models are considered, such as integral methods, two-equation models (also with extra equation for the intermittency), and Differential Stress Models. Comparison is made with experiments, DNS and LES. A few models (including the low-Reynolds-number $k-\epsilon$ model of Launder & Sharma) are shown to be able to accurately predict the transition onset, but the length of the transition region is underpredicted. Such models do not contain a wall-distance parameter (such as y^+) to account for the near-wall turbulence damping, but only a turbulence-based Reynolds number. Results are very much dependent on the initial profiles for the turbulence equations in the laminar regime. In particular there is a strong effect of the prescribed turbulent length scale. Fur-

ther improvement of the turbulence models is expected from combining them with a separate stability method (such at PSE) to predict the transition onset. The NASA Transition Project has shown good PSE predictions for transition at nonzero free-stream turbulence levels. Once the transition onset is know, the turbulence model can used to represent the transition region.

This session was ended by the paper of Solomon, Walker & Gostelow (University of Tasmania) on a new model for the transition length in boundary layers with moderate to strong favourable or adverse pressure gradient and various free-stream turbulence levels. An experimental correlation is given for the propagation rate, spreading rate and spreading angle of turbulent spots, which in turn appear in the relation for the intermittency, that fixes the transition length.

Session 6: Asymptotic analysis

As the Reynolds number in aeronautical applications is usually very large (the typical overall Reynolds number is in the range $10^6 - 10^8$) analytical solutions of the flow equations might be sought in the form of asymptotic expansions using $\epsilon = R^{-1}$ as the small expansion parameter. In this way Prandtl derived that the boundary-layer equations are a first asymptotic approximation of the boundary layer close to the wall. The asymptotic theory has also proven to be useful in analysing the stability and transition of the boundary layers, though the asymptotic analysis becomes gradually more complicated as multi-deck layers have to be distinguished and matched. This is by no way an easy task and requires thorough mathematical analysis.

An often heard criticism on some of the results obtained with asymptotic theory is that their range of applicability is at Reynolds numbers far above what is met in applications. However, asymptotic transition methods are not intended to replace the new computational approaches such as PSE and DNS methods. The strength of asymptotic analysis is that it can isolate the underlying physical mechanisms of transition. In this way asymptotic theory can direct the PSE and DNS with respect to the scales of the problem (and thus the required numerical resolution) as well as the dominant parameters of the problem. Furthermore, parameter variation (such as frequencies and wavelengths) and trend studies can easily be carried out with the analytical methods, whereas they are computationally too demanding for PSE and DNS approaches.

F.T. Smith (University College London) was invited to give the first presentation in this session. He has given an overview on recent work on the combination of (asymptotic) theory and its computational solutions, specifically for the last stage of transitions in incompressible boundary layers, characterized by spikes and nonlinear spots. Nonlinear TS waves or vortex-wave interactions can be described by 2D or 3D interacting boundary-layer equations (IBL), which have links with the PSE. The IBL can lead to a singularity within a finite time, where both the pressure gradient and the skin friction become unbounded locally. This

breakup is associated with the formation of short scales owing to sublayer eruption and shows up as the first spike in transition experiments. The repeated break-up process is probably connected with intermittency. The integral criterion that defines the breakdown in the IBL also applies to 3D transition over surface roughness elements. A comparison of the analytical breakdown with DNS results was made. The formation and propagation of spots was also analysed. The spot dynamics can be split up in an inviscid regime and a viscous-inviscid regime. The former regime, the Euler stage, has been solved as a 3D initial-value problem for a localized input disturbance. The latter regime can be described by linking 3D boundary-layer equations to unsteady Euler equations. Good results with the spot description are obtained; for example the analysis gives a spot spreading angle of 11°, which is close to the experimental value.

Duck (University of Manchester, UK) presented solutions of the inviscid triple-deck equations. Triple deck theory can describe the lower branch of the neutral stability curve of the Blasius boundary layer, and it appears also when describing the earlier stages of transition. For the high-frequency problem the viscous triple deck equations reduce to the inviscid triple deck equations. The latter equations are numerically solved with Fourier modes in spatial direction and a finite-difference time integration. For the 2D problem there was no evidence for any solution breakdown, but the 3D solution indicates a finite-time breakdown.

Kazakov (Central Aero-Hydrodynamic Institute Zhukovsky) has used a finite-difference numerical method to solve the unsteady, two-dimensional, viscous triple-deck equations. For increasing time wave structures with multiple separation regions appear. However, the finite-time breakdown as revealed in the studies by F.T. Smith *c.s.* is not found. That would probably need a further increase of the spatial and temporal numerical resolution.

Session 7: Disturbance sources and receptivity

Experiments showed that the n factor in the e^n method was actually not a universal constant for all experimental configurations, but it is dependent on the external disturbance level. Morkovin (1969) has denoted the process in which disturbances enter the boundary layer as *receptivity.*

Different receptivity sources are summarized below:

Free-stream turbulence
Outside the boundary layer the amount of turbulence in the free-steam flow can be characterized by its kinetic energy and its length scale. The turbulent kinetic energy of the free-stream turbulence can be referred to as the turbulence level, defined as

$$Tu = \frac{\sqrt{\frac{1}{3}(\overline{u'^2} + \overline{v'^2} + \overline{w'^2})}}{U}. \tag{8}$$

Here a prime denotes a fluctuation and an overbar denotes a time-averaged value. Although the turbulence also depends on its length scale (or time scale), its effect on receptivity has not been studied very much so far. For increasing turbulence levels transition is enhanced, implying a lower critical Reynolds number and a lower n factor. Van Ingen (1977) has given the following empirical relation between the n factor for the onset of transition and the free-stream turbulence level Tu:

$$n = 2.13 - 6.18\ {}^{10}\log Tu, \tag{9}$$

where Tu must be given in percent. For in-flight aircraft the free-stream turbulence level is very low, say $Tu << 0.01\%$. Therefore good wind tunnels for aircraft aerodynamics are designed such that the free-stream turbulence level is low, typically 0.1% or lower, which corresponds, according to equation (9) to n factors above 8. Therefore the n factor is only a universal constant when the transition experiments for different configurations are performed in the *same* wind tunnel.

Equation (9) no longer holds for very low free-stream turbulence levels, typically below 0.1%, as other sources dominate the receptivity process. For higher free-stream turbulence levels linear, exponentially growing instability mechanisms, such as Tollmien-Schlichting waves, are by-passed, and Morkovin has denoted this type of transition as *by-pass transition.*

Sound

Pressure waves are another disturbance source. For example, the n factor for a given wind tunnel can be further increased when dampers are used to absorb the noise. Sound can become a dominant receptivity source if there is some mechanism to transfer the relatively long wave length of the sound waves into the short wave lengths (typically a few times the boundary-layer thickness) of unstable Tollmien-Schlichting waves that initiate the transition. Such a mechanism may be provided by leading-edge curvature, surface inhomogeneities or waviness, discontinuity in the surface curvature, or strong streamwise pressure gradients.

Due to the relatively large wave length of the sound waves, in receptivity computations the wave length can be set to infinity. Hence its effect can be analysed by imposing the following time-dependent streamwise velocity at the outer edge of the boundary layer

$$u' = \epsilon \sin(2\pi f t). \tag{10}$$

for all x (where f denotes the frequency and t denotes time). Here ϵ is the (small) amplitude level of the sound wave.

Wall roughness

Only for very smooth walls, the transition can be determined by linear stability theory. Wall roughness may lead to immediate transition. For aerofoils in wind tunnels this may be established by gluing sandpaper or tape to the surface. In flight, insects caught by the wing might introduce sufficient wall roughness to

give an early transition. This actually is one of the reasons why it is difficult to maintain a laminar flow over large part of the wing during flight.

The theory of receptivity due to wall roughness addresses how the shape and distribution of very small elements introduces disturbances in the flow. The interaction between wall roughness and sound waves can be a relevant receptivity mechanism also.

The invited lecture of Alfredsson (KTH, Stockholm) describes how streamwise-oriented streaky structures, introduced by disturbances coming from the free stream or from the wall, can be the first stage of transition. Small-amplitude disturbances introduce wave packets, large-amplitude disturbances give turbulent spots, whereas intermediate disturbances where found to generate long streaky structures. The latter type is found in experiments for by-pass transition due to moderate free-stream turbulence levels (where Tu is in between 1 and 10%). DNS indicate that those streaky structures are due to the algebraic transient growth of oblique TS waves, leading to subcritical instability and transition. The development of the streaky structure was measured by introducing a localized disturbance in the free stream. The disturbance penetrates into the boundary layer and causes a maximum perturbation in the middle of the boundary layer. The amplitude of the streaky structure shows a downstream decay, unless a TS wave is introduced also; the nonlinear interaction leads to amplitude growth and secondary instability of the structure, followed by breakdown into turbulence.

Kozlov & Grek (Institute of Theoretical and Applied Mechanics, Novosibirsk, Russia) have presented an experimental study for the influence of riblets on different transitional structures. Riblets are known to reduce the wall-shear stress for the fully turbulent regime. Experiments in the transitional regime were made in a low-speed wind tunnel with streamwise-oriented V-grooved riblets in the flat surface. The riblets were found to suppress cross-flow vortices and Görtler vortices. Also the Λ structures in the nonlinear stage of transition were damped by the riblets. In contrast to this, Tollmien-Schlichting waves were amplified by the riblets. This seems to agree with some kinds of shark skins, which have riblet-like structures only at places where the boundary-layer will be turbulent, but not at places where the boundary layer is laminar or transitional.

The paper by Laurien (Technical University of Braunsweig, Germany) describes new DNS for the spatial and temporal evolution of a local disturbance introduced in a compressible boundary layer at $Re_\delta = 5800$ and Mach number 0.65. Fourier modes are used in both horizontal directions and sixth-order finite differences are used in normal direction. When the amplitude of the initial disturbance is small, the disturbance decreases for increasing time, but for a larger initial amplitude the disturbance is unstable and increases in time. The development of the growing structure (probably leading to a turbulent spot) closely resembles existing DNS for incompressible flows.

Corke & Haddad (Illinois Institute of Technology, Chicago, USA) have studied the receptivity to sound on a parabolic leading edge, by numerically solving the two-dimensional, incompressible Navier-Stokes equations. The sound waves

were represented by small amplitude time oscillations of the free-stream velocity. The free-stream sound forces finite-amplitude TS waves in the leading-edge boundary layer. The receptivity is defined here as the ratio between the maximum amplitude of the TS wave and the amplitude of the free-stream oscillation. The computations show that the receptivity (coefficient) increases for decreasing nose radius, and becomes maximum for a sharp leading edge.

The last paper of this session was presented by Semionov, Kosinov & Maslov (Institute of Theoretical and Applied Mechanics, Novosibirsk, Russia). Hot-wire experiments were performed for the receptivity due to sound for a supersonic boundary layer along a flat plate at Mach number 2. The sound waves were generated by the boundary layer along another plate (plate 1) that was placed in parallel below the test plate (plate 2); the nose of plate 1 was somewhat ahead of the nose of plate 2. Sound waves at plate 1 are introduced by the TS waves in the transition regime as well as artificially induced pressure fluctuation in the surface. First the acoustic disturbance level in the plane of the test plate was measured (while the plate itself was removed). Second, the receptivity coefficients inside the boundary layer along the test plate were measured. It is found that only downstream propagating acoustic disturbances are received by the boundary layer.

Session 8: High-speed flows

The renewed interest in supersonic civil aircraft and in space planes, has given new impetus to research into stability and transition of supersonic and hypersonic boundary layers. Delay of transition will reduce the viscous drag and thermal loads. Far less is known for the transition of high speed flows, compared to low-speed flows, as the theory is more complex and accurate experimental data are more difficult to obtain.

The linear theory for supersonic and hypersonic boundary layers was mainly developed by Mack (1984). A sufficient condition for the existence of an inviscid instability is the (generalized) inflection-point criterion that states that $\frac{\partial}{\partial y}\rho\frac{\partial u}{\partial y} = 0$ somewhere in the boundary layer. This shows that the compressible boundary layer at zero pressure gradient can have an inviscid instability, whereas the incompressible counterpart is stable. Furthermore, the inviscid linear stability problem can have multiple solutions for a Mach number above about 2.2. The first mode is also found in incompressible flow. The additional modes (second mode and higher) are referred to as Mack modes or acoustic modes. In contrast to the incompressible case, oblique waves for boundary layers at $M > 1$ are less stable than 2D waves. But for the second mode, 2D waves are most unstable. Inclusion of the viscosity stabilizes the first mode. For $M > 4$ the second mode grows faster than the 3D first mode, and becomes the dominant instability mechanism.

The transition of high-speed flows can be delayed by wall cooling or suction. Cooling only works if the first mode is unstable, as it has a destabilizing effect

on the second mode. Suction is no longer practical for hypersonic speeds, where the air temperature has become too high for the materials that can be used in the suction system.

As supersonic aircraft have wings with a strong sweep angle, besides the above mentioned first and second linear modes, also cross-flow instability, attachment line instability, or leading edge contamination can occur. The latter instabilities can be suppressed by reduced sweep angle, applying suction, smoother surface, or reduced leading-edge radius.

At the colloquium, Bertelrud & Graves (NASA Langley and Lockheed, USA) presented data from flight experiments for transition at supersonic Mach number. The data can provide the n factor in the e^n method or the input disturbance level for the PSE method. Fight data are particularly needed for high-speed flows, as the disturbance level in wind tunnels is usually much too high. A flight experiment was performed for a flat plate with an elliptical nose, mounted underneath an F-15 at Mach 2. The instrumentation included pressure taps and surface hot films. The transition location and dominant frequencies could be derived from the measured unsteady signals. The same equipment will also be used in new flight experiments at hypersonic speeds (Mach 6 to 8), where a smooth metallic glove will be mounted on the boost of the Pegasus launch vehicle.

Zanchetta & Hillier (Imperial College, London) have performed measurements for the transition in the boundary layer along a cone at the hypersonic Mach number 9. The unsteady wall-heat transfer was measured with 65 film gauges, The surface temperature was also visualized with liquid crystals. The transition location is dependent on the Reynolds number based on the radius of the blunt nose Re_n. For relatively low Re_n the transition is characterized by high-frequency oscillations followed by a sudden break down into turbulence. For increasing Re_n transition is first delayed, but above some critical value further increase of the Reynolds number moves the transition back to the nose. The latter phenomenon is denoted as the 'reversal regime', and there the transition location strongly depends on the surface roughness. The transition region is relatively large, and has low-frequency events.

Wendt (DLR, Göttingen, Germany) has performed hot-wire measurements for transition in the boundary layer along a cone and a flat plate at Mach 5. Linear stability theory predicts that the high-frequency second mode induces the primary instability (corresponding to frequencies above 200 kHz for the present configurations). However, the experiments do not show this behaviour. Instead mainly lower frequencies are amplified; up to 50 kHz for the plate and up to 200 kHz for the cone. Comparison with the theory shows that the measured frequencies correspond to oblique first-mode unstable waves.

Kosinov, Semionov & Yermolaev (Institute for Theoretical and Applied Mechanics, Novosibirsk, Russia) presented a paper describing hot-wire experiments for transition in boundary layer at Mach 2 and 3. Disturbances were introduced through the surface of the plate. The experiments are focussed on the nonlinear transition regime. In earlier experiments at relatively low Reynolds

numbers only low-frequency subharmonic waves were found. The present experiments also show the appearance of high-frequency oscillations. The cause of the amplification of the high-frequencies in the nonlinear regime is not yet clear.

Eissler & Bestek (University of Stuttgart, Germany) have closed the session on high-speed flows with a DNS study for transition in a supersonic boundary layer at Mach 4.8. As experiments for high-speed flows are quite difficult, DNS might be a valuable alternative tool to get insight in such flows. The 3D compressible Navier-Stokes equations were solved using a 4th-order finite-difference scheme in streamwise and normal direction, Fourier modes in spanwise direction, and the 4th order explicit Runge-Kutta scheme for the time integration. DNS were performed for different choices of the boundary condition at the wall for the base flow temperature and the temperature perturbation, including a constant, adiabatic, and mixed (radiation-like) condition, respectively. The latter condition seems to be most realistic. The transition strongly depends on the thermal boundary condition; for example, in agreement with linear stability theory, a lower wall temperature destabilizes second-mode waves. Further downstream, three-dimensional structures being characteristic for the fundamental type of breakdown are computed.

Discussion on the future directions of research

The colloquium was closed with a general discussion on the future directions of research, chaired by Van Ingen. The main contributions to the discussion are reproduced below.

Van Ingen:
Now we have come to the end of this colloquium, we may know what still has to be done in the coming years. A main question is whether we have enough information to design a laminar-flow wing. Do we for example agree on the proper integration strategy for the three-dimensional e^n method?

Herbert:
We do not have sufficiently clear data to test any strategies. There is a need for non-proprietary benchmark experiments. There is currently work going on for these strategies at ONERA to calculate these flows with PSE. We also work on that too. We also work on DNS, but that is for somewhere in the future. But even then we do not know how to check. Perhaps Ian Poll, or someone else, can provide us with wind tunnel experiments for 3D flow instabilities.

Saric:
What is a 3D problem?

Herbert:
Normally you have big problems on the wing in the neighbourhood of an engine; everything is 3D. But the industries do not give me the geometry. They have the data from experiments. We need a real 3D flow, with sufficient accuracy such that we can compare something like cross-flow vortices.

Saric:
3D experiments are done at DLR.

Herbert:
That is not what I mean. That is a 2D geometry. I talk about a 3D geometry.

Saric:
First consider Bippes' experiments and my own experiments. Thereafter we can go to more complicated geometries.

Herbert:
If we talk about integration strategies in a 3D boundary layer over an infinite wing, then it is clear. But the question is, what shall we do in an actual 3D flow. That means a 3D boundary layer that depends on three spatial variables, not on two.

Bertolotti:
As I understand correctly, do you already have, or are you working on, the PSE for fully 3D mean flows?

Herbert:
That is right. I did not mention it in my lecture.

Van Ingen:
Do we need more experiments?

Poll:
There are two issues. One in which we try to understand the physics of transition. The other is that you do not necessarily need to understand the details of the physics to design a laminar-flow aircraft. The idea that one worries about the tiniest suction input re-supposes that somehow you have to minimize all this in order to get some kind of performance benefit. But it would also be good to design for half of what is available rather than 99%.

Van Ingen:
You could also turn it around: suck double the amount of the full performance benefit. This is not wasting the advantage, because the suction amounts are rather small. Keeping some safety margin would keep you in a region were design would be easier.

Alfredsson:
Concerning the question whether we need more experiments: Maybe that is not really what is needed. What is needed is that the theory tries to replicate the experiments. Then we can make a direct comparison. Often I feel that the theory does not do that. The experiments must be taken for what they are, but theoreticians can more easily apply the experimental boundary conditions.

Van Ingen:
Theoreticians and experimentalists should use the same format. They should together design experiments and computations to get the right things.

Herbert:
I was in fact very pleased to see the progress of the experiments by Bippes and his coworkers, as well as Bill Saric and his group, and also the DNS results by Wintergerste and Kleiser, in spite of the fact that they have not answered all my questions. Still open is the question on the mechanism of breakdown for large stationary cross flow vortices. What is also open is the roll of unsteady cross flow vortices in many cases, in particular in flight experiments. There is no information about whether they are important or not important. It is also important to get input for Navier-Stokes and PSE results. What is highly desirable is an easier relation between external influences, like free-stream turbulence, surface quality, vibrations, noise, to the initial disturbance levels and the disturbance levels in the transition region. Also open is the question what is the atmospheric environment. To document this in some way would be very interesting.

Saric:
Also for experiments it would be a lot easier if you could design your experiments with a good theoretical model for receptivity. So far we raised a few issues on the cross-flow boundary-layer problems with receptivity, such as roughness receptivity and its role in unsteady disturbances. In experiments it is hard to do with a big matrix of conditions and sort it out. If we have analytical models - maybe Frank Smith can provide them- this would really be something that would guide us very strongly with the experiments.

Bippes:
All the experiments for cross-flow instabilities have shown that the appearance of high frequencies in the secondary instability is immediately followed by the final breakdown. I think it would be meaningful to calculate this with nonlinear PSE. This would be easier to do than finding the proper integration strategy for the e^n method.

Herbert:
I have another point: the relation to industrial applications. Are we doing something useful? The industry wants us to provide methods that can be used finally by untrained engineers. I would not know how to do that.

Cebeci:
I have been working in industry for about thirty years, and revealed that transition is a complicated phenomenon. We also have to realize what industry would like to have in the area of transition. Applications are laminar flow control and transition in high-lift systems. People are not going to ask you to document the wind tunnel. What industries, like Boeing and McDonnell Douglas, really need is the development and evaluation of an accurate and robust user-friendly design method. This does not mean that the user has to have any advanced degree. Codes must be developed, and have been developed, that can be used by an engineer.
When the e^n method came about 40 years ago, people said it is an empirical correlation, the transition is maybe linear in its initial stage, but it is nonlinear in its later stages. But what has happened. Around 1970's when the Navy was

testing torpedos, they found that the only method that could predict transition was the e^n method. Now we have PSE and DNS, and a lot of experimental data, for example taken by Arnal. Let those who are involved with PSE methods take their codes and apply them and show whether these methods are better or not than the e^n method.
My last comment is about the operating costs. People make studies on the laminar flow control assuming that you could find a certain suction rate that will maintain a laminar flow. When you increase the suction rate, then there is suction drag. So from a technological point of view you can come up with a design. But as far as the operating conditions are concerned, there are a lot of other issues that must be considered. A little bit roughness, ice or insects can make a big difference. We must also consider whether airlines will really buy a wing for an airplane with laminar flow control. At a meeting like this we can only talk about whether we have enough technology to design a laminar wing under ideal conditions.

Stock:
I am really concerned about laminar flow applications by industry. Ten years ago the interest in laminar flow started and there was really a boom. There was a collaboration between engineers from the industries, research centres, and universities, and the outcome was ATTAS. Now we are in a status that we have a separation in industry. There is a group that has to go to NLF; those working on regional aircraft at low Mach numbers, and with low leading edge sweep. The other group makes transporter type aircraft, like Boeing and Airbus, which fly at high Mach numbers and consequently have high sweep. They have to do something at the leading edge, like sucking, to get rid of the cross-flow instability. The regional aircraft has the problem with LFC that due to the short flight distance, it has to be laminar in cruise, and also in climb and descent.
Aerodynamics of laminar flow is not the only thing. It is now really time that new disciplines come in and they will do, such as materials and structures. But there is still a next discipline entering the field: system engineering. For example, a suction device on the leading edge needs about 20 different chambers to avoid outflow, and they have to be glued to a Titanium sheet. So far no conclusive research was done on the fabrication of 5 μm holes in such a sheet. Only recently people started to think about what happens to a little hole, where a vortex can be created. If you oversuck, you transport transition upstream instead of preventing it.
First the feasibility has to be shown that the system works. If then you can demonstrate that the direct operation costs are not increased above the gain in fuel we have a chance to come into the market.
So far this scenario. What I heard in the sessions were remarks on what we can do and cannot do. Industry cannot do DNS, as we cannot wait 120 hours. And as far as I understood, in DNS mostly output is input; you postpone the transition location problem to the initialization problem. I heard that the e^n method is rather stupid. This community has to give us something at hand that we can use. We have to freeze at least for 5 years the goals in order to get the

rest of the people accustomed to it. If we fail, the money will be reduced and we will really drop down to the situation in 1984.

Atkin:
I have been involved in transition and turbulence in both industry and research. There is a real danger that we get polarization. There is a lot of sense in having a variety of methods. Those who are defining aircraft configurations need to know how the the skin friction and form parameters influence their drag estimation. What is perhaps missing is a good dialogue, and this is true in turbulence modelling as well. There you have people at university solving very difficult problems, and people in industry who are still using simple one-equation models. We need to talk with each other, because otherwise we will not get money, and we are actually all out of business in a few years. It is not good enough to say to industry that their methods are physically inconsistent, do not use it. Because it is all they have, they have to use it.

Participant:
It seems these days that we are discussing only stability analysis, PSE, and DNS. Does that mean that the good, old empirical relations are thought to be hopeless and abandoned completely.

Saric:
Yes.

Van Ingen:
If they are good, old does not matter. One of my teachers often said: the real engineer is someone who uses corrupt data, but can still make a good product. Some of that is true of course. People who build and sell aircraft do not wait until we have solved all these problems.

On behalf of the participants Bill Saric thanks the organizers for the very good colloquium.
Van Ingen thanks the Royal Netherlands Academy of Arts and Sciences and the J.M. Burgers Centre for their support. *Then the colloquium is closed.*

References

Abu-Ghannam, B.J. & Shaw, R. 1980 – Natural transition of boundary layers-The effects of turbulence, pressure gradient, and flow history. *J. Mech. Eng. Science* **22**, 213-228.

Bertolotti, F.P., Herbert, Th., & Spalart, P.R. 1992 – Linear and nonlinear stability of the Blasius boundary layer. *J. Fluid Mech.* **242**, 441-474.

Craik, A.D.D. 1971 – Nonlinear resonant instability in boundary layers. *J. Fluid Mech.* **50**, 393-413.

Dagenhart, J.R., Saric, W.S., Mousseux, M.S. & Stack, J.P. 1989 – Cross-flow vortex instability and transition on a 45-degree swept wing. *AIAA* 89-1892.

Dhawan, S. & Narasimha, R. 1958 – Some properties of boundary layer flow during the transition from laminar to turbulent motion. *J. Fluid Mech.* **3**, 418-437.

Emmons, H.W. 1951 – The laminar-turbulent transition in a boundary layer. *J. Aero. Sci.* **18**, 490-498.

Gaster, M. 1965 – A simple device for preventing turbulent contamination on swept leading edges. *J. Roy. Aeron. Soc.* **69**, 788-789.

Gregory, N., Stuart, J.T. & Walker, W.S. 1955 – On the stability of three-dimensional boundary layers with applications due to a rotating disk. *Phil. Trans. Roy. Soc. London A* **248**, 155-199.

Hall, P., Malik, M.R., & Poll, D.I.A. 1984 – On the instability of an infinite swept attachment line boundary layer. *Proc. Roy. Soc. Lond. A* **395**, 229-245.

Herbert, Th. 1988 – Secondary instability of boundary layers. *Ann. Rev. Fluid Mech.* **20**, 487-526.

Herbert, Th. & Bertolotti, F.P. 1987 Stability analysis of nonparallel boundary layers. *Bull. Am. Phys. Soc.* **32**, 2079.

Kachanov, Y.S. & Levchenko, V.Y. 1984 – The resonant interaction of disturbances at laminar-turbulent transition in a boundary layer. *J. Fluid Mech.* **138**, 209-247.

Klebanoff, P.S., Tidstrom, K.D., and Sargent, L.M. 1962 – The three-dimensional nature of boundary-layer instability. *J. Fluid Mech.* **12**, 1-34.

Kohama, Y., Saric, W.S., Hoos, J.A. 1991 – A high-frequency, secondary instability of cross-flow vortices that leads to transition. *Proc. R.A.S Conf. on 'Boundary-Layer Transition and Control'*, Cambridge, UK.

Mack, L.M. – 1984 Boundary-layer linear stability theory. AGARD Report 709.

Malik, M.R., Li, F., and Chang, C.-L. 1994 – Crossflow disturbances in three-dimensional boundary layers: nonlinear development, wave interaction and secondary instability. *J. Fluid Mech.* **268**, 1-36.

Müller, B. & Bippes, H. 1988 – Experimental study of instability modes in a three-dimensional boundary layer. In: Fluid Dynamics of Three-Dimensional Turbulent Shear Flows and Transition. AGARD CP-438.

Morkovin, M.V. 1969 – On the many faces of transition. In: Viscous Drag Reduction, C.S. Wells (ed.), Plenum Press.

Poll, D.I.A. 1985 – Some observations of the transition process on the windward face of a long yawed cylinder. *J. Fluid Mech.* **150**, 329-356.

Rayleigh, Lord 1880 – On the stability of certain fluid motions. *Proc. Math. Soc. London* **11**, 57-70.

Saric, W.S. 1994 – Physical description of boundary-layer transition: experimental evidence. AGARD-R-793.

Schlichting, H. 1933 – Zur Entstehung der Turbulenz bei der Plattenströmung. Nachr. Ges. Wiss. Göttingen, Math. Phys. Klasse 182-208; also *ZAMM* **13**, 171-174 (1933).

Schubauer, G.B. & Skramstad, H.K. 1947 – Laminar boundary layer oscillations and transition on a flat plate. NACA Report 909.

Smith, A.M.O. & Gamberoni, N. 1956 – Transition, pressure gradient and stability theory. Douglas Aircraft Co. Report ES 26388, El Segundo, California.

Tollmien, W. 1929 – Über die Entstehung der Turbulenz. Mitt. Nachr. Ges. Wiss. Göttingen, Math. Phys. Klasse 21-44; English translation in NACA TM 609 (1931).

Van Ingen, J.L. 1956 – A suggested semi-empirical method for the calculation of the boundary layer transition region. Delft University of Technology, Faculty of Aerospace Engineering, Report VTH-74, Delft, The Netherlands.

Van Ingen, J.L. 1977 – Transition, pressure gradient, suction, separation and stability theory. In: Laminar-Turbulent Transition, Agard CP 224, pp. 20.1-20.15.

Author's address

Faculty of Aerospace Engineering
Delft University of Technology
Kluyverweg 1, 2629 HS Delft, The Netherlands.

Introduction

H.H. Fernholz

Preliminary Measurements of the Distribution of the Velocity of a Fluid in the Immediate Neighbourhood of a Plane, Smooth Surface by J.M. Burgers and B.G. van der Hegge Zijnen – Revisited and Discussed –

Abstract

This is a brief historical excursion to revisit some hot-wire measurements in a flat-plate laminar-transitional-turbulent boundary layer which were performed before 1924. Using calculated skin-friction data, the measured mean velocity profiles are presented in inner-law coordinates and compare well with more recent measurements.

Introduction

When reading in the recently published "Selected papers" of J.M. Burgers (1995), I was intrigued by the hot-wire measurements performed by van der Hegge Zijnen and Burgers in the early twenties of this century. Since the data were presented in tables, it was easy to process them and to plot them in inner-law coordinates. These are the first hot-wire measurements ever taken in a boundary layer and, before discussing them, it seems to be appropriate to briefly set the "boundary layer scene" at Delft and in Europe at the time. J.M. Burgers was appointed as ordinary professor of "Aerodynamics Hydrodynamics and their application" at the Technical University of Delft at the age of 23 in 1918. His laboratory was functioning in the beginning of 1921 and so was an open return wind-tunnel of the Eiffel type with a test section of $4 \times 0.8 \times 0.8$ m (Fig. 1). In the same year B.G. van der Hegge Zijnen joined Burgers' group and probably designed and built the hot-wire probe and the CT-anemometer and performed the measurements in the boundary layer (van der Hegge Zijnen, 1924).

L. Prandtl had presented his boundary-layer theory to a small scientific community in 1904 and his doctoral student H. Blasius had solved the equations for the 2-D incompressible laminar boundary layer with zero pressure gradient in 1907. An important result was the Blasius skin-friction formula $c_f = 0.664/\sqrt{Re_x}$. Transition from a laminar to a turbulent boundary layer was probably discovered by Prandtl (1914) when he investigated the drag of spheres. Finally the principle of hot-wire measurements had been brought to general attention by L.V. King (1914). Burgers and van der Hegge Zijnen quote earlier

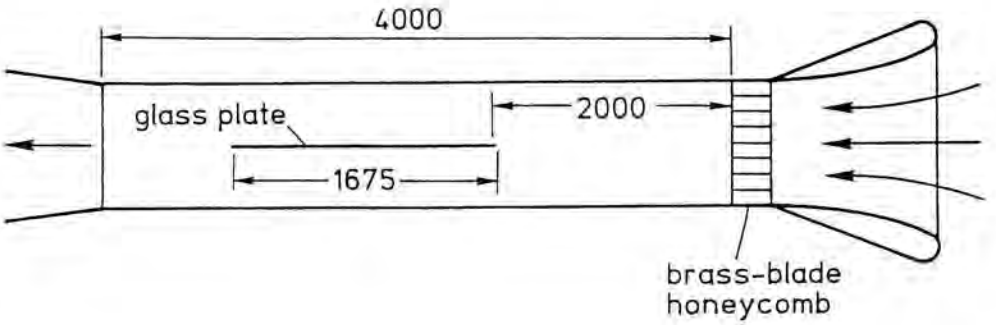

Figure 1: The closed test section of the Eiffel-type open windtunnel at Delft (length in mm).

measurements in a boundary layer than their own by Riabouchinsky (1914) "but the St. Petersburg group did not supply sufficient data for a detailed study of the flow in the boundary layer". So Burgers decided to investigate the problem in Delft and the goals were clearly stated:

- "obtaining data of the distribution of the velocity in the boundary layer;
- to ascertain if the upstream part of the boundary layer showed the laminar motion, corresponding to Blasius' formula;
- to obtain data on the change from the laminar state of motion to the turbulent one;
- to determine the gradient $(\partial\overline{u}/\partial y)_{y=0}$".

Where and how did they perform their measurements? The test plate was made of polished glass with a leading edge formed by two circular arcs (0.75 m radius of curvature). The plate did not span the tunnel width (0.40 m wide) and had a length of 1.675 m. The hot-wires were made of platinum-iridium with diameters of 200 to 15 μm and lengths between 21 and 29 mm. The wall distance was set by a micrometer screw and the near-wall distance was controlled by the wire/image method. The probes were calibrated in the irrotational flow against a Pitot-static tube. The freestream velocity u_∞ was kept constant at 8 m/s at each respective measuring station and the atmospheric pressure and the temperature were measured for each velocity profile. Only mean-velocity data are available.

Discussion of data

Burgers & van der Hegge Zijnen could not measure the skin friction and so determined it from the wall slope of the mean-velocity profile. These data (•) are

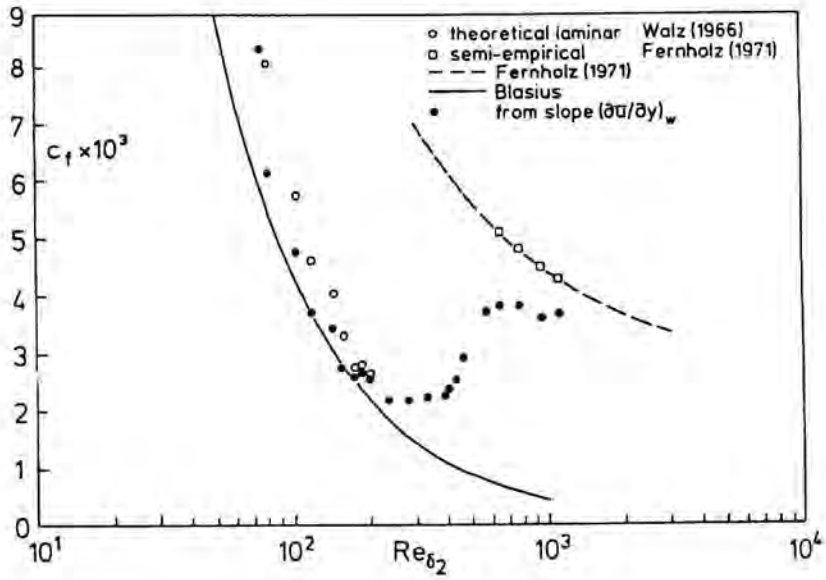

Figure 2: Comparison of skin-friction data determined from the wall slope $(\partial\overline{u}/\partial y)_w$ and from semi-empirical relations in a zero-pressure gradient 2-D boundary layer. Data from Burgers & van der Hegge Zijnen (1924).

plotted as $c_f = 2\overline{\tau}_w/\rho U_\infty^2$ against $Re_{\delta_2} = U_\infty \delta_2/\nu$ in Fig. 2 where δ_2 is the momentum loss thickness, $\overline{\tau}_w$ the mean skin friction and U_∞ the free stream velocity. They are compared in the upstream region with the skin-friction formula of Blasius for a zero-pressure gradient laminar boundary layer. They were also recalculated from the velocity profiles (o) by the skin-friction formula of Walz (1966) which is of the form

$$c_f = \frac{3.452}{Re_{\delta_2}}(H_{32} - 1.515)^{0.716}, \tag{1}$$

and thus can take account of the pressure gradient dp/dx in the streamwise direction. Since the data lie above the curve of Blasius a favourable pressure gradient must have been present (this is also discussed by Hansen, 1928). There is still no reliable calculation method for the skin friction in a transitional boundary layer; so we can only show Burgers' "slope data".

The downstream boundary layer is apparently turbulent and the "slope method" becomes rather inaccurate. Skin friction (⊗) was therefore also determined from a semi-empirical relationship (Fernholz, 1971) and compared with the Delft data which are definitely low. The skin-friction data, determined as given in the legend of Fig. 3, were used to plot the mean-velocity profiles in inner-law scaling in Fig. 3. It is astonishing how well the measurements agree with the linear law in the viscous sublayer and how they show the typical be-

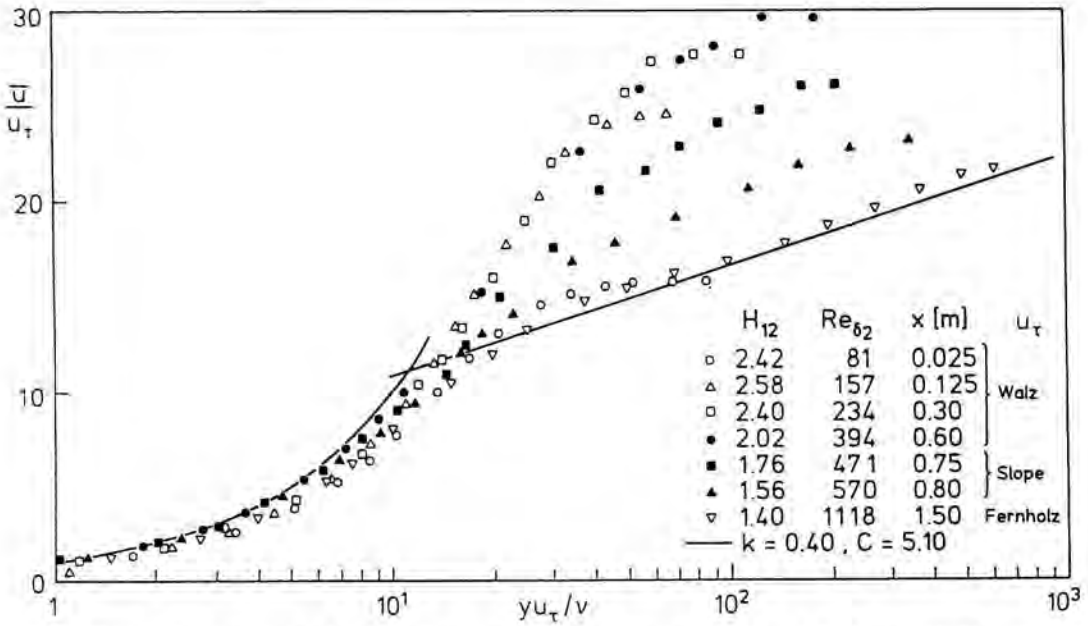

Figure 3: Mean velocity profiles in a zero-pressure-gradient 2-D boundary layer in inner-law scaling. Data from Burgers & van der Hegge Zijnen (1924).

haviour in a transitional and for the last profile (∇) in a turbulent boundary layer (e.g. following the logarithmic law of the wall). Fig. 4 presents the development of the relevant boundary-layer parameters, such as the shape parameter H_{12}, the Reynolds number Re_{δ_2}, and the skin-friction parameter c_f against the streamwise distance x. The different flow regimes can be determined clearly but again it seems to be appropriate to quote Burgers and van der Hegge Zijnen (1924) on the transition regime:

> "... the character of the motion changes at $x = 0.75$ m. ... The conclusion is allowed that here the two manners of motion are present at the same time: the laminar one at $x < 0.75$ m, the turbulent one at $x > 0.75$ m. .... It was observed that the needles both of the galvanometer and of the ammeter were very quiet during the measurements at the former part of the glassplate ... . The fluctuations showed a maximum in the region of transition; in this region they were so intense, that they could be observed by the eye from the glittering of the wire. Probably this phenomenon has to be ascribed to the formation of large vortices or irregular waves, which mark the breaking down of the laminar motion. ... These fluctuations gave the greatest disturbances for values of y between about 0.25 and 1 mm" (corresponding with $y^+ = 5.8$ and 23 at $x = 0.80$ m which is very close to the critical layer).

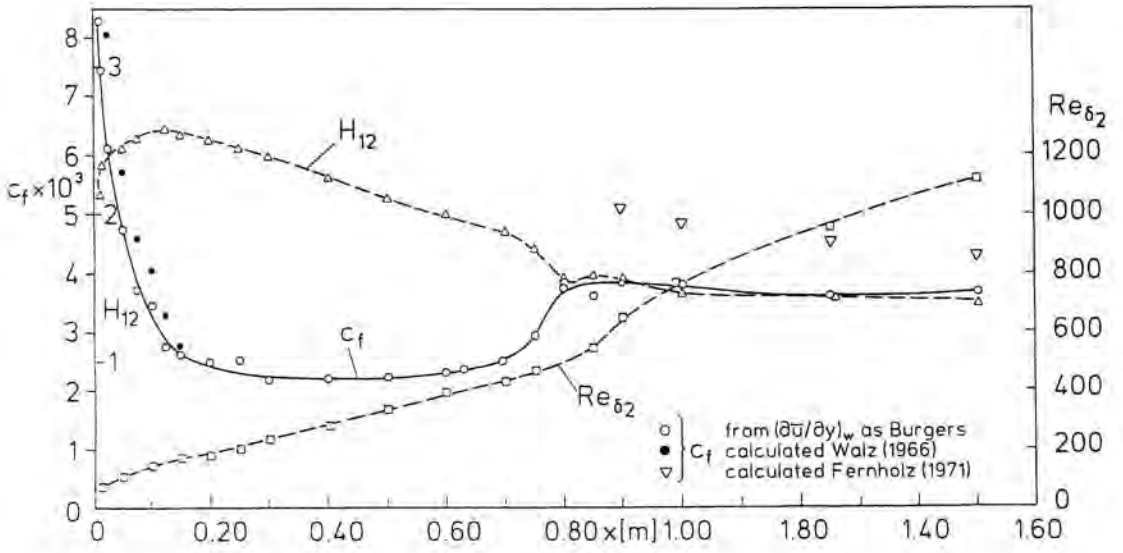

Figure 4: Streamwise development of the Reynolds number Re_{δ_2}, the shape parameter H_{12} and the skin-friction coefficient c_f in a zero-pressure-gradient 2-D boundary layer. Data from Burgers & van der Hegge Zijnen (1924) (lines are for visual aid only).

The first transition diagram $\delta/(\nu x/U_\infty)^{1/2}$ against Re_x was presented by Hansen (Aachen, 1928) who also used and discussed the measurements from Delft.

Finally one should mention some conclusions of Burgers and van der Hegge Zijnen about the velocity distribution and about transition:

i) For values of $y < 0.2$ mm the mean velocity u becomes approximately a linear function of y.

ii) In the turbulent part values of the mean velocity u can be represented for values of $y > 1.25$ mm by a power law

$$u/u_\infty = (y/\delta)^{1/7} . \tag{2}$$

iii) The region of transition marks itself by an inflection of the curve of the boundary layer thickness δ.

iv) The transition from the laminar state of motion to the turbulent one is influenced by the magnitude of the disturbance of the air current.

References

Blasius, H. 1907 – Grenzschichten in Flüssigkeiten mit kleiner Reibung. Diss. Göttingen. *Z. Math. Physik* **56**, 1-37 (1908).

Burgers, J.M. & van der Hegge Zijnen 1924 – Preliminary measurements of the distribution of the velocity of a fluid in the immediate neighbourhood of a plane, smooth surface. *Selected Papers of J.M. Burgers* pp. 25-56. Kluwer Academic Publ. Dordrecht (1995).

Fernholz, H.H. 1971 – Ein halbempirisches Gesetz für die Wandreibung in kompressiblen turbulenten Grenzschichten bei isothermer und adiabater Wand. *ZAMM* **51**. T 148-149.

Hansen, M. 1928 – Die Geschwindigkeitsverteilung in der Grenzschicht an der längsangeströmten ebenen Platte. *ZAMM* **8**, 185-199. NACA 585 (1930).

Hegge Zijnen van der, B.G. 1924 – Measurements of the velocity distribution in the boundary layer along a flat surface. Thesis Delft.

King, L.V. 1914 – On the convection of heat from small cylinders in a stream of fluid. *Phil. Trans.* **215**, 373.

Nieuwstadt, F.T.M. & Steketee, J.A. 1995 – Selected papers by J.M. Burgers. Kluwer Academic Publ. Dordrecht.

Prandtl, L. 1904 – Über Flüssigkeitsbewegung bei sehr kleiner Reibung. Verh. III Intern. Math. Kongr. Heidelberg, 484-491.

Prandtl, L. 1914 – Über den Luftwiderstand von Kugeln. *Nachr. Ges. Wiss. Göttingen, Math. Phys. Klasse*, 177-190.

Riabouchinsky, D. 1914 – Etude experimentale sur le frottement de l'air. *Bull. Inst. Aérod. de Koutchino*, fasc. V, p. 51.

Walz, A. 1966 – Strömungs- und Temperaturgrenzschichten. G. Braun Verlag Karlsruhe.

Author's address

Hermann-Föttinger-Institut für Strömungsmechanik
Technische Universität Berlin
Strasse des 17. Juni 135
10623 Berlin, Germany

N. Voogt

Flight Testing of a Fokker 100 Test Aircraft with Laminar Flow Glove

Abstract

Within the framework of the ELFIN project for laminar flow investigation a natural laminar flow glove was designed, built and tested in flight on a Fokker 100 test aircraft. The glove design is described and some of the flight test results are discussed.

Introduction

For at least five decades research has been going on in the area of drag reduction by various means of laminar flow control. Not only the impressive potential for drag savings up to 15 percent but also the associated reductions in fuel consumption and pollutive emissions are driving the pursuit of laminar flow technology. Especially the environmental factors will be of major importance in view of the predicted doubling or even tripling of air traffic within the next decades.

Although a large knowledge base has accumulated during many years of laminar flow research, practical application on commercial transport aircraft has not been feasible due to severe surface quality and contamination requirements. Recent advances in aerodynamics, computational design capabilities, materials, structures and aircraft systems have stimulated national research programs in the USA and some European countries, notably France and Germany (see Wagner *et al.*, 1988, Bulgubure & Arnal, 1992; Dxiomba *et al.*, 1989).

In 1989 the ELFIN project [European Laminar Flow INvestigation] was initiated as one of the largest projects within the Brite/Euram Aeronautics Program supported by the EC. The objective of the ELFIN project is to strengthen the laminar flow technology basis by combining European resources in conducting windtunnel and flight tests as well as in advancing prediction methods.

The project is in its second phase and is building on results obtained in ELFIN I which was the first phase and which ended in 1992. ELFIN I was split up in four strongly related tasks shown in Fig. 1:

- task 1: windtunnel testing at transonic speed on a large-scale model with leading edge suction
- task 2: developing testing techniques and suction devices
- task 3: developing effective computational methods for predicting transition from laminar to turbulent flow
- task 4: flight testing of a natural laminar flow wing

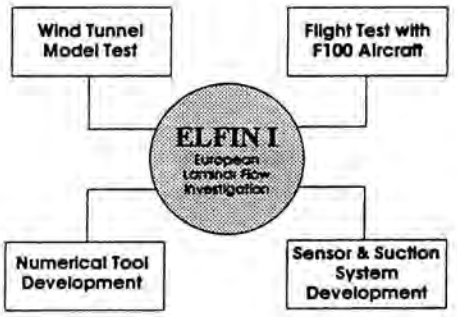

Figure 1: Main topics in ELFIN I.

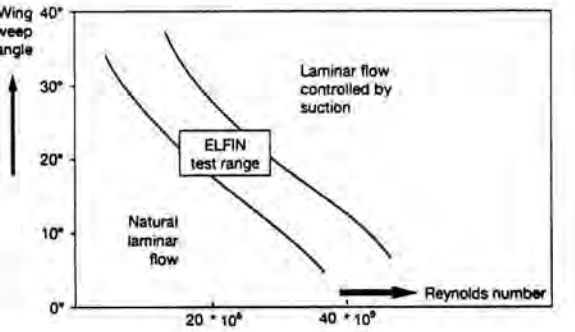

Figure 2: Flight test range Fokker 100 with glove.

The ELFIN I project proved to be a successful cooperation with 24 organizations in 11 countries comprising participation of all large aerospace companies, research institutes and a number of universities.

This paper will describe activities in task 4 where scientists and engineers from 12 organizations from all over Europe worked together in a unique cooperation to design, build and flight test a natural laminar flow wing glove on a Fokker 100 test aircraft.

ELFIN flight test objectives

The ELFIN flight testing builds on previous experience with an ATTAS VFW 614 test aircraft which was equipped with a part-span, part-chord glove. One objective of those tests (1986-1989) was to correlate results from flight tests and transonic as well as low speed windtunnel experiments. The other objective was to validate new advanced measuring techniques for boundary layer investigation. In contrast with the ATTAS flight testing which was limited to the lower transonic Mach number range the aim of ELFIN flight testing was to cover a range of Mach numbers and Reynolds numbers which are representative for modern regional aircraft.

The first objective was to validate and calibrate existing prediction methods for boundary layer stability. Although several methods of varying physical complexity are available, their usefulness can only be established by correlation with full-scale experimental data. The ELFIN flight testing was essential in creating a data base for this purpose.

The second objective was to measure the performance of the glove in terms of drag reduction potential. For that purpose advanced, but well-proven instrumentation was to be applied to establish the extent of laminar flow for a wide range of operating conditions.

The third objective was to establish limits for application of natural laminar flow. Within laminar flow technology three application areas can be distinguished:

- natural laminar flow - NLF - where a specific wing shape generates favourable surface pressure gradients to stabilize the laminar boundary layer. NLF can be applied from general aviation to medium-sized aircraft.
- hybrid laminar flow control - HLFC - where limited suction is used in combination with a favourable pressure distribution. HLFC is applicable to medium-sized aircraft with moderate sweep angles.
- laminar flow control - LFC - where extensive suction is required in combination with an appropriate airfoil shape. LFC is applicable to large aircraft with high leading edge sweep angles.

Throughout the various application areas wing sweep angle, Reynolds number and leading edge curvature are important parameters in connection with the various types of instabilities [Tollmien-Schlichting, cross flow and attachment line instabilities] which can provoke transition to turbulent flow.

Since no clear boundaries are known to exist between the area where NLF can be applied and the other areas where suction is required the "in between" region, as shown schematically in Fig. 2, was investigated.

This figure also illustrates the suitability of the Fokker 100 as a test aircraft in view of the leading edge sweep angle of 21.5 degrees in the mid-wing region and the range of its operational Reynolds numbers (between 15 and 30 million).

Design of the NLF glove

The NLF wing glove was designed for cruise conditions which are representative of those for future regional airliners. In order to obtain the best aerodynamic performance at a range of operating conditions the glove should be located in the wing area which is least disturbed by three-dimensional effects from wing root and wing tip. Therefore the mid-wing region of the Fokker 100 (starboard) wing with a span of about three meter was selected (Fig. 3).

Fairings of about one metre wide were incorporated at both ends of the glove to enable the transition from the turbulent flow pattern on the Fokker 100 to the laminar type of pressure distribution as required on the glove. The following design requirements were set:

- the glove should be designed for a design point at a Mach number of $M = 0.75$ and a lift coefficient of $C_L = 0.40$ for a Reynolds number of of 22 million. The aim was to reach a laminar flow extent of 50 percent chord length on upper and lower glove surfaces. In addition sufficient laminarity should be achieved for a range of lift coefficients between $C_L = 0.25$ and $C_L = 0.55$.
- aircraft transonic characteristics should not be affected by the presence of the glove.

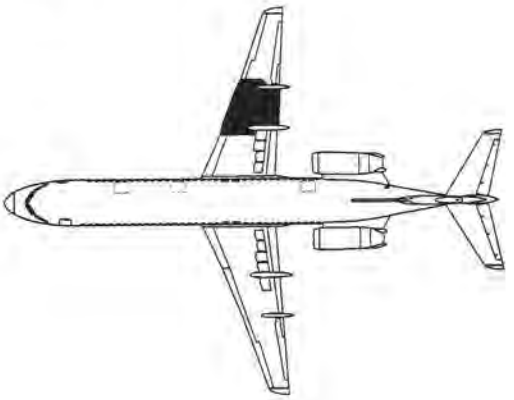

Figure 3: Glove location on Fokker 100.

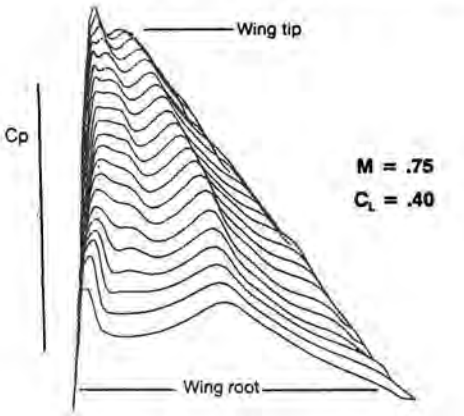

Figure 4: Transonic pressure pattern on Fokker 100 upper surface.

- a minimum clearance of 10 mm should be taken between existing wing and glove contour and a maximum leading edge extension of about 5 percent chord.

Preliminary infinite sheared laminar wing design studies by several design teams indicated that a leading edge sweep angle of 20 degrees would be required to satisfy the 50 percent laminarity requirement. Since the leading edge sweep angle in the mid-wing region on the Fokker 100 wing is somewhat larger the glove planform was adapted accordingly.

The design process was hampered by several complicating factors:

- the large discrepancy at the design point between actual "turbulent" flow condition on the Fokker 100 wing (Obert, 1988) and the required flow condition. The transonic flow pattern on the Fokker 100 wing at $M = 0.75$ is characterized by a double-shock system on the upper surface as shown Fig. 4. At the same condition the lower surface pressure distribution shows a suction peak in the nose region (Fig. 5) which is associated with leading edge droop introduced to optimize low-speed, high-lift characteristics (Obert, 1988). Fig. 5 also shows the very different pressure distributions required for laminar flow.
- the three-dimensional interaction between the Fokker 100 flow pattern and the NLF flow pattern on the glove.

Especially the problem of embedding the laminar type pressure distribution on the glove in the double-shock pressure pattern demanded much attention and required specially adapted fairing airfoils at both ends of the glove as well as three different airfoil sections on the glove itself.

Final glove contours are shown in Fig. 6 together with the modified planform and the original Fokker 100 wing sections. The 20 degrees swept leading edge on the glove is continued on the inboard fairing. Connection with the existing inboard wing is made through a narrow area with zero leading edge sweep. This

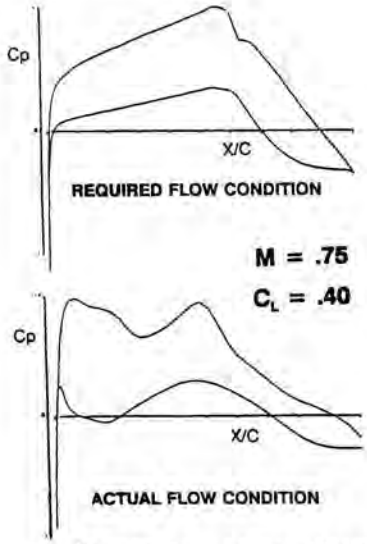

Figure 5: Actual (Fokker 100) and required flow condition on glove.

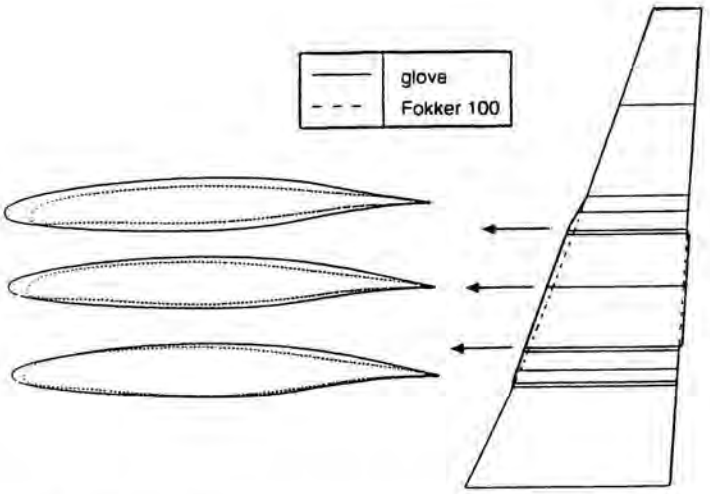

Figure 6: Wing sections on glove and on Fokker 100.

is used as a safeguard against attachment line instabilities propagating from the inboard wing.

The influence of the glove on the pressure patterns in the design condition is shown in Fig. 7. At this condition the flow on the glove seems to be isolated from the flow pattern on the rest of the wing.

For higher lift coefficients at the same Mach number, however, the pressure distribution will be affected by three-dimensional influences mainly from the inboard wing. Shown in Fig. 8 are computed pressures on the glove - inboard, mid and outboard - for higher lift coefficient. This result shows that eventually the double-shock type pressure distribution will dominate the flow field again, and obviously more clearly at the inboard end of the glove.

The final glove design (see Dressler *et al.*, 1992) was performed by a joint German team of Deutsche Aerospace Airbus and research institute DLR and the result was evaluated by the other partners. Predictions of the chordwise extent of laminar flow covered a range from 30 to well over 50 percent depending on the different methodologies used. This fact again illustrated the need for a full-scale NLF data base.

Windtunnel experiment

After the glove design was finalized an existing half model of the Fokker 100 was modified to represent glove and fairings. The glove was made of epoxy-resin allowing for infrared measurements of transition and shock patterns. A pressure measuring section was incorporated in the middle of the glove and in addition a number of pressure taps at both ends of the glove to check two-dimensionality.

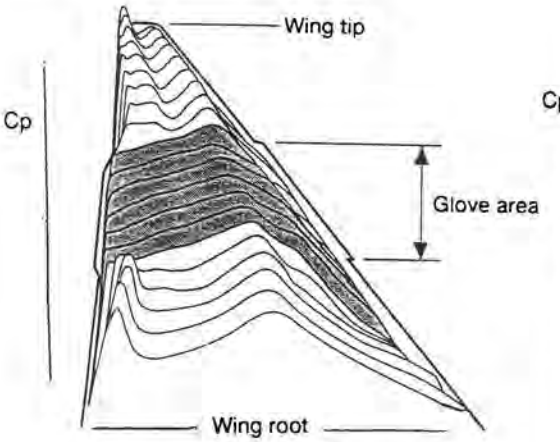

Figure 7: Upper surface pressure pattern at glove design condition.

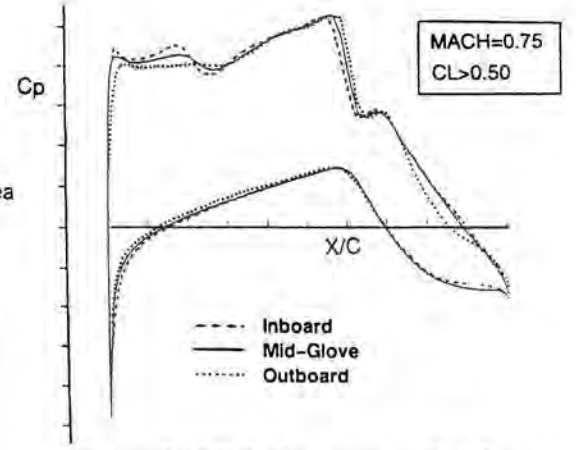

Figure 8: Off-design pressure distribution on glove.

The model was tested in the High Speed Tunnel of NLR at Mach numbers between $M = 0.19$ and $= 0.80$ and at Reynolds numbers between 2.4 and 8.5 million.

Objectives for the windtunnel tests were to investigate:

- effect of the glove on aircraft characteristics and therefore on flight safety aspects.
- the integration of the laminar flow type of pressure distribution and the Fokker 100 flow pattern.

The experiment showed an excellent correlation between measured pressures and results from some of the viscous transonic computations such as the DLR result shown in Fig. 9 for a Reynolds number of $Re = 5 \times 10^6$. The high-speed tests showed no major changes in aerodynamic characteristics due to the presence of the glove. Effects of transition shifts were established by testing with natural transition and fixation near the nose of the glove. From these data it could be concluded that a sudden movement of transition over 50 percent chord - which can be expected when flying through ice clouds - could be adjusted for by aileron deflection of less than 1 degree and elevator deflection of less than 0.4 degrees.

Low-speed test data revealed a substantial loss in maximum lift of $\Delta C_L = 0.12$ as compared with the original half model data. In addition infrared images showed a different wing stall behaviour. Although loss of maximum lift was not unexpected in view of the different nose shapes on glove and original wing this result required restricted operation of the test aircraft in low-speed, high angle-of-attack conditions.

During the second ELFIN phase a further investigation was made of this phenomenon and an existing two-dimensional windtunnel model representing

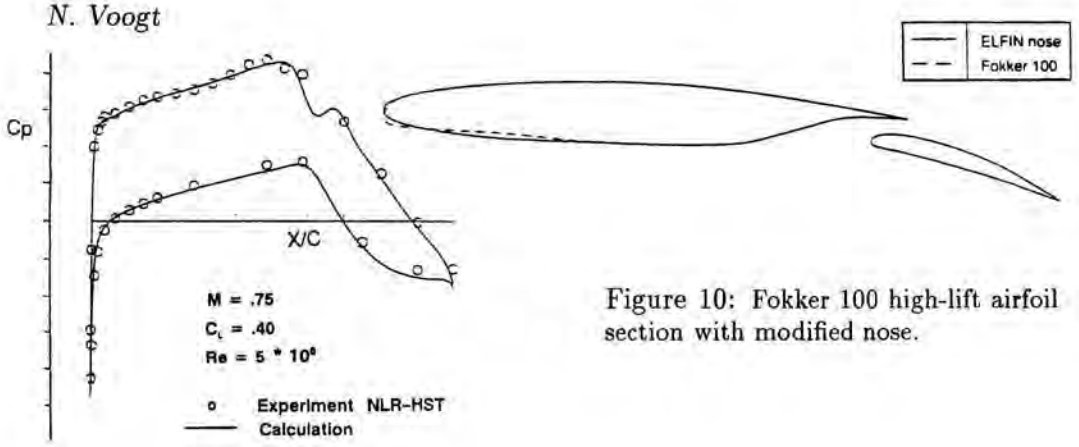

Figure 9: Computed and measured pressure on glove in windtunnel.

Figure 10: Fokker 100 high-lift airfoil section with modified nose.

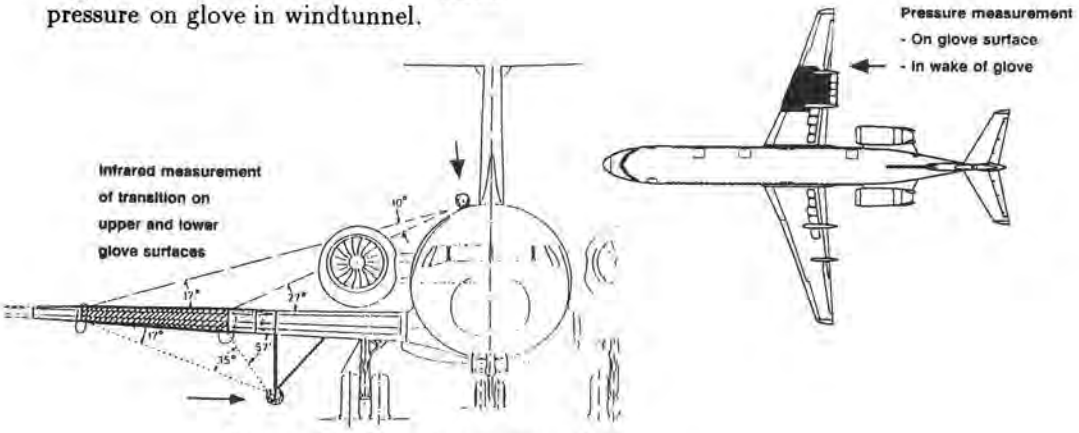

Figure 11: Main instrumentation.

a mid-wing section of the Fokker 100 with high-lift devices was modified to incorporate the nose section of the ELFIN mid-glove contour (Fig. 10). Also in this case windtunnel tests as well as computations showed a substantial loss in maximum lift especially with deflected high-lift devices.

Glove build-up and instrumentation

The instrumentation on the test aircraft was strongly interrelated with the glove structural build-up. The main element, essential for the measurement of transition, was the infrared system. As shown in Fig. 10 two infrared camera systems were installed to monitor transition on upper and lower surfaces of the glove. For effective measurement in level flight the infrared system requires a small temperature gradient between glove and surrounding air so that laminar and turbulent flow regions with their different heat exchange rates can be visualized. The glove surface was heated by means of specially made thin carbon fibre

heating elements inside the glove skin. To support analysis of infrared images complementary data was supplied by hotfilm sensors in the leading edge region and at the glove inboard end.

To provide experimental data for validation of boundary layer stability methods detailed pressure measurements were made in two rows each containing 120 flush-mounted pressure taps at both ends of the glove. In the wake of the glove static and total pressures were measured by means of several rakes to derive section drag data. The rakes were installed on a beam mounted between the flap track fairings (Fig. 11).

A schematic cross-section showing the glove structure with the embedded instrumentation, wiring and tubing is shown in Fig. 12. A substructure of profiled wooden ribs was filled-in with polyurethane foam shaped to the glove profile (minus outer skin). On top of the substructure a prefabricated composite skin was glued consisting of a glass fibre woven cloth construction which contained the carbon fibre heating elements within the lay-up. A skin thickness of about 3 mm was selected as a compromise between having enough thickness to maintain profile shape and having little thickness to minimize loads.

Flight testing

With the glove installed the Fokker 100 test aircraft has an asymmetrical configuration and although windtunnel tests did not indicate potential problems in the high-speed regime some precautions were taken:

- well ahead in time of the glove mounting, critical instrumentation elements such as the infrared camera installation were tested in flight to ensure their operation without vibration or excessive drag.
- in view of potential low-speed, high-lift problems (reduced maximum lift, flaps inoperative) higher take-off and landing speeds had to be prescribed and ground runs were made at high angle-of-attack conditions.

During ground run testing the aircraft showed a strong and unexpected tendency to roll. It appeared that the starboard wing produced more lift than anticipated. The phenomenon could be explained when the beam carrying the wake rakes was included in the computational model. Especially in ground effect the additional lift on the beam as found to be responsible for this effect which could easily be compensated for by aileron deflection.

No further complications occurred and the planned range of flow conditions could be covered in 15 flight hours during which more than 100 recordings were efficiently obtained thanks to flawless operation of the instrumentation.

Infrared images and hotfilm signals were evaluated and stored onboard the aircraft while simultaneously recorded and transmitted pressure distributions such as shown in Fig. 13 were evaluated at a ground station.

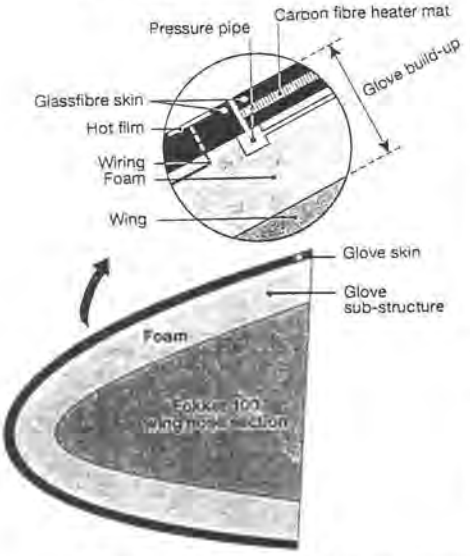

Figure 12: Glove build-up structure.

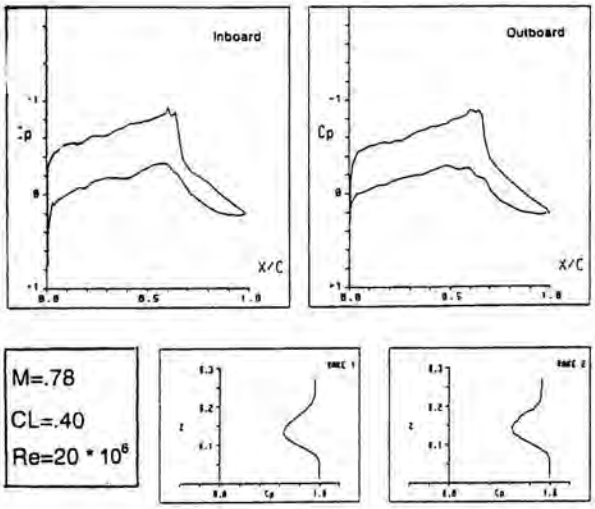

Figure 13: Example of recorded pressures on glove and in wake.

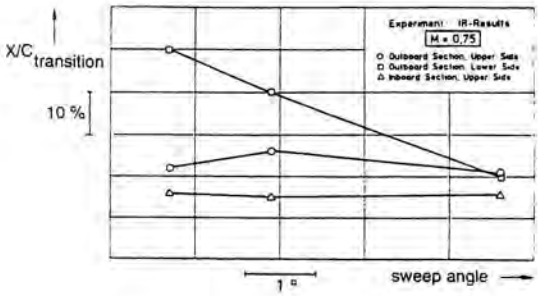

Figure 14: Effect of wing sweep angle on transition.

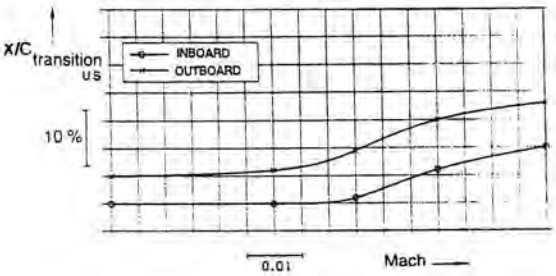

Figure 15: Effect of Mach number on upper surface transition.

Flight test results

During the first three flights (10 flight hours) a large part of the intended range of flight test points representing the most interesting flow conditions could be recorded. Some of the results are summarized in Figs 14 and 15. The important effect of sweep angle variation - simulated by sideslipping the aircraft - is shown in Fig. 14. Transition on the lower surface at the design Mach number is strongly affected by variation in leading edge sweep angle whereas no clear correlation with sweep angle could be established for the upper surface. Lower surface transition is apparently dominated by cross flow instabilities.

Mach number variation has an effect on both surfaces since the pressure distribution steepens up and the flow more strongly accelerates up to 50 or 60

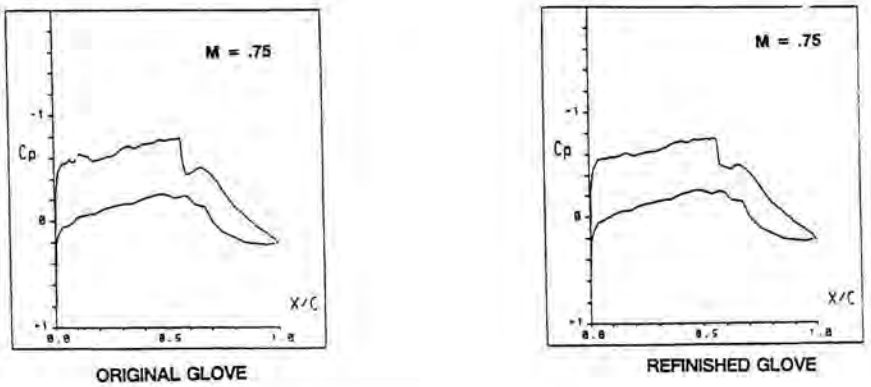

Figure 16: Recorded pressures on original and refinished glove.

percent chord on both surfaces when the Mach number increases. The effect of Mach number around the design condition on measured upper surface transition is shown in Fig. 15. The - not very strong - effect is similar for inboard and outboard ends of the glove but the extent of laminar flow is consistently larger on the outboard end. This effect can also be noticed in Fig. 14 and it indicates that on the aircraft in flight the flow on the glove is less two-dimensional than the flow measured on the windtunnel model. Further evidence of surface irregularity was found when comparing measured pressures near the design condition with computed results for the design case.

Although the glove surface - which during manufacturing was checked against templates - seemed sufficiently smooth before the tests, the measured pressures showed irregularities associated with surface waviness. Accurate measurement of the glove after the first three flights showed that the glove did not satisfy the severe waviness requirements set for laminar flow surfaces but complied with the less severe requirements for surface waviness on present day commercial airliners.

It was decided to refinish the main part of the glove upper surface to the highest possible standard and to measure a second set of datapoints. Fig. 16 shows an example of an improved measured outboard pressure distribution close to the design condition indicating that the main irregularities have disappeared.

The effect of the improved glove surface quality on the extent of laminar flow is shown in Fig. 17 where results for similar flow conditions are compared. The spanwise extent has become more regular and in chordwise direction an additional 10 to 15 percent of flow laminarity is recorded. This gain was found for most of the test conditions which could be compared. The turbulent wedge shown in Fig. 17 on the original glove surface is due to a surface irregularity caused by insect impact.

In-flight pressure measurements confirmed that three-dimensional effects become important for higher lift coefficients (see also Fig. 8). A result of such measurements is shown in Fig. 18 where differences between inboard and out-

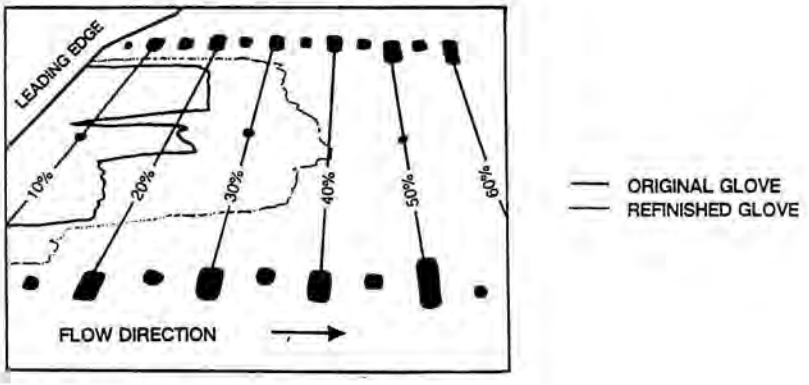

Figure 17: Effect of glove refinishing on transition.

board recordings are similar to those shown in Fig. 8. It was however found that the measured lift coefficient at this flow condition was somewhat lower than anticipated on the basis of computations.

Apart from surface quality imperfections the extent of laminarity at a certain flow condition was also influenced by "environmental" conditions such as ice clouds and insects. During encounters with ice crystals in cirrus clouds laminarity disappeared only temporarily but most of the insects picked up during take-off left their turbulent "signature" during the remainder of the flight. Examples of disturbances related to insect impact are shown in Fig. 17 and also in Fig. 19 where signals are shown from hotfilm sensors placed along the glove leading edge to detect any attachment line instabilities. The sensors at both ends of the glove show a laminar signal whereas the middle one detects transition. This local transition is most likely caused by a small disturbance resulting from insect impact.

Because of the large number of insect impacts observed during the first flights in late November 1991 take-offs during the second series of flights in May 1992 were made early in the morning to minimize risk of insect encounters. This strategy appeared to be very effective.

Concluding remarks

As part of the ELFIN project and within the time frame of two years a full-chord, part-span natural laminar flow glove was designed, built and tested in flight on a Fokker 100 test aircraft. Combination of available knowledge and experience on a European level proved very effective.

During 15 flight test hours an extensive database was collected with more than 100 recordings covering a wide range of flow conditions for two types of glove surface quality. This database was an essential element for validation and

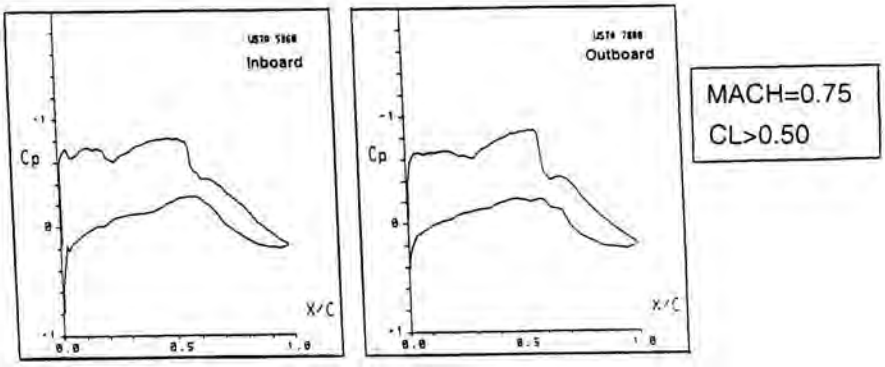

Figure 18: Pressure recordings at off-design condition.

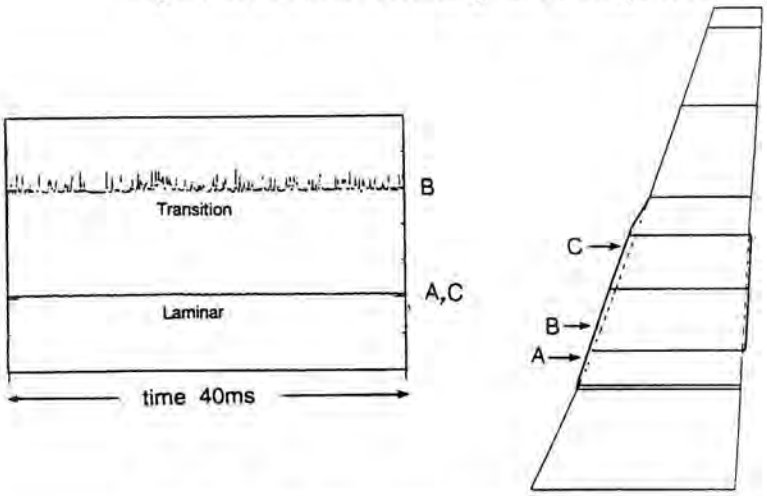

Figure 19: Hotfilm signal recordings at leading edge.

calibration of prediction methods for boundary layer stability which are applied to aerodynamic design.

A major step has been made in understanding laminar flow aerodynamics although an adverse effect, such as reduction in maximum lift at low speed as observed in this application, requires further attention. Other application aspects such as surface quality requirements will imply new manufacturing and maintenance standards.

Therefore any future application of laminar flow technology, which potential was demonstrated by this project, requires a combination of aerodynamic (design) -, production (surface quality) - and systems (clean leading edge, suction) -technologies.

Acknowledgement

The author wishes to acknowledge the support of the European Commission and the important contributions of many colleagues from aircraft manufacturers, research institutes and universities throughout Europe who together made ELFIN flight testing a great success.

References

Bulgubure, C. & D. Arnal 1992 – Dassault Falcon 50 laminar flow flight demonstrator. Proceedings of First European Forum on Laminar Flow Technology.

Dressler, U., H. Hansen, S. Rill, K.H. Horstmann, C.H. Rohardt & G. Wichmann 1992 – Design of the Fokker 100 Natural Laminar Flow Glove. Proceedings of First European Forum on Laminar Flow Technology.

Dziomba, B., R. Henke, F.X. Münch & J. Szodruch 1989 – Laminar Wing Testing Techniques in Windtunnel and Flight. ICIASF, Göttingen.

Obert, E. 1988 – The aerodynamic development of the Fokker 100. ICAS-88 -6.1.2.

Wagner, R.D., D.V. Maddalon, D.W. Bartlett & F.S. Collier Jr. 1988 – Fifty years of Laminar Flow Flight Testing. SAE paper 881393.

Author's address

Fokker Aircraft B.V.
Amsterdam, The Netherlands

Session 1:
Tollmien-Schlichting Waves and Subsequent Instabilities

Y.S. Kachanov

Three-Dimensional Instabilities in Boundary Layers

Abstract

The paper is devoted to a survey of experimental studies of the stability of both 2D and 3D boundary layers with respect to 3D stationary and traveling waves inclined at various angles to the flow, including Tollmien-Schlichting (TS) waves and cross-flow instability modes. These results are compared with theoretical ones obtained by different authors by means of the stability theory, Parabolized Stability Equations (PSE), asymptotic theory and Direct Numerical Simulation (DNS).

Introduction

The problem of boundary-layer transition has three main aspects: (i) the laminar-flow receptivity to external perturbations, (ii) the linear boundary-layer instability, and (iii) the nonlinear flow breakdown. The present paper is devoted to the second aspect. The experiments, described in the paper, were conducted in the Institute of Theoretical and Applied Mechanics in Novosibirsk during past several years. The theoretical results used for comparison were obtained in different groups in Moscow, Berlin and Seattle (the linear stability theory), Stockholm (PSE), London (asymptotic theory), and Stuttgart (DNS).

The linear hydrodynamic stability theory is undoubtedly the most developed branch of our knowledge about transition. This theory is very important for engineering methods of transition prediction (for example for the e^n-method). At the same time, the three-dimensional instability of both 2D and 3D basic flows has not been studied in detail until now. More recent studies can provide some quantitative stability characteristics of boundary layers that could be used for comparison with theoretical approaches and for quantitative verification of 3D computer codes. Some recent results of such quantitative comparisons are presented below. In contrast to most other studies the experiments described here were conducted at *controlled* disturbance conditions with excitation of instability modes by means of disturbance sources of different types. Such experimental conditions, together with special methods of analysis of the data, give the possibility to obtain very detailed information on the flow stability to 3D stationary and traveling modes.

3D instability of the Blasius boundary layer

The first successful experimental investigation of 3D instability waves in the flat-plate boundary layer was conducted by Gaster & Grant (1975) and the results of this study were compared with calculations by Gaster (and, recently, with DNS by Konzelmann, 1990). Later a complete set of stability characteristics of the Blasius boundary layer was obtained experimentally by Gilyov *et al.* (1983). In the paper by Kachanov & Michalke (1994) the experimental data obtained by Gilyov *et al.* were used for additional processing and for a quantitative comparison with the results of calculations carried out by Michalke within the framework of the parallel linear stability theory (PLST). Another set of measurements in the Blasius flow was conducted very recently. The first results of the data processing are published by Kachanov & Obolentseva (1996). The goal of these experiments is to investigate the stability characteristics in more detail, including measurements at various distances from the wall, in order to obtain the eigenfunctions of the 3D TS modes (inclined at different angles to the flow direction) as well as to investigate the non- parallel effects and criteria of instability in the 3D case.

In the experiments by Gilyov *et al.* (1983) and Kachanov & Obolentseva (1996) the disturbances (harmonic in time) were introduced into the boundary layer by means of localized disturbance sources of two types, namely by a "point" source and by a circular membrane-type vibrator. In both cases during the data processing the wave trains were decomposed into normal oblique TS waves inclined at various angles to the flow direction. This procedure was used for the first time by Gilyov *et al.* (1983) and described in detail by Kachanov & Michalke (1994).

The structure of the mean flow, realized at the conditions of experiments by Gilyov *et al.* (1983) and Kachanov & Obolentseva (1996), corresponds locally to the Blasius boundary layer with very high accuracy.

Dispersion characteristics of 3D TS modes in Blasius flow

The dependences of the nondimensional streamwise wavenumber $\alpha_r\delta_1$ (where δ_1 is the boundary-layer displacement thickness) on the propagation angle θ (where $\theta = \tan^{-1}[\beta/\alpha_r(\beta)]$ and β is the spanwise wavenumber) for three different frequency parameters $F = \omega\nu/U_o^2$ are shown in Fig. 1 (where ω is the disturbance frequency and ν is the kinematic viscosity). A comparison of the experimental points obtained by Gilyov *et al.* (1983) and Kachanov & Obolentseva (1996) (new experiments) with the results of the PLST by Michalke (see Kachanov & Michalke, 1994), non-parallel PSE approach by Hanifi (1995), and DNS by Ebert (1995) demonstrate a good quantitative agreement in a wide range of the propagation angles from 0 to 50°. At very large propagation angles the PLST predicts some unexpected growth of the streamwise wavenumbers (shown in Fig. 1 for $F = 94.1 \cdot 10^{-6}$) that is not observed in the experiments. In this range the PSE and DNS give better agreement with the experimental results. Note that the data obtained by means of the localized disturbance sources (with

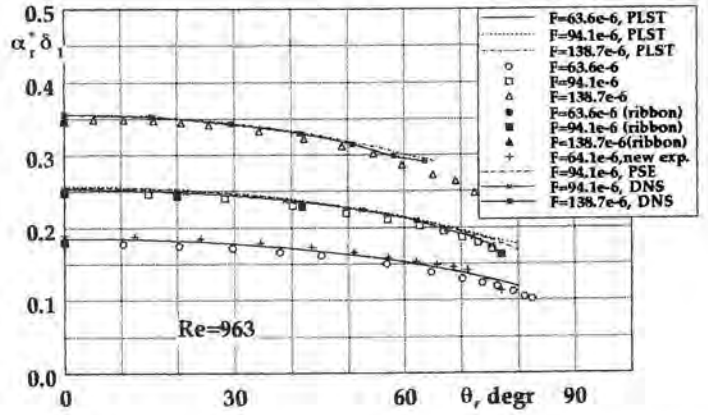

Figure 1: Streamwise wavenumbers of 3D TS waves versus propagation angle for the Blasius flow.

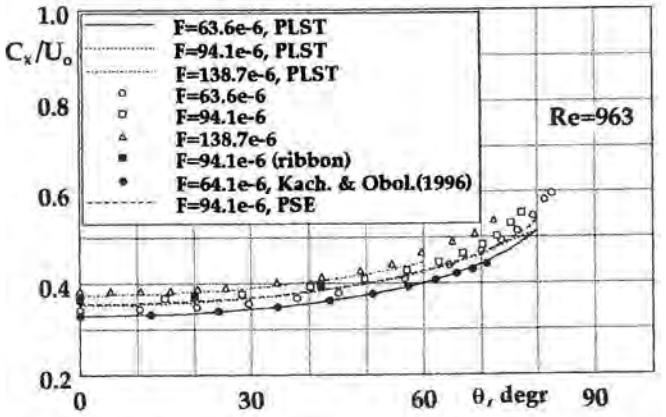

Figure 2: Phase velocity of 3D TS waves versus propagation angle for the Blasius flow.

the subsequent Fourier decomposition) agree very well with those obtained by means of an inclined (or flat) vibrating ribbon; the corresponding points for $\theta = 0$ practically merge in Fig. 1. As was shown by Kachanov & Michalke (1994) the data from the experiments by Gilyov *et al.* (1983) are in a very good agreement with the results by Ross *et al.* (1970) obtained for 2D waves with the help of a vibrating ribbon.

Downstream phase velocities ($C_x = \omega/\alpha_r$), shown in Fig. 2, demonstrate the very good agreement between theories and experiment, especially for angles less than 50°. The PSE results by Hanifi (1995) almost coincide with the PLST data by Michalke (except for very high propagation angles, shown for $F = 94.1 \cdot 10^{-6}$). A very good agreement of the phase velocities obtained by Gilyov *et al.* (1983) with the experimental data by Schneider (1989) is found by Kachanov & Michalke (1994). Note that the Schneider's (1989) results were obtained under completely

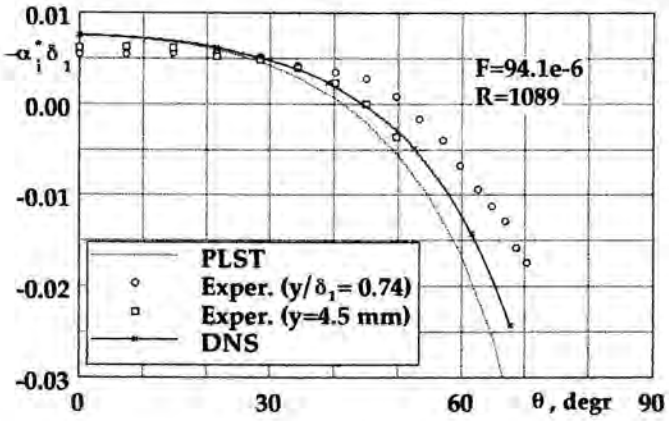

Figure 3: Growth rates of 3D TS waves versus propagation angle. Blasius flow.

different experimental conditions in a water flow, without Fourier decomposition, with excitation of the oblique waves by means of a set of heating elements.

Amplification rates of 3D TS modes in Blasius flow

The comparison of the growth rates $-\alpha_i$ represents a much more complicated problem. Good quantitative agreement for $-\alpha_i$ between the experimental and theoretical values has never been obtained for the flat-plate boundary layer; not for 3D modes, and even not 2D modes. Some typical problems, which arise in this field, were discussed for the 2D instability waves by Fasel & Konzelmann (1990), Bertolotti (1991), Bertolotti *et al.* (1992), and Klingmann *et al.* (1993).

Dependences of nondimensional amplification rates $-\alpha_i\delta_1$ on the propagation angle θ shown in Fig. 3 are obtained in both experiment and theory (the PLST by Michalke and DNS by Ebert, 1995) for the frequency parameter $F = 94.1 \cdot 10^{-6}$ and the Reynolds number $Re = 1089$. It is seen that the theoretical approaches and experiment demonstrate a very similar general behaviour of the growth rates with propagation angle. For not too large values of θ all theories (including the PSE calculations by Hanifi, 1995) are in a rather good agreement with the experiments and with each other. At the same time the theoretical data deviate from the experimental points for high propagation angles. Especially this is true for the PLST results. This is consistent with the theoretical study of Bertolotti (1991) who found that the parallel-flow approach gives lower growth rates, especially for high propagation angles. The experimental data obtained outside the boundary layer (at $y = 4.5$ mm) display better agreement with the PLST and DNS rather than the points measured near the inner disturbance maximum (at $y/\delta_1 = 0.74$). Note that these data are obtained inside the neutral stability curve (for the 2D waves). Very similar results are observed at another value of the Reynolds number ($Re = 1129$) and for the same frequency parameter.

The agreement between the PLST and experiment is better in the vicinity of the lower branch of the neutral stability curve at $F = 63.6 \cdot 10^{-6}$ and $Re = 1071$

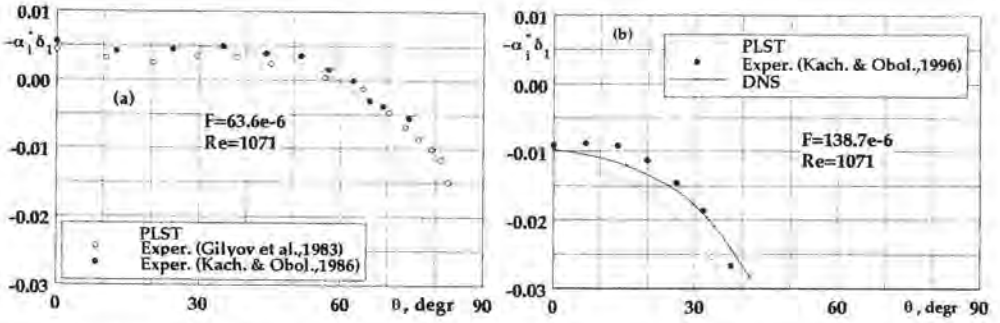

Figure 4: Growth rates of 3D TS waves versus propagation angle for the Blasius flow.

(Fig. 4a). However the PLST (by Michalke) still predicts somewhat lower growth rates for the modes propagated at angles higher than approximately 65°. Near the upper branch, for $F = 138.7 \cdot 10^{-6}$ and $Re = 1071$ (Fig. 4b), the difference between the PLST and the experimental is largest, while the DNS (by Ebert, 1995) predict the experimental growth rates much better.

Non-parallel effects and criteria of instability

There are several causes for the discrepancies between the experimental and theoretical growth rates. One of them is the dependence of the shape of the eigenfunctions on the propagation angle (see Gilyov *et al.*, 1983 and Bertolotti, 1991). The main experimental results presented in Figs 3 and 4 are obtained at a constant nondimensional distance from the wall $y/\delta_1 = 0.74$ that is close to the disturbance maxima but does not coincide with them exactly. Meanwhile the theoretical data (PSE and DNS) are obtained for the exact positions of the maxima. This explains, at least partially, why in the experiments the quasi-2D modes have usually lower growth rates compared even to non- parallel PSE and DNS, whereas the strongly 3D modes have larger growth rates.

The discrepancies, observed between the PLST and experiment, are consistent with the results obtained by Bertolotti (1991) who found that this theory underestimates the growth rates of the 3D modes. This difference increases with the propagation angle. In our recent experiments (Kachanov & Obolentseva, 1996) we found that the growth rates of the 3D modes in the Blasius flow depend significantly on the non-dimensional distance from the wall where they were measured. This dependence (conditioned by the downstream growth of the boundary layer) turned out to be very strong for those perturbations that correspond to the vicinity of the upper branch of the 2D neutral stability curve, it becomes weaker for lower frequency parameters, and it is very weak near the lower branch. This observation is also consistent with the results by Bertolotti (1991).

Similar to the case of the 2D instability waves (see Fasel & Konzelmann, 1990 and Bertolotti *et al.*, 1992) the question about the criteria of instability for the 3D modes needs additional investigation. Depending on the method of definition

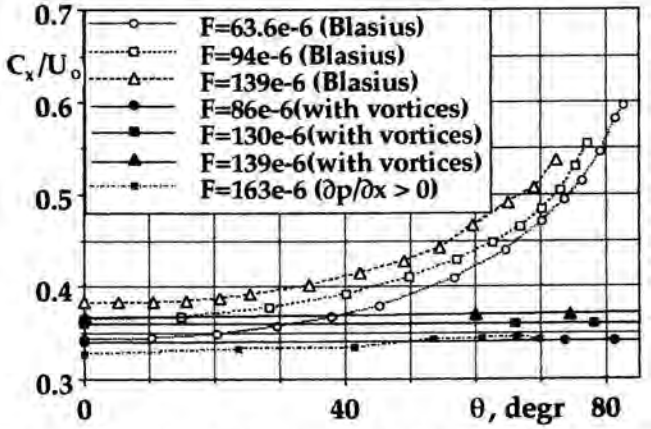

Figure 5: Influence of vortices and pressure gradient on dispersion curves for 3D TS waves.

of the growth rates, the flow can be regarded as stable or unstable with respect to the same 3D wave.

Influence of streamwise vortices in Blasius flow

A first experimental study of the influence of stationary 3D perturbations of the mean flow (the streamwise vortices) on the stability of Blasius boundary layer to 2D and 3D waves was conducted by Kachanov & Tararykin (1987). More recently a similar problem was investigated by Bakchinov *et al.* (1995) for the case of much more intensive streamwise vortices produced by roughness elements.

Kachanov & Tararykin (1987) found that even when the streamwise vortices (introduced into the flow by means of a special slit generator) have amplitudes close to 10 %, they almost do not influence the growth rates of the 2D instability waves and do not lead to a growth of the 3D TS modes although some local mean velocity profiles have inflexion points and are expected to be more unstable than the original Blasius profile. Moreover, it is found that the streamwise vortices even stabilized the flow with respect to the 2D TS waves. This is an evidence that the local notions are not applicable when investigating the boundary-layer instability. Later observations by Bakchinov *et al.* (1995) corroborate this result in a case of not very high amplitudes of the vortices.

Another important observation of the experiments by Kachanov & Tararykin (1987) is that the streamwise vortices influence significantly the dispersion characteristics of the 3D waves. Without these vortices the downstream phase velocity of the 3D modes increases with the propagation angle (see Fig. 2). The vortices are found to result in an almost complete disappearance of the dependence of the phase velocities on the propagation angle (Fig. 5, points "with vortices"). Disappearance of the dispersion can play an important role at late,

weakly nonlinear, stages of transition where some resonant interactions between 2D and 3D instability waves occur.

3D instability of the 2D boundary layer on an airfoil

An experimental study of the 3D instability of a boundary layer on an airfoil at low Reynolds numbers was carried out by Gilyov *et al.* (1988). At the incidence studied the boundary layer was subjected to both favourable and adverse pressure gradients and had a 2D laminar separation point at a distance $x \approx 400$ mm from the leading edge. A localized wave train of TS waves with frequency 85 Hz (the Strouhal number $St = \omega\delta_2/U_o \approx 0.0088$) was introduced into the boundary layer by means of a "point" source similar to that used in experiments by Gaster & Grant (1975) and by Gilyov *et al.* (1983). After Fourier decomposition of the wave train into normal (i.e. harmonic in time and space) oblique modes the stability characteristics of this flow with respect to various 3D waves were obtained.

Growth rates of 3D TS waves on an airfoil

The disturbance behaviour was studied in three different regions of the flow development. In region I the pressure gradient was favourable ($\partial p/\partial x < 0$) and in region II adverse ($\partial p/\partial x > 0$). Region II was subdivided into two subregions II.1 and II.2 that correspond to the flow before and after the separation point.

In region I the flow is found to be stable and all the 3D modes attenuate downstream. In region II.1 all the studied 3D modes are amplified, and the most rapidly growing waves are the two-dimensional ones (qualitatively the same as in the Blasius flow at subsonic speeds, see Figs 3 and 4). At the same time, in region II.2 the most amplified modes are found to be the three-dimensional ones. This phenomenon looks similar to the case of a supersonic boundary layer. A fast growth of the 3D modes leads to a rapid increase of the three-dimensionality within the separation zone observed usually in experiments.

Comparison of the growth rates of the 3D instability modes in region II.2 obtained by Gilyov *et al.* (1988) with some theoretical data is shown in Fig. 6. The growth rates $-\alpha_i\delta_2$ (where δ_2 is the momentum thickness) calculated by Michalke (see Dovgal *et al.*, 1994) within the framework of inviscid PLST are shown in Fig. 6a together with the experimental data. The agreement is rather good. At the same time, the theory does not predict the maximum at $\theta \approx$ 40-45° observed in the experiment. The viscosity does not change this result qualitatively. Comparison with the asymptotic theory by Stewart & Smith (1987), shown in Fig. 6b, somewhat clarifies the question. Stewart & Smith (1987) have shown that the boundary-layer growth influences significantly the amplification rates of the 3D modes. In the region behind the separation point the three-dimensional modes are shown to grow most rapidly when the parameter $-A'$ (a measure of the flow non-parallelism) increases. This fact is consistent

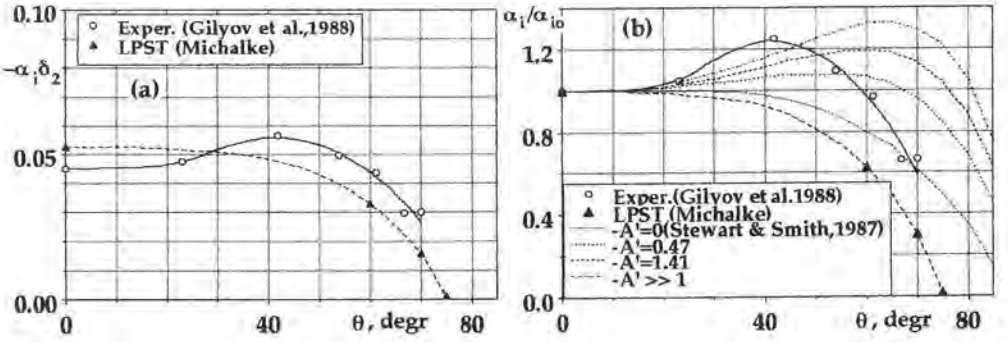

Figure 6: Growth rates of 3D TS waves versus propagation angle for the adverse pressure gradient case.

with the experiment despite the propagation angle of the most amplified modes is somewhat different in the theory.

Dispersion characteristics of 3D TS waves on airfoil

In contrast to the case of Blasius flow it is shown in the experiments by Gilyov *et al.* (1988) that in region II as a whole the streamwise wavenumber is almost independent of the spanwise wavenumber and propagation angle (Fig. 5, "$\partial p/\partial x > 0$"). The dispersion (i.e. the dependence of the phase velocity on the wave angle) disappears when the region of the adverse pressure gradient begins on the airfoil. Meanwhile in region I this dispersion becomes even stronger than in the Blasius flow and, in contrast to region II, it depends significantly on the downstream coordinate and changes together with the local pressure gradient.

Such disappearance of the dispersion of the 3D modes looks very similar to that observed in the Blasius boundary layer disturbed by the streamwise vortices (see Fig. 5, "with vortices"). Most probably, the cause of this phenomenon is the same in the two cases and associated with a prevailing role of the inviscid instability in the flow with inflexional velocity profiles. This instability appears in the two cases under influence of either the streamwise vortices or the adverse pressure gradient. It is well known that the most unstable inviscid modes propagate with the phase speed close to the flow velocity in the inflexion point.

Instability of 3D boundary layer on a swept wing

One of the most important types of instability in 3D boundary layers is the cross-flow instability. Some recent studies of this instability are discussed in reviews by Reed & Saric (1989), Arnal *et al.* (1990), Bippes (1990), Saric (1994) and others. In the transition process on the swept wings both the stationary and traveling cross- flow instability modes play an important role. In the present

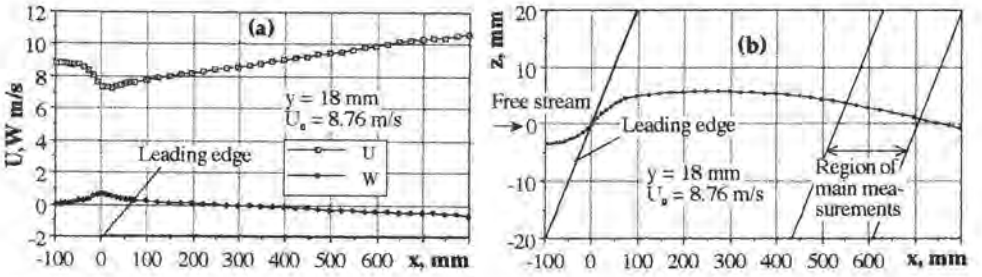

Figure 7: Inviscid-flow velocities (a) and streamline (b) over the swept-wing model.

paper we concentrate on a brief review of some recent experimental results on the cross-flow instability obtained at controlled disturbance conditions.

Experimental conditions and swept-wing mean flow

The mean flow on an initial section of a swept wing was simulated by means of a flow over a model of a swept plate with the pressure gradient induced by a contoured wall bump put onto the test-section wall just above the plate. Both the plate and the bump had the same sweep angle $\chi = 25.0°$. For more details see Kachanov *et al.* (1989) and Kachanov & Tararykin (1990). The main results presented below correspond to a local coordinate system (x^*, z^*) with the x^*-axis directed along the vector U_o of the potential flow near the external edge of the boundary layer. In another coordinate system (x, z) the x-coordinate is parallel to the free-stream velocity and to the axis of the wind-tunnel.

The disturbances were either stationary (the cross-flow vortices) or harmonic in time (the traveling cross-flow waves) and were introduced into the flow by means of several generators. In particular the following disturbance generators were used: (*a*) a steady blowing and suction through a set of slits, (*b*) periodic (along the span) roughness elements, and (*c*) isolated roughness elements. The traveling waves were generated by means of 3 different sources: (*d*) an electromagnetic circular vibrator flush-mounted with the model surface (see for more details Ivanov & Kachanov, 1994a), (*e*) a similar pneumatic vibrator, and (*f*) a linear source consisting of a spanwise slit in the model surface with a system of 83 pipes below it, which are connected to eight loudspeakers. Several frequency parameters were studied: $F \cdot 10^6 = 0$, 7.7, 16.2, 23.8, 35.4, 48.8, 68.6, and 82.4 which correspond to disturbance frequencies: $f = 0$, 3.95, 8.3, 12.15, 18.0, 25.0, 35.0 and 42.0 Hz.

The structure of the 3D mean flow field over the model was measured carefully in both the potential flow and the boundary layer by Kachanov *et al.* (1989, 1990), Kachanov & Tararykin (1990) and Kachanov & Ivanov (1994a, 1994b). It was found that the characteristics of the potential flow over this model are almost independent of the spanwise z'-coordinate in the region of all the main measurements. Downstream distributions of the U- and W-components of the potential flow velocity are shown in Fig. 7a. The shape of the corresponding

streamline of the inviscid flow is shown in Fig. 7b. In the region of the main measurements the pressure-gradient parameter β_H (Hartree parameter) was approximately equal to 0.4 to 0.5, the local yaw angle of the flow was $\chi \approx$ -1 to -2°, the local sweep angle was equal to about 23 to 24°.

The measurements conducted inside the boundary layer and their comparison with calculations by Fyodorov (see Kachanov *et al.*, 1989) testify that the structure of the mean flow over the model (in the region of the main measurements) is almost completely adequate for a swept-wing flow.

Amplification rates of cross-flow modes

The growth rates of both the stationary and traveling cross-flow instability modes were obtained in the experiments by Kachanov *et al.* (1990), Kachanov & Tararykin (1990), Ivanov & Kachanov (1994b) and Gaponenko *et al.* (1995a, 1995b) after decomposition of disturbances to normal oblique modes. Using the linear source f (mentioned above) the author recently obtained (together with colleagues Borodulin & Gaponenko) some stability characteristics of the swept-wing flow directly without the complicated procedure of the Fourier decomposition.

Dependences of the disturbance growth rates on the spanwise wavenumber $\beta^*\delta_1$ are shown in Fig. 8 for two of frequencies studied (including the stationary perturbations). The points were obtained by means of four different methods of disturbance excitation and at several levels of excitation. The lines in Fig. 8a represent the PLST results by Fyodorov (see Kachanov *et al.*, 1990). It is seen that within the experimental accuracy (around ± 0.003) the results obtained for different types and levels of excitation coincide with each other and correlate very well with the results of calculations. Crouch (1994) conducted recently a calculation for the conditions of our experiments for the frequency 18.0 Hz. His curve is also in good agreement with the experimental data.

The results obtained for all values of the frequency parameter show two distinct maxima in the dependences of the growth rate $\alpha_i^*\delta_1$ on the spanwise wavenumber β^*. These maxima are located around $\mid \beta^*\delta_1 \mid \approx 0.4$ - 0.6 and are attributed to the two kinds of instability modes propagated upstream the cross-flow (for $\beta^* > 0$) and along the cross-flow direction (for $\beta^* < 0$). The former mode is the most unstable one. The amplification maxima are localized near very large values of the disturbance propagation angles θ^* with $\mid \theta^* \mid$ between 80 and 90°. This is a very typical property of the cross-flow instability modes predicted by all theories (see for example Dallmann & Bieler, 1987).

Dispersion characteristics and eigenfunctions of cross-flow modes

The dispersion curves (i.e. the streamwise wavenumbers $\alpha_r^*\delta_1$ versus the spanwise wavenumbers $\beta^*\delta_1$) are shown in Fig. 9 for several disturbance frequencies in the case of traveling modes. It is seen that in the coordinate system (x^*, z^*) they are almost symmetric. For all frequencies the typical values of $\alpha_r^*\delta_1$ are

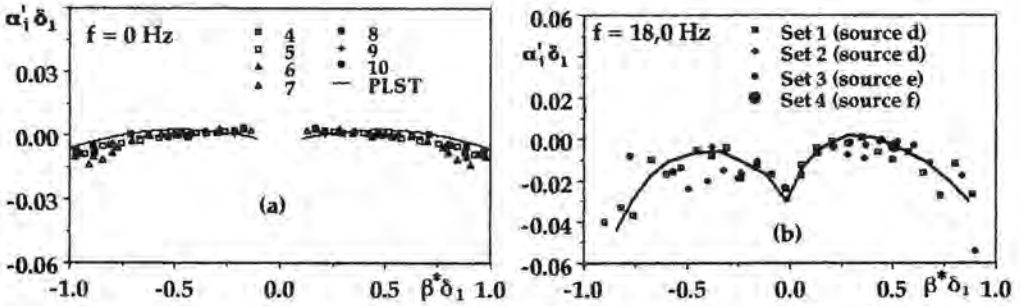

Figure 8: Growth rates of cross-flow instability modes versus spanwise wavenumber.

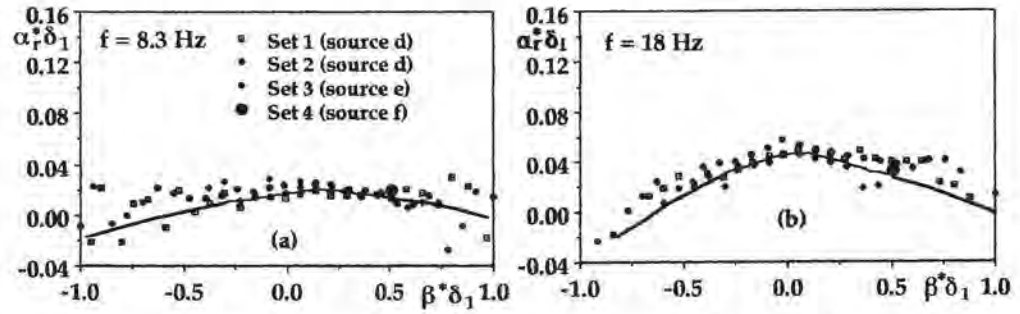

Figure 9: Dispersion curves for cross-flow instability modes.

an order less than those of $\beta^*\delta_1$. The curve obtained for the frequency 25.0 Hz calculated recently by Crouch (1994) for the experimental conditions was found to be in good agreement with the experiment. In the case of stationary cross-flow vortices experimental values of the angles θ^* between the wavevectors of the stationary modes and the x^*-axis were determined. They were found to be almost independent of the spanwise wavenumber. The values of this angle are around 88- 89° and they are in a good agreement with the theoretical results by Fyodorov (see Kachanov *et al.*, 1990) obtained for the experimental conditions.

The eigenfunctions of the cross-flow instability normal modes were also measured by means of two different methods: (i) after spatial Fourier decomposition of the wave trains, and (ii) in direct measurements using the linear source *f*. The shape of the eigenfunctions was shown to agree with the stability theory and confirms the correctness of the choice of wall distances used for the main stability measurements (near the maxima of the u-component of the fluctuations). The phase part of the eigenfunctions of the traveling modes is found to be in a qualitative agreement with the linear stability theory by Takagi & Itoh (1994).

For most unstable traveling modes (with $\mid \beta^*\delta_1 \mid \approx 0.4$ - 0.6) the phase velocities C_k along their wavevectors were found to be very small (around $0.05U_o$, see Fig. 10a). These values are typical for the cross-flow instability waves and observed in theory and in the "uncontrolled" experiment by Deyhle *et al.* (1992). However the quasi-2D modes (with β^* close to zero) propagated with a velocity

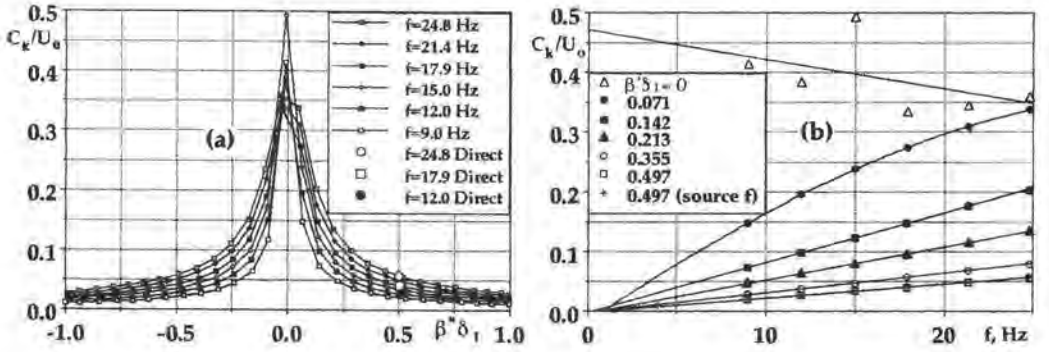

Figure 10: Phase velocities of cross-flow instability modes versus spanwise wavenumber for various frequencies (a) and versus frequency for several spanwise wavenumbers (b).

C_k, which is around 0.3 - 0.6 of U_o. It is interesting that the downstream (along x^*-coordinate) phase velocities C_x^* of almost all the instability modes for all frequencies are rather close to each other and equal to half the edge velocity. Dependences of the phase velocity C_k on the disturbance frequency (Fig. 10b) demonstrate that a limit transition for the dispersion characteristics at $f \to 0$ exists for almost all values of the spanwise wavenumber except for the modes with zero spanwise wavenumber (i.e. with the wave front perpendicular to the flow direction).

The group velocities of traveling modes were determined with the help of the formulas $C_{gx}^* = \partial\omega/\partial\alpha_r^*$ and $C_{gz}^* = \partial\omega/\partial\beta^*$ using the dispersion curves like those shown in Fig. 9. The streamwise component C_{gx}^* of the group velocity vector is found to be rather close to half the free-stream velocity (mainly between 0.4 and 0.8) for almost all modes. (This is very similar to the behaviour of the downstream phase velocity C_x^*.) Meanwhile, the values of the spanwise component of the group velocity vector C_{gz}^* are mainly very small (usually less than $0.05U_o$) and close to the phase velocity C_k of the most unstable modes. The absolute values of the inclination angle ψ_g^* of the group velocity vectors were found to be very small also (mainly less than 5°). (Compare them with the propagation angles of these modes, which are close to $\pm$ 85°!) An inclination angle ψ_g^* of the group-velocity vector for the stationary modes (the cross-flow vortices) was found to be very close to the x^*- axis too. For the most unstable modes the inclination angle is ψ_g^* = -1.0° in experiment and ψ_g^* = -1.6° in theory by Fyodorov (see Kachanov *et al.*, 1990), i.e. a difference between the theory and experiment is less than 1°.

Having reached the end of this section, it is important to note that all the experimental results, obtained by means of different disturbance sources with and without Fourier decomposition, correlate with each other very well and demonstrate the good experimental accuracy and reliability of the data obtained.

Conclusions

- The 3D linear stability theory is still not compared quantitatively in an appropriate way with experimental data, even not in the classic case of the Blasius boundary layer.
- Qualitative agreement between the 3D stability theory and experiment is mainly achieved including the case of traveling waves in the swept-wing boundary layer.
- Non-parallel effects are very significant for the 3D instability even in the Blasius flow. This is in contrast to the case of the 2D instability. Those effects need additional studies, in particular for the 3D boundary layers.
- The problem of 3D instability of 2D boundary layers with pressure gradients (especially those with adverse pressure gradients) needs a more detailed investigation (including non-parallel effects).

Acknowledgements

This work was supported by the Russian Foundation for Basic Research (Grant No 94-01-00062) and the International Science Foundation (Grants No NQY000 and NQY300). The author is greatly indebted to these institutions as well as to his colleagues Dr. O.I. Tararykin, Dr. V.I. Borodulin, A.V. Ivanov, V.R. Gaponenko and T.G. Obolentseva. It would have been impossible to conduct the experiments described above without them.

References

Arnal, D., Casalis, G & Juillen, J.C. 1990 – Experimental and theoretical analysis of natural transition on "infinite" swept wing. In: *Laminar-Turbulent Transition* (D.Arnal and R.Michel eds.), Springer-Verlag, Berlin, pp. 311-325.

Bakchinov, A.A., Grek, G.R., Klingmann, B.G.B. & Kozlov, V.V. 1995 – Transition experiments in a boundary layer with embedded streamwise vortices. *Phys. Fluids.* **7**, 820-832.

Bertolotti, F.P. 1991 – *Linear and nonlinear stability of boundary layers with streamwise varying properties.* PhD thesis. The Ohio State Univ., USA.

Bertolotti, F.P., Herbert T. & Spalart, P.R. 1992 – Linear and nonlinear stability of the Blasius boundary layer. *J. Fluid Mech.* **242**, 441-474.

Bippes, H. 1990 – Instability features appearing on swept wing configurations. In: *Laminar-Turbulent Transition* (D. Arnal and R. Michel eds), Springer-Verlag, Berlin, pp. 419-430.

Crouch, J.D. 1994 – Private communication.

Dallmann, U. & Bieler, H. 1987 – Analysis and simplified prediction of primary instability of three-dimensional boundary layer flows. *AIAA-87-1337.*

Deyhle, H., Höhler, G. & Bippes, H. 1992 – Experimental investigations of instability wave propagation in a 3D boundary-layer flow. *Preprint,* DLR, Inst. Exper. Fluid Mech., Göttingen. (presented to *AIAA Journal.*)

Dovgal, A.V., Kozlov, V.V. & Michalke, A. 1994 – Laminar boundary layer separation: instability and associated phenomena. *Progr. Aerospace Sci.* **30**, 61-94.

Ebert, K.U. 1995 – *Untersuchung nichtparalleler Effekte dreidimensionaler Störwellen.* PhD thesis. (Research adviser U. Rist) Institut für Aerodynamik und Gasdynamik, Universität Stuttgart, Germany.

Fasel, H. & Konzelmann, U. 1990 – Non-parallel stability of a flat plate boundary layer using the complete Navier-Stokes equations. *J. Fluid Mech.* **221**, 311-347.

Gaponenko, V.R., Ivanov, A.V. & Kachanov, Y.S. 1995a – Experimental study of cross-flow instability of a swept-wing boundary layer with respect to traveling waves. In: *Laminar-Turbulent Transition* (R. Kobayashi ed.), Springer-Verlag, Berlin, pp. 373-380.

Gaponenko, V.R., Ivanov, A.V. & Kachanov, Y.S. 1995b – Experimental study of a swept-wing boundary-layer stability with respect to unsteady disturbances. *Thermophysics & Aeromechanics.* **2**, 333-359 (in Russian).

Gaster, M. & Grant, T. 1975 – An experimental investigation of the formation and development of a wave packet in a laminar boundary layer. *Proc. Roy. Soc. London.* **A 347**, 253-269.

Gilyov, V.M., Kachanov, Y.S. & Kozlov, V.V. 1983 – Development of a spatial wave packet in a boundary layer. *Izv. Sib. Otd. Akad. Nauk SSSR, Ser. Tekh. Nauk.* **13**, 27-37 (in Russian). (See also Kachanov, Y.S. 1985, In: *Laminar-Turbulent Transition* (V.V. Kozlov ed.), Springer, pp. 115-123.)

Gilyov, V.M., Dovgal, A.V., Kachanov, Y.S. & Kozlov, V.V. 1988 – Development of spatial disturbances in a boundary layer with pressure gradient. *Izv. Akad. Nauk SSSR, Mekh. Zhidk. i Gaza.* **3**, 85-91 (in Russian).

Hanifi, R. 1995 – Private communication.

Ivanov, A.V. & Kachanov, Y.S. 1994a – A method of study of the stability of 3D boundary layers using a new disturbance generator. In: *International Conference on the Methods of Aerophysical Research. Proceedings. Part 1,* Institute of Theoretical & Applied Mechanics, Novosibirsk, pp. 125-130.

Ivanov, A.V. & Kachanov, Y.S. 1994b – Excitation and development of spatial packets of instability waves in a three-dimensional boundary layer. *Thermophysics & Aeromechanics.* **1**, 287-305.

Kachanov, Y.S. & Michalke, A. 1994 – Three-dimensional instability of flat-plate boundary layers: Theory and experiment. *Eur. J. Mech., B/Fluids.* **13**, 401- 422.

Kachanov, Y.S. & Obolentseva, T.G. 1996 – Development of three-dimensional disturbances in Blasius boundary layer. Part 1. Wave trains. *Thermophysics and Aeromechanics.* **3** (in Russian).

Kachanov, Y.S. & Tararykin, O.I. 1987 – Experimental study of stability of a relaxing boundary layer. *Izv. Sib. Otd. Akad. Nauk SSSR, Ser. Tekh. Nauk.* **18**, 9-19 (in Russian).

Kachanov, Y.S. & Tararykin, O.I. 1990 – The experimental investigation of stability and receptivity of a swept-wing flow. In: *Laminar-Turbulent Transition* (D.Arnal and R.Michel eds.), Springer-Verlag, pp. 499-509.

Kachanov, Y.S., Tararykin, O.I. & Fyodorov, A.V. 1989 – Experimental simulation of swept-wing boundary layer in the region of secondary flow formation. *Izv. Sib. Otd. Akad. Nauk SSSR, Ser. Tekh. Nauk.* **3**, 44-53 (in Russian).

Kachanov, Y.S., Tararykin, O.I. & Fyodorov, A.V. 1990 – Investigation of stability of boundary layer on a model of a swept wing to stationary disturbances. *Izv. Sib. Otd. Akad. Nauk SSSR, Ser. Tekh. Nauk.* **5**, 11-21 (in Russian).

Konzelmann, U. 1990 – *Numerische Untersuchungen zur raumlichen Entwicklung dreidimensionaler Wellen-paket in einer Plattengrenzschichtstromung.* Ph.D. thesis. Universität Stuttgart, Stuttgart.

Klingmann B.G.B., Boiko A.V., Westin K.J.A., Kozlov V.V. & Alfredsson P.H. 1993 – Experiments on the stability of Tollmien-Schlichting waves in the flat-plate boundary layer. *Eur. J. Mech., B/Fluids.* **12**, 493-514.

Reed, H.L. & Saric, W.S. 1989 – Stability of three-dimensional boundary layers. *Annu. Rev. Fluid Mech.* **21**, 235-284.

Ross, J.A., Barnes, F.H., Burns, J.G. & Ross, M.A.S. 1970 – The flat plate boundary layer. Part 3. Comparison of theory with experiment. *J. Fluid Mech.* **43**, 819-832.

Saric, W.S. 1994 – Low-speed boundary-layer transition experiments. In: *Transition: Experiments, Theory & Computations* (T.C. Corke, G. Erlebacher, M.Y. Hussaini eds.), Oxford, pp. 1-114.

Schneider, S.P. 1989 – *Effects of controlled three-dimensional perturbations on boundary layer transition.* PhD thesis. Calif. Inst. of Tech., Pasadena.

Stewart, P.A. & Smith, F.T. 1987 – Three-dimensional instabilities in steady and unsteady non-parallel boundary layers, including effects of Tollmien-Schlichting disturbances and cross flow. *Proc. Roy. Soc. London.* **A 409**, 229- 248.

Takagi, S. & Itoh, N. 1994 – Observation of traveling waves in the three-dimensional boundary layer along a yawed cylinder. *Fluid Dyn. Research.* **14**, 167-189.

Author's address

Institute for Theoretical and Applied Mechanics
Russian Academy of Science
630090 Novosibirsk, Russia

B.F.A. van Hest, H.F. Groenen & D.M. Passchier

Nonlinear Development and Breakdown of TS-waves in an Adverse Pressure Gradient Boundary Layer

Abstract

The *natural* transition process in boundary layers subjected to an adverse pressure gradient (APG) and low free stream turbulence intensities has been studied experimentally using hot-wire anemometry. The initial growth of Tollmien-Schlichting waves is shown to agree with linear stability theory. The TS-wave amplitude distribution across the boundary layer shows two near-wall maxima. The nonlinear development of the Tollmien-Schlichting waves is shown to be of a combined resonance, with fundamental resonance observed at the first near-wall maximum and subharmonic resonance at the second maximum. Breakdown to turbulence occurs at the second near-wall maximum. The streamwise intermittency distribution is found to follow Narasimha's universal intermittency distribution, while Klebanoff's fit in normal direction needs a modification.

Introduction

The transition from laminar to turbulent boundary layer flow, subject to small free stream disturbances, begins with the generation of instability waves, known as Tollmien-Schlichting waves, in the boundary layer. After a region of exponential growth the waves reach a finite amplitude and nonlinear processes set in. These processes lead to a local breakdown of the flow and the formation of turbulent spots. The length of the transition region is determined by the growth rate of the turbulent spots.

Although linear amplification and subsequent nonlinear processes have been verified extensively for zero pressure gradient (ZPG) flow (see e.g. Klingmann *et al.*, 1993 and Kachanov & Levchenko, 1984), stability data for flow with adverse pressure gradients is still scarce. Recent experiments (Gostelow *et al.*, 1995, van Hest *et al.*, 1995) have shown that an adverse pressure gradient dramatically increases the spot growth rates.

This paper presents the later stages of development and subsequent breakdown of natural TS-waves in a low-speed boundary layer with adverse pressure gradient. We will focus on the growth of the TS-waves and their sub- and higher harmonics, the break-down position and the subsequent growth of turbulent spots in the transition region. The obtained experimental data can be used

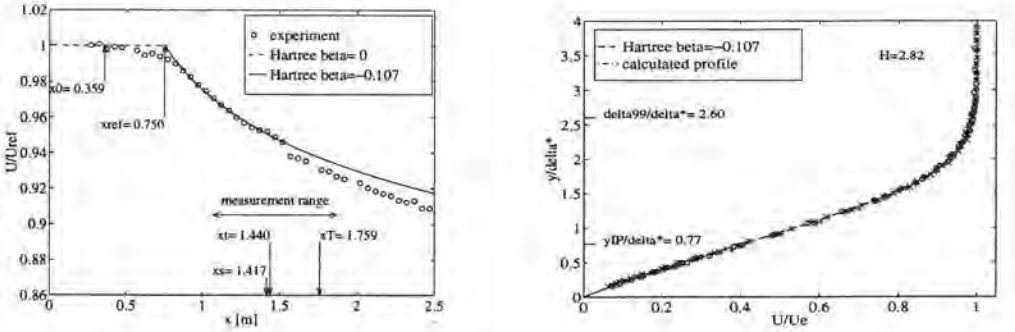

Figure 1: Comparison between measured and Hartree $\beta = -0.10$ pressure distribution (left). Measured and Hartree $\beta = -0.10$ velocity profiles (right).

to develop more accurate models for the prediction of the transition onset and transition length of boundary layers along aircraft fuselage and wings.

Experimental procedure

The measurements were conducted on the flat test wall of a closed return wind tunnel. Different pressure gradients can be imposed by the flexible wall opposite of the test wall. The imposed pressure gradient (Fig. 1 left) varied from nearly neutral over the first 0.75 m, to Hartree $\beta = -0.107$ further downstream. The laminar velocity profiles (Fig. 1 right), measured in between $1.070 \leq x \leq 1.320$ m, have a shape factor $H = 2.82 \pm 0.04$, which corresponds to a Falkner-Skan profile with $\beta = -0.107$. The reference velocity was $U_{ref} = 10$ m/s, measured at $x_{ref} = 0.27$ m, and the free stream turbulence level was $Tu = 0.09$ %.

Velocity measurements were performed with Constant Temperature Anemometers with both single and cross hot-wires. At each position at least 1.2×10^5 samples, depending on the local turbulence intensity in the boundary layer, were taken at a sampling rate of $f_s = 4000$ Hz.

Tollmien-Schlichting wave development

Linear growth

The power spectral density was calculated from the discrete time series of the fluctuating velocity signal using the Fast Fourier Transform algorithm and the Welch averaging method. The power spectral density $P(f)$ is defined such that

$$\overline{u^2} = \int_0^\infty P(f)df. \tag{1}$$

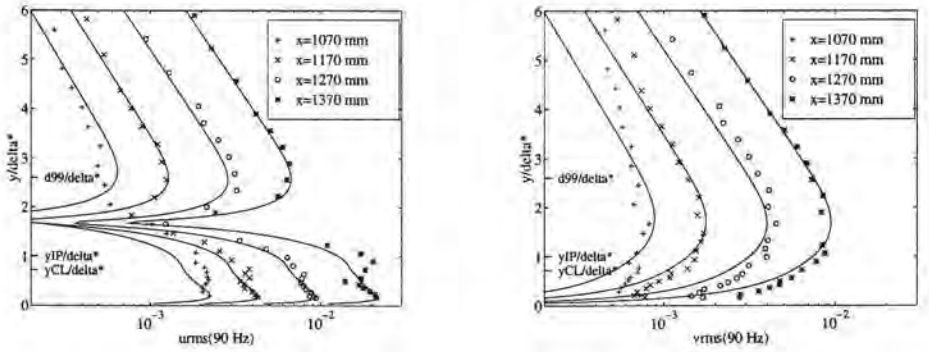

Figure 2: Measured and calculated TS-wave amplitude distributions at four streamwise positions in the frequency band of the most amplified TS-wave.

The velocity spectra showed a broad maximum in the frequency range between 50 and 130 Hz, with three discrete peaks (probably caused by larger initial background disturbances) at $f = 69$ Hz, $f = 90$ Hz and $f = 109$ Hz. This frequency range corresponds to the most amplified Tollmien-Schlichting waves according to linear stability theory. In the remainder of this paper, we will consider only the central maximum at $f = 90$ Hz. The development of the amplitude distribution of the streamwise and normal velocity fluctuations in the frequency band 90 ± 2 Hz is presented in Fig. 2. All the experimental amplitude distributions of the streamwise component of fluctuating velocity show a second near-wall maximum located at $y/\delta^* \approx 0.9$ (close to the critical layer and the inflexion point in the velocity profile). This second near-wall maximum is not present in the eigen functions calculated on the basis of linear stability theory (shown by the solid lines). In an earlier experiment with an APG boundary layer (see Wubben *et al.*, 1990), it was suggested that the second maximum was due to the effect of nonlinear interactions but no supporting evidence was given. Linear stability calculations for oblique Tollmien-Schlichting waves (Rist, 1996) show that three-dimensional TS-waves have a maximum at the position of the second near-wall maximum. Therefore, the experiments suggest that both two-dimensional and three-dimensional Tollmien-Schlichting waves are present in our flow at the same time.

The amplitude growth of the TS-wave and its subharmonic and higher harmonics were followed in the streamwise direction at the height of the first and second near-wall maxima (see Fig. 3). The growth of the TS-waves at both near-wall maxima agrees well with linear stability theory (solid line) up to $x = 1.320$ m, which is approximately two TS-wavelengths upstream of the onset of transition. At the first maximum both the subharmonic and second harmonic grow rapidly downstream of $x = 1.220$ m, where the rms-value in the 90 Hz-frequency band has an amplitude of 0.1 % of the edge velocity. At the second maximum, the subharmonic grows continuously from the first measurement position at $x = 1.070$ m with an enhanced growth downstream of $x = 1.270$ m (where

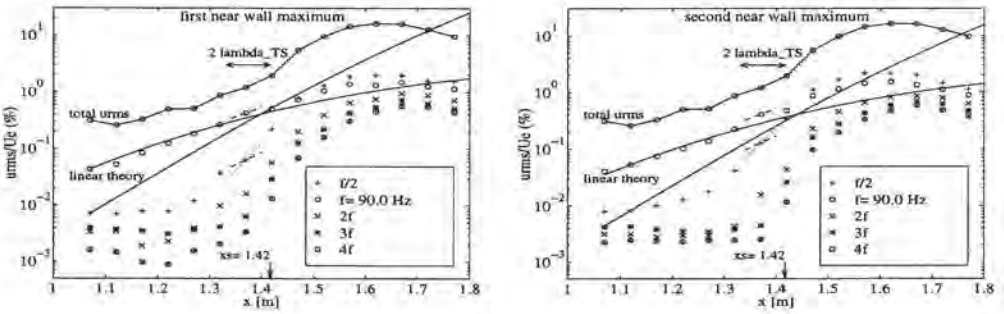

Figure 3: Amplitude of the subharmonic, fundamental and higher harmonics at the first near-wall maximum (left) and second near-wall maximum (right).

$u_{rms}(90\text{ Hz})/U_e = 0.1\ \%$). Although the subharmonic modes are unstable, their amplification rate is much smaller than predicted by linear theory (solid line). Secondary instability calculations for subharmonic resonance (Rist, 1996) performed for a 2D base profile and 2D eigenfunctions with $A_{rms}/U_e = 0.7\ \%$ (at $x = 1.370\ m$) and oblique subharmonic waves with $\phi = 60°$ provide the correct growth rate (dotted line). It must be noted, however, that the actual propagation angle of the oblique subharmonic waves in this experiment is unknown.

Tollmien-Schlichting wave resonance

Nonlinear interactions between Tollmien-Schlichting waves with the fundamental frequency and oblique subharmonics or oblique fundamental waves can be regarded as a form of three-wave interaction which causes a constant phase difference between the waves involved. As the present experiment considers natural Tollmien-Schlichting wave growth, in contrast with vibrating-ribbon experiments, there is no direct method to determine whether a constant phase difference between the different frequencies exists. Therefore, the use of bispectral analysis (see Corke, 1987) has been adopted to determine nonlinear interactions between different waves. The bispectrum $B_u(f_1, f_2)$ is defined as

$$B_u(f_1, f_2) = E\left[\tilde{u}(f_1)\tilde{u}(f_2)\tilde{u}^*(f_1 + f_2)\right], \tag{2}$$

with $\tilde{u}(f)$ the Fourier transform, $\tilde{u}^*(f)$ its complex conjugate and $E[\ ]$ the expectation operator. Because the velocity signal is a real signal and auto-bispectra are calculated, a number of symmetry relations can be used to reduce the frequency plane for which the bispectrum is calculated to the area given by

$$\begin{array}{lll} 0 & \leq f_2 & \leq \frac{1}{4} f_s \\ f_2 & \leq f_1 + f_2 & \leq \frac{1}{2} f_s - f_2. \end{array} \tag{3}$$

The physical interpretation of the bispectrum is that it measures the degree of energy-transfer between to waves of frequencies f_1 and f_2, by which a third wave is generated with the sum or difference frequency $f_3 = f_1 \pm f_2$. Because the amplitude of the Tollmien-Schlichting waves, and as a consequence the absolute value of the energy transfer, changes in streamwise direction it is more interesting to determine the normalized bispectrum, called the bicoherence spectrum or bicoherence. The bicoherence is defined as a measure for the degree of phase locking between two waves.

$$b_u^2(f_1, f_2) = \frac{|B_u(f_1, f_2)|^2}{E\left[|\tilde{u}(f_1)\tilde{u}(f_2)|^2\right] E\left[|\tilde{u}^*(f_1 + f_2)|^2\right]}, \tag{4}$$

with $0 \leq b_u^2 \leq 1$. A bicoherence of one indicates a quadratic interaction between a frequency pair (f_1, f_2), resulting in a third wave with sum or difference frequency f_3. For values in between zero and one a partial interaction takes place, which means that part of the waves with frequency f_3 are caused by the quadratic interaction, whereas the rest are spontaneous oscillations. A value of zero at a frequency pair (f_1, f_2) means that no phase relationship between those frequencies is present. Because of the presence of noise in experimental signals, the bicoherence will always be in the range between zero and one. We will speak of quadratic interactions when the bicoherence lies above the mean noise level plus one standard deviation in the noise level, which is calculated in a part of the frequency plane without interactions. We will present the bicoherence spectra, with the frequency f_1 fixed (at the Tollmien-Schlichting frequency and its sub- or higher harmonic), as a function of the second frequency f_2.

Special attention must be given to interpreting the bicoherence spectra. When a high bicoherence is observed at (f_1, f_2), three possible interactions could have taken place, namely (i) the sum or difference frequency results from the interaction between f_1 and f_2, (ii) f_1 interacts with the sum or difference frequency to give f_2, or (iii) f_1 is the result of interaction between f_2 and the sum or difference frequency. When the origin of a mode is known, like in the present case where the TS-frequency is known from linear stability theory and frequency spectra, this is not a problem. In other cases the order of interacting frequencies has to be determined from the streamwise development of the bicoherence.

From $x = 1.270$ m to 1.420 m the bicoherence spectra (see Fig. 4) show a phase locking between the fundamental frequency $f_1 = 90$ Hz and its harmonics f_1, $2f_1$, $3f_1$, etc at the first near-wall maximum. Further, a resonance is found between two of the three discrete frequencies in the velocity spectra, i.e. interactions between $f_1 = 90$ Hz and $f_2 = 69$ Hz take also place. These interactions produce high levels of bicoherence at (f_1, f_2), $(f_1 + f_2, f_2)$ and $(2f_1, f_2)$. A subharmonic resonance is displayed at the second maximum. At the first streamwise position, the same interactions are found as in the case of the fundamental resonance. Further downstream, maxima in the bicoherence appear at $(\frac{1}{2}f_1, \frac{1}{2}f_1)$, $(\frac{1}{2}f_2, \frac{1}{2}f_2)$ and at $(f_1 - f_2, \frac{1}{2}f_2)$ and $(f_1 - f_2, \frac{1}{2}f_1)$. One TS-wavelength before breakdown, the bicoherence becomes larger at higher frequencies up to approxi-

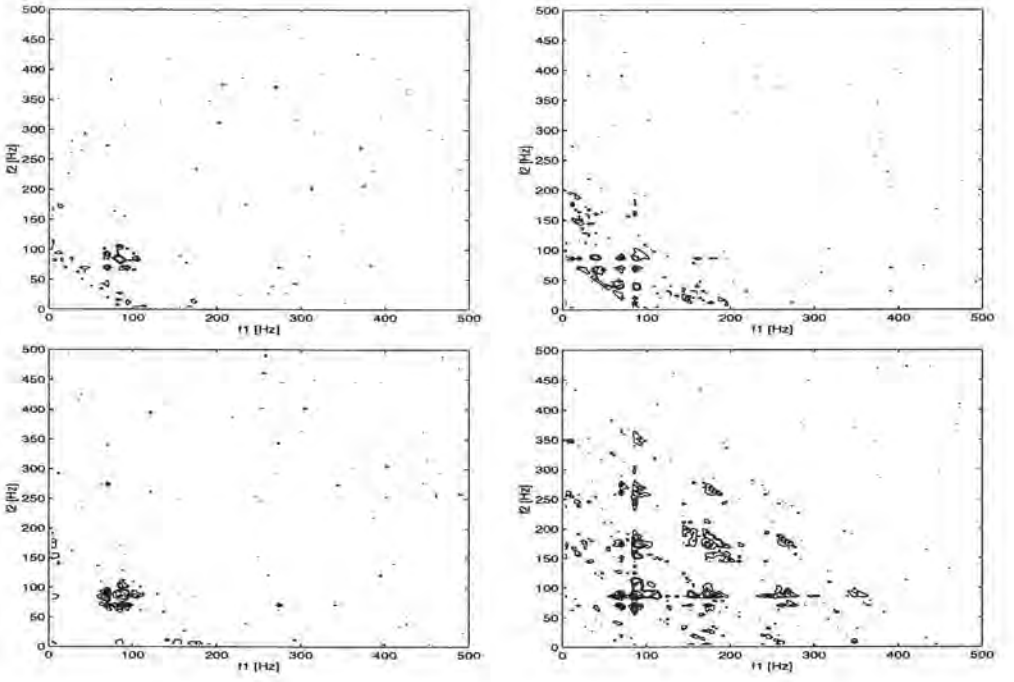

Figure 4: Streamwise development of the bicoherence spectra at the second (upper graphs) and first (lower graphs) near-wall maximum, at $\Delta x = 2\lambda_{TS}$ and $\Delta x = \lambda_{TS}$ upstream of transition onset and at transition onset.

mately $4f_1$. In the transition region the bicoherence continues to spread to higher frequencies but the absolute value of the bicoherence is reduced drastically, first at the lowest frequencies and next for the complete frequency domain.

From the above mentioned results we believe that the measured secondary instability of the TS-waves is of a mixed type, in which both the higher harmonics and subharmonics are amplified through a phase-locking mechanism. This mechanism differs for different positions in the boundary layer.

Breakdown and intermittency

At $x = 1.420\ m$ the TS waves break up and natural turbulent spots appear at approximately the height of the inflexion point. The turbulent spots were detected by comparing a *detection function*, taken as the short time average of $|d^2u/dt^2|$, with a threshold level. Next, the velocity record was divided into laminar and turbulent regions. The fraction of time that the flow is turbulent, i.e. the intermittency γ, is shown in Fig. 5 left across the boundary layer. Klebanoff (1956) presents the following fit to the intermittency distribution for

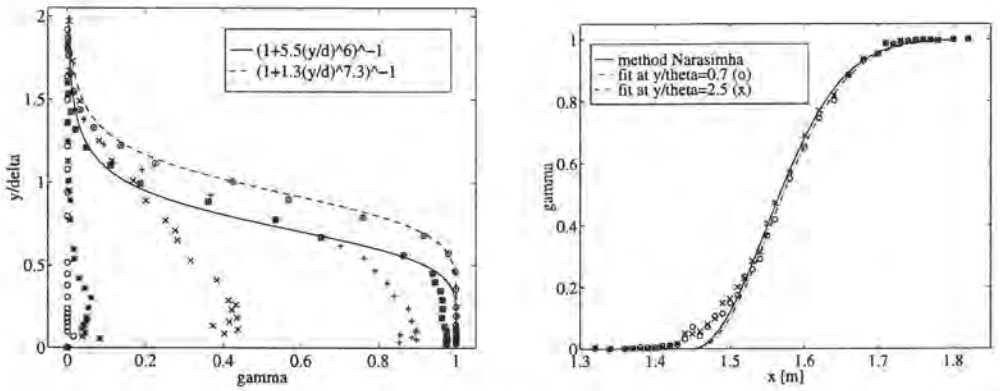

Figure 5: Intermittency distribution across the boundary layer (left graph) in the transition region and initial turbulent boundary layer at $x = 1.370(\bigcirc)$, $x = 1.470(*)$, $x = 1.570(\times)$, $x = 1.670(+)$, $x = 1.770(\otimes)$ and $x = 1.870\ m(\odot)$. Intermittency in streamwise direction (right graph), measured at two wall distances ($y/\delta^* = 0.2$ & $y/\delta^* = 0.9$).

(*fully developed*) ZPG turbulent boundary layers

$$\gamma(y) = \left[1 + c_1 \left(\frac{y}{\delta}\right)^{c_2}\right]^{-1}, \tag{5}$$

with $c_1 = 5.5$ and $c_2 = 6$. A modification is necessary to fit this relation to our APG *turbulent* boundary layer (at the, last, *turbulent* stations). New values are given by $c_1 = 1.3$ and $c_2 = 7.3$. It must be remarked that these values depend on the definition of the boundary layer thickness (which is not given by Klebanoff). A second explanation for the difference may be the short distance between the turbulent stations and the end of transition.

Through the transition region the intermittency increases from zero at onset to one in the turbulent boundary layer (shown in Fig. 5 right at the wall distance of the two near-wall maxima in the Tollmien-Schlichting wave amplitude distribution). The curve follows the 'universal' intermittency distribution as proposed by Narasimha, except at the beginning, which is possibly due to the large negative spikes in the velocity signal prior to breakdown. This gives high values of $|d^2u/dt^2|$ and therefore causes an early detection of small patches of 'turbulence'. Narasimha's 'universal' intermittency distribution is given by

$$\gamma(x) = 1 - \exp\left[-n_t\sigma\frac{(x - x_t)^2}{U_e}\right], \tag{6}$$

with $n_t\sigma = 0.411\frac{U_e}{\lambda^2}$, x_t the start of transition and $\lambda = x_{\gamma=0.75} - x_{\gamma=0.25}$ a characteristic parameter for the length of the transition region. A fit of equation 6 to the experimental data with $n_t\sigma$ given by a relation for the spot formation

and growth, $n_t\sigma = n_t \tan\alpha(U_e/U_{te} - U_e/U_{le})$ (see Chen & Thyson, 1971), results in a spot formation rate $n_t = 1.05 \times 10^3$, a spanwise growth $\alpha = 16.5°$ and trailing edge velocity[1] $U_{te}/U_e = 0.38$. These values agree well with results from a triggered turbulent spot experiment with the same local pressure gradient (see van Hest, 1995). This result gives confidence in models for the length of the transition region based on experiments with triggered turbulent spots.

Conclusions

- Linear stability theory provides a good prediction of TS-wave growth.
- In the present experiments both 2D and 3D TS-waves seem to be present in the flow, resulting in measured TS-wave amplitude distributions with two near-wall maxima.
- Phase-locking between fundamental and higher harmonics and between fundamental and subharmonics is observed respectively at the first and second near-wall maxima of the TS-wave amplitude distribution.
- Breakdown to turbulence occurs at the second near-wall maximum.
- The normal intermittency distribution in APG flow needs a modification compared to Klebanoff's definition. This may depend on either the definition of the boundary layer thickness or the 'state-of-development' of the turbulent boundary layer.
- The streamwise intermittency distribution agrees with Narasimha's universal distribution. A fit to the experimental intermittency provides spot propagation parameters in agreement with triggered spot experiments.

References

Chen, K.K. & Thyson, N.A. 1971 – Extension of Emmons' spot theory to blunt bodies, *AIAA* **9**, 821-825.

Corke, T.C. 1987 – Measurements of resonant phase locking in unstable axisymetric jets and boundary layers, *Non-linear Wave Interactions in Fluids*, volume 87 of *AMD*, 37-65.

Gostelow, J.P., Melwani, N., Solomon, W.J., & Walker, G.J. 1995 – Effects of a self-similar adverse pressure distribution on turbulent spot development, *AIAA* **95-2254**.

Hest, B.F.A. van, Passchier, D.M., & van Ingen, J.L. 1995 – The development of a turbulent spot in an adverse pressure gradient boundary layer, IUTAM symposium *Laminar-Turbulent Transition* Sendai, Japan, pp. 255-262.

Kachanov, Y.S. & Levchenko, V.Y. 1984 – The resonant interaction of disturbances at laminar-turbulent transition, *J. Fluid Mech.* **138**, 209-247.

[1]It has been shown that the leading edge velocity ($U_{le}/U_e = 0.89$) is almost constant.

Klebanoff, P.S. 1956 – Characteristics of turbulence in a boundary layer with zero pressure gradient, NACA *Technical Report* TN 3178.

Klingmann, B.G.B., Boiko, A.V., Westin, K.J.A., Kozlov, V.V. & Alfredsson, P.H. 1993 – Experiments on the stability of Tollmien-Schlichting waves, *Eur.J.Mech., B/Fluids* **12**, 493-514.

Rist, U. 1996 private communication, Universität Stuttgart, Germany.

Wubben, F.J.M., Passchier, D.M. & van Ingen, J.L. 1990 – An experimental investigation of Tollmien-Schlichting instabilities in an adverse pressure gradient boundary layer, IUTAM Symposium *Laminar-Turbulent Transition* Toulouse, France, 31-42.

Authors' address

Delft University of Technology
Faculty of Aerospace Engineering
Kluyverweg 1
2629 HS Delft, The Netherlands

S. Bake °, Y.S. Kachanov ▷ & H.H. Fernholz °

Subharmonic K-Regime of Boundary-Layer Breakdown

Abstract

The paper is devoted to an experimental study of the nonlinear stages of the laminar-turbulent transition of a 2-D boundary-layer flow close to the Blasius flow. The possibility of a realization of some phenomena typical for the K-regime of boundary-layer transition initiated by subharmonic resonance at very late but still deterministic stages of the N-regime of transition are investigated. A novel disturbance source was used for the generation of instability waves of the necessary frequency and spanwise wavenumber spectrum. In the main part of the measurements (case I) the generator introduced a large-amplitude 2-D fundamental instability wave and a pair of low-amplitude oblique subharmonics with spanwise wavenumbers $\pm\beta_{1/2}$. The phase angle between the fundamental and the subharmonic waves was chosen to be favourable for the subharmonic resonance. In this case the transition process is found to begin with a rapid resonance growth of the subharmonic modes typical for the N-regime of transition. However at late stages of the disturbance development the local behaviour of the perturbations at the tips of the Λ-structures is very similar to the K-regime of breakdown with the formation of coherent structures associated with spikes in the time-traces of the hot-wire signal. A row of consecutive spikes appeared coinciding with the streamwise spacing of the subharmonic wavelength but their properties were found to be qualitatively the same as those usually observed in the K-regime.

Introduction

The nonlinear stage of the laminar-turbulent transition process in a boundary-layer is the last phase before the final randomisation and breakdown to turbulence. In contrast to the preceding linear stage many aspects of the last stage are still unclear. In a relatively short region where the disturbances reach amplitudes of the order of 1-2% of the free-stream velocity the flow transforms rapidly from a deterministic laminar flow into a stochastic turbulent one. Recent progress in the understanding of the nonlinear phase is associated with the recognition of the importance of resonance phenomena (for an overview see Kachanov, 1994).

Two main regimes of the 2-D boundary-layer breakdown have been identified. First the K-regime (after Klebanoff *et al.*, 1962) and second the N-regime (new or Novosibirsk). The former is induced by a fundamental wave with an amplitude modulation in spanwise direction leading to the formation of 'peaks' and 'valleys'

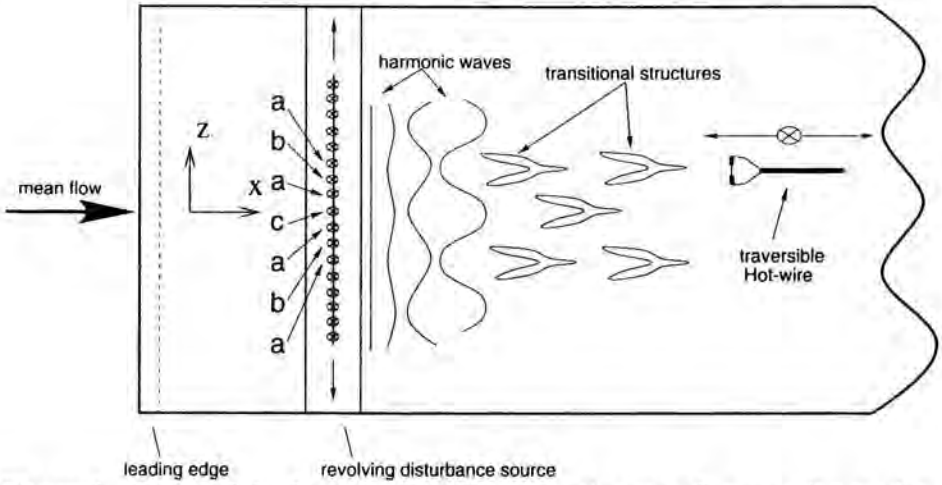

Figure 1: Sketch of the flow phenomena in the axisymmetric measuring section.

in the disturbance distribution and the formation of Λ-vortices in an aligned order (Saric *et al.*, 1984). The most characteristic feature of the K-regime is the appearance of spikes, i.e. of low speed flashes, at late stages attributed to ring-vortices snatched away from the tip of the Λ-vortices (see Hama & Nutant, 1963; Borodulin & Kachanov, 1993; Rist & Kachanov, 1995).

The N-regime is initiated by the interaction of a 2-D fundamental wave and a pair (or more) of oblique subharmonic waves (Kachanov *et al.*, 1977; Kachanov & Levchenko, 1984). The phase angle between them has to be favourable for a parametric resonance which leads to a rapid amplification of the subharmonic amplitude and to the formation of Λ-vortices in a staggered order. The breakdown of the Λ-vortices in the N-regime is characterised by a gradual broadband filling of the disturbance spectrum but the formation of spikes as in the K-regime has not been observed experimentally (e.g. Corke & Mangano, 1989). However, Laurien & Kleiser (1989) indicated the possibility that the breakdown of Λ-vortices in the N-regime can probably occur in the same way as in the K-regime if the initial amplitude of the subharmonic is high enough (for discussion see also Kachanov, 1994).

Experimental set-up and procedure

The experiment was conducted in the Laminar Wind Tunnel of the Hermann-Föttinger-Institute in Berlin. It is a closed-circuit tunnel with an axisymmetric test section made of Plexiglas tubes with an inner diameter of 441 mm and a total length of 6000 mm. The boundary-layer of the nozzle is blown out and the boundary-layer under investigation develops downstream at the elliptic leading edge of the test section. All measurements are made at the inner wall of the Plexiglas tube as illustrated in Fig. 1.

A ring shaped disturbance source (based on the experimental experience of Gaponenko & Kachanov, 1994) was inserted between the measurement sections

to excite the flow. The source consists of a slit in the wall with 0.5 mm width and 260 mm length in spanwise direction. The slit is connected to loudspeakers via 32 plastic tubes with a spanwise spacing of 8 mm. Time-periodic volume fluctuations are produced by an excitation system consisting of a micro-computer, DA-converters, amplifiers and loudspeakers. The ring with the disturbance source can be rotated to vary the spanwise position (z-direction) relative to the hot-wire probe.

A constant-temperature hot-wire anemometer with linearizer was used to measure the streamwise component of the time-mean and fluctuation velocities U and u. The hot-wire of 5 μm diameter and 1 mm active length is mounted on an x-y traverse. The hot-wire signal is sampled and analysed with a Tektronix Fourier analyser in a way that phase locked ensemble averaged or instantaneous time-series triggered by the excitation signal were stored. The amplitude and phase values of the waves were determined by a Fourier transformation of the time series.

The free-stream velocity U_∞ was fixed at 7.2 m/s resulting in a Reynolds number of $Re_{\delta 1}$=785 at the position of the disturbance source (x=547 mm, Δx = 0 mm). The mean flow distribution $U(y)$ in the boundary-layer was close to that of a Blasius profile despite the slight favourable pressure gradient due to the growth of the boundary layer in the test section. The free-stream turbulence intensity was below Tu_∞=0.08% in a frequency range between 0.1 and 1000 Hz.

The boundary-layer was excited through the slit in the wall with a two-dimensional fundamental wave and/or a pair of three-dimensional oblique subharmonic waves. The fundamental frequency was f=62.5 Hz corresponding to a nondimensional frequency parameter $F = 2\pi f\nu/U_\infty^2 = 115.5 \cdot 10^{-6}$ at the position of the source. The subharmonic spanwise wavenumber was
$\beta_{1/2} = \pm 2\pi/32$ mm $= \pm 0.196$ rad/mm.

Four cases of excitation were investigated:

Case I : A 2-D fundamental instability wave with large amplitude A_1 and phase angle φ_1 and a pair of oblique subharmonics with low amplitudes $A_{1/2}$, phase angle $\varphi_{1/2}$ and spanwise wavenumber $\pm\beta_{1/2}$. The phase angle between the fundamental and the subharmonic waves was chosen to be favourable for subharmonic resonance according to earlier measurements (Kachanov & Levchenko, 1984).

Case II : Only the pair of oblique subharmonic waves with the same spanwise wavenumber $\pm\beta_{1/2}$ and the same low amplitude as in case I.

Case III : Only the 2-D fundamental wave with the same amplitude as in case I.

Case IV : The same as case I but with the phase angle between the fundamental and the subharmonic waves opposite to the resonant case.

The initial conditions at 50 mm downstream of the source are shown in Fig. 2.

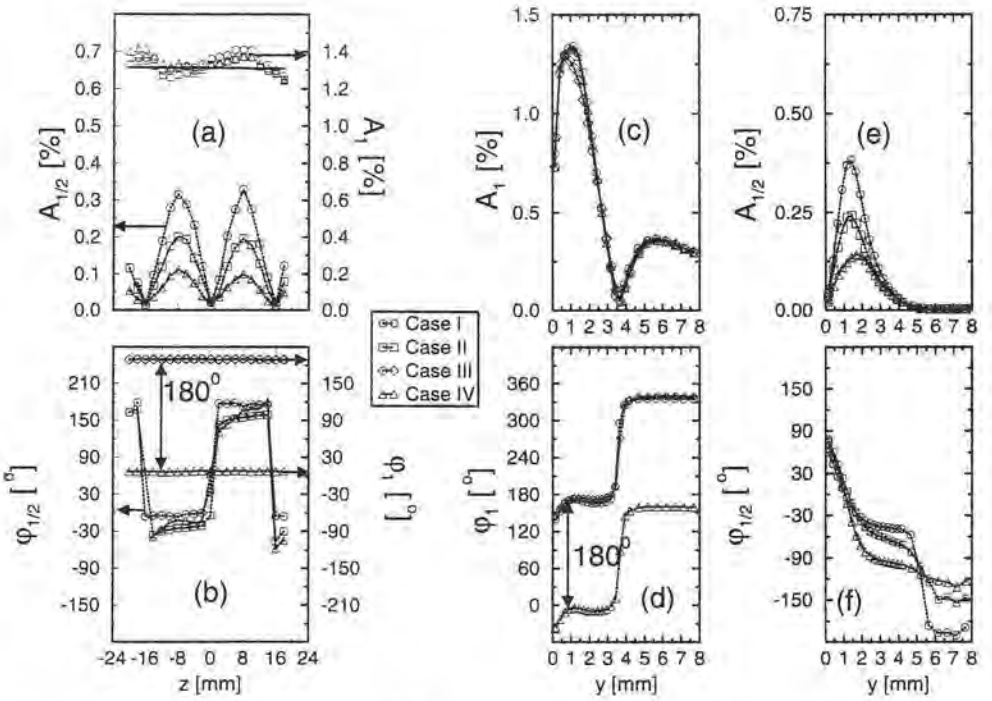

Figure 2: Initial Conditions of the excitation at 50 mm downstream of the source. (a),(b) spanwise distribution. Amplitude (c) and phase (d) of the fundamental wave. Amplitude (e) and phase (f) of the subharmonic wave.

Experimental results

The downstream development of the instability waves is shown in Fig. 3. In case I an exponential growth of the 3-D subharmonic waves was observed and the phase angles (calculated in degrees of the fundamental period) of the fundamental and the subharmonic waves show a synchronisation i.e. they have the same phase-velocity. This is the main condition for the existence of three-wave nonlinear resonance and in particular of the parametric resonant amplification (Craik, 1971; Herbert, 1984).

In case II the subharmonic amplitude decreases downstream according to linear stability theory (outside the neutral stability curve).

The fundamental amplitude in case III behaves in the same way as in case I and IV. This shows that it is not influenced by the nonlinear interaction with the subharmonic wave and plays only a 'catalytic' role in the whole process (e.g. Herbert, 1988; Kachanov, 1994).

In case IV when the initial phase shift between the fundamental and the subharmonic wave was introduced opposite to the resonant case (I) the amplitude of the subharmonic attenuates initially even faster than in case II. This is followed by a slight growth of the subharmonic amplitude probably because

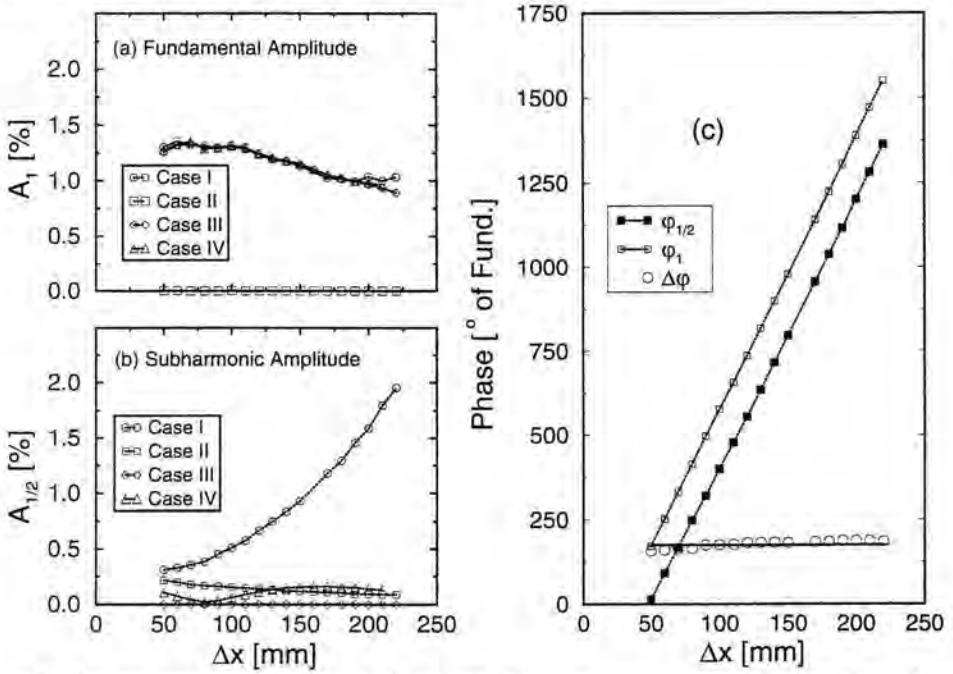

Figure 3: Downstream development of the instability waves at a spanwise position where the subharmonic amplitude has a maximum and at y/δ_1=0.7. (a), (b) Amplitudes. (c) Phase angles.

of an amplification of a very small but remaining resonant component of the subharmonics.

The resonant growth of the subharmonic waves results in an intensive spanwise modulation of the flow with formation of 'peaks' and 'valleys' with a spanwise distance $\pi/\beta_{1/2}$. In Fig. 4 the typical Λ-shaped disturbance structure can be seen in a staggered order characteristic of the N-regime or subharmonic type of boundary-layer breakdown. The Λ-vortices are inclined to the wall and show strong vorticity concentration in the "legs" and at the "tip". Thus until this stage of the transition development we find all typical attributes of the N-regime of breakdown which are well known from previous experimental and theoretical studies. At the same time, the subsequent development of disturbances turned out to be qualitatively the same as in the K-regime. In particular as shown in Fig. 5, in the peak positions the first, second, third and so on 'spike', and other phenomena typical for the K-regime (Klebanoff*et al.*, 1962) were observed further downstream. No significant differences in the disturbance behaviour near the peak position were found between this late stage of the N-breakdown and the corresponding stage of the K-breakdown except for the order of the Λ-structures and the frequency of their passing by. Consequently, we can speak of a "convergence" of mechanisms of the N- and K-breakdown at late stages of disturbance development, meaning a qualitative similarity of the local process near the planes of symmetry of the Λ-structures.

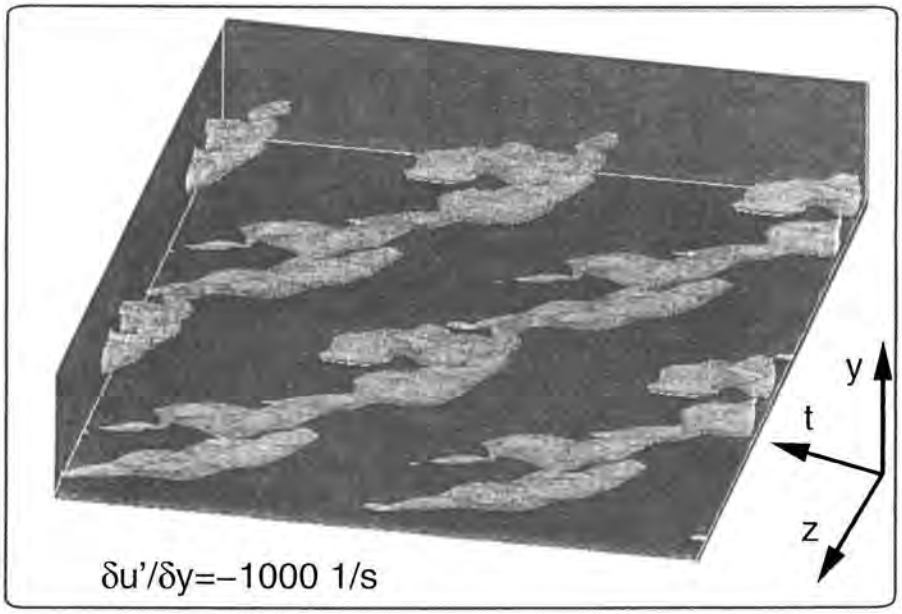

Figure 4: Iso-surfaces of one value of an estimate of the spanwise vorticity fluctuation $\delta u'/\delta y = \omega_z'$ over two spanwise and two streamwise periods of the subharmonic wave. Measured at $\Delta x = 380$ mm.

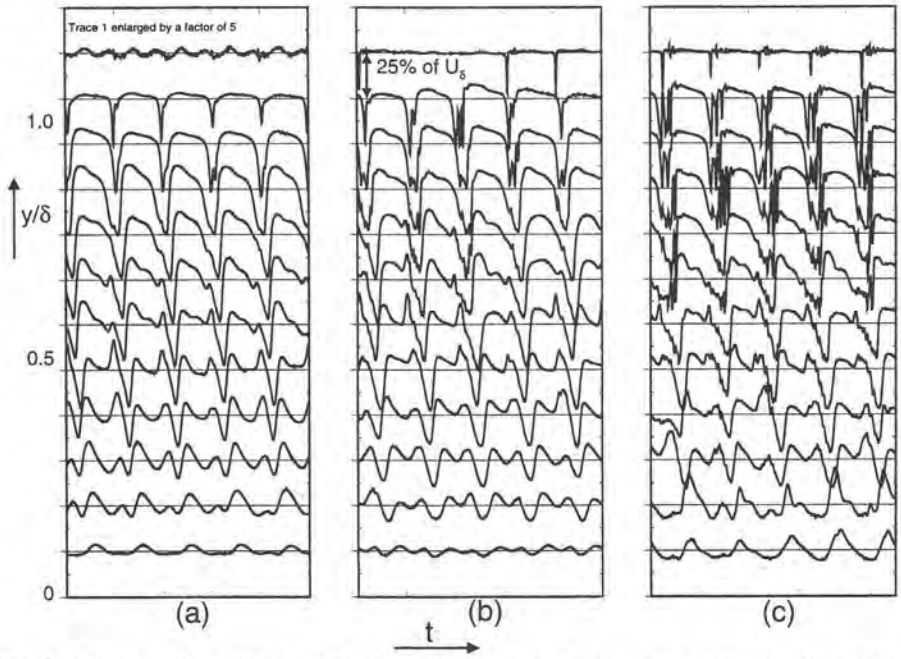

Figure 5: Time-series obtained far from the source at various distances from the wall in the peak position. Five periods of subharmonic frequency are shown. (a) $\Delta x = 420$ mm. (b) $\Delta x = 440$ mm. (c) $\Delta x = 460$ mm.

Conclusions

The N-regime of the boundary layer transition is reproduced under controlled disturbance conditions by the excitation of a 2-D fundamental wave and a pair of 3-D subharmonics. It is shown that introduced separately modes are stable or close to neutrally stable and transition (N-regime) occurs only when the conditions for subharmonic resonance are satisfied. In this case detailed hot-wire measurements show the formation of Λ-structures in staggered order with the subharmonic frequency as observed in other studies of the N-regime. However, the further disturbance development was found to be qualitatively the same as usually observed in the other regime of breakdown – the K-regime. That is namely the formation of typical Δ-wing shaped 3-D high-shear layers and, especially, the formation of a first, second, third, etc. spike in the peak position of the Λ-structures.

The results testify that at late stages of the N-breakdown local physical mechanisms of the nonlinear disturbance development are qualitatively the same as those characteristic of the K-regime of transition.

References

Borodulin, V.I. & Kachanov, Y.S. 1993 – Experimental study of nonlinear stages of a boundary-layer breakdown. *Nonlinear Stability of Nonparallel Flows*, IUTAM Symp. 1993 Potsdam/NY USA, eds. Lin, N., Buter, T.A., Reed, H.L., Springer.

Corke, T.C. & Mangano, R.A. 1989 – Resonant growth of three-dimensional modes in transitioning Blasius boundary-layers. *J. Fluid Mech.* **209**, 93-150.

Craik, A.D. 1971 – Nonlinear resonant instability in boundary-layers. *J. Fluid Mech.***50**, 393.

Gaponenko, V.R. & Kachanov, Y.S. 1994 *Proc. ICMAR'94*, Novosibirsk, pp. 90-97.

Hama,F.R. & Nutant, J. 1963 – Detailed flow observations in the transition process in a thick boundary layer. *Proc. Heat Transfers & Fluid Mech. Inst.*, pp. 77-93, Palo Alto, Calif.: Stanford Univ. Press.

Herbert, T. 1988 – Secondary instability of boundary-layer. *Annu. Rev. Fluid Mech.* **20**, 487-526.

Kachanov, Y.S., Kozlov, V.V. & Levchenko, V.Y. 1977 – Nonlinear development of a wave in a boundary-layer. *Izv. Akad. Nauk SSSR, Mekh. Zhidk. Gaza.* **3**, 49-53 (In Russian) (Transl. *Fluid Dyn.* **12**, 1978, 383-390).

Kachanov, Y.S. 1994 – Physical mechanisms of laminar boundary-layer transition. *Ann. Rev. Fluid Mech.* **26**, 411-482.

Kachanov, Y.S. & Levchenko, V.Y. 1984 – The resonant interaction of disturbances at laminar-turbulent transition in a boundary-layer. *J. Fluid Mech.* **138**, 209-247.

Klebanoff, P.S., Tidstrom, K.D. & Sargent, L.M. 1962 – The three-dimensional nature of boundary-layer transition. *J. Fluid Mech.* **12**, 1-34.

Laurien E. & Kleiser, L. 1989 – Numerical simulation of boundary-layer transition and transition control. *J. Fluid Mech.* **199**, 403-440.

Rist, U. & Kachanov, Y.S. 1995 – Numerical and experimental investigation of the K-regime of boundary-layer transition. *Laminar-Turbulent Transition*, IUTAM Symp. 1994 Sendai/Japan, ed. R. Kobayashi. Springer.

Saric, W.S. & Thomas, A.S.W. 1984 – Experiments on the subharmonic route to turbulence in boundary layers. In *Turbulence and Chaotic Phenomena in Fluids*, ed. T. Tatsumi, pp. 117-22. North-Holland, Amsterdam.

Authors' addresses

°Hermann-Föttinger-Institut
für Strömungsmechanik
Technische Universität Berlin
Strasse des 17. Juni 135
10623 Berlin, Germany

▷Russian Academy of Science
630090 Novosibirsk, Russia

M. Baumann ° & W. Nitsche ▷

Investigation of Active Control of Tollmien-Schlichting Waves on a Wing

Abstract

Experiments were performed to delay the laminar-turbulent transition on a wing by means of active wave cancellation. For this purpose an active wave control system (AWC) was integrated in the instability region of an unswept airfoil (NACA 0012; $c = 800$ mm; $Re_c = 0.8 \cdot 10^6$). Natural 2D flow instabilities were sensed by a surface hot-film-probe, a downstream located actuator (suction/blowing slot) was used to produce a cancelling wave and a further downstream located hot-wire was used to obtain a quality signal of the cancellation process. The sensor-actuator system was operated by a DSP controller (Digital Signal Processor) running an LMS adaptive FIR filter algorithm which performs a feedforward control of the cancellation process. In the experiments, an attenuation of 'natural' broadband TS-waves of 12 dB up to 25 dB was observed at the downstream located error sensor. The highest attenuation rates were obtained when 'natural' instability waves were periodically pre-triggered very lightly by a second suction/blowing slot upstream of the AWC system.

Introduction

Several methods are known to delay the laminar-turbulent transition of boundary layers. These methods can be divided into those which modify the mean velocity profile, such as a negative pressure gradient, suction through the wall or wall cooling in air (wall heating in water) and those which directly influence unstable oscillations dynamically using a wave superposition principle. The linear stability theory of laminar boundary layers suggests the possibility to cancel or to reduce naturally occurring instability waves with artificially excited waves due to linear wave superposition.

In several experimental and numerical investigations the feasibility of active wave cancellation has been verified, but mainly under simplified test conditions such as artificially induced sinusoidal TS-waves instead of randomly occuring natural waves. The basic experimental works of Milling 1981, Liepmann, Nosenchuck & Brown 1982a, 1982b, Thomas 1983 and Gilev & Kozlov 1985, 1987 have clearly shown the feasibility of cancelling artificially induced sinusoidal TS-waves in flat-plate experiments in water and air by means of flush mounted vibrating ribbons, heating strips or periodic suction and blowing through a small slot in the wall. Pilipenko & Shapovalov 1987 were able to reduce 'natural' TS-waves by pure sinusoidal blowing and suction through a slot on a wing. Advanced

attempts to cancel artificially induced broadband TS-waves using feedforward control devices were made by Ladd 1988 on an axisymmetric body with strip-heaters in water, and by Pupator & Saric 1989 on a flat plate employing vibrating ribbons. In both works a very good success in reducing the disturbance levels was reported, e.g. in the work of Pupator & Saric the disturbance level could be reduced by an order of magnitude when compared to the case without control. Later experiments of Ladd 1990 indicated an amplitude reduction of natural TS-waves by approximately 50 % using a simplified feedforward controller compared to his previous work (Ladd 1988) and a suction/blowing-actuator instead of the strip-heater.

Experiments without artificial excitation of instability waves are generally described as conducted under natural conditions, but it is well known that results of such sensitive transition experiments are influenced by disturbances present in the wind- or water tunnel used. Hence, the experiments presented here and which are described in detail in Baumann & Nitsche 1995, can also be classified as conducted under 'natural' conditions. A special case with artificially pre-triggered TS-waves is also presented.

Experimental apparatus

The sensors and the actuator for active TSwave control were located in the instability region of an unswept NACA 0012 wing with a chord of $c = 800$ mm. The experiments were carried out at a velocity of $U_\infty = 14.5$ m/s ($Re_c = 0.8 \cdot 10^6$) in a small closed test section of a wind tunnel at the Institut für Luft- und Raumfahrt of the Technical University Berlin. The freestream turbulence level was approximately 0.2 %. The angle of attack was chosen as $\alpha = 0.36°$ with respect to wall effects in the test section. The adverse pressure gradient obtained $\Delta cp/\Delta x = 0.6$ ($cp_{0.2} = -0.67, cp_{0.5} = -0.49$) corresponds to higher angles of attack under real freestream conditions.

The principle of the active wave control system used on the wing is shown in Fig. 1. The perturbations (TS-waves) are sensed by the first sensor (flush mounted hot-film probe) and from this signal an adaptive controller generates a driver signal for the actuator located downstream ($x/c = 0.43$) to produce an appropriate cancelling wave. The actuator is based on the principle of periodic blowing and suction through a small slot. The actual cancellation effect takes place over a few wave periods downstream. The error sensor (hot-wire probe) delivers a quality or error signal for the optimization or adaptation of the controller in order to achieve a minimum of residual disturbances. The adaptive controller performs a closed loop control due to the continuous adaptation of the unknown transfer function between the perturbation signal and the best possible cancelling signal of the actuator.

The location of the disturbance sensor (surface hot-film probe) was chosen far enough from the actuator to prevent an upstream coupling, which would disturb the adaptation process of the controller (Fig. 1). Additionally small piezofoil-sensors (Nitsche, Mirow & Szodruch 1989) have also been tested as disturbance

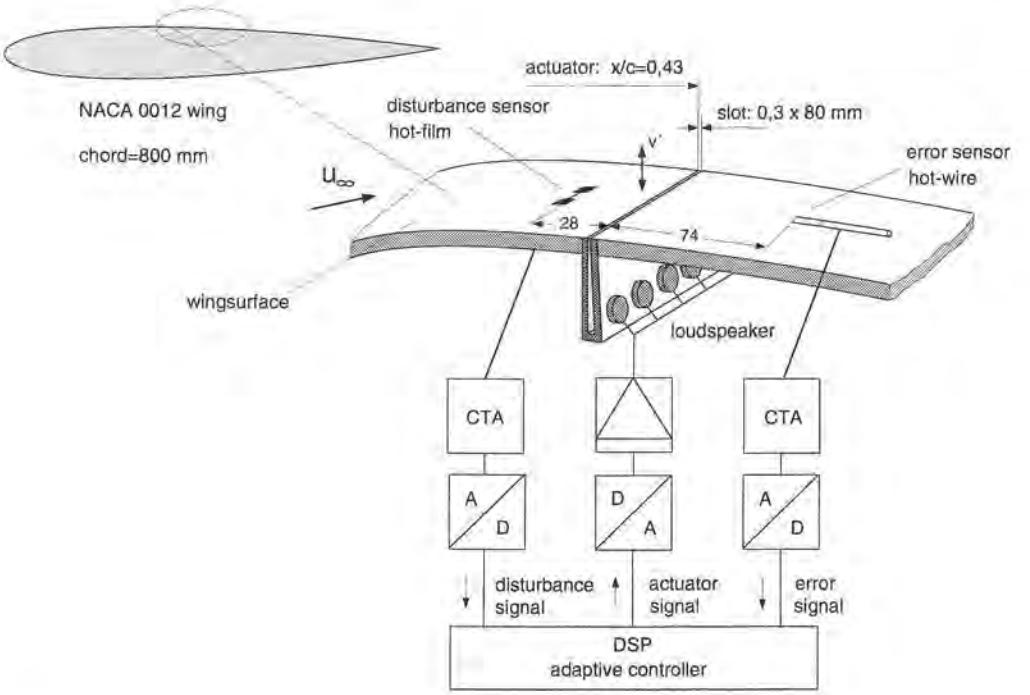

Figure 1: Principle sketch of the developed AWC-System on the NACA test wing.

sensors, but they react more sensitively to upstream coupling due to acoustic effects, which can be observed especially when the adaptation process is not completely finished (Baumann & Nitsche 1995).

The location of the hot-wire error sensor had also to be chosen carefully. It was necessary to keep a certain relaxation distance from the actuator until a homogeneous residual disturbance remains in the boundary layer. Originally, flush mounted hot-film- and piezofoil sensors were too close to the actuator, thus making the wall fixed hot-wire necessary. The wall distance of the hot-wire was chosen approximately to measure the maximum of the u'-fluctuations across the boundary layer. Both sensors were operated in constant-temperature mode (CTA) and their signals were digitalized by A/D-converters of the adaptive control device.

The actuator (Fig. 2) employed consists of a row of small loudspeakers moving the air in a specially shaped cavity which ends as a small slot (0.3 mm wide) in the wing surface and produces a v' velocity component. The chosen geometry combines the advantages of a minimal volume of the wedge shaped cavity and an equalizing effect on differences in the power of any loudspeaker. This results in a good dynamic response of the slot-actuator and in very low deviations in the perturbation velocity v' along the slot. It is known that wedges of 3D-disturbances develop downstream from the lateral ends of the 80 mm long slot, thus only a small area of controlled 2D-disturbances downstream of

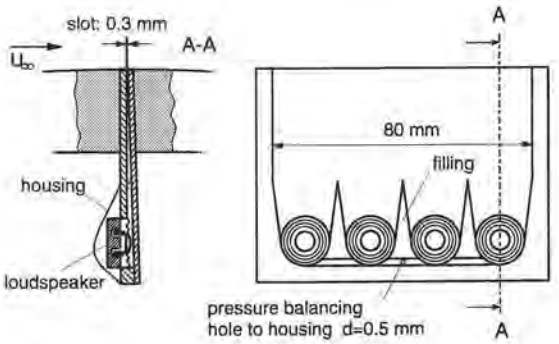

Figure 2: Principle of the suction/blowing-slot actuator.

the mid region of the slot remains. A second actuator (120 mm long) was located upstream ($x/c = 0.25$) of the main sensor-actuator system to enable simplified test conditions with artificial perturbations (excitation with random noise or sinusoidal signals) during the pre-tests of the AWC system.

Adaptive controller

In general, a controller for a sensor-actuator system has two primary functions: to find the time delay between the sensor signal and the actuator signal with respect to the relevant group velocity of the TS-waves and to find the amplification between the signals in order to achieve the best cancellation. Thus, a controller has at least to adapt the delay time and the amplification factor. Ladd 1990 reported an approximately 50 % reduction of 'natural' TS-waves with such a controller. In some preliminary experiments similar values were reached with a very carefully adjusted so-called 'Delay & Amplify' device. In other previous flat-plate experiments we indicated some fluctuations of the group velocity of TS-waves and we further assume that local receptivity effects at the boundary layer actuator and the actuator itself also include nonlinear effects. For these reasons it would be valuable to have a controller which is able to cover most of the still unknown effects with a very fast self adapting transfer function.

Much recent research handles similar problems in active noise control (ANC) applications with modern DSP-based (Digital Signal Processor) electronic devices. The problem of active wave control (AWC) is quite different, but similar tools can be used (Bellanger 1987, Elliott 1993). Especially, the relatively long travel times of TS-waves over the sensor-actuator system require a more complicated controller design. On the other hand the long travel times give enough computing time to model the transfer function more precisely. Fig. 3 shows a block diagram of the implemented feedforward control algorithm, called 'filtered-x-LMS'. The physical transfer function between the disturbance sensor and the actuator (Path 1) is modelled by FIR-filter 1 (Finite Impulse Response). The filter coefficients are derived through an instantaneous adaptation by an LMS-algorithm (Least Mean Square) in order to minimize the signal of the error sensor,

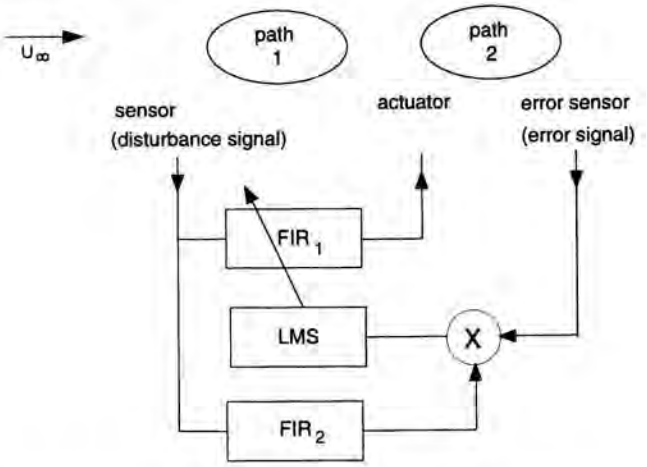

Figure 3: Principle of the adaptive controller (filtered-x-LMS).

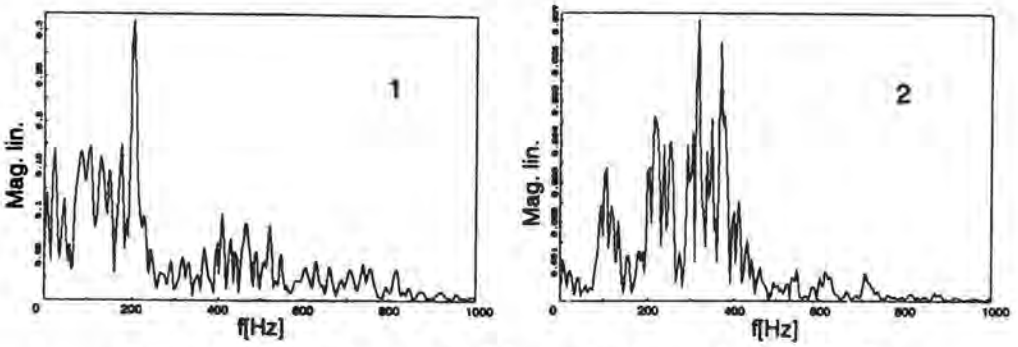

Figure 4: Amplitude spectra of the first and second path FIR filter.

and so minimize the mean square of the error signal. The high time delay between the actuator signal and error signal requires a second FIR-filter 2 to build an internal model of the physical signal path from the actuator to the error sensor (Path 2) ensuring the convergence of the LMS-algorithm. So the disturbance signal is filtered and multiplied by the error signal to generate a filtered reference signal for the LMS-algorithm, which explains the name: 'filtered-x-LMS'. The FIR-filter 2 can be adapted in a pre-training phase by sending random noise to the actuator. In the configuration used each filter vector has 300 coefficients and a sampling rate of 8 kHz was chosen. This means that the whole filter vector of FIR 1 was varied within one sampling period.

The special value of having a fast adapting LMS-algorithm is that the filter coefficients keep moving and thus result in the ability to actually build a more precise transfer function than a well adapted static FIR-filter would be able to do. In consequence the huge amount of fast calculations requires a sophisti-

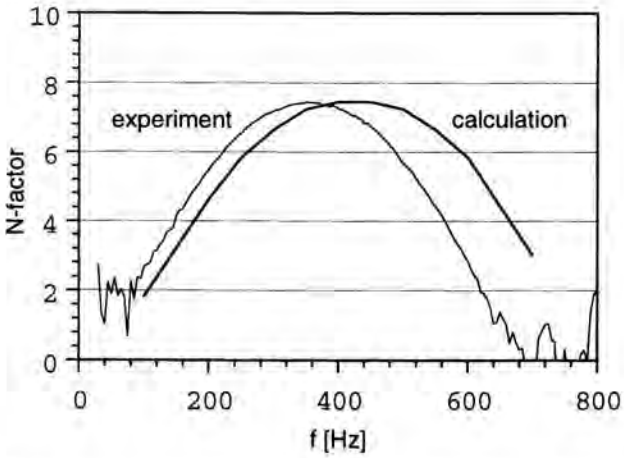

Figure 5: N-factors against frequency at $x/c = 0.5$ (calculation from DASA Bremen).

cated RISC processor like a digital signal processor (DSP). For this reason a fifty megaflop DSP with 16 Bit A/D- and D/A-converters programmed in assembly language was used. The typical convergence time (full adaptation of FIR 1 from zero state) was one minute. Nevertheless the adaptation can follow small fluctuations such as small changes in the angle of attack within increments less than a second, because of the high update frequency. The obtained frequency responses of the adapted filters look very nonuniform. Fig. 4 shows such amplitude spectra of both adapted FIR-filters. They could be of theoretical interest as numerically found transfer functions, but they also include the properties of sensors, the actuator and their amplifiers. Both filters also have a group delay which corresponds to the expected group velocity of the TS-waves.

Stability of the laminar boundary layer

Using the slot-actuators, it was possible to excite very clean sinusoidal TS-waves (excitation by 30 dB of the single frequency above the background perturbations), indicated by the sensors. This made it easy to measure the frequency response between the excitation signal of the first actuator and the hot-film signal in a sine-sweep procedure to indicate the instability frequency range. Fig. 5 shows a comparison between calculated data (performed by DASA Airbus Bremen) and the measured frequency response, scaled as N-factors over the excitation frequency at the hot-film location $x/c = 0.5$. The experiments had to be performed with a reduced angle of attack of $\alpha = 0.36°$ compared to the earlier planned and calculated case with $\alpha = 1.0°$, which could almost entirely explain the difference of the two curves. The second actuator shows a similar behaviour to the first one, except that the boundary layer reacts much more unstably on excitation at the second actuator location. For $\alpha = 1.0°$, the hot-wire already

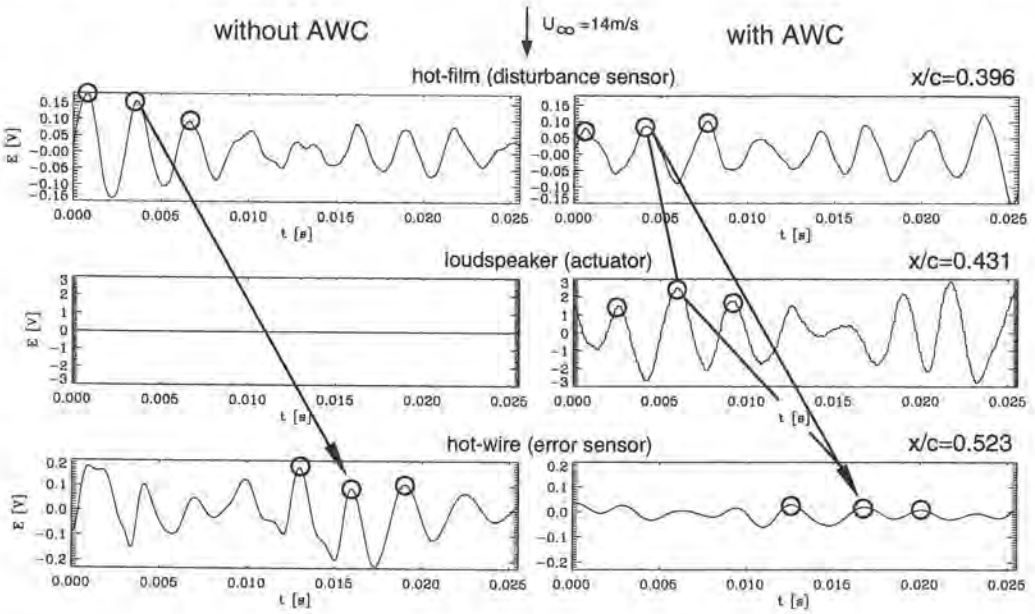

Figure 6: Time traces of the sensor-actuator system without and with control (AWC).

indicates a strong non-linear stage of the 'natural' instability waves, hence the unsuitability of this case for cancellation experiments.

Results of active wave control

During the development phase of the described AWC-system on a wing many simplified pre-tests with artificially excited perturbations were conducted. The results presented, however, will only illustrate the performance of the system under 'natural' flow conditions. Fig. 6 shows two sets of three time traces in downstream order (disturbance sensor, actuator, error sensor). The left set indicates large disturbances at the error sensor, when the actuator is switched off. It can be recognised that some signal peaks correspond to each other and are marked in the figure. The right set shows the three traces when operating the active control device. The signal of the error sensor indicates a significant amplitude reduction of the residual perturbations compared to the case without control. The actuator signal looks similar to that of the disturbance sensor. Characteristic peaks are also marked, indicating different delays from sensor to actuator and actuator to error sensor, which correspond to the different distances.

A comparison of the averaged power spectra of the error sensor signal (with and without AWC) gives a detailed view of the attenuation performance. Fig. 7 shows the power spectra of one of the best obtained damping results. It shows amplitude reductions between 10 dB and 15 dB in the instability frequency range from 200 Hz to 500 Hz. A characteristic value can be found with 12 dB

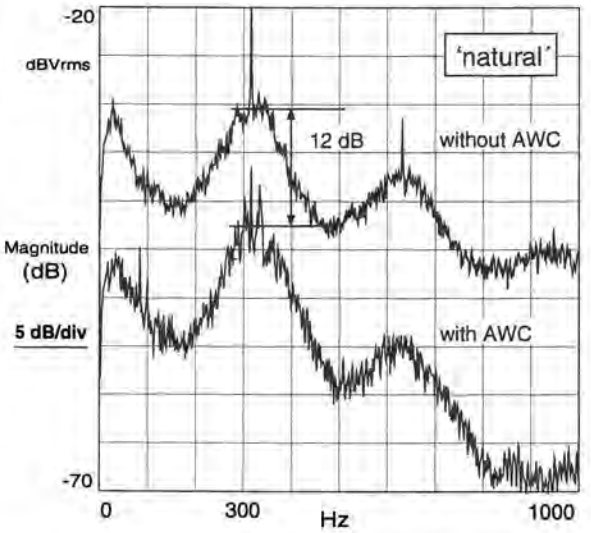

Figure 7: Power spectra of the error sensor with and without AWC, 'natural case'.

at 330 Hz. Much higher differences are reached from 800 Hz to 1000 Hz, which is outside the unstable frequency range and therefore is easier to cancel.

A critical view on the spectra shows why the test conditions have to be classified as quasi natural or even "natural". Especially, the two peaks (at 315 Hz and 630 Hz) in the spectra of Fig. 7 and also of Fig. 8 obviously result from disturbances of the wind tunnel. The AWC-system shows its best performance when reducing peaks in the disturbance spectra, like that at 315 Hz. This depends on the LMS-algorithm and is also known from ANC-applications. As a consequence of this a further experiment was performed with an artificial sinusoidal excitation on the first actuator with a frequency of 344 Hz, which marks the centre of the unstable frequency range. The amplitude was chosen carefully so that the signal of the first sensor indicated almost no change in amplitude but seemed to be more uniform, which looks as though it was triggered periodically. Under these conditions better cancellation effects were observed. The averaged power spectra of Fig. 8 indicate an attenuation between 15 dB and 25 dB. It is to be noticed that an excitation peak at 344 Hz can not be recognized. So it seems to be possible to force a random instability wave with a very small additional artificial excitation to a more uniform 2D-state which is easier to cancel.

Conclusions

Airfoil experiments employing AWC (Active Wave Control) have been successfully conducted. In particular it has been demonstrated that an LMS adaptive FIR-filter (filtered-x-LMS algorithm) in conjunction with a suction/blowing-slot

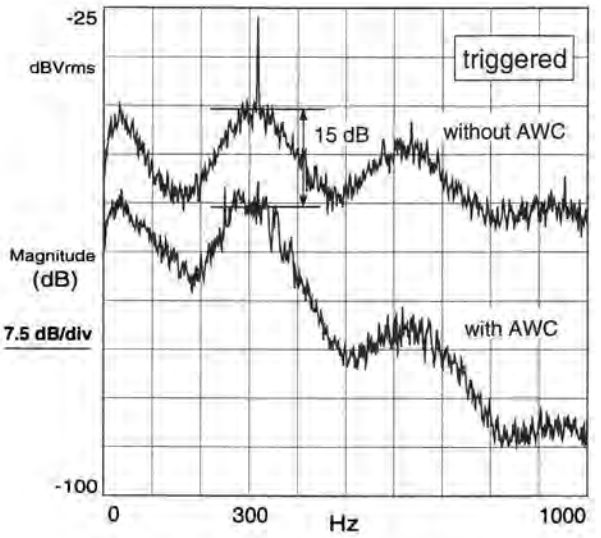

Figure 8: Power spectra of the error sensor with and without AWC, artificially triggered (sine, $f = 344$ Hz).

actuator has the ability to reach very high cancelling effects on 'natural' TS-waves. Amplitude reductions from 12 dB up to 25 dB compared to the case without AWC were observed. This is equivalent to damping factors of 4 up to 18 or expressed as 'negative N-factors' by $N = -1.4$ up to $N = -2.8$. It is of particular interest that the highest attenuation was obtained in case of an artificial triggering of the 'natural' instability waves. This can be explained by the fact that natural instability waves, when artificially 2D-triggered, become less random and probably are forced to a clean 2D-development. In addition, the FIR-filter of the controller can be more precisely adapted to pre-triggered perturbations by the LMS-algorithm and hence cancels TS-waves more effectively.

Questions concerning local effects of the cancellation process and especially concerning the artificial triggering still remain unanswered in this work. But the results obtained give a good basis for further investigations in future work. Especially, active control of artificially pre-triggered 2D-waves (TS-waves) could be a promising research field to understand the local mechanism of such a 'TS-lock-in effect'. It is also of interest to study experimentally whether the method can be used to cancel 3D (primary, secondary) instabilities.

Acknowledgements

The work was partly sponsored by the DASA Airbus (Bremen). Special thanks are to Dr. G. Schrauf, who performed the stability calculations.

References

Baumann, M., Nitsche, W. 1995 – Aktive Grenzschichtbeeinflussung laminar-turbulenter Profilströmungen, ILR-Mitteilung 293 (Jan. 1995), TU-Berlin.

Bellanger, M.G. 1987 – Adaptive Digital Filters and Signal Analysis, New York 1987.

Elliott, S.J., Nelson, P.A. 1993 – Active Noise Control. *IEEE Signal Processing Magazine*, October 1993, 12-35.

Gilev, V.M., Kozlov V.V. 1985 — Use of Small Localized Wall Vibrations for Control of Transition in the Boundary Layer. *Fluid Mechanics-Soviet Research*, **14**, 50-54.

Gilev, V.M., Kozlov V.V. 1987 – Effect of Altering Injection an Suction on Transition in the Boundary Layer. *Fluid Mechanics-Soviet Research*, **16**, 61-68.

Ladd, D.M. 1988 – Active control of 2-D instability waves on an axisymmetric body. *Experiments in Fluids*, **6**, 69-70.

Ladd, D.M. 1990 – Control of Natural Laminar Instability Waves on an Axisymmetric Body. *AIAA Journal*, **28**, 367-369.

Liepmann, H.W., Brown, G.L., Nosenchuck, D.M. 1982a – Control of laminar-Instability waves using a new technique. *J. Fluid Mech.*, **118**, 187-200.

Liepmann, H.W., Nosenchuck, D.M. 1982b – Active control of laminar-turbulent transition. *J. Fluid Mech.*, **118**, 201-204.

Milling, R.W. 1981 – Tollmien-Schlichting wave cancellation. *Phys. Fluids*, **24**, 979-981.

Nitsche, W., Mirow, P., Szodruch, J. 1989 – Piezoelectric Foils as a Means of Sensing Unsteady Surface Forces. *Experiments in Fluids*, **7**, No. 2, 111-118.

Pilipenko, A.A., Shapovalov, G.K. 1987 – Control of Transition to Turbulence in the Boundary Layer by Cancellation of Tollmien-Schlichting Waves by Means of Induced Perturbations. *Fluid Mechanics-Soviet Research*, **16**, 78-85.

Pupator, P.T., Saric, W.S. 1989 – Control of random disturbances in a laminar boundary layer. AIAA Paper 89-1007.

Thomas, A.S.W. 1983 – The control of boundary-layer transition using a wave-superposition principle. *J. Fluid Mech.*, **137**, 233-250.

Authors' address

o Research Scientist
▷ Professor of Aerodynamics
Technische Universität Berlin
Institut für Luft- und Raumfahrt, Sekr. F2
Marchstr. 14, 10587 Berlin, Germany

U. Rist

DNS of Boundary-Layer Instability and Transition using the Spatial Approach

Abstract

Starting with the work of Fasel (1976), the research group at the University of Stuttgart has developed numerical methods for the realistic Direct Numerical Simulation of controlled laminar-turbulent transition in boundary layers using the spatial model. This paper presents results of K-type transition simulations in zero and adverse pressure gradients. Subsequently it is shown that such simulations can also be used for boundary layers in 'real-life' aeronautical applications, such as airfoils. For such a flow, the influence of steady suction at the wall is investigated and compared with experimental data.

Introduction

Laminar-turbulent transition in boundary layers plays a significant role in many practical applications. For instance, delaying the onset of transition on an aircraft wing reduces the skin friction drag, thus decreasing the fuel consumption of the airplane. Airfoils with a large portion of laminar flow based on a design that avoids strong adverse pressure gradients are only feasible for small aircraft, operating at relatively low Reynolds numbers where no wing sweep is necessary. Larger and faster aircraft need laminar flow control (LFC) devices to enforce laminar flow. Designing and optimizing such devices undoubtedly requires a good knowledge of the transition mechanisms.

Transition in boundary layers is a spatially evolving complex process influenced by many parameters, such as free-stream turbulence, Reynolds number, pressure gradient, etc. In order to reduce the number of these parameters, transition research has focussed on so-called 'controlled' transition in simple model flows, like, for instance, the flat-plate boundary layer. In such experiments, some kind of a wave maker is used to excite disturbances in the boundary layer. The streamwise evolution of these disturbances is then examined using, for instance flow visualization and hot-wire measurements.

In addition to experimental and theoretical work, Direct Numerical Simulations (*DNS*) based on the solution of the complete Navier-Stokes equations have played an increasingly important role in transition research during the past decade. The basic approach is similar to that of controlled experiments. Some regular perturbations are introduced into the integration domain, and their subsequent unstable, nonlinear development is computed. Two basically different kinds of numerical models have been used until the beginning of the 1990s, the

'temporal' and the 'spatial' model. The advantages and disadvantages of both models are not reviewed here, they have already been discussed elsewhere (cf. Fasel, 1990, Kleiser & Zang, 1991).

In the spatial model the streamwise evolution of disturbances is simulated in a fixed integration domain extending over a large downstream distance. With this model, realistic simulations of controlled experiments are possible, even in flows with large streamwise gradients including feedback by local flow reversal. However, elaborating a properly working numerical method for this model is a difficult task due to the boundary conditions and high demands on numerical stability and accuracy.

Today, the computationally less demanding temporal model with its underlying unphysical assumptions has been widely supplanted by the spatial model. The numerical results obtained by the research group of H. Fasel at the University of Stuttgart, for instance, compare favourably well with available theoretical and experimental data. The vibrating-ribbon experiments of Kachanov (1987) for the fundamental breakdown in a Blasius boundary layer simulated by Rist and the nonlinear development of a three-dimensional wave packet according to the wave-packet experiments by Gaster & Grant (1975) simulated by Konzelmann proved to be the first successful DNS of controlled transition experiments using the spatial approach (see Fasel, 1990).

This paper presents some results of two of the major investigations performed in the past several years at the University of Stuttgart: K-type transition in boundary layers with zero and adverse pressure gradient. It is then shown that these simulations can be easily extended to LFC studies in boundary layers of 'real-life' airfoils including suction at the wall.

Numerical model

The latest version of the DNS-scheme originally developed by Fasel (1976), extended to three-dimensions by Fasel *et al.* (1990), improved by Kloker *et al.* (1993) and by Kloker (1993), is described here. Only a general outline of the numerical model is given; details are available in the mentioned references and in Rist & Fasel (1995). Many of the basic features of our numerical scheme (disturbance flow formulation, 'relaminarization zone' at the outflow boundary, forcing at the wall, pseudo-spectral formulation, high-order finite difference discretizations, explicit time integration, etc.) are equally applicable for other flows, like separated flows, free shear layers, compressible boundary layers, 3D boundary layers, and Taylor-Couette flow, for example.

The basic configuration of the integration domain for boundary layers is relatively simple. As shown in Fig. 1, a finite rectangular box is selected to represent a certain region of the flow over a flat plate. The integration domain extends in streamwise direction from $x = x_0$ to $x = x_N$, covering typically more than ten Tollmien-Schlichting wave lengths, and y_u is chosen to cover approximately three boundary layer thicknesses (δ) at the outflow boundary. In the spanwise direc-

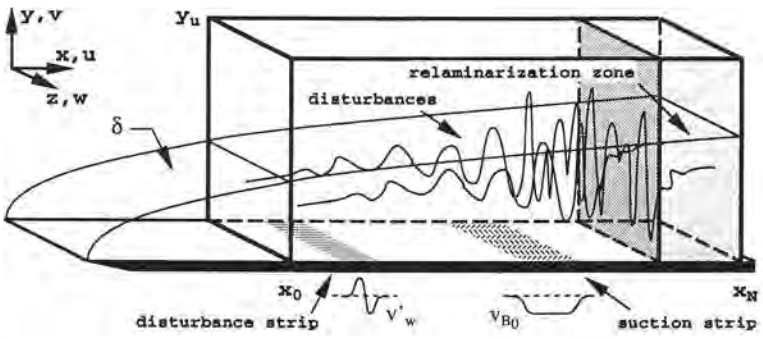

tion, the flow is assumed to be periodic with a chosen fundamental wavelength λ_z.

Governing equations

The numerical method is based on the three-dimensional Navier-Stokes equations for incompressible flow in vorticity-velocity formulation. The vorticity components are denoted by ω_x, ω_y and ω_z, and u, v and w are the velocity components in the x, y and z directions, respectively (see Fig. 1).

The equations are split into a set of equations for a two-dimensional steady base flow and a three-dimensional disturbance flow, i.e., for all variables $f = [u, v, \ldots, \omega_z]$ we have $f(x, y, z, t) = f_B(x, y) + f'(x, y, z, t)$. This allows the calculation of different base flows by prescribing different free-stream velocity distributions without altering the boundary conditions for the calculation of the disturbance flow. Thus, for investigations of the effects of different streamwise pressure gradients or steady suction at the wall, only a new base flow needs to be computed and specified for the calculation of the disturbance flow. The base flow is calculated from the 2D Navier-Stokes equations, *i.e.*, one vorticity-transport equation and two Poisson equations for the velocity components. The disturbance flow is described by three vorticity-transport equations and three Poisson equations for the velocity components. The detailed set of equations can be found in Fasel *et al.* (1990), Kloker *et al.* (1993) or Rist & Fasel (1995), for instance.

Boundary conditions

An arbitrary streamwise pressure gradient can be imposed on the base flow by prescribing the streamwise velocity distribution $U_e(x)$ of the external flow at the free-stream boundary of the base flow calculation. Three different base flows are considered in this paper, one with $U_e(x) = 1$ (Blasius boundary layer), one with $U_e(x) = (x/x_0)^{-0.0826}$ (strongly decelerated Falkner-Skan boundary layer

with Hartree parameter $\beta_H = -0.18$), and one where $U_e(x)$ is taken from an experiment to represent the velocity distribution of an airfoil. In any case the vorticity at the free-stream boundary is set to zero and $\partial v_B/\partial y = -dU_e/dx$ is specified for the calculation of v_B.

At the inflow boundary, Falkner-Skan profiles ($\equiv$ Blasius profiles for $\beta_H = 0$) corresponding to the imposed distribution of the streamwise pressure gradient are specified for the *base flow* variables. For a flow that does not belong to the Falkner-Skan family, as the airfoil boundary layer for instance, the streamwise velocity component $u_B(y)$ is taken from the Falkner-Skan velocity profile corresponding to the local pressure gradient and the local displacement thickness. Then, the $v_B(y)$ profile is integrated by using the continuity equation. At the outflow boundary, all equations are solved neglecting the second derivatives with respect to x, i.e., the equations are parabolized in the streamwise direction. At the wall, the velocity components are zero, except for the suction strip. The effect of suction through a porous strip is simulated by prescribing a normal velocity distribution $v_{B,0}(x)$ at the wall as sketched in Fig. 1.

A detailed description of the boundary conditions used for the calculations of the three-dimensional *disturbance flow* is given by Fasel *et al.* (1990), Kloker *et al.* (1993), and Rist & Fasel (1995). At the wall, all disturbance velocity components are zero, except within the disturbance strip, where the normal velocity component v'_w can be prescribed as a function of x, z, and t in order to introduce controlled time-periodic 2-D and 3-D disturbance waves. At the free-stream boundary, vanishing vorticity fluctuations and an exponential decay of the velocity disturbances are assumed. At the inflow boundary, all velocity and vorticity disturbances are set to zero. A harmonic wave condition in x-direction is applied at the outflow boundary. In addition, an artificial suppression of disturbances is introduced in the 'relaminarization zone' upstream of the outflow boundary (see Fig. 1) to substantially reduce the disturbance level at this boundary (cf. Kloker *et al.*, 1993 for details). Thus, possible undue reflections caused by large amplitude, broad-band disturbances passing the outflow boundary are prevented.

Numerical method

For the numerical solution of both the base flow and the disturbance flow equations a fourth-order accurate finite-difference discretization is employed in the streamwise direction and normal to the wall, which allows for a proper treatment of the effects of the spatially varying boundary layer. The discretization in the spanwise direction for the disturbance flow is done by using a Fourier series

$$f'(x,y,z,t) = \sum_{k=-K}^{K} F_k(x,y,t)\, e^{ik\gamma z} \tag{1}$$

to exploit the periodicity with respect to z, where the complex $F_k = [U_k, V_k, \ldots, \Omega_{zk}]$ represent all disturbance variables in spectral space, and γ is the basic spanwise wavenumber defined by $\gamma = 2\pi/\lambda_z$.

For the base flow, the vorticity-transport equation is integrated by a semi-implicit Euler scheme in artificial time until convergence to a steady state is achieved. For the disturbance flow, the integration in time is performed by an explicit four-stage Runge-Kutta scheme of fourth-order accuracy. The time integration is coupled with a fourth-order accurate discretization of the x-convection terms using central, upwind, downwind, and again central finite differences in each of the four stages, respectively. The sequence of upwind and downwind differences is altered for every time step. It can be shown that this technique effectively damps out small-scale oscillations that cannot be accurately discretized on a given grid at no additional computational cost (Kloker, 1993). The V_k-Poisson equation is solved with a multi-grid method using SOR line iteration technique (LU-decomposition in y, iteration in x). The equations for U_k and W_k are reduced to ODEs and directly solved.

Numerical results

As already stated, the numerical simulation is performed in two steps. First, the steady two-dimensional base flow is calculated, i.e., a boundary layer under combined effect of streamwise pressure gradient and local suction through a narrow suction strip (if necessary). Second, two- and three-dimensional disturbance waves with prescribed frequency and amplitude are introduced into the domain by periodic blowing and suction through a narrow disturbance strip at the wall (shown schematically in Fig. 1). After several periods of forcing, the streamwise evolution of these disturbances can be observed in the unsteady numerical results like in a wind tunnel experiment.

Using periodic disturbance input, a periodic wave train is generated which travels downstream as sketched in Fig. 1. The numerical method was carefully validated by extensive comparisons with results from linear (spatial) stability theory, secondary instability theory and experiments (Fasel *et al.*, 1990).

K-type transition

DNS of the K-type controlled transition experiments by Kachanov *et al.* (1985) have been performed by Rist (cf. Rist & Fasel, 1995), using $K = 8$ in equation (1), and extensively compared with the available experimental data (Kachanov, 1987 & 1994). In order to document the good agreement of the DNS with the experiments, new comparisons for later stages of transition are shown here in Figs 2 to 4 using data computed by Kloker (1993) with $K = 15$.

In Fig. 2, u'-rms amplitudes are shown together with amplitudes (A_h) and phases (ϕ_h) from a Fourier decomposition of the x-velocity component $u(x,y,z,t) = \sum_h A_h(x,y,z)\cos[hf_1t - \phi_h(x,y,z)]$, where f_1 is the fundamental disturbance frequency. The direct quantitative comparison of the DNS results with experimental data for $\bar{y} = 4$ mm at the spanwise 'peak' and 'valley' stations in Figs 2(a) and 2(b) shows excellent agreement. It should be noted here that only the disturbance amplitudes of the 2D TS-wave and its spanwise modulation at the

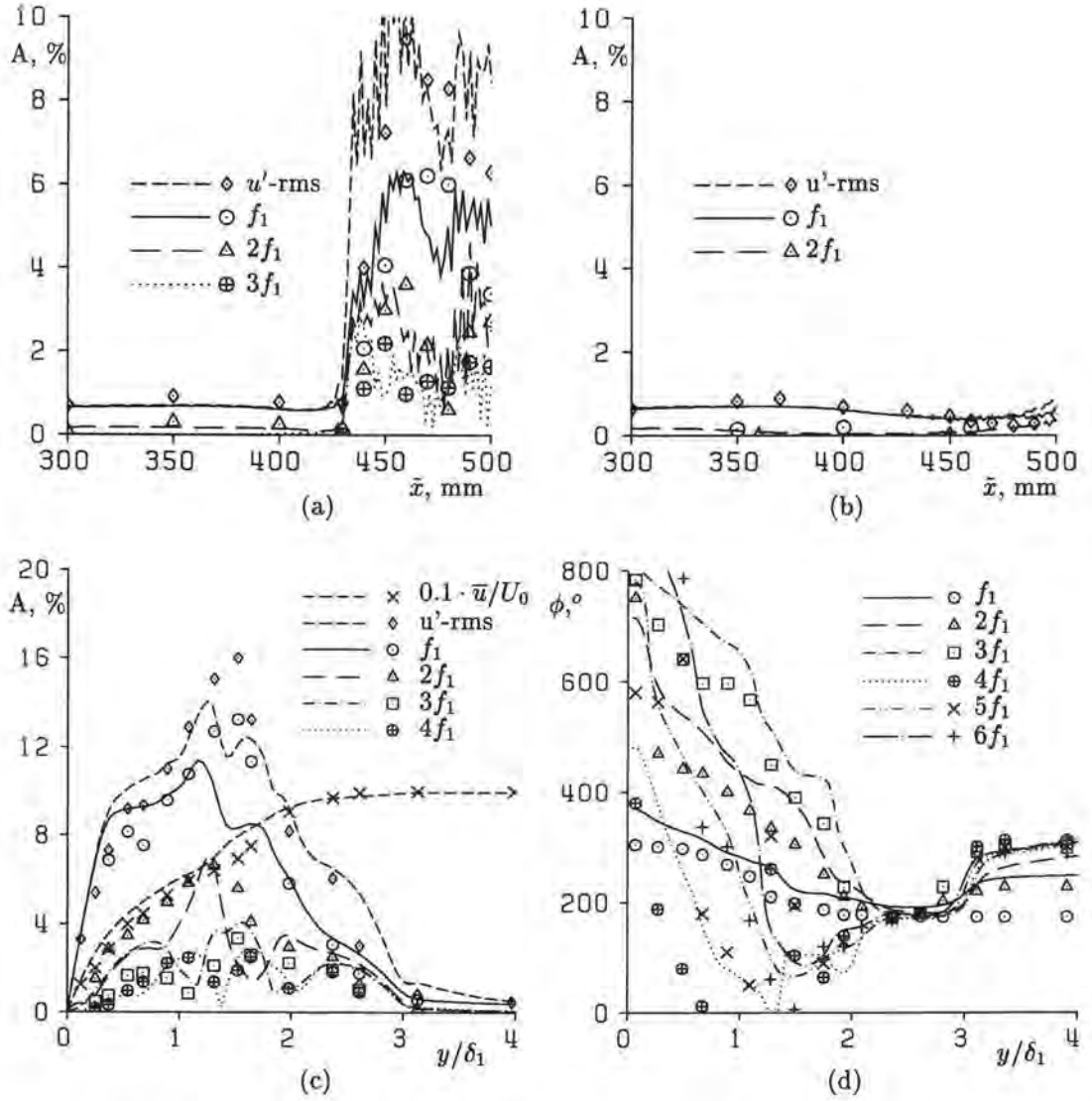

Figure 2: Comparison of u'-disturbances. Lines = DNS, symbols = experimental measurements by Kachanov *et al.* (1985), f_1 = disturbance frequency.
(a) amplitude (A) at $\tilde{y} = 4$ mm, z at 'peak'
(b) amplitude (A) and mean flow ($\overline{u}$) at $\tilde{y} = 4$ mm, z at 'valley'
(c) amplitude (A) at $\tilde{x} = 450$ mm, z at 'peak'
(d) phase profile (ϕ) at $\tilde{x} = 450$ mm, z at 'peak'

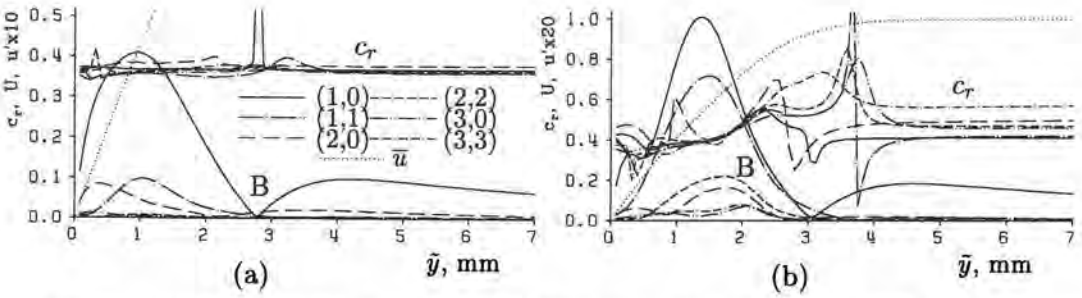

Figure 3: Comparison of phase speeds c_r with mean-velocity $\overline{u}$ and spectral amplitudes B for various frequency-spanwise-wave-number modes (h,k). a. $\tilde{x} = 350$ mm; b. $\tilde{x} = 410$ mm.

disturbance strip placed at $x = 250$ mm were adjusted in such a way that the experimental amplitudes at $x = 300$ mm were closely met.

Two regions can be distinguished in the results for the 'peak' station: a rather modest weakly nonlinear disturbance development upstream of $\tilde{x} \approx 430$ mm, followed by a highly nonlinear region with several 'spikes' per disturbance cycle. The sudden increase of the peak rms- and higher-harmonic amplitudes is due to these spikes which are cut for $\tilde{x} \geq 430$ mm. Figs 2(c) and 2(d) show a quantitative comparison of the amplitude and phase profiles, respectively for the highly nonlinear 'two-spike stage' at $\tilde{x} = 450$ mm which also exhibits a remarkable agreement. The first spike is situated between $y/\delta_1 = 2.4$ and 2.8 ($\tilde{y} \approx 4$ mm) where the phases are equal to 180° due to their normalization with respect to the passage of the first spike.

In Figs 3 and 4 the disturbances are examined in the frequency-spanwise-wave-number spectrum defined by $u(x,y,z,t) = \sum_h \sum_k B_{h,k}(x,y) \cos[k\gamma z - hf_1 t - \theta_{h,k}(x,y)]$. The phase speeds $c_{r\,h,k} = hf_1/(\partial\theta_{h,k}/\partial x)$ of the modes (h,k) in Fig. 3 exhibit new, interesting features. Upstream of $\tilde{x} \approx 400$ mm, the phase speeds versus y are practically constant and all modes are phase-locked to the 2D wave. Thus, the disturbances show 'wave-like' behaviour and the flow field in this stage is defined by nonlinear waves. Fig. 3 clearly shows that the nonlinear interaction is not confined to the critical layer (i.e., the y-position where the mean flow $\overline{u}$ equals the phase speed): Except for mode (1,0), all phase speeds are significantly different from their linear values due to the phase lock observed above. In addition, there is no observable increase of higher harmonic amplitudes in the critical layer by nonlinear interactions. Only the fundamental 2D and 3D disturbance amplitudes [modes(1,0) and (1,1)] exhibit a maximum in the critical layer, but this is already there in the linear case.

Further downstream in the spike stage, shown in Fig. 3(b), the 'wave-like' behaviour disappears: the phase speeds change with respect to y, especially inside the boundary layer. Outside, they are no longer phase-locked. At this stage it is much more difficult to define a critical layer and to attribute a special nonlinear significance to it. The only distinct feature that can be observed is a

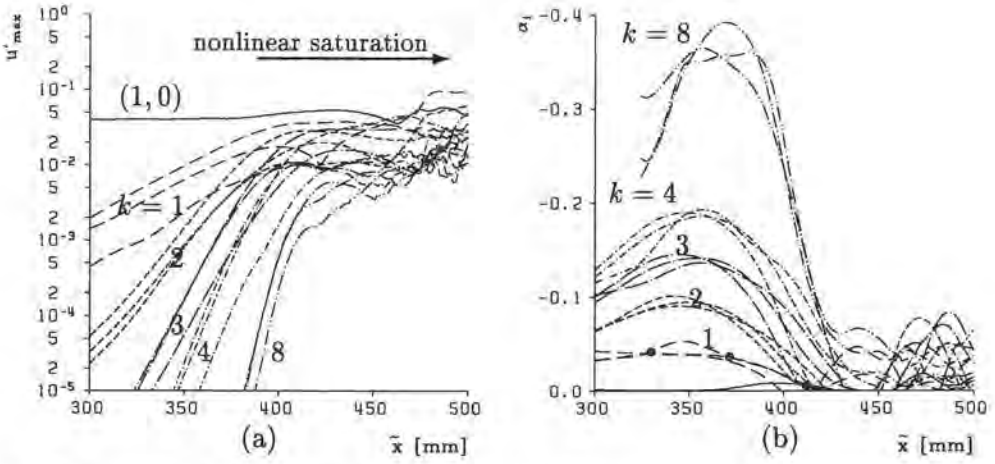

Figure 4: Amplitude maxima (a) and amplification rates α_i (b) for various spectral modes: frequencies $0, f_1, 2f_1$, spanwise wave numbers $k = 1, 2, 3, 4, 8$. ($\oplus$) = Floquet theory, Fasel *et al.* (1988).

region of equal phase speed at $\tilde{y} \approx 2$ mm where the first spike is just being formed. Since spikes are the manifestation of small Ω-shaped vortices, we suppose that this part of the flow field must be governed by nonlinear dynamic interactions of local fluid-flow structures in contrast to the wave interactions in the first sector.

Both regimes also appear in Fig. 4 where the y-maxima of the B-amplitudes defined above and the amplification rates $\alpha_i = -d/dx(B_{max})$ are shown for various frequency-spanwise-wave-number modes $[(h,k), 0 \leq h \leq 2, k > 0]$ versus x. It is quite evident that the initial amplification rates of the spanwise higher harmonics grow (linearly) with the spanwise wave number for $\tilde{x} < 400$ mm. The initial fan-out and deviation from linear increase of the modes with $k = 3, 4, 8$ should not be considered, since these modes are initially affected by the numerical round-off error due to their extremely small amplitudes ($B_{max} < 10^{-6}$) for small x.

Comparisons of the amplification rates α_i with an extension of Herbert's (1988) secondary instability theory are also shown. They reveal that the amplification of modes (1,1) and (1,0) is due to a 'combined' subharmonic-fundamental resonance with the 2D modes (1,0) and (2,0) (Fasel *et al.*, 1988). The possibility whether or not such a resonance could amplify other modes as well has also been checked. It turned out that α_i due to secondary instability is largest for $k = 1$, so that the modes with higher k must be considered as higher harmonic disturbance components of the fundamental disturbances. This hypothesis has been further checked in a number of test calculations using different initial amplitudes for these modes. It turned out that the local amplitudes (and amplification rates) of the higher harmonics do not depend on their initial disturbance amplitude but on the local amplitude of the waves that are amplified by the 'combined' resonance. Thus, it appears that this resonance is the kernel that drives the flow

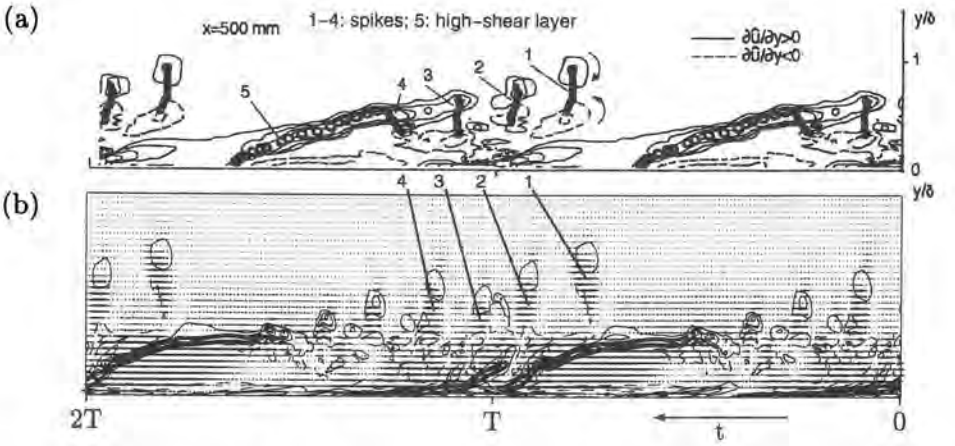

Figure 5: Experimental (a) and numerical (b) contours of $\partial u'/\partial y$ at $\tilde{x} = 500$ mm. (b) together with u'.

through the first stage of K-type transition.

In the second stage, nonlinear effects lead to a saturation of all amplitudes on a high level as can be observed in Fig. 4. So far, no wave resonances could be discovered in the numerical data. This absence might be due to the appearance of local dynamics that apparently replace the 'wave-like behaviour' observed in the first regime.

Simulations of the late-stage structures downstream of $\tilde{x} = 450$ mm have been started recently using $K = 64$ in eq. (1), see Rist & Kachanov (1994). Fig. 5 shows a comparison of the instantaneous shear $\partial u'/\partial y$ at $\tilde{x} = 500$ mm for the peak station from the DNS with data from Kachanov (1994). Spikes and a high-shear layer close to the wall are mapped out by black dots and circles, respectively in the experimental data. Regions of large negative u' indicate spikes in the numerical results. Instead of only four in the experiment, five or six spikes can be observed in the DNS. Besides that, the qualitative features in both data sets are identical: a high-shear layer traversing the entire boundary layer and several spikes (Ω-vortices) at its downstream end. However, there is no doubt that further analysis of these new data is required to learn more about possible interactions of such structures with the near-wall region, for instance.

Application to a boundary layer with adverse pressure gradient

Kloker (1993) has used a Falkner-Skan-type boundary layer with Hartree parameter $\beta_H = -0.18$ for comparison with the K-type simulation in the previous section. At first glance the results look very much like those for the Blasius boundary layer (cf. Fig. 6). Aligned Λ-vortices are forming out of a spanwise modulation of the large-amplitude TS-wave and Ω-vortices appear together with spikes at the spanwise peak stations. The downstream disturbance development,

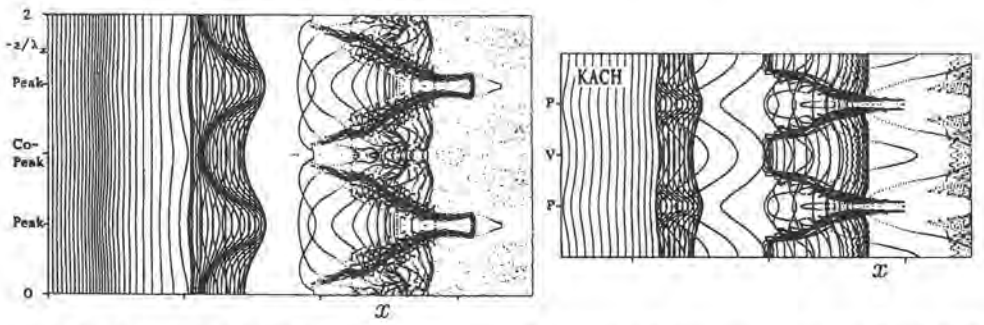

Figure 6: Simulated time-lines. Comparison between adverse pressure gradient (left) and zero pressure gradient boundary layer (right).

however, although quite similar in the peak plane, is drastically more violent at the spanwise valley station in the case with adverse pressure gradient than with zero pressure gradient (Kloker & Fasel, 1995). A closer look at the results indicated that the breakdown occurs much earlier there than at the peak station. This is why Kloker called this station a 'Co-Peak' station instead of 'Valley'. A new secondary vortex system close to the wall, centred around this station, induces a (lower) quite characteristic high-shear layer in between neighbouring Λ-vortices and accelerates transition at the 'Co-Peak' station. This event proceeds much more rapidly than the formation and breakdown of the well-known (upper) high-shear layer on top of the Λ-vortex. These violent dynamic events are apparent in Fig. 6 but could be perceived much better in an animation.

Application to an airfoil with suction

The base flows of wind-tunnel experiments on a NACA 64_2-A-215 airfoil with suction performed by van Ingen (1965) have been calculated. Between 30% and 90% of the airfoil chord (c) the wing section has been divided into 20 suction chambers, each of which was adjustable separately in order to prevent flow separation with only minimal viscous drag by suction through a porous surface. Bestek *et al.* (1994) have simulated this flow by prescribing the velocity distribution shown in Fig. 7(a) at the free-stream boundary of the integration domain. Two calculations have been performed: one without suction at the wall with the integration domain reaching from $s/c = 0.2$ to 0.55, and one with the suction velocity of van Ingen extending to $s/c = 0.72$.

Fig. 7(b) shows a comparison of the DNS results with the experiments for the streamwise distributions of the displacement thickness δ_1 and the momentum thickness δ_2 for both cases. Without suction the strong growth of both indicates the inclination to separation. For the suction case, δ_1 and δ_2 grow only moderately. For both cases, the numerical and experimental results are in good agreement. The neglection of the airfoil surface curvature in the numerical model is justified due to the small ratio of boundary-layer thickness to surface curva-

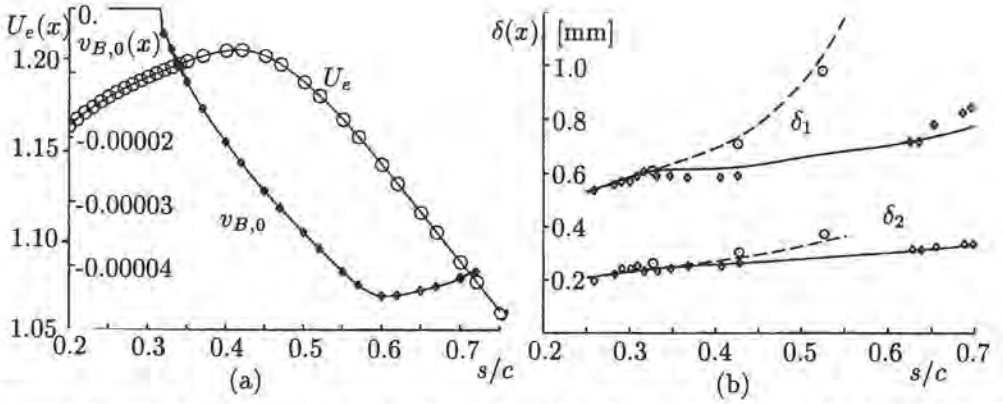

Figure 7: (a) Free-stream velocity U_e and wall-suction velocity $v_{B,0}$ for the DNS of a NACA 64_2-A-215 airfoil boundary layer with suction. (b) Comparison of boundary layer growth. Symbols = experiments v. Ingen (1965).

ture radius within the considered chord region. Thus, the basis for subsequent simulations of disturbance control in practical applications is prepared.

Conclusions

A numerical method has been developed and optimized over the past several years that can now be used to perform high-resolution spatial DNS of instability and transition in various boundary-layers of practical interest, provided a high-performance, large-memory computer is available. The results shown here demonstrate a good quantitative agreement with available experimental data. Research within the next few years must focus on flow control in such flows, on boundary-layer receptivity, and on understanding the late-stage structures of transition to turbulence in 2D as well as in 3D mean flows.

Acknowledgements

The work reviewed here would have been impossible without the long-term funding by the Deutsche Forschungsgemeinschaft, the Stiftung Volkswagenwerk, the Bundesministerium für Forschung und Technologie, the generous support of computer time provided by the University of Stuttgart, and continuous stimulation by its initiator Hermann Fasel.

References

Bestek, H., Kloker, M. & Müller, W. 1994 – Spatial direct numerical simulation of boundary layer transition under strong adverse pressure gradient. AGARD-Symposium *Application of Direct and Large Eddy Simulation to Transition and Turbulence*, Chania, Crete, Greece, AGARD-CP 551, pp. 32-1-32-12.

Fasel, H.F. 1976 – Investigation of the stability of boundary layers by a finite-difference model of the Navier-Stokes equations. *J. Fluid Mech.* **18**, 355-383.

Fasel, H.F. 1990 – Numerical simulation of instability and transition in boundary-layer flows. In: *Laminar-Turbulent Transition* (D. Arnal and R. Michel, eds), Springer, Berlin, pp. 587-598.

Fasel, H.F., Rist, U. & Konzelmann, U. 1988 – Numerical investigation of the effects of longitudinal vortices on the onset of transition in a flat-plate boundary layer. AGARD-Symposium *Fluid Dynamics of Three-Dimensional Shear Flows and Transition*, Cesme, Turkey, AGARD-CP 438, pp. 7-1-7-13.

Fasel, H.F., Rist, U. & Konzelmann, U. 1990 – Numerical investigation of the three-dimensional development in boundary-layer transition. *AIAA J.* **28**, 29-37.

Gaster, M. & Grant I. 1975 – An experimental investigation of the formation and development of a wave packet in a laminar boundary layer. *Proc. Roy. Soc. London A* **341**, 253-269.

Herbert, T. 1988 - Secondary instability of boundary layers. *Ann. Rev. Fluid Mech.* **20**, 487-526.

Ingen van, J.L. 1965 – Theoretical and experimental investigations of incompressible laminar boundary layer with and without suction. TU Delft, Report VTH-**124**.

Kachanov, Y.S. 1987 – On the resonant nature of the breakdown of a laminar boundary layer. *J. Fluid Mech.* **184**, 43-74.

Kachanov, Y.S. 1994 – Physical Mechanisms of laminar-boundary-layer transition. *Ann. Rev. Fluid Mech.* **26**, 411-482.

Kachanov, Y.S., Kozlov, V.V., Levchenko, V.Y. & Ramazanov, M.P. 1985 – On nature of K-breakdown of a laminar boundary-layer; new experimental data. In: *Laminar-Turbulent Transition* (V.V. Kozlov ed.), Springer, Berlin, pp. 61-73.

Kleiser, L. & Zang T.A. 1991 – Numerical Simulation of Transition in Wall-Bounded Shear Flows. *Ann. Rev. Fluid Mech.* **23**, 495-537.

Kloker, M. 1993 – Direkte numerische Simulation des laminar-turbulenten Strömungsumschlages in einer stark verzögerten Grenzschicht. Dissertation, Univ. Stuttgart.

Kloker, M., & Fasel, H.F. 1995 – Direct numerical simulation of boundary-layer transition with strong adverse pressure gradient. In: *Laminar-Turbulent Transition* (R. Kobayashi ed.), Springer, Berlin, pp. 481-488.

Kloker, M., Konzelmann, U. & Fasel, H.F. 1993 – Outflow boundary conditions for spatial Navier-Stokes simulations of transitional boundary layers. *AIAA J.* **31**, 620-628.

Rist, U. & Fasel, H.F. 1995 – Direct numerical simulation of controlled transition in a flat-plate boundary layer. *J. Fluid Mech.* **298**, 211-248.

Rist, U. & Kachanov, Y.S. 1995 – Numerical and experimental investigation of the K-regime of boundary-layer transition. In: *Laminar-Turbulent Transition* (R. Kobayashi ed.), Berlin, pp. 405-412.

Author's address

Institut für Aerodynamik und Gasdynamik
Universität Stuttgart
Pfaffenwaldring 21, 70550 Stuttgart, Germany

V.A. Gushchin

Direct Numerical Simulation of Transitional Separated Fluid Flow Around a Circular Cylinder

Abstract

The transitional separated fluid flow around a circular cylinder is simulated numerically. The main idea of the simulation is based on the existence of large scale organized structures in the boundary layer and the near wake of the body and the possibility of modeling the dynamics of such structures using the complete Navier-Stokes equations without any turbulence models. The SMIF method is used, which is an efficient numerical method previously developed by the author with explicit hybrid non-oscillating (monotonic) finite difference scheme based on the combination of modified central and upwind difference schemes with a special switch condition and has second order accuracy and minimal scheme viscosity. It works in a wide range of Reynolds numbers. A comparison with experimental data for subcritical and critical Reynolds numbers is made.

Introduction

The transition from laminar to turbulent flow is one of the more important and less investigated phenomena in fluid dynamics. The difficulties of an experimental study of such regimes are connected with the complexity of the flow. The transitional separated fluid flow around finite bodies depends on many different factors such as the turbulence level and uniformity of the oncoming flow, the shape and smoothness of the surface of the body, etc. Therefore mathematical modeling may be one of the more effective approaches for such investigations. For the mathematical modeling it is necessary to develop an adequate physical and numerical model of the phenomena. In the past years more and more attention has been paid to the existence of an organized motion of large scale structures in laminar and turbulent boundary layers, in free shear layers, in jets, in the wake of finite bodies, etc. (Townsend, 1956; Cantwell, 1981). It is obvious that the construction of a universal model is impossible and each model (suitable for some classes of flows) should be based on the reasonable combination of determinism and chaos, possibly with taking the intermittency into account.

Our attempts are directed to the adequate reproduction of large scale (ordered, organized, coherent) structures, where the most part of the motion energy are concentrated. This investigation is based on the direct numerical simulation (without any turbulence models) using the complete Navier-Stokes equations to resolve the large scale structures (discrete model).

Foundation of the problem and numerical method

Let us consider the incompressible viscous fluid flow past a circular cylinder with radius R which is described by the Navier-Stokes equations. The transformation $x = r(z)cos\theta$, $y = r(z)sin\theta$ is used to resolve the boundary layer and the outer flow, where $r(z) = exp(z) - z - \frac{z^2}{2!} - \frac{z^3}{3!} + \eta z$ and $\eta = \eta(Re) = 4\sqrt{\frac{2}{Re}}$. Such transformation maps the investigated domain on the semistripe $\{(z,0): 0 \leq z \leq z_\infty, 0 \leq \theta \leq 2\pi\}$ and enables to use a finer spatial grid (with constant step size for z) in the boundary layer. Let u and v be the velocity components along z and θ respectively. The no-slip conditions on the rigid body are: u=0, v=0, and the velocities at "infinity"($z = z_\infty$) are $u = cos\theta$, $v = -sin\theta$.

The outer boundary z_∞ was taken as z_∞=5 (r_∞=105 R, where R is the radius of the cylinder). The number of grid points was 100 x 60 in z and θ directions respectively except for $Re = 10^6$ (100 x 120). So the number of the grid points in radial direction inside the boundary layer was between 10 and 15 for Reynolds numbers between 10^4 and 10^6. The influence on the solution of z_∞ and the form of the boundary conditions at infinity, the grid size and time steps were investigated in Gushchin (1985). For the calculation of fluid flows with large gradients of hydrodynamic parameters it is necessary to use an effective numerical method with finite difference schemes that have the following properties: high order of accuracy (second or higher), minimal numerical viscosity, monotony of the scheme, and applicable in a wide range of Reynolds numbers. The Splitting on physical factors Method for Incompressible Fluid flows -SMIF (Gushchin & Konshin, 1992) uses an explicit hybrid finite difference scheme which is based on the combination of a modified central difference scheme (MCDS) and a modified upwind difference scheme (MUDS) with a special switch condition and possesses all the properties mentioned above. The SMIF method was used for the calculation of 2D and 3D steady and unsteady, internal and external, homogeneous and nonhomogeneous, and also free surface fluid flows. The method is portable for convenient and parallel architectures.

The method was tested in calculations of steady and periodic separated fluid flows past a circular cylinder for small and moderate Reynolds numbers (Gushchin, 1985). The results are in a good agreement with experimental data and calculations of other authors.

Results

For the Reynolds numbers $10^2 < Re < 2 \cdot 10^3$ ($Re = \frac{U_\infty D}{\nu}$, where U_∞ is the velocity of a uniform flow at "infinity", D is the diameter of the cylinder, ν is the kinematic viscosity) the flow is periodic and laminar, but some secondary effects take place: the loss of stability in the separated boundary layer (Kelvin-Helmholtz instability in a free shear layer), secondary vortices near the body surface, and secondary separation in the vicinity of the separation point. The life time for each secondary effect arising twice per period is about one tenth of the main period.

Parameters	Experiment	Numerical results
Sh	0.179	0.18
L/D	4.22	3.5-4.0
$\overline{P}(\pi)$	1.019	1.0
θ_s	103°	95°
L_s/D	1.0	0.7
$\overline{C}_d$	1.237	1.0

Table 1: $Re = 1.4 \cdot 10^5$ Comparison with experimental data of Cantwell & Coles (1983).

For the Reynolds numbers $2 \cdot 10^3 < Re < 1.5 \cdot 10^5$ the characteristic features are the following:

- The flow is three dimensional.
- The flow in the boundary layer is unsteady but still laminar.
- Outside the boundary layer the flow is turbulent with large-scale structures in the wake.

Let us compare the numerical results with the experimental data of Cantwell & Coles (1983) for large subcritical Reynolds numbers ($Re = 1.4 \cdot 10^5$), where the boundary layer is still laminar. For this purpose we make some additional treatment of the obtained solution. Let $\overline{f}(x) = \frac{1}{kT} \int_{t_0}^{t_0+kT} f(x,t)dt$ be the time-mean over k periods T of the function $f(x,t)$ (velocity components, pressure, etc.), where t_0 is an arbitrary time moment in the well developed periodic flow regime. Then $f(x,t) = f(x,t) - \overline{f}(x)$ is the deviation (fluctuation) of the function $f(x,t)$ with respect to the time-mean value $\overline{f}(x)$. Time-averaging of periodic flows allows us to find time-mean flow patterns and flow characteristics (drag coefficients, angles of separation, length of the separated zone, pressure in the front and rear stagnation points of the cylinder), the amplitudes of these characteristics near the time-mean values and their dependence on the Reynolds number in the considered range of Reynolds number. Such mathematical treatment of the results allows us to calculate the second and higher order moments, and brings together computational and laboratory experiments. In Table 1 the quantitative comparison of some frequency, geometric, local and integral characteristics is shown. Here $Sh = \frac{D}{U_0 T}$ is the Strouhal number; l/D is the distance passed by the vortex during the period T; $\overline{P}(\pi)$ is the pressure in the front stagnation point; θ_s is the angle of separation; L_s/D is the length of the "recirculation" zone calculated from the rear critical point of the time-mean flow; and $\overline{C}_d$ is the total drag coefficient.

Table 2 compares the extreme values of some second moments (the energetic characteristics of the oscillating motion) and their coordinates in the investigated domain. Here only the periodic part is taken (in table 2 total values for the second moments from the experiment are shown in brackets, Cantwell & Coles,

Parameters	Experiment	Numerical results
$\overline{u'^2}$	0.085 (0.22)	0.075 (0.22)
x/D	1.0	1.0 (0.7)
y/D	± 0.45	± 0.45 (± 0.35)
$\overline{v'^2}$	0.25 (0.43)	0.22 (0.48)
x/D	1.7	1.6 (0.6)
y/D	0	0 (0)
$\overline{u'v'}$	± 0.055 (± 0.12)	± 0.07 (± 0.11)
x/D	1.3	1.3 (0.8)
y/D	± 0.4	± 0.35 (± 0.35)

Table 2: $Re = 1.4 \cdot 10^5$, comparison with experimental data of Cantwell & Coles (1983).

1983). There are a few local extrema in the investigated domain in the numerical calculations. In table 2 only one local extreme value is shown for the second moment, and in brackets the absolute extreme values are shown. As may be seen from tables 1 and 2 the numerical results and experimental data are in a good agreement.

Thus from the previous analysis the following conclusion may be drawn: the large scale structures in the near wake are adequately reproduced by our numerical solution of the Navier-Stokes equations provided sufficient resolution is used to represent the molecular mechanism, which is responsible for the separation from the surface of the cylinder. In the near wake this mechanism is not so important. It means that near the solid surface it is necessary to use a fine enough grid. This grid may be more coarse outside the boundary layer but it must be fine enough for the resolution of separated vortices.

This numerical approach was used to calculate the transitional separated regimes for critical Reynolds numbers between $2 \cdot 10^5$ and $5 \cdot 10^5$. Here it is advisable to use a finite-difference grid near the body, which allows us to reproduce the large scale vortex structures typical for the boundary layer.

It is well known that for large subcritical Reynolds numbers $Re < 2 \cdot 10^5$ laminar separation of the boundary layer takes place and the angle of separation is $\theta_l \approx 100°$ (calculated from the rear critical point). The turbulization of the separated boundary layer takes place in the near wake. At supercritical Re ($> 4 \cdot 10^5$) the separated boundary layer is turbulent. The angle of separation in this case is $\theta_t \approx 70°$. Both for laminar and turbulent separations the periodic motion with one main frequency takes place in the wake: for the laminar case the Strouhal number is Sh=0.2 and for the turbulent case Sh=0.28. In the last case this is probably connected with the decrease of the distance between the separation points, the vortices are shed more often and the wake becomes narrower.

At critical Reynolds numbers in the transitional regime the periodicity is absent, whereas in experiments wide range of frequencies is registered. The

Parameters	θ_l	θ_t	C_d	Sh
Experiment	90°	45°	0.48	0.5
Numerical results	93°	48°	0.32	0.42

Table 3: $Re = 4 \cdot 10^5$; Comparison with experimental data of Bychkov & Larichkin (1987)

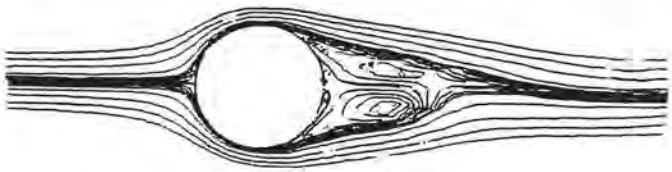

Figure 1: $\overline{\Psi} = const.$; $Re = 4 \cdot 10^5$.

existence of the bubble, its size and place may be one of the reasons for the non-periodic lift force. A flow with nonzero lift force coefficient is indeed possible (Schewe, 1986). The separated structures were observed in calculations at Reynolds numbers between $2 \cdot 10^5$ and $4 \cdot 10^5$. The time-averaged flow pattern ($\overline{\Psi}$= const, Ψ is the streamfunction) for $Re = 4 \cdot 10^5$ is shown in Fig. 1. The comparison of our numerical results with experimental data of Bychkov & Larichkin (1987) is given in Fig. 2 where the time-mean surface pressure $\overline{P}(\theta)$ is shown, and in Table 3. The presence of two "plateaus" in every semi-plane confirms the existence of two separation points on the cylinder surface as found in experiments. Here θ_l corresponds to the laminar separation point and θ_t to the turbulent separation point. There is a bubble between these two points. Curve 1 corresponds to the numerical results ($Re = 4 \cdot 10^5$), curve 2 is the laminar regime of the separation in the experiment of Fage & Falkner (1921) for $Re = 1.1 \cdot 10^5$, curve 3 is the turbulent regime in the experiment of Roshko (1961) for $Re = 8.4 \cdot 10^5$, and the circles are the transitional regime in the experiment of Bychkov & Larichkin (1987) for $Re = 4 \cdot 10^5$.

For a more detailed comparison of the spectral characteristics of the flow with experimental data of Farell & Blessmann (1983) the numerical calculations were used to investigate the spectral density of velocity fluctuations. In both calculations and experiment the dependence on time of the absolute value of the total velocity was recorded in four points in the vertical wake cross section located at $x = 2.07D$ from the centre of the cylinder. The points had different y coordinates. Then a spectral analysis of the time dependences of the absolute values of the velocity was made. On the diagrams depicted in Fig. 3 for different Reynolds numbers and different wake points the nondimensional frequency (Strouhal number) is along the abscissa axis and the spectral density of the velocity fluctuation $S(f)/\sigma$ is along the other axis. Here $S(f) = \overline{u'^2}(f)$ is the square of the velocity fluctuations for some frequency f and $\sigma = \overline{u'^2}$ is

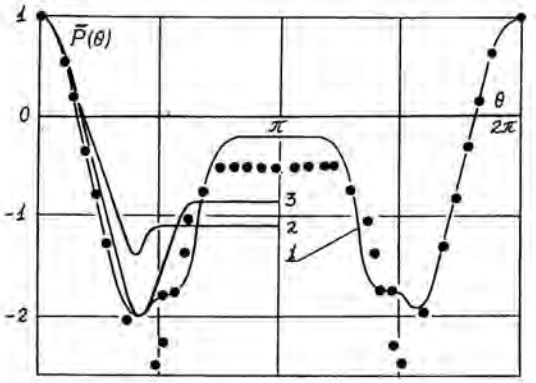

Figure 2: $\overline{P}(\theta)$-surface pressure.

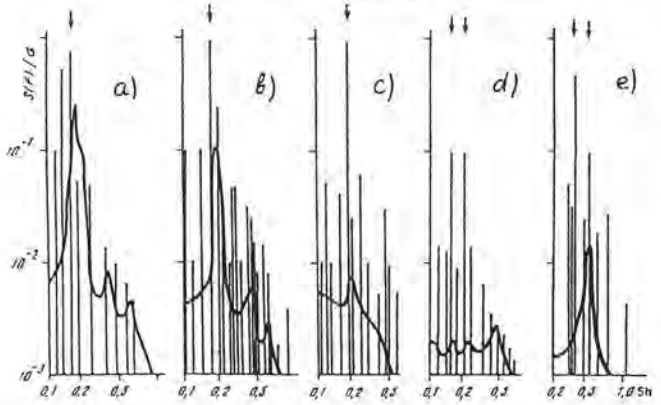

Figure 3: Spectral density of velocity fluctuation. a) $y = 0.57D$, $Re = 1.27 \times 10^5$, $Sh = 0.18$; b) $y = 0.57D$, $Re = 2.32 \times 10^5$, $Sh = 0.18$; c) $y = -0.5D$, $Re = 3.44 \times 10^5$, $Sh = 0.20$; d) $y = 0, Re = 3.74 \times 10^5$, $Sh = 0.34$, $Sh = 0.42$; e) $y = -0.2D$, $Re = 3.80 \times 10^5$, $Sh = 0.34$, $Sh = 0.42$.

the time-averaged of the squared velocity fluctuations. The experimental data are shown on diagrams by solid lines. The numerical results give us a discrete spectrum.

It is well known (and the same was observed in our calculations) that when the Reynolds number increases from 10^5 until $3 \cdot 10^5$ the Strouhal number increases from 0.18 until 0.20. When the Reynolds number increases (but $Re < Re_{cr}$) a sharp rise of Strouhal number takes place until 0.4 - 0.5. In the calculations at $Re = 3.8 \cdot 10^5$ the value $Sh = 0.42$ (Fig. 3e) was obtained. Moreover in the calculations at $Re = 3.74 \cdot 10^5$ and at $Re = 3.8 \cdot 10^5$ another additional frequency with $Sh = 0.34$ was observed (see Fig. 3d, e). The similar phenomenon was observed previously in some experiments (Bearman, 1969).

The dependences of time-mean total drag coefficient and of the Strouhal number Sh on the Reynolds number are shown in Figs 4 and 5, respectively.

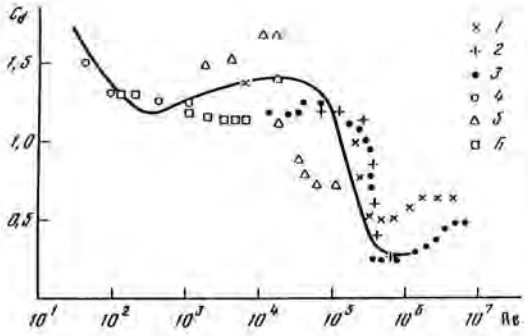

Figure 4: The dependence of the total drag coefficient $\overline{C}_d$ on the Reynolds number Re.

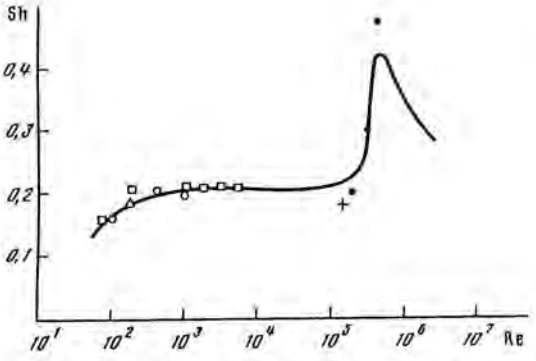

Figure 5: The dependence of the Strouhal number Sh on the Reynolds number Re.

The crisis of $\overline{C}_d$ and the sharp rise of the Strouhal number take place and are simulated numerically (without any turbulence models) for critical $Re = 4 \cdot 10^5$. As seen from Fig. 4 and 5 the numerical results denoted by the solid line are in a good agreement with experimental data (1 = Cantwell & Coles, 1983; 2 = Achenbach & Heinecke, 1981; 3 = Schewe, 1986) and calculations of other authors (4 = Jordan & Fromm, 1972; 5 = Kawamura *et al.*, 1986; 6 = Braza *et al.*, 1986). Moreover from the calculation the following formula is found for time-mean friction drag coefficient

$$\overline{C}_{d_f} = 1.879/(\log Re)^{2.58} ,$$

which coincides up to a constant multiplier with the well known Prandtl-Schlichting law (Schlichting, 1979) for a smooth flat plate for turbulent regime at $Re < 10^9$.

Conclusion

The direct numerical simulation of transitional separated fluid flow around a circular cylinder is based on the resolution of large ordered structures existing inside and outside the boundary layer. A spatial transformation of the radial coordinate was applied. The SMIF-method with explicit hybrid finite differences (second order accuracy, minimal scheme viscosity, workable in a wide range of Reynolds number, monotony) is used.

The obtained numerical results and comparison with experimental data confirm the applicability of the previously developed numerical approach for direct numerical simulation of transitional separated fluid flows.

Acknowledgement

This research has been supported in part by the Russian Foundation for Basic Researches (grant 94-01-00395 and 96-01-00546). The author is grateful to Dr. V.N. Konshin for performing some of the numerical calculations.

References

Achenbach, E. & Heinecke, E. 1981 – On vortex shedding from smooth and rough cylinder in the range of Reynolds numbers from 6×10^3 to 5×10^6. *J. Fluid Mech.* **109**, 239-251.

Bearman, P.W. 1969 – On vortex shedding from a circular cylinder in the critical Reynolds number regime. *J. Fluid Mech.* **37**, 577-585.

Braza, M., Chassaing, P. & Ha Minh H. 1986 – Numerical study and physical analysis of the pressure and velocity fields in the near wake of a circular cylinder. *J. Fluid Mech.* **165**, 79 -130.

Bychkov, N.M. & Larichkin, V.V. 1987 – The pressure and the pulsations on a cylinder at low distance from a screen [in Russian]. ITAM Rept. N1658, Novosibirsk, ITAM SB AS USSR.

Cantwell, B.J. 1981 – Organized motion in turbulent flow. *Ann. Rev. Fluid Mech.* **13**, 457-515.

Cantwell, B. & Coles, D. 1983 – An experimental study of entrainment and transport in the turbulent near wake of a circular cylinder. *J. Fluid Mech.* **136**, 321-374.

Fage, A. & Falkner, V.M. 1921 – Further experiments on the flow around a circular cylinder. ARC RM., 1369.

Farell, C. & Blessmann, J. 1983 – On critical flow around a smooth circular cylinder. *J. Fluid Mech.* **136**, 375-391.

Gushchin V.A. 1985 – Numerical investigation of separated fluid flows around a circular cylinder. Steady and periodic regimes. Computing Centre AS USSR, Moscow (in Russian)

Gushchin, V.A. & Konshin, V.N. 1992 – Computational aspects of the splitting method for incompressible flow with a free surface. *Computers and Fluids* **21**, 345-353.

Jordan, S.K. & Fromm, J.E. 1972 – Oscillatory drag, lift and torque on a circular cylinder in a uniform flow. *Phys. Fluids* **15**, 371-376.

Kawamura, T., Takami, H. & Kuwahara K. 1986 – Computation of high Reynolds numbers flow around a circular cylinder with surface roughness. *Fluid Dynamics Research* **1**, 145-162.

Roshko, A. 1961 – Experiments on the flow past a circular cylinder at very high Reynolds number. *J. Fluid Mech.* **10**, 345-356.

Schlichting, H. 1979 – Boundary layer theory.

Mc-Graw-Hill Schewe, G. 1986 – Sensitivity of transition phenomena to small perturbations in flow around circular cylinder. *J. Fluid Mech.* **172**, 33-46.

Townsend, A.A. 1956 – The structure of turbulent shear flows. Cambridge University Press.

Author's address

Institute for Computer Aided Design RAS,
19/18, 2nd Brestskaya str.,
Moscow 123056, Russia
E-mail: gushchin@inapro.msk.su

Session 2:
Cross-Flow Instabilities

M.S. Reibert°, W.S. Saric°, R.B. Carrillo Jr.° & K.L. Chapman▷

Nonlinear Stability, Saturation, and Transition in Swept-Wing Flows

Abstract

Stability experiments are conducted in the Arizona State University Unsteady Wind Tunnel on a 45° swept airfoil. The pressure gradient is designed to provide purely crossflow-dominated transition; that is, the boundary layer is subcritical to Tollmien-Schlichting (TS) disturbances. The airfoil surface is hand polished to a 0.25 μm rms finish. Under these conditions, stationary crossflow disturbances grow to nonuniform amplitude due to submicron surface irregularities near the leading edge. Spectral decompositions isolate single-mode growth rates for the fundamental and harmonic disturbances. The measurements show early nonlinear growth causing amplitude saturation well before transition. Comparisons with nonlinear PSE calculations show excellent agreement in both the amplitude saturation and the disturbance mode shape.

Background and motivation

The present swept-wing research program experimentally investigates the fundamental nature of the crossflow instability which leads to transition in three-dimensional boundary layers. Gregory *et al.* (1955) provide the theoretical basis for the instability. It results in an Orr-Sommerfeld type solution that can be implemented in a variety of ways. See Mack (1984) for the development of the details of the instability. Reed & Saric (1989), Saric (1992b) and Arnal (1992) review the literature.

Fundamentals

In contrast to Tollmien-Schlichting (TS) instabilities, the crossflow problem exhibits stationary ($f = 0$) as well as traveling disturbances. The traveling waves are more amplified according to linear theory, however many experiments are dominated by stationary waves. Müller & Bippes (1988), Bippes *et al.* (1991), and Deyhle & Bippes (1996) have shown that traveling waves are observed in tunnels rich in unsteady freestream disturbances, whereas stationary waves dominate in a low-turbulence environment. Since the flight environment is more benign than the wind tunnel, one expects the low-turbulence results to be more important.

One of the important results to come out of the DLR experiments is the set of data that show early saturation of the stationary disturbance amplitude and

the failure of linear theory to predict the growth of the instability (Bippes & Nitschke-Kowsky, 1990; Bippes *et al.*, 1991; Deyhle *et al.*, 1993). Dagenhart *et al.* (1989, 1990) and Radeztsky *et al.* (1994) observed similar behaviour. Kohama *et al.* (1991) showed that the *stationary* crossflow vortex controls transition by causing a high-frequency secondary instability resulting from the nonlinear mean-flow distortion. More recently, Deyhle & Bippes (1996) document the role of freestream disturbances with regard to traveling crossflow waves. Radeztsky *et al.*show that the receptivity process for stationary waves is strongly influenced by surface roughness, i.e., initial amplitudes. Insofar as stationary crossflow waves are concerned, it is clear that a successful transition prediction scheme must account for the initial conditions and the nonlinear growth of the disturbance. It is this aspect of the problem which we address in this paper.

Objectives

In earlier ASU experiments, Dagenhart *et al.* (1989, 1990) found that naturally occurring stationary crossflow waves of moderate amplitude have lower growth rates than predicted by linear theory. Under the same conditions, Radeztsky *et al.* (1993) investigated the sensitivity to surface roughness and showed early saturation of the natural stationary disturbance amplitude. Later experiments by Radeztsky *et al.* (1994) examined the growth of very weak crossflow waves in an attempt to close the gap between previous experimental results and linear theory. Even for these weak waves, linear theory completely failed to predict the disturbance growth.

In all of the early experiments measuring the growth of the stationary crossflow wave (Dagenhart *et al.*, 1989, 1990; Bippes *et al.*, 1991), the initial conditions for the disturbance amplitude came from the unknown natural roughness of the surface. Although a dominant wavelength appears, the resulting stationary structure is nonuniform in span and contains many fundamental disturbance modes of unknown amplitude. Consequently, comparisons with single-mode numerical predictions are not possible.

The same NLF(2)-0415 airfoil (Somers & Horstmann, 1985) is used as in the previous experiments. With a 45° sweep and a $-4°$ angle of attack, the favourable pressure gradient produces considerable crossflow while suppressing TS modes. Arrays of 6 μm roughness elements near the leading edge produce *uniform* stationary disturbances without excessive initial amplitudes. Spectral techniques are used to identify and follow specific stationary modes, thus providing single-wavelength growth rates for comparison with theoretical calculations.

The experiment

Facility and model

The Unsteady Wind Tunnel at Arizona State University is a low-speed, low-turbulence, closed-circuit facility used to study the stability and transition of

laminar boundary layers (Saric, 1992a). The airfoil model is mounted vertically in the 1.4 m x 1.4 m x 5 m test section. The aluminum surface is hand polished to a 0.25 μm rms finish so that even micron-sized roughness elements are well above the background roughness level.

Measurement techniques

Two standard hot-wire scanning methods are used to investigate the stationary crossflow waves. These are described below.

Wall-normal scans

Wall-normal boundary-layer scans provide a detailed map of the stationary structure. These maps are constructed by taking a spanwise series of mean-flow boundary-layer profiles at constant x/c. Once the scans are aligned with the airfoil surface, disturbance profiles are generated from which a stationary crossflow mode shape is computed. The disturbance growth is calculated by tracking the size of the mode shape at various chord positions. Three different measures of the mode shape size are used to characterize the disturbance amplitude: the maximum of the mode, the integral of $|u'|$ with respect to y, and the integral of $|u'|^2$ with respect to y. When the disturbance growth is cast in terms of the amplification factor N, all three measures collapse onto a single N-factor curve. These results, however, cannot (in general) be quantitatively compared with single-wavelength linear predictions since all amplified stationary modes are lumped into a single mode shape.

Single-wavelength information can be extracted from a boundary-layer map by taking a spanwise slice across the profiles at a constant height above the airfoil surface. The resulting velocity vs. span trace can be decomposed using spectral techniques to resolve the wavenumber content. Reasonable resolution in the wavenumber domain, however, requires a large spanwise extent of the measurement region. Consequently, this technique can quickly become prohibitively time consuming.

Spanwise scans

Individual-wavelength growth rates are obtained by restricting hot-wire measurements to a single spanwise scan at a constant height above the airfoil surface. With this technique, data are acquired along the entire span of the measurement region (240 mm) at much higher (spanwise) resolution than the wall-normal scans. Since data are collected at only one height in the boundary layer, these scans progress very quickly (typically 75 minutes per scan compared to nearly 45 hours for a full set of wall-normal scans with the same spanwise extent and resolution). The disadvantage of this technique is that the details of the stationary structure are not captured. For this reason, a disturbance mode shape (produced with a small set of wall-normal scans) is used to guide the spanwise scans.

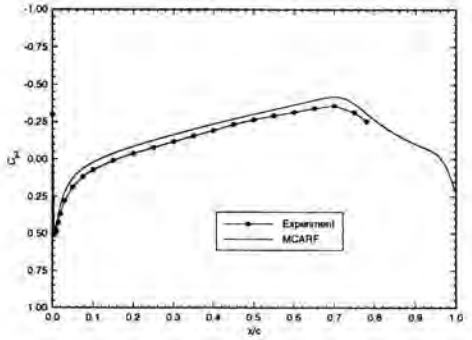

Figure 1: Experimental and theoretical swept C_p distribution at $Re_c = 2.4 \times 10^6$. The theory is computed with the NASA Langley code MCARF.

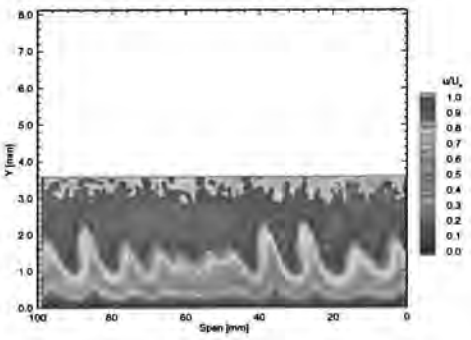

Figure 2: Streamwise velocity contours at $x/c = 0.45$, $Re_c = 3.0 \times 10^6$. No artificial roughness.

Results

Basic state

The basic state is documented with pressure measurements and mean-flow boundary-layer profiles. Fig. 1 shows the measured and theoretical C_p distribution over the airfoil upper surface. The experimental data are the average readings from two sets of pressure ports in the airfoil surface. The theoretical curve is the inviscid solution from the NASA Langley code MCARF. The agreement, especially in terms of the pressure gradient, is good over the entire measurement region.

Boundary-layer maps

Fig. 2 is a contour plot of the streamwise velocity u/U_e in the (y, z) plane. The flow is toward the reader, and the stationary vortices are turning in the right-handed sense. These data are acquired at $x/c = 0.45$, $Re_c = 3.0 \times 10^6$, with no artificial roughness on the airfoil. The nonuniformity of the naturally occurring stationary waves is caused by submicron surface irregularities near the leading edge. Fig. 2 displays a strong feature at a 12 mm spacing, which is approximately the most amplified stationary wavelength. At the same time, the richness in the spectral content is evident. This is typical of all of the earlier data (Bippes & Nitschke-Kowsky, 1990; Bippes *et al.*, 1991; Deyhle *et al.*, 1993; Dagenhart *et al.*, 1989, 1990), and indicates both nonlinear behaviour and multiple modes. Thus, even a nonlinear calculation that included only a single spanwise mode would be inappropriate to characterize the disturbance motion.

In order to generate spanwise-uniform stationary crossflow waves, initial conditions are controlled by applying a full-span array of roughness elements at

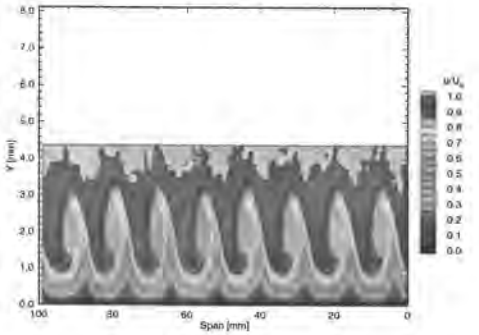

Figure 3: Streamwise velocity contours at $x/c = 0.45$, $Re_c = 2.4 \times 10^6$. A full-span array of 6 μm roughness with 12 mm spacing is at $x/c = 0.023$.

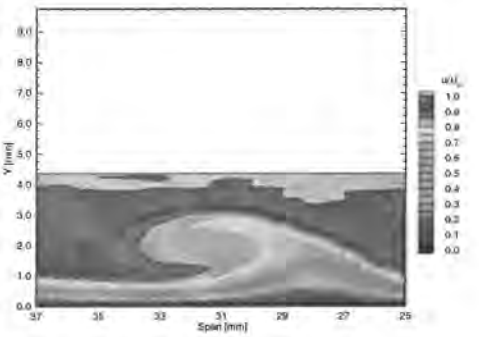

Figure 4: Single stationary crossflow vortex isolated from Figure 3 and plotted on a 1:1 scale.

$x/c = 0.023$ (near the neutral point of the instability) following Radeztsky *et al.* (1993). The roughness height is $k = 6$ μm, and the 3.7 mm diameter elements are spaced 12 mm apart in span, corresponding to the most amplified wavelength according to linear theory. Fig. 3 shows the streamwise velocity contours at $x/c = 0.45$ and $Re_c = 2.4 \times 10^6$ with this roughness distribution. Under these conditions, the roughness Reynolds number, Re_k, is 0.1. The uniformity of the fundamental 12 mm mode is striking, and allows for meaningful comparisons with single-mode theoretical predictions. A single vortex is isolated in Fig. 4 and plotted on a 1:1 scale. The crossflow vortex produces regions of upwelling and downwelling which transport low- and high-momentum fluid, respectively. The symmetry of the co-rotating vortex distorts this momentum transfer giving an apparent rollover of low-momentum fluid that appears above high-momentum fluid.

Fig. 5 shows the 100 boundary-layer profiles from which Fig. 3 is generated. The profiles are obtained at 1 mm intervals in the swept span direction. The dots indicate the spanwise average of the profiles, which accounts for basic state plus the mean-flow distortion [(0,0) mode]. It should be emphasized that these are mean profiles and not an unsteady oscillation in the boundary layer. One can clearly see how the stationary vortex structure has distorted the mean flow, resulting in accelerated, decelerated, and doubly inflected profiles existing millimetres apart. The nonlinearities are indicated by the distortion of the averaged profile in the vicinity of $y \approx 2.8$ mm. This distortion of the basic state leads to the secondary instability which controls the transition to turbulence (Kohama *et al.*, 1991).

Disturbance profiles are generated by subtracting the basic state plus mean-flow distortion (i.e., the spanwise average profile) from the individual boundary-layer profiles (Fig. 6). From these data, the crossflow mode shape is generated by computing the spanwise rms of the disturbance profiles (Fig. 7). This mode

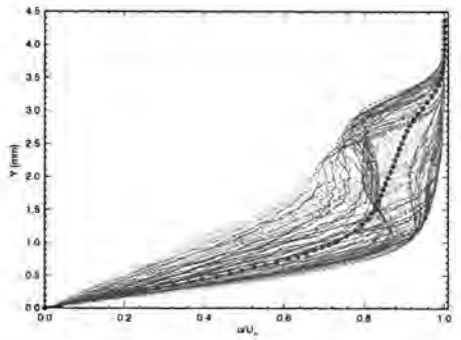

Figure 5: Spanwise array of boundary-layer profiles at $x/c = 0.45$, $Re_c = 2.4 \times 10^6$. A full-span array of 6 μm roughness with 12 mm spacing is at $x/c = 0.023$. The dots indicate the mean of the profiles.

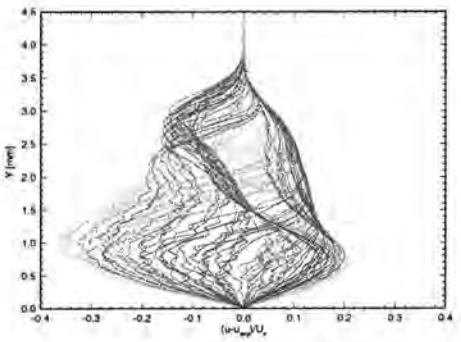

Figure 6: Spanwise array of disturbance profiles at $x/c = 0.45$, $Re_c = 2.4 \times 10^6$. A full-span array of 6 μm roughness with 12 mm spacing is at $x/c = 0.023$.

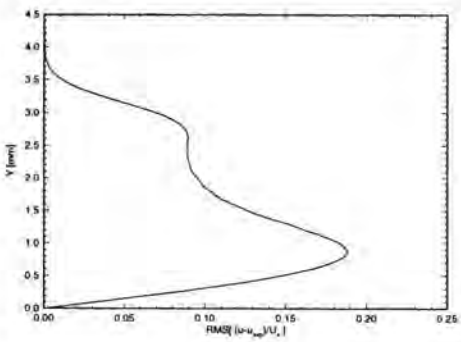

Figure 7: Stationary crossflow mode shape at $x/c = 0.45$, $Re_c = 2.4 \times 10^6$. A full-span array of 6 μm roughness with 12 mm spacing is at $x/c = 0.023$.

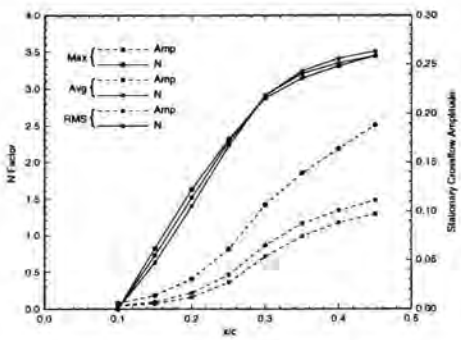

Figure 8: Disturbance amplitude distribution at $Re_c = 2.4 \times 10^6$. A full-span array of 6 μm roughness with 12 mm spacing is at $x/c = 0.023$. The reference point for the N-factor calculations is $x/c = 0.10$.

shape contains the fundamental disturbance and all amplified harmonics.

The total disturbance amplitude is computed using three measures of the mode shape size as outlined above. Growth rates are obtained by repeating this procedure at several chord positions. Fig. 8 shows the disturbance amplitude distribution for 6 μm roughness with 12 mm spacing at $Re_c = 2.4 \times 10^6$. The dashed lines represent the absolute size of the mode shape as computed by each of the three measures. The solid lines show the corresponding amplification factor N. The ability of the N-factor to collapse the data onto a single curve is typical. The nonlinear saturation is clearly evident, and occurs well before the transition location of $(x/c)_{tr} = 0.52$. It is worth emphasizing that these measures record the *total* disturbance amplitude since all amplified wavelengths are present in the mode shape.

Fig. 9 compares the experimental N-factor (as computed from the maximum of the mode shape profiles) with various theoretical predictions of Haynes & Reed (1996). The nonlinear parabolized stability equations (NPSE) results are computed using initial amplitudes provided by the experiment. The agreement is excellent, especially in predicting the amplitude saturation. (At this time, the Haynes & Reed formulation does not contain curvature, which is known to be stabilizing and may account for the small differences in the disturbance growth.) In contrast, the Orr-Sommerfeld and linear PSE results fail to predict the details of the disturbance growth. The early qualitative agreement with the linear PSE results indicates that the nonlinear effects are initially weak up to $x/c = 0.20$, at which time the growth rates depart from linear behaviour. It is at this location that the spanwise average of the boundary-layer profiles first begins to exhibit the distortion shown in Fig. 5.

Wavelength separation

As pointed out previously, crossflow amplitudes computed from mode-shape profiles contain all amplified stationary modes. To decompose the wavenumber content of the disturbance, the spanwise scan technique discussed above is used. Fig. 10 shows the spanwise velocity profile at $x/c = 0.45$ for $Re_c = 2.4 \times 10^6$. The roughness configuration is $k = 6$ μm with 12 mm spanwise spacing. The data are acquired at $y = 0.9$ mm above the airfoil surface, corresponding to the maximum of the mode-shape profile. The strong distortion of the boundary-layer is evident, as is the spanwise uniformity of the stationary structure.

The FFT-based power spectral density (PSD) is shown in Fig. 11. The dominance of the fundamental 12 mm mode is clear. However, the superharmonics at $\lambda_s = 6$ mm and 4 mm are also amplified. (The amplitude of the 4 mm mode is too small to appear on the scale of Fig. 11.) This wave doubling was observed by Saric & Yeates (1985) and predicted by Reed (1988). Disturbance amplitudes are computed by integrating the peaks of the PSD. When repeated at several chord positions, the growth rates of Fig. 12 are obtained. The dashed lines represent the rms amplitude of the individual modes, while the amplification factor N is plotted with solid lines. At each chord location, the spanwise scan is taken

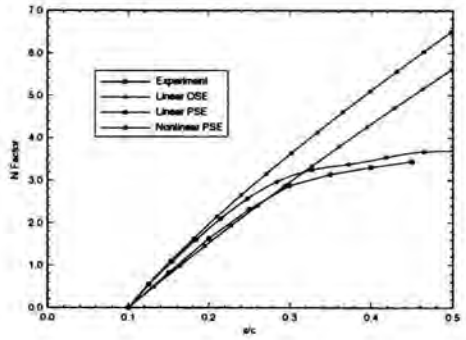

Figure 9: Measured and theoretical N-factor for $Re_c = 2.4 \times 10^6$. A full-span array of 6 μm roughness with 12 mm spacing is at $x/c = 0.023$. The reference point for the N-factor calculations is $x/c = 0.10$.

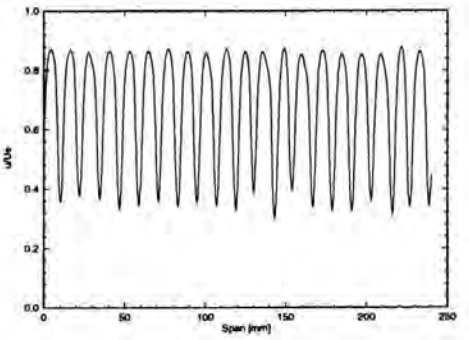

Figure 10: Spanwise hot-wire scan at $x/c = 0.45$, $Re_c = 2.4 \times 10^6$, $y = 0.9$ mm. A full-span array of 6 μm roughness with 12 mm spacing is at $x/c = 0.023$.

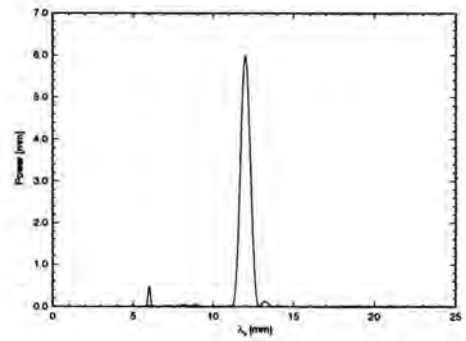

Figure 11: FFT power spectrum of spanwise hot-wire scan at $x/c = 0.45$, $Re_c = 2.4 \times 10^6$, $y = 0.9$ mm. A full-span array of 6 μm roughness with 12 mm spacing is at $x/c = 0.023$.

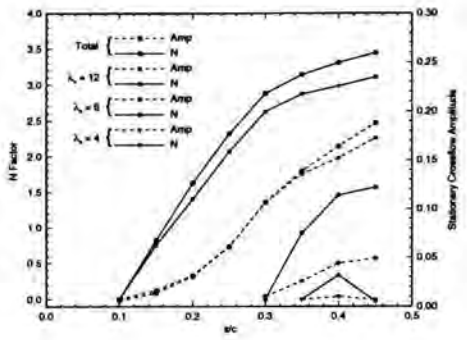

Figure 12: Total and single-mode amplitude distribution at $Re_c = 2.4 \times 10^6$. A full-span array of 6 μm roughness with 12 mm spacing is at $x/c = 0.023$. N-factors are relative to the point at which the disturbance is first detected.

at the boundary-layer height corresponding to the maximum of the mode-shape profile. This permits us to compare the amplitude of the individual modes with that of the total disturbance as computed from the maximum of the mode shape (indicated on Fig. 12 by the lines marked "Total"). It is a remarkable verification of the two different measurement techniques that the amplitudes of the total and fundamental ($\lambda_s = 12$ mm) disturbances agree for $x/c < 0.30$. For $x/c > 0.30$, the amplitude of the fundamental diverges from the total disturbance, and the harmonic at $\lambda_s = 6$ mm becomes measurable. In the region of strong nonlinear interaction and amplitude saturation ($x/c \geq 0.35$), the 6 mm component shows significant energy and the 4 mm mode becomes unstable.

Conclusions

Stationary crossflow waves are investigated on a swept airfoil within a low-disturbance environment. It is shown that even though the surface is polished to 0.25 μm rms roughness, stationary crossflow waves still dominate the transition process. Because the initial roughness is nonuniform, the resulting disturbance motion is nonuniform and is complicated by the presence of many different modes. Because of this, comparisons with different theoretical and computational schemes are unnecessarily rendered much more difficult.

Systematic introduction of equally spaced 6 μm roughness elements ($Re_k = 0.1$) is shown to produce an ideal fundamental mode at that spacing. When the roughness elements are placed at the most amplified linear-mode wavelength of $\lambda_s = 12$ mm, disturbance growth, departure from linearity, and saturation amplitude are documented. Evidence of growth at the 6 mm and 4 mm harmonics is shown. There is no evidence of wavelength doubling (i.e., components at 24 mm or 36 mm). Comparisons with computations using nonlinear parabolized stability equations are very good. It is possible to conclude that the introduction of systematic weak roughness provides the necessary data base for comparisons with theory and computations.

These data continue to illustrate the extreme sensitivity to leading-edge roughness. Strong nonlinear distortion of the mean flow is observed, as is the nonlinear saturation of the disturbance amplitude. This saturation occurs well before the transition to turbulence. Linear theory fails to capture these details of the disturbance growth. On the other hand, NPSE calculations agree remarkably well with the experimental data.

Acknowledgements

This work was supported by NASA Langley Research Center Grant NCC-1-94. Mr. Reibert was supported by NASA Langley Research Center Fellowship NAG-1-1111. Mr. Carrillo was supported by the National Science Foundation Fellowship Program. Mr. Tim Haynes' numerical calculations and technical discussions

are gratefully acknowledged. The technical support of Mr. Dan Clevenger is greatly appreciated.

References

Arnal, D. 1992 – Boundary-layer transition: Prediction, application to drag reduction. In *Special Course on Skin Friction Drag Reduction*, AGARD R-786.

Bippes, H. 1990 – Instability feature appearing on swept wing configurations. In *Laminar-Turbulent Transition* (eds. Arnal, D. and Michel, R.), vol. 3, pp. 419-430. Springer-Verlag, New York.

Bippes, H. 1991 – Experiments on transition in three-dimensional accelerated boundary-layer flows. In *Proc. R.A.S. boundary Layer Transition and Control*, Cambridge, U.K.

Bippes, H. & Nitschke-Kowsky, P. 1990 – Experimental study of instability modes in a three-dimensional boundary layer. *AIAA J.* **28**(10), 1758-1763.

Bippes, H., Müller, B. & Wagner, M. 1991 – Measurements and stability calculations of the disturbance growth in an unstable three-dimensional boundary layer. *Phys. Fluids* **3**(10), 2371-2377.

Dagenhart, J.R., Saric, W.S., Mousseux, M.C. & Stack, J.P. 1989 – Crossflow vortex instability and transition on a 45-degree swept wing. AIAA Paper 89-1892.

Dagenhart, J.R., Saric, W.S., Hoos, J.A. & Mousseux, M.C. 1990 – Experiments on swept-wing boundary layer. In *Laminar-Turbulent transition* (eds. Arnal, D. and Michel, R.), vol. 3, pp. 369-380. Springer-Verlag, New York.

Deyhle, H. & Bippes, H. 1996 – Disturbance growth in an unstable three-dimensional boundary layer and its dependence on environmental conditions. To appear in *J. Fluid Mech.*

Deyhle, H., Höhler, G. & Bippes, H. 1993 – Experimental investigation of instability wave propagation in a 3-D boundary-layer flow. *AIAA J.* **31**(4), 637-645.

Gregory, N., Stuart, J.T. & Walker, W.S. 1955 – On the stability of three-dimensional boundary layers with applications to the flow due to a rotating disk. *Phil. Trans. Roy. Soc. Lon. A* **248**(943), 155-199.

Haynes, T.S. & Reed, H.L. 1996 – Computation in nonlinear saturation of stationary crossflow vortices in a swept-wing boundary layer. AIAA Paper 96-0182.

Kohama, Y., Saric, W.S. & Hoos, J.A. 1991 – A high-frequency secondary instability of crossflow vortices that leads to transition. In *Proc. R.A.S. Boundary Layer Transition and Control*, Cambridge, U.K.

Mack, L.M. 1984 – Boundary-layer linear stability theory. In *Special Course on Stability and Transition of Laminar Flows,* AGARD R-709.

Müller, B. & Bippes, H. 1988 – Experimental study of instability modes in a three-dimensional boundary layer. In *Fluid Dynamics of Three-Dimensional Turbulent Shear Flows and Transition,* AGARD CP-438.

Radeztsky, R.H. Jr, Reibert, M.S. Saric, W.S. & Takagi, S. 1993 – Effect of micronsized roughness on transition in swept-wing flows. AIAA Paper 93-076.

Radeztsky, R.H. Jr, Reibert, M.S. & Saric, W.S. 1994 – Development of stationary crossflow vortices on a swept wing. AIAA Paper 94-2373.

Reed, H.L. & Saric, W.S. 1989 – Stability of three-dimensional boundary layers. In *Annual Review of Fluid Mechanics* (eds. Lumley, J.L., Van Dyke, M. and Reed, H.L.), vol. 21, pp. 235-284. Annual Reviews Inc., Palo Alto, California.

Saric, W.S. 1992a – The ASU transition research facility. AIAA Paper 92-3910.

Saric, W.S. 1992b – Laminar-turbulent transition: Fundamentals. In *Special Course on Skin Friction Drag Reduction,* AGARD R-786.

Saric, W.S. & Yeates, L.G. 1985 – Experiments on the stability of crossflow vortices in swept-wing flows. AIAA Paper 85-0493.

Somers, D.M. & Horstmann, K.H. 1985 – Design of a medium-speed natural-laminar-flow airfoil for commuter aircraft applications. *DFVLR-IB/29-85/26.*

Authors' addresses

[a]Arizona State University
Mechanical and Aerospace Engineering
Box 87-6106
Tempe, AZ 85287-6106, USA

[b]Clarkson University
Mechanical and Aeronautical Engineering
Box 5725
Potsdam, NY 13699-5725, USA

T. Lerche & H. Bippes

Experimental Investigation of Cross-Flow Instablility Under the Influence of Controlled Disturbance Excitation

Abstract

A three-dimensional boundary-layer flow on a 45° swept flat plate with imposed pressure gradient is investigated experimentally utilizing controlled introduction of single mode disturbances. The base flow is subject to cross-flow instability, for which the nonlinear evolution largly depends on the initial amplitudes of stationary cross-flow vortices and oblique traveling waves. Both could independently be initiated experimentally by means of fixed roughness elements and a newly developed unsteady disturbance generator, respectively. The instability development and transition process has been investigated for different combinations of initial conditions by means of hot-wire anemometry.

The experimental set-up

The present DLR transition experiment basically consists of a 45° swept flat plate and a displacement body which imposes a nearly constant negative pressure gradient (for more details see *e.g.* Müller & Bippes, 1988).

The leading edge has a non-symmetrical Clark-Y profile without curvature discontinuity on the upper side. The attachment line is at $x_c/c \approx 0.02$ due to an angle-of-attack of -1.0°. Experiments were carried out in the 1 × 0.7 m^2 wind tunnel at DLR Göttingen with $Tu = 0.15$ % in the frequency range between 2 Hz and 2 kHz. Infinite swept conditions could be achieved to a good degree of approximation by using two end plates (Fig. 1) with potential streamline curvature. Distinguished must be the chord oriented coordinate system (index c) and the streamline oriented coordinate system (index s). The latter is locally tangential to potential streamlines at the edge (index e) of the boundary layer. Specially designed subminiature V-type hot-wire probes have been used to measure the wall parallel velocity components. All measurements are non-dimensionalized by the local velocity Q_e at the edge of the boundary-layer. The freestream velocity Q_∞ has been determined from the settling-chamber velocity by taking the blockage effect of the model into account.

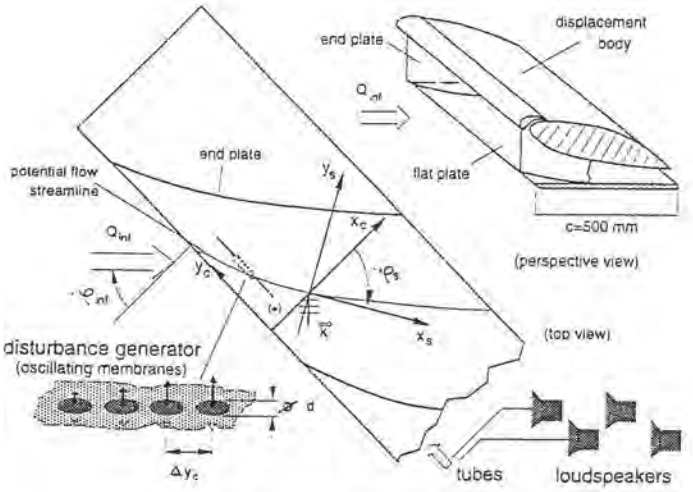

Figure 1: Experimental set-up.

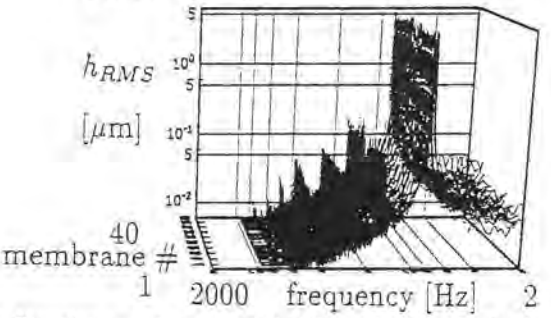

Figure 2: Fourier spectra of excitation membrane displacements.

The newly developed single mode disturbance generator

The newly developed disturbance generator was centered between the two end plates at $x_c/c = 0.13$. 40 equally spaced circular membranes are flush mounted parallel to the leading edge on the upper surface of the flat plate, i.e. in spanwise direction. One generator version with membranes of 40 μm polyurethane, diameters $d = 2$ mm and spacings Δy_c=6 mm was compared to a second version with membranes of 15 μm polyester, diameters d =2.5 mm and spacings of Δy_c=4.5 mm.

The membranes oscillate sinusoidally with adjustable displacement amplitude and phase shift by means of pressure fluctuations. The pressure fluctuations are produced by 20 loudspeakers which are connected via tubes. A system of 20 programmable signal generators using a common clock and trigger signal was built up to drive the loudspeakers. The limitation to 20 channels implies a symmetry condition that limits the phase shifts between two membranes to multiple integers of 18°. The phase shifts of the excitation signals assigned the

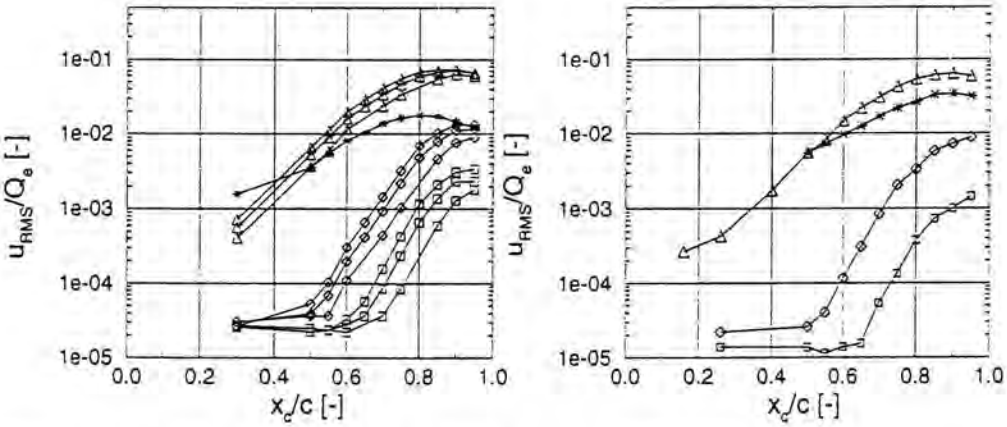

Figure 3: Amplification curves for excitation levels of 50%, 75% and 100% $\equiv$ 30 μm for case (1,1) (left) and 100% for case (0,1)+(1,1) (right) at $Q_\infty = 12.5$ m/s. $*$: stationary, $\triangle$: fundamental, $\diamond$: first harmonic, $\square$: second harmonic.

spanwise wavelength of initiated cross-flow waves. The signal of one channel was used to trigger the measurements and has been recorded as a reference signal of the hot-wire measurement data.

Displacement amplitudes and phase shifts were measured and set by means of a commercially available laser optical device with an accuracy of 0.2 μm/mV. Fig. 2 shows as an example the variation of displacement amplitudes spectra of the second generator version, measured in the centre of the membranes ($h_{RMS} = \sqrt{\Delta f \cdot G}$ with $\Delta f = 1$ Hz and G denoting the power spectral density). Besides the excitation frequency of $f = 82$ Hz the higher harmonics appearing are smaller by more than one order of magnitude. The maximum amplitudes of the first and second disturbance generator were in the order of 30 and 10 μm, respectively. The phase shifts were found to differ by approximately ± 4.5 % from the adjusted value. Both disturbance generators could be used to excite traveling waves with frequencies from 20 to 200 Hz.

Linear and weakly nonlinear instability regime

Measurements were carried out at the relatively low freestream velocity of $Q_\infty = 12.5$ m/s in order to qualify the effectiveness of the integrated disturbance generator and to obtain data for comparison with numerical computation. For this case no transition occurred on the model surface.

Excited traveling waves became measurable only 10 mm behind the membranes at $x_c/c = 0.15$ where the amplitude of the fundamental mode amounts to only 0.02 % of the freestream velocity. Furthermore, it was found that the disturbance amplitudes scale linearly with the excitation level (in a semi-logarithmic plot) up to 60% chord, thus indicating the linear range of amplification. Fig. 3

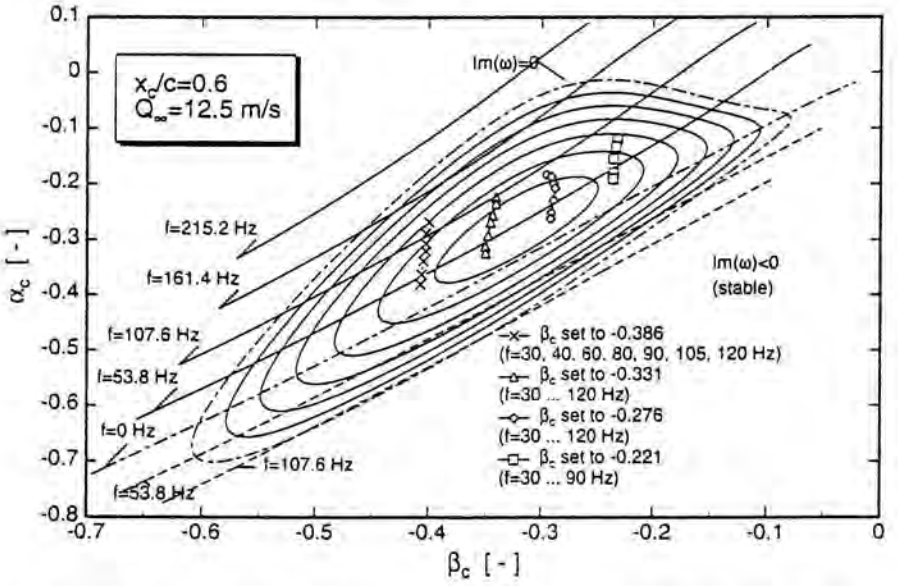

Figure 4: Wavenumber stability diagram for freesteam velocity $Q_\infty = 12.5$ m/s at location $x_c/c = 0.6$. Closed curves are curves of constant amplification rate. × △ ◇ □: measurements.

shows exponential growth of the excited 80 Hz wave with spanwise wavenumber $\beta_c = 2\pi/\lambda_c = 0.37$ denoted by (1,1) until from $x_c/c \geq 0.6$ on, nonlinearly generated harmonics become significant and amplitude saturation sets in.

This (1,1) wave was experimentally found to have maximum amplification rate. For comparison, a 82 Hz wave with $\beta_c = 0.42$ was excited using the second disturbance generator. Again, these parameters were determined to yield the most amplified wave. They match the former results almost perfectly although the stationary vortices have been initiated by 13 roughness elements at $x_c/c = 0.076$ (diameter d=2mm, height h=18 μm, $\beta_c = 0.45$) denoted by (0,1) to increase the maximum stationary amplitude $(max[u_s] - min[u_s])/[2Q_e]$ from 2 to 3 %.

Additionally, wavenumber components of initiated waves were determined from two parallel spanwise hot-wire traverses with z=const. and 60 mm length at 60 and 61 % chord. The spanwise phase $\phi(y_c)$ distributions of the excited fundamental modes were determined from a cross spectra calculation of the hot-wire signals and the reference signal. The phase distributions $\phi(y_c)$ obtained from two parallel traverses are two parallel linear curves. The spanwise wavelength was calculated from $\partial y_c/\partial\phi \cdot 360°$. The displacement Δy_c of the linear phase curves was used in conjunction with the known measurement displacement Δx_c to calculate a propagation angle $\Psi_c = \arctan[\Delta x_c/\Delta y_c]$. Values of the spanwise wavenumber component β_c and chord oriented component α_c normalized with $l_{ref} = \sqrt{\nu x_c/u_{c,e}} = 0.79$ mm for different excitation frequencies and

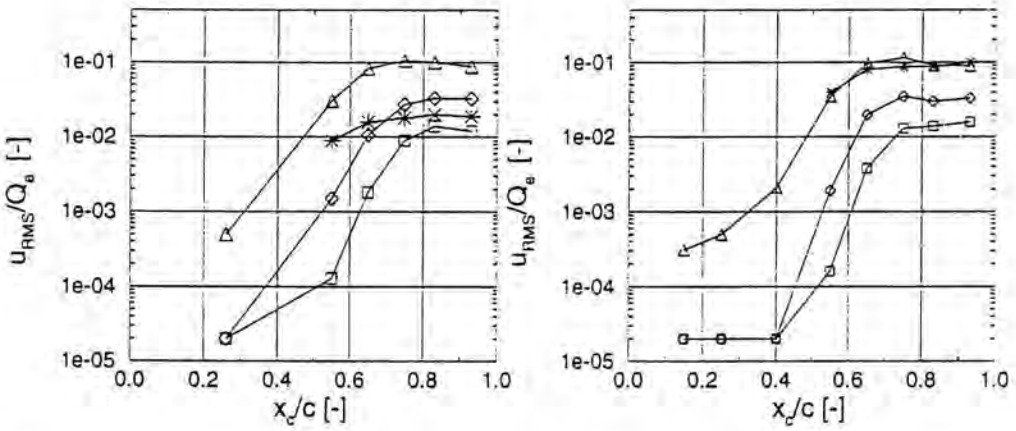

Figure 5: Amplification curves for case (1,1) (left) and case (0,1)+(1,1) (right) at $Q_\infty = 16.3$ m/s. $\star$:stationary, $\triangle$: fundamental, $\diamond$: first harmonic, $\square$: second harmonic.

spanwise wavenumbers are plotted in Fig. 4 (denoted by symbols) together with local linear stability calculation results provided by Koch (1995). The measured wavenumber components are satisfactorily matched by numerical predictions. However, it should be noted that less amplified traveling waves could not be initiated.

Nonlinear interactions and saturation

Nonlinear effects have been studied at a freestream velocity of $Q_\infty = 16.3$ m/s, where the onset of laminar to turbulent breakdown can be observed near the end of the model.

Like figure 3, figure 5 shows the development of maximum amplitudes for two cases. Case (1,1) implies controlled excitation of a 82 Hz and $\beta_c = 0.42$ traveling wave, whereas case (0,1)+(1,1) includes the additional initiation of stationary vortices with $\beta_c = 0.45$ by application of 15 roughness elements of diameter d =2.5 mm and height h =18 μm at $x_c/c = 0.076$. The amplitude development of the traveling waves was found to be very similar although the saturation amplitude of the stationary vortices $(max[u_s] - min[u_s])/[2Q_e]$ differs significantly between 2 % for case (1,1) and 10 % for case (0,1)+(1,1).

The effect of large amplitude vortices on the traveling modes is demonstrated in Fig. 6, where the spanwise distribution of fluctuation velocity profiles for case (1,1) and case (0,1)+(1,1) is compared at location $x_c/c = 0.93$. The strong amplitude variation for case (0,1)+(1,1) clearly indicates a superposition of several waves with equal frequency but different spanwise wavenumbers.

This finding is confirmed by Fig. 7 which shows the corresponding phase distributions. It is furthermore in agreement with predictions of secondary instability theory by Fischer *et al.* (1993) and direct numerical simulation results

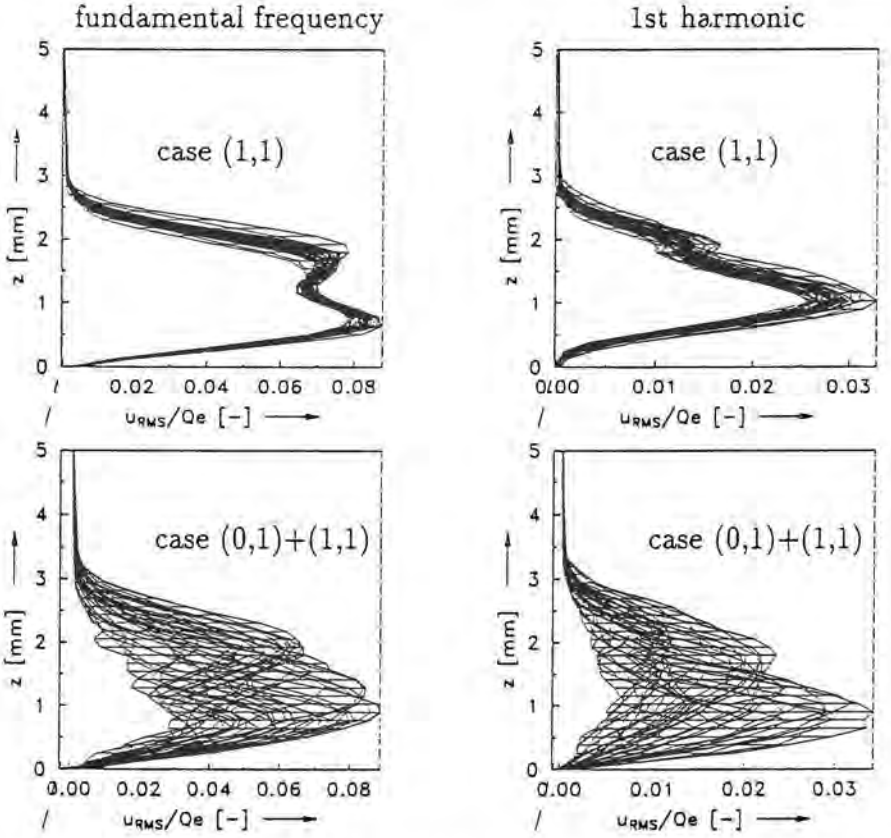

Figure 6: Spanwise modulation of fundamental 82 Hz (left) and first harmonic 164 Hz (right) for case (1,1) (top) and case (0,1)+(1,1) (bottom) at $x_c/c = 0.93$.

obtained by Müller *et al.* (1994). Further investigations will be aimed at a more detailed modal analysis of these phase distributions.

Another important interaction between stationary vortices and traveling waves is documented in Fig. 8 where mean velocity profiles $u_s(z)$ of one identical spanwise wavelength are compared for case (0,1) and case (0,1)+(1,1). The spanwise variation of u_s decreases, when excited traveling waves are present. This confirms earlier indications from measurements as well as Müller's (1994) numerical results that traveling modes extract energy from stationary modes and thus inhibit their amplitude growth.

Conclusions

A new type of disturbance generator has been developed and tested. It has proven to be a well-suited device for excitation of single, oblique traveling waves in a three-dimensional boundary-layer to follow their downstream development

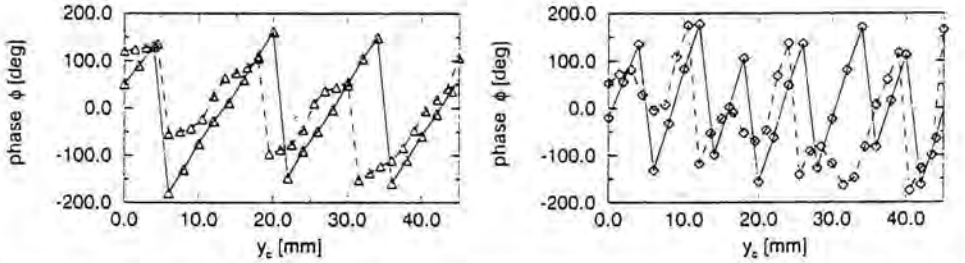

Figure 7: Spanwise phase distribution measured at z=1.0 mm and $x_c/c = 0.93$ of 82 Hz modes (left) and 164 Hz modes (right) for case (1,1) and case (0,1)+(1,1) (dashed lines).

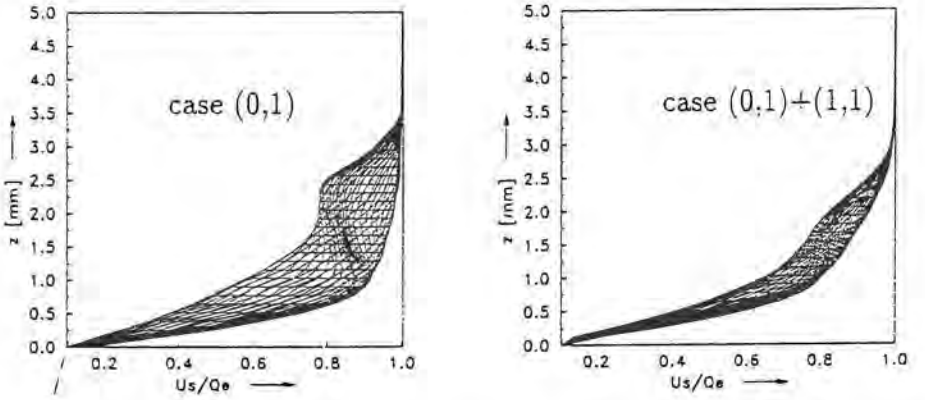

Figure 8: Spanwise modulation of u_s profiles for case (0,1) (left) and case (0,1)+(1,1) (right) at $x_c/c = 0.93$.

for comparison with theory. The traveling wave characteristics have been found to be in agreement with local, linear stability theory predictions.

Interactions between stationary and traveling cross-flow vortices can now be analysed by utilizing the important phase information of one reference excitation signal. It has been shown that large amplitude stationary cross-flow vortices lead to the nonlinear amplification of modes with equal frequency but different spanwise wavenumbers. These modes contribute to laminar to turbulent transition as could be seen from the appearance of a high-frequency secondary instability towards the end of the plate. This high-frequency instability was found to be in agreement with observations of Kohama *et al.* (1991) and predictions of Fischer *et al.* (1993) and Malik *et al.* (1994) but also seems to be phase-coupled to the excited traveling wave. As another finding, large initial amplitudes of traveling modes attenuate significantly the growth of unsteady modes.

Cross-flow modes with equal frequency but different spanwise wavenumbers also largely increase the spatial flow complexity. This could be seen from recon-

structed phase-averaged velocity fields which could be decomposed by Proper Orthogonal Decomposition (see *e.g.* Lumley, 1967) to obtain coherent structures. However, this work and the finding of a high-frequency secondary instability has to be elaborated in more detail and will be presented at the 6th European Turbulence Conference at Lausanne, July 2-5, 1996.

References

Fischer, T.M., Hein, S. & Dallmann, U. 1993 – A theoretical approach for describing secondary instability features in three-dimensional boundary-layer flows. *AIAA paper* 93-0080.

Koch, W. 1995 – private communication, DLR Göttingen.

Kohama, Y., Saric, W.S. & Hoos, J.A. 1991 – A high-frequency, secondary instability of cross-flow vortices that leads to transition. *Proc. R.A.S Conf. on 'Boundary-Layer Transition and Control'*, Cambridge, UK.

Lumley, J.L. 1967 – The structure of inhomogeneous turbulence, in *Yagolm, A.M., Tatarski, V.I. (ed.), Atmospheric Turbulence and wave propagation*, Dokl. Nauk. Moscow, pp. 166–178.

Malik, M.R., Li, F. & Chang, C.-L. 1994 – Cross-flow disturbances in three-dimensional boundary layers: nonlinear development, wave interaction and secondary instability. *J. Fluid Mech.* **268**, 1-36.

Müller, B. & Bippes, H. 1988 – Experimental study of instability modes in a three-dimensional boundary-layer. *Proc. AGARD Symp. on 'Fluid Dynamics of Three-Dimensional Turbulent Shear Flows and Transition'*, Cesme, Turkey.

Müller, W., Bestek, H. & Fasel, H. 1994 – Spatial direct numerical simulation of transition in a three-dimensional boundary-layer. *Proc. IUTAM Symp. ' Laminar-Turbulent Transition'*, Sendai, Japan.

Authors' address

Deutsche Forschungsanstalt für Luft- und Raumfahrt e.V.
Institut für Strömungsmechanik
Bunsenstraße 10
37073 Göttingen
Germany

T. Wintergerste & L. Kleiser

Direct Numerical Simulation of Transition in a Three-Dimensional Boundary Layer

Abstract

Transition to turbulence in a three-dimensional boundary layer is investigated by a highly resolved direct numerical simulation adapted to a transition experiment made at DLR Göttingen. A parallel base flow is defined locally by Falkner-Skan-Cooke similarity profiles. As shown earlier, the temporal simulation results can be related to the spatial disturbance development in the experiment and show good agreement with measurements. The crossflow vortices, which develop as a primary instability of the laminar flow, break down at the late stages of the transition process. At the end of transition, the shape factor and local skin friction coefficient of the computed mean velocity profile reach their turbulent levels. Particular attention is given to the development of flow structures in the breakdown stage. A new three-dimensional vortical structure is found to emerge which propagates with approximately 70% of the free-stream velocity in the streamwise direction. Vortical structures are identified by different criteria based on local pressure minima or the velocity-gradient tensor ∇u.

Introduction

Transition to turbulence in the swept wing boundary layer of a modern aircraft can be caused by different instability mechanisms. The crossflow instability dominates regions on the wing where a strong favourable pressure gradient exists. This instability is characterized by the presence of co-rotating stationary crossflow vortices and travelling waves which are both linearly unstable. For an overview readers are referred to the paper by Reed & Saric (1989).

Experiments and theoretical investigations have shown that nonlinear interactions play an important role already at early stages of the transition process. These stages are characterized by interactions between the crossflow vortices and the travelling waves. At the highly nonlinear stages of transition, a secondary instability with a frequency a magnitude larger than the travelling primary disturbances was observed in the experiments by Kohama *et al.* (1991). This instability was also observed in theoretical investigations by Malik *et al.* (1994) based on PSE in a swept Hiemenz flow. They found that the high-frequency instability is associated with a shear layer on the upper side of the crossflow vortex. The processes at the late stages which lead to the breakdown of the crossflow vortex and to the onset of turbulence are not yet fully understood.

Our investigations are adapted to the transition experiment by Bippes *et al.* (1991). Various attempts have been made at clarifying the transition process

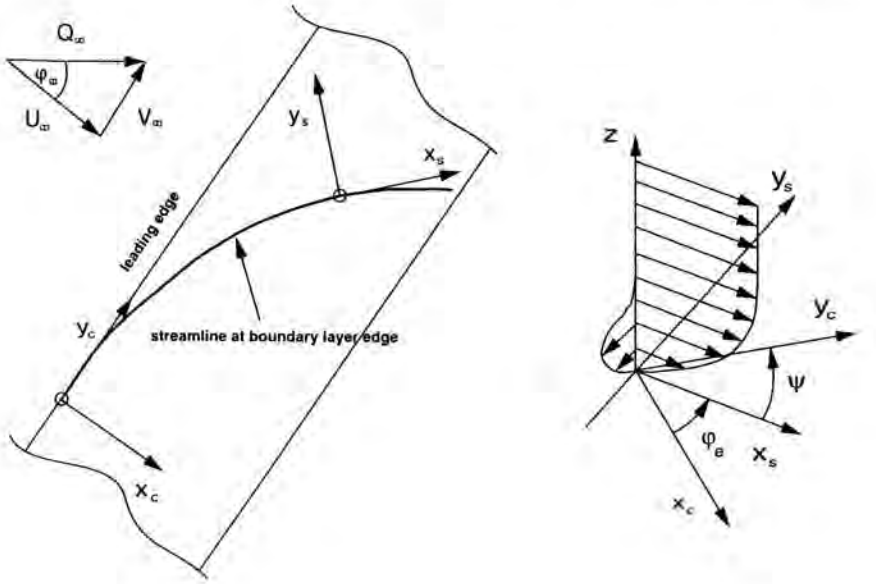

Figure 1: Sketch of the DLR swept plate transition experiment (Bippes *et al.*, 1991).

observed in this experiment. Fischer & Dallmann (1992) find a good agreement between the results of the secondary stability of the crossflow-vortex modulated base flow and the experiment. Meyer and Kleiser (1989,1990) and Wagner (1992) carried out temporal simulations of the 3D-boundary layer transition. They observed a strong deformation of the mean flow which agrees well with the experimental observations. These simulations reached a highly developed stage of transition but they were not fully resolved in the late breakdown stage of the crossflow vortices.

In this contribution we present a continuation of the latter work which includes the complete breakdown process. Our interest will be focussed on the flow phenomena occurring in the late stages of transition where the crossflow vortices break down and the boundary layer becomes turbulent.

Base flow

The simulation presented here is adapted to the DLR transition experiment (Bippes *et al.*, 1991) in which a three-dimensional boundary layer develops on a swept flat plate. A displacement body above the plate is used to generate an approximately constant negative pressure gradient normal to the leading edge. A sketch of the various coordinate systems which are used is given in Fig. 1. The coordinate system aligned with the local streamline direction is denoted by (x_s, y_s). In the vortex-oriented system the coordinate x_v points into the direction of the crossflow vortex axis, which is determined from linear stability analysis. It

includes a small angle ϵ with the x_s direction. The angle ϵ is determined by linear stability analysis as the angle between the local streamline and the most amplified primary disturbance, i.e. the crossflow. The simulations have been carried out in the vortex-oriented system. The wall-normal direction is denoted by z. All quantities are nondimensionalized by the reference length $\tilde{d} = [(\tilde{\nu}\tilde{x}_c)/\tilde{U}_{0c,e}]^{1/2}$ (where $\tilde{\nu}$ is the kinematic viscosity and an index "0" refers to the undisturbed laminar base flow) and the magnitude of the local velocity at the boundary layer edge $\tilde{Q}_{0,e}$. The local Reynolds number is defined by $Re = (\tilde{Q}_{0,e}\tilde{d})/\tilde{\nu}$.

The boundary layer can be approximated locally by Falkner-Skan-Cooke (FSC) similarity solutions (Cooke, 1950) as demonstrated by Meyer & Kleiser (1989). The profiles depend on the local sweep angle φ_e and the Hartree parameter β_h. These parameters are taken from the experiment. Our computation simulates the development of the disturbances in the rearward region of the plate. In this region the two parameters φ_e and β_h are nearly constant. We have chosen a position of 80% chord-length of the plate. Under the conditions of the experiment, this results in a local Reynolds number of $Re = 826$, a sweep angle of $\varphi_e = 46.9°$ and a Hartree parameter of $\beta_h = 0.63$.

Numerical method

The nonlinear development of the streamwise and spanwise periodic disturbances is computed by solving the three-dimensional incompressible time-dependent Navier-Stokes equations. A Fourier/Chebychev spectral method is used for the spatial discretization. For the time integration a four-stage third-order Runge-Kutta scheme is employed for the nonlinear terms and an implicit Crank-Nicolson scheme for the viscous terms. The nonlinear term is computed aliasing-free in the wall-parallel directions. Earlier simulations by Meyer & Kleiser (1989) and Wagner (1992) showed that the results of the temporal simulation are in good agreement with the experimental results at corresponding stages of the development.

Results

In the present investigations we are mainly interested in the processes occurring in the highly nonlinear stages of transition, when the stationary crossflow vortex breaks down and the flow becomes turbulent. The spatial discretization of the computational domain has been increased up to $N_x \cdot N_y \cdot N_z = 240 \cdot 192 \cdot 160$ grid points. This number is increased by a factor of 3/2 in the wall-parallel directions for the alias-free calculation of the nonlinear terms.

The streamwise and spanwise wave numbers are chosen as $\alpha_v = 0.08$ and $\beta_v = 0.48$. The computational domain captures one crossflow vortex in the spanwise direction. The streamwise length of the domain is chosen from secondary stability theory. The initially excited travelling disturbance with the streamwise wavenumber α_v and spanwise wavenumber β_v gives the maximum

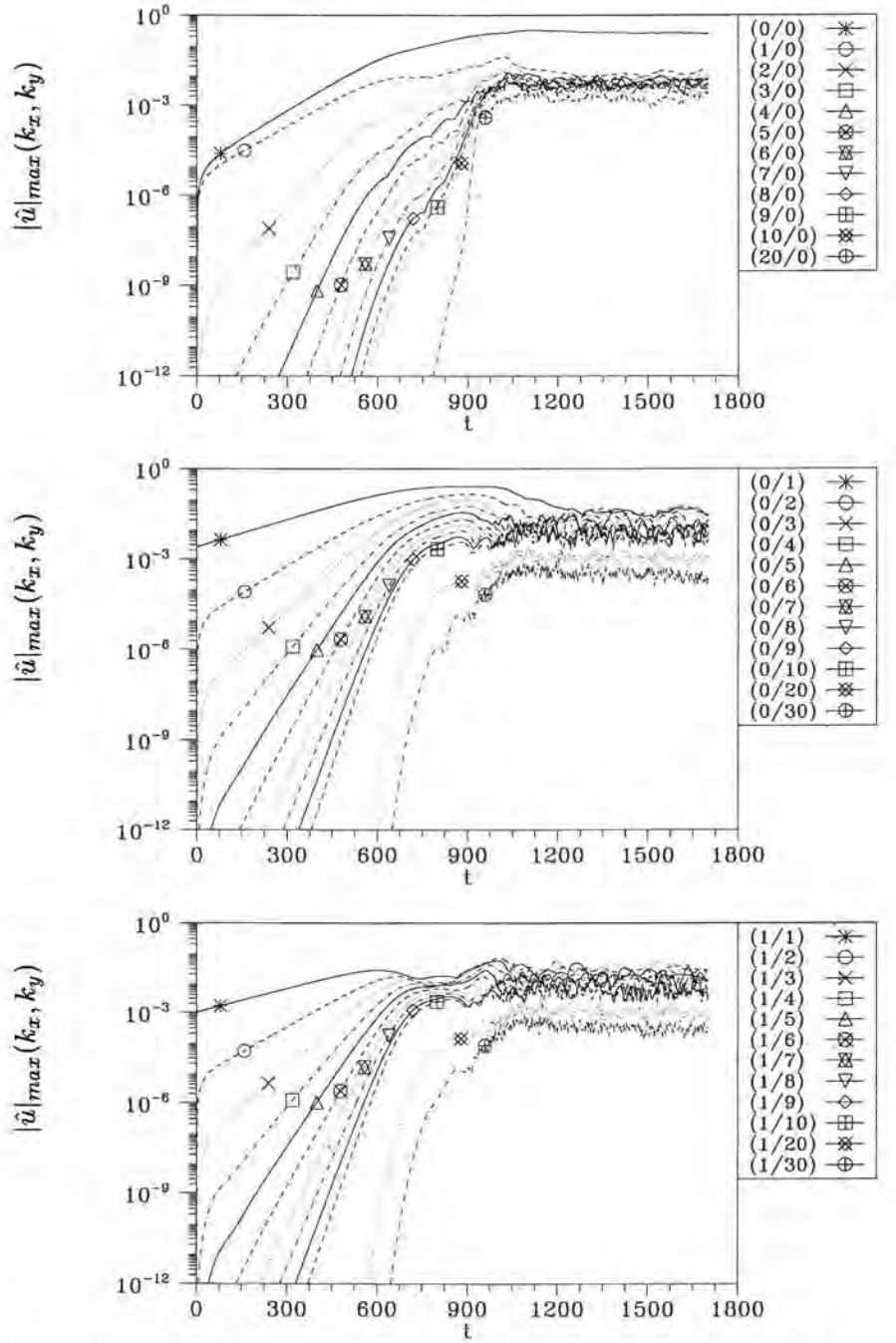

Figure 2: Development of the maximum in the wall-normal direction of the Fourier amplitudes $|\tilde{u}|(k_x, k_y)$.

secondary amplification rate as predicted by the secondary stability theory (Fischer & Dallmann, 1992). As initial disturbances a crossflow vortex with an amplitude of $A_{CF} = 0.25\%$ of the free-stream velocity U_v and a travelling three-dimensional disturbance with an amplitude of $A_{tr} = 0.1\%$ were superimposed. The temporal development of the maximum in the wall-normal direction of the Fourier-amplitudes $|\hat{u}|(k_x, k_y)$ is shown in Fig. 2. Both initial modes grow exponentially up to the time $t \approx 600$ as predicted by the linear stability theory. The higher harmonic modes are generated in a regular cascade by the nonlinearity of the Navier-Stokes equations. Between time $t \approx 700$ and $t \approx 920$ the longitudinal vortex modes $\hat{u}(0, k_y)$ reach an approximate saturation, while the travelling wave modes $\hat{u}(k_x, 0)$ are still growing. The maximum of the amplitude of the crossflow vortex reaches a value of $A_{CF} \approx 13\%$ and the amplitude of the travelling wave $A_{tr} \approx 3\%$. Beyond the time $t \approx 920$ the maxima of the Fourier modes are highly fluctuating, and the boundary layer becomes turbulent.

Viewed in streamwise direction, the crossflow vortex rotates in counter-clockwise direction. Thus, the vortex moves slow fluid from the lower part to the upper part of the boundary layer and generates layers of high shear $\partial u/\partial y$ and $\partial u/\partial z$. Faster fluid from the upper part of the boundary layer moves closer to the wall. Velocity profiles with two inflection points can be obtained due to the upward motion of the slow fluid.

Fig. 3b shows the vortical structures identified by the same criterion at a later time $t = 920$. In addition to the crossflow vortex, a new three-dimensional structure is formed in the downstream part of the domain. The foot-print of this new structure can also be found in the wall-pressure distribution, where it marks a strong minimum. Downstream of the three-dimensional vortex a region of high pressure fluctuations is observed. The identification of this flow structure as a vortex can also be confirmed by calculating streamlines in a moving frame of reference. This vortex, which generates new shear layers, moves downstream rapidly and initiates the local breakdown of the crossflow vortex. The visualization of the flow fields at later times shows that the breakdown spreads from this new vortex while in the remaining part of the flow the saturated crossflow vortex persists (Fig. 3c). When the spreading has covered the full domain the entire flow field becomes turbulent (Fig. 3d).

The identification of vortical structures by isosurfaces of low static pressure can only capture vortices with the largest pressure minimum. This criterion fails if vortical structures with different strength appear in the flow. In Fig. 4 the identification of vortical structures by a "*second eigenvalue criterion*" is shown at two earlier times in order to investigate the emergence of the new structure mentioned above. This criterion, which is based on the velocity gradient tensor ∇u, was first used by Jeong & Hussain (1995). It can also be interpreted as locating the "inflection points" of the pressure field, and it allows to determine vortices with different core pressure minima.

Next, the breakdown of the crossflow vortex and the onset of turbulence is investigated by visualizations of the vortical structures which appear in the flow. These structures are important for the energy transfer from the large

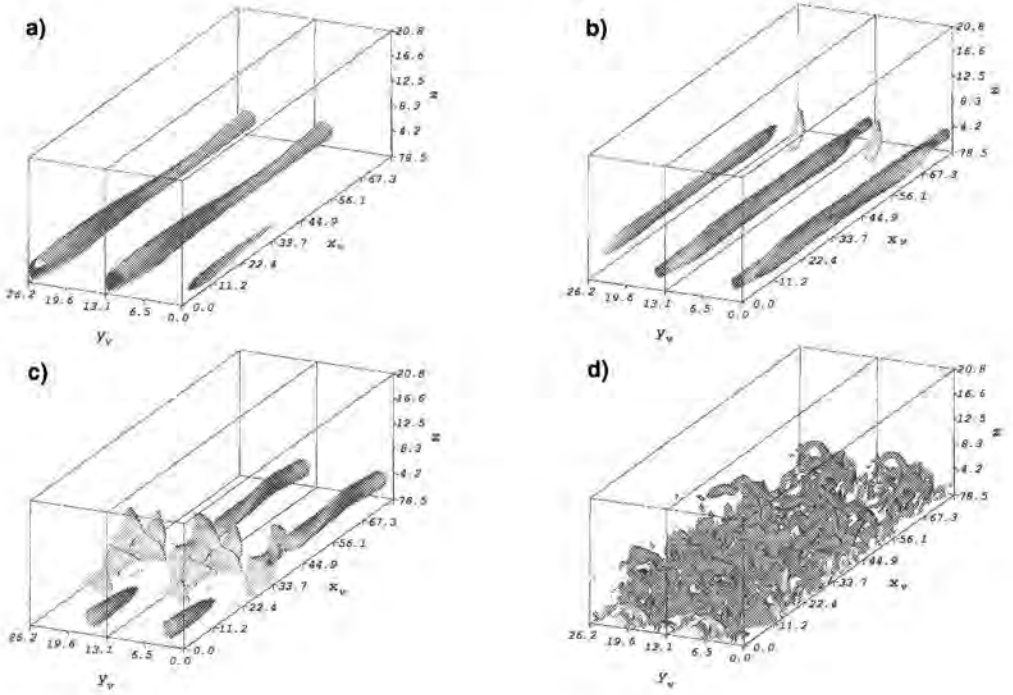

Figure 3: Visualization of vortical structures by isosurfaces of low static pressure. For visualization twice the computational domain in the spanwise direction y is shown. a): $t = 800$, $p_{iso} = -0.0022$; b): $t = 920$, $p_{iso} = -0.0031$; c): $t = 970$, $p_{iso} = -0.004$; d): $t = 1300$, $p_{iso} = -0.005$.

scales to the smaller ones. Different criteria for their identification can be applied to the three-dimensional flow field (e.g. Wintergerste *et al.*, 1995). In Fig. 3a the crossflow vortex is visualized by the most common criterion - isosurfaces of low static pressure - at time $t = 800$ where a near-saturation state of the crossflow vortex is obtained. The modulation in the x_v−direction is caused by the imposed travelling wave.

Fig. 4 shows that a second near-wall streamwise vortex next to each crossflow vortex has been generated at time $t = 800$. This secondary vortex is much weaker than the crossflow vortex. While the centre of the crossflow vortex is located at a height of 50% of the laminar boundary layer thickness δ this vortex is located at a height of approximately $0.15\,\delta$. The new vortex is induced by the co-rotating crossflow vortices in the presence of the wall and rotates in clockwise direction, that is opposite to the rotation direction of the main vortex. Such a near-wall streamwise vortex was also found by Malik *et al.* (1994) in their simulation of swept Hiemenz flow. At time $t = 850$ it moves to the upper side of the crossflow vortex. The interaction of these two vortical structures with the travelling wave which has grown to finite amplitude then leads to the three-dimensional vortical

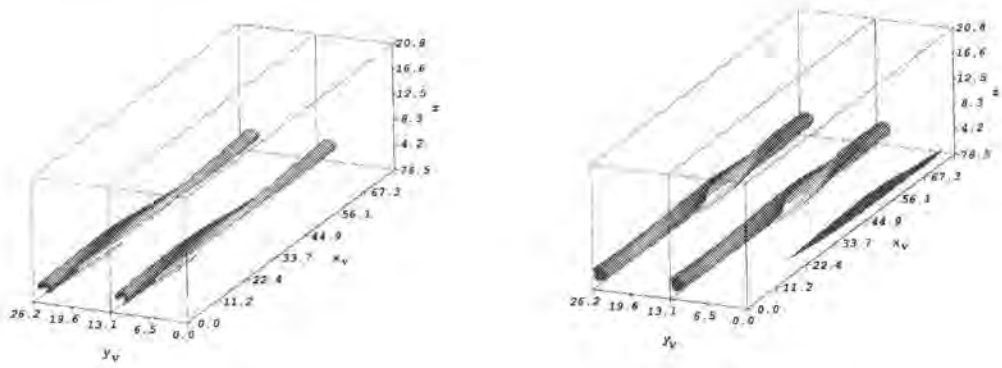

Figure 4: Visualization of the vortical structures by the second eigenvalue criterion. Left: Time $t = 800$; Right: Time $t = 850$. The isovalue is set to -0.001.

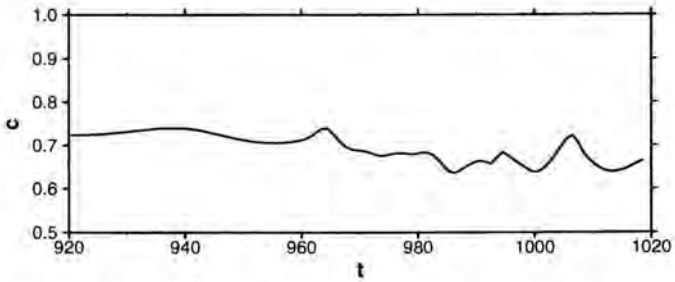

Figure 5: Propagation velocity of the new three-dimensional vortical structure from time $t = 920$ to $t = 1020$.

structure which was visualized in Fig. 3 by isosurfaces of low static pressure. This structure moves to the upper part of the crossflow vortex with increasing time. As mentioned above, a foot-print of this structure can be found in the wall-pressure distribution already at early times of its appearance.

In order to estimate the propagation velocity of the new three-dimensional vortical structure, we consider the correlation of the wall-pressure distribution at two time steps t and $t + \tau$ given by

$$R(\tau, \Delta l)|_{(t,l)} = \frac{\overline{p_{wall}(t,l) \cdot p_{wall}(t+\tau, l+\Delta l)}}{\sqrt{\overline{p_{wall}(t,l)^2} \cdot \overline{p_{wall}(t+\tau, l+\Delta l)^2}}}. \qquad (1)$$

Here $p_{wall}(t,l)$ is the wall-pressure fluctuation in a $(x,y)-$window which encloses the foot-print of the vortex, whose streamwise position is denoted as l. Averages are taken over the window. From the shift of the maximum of the correlation function the propagation velocity of the vortical structure can be estimated. In Fig. 5 the propagation velocity of the three-dimensional vortical structure

from time $t = 920$ to $t = 1020$ is shown. One can see that the propagation velocity is approximately 70% of the free-stream velocity. This velocity is an order of magnitude larger than the phase velocities of the most-amplified primary travelling waves.

Conclusions

The complete transition process in a three-dimensional boundary layer has been simulated using the temporal model. After the crossflow vortices, which are excited as primary disturbances, have grown to finite amplitude, small secondary streamwise vortices appear close to the wall next to each crossflow vortex. The breakdown of the crossflow vortices appears to originate from the interaction of these vortices with finite-amplitude travelling waves. From this interaction new three-dimensional vortices emerge which locally initiate the final breakdown of the crossflow vortices. The three-dimensional vortices move downstream with a propagation velocity of approximately 70% of the free-stream velocity, which is an order of magnitude larger than the phase velocity of the initially excited travelling wave. This local breakdown finally spreads over the entire domain and makes the flow turbulent.

References

Bippes, H., Müller, B. & Wagner, M. 1991 – Measurements and stability calculations of the disturbance growth in an unstable three-dimensional boundary layer. *Physics of Fluids A* **3**, 2371-2377.

Cooke, J.C.,1950 – The boundary layer of a class of infinite yawed cylinders. *Proc. Cambridge Phil. Soc.* **46**, 645-648.

Fischer, T.M. & Dallmann, U. 1992 – Primary and secondary stability analysis of a three-dimensional boundary-layer flow. *Physics of Fluids A* **3**, 2378-2391.

Jeong, J. & Hussain, F. 1995 – On the identification of a vortex. *Journal of Fluid Mechanics* **285**, 69-94.

Kleiser, L. & Zang, T.A. 1991 – Numerical simulation of transition in wall-bounded shear flows. *Annual Review of Fluid Mechanics* **23**, 495-537.

Kohama, Y., Saric, W.S. & Hoos, J.A. 1991 – A high frequency secondary instability of crossflow vortices that leads to transition. In: *Proc. of Boundary Layer Transition and Control Conference*, The Royal Aeronautical Society, Cambridge UK, 4.1-4.13.

Malik, M.R., Li, F. & Chang, C.-L. 1994 – Crossflow disturbances in three-dimensional boundary layers: non-linear development, wave interaction and secondary instability. *Journal of Fluid Mechanics* **268**, 1-36.

Meyer, F. & Kleiser, L. 1989 – Numerical investigation of transition in 3D boundary layers. In: *AGARD-CP-438*, 16-1-16-17.

Meyer, F. & Kleiser, L. 1990 – Numerical simulation of transition due to cross-flow instability. In: *Proc. of Third IUTAM Symposium on Laminar-Turbulent Transition*, Editors: D. Arnal and R. Michel, Springer Verlag, 609-619.

Reed, H.L. & Saric, W.S. 1989 – Stability of three-dimensional boundary layers. *Annual Review of Fluid Mechanics* **21**, 235-284.

Wagner, M. 1992 – Numerische Untersuchungen zum laminar-turbulenten Übergang in zwei- und dreidimensionalen Grenzschichten, *Doct. Dissertation, Universität Karlsruhe, Report DLR-FB 92-36.*

Wintergerste, T., Wilhelm, D. & Kleiser, L., 1995 – Visualization of time-dependent three-dimensional transitional and turbulent flow fields. In: *Visualization Methods in High Performance Computing and Flow Simulation. Proceedings of the International Workshop on Visualization, Paderborn Jan. 18-21, 1994*, Editors: W. Borchers, G. Domick, D. Kröner, R. Rautmann and D. Saupe, International Science Publishers.

Authors' address

Swiss Federal Institute of Technology
Institute of Fluid Dynamics
ETH Zentrum
CH-8092 Zürich, Switzerland

C.J. Atkin° & D.I.A. Poll▷

Correlation Between Linear Stability Analysis and Crossflow Transition Near an Attachment Line

Abstract

Results of exhaustive linear stability calculations are presented for the boundary layer flow near the attachment line of a yawed cylinder, the flow being that studied at length by Poll (1985). The results are represented following some dimensional analysis and demonstrate a clear transition onset position for all yaw angles and Reynolds numbers. Linear stability theory yields an unambiguous e^N correlation, in contrast to previous attempts to apply the method to crossflow instability.

Introduction

The problem of transition on or near the leading edge of swept wings has been the subject of investigation for some years now. In addition to the problem of designing a laminar flow wing, where the leading edge is the most critical region, the phenomenon also impacts on the study of Reynolds number effects for wind-tunnel-to-flight extrapolation.

This particular investigation concerns crossflow transition close to a laminar attachment-line flow which derives initially from the instability associated with the inflectional nature of the velocity profiles in three-dimensional boundary layers. The principle of crossflow instability has been well documented since the work of Gregory *et al.* (1955) but the subsequent processes leading to transition are not universally understood, although progress has been made with respect to some specific mechanisms (see for example Bippes, 1991).

Prediction has proved a difficult exercise because the transition process is affected by a large number of parameters and it is not always clear exactly when and how these parameters should be taken into account. Current approaches to prediction vary from fully empirical criteria such as those discussed by Arnal *et al.* (1984) to direct numerical simulations (see Reed, 1994). The former methods attempt to generalise the transition phenomena and suffer from an insufficient treatment of the physics of the flow, while the latter, which investigate specific transition scenarios, are quite expensive and require extremely detailed information about the external flow and the initial disturbance environment. As such they are limited in scope for use in design. In between there are approaches which retain and discard varying amounts of physics such as the e^N approach

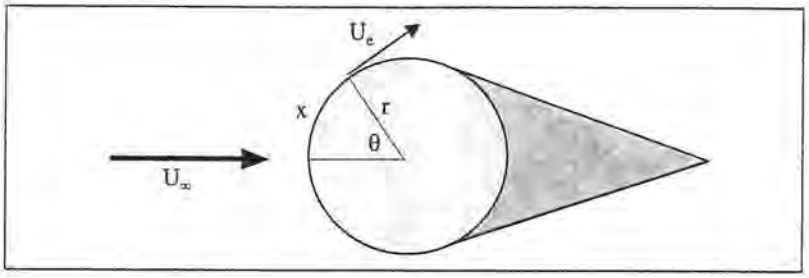

Figure 1: Cross-section of the yawed cylinder model. x is the distance along the surface, U_e the local velocity and U_∞ the free stream velocity all measured normal to the leading edge.

of Van Ingen (1956) and Smith & Gamberoni (1956) and the PSE method of Herbert (1991) and Bertolotti (1991).

The semi-empirical e^N method has been criticised in recent years because it often fails to yield a consistent N-factor correlation across a range of wind tunnel and flight test measurements, particularly for crossflow transition, and for its inability to account for receptivity or non-linear effects which are known to exist. However the method has been used with success to predict effects of suction and heat transfer on the growth of instabilities in the boundary layer, particularly when using a given wind tunnel. The method obviously works best when the position of transition is largely dictated by the exponential growth of small-amplitude disturbances.

More sophisticated methods yield more convincing results but for aerodynamic design simple e^N is already regarded as an expensive exercise and the modelling of receptivity and of non-linear effects may push the cost of transition analysis beyond the levels allowable for rapid design iterations. This is the motivation for persisting with the technique in the face of its mathematical limitations. The majority of effort on the e^N method is now concentrated on finding reliable correlations between wind tunnels and for extrapolating from wind tunnel to flight.

In this paper, which describes work performed late in 1993 at British Aerospace Regional Aircraft Ltd and at the Manchester School of Engineering, the authors present very consistent N-factor results for the flow over a yawed cylinder measured in different wind tunnels and using different models. The raw data have been in the literature for some time but the presentation and the stability analysis are new.

Experimental arrangement

The flow being studied is that near the attachment line of an infinite-yawed cylinder (see Poll, 1985 for experimental details). A cross-section is shown in Fig. 1. The original data obtained at Cranfield were supplemented by tests performed

at the Goldstein Aeronautics Laboratory at Manchester University on a cylinder of twice the dimensions; the latter cylinder was laser-drilled for surface suction, although no suction results are presented here. In both sets of experiments the transition was set at given chordwise positions by varying the tunnel speed (and therefore local Reynolds number) for a particular angle of sweep. The variables in this problem therefore include model manufacture, surface finish, wind tunnel noise and tunnel turbulence intensity (up to 0.16%). These are all factors which are known to influence transition under various circumstances (see Bippes, 1991 and Saric, 1994).

The relevance of the yawed cylinder model to full-scale leading edges can be determined from dimensional analysis. In general the chordwise velocity distribution (see Fig. 1) for a lifting aerofoil can be expressed as a power series:

$$\frac{U_e}{U_\infty} = A\left(\frac{x}{l}\right) + B\left(\frac{x}{l}\right)^2 + C\left(\frac{x}{l}\right)^3 + \cdots, \tag{1}$$

where l, A, B and C are constants. In the vicinity of the attachment line:

$$\frac{U_e}{U_\infty} \cong A\left(\frac{x}{l}\right) = \left(\frac{dU_e}{dx}\right)_{x=0} \frac{x}{U_\infty} = K\frac{x}{U_\infty}. \tag{2}$$

We now assume the leading edge flow to be infinite-swept, the free stream to be isentropic and homenthalpic, and the wall temperature to be constant at T_w. We restrict the analysis to flows without surface suction and concentrate on integral properties: that is, we do not consider wall-normal variations. Any property q of the boundary layer flow in the vicinity of the attachment line is thus a function of the following variables:

$$q = f(y,\ x,\ K,\ V_A,\ \rho_A,\ \mu_A,\ T_A,\ T_w,\ c_p,\ R), \tag{3}$$

where V is the spanwise velocity, R the gas constant and the subscript A refers to conditions at the attachment line. We neglect surface finish, tunnel turbulence and tunnel noise in the analysis. From Buckingham's Π theorem, nine independent variables and four dimensions (mass, length, time and temperature) yield five dimensionless groups. We choose:

$$\sqrt{\frac{V_A^2}{\nu_A K}} = \overline{R},\ \left(\frac{x^2 K}{\nu_A}\right) = \frac{U_e x}{\nu_A} = R_x,\ M_A,\ \gamma \quad \text{and} \quad \frac{T_w}{T_A}. \tag{4}$$

By limiting our consideration to air and to adiabatic flow, we conclude that any dimensionless property Q of the boundary layer flow is governed by the parameters:

$$Q = f\left(\overline{R},\ R_x,\ M_A\right). \tag{5}$$

This tells us that the wing sweep is not *explicitly* a parameter in the problem. In terms of compressibility, the relevant Mach number is the *spanwise* Mach number

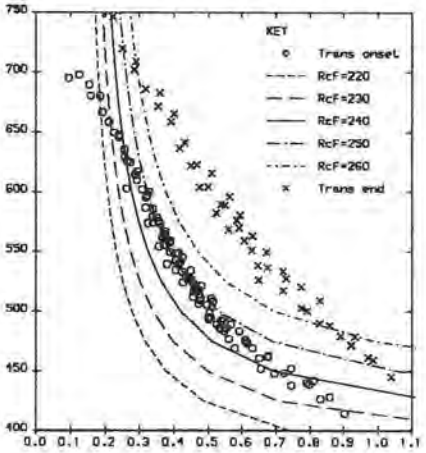

Figure 2: Transition onset and completion for a yawed cylinder plotted with curves of constant crossflow Reynolds number.

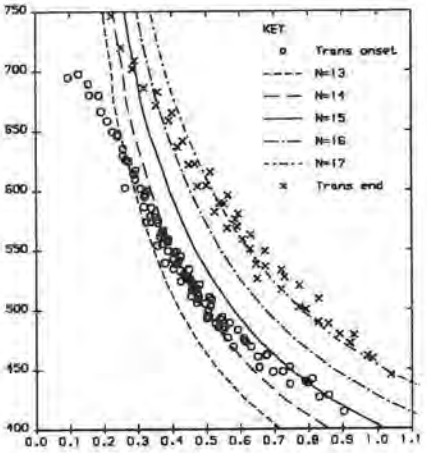

Figure 3: Transition onset and completion plotted with N-factor curves calculated for a cylinder yawed at 30°, using integration strategy 1.

which, for all current transport wing applications, is in the low subsonic regime. To a good approximation, then, the flow near the attachment line depends on $\overline{R}$ and R_x alone, whether on a low speed cylinder model or a transport aircraft leading edge. The cylinder model can thus provide data directly relevant to the full scale aircraft.

The power of the dimensional analysis is demonstrated by re-plotting the results of Poll (1985) and adding the more recent data collected at Manchester in Fig. 2. The data generally cover values of $\overline{R}$ above those currently encountered on transport aircraft ($\overline{R}$ >400) and extend into the region where one finds attachment line instability,$\overline{R}$ >581. Work is in progress at the present time to extend the range of data to lower values of $\overline{R}$ and higher values of R_x. The impressive collapse justifies the neglect of surface finish and tunnel turbulence and noise levels in the above dimensional analysis. However Bippes (1991) and Saric (1994) both find that transition dominated by stationary crossflow vortices is strongly dependent on these parameters, which suggests that transition in these experiments is determined not by the stationary modes but by some other mechanism. Whether this is due to the magnitude of the tunnel turbulence or whether this is a feature of transition in strongly accelerating flow remains to be established.

The advantages of this collapse is that the yawed cylinder flow is expressed as a two-parameter problem where both parameters have been fully explored. The results are then a useful benchmark for empirical transition prediction methods, such as the crossflow Reynolds number R_{cf} which is also plotted on Fig. 2. R_{cf} is defined here as $w_{max}\ y_{10\%}/\nu_e$ where w is the crossflow velocity within

the boundary layer and $y_{10\%}$ is the height at which w drops to one-tenth of its maximum value w_{max}. The correlation between R_{cf} and the experimental results is good only between $500 \leq \overline{R} \leq 600$.

Boundary layer and stability analysis

The cylinder boundary layer flow was calculated for various yaw angles, assuming that the chordwise velocity distribution was that given by potential flow:

$$\frac{U_e}{U_\infty} = 2\sin\theta = 2\frac{x}{r}\frac{\sin\theta}{\theta}, \tag{6}$$

if θ is small:

$$\frac{U_e}{U_\infty} \cong 2\frac{x}{r}, \tag{7}$$

which represents swept Hiemenz flow. This has an analytical solution (see Rosenhead, 1963) and these analytical profiles were also used for stability calculations. The cylinder experiment was used to evaluate the 'black box' operation of a linear stability method developed at British Aerospace Regional Aircraft Ltd and validated during the European Laminar Flow Investigation programme (ELFIN). The code employs the spatial formulation described by Mack (1984) and the compact-difference scheme of Malik (1988). The method also accounts for the curvature terms arising from the use of body- and streamline-conforming coordinates (see for example de Bruin, 1990). Aside from the modelling deficiencies already described, linear stability theory also suffers from the need to know the frequency ω, spatial wavenumber k and the phase speed direction φ of an unstable wave in the boundary layer *before* being able to calculate the amplification rate α_i. However for flows which are often revisited, such as aerofoil flows at subsonic and transonic speeds, one can find empirical relations expressing k and ω as functions of R_x and φ. These are sufficiently reliable to allow automated stability calculations without the need for manual input of frequencies or other wave properties: this approach was proven during the calculation of the cylinder N-factors for the full range of $\overline{R}$ and R_x. In three-dimensions one must find all the amplified modes within the boundary layer for each combination of R_x, φ and ω. The amplification rates are then integrated with respect to x (and therefore R_x) subject to certain constraints on ω and φ: the frequency of each disturbance is invariant, but having assumed locally parallel mean flow, one must further assume a relation $f(\varphi) = \textit{constant}$ to determine how the physical properties of the wave vary with R_x: this is the ray tracing or 'integration strategy' problem. Some workers take φ to be constant, but Mack (1983) suggested that, for infinity-yawed flows, the spanwise wavenumber (SWN) should be constant:

$$f(\varphi) = k\sin(\varphi + \phi) = k_z, \tag{8}$$

where ϕ is the angle between the local streamline and the x vector normal to the leading edge. This approach yields $m \times n$ integrations as follows:

$$N_{a,b} = \int_{\alpha_i=0}^{R_{x'}=R_x} \alpha_i\,(x',\ \omega=\omega_a,\ f(\varphi)=k_{z,b})\,dx' \quad \text{for} \quad \begin{matrix} a=1,\ldots,m \\ b=1,\ldots,n \end{matrix} \tag{9}$$

One must ensure that the 'worst' case (largest N-factor) is included in the analysis; fortunately it is quite simple to determine an appropriate range of k_z values at an early stage in the calculations. Arnal (1984) and others have used the 'envelope' strategy, which involves maximising $\alpha_i(\varphi)$ at each boundary layer station R_x such that:

$$(\partial\alpha_i/\partial\varphi)\,|_\omega = 0. \tag{10}$$

This approach reduces the number of N-factor curves to m:

$$N_a = \int_{\alpha_i=0}^{R_{a'}=R_x} \alpha_{i,\ max}\,(x',\ \omega=\omega_a)\,dx' \quad \text{for} \quad a=1,\ldots,m. \tag{11}$$

Maximising $\alpha_i(\varphi)$ may be marginally less expensive than the 'shotgun' approach required for the SWN strategy, but there is a risk that it converges only to a local rather than an absolute maximum in the α_i vs. φ curve: hence it can be ambiguous.

An envelope of most-amplified modes $N_{max} = f(R_x)$ is compiled from the $m \times n$ or m integrations and the analysis is repeated for different $\overline{R}$ to obtain $N_{max} = f\left(\overline{R}, R_x\right)$. Selected curves of constant N_{max} can then be plotted against the experimental data. For each boundary layer calculation in this investigation eigenvalues were obtained over a range of 17 R_x stations, 10 frequencies and 20 values of k_z. Total CPU time for 15 values of $\overline{R}$ was 45 minutes on an 8-bit Silicon Graphics Indy 4600 workstation running at 100 MHz.

Results

Fig. 3 shows the stability results for the cylinder at 30° sweep using the SWN strategy. The correlation is significantly better than that with R_{cf} (Fig. 2) particularly at lower values of $\overline{R}$ where the curves are tangential to the experimental results. Transition onset corresponds to $N = 14 \pm 1$ for the range $400 \leq \overline{R} \leq 650$, above which one encounters attachment line instabilities which would affect the experimental results but which are not modelled in the stability analysis. Fig. 4 confirms that the results are practically identical when the analysis is performed on swept Hiemenz flow except for large R_x, small $\overline{R}$: this is the region where the approximation $\sin\theta \cong \theta$ implicit in equation (7) is invalid. These differences are magnified at larger sweep angles.

Fig. 5 shows how the envelope strategy improves the fit, giving a different N value of about 18 for most of the $\overline{R}$ range. Integrating with constant φ yields a slightly worse fit than the two examples shown, particularly at lower values of

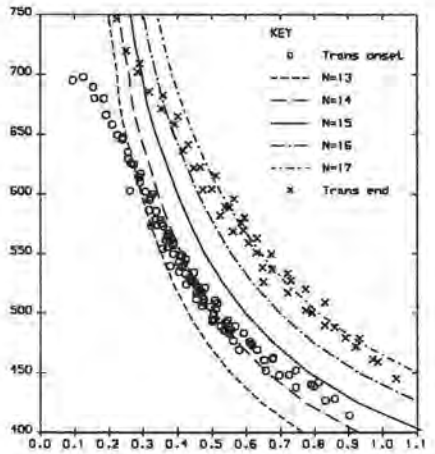

Figure 4: Transition positions and N-factor curves (SWN strategy) for swept Hiemenz flow.

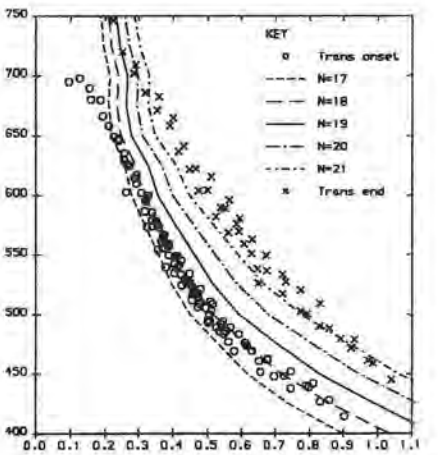

Figure 5: Transition positions and N-factor curves (**envelope strategy**) for a cylinder yawed at 30°.

$\overline{R}$, giving $15 \leq N \leq 18$, but all three methods would probably satisfy engineering requirements for this particular set of data.

Fig. 6 shows the effect of surface and streamline curvature treatment for the SWN strategy. The quality of the N-factor correlation does improve markedly below $\overline{R}$=600 to give a very narrow band around N=15. Surface curvature improves the fit while streamline curvature increases N. For the envelope strategy curvature increases N to about 18.5, but the fit is slightly poorer. Finally, Fig. 7 shows the detrimental effect of considering only stationary modes. This result is unaffected by either integration strategy or curvature effects.

Conclusions

Dimensional analysis of the flow near a swept attachment line has shown that transition position is a function of $\overline{R}$ and R_x. The variations in surface finish and wind tunnel environment during the experiments have not had a discernible effect on the results. The results of the linear stability analysis generally correlate well with the experimentally measured transition onset positions. The correlation is a significant improvement on that obtained with the crossflow Reynolds number. Best results are obtained from the envelope integration strategy and from the spanwise wavenumber strategy with curvature terms included. The latter strategy has a better physical basis for infinite-swept flows. Including curvature terms in the analysis alters the value of the N-factor for both integration strategies, but only improves the correlation for the SWN strategy.

The experimental observations (Poll, 1985) reveal the presence of both stationary and travelling disturbances ahead of the transition region. The linear

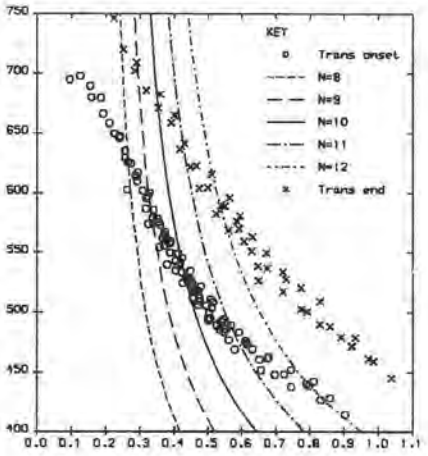

Figure 6: Transition positions and N-factor curves (SWN strategy) for a cylinder yawed at 30° *including surface and streamline curvature effects.*

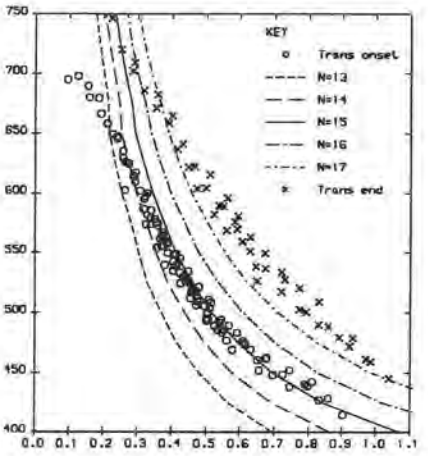

Figure 7: Transition positions and *stationary mode* N-factors (SWN strategy) for a cylinder yawed at 30°.

stability analysis, however, only correlates well when travelling modes are considered, prompting one of two conclusions: that in this flow there is a significant region of linear-theory-type wave growth, the travelling modes proving dominant over the stationary modes; or that the results presented here are a fantastic coincidence, given that linear stability analysis may be totally inapplicable to this problem. The dominance of stationary modes is usually associated with higher free-stream turbulence levels, but it is not clear how the presence of a strong, uniform chordwise velocity gradient influences the transition behaviour.

The values of N-factor from the SWN strategy are believed to be higher than those previously recorded for any type of disturbance in a wind tunnel. The work of Malik *et al.* (1994) suggests that non-parallel effects would be small. This does not invalidate the use of the e^N method as an engineering tool, but confirms that there are different flow fields requiring different values of N. Neither does the quality of the N-factor correlation imply that the transition process is wholly linear: simply that here the non-linear growth is either short in extent or can be represented by an extension of the linear growth regime. Future work will extend the experimental database to flows with suction and to situations where $\overline{R} < 400$ and/or $R_x > 1$ million.

Acknowledgements

The authors would like to acknowledge the support of British Aerospace Regional Aircraft Ltd, Manchester University School of Engineering, and the UK Department of Trade and Industry.

References

Arnal, D., Coustols, E. & Juillen, J.C. 1984 – Experimental and theoretical study of transition phenomena on an infinite swept wing. *La Recherche Aérospatiale* **1984-4**.

Arnal, D. 1984 – Boundary layer transition: predictions based on linear theory. *AGARD report* **R-793**, 2-1.

Bertolotti, F.P. 1991 – Linear and non-linear stability of boundary layers with streamwise varying properties. *Ph.D. Thesis, Ohio State University, Columbus, Ohio.*

Bippes, H. 1991 – Experiments on transition in three-dimensional accelerated boundary layer flows. *Proc. R.Ae.S. Conf. Boundary Layer Transition and Control*, Cambridge.

De Bruin, A.C. 1990 – Linear boundary layer stability theory in orthogonal curvilinear co-ordinates. *NLR* **TR 90385 L.**

Gregory, N., Stuart, J. T. & Walker, W. S. 1955 – On the stability of three-dimensional boundary layers with applications to the flow due to a rotating disk. *Phil. Trans. Roy. Soc. Lond. A* **248**, 155-199.

Herbert, Th. 1991 – Boundary layer transition – analysis and prediction revisited. *AIAA paper* **91-0737**.

Mack, L.M. 1984 – Boundary layer stability theory. AGARD report R-709, paper no. 3.

Malik, M.R. 1988 – Numerical methods for hypersonic boundary layer stability. *High Technology Corporation Report* **88-6**.

Malik, M.R., Li, F. & Chang, C.L. 1994 – Crossflow disturbances in three-dimensional boundary layers: non-linear development, wave interaction and secondary instability. *J. Fluid Mech.* **268**, 1-36.

Poll, D.I.A. 1985 – Some observations of the transition process on the windward face of a long yawed cylinder. *J. Fluid Mech.* **150**, 329-356.

Reed, H.L. 1984 – Direct numerical simulation of transition: the spatial approach. *AGARD report* **R-793**, paper no. 5.

Rosenhead, L. 1963 – Laminar boundary layers. *Oxford University Press*, pp. 232 & 471.

Saric, W.S. 1984 – Physical description of boundary layer transition: experimental evidence. *AGARD report* **R-793**, paper no. 1.

Smith, A.M.O. & Gamberoni, N. 1956 – Transition, pressure gradient and stability theory. *Douglas Aircraft Company Report* **ES 26388**.

Van Ingen, J.L. 1956 – A suggested semi-empirical method for the calculation of the boundary layer transition region. *Delft University of Technology, Dept. of Aero. Eng., Report no* **VTH-74**.

Authors' addresses

°Defence Research Agency
Farnborough
Hants, GU14 6TD
United Kingdom

▷College of Aeronautics
Cranfield University
Beds, MK41 XXX
United Kingdom

K.L. Chapman°, M.N. Glauser° M.S. Reibert▷ & W.S. Saric▷

Proper Orthogonal Decomposition Applied to Boundary-Layer Transition on a Swept Wing

Abstract

Proper orthogonal decomposition (POD), a technique generally used in the study of turbulent flows, is used to analyze experimental signals from multi-point measurements in transitional flow over a 45° swept wing. The data used in this analysis include surface shear stress and two-component velocity measurements from two separate experiments in a highly three-dimensional flow with crossflow-dominated transition. Measurements were obtained across the span at constant chord locations just before and after transition. Streamwise surface shear-stress measurements were acquired through transition to turbulence. The POD solution produces energy-based modes which statistically determine the spatial evolution of the particular flow field. These results reflect physical events in the flow which may provide valuable information to developing flow control strategies.

Experiments

Flow transition is a common phenomenon on aircraft surfaces, particularly on swept wings. The goal of this research effort is to use proper orthogonal decomposition (POD) to statistically capture swept-wing flow evolution in space from multi-point measurements. The data used in this analysis were obtained via multi-element hot-film and cross-wire anemometry on a 45° swept wing (shown in Fig. 1) with a chord length of $c = 1.83$ m at the Arizona State University Unsteady Wind Tunnel facility. Wall liners, contoured to the inviscid streamlines,

Figure 1: 45° swept wing with wall liners at the Arizona State University Unsteady Wind Tunnel.

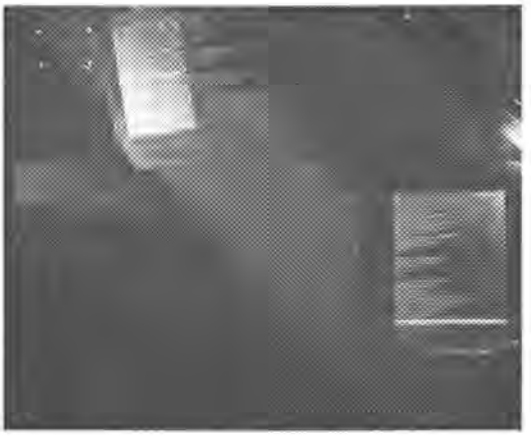

Figure 2: Dagenhart *et al.* (1989) experiment: Placement of hot-film array with naphthalene surface flow visualization results shown. Flow is left to right.

are used to simulate a wing of infinite span. The experiments were designed to produce a highly three-dimensional flow consisting of stationary crossflow vortices which dominate transition starting near $x/c = 0.52$ at a Reynolds number of $Re_c = 2.4 \times 10^6$. Naphthalene surface flow visualization and single hot-wire velocity scans are used to determine the boundary-layer state.

An experiment performed by Dagenhart *et al.* (1989) included spanwise surface shear-stress measurements in the laminar regime and streamwise measurements through transition. The surface-mounted hot-film arrays were aligned to the visualized crossflow vortex axis as shown in Fig. 2. The crossflow array consisted of 13 sensors spaced 1.3 mm apart, covering a range of 15.3 mm in span. The streamwise array consisted of 13 hot-film sensors spaced 2.54 mm apart, covering a range of 30.48 mm. For a more detailed description of this experiment, refer to Dagenhart *et al.* (1989).

A second experiment by Chapman *et al.* (1996) was based on the analysis of the Dagenhart experiment and designed with the POD technique in mind. A series of 6 μm thick roughness elements spaced 12 mm apart were placed downstream of the attachment line across the entire span at $x/c = 0.023$ to force the dominant crossflow vortex wavelength, thus isolating the dominant mode in the flow. The data acquired from this experiment included two-point, two-component velocity measurements in span at two chord locations; at $x/c = 0.50$, just before transition, and at $x/c = 0.58$ in the turbulent region. These correlation measurements (outlined in Fig. 3) for each of the two chord locations were made at a single height of $y = 3.0$ mm in the boundary layer at 8 span locations spaced 4 mm apart. The cross-wire measurements were taken above surface-mounted hot-film arrays used to supplement the data from the Dagenhart experiment. Only the cross-wire data will be analyzed here. Refer to Chapman *et al.* (1996) for a more detailed description of the experiment.

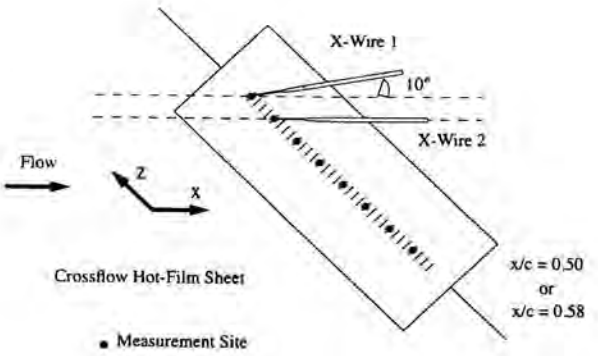

Figure 3: Chapman *et al.* (1996) experiment: Schematic of cross-wire experiment at x/c=0.50 and x/c=0.58 with crossflow hot-film sheets used to define measurement grid points.

Proper orthogonal decomposition

Proper orthogonal decomposition (POD) is a mathematically unbiased method for extracting a system of eigenfunctions through the solution of an integral eigenvalue equation. It was introduced to the study of inhomogeneous turbulent flows by Lumley (1967) as a way of identifying large-scale structures, i.e., those events in the flow which have the largest mean-square projection on the flow field. In general, it is an objective method that decomposes a system of signals into various modes on an energy basis without imposing a basis set as in Fourier decomposition, but determines the appropriate modes directly from the data. Hence, POD includes the results of the flow non-linearities in the solved eigenfunctions, unlike conventional linear-theory methods. For a summary of POD and applications in turbulence, refer to Berkooz *et al.* (1993).

Lumley (1967) defined coherent structures as those events in the flow with the largest mean-square projection on the random velocity field, i.e., those with the maximum energy. Defining $\vec{\phi}(\vec{x},t)$ as the candidate structure and maximizing this projection leads to the following integral eigenvalue problem:

$$\int\int\int\int R_{ij}(\vec{x},\vec{x}',t,t')\phi_j^{(n)}(\vec{x}',t')d\vec{x}'dt' = \lambda^{(n)}\phi_i^{(n)}(\vec{x},t), \tag{1}$$

with a symmetric kernel that is the velocity cross-correlation tensor,

$$R_{ij}(\vec{x},\vec{x}',t,t') = \overline{u_i(\vec{x},t)u_j(\vec{x}',t')}. \tag{2}$$

The eigenvalues, $\lambda^{(n)}$, which represent an energy distribution across the POD modes, $\phi^{(n)}(\vec{x},t)$, reflect the projection. Theoretically, Eq. (1) has an infinite number of orthonormal solutions. However, it is maximally discretized experimentally to the number of measurement sites.

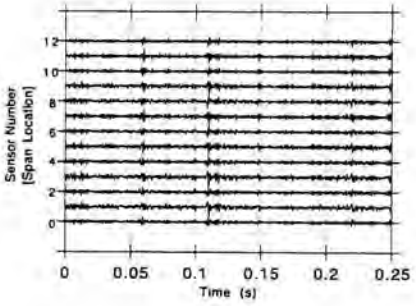

Figure 4: Simultaneously measured spanwise hot-film time histories in the laminar regime. Sensor spacing is 1.3 mm.

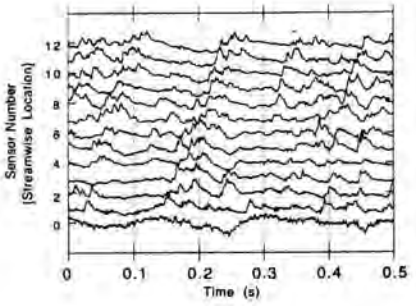

Figure 5: Simultaneously measured streamwise hot-film time histories through transition. Sensor spacing is 2.54 mm.

In this study, POD is applied to the surface shear-stress measurements of the Dagenhart experiment and to the two-component velocity measurements of the Chapman experiment, treating each component independently. Therefore, for these scalar solutions, Eq. (1) becomes

$$\int R_{11}(x,x')\phi_1^{(n)}(x')dx' = \lambda^{(n)}\phi_1^{(n)}(x), \tag{3}$$

where the discrete variable, n, is the POD mode number maximally discretized to the number of measurement sites. Note that in Eq. (3), R_{11} is formed with either shear stresses or velocities and x denotes the coordinate in either the spanwise or streamwise measurement grids, as appropriate, since each data set is treated as an independent system. Only the one-dimensional POD solution is presented here. From these solutions, it is possible to statistically determine the spatial evolution of the eigenmodes across each measurement range.

Proper orthogonal decomposition results

Surface shear-stress solutions

POD was applied to the spanwise surface shear-stress data in the laminar regime shown in Fig. 4 and to the streamwise surface shear-stress data through transition shown in Fig. 5. The solutions are obtained using two-point correlation tensors normalized by the appropriate root-mean-square values.

In Fig. 6, the resulting eigenvalues plotted as a function of POD mode number for these data show the contribution of each mode to the total energy of the measured surface shear-stress fields. The spanwise eigenvalues contain 98% of the total energy in the first three modes, whereas only 69% of the total energy

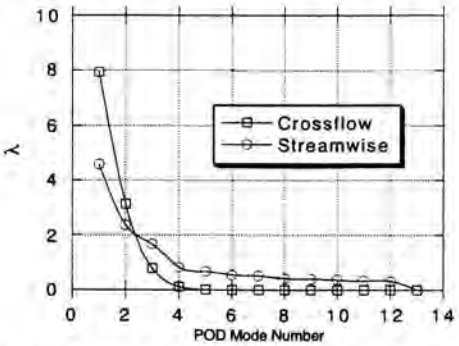

Figure 6: Eigenvalues from the one-dimensional POD solution for the surface shear-stress data showing the energy distribution across POD modes for each regime.

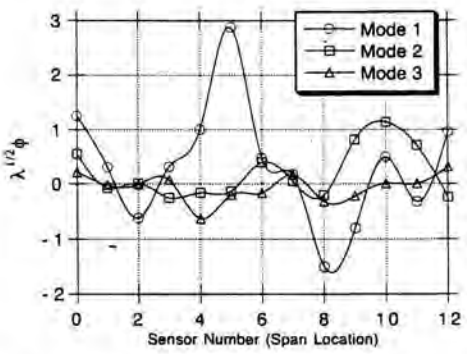

Figure 7: Spatial evolution of the first three spanwise modes in the laminar regime.

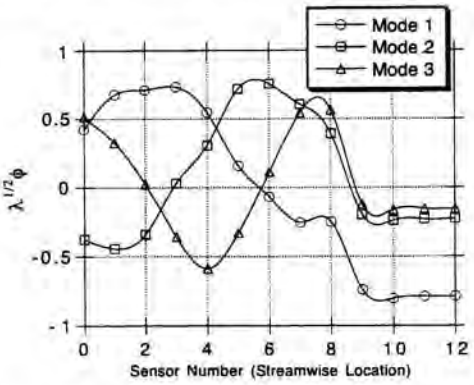

Figure 8: Spatial evolution of the first three streamwise modes through transition.

is in the first three modes of the streamwise solution. In fact, six modes are needed to represent over 80% of the field's total measured energy. Thus, the use of higher modes in the analysis of transitional flows is a necessity.

The first three eigenfunctions for the spanwise and streamwise solutions are plotted in Figs. 7 and 8, respectively, and are weighted by $\lambda^{1/2}$ to distinguish them as characteristic surface shear stresses. High modal amplitudes statistically correspond to regions of high shear. The spatial evolution of the first spanwise mode in Fig. 7 captures the dominant wavelength of the co-rotating crossflow vortices, determined to be approximately 9.0 mm from flow visualizations and mean-velocity boundary-layer scans. Hence, the spatial wavelength is expected to span across seven hot-film sensors. This is captured by the first mode from sensor number 2 through 8 inclusive. A second vortex of weaker amplitude is also captured by the first two modes from sensors 8 through 12 inclusive. In the cross-wire experiment, this type of non-uniformity of the vortices was removed through the use of roughness elements, effectively isolating the wavelength to

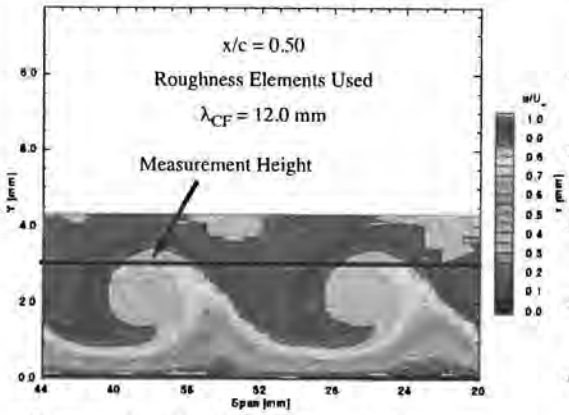

Figure 9: Typical mean velocity contour plot of stationary crossflow vortices (2:1 scale).

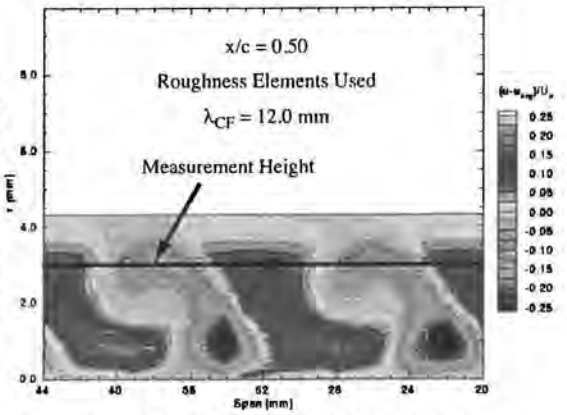

Figure 10: Typical disturbance contour plot of stationary crossflow vortices (2:1 scale).

the first mode. Higher spanwise modes provided very little information.

The spatial evolution of the streamwise modes in Fig. 8 reveal important characteristics of flow transition. From observation of the time history data in Fig. 5, one sees the onset of turbulence occurring near sensor number 9. This event is dramatically captured in the first three eigenmodes. The functions spatially evolve from high amplitude periodic waveforms to fairly constant values at the onset of turbulence. The fact that the first three modes are at the same amplitude in the transition region supports the absolute need for the inclusion of higher modes when modelling this regime. It also suggests that the dominant three modes are of equal importance. In the turbulent regime, the energy in the flow becomes organized and may be adequately represented by simply the first three modes. This is comparable to other POD applications in turbulent flows where increasing mode number reflects a significant decrease in energy. Therefore, the solution of the POD through transition to turbulence statistically reveals a spatial organization of energy which requires higher modal information in transitioning regions, but needs only the first three modes in turbulent regimes.

Individual velocity component solutions

The POD was also applied to the two-point cross-wire data taken at a height of $y = 3.0$ mm in the boundary layer. Fig. 9 shows a typical mean velocity contour plot of the stationary crossflow vortices obtained by single hot-wire scans. Fig. 10 is a statistical picture of the flow disturbances, i.e., the fluctuations about the mean, for the data shown in Fig. 9. The physics of the solved eigenfunctions at $y = 3.0$ mm can then be appropriately mapped to this plot.

The eigenvalues for the u and w components of velocity are shown in Fig. 11 for $x/c = 0.50$ and $x/c = 0.58$. The turbulent solutions are at an entirely higher energy level suggesting the fluctuating components have acquired more energy

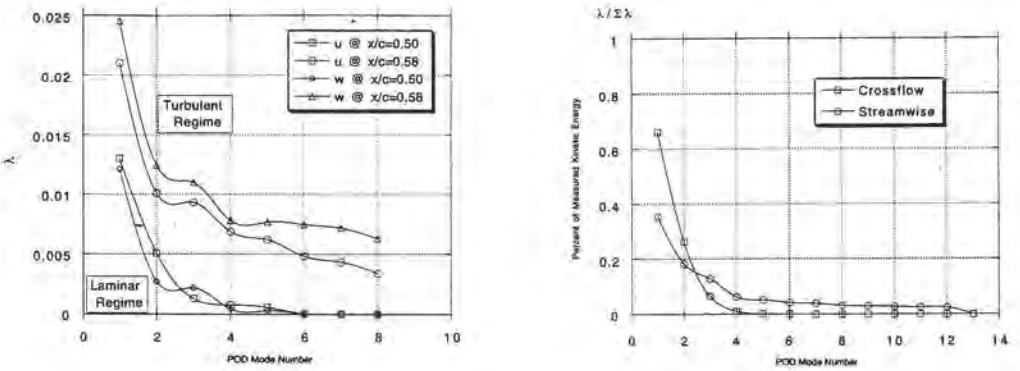

Figure 11: Eigenvalues from the one-dimensional POD solution for the velocity component data.

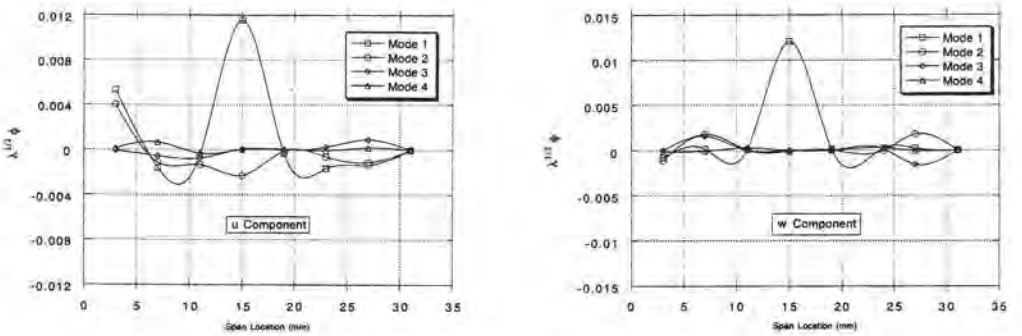

Figure 12: Spatial evolution of the first four eigenmodes for both u and w velocity components in the laminar regime at $x/c = 0.50$.

from the mean flow. Also, the eigenvalues demonstrate that only the first three POD modes are significant in the laminar regime, yet higher modes are active in the turbulent regime, consistent with the shear-stress analysis.

The spanwise evolution of the first four eigenmodes of both components in the laminar regime, shown in Fig. 12, demonstrate the effectiveness of the POD in capturing the crossflow vortex wavelength of $\lambda_{CF} = 12$ mm entirely in the first mode. The vortex structure in the first mode ranges from 7 mm to 19 mm on the measurement grid which can be mapped to the disturbance contour plot in Fig. 10. The circles in Fig. 10 represent five typical measurement points that could be characterized by the five eigenfunction points ranging from 7 mm to 27 mm for the first modes of each component in Fig. 12. In this range, the first modes show two points of relatively low disturbances (each represented by o in Fig. 10) followed by a large amplitude event (represented by • in Fig. 10) and then two more points of relatively low amplitude velocity disturbances.

The spanwise evolution of the first four eigenmodes for the u and w compo-

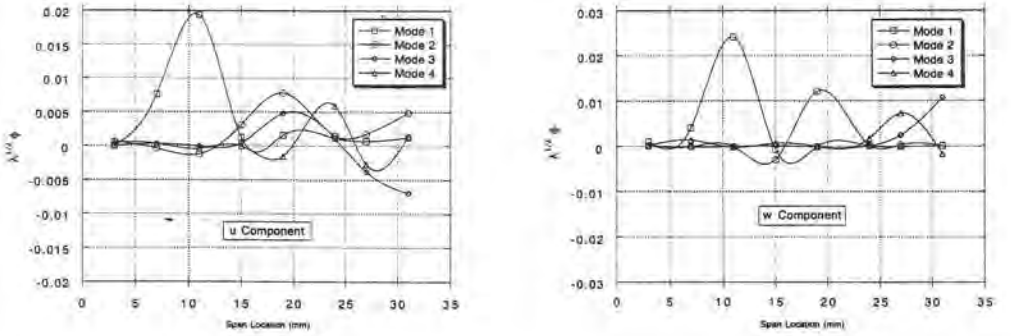

Figure 13: Spatial evolution of the first four eigenmodes for both u and w velocity components in the turbulent regime at $x/c = 0.58$.

nents in the turbulent regime are shown in Fig. 13. The same events in the first modes of the laminar solution which capture the crossflow vortex wavelength are retained and increase in amplitude in the turbulent solutions. This suggests that the initial structures present in the flow field before transition acquire energy and remain intact in the turbulent regime. Flow visualization results show the crossflow vortex axis to be angled approximately 6° from the x coordinate axis thus explaining the 4 mm shift of the vortex structure position (from 15 mm at $x/c = 0.50$ to 11 mm at $x/c = 0.58$). The turbulent solution shows higher modes are now significant and have amplitudes nearly half of the first mode.

Conclusions

Proper orthogonal decomposition has been shown to be a useful and objective tool in analyzing transitional flow. Large scale events, such as the crossflow vortex wavelength are easily tracked and can be used for structure identification purposes where supplemental experiments such as flow visualization are not available. The POD modes clearly identify the onset of turbulence when applied to multi-point streamwise measurements. The POD solution provides a set of eigenfunctions decomposed on an energy basis which can then be used in developing flow control strategies and flow models.

Acknowledgements

This work is supported under NASA Grant NAG2-724 by NASA Dryden Flight Research Center. The authors would like to thank Mssrs Dan Clevenger, Edmund Hamlin, and Paul Harney for their contributions to this research effort.

References

Berkooz, G., Holmes, P. & Lumley, J. L. 1993 – The proper orthogonal decomposition in the analysis of turbulent flows. *Ann. Rev. Fluid Mech.* **25**, 539-575.

Chapman, K.L., Glauser, M.N., Reibert, M.S. & Saric, W.S. 1996 – A multipoint correlation analysis of a crossflow-dominated boundary layer. AIAA 96-0186.

Dagenhart, J.R., Saric, W.S., Mousseux, M.C. & Stack, J.P. 1989 – Crossflow-vortex instability and transition on a 45-degree swept wing. AIAA 89-1892.

Lumley, J.L. 1967 – The structure of inhomogeneous turbulent flows. *Atmos. Turb. and Radio Wave Prop.*, edited by Yaglom & Tatarsky, Nauka, Moscow, pp. 166-176.

Rempfer, D. 1996 – Investigations of boundary layer transition via Galerkin projections on empirical eigenfunctions. *Phys. Fluids* **8**, 175-188.

Saric, W.S. 1994 – Low-speed boundary-layer transition experiments. *Transition: experiments, theory and computations*, edited by Corke, Erlebacher & Hussaini, Oxford Press.

Authors' addresses

°Clarkson University
Mechanical and Aeronautical Engineering
Box 5725
Potsdam, NY 13699, USA

▷Arizona State University
Mechanical and Aerospace Engineering
Box 87-6106
Tempe, AZ 85287-6106, USA

Session 3:
Attachment-Line Instabilities

D. Arnal°, J. Reneaux▷ & G. Casalis°

Numerical and Experimental Studies Related to Skin Friction Drag Reduction Problems

Abstract

This paper gives an overview of some recent investigations conducted at ONERA in order to improve the techniques for laminar flow control. The first part deals with the problem of leading edge contamination. It is shown that suction and the Gaster bump can significantly increase the Reynolds number at which contamination occurs. The second part of the paper is devoted to applications of numerical tools aimed at predicting the onset of transition.

Introduction

Among the different techniques which could be applied to reduce the drag of transport aircraft, laminar flow technology seems to have the greatest potential. The importance of the problem and the associated economic gains are highlighted by the large number of studies currently being carried out in the United States and in Europe. In France, ONERA is deeply involved in several national and European programmes (Falcon 900, A 320 fin, ELFIN project). Besides practical results directly applicable to free flight conditions, these numerical and experimental studies gave the opportunity to obtain fundamental information concerning the transition problem. The objective of this paper is to give a survey of these results, by showing how such studies have improved our knowledge of the transition mechanisms and our capability to model them.

For swept wings, a substantial region of laminar flow can be maintained by controlling the development of crossflow and/or Tollmien-Schlichting (TS) disturbances. This control can be carried out either by adequately shaping the wing (NLF: Natural Laminar Flow) or by applying suction at the wall (LFC: Laminar Flow Control). Given the typical leading edge sweep angles and chord Reynolds numbers of transport aircraft wings, most of the research effort is devoted to the combination of these techniques (HLFC: Hybrid Laminar Flow Control). However, it is first necessary to ensure that the attachment line boundary layer is laminar, i.e. to avoid the problems of leading edge contamination. This phenomenon, by which the turbulence of the fuselage boundary layer is convected along a swept leading edge, is likely to occur on transport aircraft causing the wing boundary layer to become fully turbulent. A survey of these problems can be found in the AGARD Report (1992).

The first part of this paper presents results obtained during wind tunnel tests for two anti-contamination devices, namely a Gaster bump and a porous leading

edge allowing to apply suction along the attachment line. The second part of the paper is devoted to the development of numerical methods aimed at predicting the transition location as accurately as possible. These methods are applied for several problems where different stabilization techniques are tested.

Leading edge contamination problems

It is well known that leading edge contamination occurs on a swept wing as soon as a leading edge Reynolds number $\bar{R}$ exceeds a critical value close to 250, see Pfenninger (1965) and Poll (1978). $\bar{R}$ is defined as:

$$\bar{R} = \frac{W_e \eta}{\nu_e}, \quad \text{with} \quad \eta = \sqrt{\frac{\nu_e}{k}},$$

where ν_e is the kinematic viscosity, W_e is the mean flow component parallel to the attachment line and K is the velocity gradient along the surface and normal to the leading edge.

As typical values of $\bar{R}$ near the root are of the order of 800-1000 for large transport aircraft, it is necessary to develop specific tools to delay the onset of leading edge contamination. This is in fact the first problem to solve for maintaining laminar flow on a wing: if the attachment line flow is turbulent, the NLF, LFC or HLFC systems will become useless.

Gaster bump

A successful device to prevent leading edge contamination is the Gaster bump (Gaster, 1967). It consists of a small fairing which is placed on the leading edge close to the wing root. It is shaped in such a way that the contaminated turbulent boundary layer is brought to rest at a stagnation point on the upstream side whilst a "clean" laminar boundary layer is generated on the downstream side.

Several Gaster bumps were tested in a water channel and in the transonic T2 wind tunnel at CERT ONERA. These experiments allowed to optimize some geometrical parameters of the bumps, while numerical investigations gave some insight into the transition mechanisms.

An example of the results is presented in Fig. 1, which shows a comparison between the measured and computed transition lines around a bump tested in the T2 wind tunnel during the preparation of flight tests performed by Dassault Aviation. Due to the strong deflection of the flow on both sides of the device, a powerful crossflow instability is generated and transition takes place at a short distance from the attachment line. Further downstream (in the spanwise direction), the transition front moves up to larger chordwise distances. When $\bar{R}$ increases, transition around the bump occurs closer and closer to the attachment line. This could explain the efficiency limitation of this kind of device.

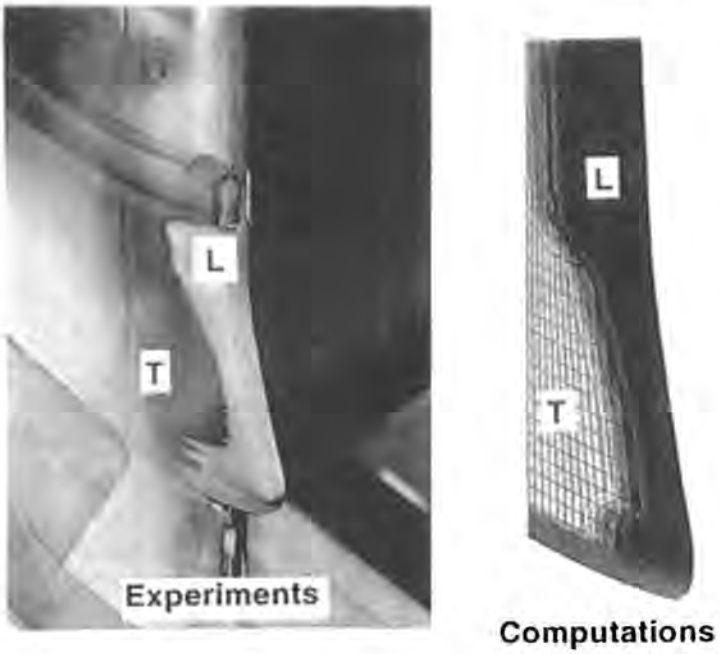

Figure 1: Transition front around a Gaster Bump, sweep angle $\varphi = 35°$, $M_\infty = 0.74$ (L: Laminar, T: Turbulent). Comparison between experiments (sublimation) and computations (transition criteria, Arnal *et al.*, 1995).

Suction (without or with Gaster bump)

The first results related to the effect of suction on contamination were obtained from DNS carried out by Spalart (1988). These computations showed that contamination can be delayed up to $\bar{R} \approx 350-400$ for $K = -1$. K is a dimensionless suction parameter:

$$K = \frac{V_w}{W_e}\bar{R}.$$

A first series of experiments carried out at CERT ONERA were performed on a small model by Juillen & Arnal (1995). With $K = -1.15$, contamination first appeared at $\bar{R} = 470$, but the small dimensions of the wind tunnel did not allow higher values of $\bar{R}$ to be investigated. Therefore ONERA decided to perform tests in the F2 wind tunnel at Le Fauga Mauzac in order to study this phenomenon at large values of $\bar{R}$. The chosen experimental support was a constant chord ($C = 1.2$ m) swept wing model generated from a symmetrical airfoil with a radius R of 0.2 m near the leading edge. The phenomenon of leading edge contamination was studied at sweep angles of 40° and 50° by fixing the model to the tunnel wall.

The objective of the tests was to delay leading edge contamination either by the use of a Gaster bump or by applying suction along the leading edge or

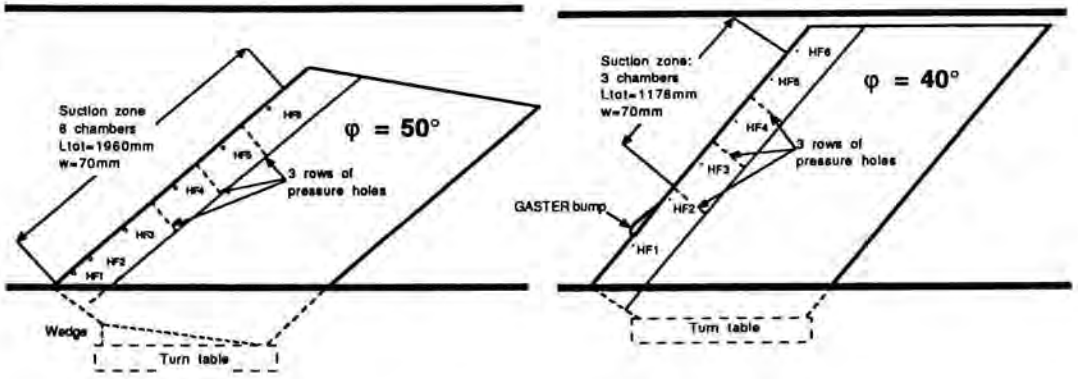

Figure 2: Experimental set-up without bump (left) and with bump (right). HF: hot films.

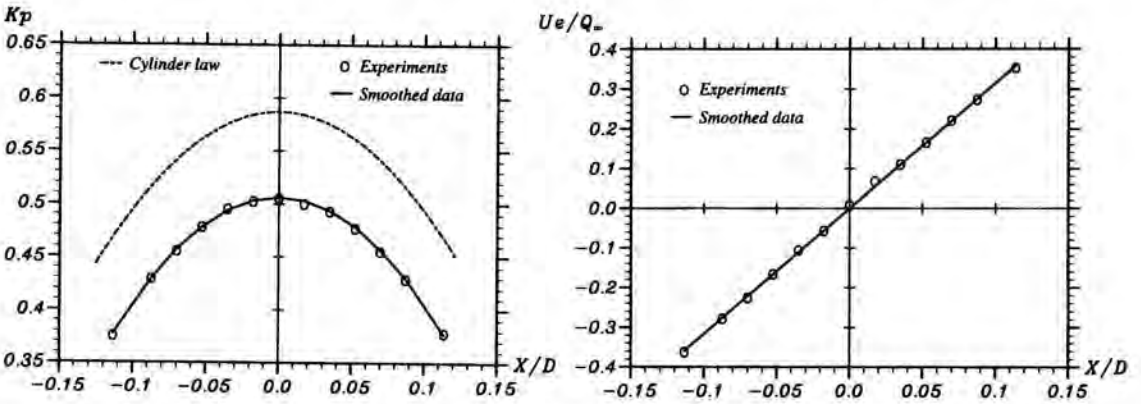

Figure 3: Experimental determination of the velocity gradient.

a combination of both. Fig. 2 shows the two leading edges which have been tested; the first one consists of six independent suction chambers fitted along the leading edge and the second one combines a Gaster bump with three leading edge suction chambers downstream of the bump. Three-dimensional computations were carried out to determine the effect of the wind tunnel walls on the pressure distributions and boundary layers of the configurations tested.

The chordwise width of the suction panel was about 70 mm, i.e. 35 mm on each side of the attachment line. The titanium perforated panel was laser drilled by AS&T company and the mean diameter of the holes was about 50 μm. The model instrumentation consisted of 3 rows of surface pressure taps aligned normal to the leading edge. Furthermore, 12 pressure taps were installed inside the suction chambers in order to evaluate the operation of the suction system. Leading edge contamination was detected by flush-mounted surface hot films. The position of the hot film is shown in Fig. 2.

The values of $\bar{R}$ were computed using pressure measurements made around

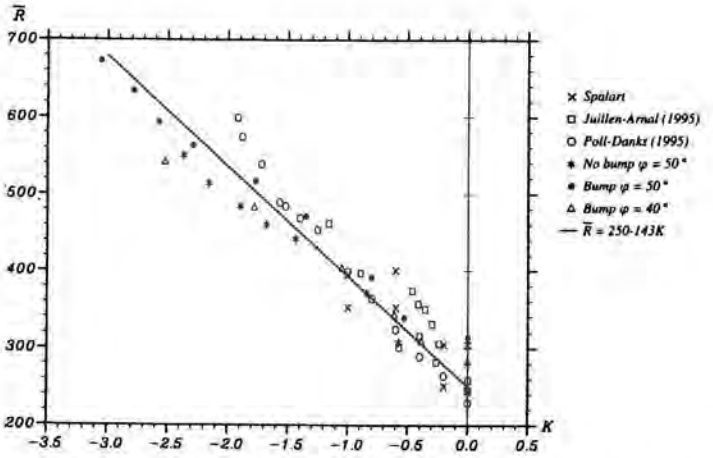

Figure 4: Leading edge contamination Reynolds numbers: summary of the results.

the leading edge. The computation of the velocity gradient K requires a precise analysis in order to be sure that small perturbations, caused for example by some defects in the geometry of the porous wall, do not introduce discrepancies into the computation. It was therefore decided to smooth the measured K_p distributions using second order polynomials (with $K_p = (P - P_\infty)/\frac{1}{2}\rho_\infty Q_\infty^2$, where P is the static pressure). Smoothing was carried out by the least square method in the interval $-0.2 < X/R < +0.2$. As an example, Fig. 3 shows the evolution of the measured pressure distribution and of the dimensionless normal velocity component U_e/Q_∞ as a function of X (curvilinear distance normal to the leading edge) for the case $Q_\infty = 60$ m/s and $\phi = 40°$. After smoothing, K and $\bar{R}$ can be accurately determined. The final values of $\bar{R}$ differ by about 10% from those of the potential flow around a circular cylinder.

Fig. 4 shows the evolution of $\bar{R}$ corresponding to the onset of leading edge contamination (first spots) as a function of the suction parameter K. The results obtained without Gaster bump for $\phi = 50°$ are compared with the DNS results by Spalart (1988) and with the experimental data currently available (Juillen & Arnal, 1995; Poll & Danks, 1995). Without suction, leading edge contamination occurs for $\bar{R} \approx 250$, as expected. Application of suction causes the onset of contamination to be delayed to $\bar{R} \approx 550$ for the maximum suction rate attainable in the experiments ($K = -2.4$).

For the configuration with a Gaster bump at $\phi = 50°$, leading edge contamination in the absence of suction occurs at $\bar{R} = 320$, a value which is lower than that obtained in other previous experiments. As soon as the flow over the bump is fully turbulent, the data with and without bump become close together (within the experimental uncertainty). The porosity of the porous leading edge fitted with the bump was larger than that of the leading edge without bump, so that the dimensionless suction parameter could be increased up to $K = -3.07$. This

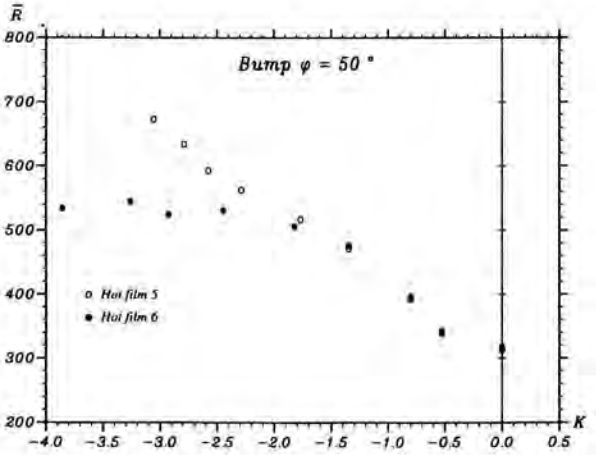

Figure 5: Leading edge contamination Reynolds numbers at two spanwise positions.

allowed to delay the onset of leading edge contamination up to $\bar{R} = 670$. The data for the onset of contamination without bump are fairly well represented by the following relationship:

$$\bar{R} = 250 - 143\ K.$$

The previous results were deduced from the time signals delivered by the hot films placed just before the end of the porous wall (hot film 6 without bump, hot film 5 with bump, see Fig. 2). The leading edge fitted with a bump was equipped with an additional sensor (hot film 6) after the end of the porous wall. Fig. 5 shows the leading edge contamination limits indicated by hot films 5 and 6 for the case with bump and $\phi = 50°$. The signals delivered by hot film 6 indicate that downstream of the sucked region, transition cannot be delayed above $\bar{R} \approx 550$, which roughly corresponds to the lower limit of "natural transition" (see next paragraph).

Numerical approaches for "natural" transition

Assuming that leading edge contamination is avoided, transition will occur through the amplification of "natural" disturbances. This linear, local stability theory and the e^n method are widely used to analyse this type of transition process. The following examples illustrate the efficiency and the limitations of the classical prediction methods and show how it is possible to improve the accuracy of these methods. The first example (localized surface heating) shows that the "old" e^n method is still useful for parametric studies. The second example (effect of suction) demonstrates how more recent approaches make it possible to take into account nonlinear phenomena. In the third example (leading edge instability), it is shown that classical TS waves are not always the most relevant ones for linear stability problems.

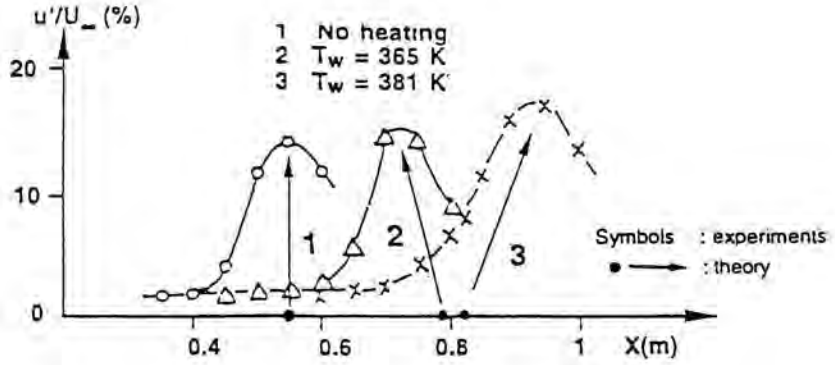

Figure 6: Effect of a localized surface heating on transition location.

Linear, local theory: application of the e^n method to the problem of localized heating

The shortcomings and limitations of the classical e^n method (based on local stability computations) are well known and have been discussed in several papers (e.g. Arnal, 1993; Arnal *et al.*, 1995). However, this method remains a very practical and efficient tool, especially for parametric studies. For a given test model and for a given disturbance environment, it is often able to predict the variation of the transition location when changing a parameter which governs the stability properties of the mean flow (pressure gradient, wall temperature, suction rate for instance).

To illustrate the usefulness of the e^n method for this kind of analysis, let us consider the problem of transition control by a localized surface heating (in air). The principle of this new stabilization technique is as follows. The wall is heated over a short streamwise distance, and a relaxation region develops downstream of the strip. In this region, the boundary layer temperature close to the wall is larger than the wall temperature, so that the boundary layer "sees" a cold wall. According to the linear stability theory, this leads to a decrease in the growth rates of the unstable disturbances.

Recent Russian papers, (Dovgal *et al.*, 1989a,b; Fedorov *et al.*, 1991) indicate that wind tunnel experiments confirmed the stabilizing effect of localized surface heating, at least for some configurations. Fig. 6 shows experimental results obtained on a two-dimensional flat plate placed in a subsonic wind tunnel (Dovgal *et al.*, 1989a). The wall is heated from $x = 0$ to $x = 0.1$ m and the wall temperature without heating is 296 K. The figure presents the streamwise evolution of the velocity fluctuations (rms values) measured near the wall without heating and for two cases with heating ($T_w = 365$ and 381 K). The efficiency of this stabilization technique is obvious. The points on the x-axis correspond to the theoretical transition location predicted by the e^n method with the value of the n factor corresponding to the case without heating. It is interesting to observe that

the theory is able to reproduce the transition movement, at least qualitatively. Other measurements (Dovgal *et al.*, 1989a) demonstrated that the best results are obtained when the heated strip is located in the area where the TS waves start to develop. Negative results (transition moves upstream) are obtained if heating is applied too far downstream of this area, because the destabilizing effect due to the heated strip becomes more important than stabilization in the relaxation region.

As far as three-dimensional flows are concerned, the experiments reported in (Dovgal *et al.*, 1989b) show that it is very difficult to observe a positive effect of the localized heating when transition is dominated by crossflow disturbances. Computations using the e^n method supported this conclusion (see Arnal, 1996).

Linear and nonlinear, non local theory: PSE approach

A new formulation of the stability analysis was proposed by Herbert (1993). The advantages of this so-called PSE approach (Parabolized Stability Equation), is that nonparallel effects are accounted for (nonlocal theory) and that nonlinear terms can be introduced into the equations.

The use of the *linear* PSE approach for transition prediction is similar to that of the classical, local theory. In particular, it is possible to integrate the (nonlocal) growth rates in the flow direction and to apply the e^n method to predict the onset of transition. Although the disturbance growth rates from local and nonlocal theories can differ significantly, particularly for three-dimensional flows (Arnal, 1995), the basic problem for transition prediction remains the same, i.e. one has to choose a value of the n factor at transition.

The *nonlinear* PSE approach is much more interesting because it is able to model resonances between different unstable modes. This can result in a steady distortion of the basic flow which is interpreted as the onset of transition. In other words, the concept of the "critical n factor" does not exist for nonlinear PSE.

As an example of application of nonlinear PSE computations, Fig. 7 shows the effect of suction on the stability properties for a two-dimensional flow (Casalis *et al.*, 1995). The results are related to a flat plate flow with a free stream velocity of 50 m/s. Suction is applied over a streamwise extent of 10 cm with a vertical suction velocity V_w equal to -1 cm/s. The numbers between parentheses denote the beginning and the end of the suction region. The left hand part of this figure shows the evolution of the amplitude $A_{2,0}$ of the primary, two-dimensional wave. The right hand part presents the variation of the amplitude $A_{1,1}$ of the secondary, oblique mode (H-type peak-valley system). It can be seen that suction location has only a minor effect on the primary mode, but this effect becomes important for the oblique mode: if suction starts upstream of $X = 0.5$ m, the secondary mode is damped up to the end of the plate. If suction starts at $X = 0.6$ or 0.7, resonance occurs. This demonstrates that suction is efficient if it is applied in the linear growth rate regime, i.e. before the appearance of the peak-valley system. Fundamental wind tunnel experiments performed by Reynolds & Saric

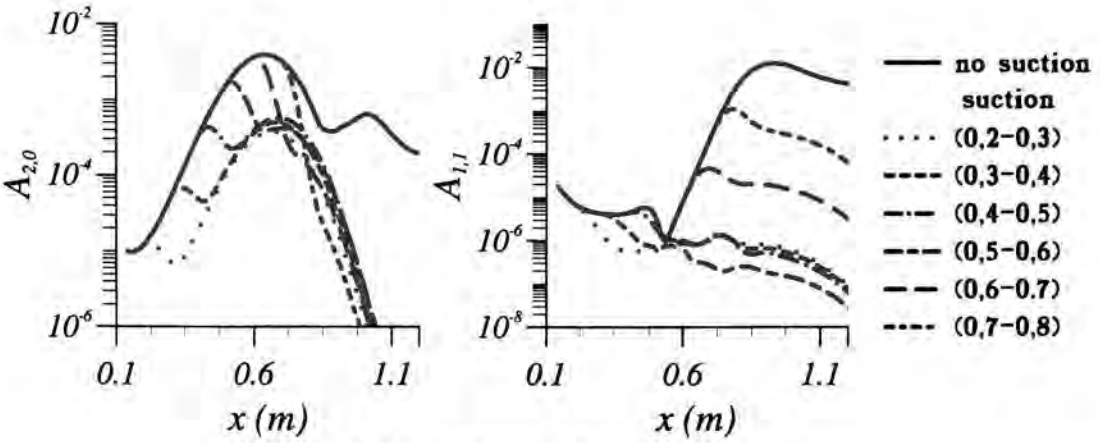

Figure 7: Effect of suction location on resonance.

(1982) indicated that suction is more effective when applied at Reynolds numbers close to the lower branch of the neutral curve, in qualitative agreement with the previous theoretical results.

"Natural" disturbances along attachment line

Even in the absence of leading edge contamination, unstable waves may appear and grow along the attachment line of swept wings. They have been observed, for instance, by Pfenninger & Bacon (1969) and by Poll (1978). This simplest way to investigate the linear problem is to use the classical, parallel theory for Tollmien-Schlichting waves (Orr-Sommerfeld equation). Based on this theory, the critical Reynolds number $\bar{R}_{cr}$ is about 670. It is also possible to follow a more rigorous approach by considering two-dimensional Görtler-Hämmerlin (GH) disturbances. In this approach, the disturbance amplitude in the X-direction normal to the leading edge depends linearly on X. The parallel flow assumption is no longer necessary, so that the GH disturbances are exact solutions of the linearized Navier- Stokes equations. The critical Reynolds number is now about 580 (see Hall *et al.*, 1984), in good agreement with the experimental data. Numerical investigations by Spalart (1988) and Lin & Malik (1995) indicated that the two-dimensional GH disturbances were the most amplified ones in the incompressible attachment line boundary layer.

Experiments on natural transition were conducted on a swept wing equipped with a suction system along the leading edge. This wing was the model without Gaster bump previously used for the investigation of leading edge contamination. The experimental set-up was modified in order to displace the apex of the model 300 mm above the wind tunnel floor, see Fig. 8. Regular waves travelling along the attachment line were detected by hot film measurements. When suction (blowing) is applied, the value of $\bar{R}$ at which the waves are observed increases (decreases) rapidly. It can be seen in Fig. 9 that the trend is in qualitative

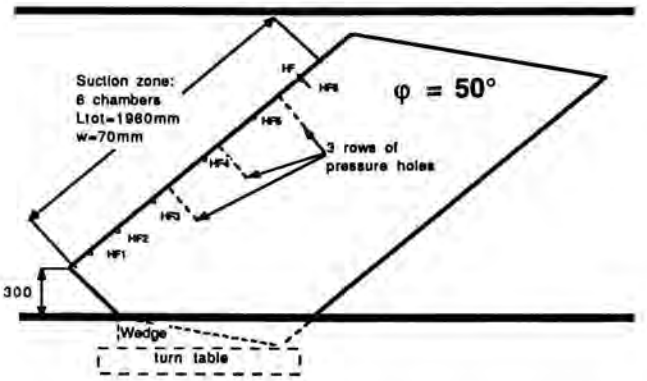

Figure 8: "Natural" transition along the attachment line of a swept model: experimental set-up.

agreement with theoretical results. In the experiments, the maximum value of $\bar{R}$ (close to 800) is fixed by the maximum wind tunnel speed.

An attempt was made to use the e_n method to predict the onset of transition along the attachment line. Fig. 10 shows the spanwise evolution of the integrated growth rates in a case with $\bar{R} \approx 740$ and $K = 0$. $Z = 0$ corresponds to the apex (stagnation point) of the model where the attachment line boundary layer starts to develop. The pressure distribution around the model was first determined by inviscid computations taking into account the presence of the wind tunnel walls. In a second step, accurate boundary layer computations along the leading edge were performed by using a three-dimensional boundary layer code (Malecki *et al.*, 1993). Then two n factors were computed, one for TS waves, the second for GH disturbances. As the boundary layer results indicate that the infinite swept wing conditions are approximately reached at $Z \approx 0.25$ m, the unstable waves leading to transition do not start to develop upstream of this point. However, if the attachment line boundary layer is assumed to be uniform all along the leading edge, i.e. if is immediately equal to 740 at the apex, then GH disturbances start to be amplified at $Z = 0$ and the n factor curve is represented by the dotted line plotted in Fig. 10. Experimentally, transition was found to occur at $Z \approx 0.6$ m. This leads to the following remarks

- when the infinite swept wing assumption is used for the GH disturbances, the n factor at transition is close to 10, in agreement with previous investigations based on the same assumptions (Arnal, 1993; Lin & Malik, 1995);
- the n factor of the GH disturbances is reduced to about 3 to 4 when the upstream flow history is taken into account;
- the n factor of the TS waves is close to zero.

In any case, a fundamental problem remains: the frequency range of the observed unstable waves is lower than that predicted by the theory (around 6 kHz

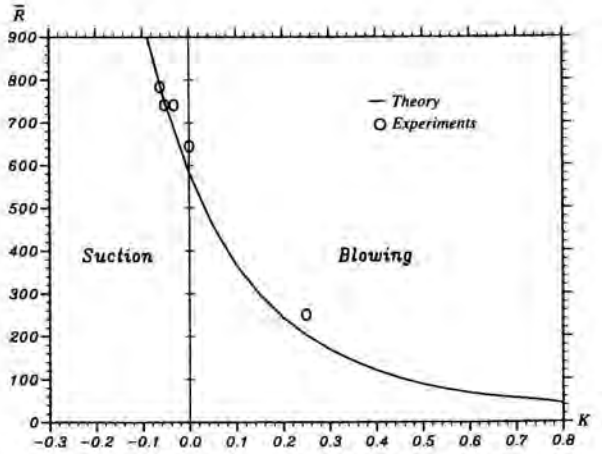

Figure 9: Suction effect on "natural" transition Reynolds number along the attachment line.

in the experiments, around 7 kHz in the computations). In fact, the measured frequency range is close to the lower branch of the neutral GH disturbances, as observed in previous experiments (Poll, 1978; Pfenninger & Bacon, 1969). This discrepancy could be explained by nonlinear phenomena which are not yet fully understood (Hall & Malik, 1986; Theofilis, 1994).

Conclusion

For the purpose of skin friction drag reduction by laminar flow control, it is often necessary to delay the onset of leading edge contamination. This can be done either by using a Gaster bump or by applying suction along the attachment line. For a given aircraft, the choice of the most appropriate device depends on the value of $\bar{R}$ near the root (leading edge radius, sweep angle, cruise conditions) and also on technological possibilities (for instance the use of anti-icing systems can make suction systems difficult to handle). Numerical and experimental investigations provided some interesting insight into the capabilities and limitations of such devices.

As far as natural transition is concerned, the e^n method remains a very efficient tool for parametric studies. Of course, there are so many routes to turbulence that a "universal" value of n cannot exist. This is true for the "old", local method, but also for the "new", nonlocal method based on linear PSE. The major improvement of nonlinear PSE is that transition occurs naturally, because resonance mechanisms are now included in the model. The new problem is the choice of correct initial conditions (amplitude, frequency, orientation) which are unknown for most of the real flow situations.

The attachment line instability is a particular problem which is likely to be important for large transport aircraft as soon as leading edge contamination is

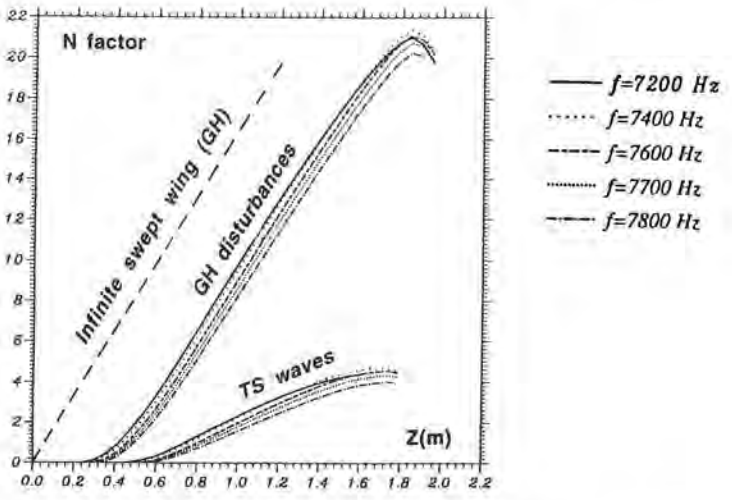

Figure 10: N factors for TS and GH disturbances.

avoided. It is now clear that GH disturbances play a major role; the present experiments showed that they can be damped by suction levels which are much lower than those necessary to relaminarize a contaminated turbulent boundary layer. However several problems still need to be solved, in particular those associated with nonlinear (subcritical ?) phenomena and with the use of the e^n method.

References

AGARD Report 786, 1992 – Special Course on Skin Friction Drag Reduction.

Arnal, D. 1993 – Prediction based on linear theory. In Progress in Transition Modelling, AGARD Report 793.

Arnal, D., Casalis G. & Juillen J.C. 1995 – A survey of the transition prediction methods: from analytical criteria to PSE and DNS. In R. Kobayashi, Editor, Laminar-Turbulent Transition, IUTAM Symp., Sendai, Springer Verlag.

Arnal, D., 1996 – Etude numérique de l'effet d'un chauffage localisé sur la transition. To be published.

Casalis, G., Copie, M.L., Airiau, C. & Arnal, D. 1995 – Nonlinear analysis with PSE approach. IUTAM Symposium on Nonlinear Instability and Transition in Three-dimensional Boundary Layers, Manchester.

Dovgal, A.V., Levchenko, V.Ya. & Timofeyev, V.A. 1989a – Laminarisation of the boundary layer through localised surface heating. In Proceedings of the Siberian Section of the USSR Academy of Sciences, Novosibirsk.

Dovgal, A.V., Levchenko, V.Ya. & Timofeyev, V.A. 1989b – Action of local heating on the transition to turbulence in a three-dimensional gas boundary layer. In Proceedings of the Siberian Section of the USSR Academy of Sciences, Novosibirsk.

Fedorov, A.V., Levchenko, V.Ya. & Tumin, A.M. 1991 – Problems of laminar-turbulent transition control in a boundary layer. *Russian J. of Theoretical and Applied Mechanics* **1**, 85-101.

Gaster, M., 1967 – On the flow along leading edges. *Aeron. Quart.* **18**.

Hall, P., Malik, M.R. & Poll, D.I.A. 1984 – On the stability of an infinite swept attachment line boundary layer. *Proc. R. Soc. London A* **395**, 229-245.

Herbert T., 1993 – Parabolized stability equations. In Progress in Transition Modelling, AGARD-FDP-VKI Special Course.

Juillen, J.C. & Arnal, D. 1995 – Experimental study of boundary layer suction effects on leading edge contamination along the attachment line of a swept wing. In R. Kobayashi, Editor, Laminar-Turbulent Transition, IUTAM Symp., Sendai, Springer Verlag.

Lin, R.S. & Malik, M.R. 1995 – The incompressible attachment line boundary layer stability. In R. Kobayashi, Editor, Laminar-Turbulent Transition, IUTAM Symp., Sendai, Springer Verlag.

Malecki, P., Cousteix J. & Houdeville, R. 1993 – Three-dimensional boundary layer calculations with two-layer turbulence models. 5th Int. Symp. on Refined Flow Modelling and Turbulence Measurements, Paris.

Pfenninger, W. 1965 – Flow phenomena at the leading edge of swept wings. AGARDograph 97, Part 4.

Pfeninnger, W. & Bacon Jr., J.W. 1969 – Amplified laminar boundary layer oscillations and transition at the front attachment line of a 45 swept flat-nosed wing with and without boundary layer suction. Viscous Drag Reduction, C.S. Wells Ed., Plenum Press.

Poll, D.I.A. 1978 – Some aspects of the flow near a swept attachment line with particular reference to boundary layer transition. Technical Report 7805./K, Cranfield, College of Aeronautics.

Poll, D.I.A. & Danks, M. 1995 – Relaminarisation of the swept wing attachment line by surface suction. In R. Kobayashi, Editor, Laminar-Turbulent Transition, IUTAM Symp., Sendai, Springer Verlag.

Reynolds, W.S. & Saric, W.S. 1982 – Experiments on the stability of the flat plate boundary layer with suction. AIAA Paper 82-1026.

Spalart, P.R. 1988 – Direct numerical study of leading edge contamination. AGARD CP 438.

Theofilis, V. 1994 – On subcritical instability of the attachment line boundary layer. AGARD CP 551.

Authors' addresses

°CERT ONERA – DERAT
2 avenue E. Belin
F–31055 Toulouse Cedex, France

▷ONERA – OA
B.P. 72
92322 Chatillon Cedex, France

D.I.A. Poll°, M. Danks▷ & M.R. Yardley▷

The Effects of Suction and Blowing on Stability and Transition at a Swept Attachment Line

Abstract

An experimental investigation has been carried out on the attachment-line flow formed on a long, inclined cylinder. When the flow is laminar, surface blowing has been applied to modify the stability characteristics and, ultimately, induce a transition to turbulence. Very substantial reductions in the transition Reynolds number have been observed. Conversely, surface suction has been used to modify a fully turbulent flow. Strong suction has been found to induce complete relaminarisation over a very wide range of Reynolds number.

Introduction

The attachment line is a common feature in the flow over many shapes of engineering interest. However, there is currently a great deal of interest in the concept of an aircraft wing designed to support extensive regions of laminar flow and, consequently, having a much lower drag than its current technology turbulent counterpart.

In the context of a laminar flow wing, the attachment-line flow is of paramount importance. It is well known, Poll (1979), that the attachment line flow can be tripped to the turbulent state at very low Reynolds number, if a sufficiently large contaminating agent is present. This may take the form of a trip wire, a skin joint, a wing fuselage junction or even an insect splat. By contrast it is also known, Hall *et al.* (1984), that, in the limit of very small forcing e.g. surface micro roughness or low free-stream turbulence, the flow exhibits a classic viscous instability which is well described by linear theory. A particularly intriguing feature of the problem is that, in terms of displacement thickness Reynolds number, there is a factor of 2.4 between the lower limit for turbulence and the linear stability, minimum critical value. To date, there has been no theoretical explanation provided for this very large difference, although the lower limit for turbulent flow has been found to be consistent with the lower "limit" for sustainable turbulence found in the DNS computations of Spalart (1988). Virtually all the plans for laminar flow wings on all but the smallest aircraft involve the use of surface transpiration to control the boundary layer instability. Therefore, it is necessary to have an understanding of the effect of transpiration at the attachment line.

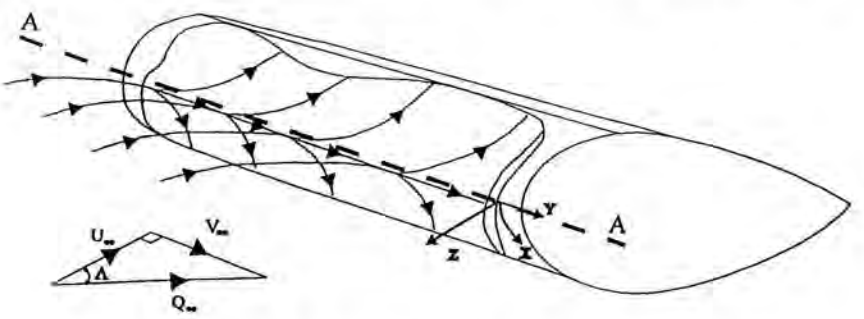

Figure 1: The flow in the vicinity of a swept attachment line.

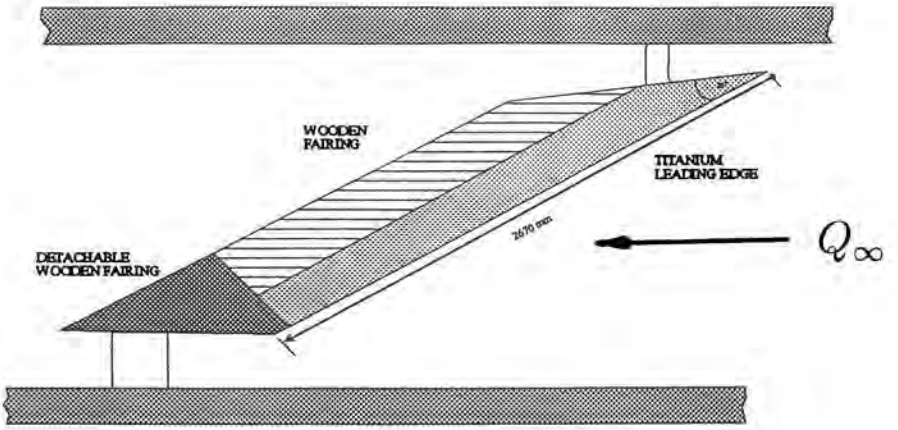

Figure 2: Sketch of the model in the wind-tunnel.

The present paper addresses issues of blowing to destabilise a laminar flow and suction to relaminarise a turbulent flow.

The attachment line flow

Fig. 1 shows a schematic of the external streamline pattern for the flow over a swept leading edge. The attachment line lies along A-A and it is the demarcation between flow which passes over the upper surface and that which passes over the lower surface. On the attachment line itself, the chordwise component of the flow at the edge of the viscous layer is zero but the spanwise component is not. Consequently a "boundary layer" is established along A-A and this may be laminar, transitional or turbulent, depending on conditions.

When the flow is incompressible, the low-speed, adiabatic flow along an infinite swept attachment line is described by the parameters

$$\overline{R} = \frac{V_e \eta}{\nu} \quad \text{and} \quad \frac{w(0)}{V_e} \ ,$$

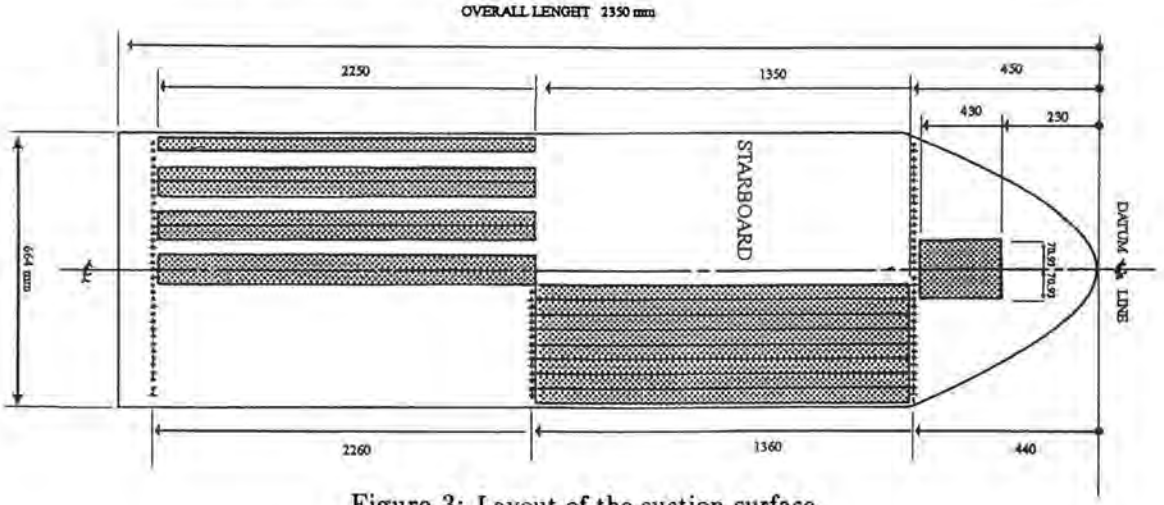

Figure 3: Layout of the suction surface.

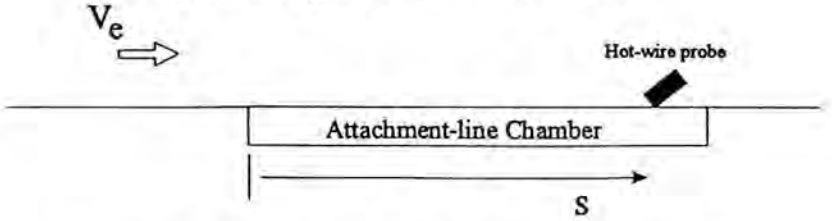

Figure 4: The spanwise length of surface transpiration, s.

with

$$\eta = \left[\frac{\nu}{dU_e/dx}\right]_{x=0}^{1/2} .$$

Here V_e is the spanwise component of the external velocity and $w(0)$ is the transpiration velocity at the wall.

Experimental arrangement

Tests have been carried out on the model shown in Fig. 2. This consists of a semi-circular forward part with a wooden fairing at the rear, giving a "teardrop" cross section. The leading edge sweep is nominally 60°, the normal-to-leading edge chord is 0.813 m and the leading edge radius is 0.202 m. All the measurements are taken on the semi-circular portion which is made from a 1.2 mm thick titanium sheet. Before being rolled to form the cylinder, the titanium sheet was laser perforated with holes of 50 μm diameter with a hole-to-hole and row-to-row spacing of 400 μm. The areas which were drilled are indicated in Fig. 3. Transpiration at the attachment line is provided by a strip of perforation which begins 1.35 m from the upstream tip and is 0.9 m long in the spanwise direction.

Perforations extend to ±35.3 mm either side of the attachment line which, in this case, coincides with the windward symmetry plane of the model. Beneath the perforation strip is a single plenum chamber. The model was mounted in the Goldstein Research Laboratory low speed, closed-return wind tunnel. This has a 2.74 m × 2.13 m test section and a maximum flow speed of 70 m/s. The free-stream, mean turbulence level is approximately constant at 0.1% over the tunnel operating range – see Mullender (1995).

Leading edge sweep may be set at any angle between 38° and 65°, giving values of $\overline{R}$ in the range 190 to 800, whilst the mean through surface velocity, $w(0)$, can be set in the range $+0.002V_e$ to $-0.01V_e$. In all the tests, an untranspired flow was established on the attachment line. This flow encountered the porous surface as shown in Fig. 4 and the transpiration velocity over the surface was invariant in s. Hot-wire anemometers were used to monitor fluctuations and surface Pitot tubes were used to make mean flow measurements - as described by Yardley (1995).

Blowing on a laminar layer

Measurements were conducted with the hot-wire at a fixed position, s, and with the free-stream speed held constant. Flow conditions were varied by slowly increasing the surface blowing rate. A typical set of spectra, covering the progression from stable laminar to turbulent flow, is given in Fig. 5. Here the value of $\overline{R}$ is 195 with s/η being 4350. For $w(0)/V_e$ below 0.00155, the laminar flow is stable. However, when the blowing rate exceeds 0.0016, a group of unstable waves appears, as indicted by the peak in the spectrum, centred on a frequency of about 400 Hz. Further increases in the blowing rate cause the energy content in this frequency range to increase. At blowing rates above 0.00172, a series of peaks appear in the spectrum. In this particular case, three additional peaks are clearly visible. These are centred upon frequencies of 800 Hz, 1200 Hz and 1600 Hz respectively i.e. they are the second, third and fourth harmonics of the 400 Hz fundamental mode. Finally, at a blowing rate of about 0.0019, the flow is turbulent and fluctuations have the appropriate spectrum.

The above behaviour was observed for all the measurements taken between an $\overline{R}$ of 195 and 545, although it should be noted that the hot-wire signals were not always as clear as those shown in Fig. 5. A more detailed description of the data may be found in Poll and Danks (1995). By considering only the central frequency of the fundamental modes, it was found that a clear correlation existed with $\overline{R}$. This is shown in Fig. 6. In principle, this result should be comparable with the theoretical work of Hall *et al.* (1984). Unfortunately, the published stability data are insufficiently detailed to allow direct comparison. However, private communication with Theofilis (1995) has revealed that the experimental data shown in Fig. 6 corresponds to the most amplified mode predicted by linear theory. Finally, Fig. 7 gives the conditions necessary for the onset of transition. It is clear that blowing produces a situation in which turbulent flow may be established at very low Reynolds number, with the value of $\overline{R}$ for transition

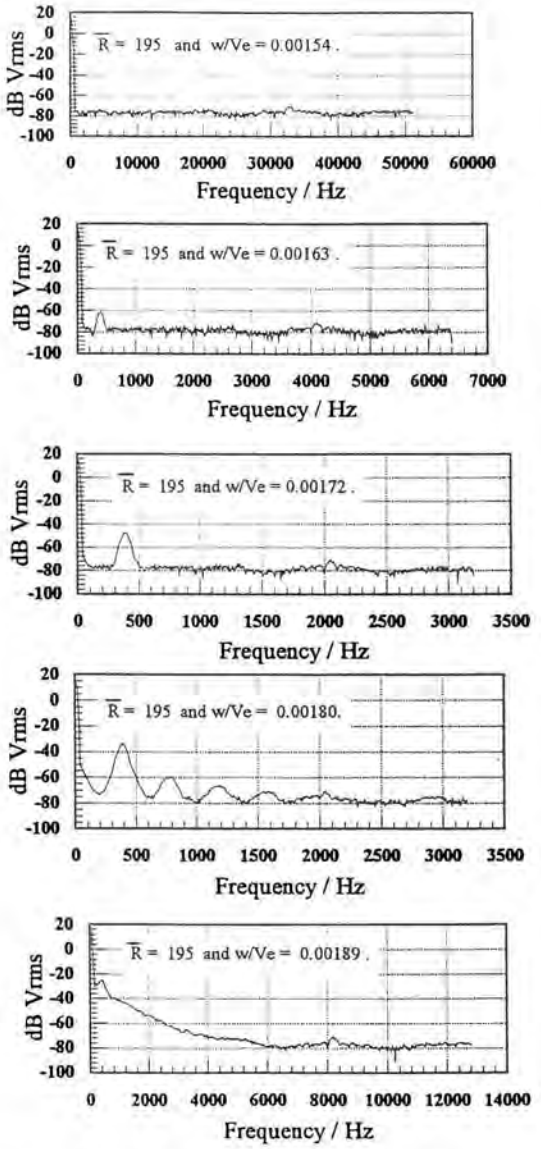

Figure 5: Attachment line boundary layer frequency spectra.

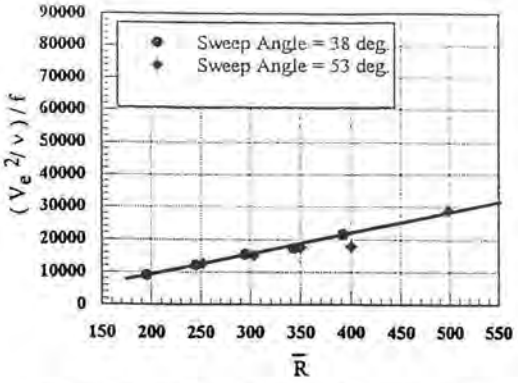

Figure 6: The variation of disturbance frequency with $\overline{R}$.

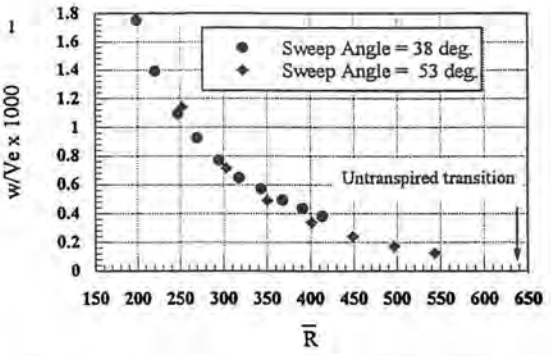

Figure 7: The transition behaviour of the blown attachment line boundary layer (s/η large).

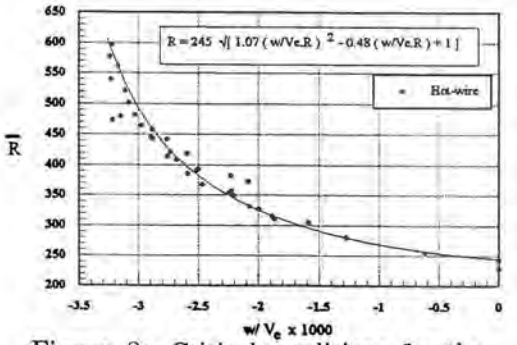

Figure 8: Critical conditions for the end of relaminarisation ($s/\eta \to \infty$).

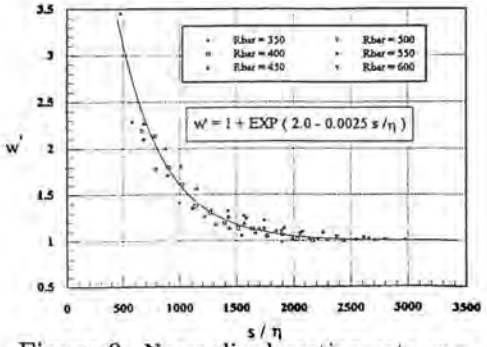

Figure 9: Normalised suction rate as a function of streamwise distance.

onset being reduced by more than a factor of 3 compared with the zero blowing case.

Suction of a turbulent layer

For this part of the investigation, a 4 mm diameter circular trip-wire was wrapped around the model at a distance of 80 mm from the upstream tip. As expected from previous work e.g. Poll (1979), with zero transpiration, transition onset began when $\overline{R}$ exceeded 245 and the flow was fully turbulent for $\overline{R}$ in excess of 280. Having established turbulent flow, the free-stream conditions were held constant and the surface suction rate was increased until the flow reverted to the laminar state, as indicated by a hot-wire at a fixed distance, s, from the leading edge of the suction strip. When the distance exceeded approximately 2000η, the results became independent of s, and the conditions for complete reversion to laminar flow are given in Fig. 8. For smaller values of s/η, the

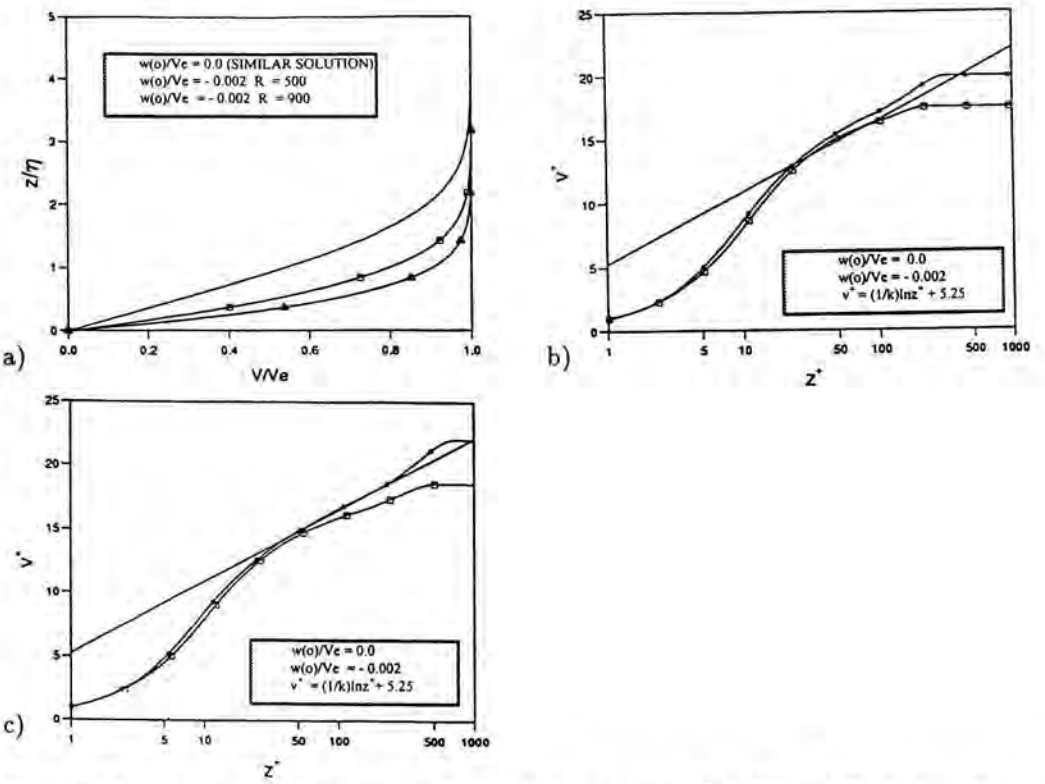

Figure 10: a) Laminar flow profiles; b) Turbulent flow at $\overline{R} = 500$; c) Turbulent flow at $\overline{R} = 900$.

data for the attainment of laminar flow could be normalised as shown in Fig. 9, where w' is the ratio of the suction required at a particular value of s/η to that required for very large s/η. A more detailed description of the data, together with approximate curve fits are given in Poll and Danks (1994) - see also Juillen and Arnal (1994).

The important points to note are that the turbulent flow can always be relaminarised with sufficient surface suction, and the data seem to indicate that a special suction rate exists, beyond which turbulent flow is physically impossible. Data from the present tests indicate that this suction level is in the region of 0.0035.

Since the suction rates required to produce relaminarisation are relatively large, there is significant distortion of the mean velocity profiles. A series of results for the case where $w(0)/V_e$ is equal to -0.002 is given in Fig. 10. It is found that the laminar flow profiles are in very good agreement with the predictions of boundary layer theory. However, the turbulent results are a challenge to the theoretician.

References

Hall, P. Malik, M.R. & Poll, D.I.A. 1984 – On the stability of an infinite swept attachment-line boundary layer. *Proc. of Roy. Soc. of Lond.* A, **395**, 229-245.

Juillen, J-C. & Arnal, D. 1994 – Experimental study of boundary layer suction on leading edge contamination along the attachment line of a swept wing. *IUTAM Symposium on Laminar-Turbulent Transition*, Sendai, Japan, Springer-Verlag 1995.

Mullender, A.J. 1995 – The application of laminar flow to aero-engine nacelles. *PhD Thesis*, University of Manchester, UK.

Poll, D.I.A. 1979 – Transition in the infinite swept attachment-line boundary layer. *The Aeronautical Quarterly*, **30**, 607-628.

Poll, D.I.A. and Danks, M. 1994 – Relaminisation of the swept wing attachment line by surface suction. *IUTAM Symposium on Laminar-Turbulent Transition*, Sendai, Japan, Springer-Verlag.

Poll, D.I.A. & Danks, M. 1995 – Non-linear instability and transition in flow near a swept leading edge. *IUTAM Symposium on Non-linear instability and transition in three dimensional boundary layer*, Manchester, UK.

Spalart, P. 1988 – Direct numerical study of leading-edge contamination. *AGARD CP 438*, paper no. 5.

Theofilis, V. 1995 – Private communications.

Yardley, M.R. 1995 – An investigation into the mechanisms of turbulent boundary layer relaminarisation on swept leading edges. *PhD Thesis*, University of Manchester, UK.

Authors' addresses

°College of Aeronautics
Cranfield University
Cranfield, Bedford
MK43 0AL, UK

▷Aerospace Division
Manchester School of Engineering
University of Manchester
M13 9PL, UK

V. Theofilis

On Secondary Destabilisation of an Attachment Line Boundary Layer in Compressible Flow

Abstract

The generalised Hiemenz model is used to describe incompressible flow in the infinite swept attachment line boundary layer. This base flow is perturbed using local spatial LST and the resulting secondary instability problem is solved at high Reynolds numbers, extending earlier work. Issues raised by compressibility are discussed next; in the absence of a simplifying theoretical assumption, such as that of Görtler & Hämmerlin, we proceed to design a DNS in order to study the instability in question. The algorithm is outlined and first results on its successful application on a relevant compressible model problem are presented.

Introduction

The investigation into secondary stability was initiated as an attempt to explain the frequencies appearing in the spectrum, distinct from the linearly unstable ones, at conditions favouring linear growth (Poll, private communications; Poll *et al.*, this volume). Although not sharply defined as such, these frequencies appear in the parameter space region where harmonics of the primary linearly growing wave are expected. A secondary instability analysis is thus called for to shed light into this problem. Within the framework of the classic, in Blasius flow, Floquet analysis (Herbert, 1988) it is impossible to introduce three-dimensional streamwise (chordwise) periodic disturbances superimposed upon the linearly growing spanwise eigenmode in a theoretically self-consistent manner. The reason is, of course, the parity of the linear eigenfunctions in the attachment line problem; these have been assumed, in theoretical analyses, to inherit the symmetry of the base flow (Görtler-Hämmerlin assumption, henceforth referred to as GH) while the incompressible DNS of Spalart (1988) has demonstrated that this assumption may be justified in the linear regime. Invoking the GH assumption to study secondary instability in the attachment line, however, results in the elimination of the dependence of the system of equations on the streamwise coordinate which, in turn, prohibits the introduction of streamwise periodic disturbances in the present problem in a formal manner.

The inability to introduce streamwise periodic disturbances into the stagnation region, while being consistent with the currently available theoretical tools, does not preclude the actual presence of such waves in an experiment. The

conjecture is then made that *if* present, streamwise periodic waves will amplify according to Floquet secondary theory. Further, use is made of the observation (Arnal, 1992; Theofilis & Poll, 1994) and theoretical prediction (Theofilis, 1995) that the classic Orr-Sommerfeld model is an adequate approximation to the infinite-swept attachment line boundary layer linear stability problem at high Reynolds numbers. Comparisons between results obtained using the set of assumptions exposed and experiments, currently performed, will test the validity of the present approach. The many analogies between attachment line flow and the Blasius boundary layer, alongside the success of Floquet theory in Blasius flow (Kachanov & Levchenko, 1984; Herbert, 1988) renders this model as the first candidate to be investigated.

In compressible flow the issue of attachment line instability is further complicated by the lack of information on experimental results which would validate the base flow (*e.g.* Reshotko & Beckwith, 1955) to be used at the stagnation region. Even less is available on the experimental validation of the various theories put forward for the linear stability of the compressible problem. From a theoretical point of view, one combines numerical solutions to the inviscid problem in the free-stream with first-order boundary layer theory near the wall, followed by linear analysis of the resulting profiles (*e.g.* Malik & Beckwith, 1988). It is well known, however, Mack (1984, for a review), that the linear stability results obtained using slightly different base flows can be profoundly different due to the presence of derivative terms in the stability equations. In our opinion it is of little practical importance to go even further and analyse the secondary stability of compressible attachment line boundary layer along these lines before the issues raised above are addressed in a satisfactory way.

In order to proceed we choose to embed the question of attachment line secondary instability within the framework of DNS. The design requirements for a DNS of the STAgnation Region (STAR) are stated and the potential of the algorithms used to meet successfully these requirements is demonstrated. Linear and nonlinear instability results are presented for a flow problem which exhibits inviscid instability, that of a free shear layer. Aside from the good documentation available there are more reasons for selecting this flow model for validation of the code. First, from a physical point of view, it is well known that the compressible flat-plate boundary layer flow is susceptible to inviscid instability through the action of the generalised inflection points developing in the base profile (Mack, 1984). While incompressible attachment line instability is viscous in nature, the analogies between the eigenvalue spectra of this flow and the Blasius boundary layer gives rise to the conjecture that inviscid instability at the attachment line itself will come in play in compressible flow. Second, crossflow instability, active in the stagnation *region* at all Mach numbers, is inviscid in nature (Reed & Saric, 1989). Finally, a purely practical reason exists in order to focus on the free shear layer, namely that best use of available computing resources can be made by developing the DNS on a model problem which exhibits instability associated with large growth rates.

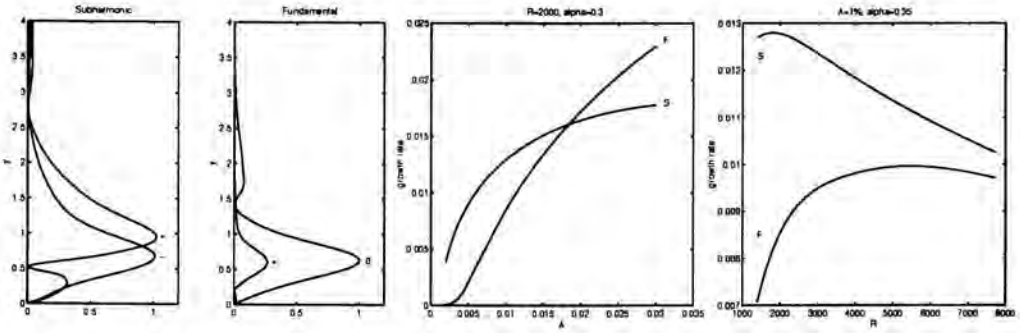

(a) (b) (c)

Figure 1: (a) Spatial structure of secondary eigenfunctions; $\bar{R}$=2000, Branch II, A = 1%; The effect of primary amplitude (b) and Reynolds number (c) on the secondary growth rate.

Review of incompressible results

Extending the approach used by Theofilis & Poll (1994) for subharmonic instability to studying fundamental disturbances as well, we use spatial LST to monitor a linearly unstable primary wave developing along the spanwise direction, which becomes unstable to three-dimensional streamwise periodic disturbances. The full body of results of this study is presented by Theofilis (1996); here a summary is presented. The spatial structure of secondary eigenfunctions at a particular set of conditions is shown in Fig. 1a. It may be seen that the secondary perturbations possess a structure analogous to that of the secondary waves found in Blasius flow; most of the activity is confined within the boundary layer, with the characteristic double-peak appearing in the subharmonic perturbation.

The effect of primary amplitude and Reynolds number on the secondary growth rate is presented in Figs 1b and 1c respectively. A number of conclusions may be drawn from these results. First, it is seen that both types of secondary instability (and presumably also detuned modes, although not studied here) may be present. As the amplitude of the primary disturbance superimposed upon the base flow $A \to 0$ the secondary growth rates are also seen to approach zero, as the case is in Blasius flow. At low A subharmonic instability is seen to be more powerful a mechanism than its fundamental counterpart. As A grows, much as in the Blasius boundary layer, fundamental instability takes over; the cross-over point is found to be $A \approx 1.8\%$. For a fixed low value of A, on the other hand, increasing the Reynolds number $\bar{R}$ results in the two instability mechanisms approaching a single one. While $\bar{R} \to \infty$ studies have not been performed, the trend obtained suggests that large $\bar{R}$ secondary instability is inviscid in nature; this prediction awaits theoretical verification.

Issues raised by compressibility

Even in incompressible flow there is no theoretical justification for the use of the GH assumption in the late linear and early nonlinear stages, although it still produces optimal results compared to other approaches in the linear regime (Arnal, 1992, and this volume). With compressibility taken into account it is not possible to use a GH-type of approach any more. The coupling of flow variables through density results in terms explicitly dependent upon the streamwise (chordwise) coordinate x appearing in the equations.

A secondary stability study based on PSE (Bertolotti, 1991), on the other hand, is physically meaningful when considering mild growth of the boundary layer. In the attachment line problem this may only be the case in compressible flow along the spanwise direction; in the incompressible regime under the GH approximation the parallel boundary layer set up along the attachment line prohibits PSE from improving the results obtained by spatial LST. However, the questions raised regarding the formal introduction of the third dimension into the compressible problem remain.

Design requirements for a STAR DNS

Our approach to solve the theoretical problems discussed has been to use DNS for the stagnation region. The fundamental requirement for a STAR DNS is that it solves for the flow in the *vicinity* of an attachment line. Physically this implies inclusion of the currently little understood region of interaction between attachment line and crossflow instability. In so doing, DNS has the potential to provide initial conditions for the theoretical study of crossflow instability further downstream in the chordwise direction; these conditions appear to be essential for the convergence of PSE methods near the attachment line, as recently experienced in the ATTAS experiments (Stolte *et al.*, 1995).

From a numerical point of view, as with any DNS, the long-time integrations suggest use of low-dispersion, low-dissipation schemes for spatial differentiation. Schemes of this nature currently include spectral single- or multi-domain and Padé 3/4/6 or 5/6/5 compact finite-differences. The ability to interchange numerical differentiation schemes has been found to be useful for diagnostic purposes by Pruett *et al.* (1995). Time-integration may be performed by a member of the $O\left((\Delta t)^3\right)$ family of Runge-Kutta schemes derived by Wray (1986) which ensure optimal memory use, given that the time-step Δt is low because of spatial discretisation requirements and the CFL-related restriction.

Finally, the issue of the outflow boundaries in a STAR DNS has to be addressed. In the incompressible limit the generalised Hiemenz base flow ensures that a strictly parallel boundary layer is set up in the spanwise direction; this can be treated numerically as homogeneous and a Fourier expansion may be utilised in this direction. The streamwise direction, on the other hand, is one of strong acceleration of the flow; as such it lends itself to application of the spatial

concept (Spalart, 1988). This may be accomplished by any of the techniques available, namely the sponge layer (Israeli & Orszag, 1981), the fringe technique (Spalart, 1988) and its windowing derivative model, the relaminarisation-zone technique (*e.g.* Eissler & Bestek, 1996) or the buffer domain approach (Streett & Macaraeg, 1989).

Application of the ideas discussed and assessment of their performance is presented next. It should be noted that the modular construction of the DNS code permits study of a variety of flow problems with minimal additional effort, concentrated mainly on the provision of base flow and the associated LST- or PSE-based initial conditions.

DNS validation results

The argumentation on the choice of the compressible free shear layer as the model base flow problem to validate the DNS approach has been presented earlier. Further, the Crocco-Busemann integral is utilised to obtain the base flow temperature pertinent to the hyperbolic tangent model for the base flow velocity; alternatively the Lock profile has also been used, or the temperature has been kept constant across the layer. The inviscid instability of this flow to three-dimensional linear disturbances is obtained by spectral collocation solution of the Lees-Lin system (Mack, 1984) and is fed as initial condition into the DNS at low amplitude.

The compressible three-dimensional Navier-Stokes equations are then marched in time with spatial derivatives in the streamwise x and spanwise z directions calculated using Fourier collocation (temporal approach) and those in the normal y direction using a choice of Chebyshev collocation or Padé 3/4/6 compact finite-differences; for the type of instability considered and the purposes of validation of the numerical techniques suffices to integrate only the Euler part of the equations. Characteristic non-reflecting boundary conditions are applied at the $|y| \to \infty$

Table 1: Convergence history for the reproduction of the 2- and 3-D LST result by DNS. A denotes amplitude of the superimposed perturbation.

Mach=0.4, α=0.409							
	ψ=0			$\psi = \pi/6$			
	LST	DNS			DNS		
		A=10^{-2}	A=10^{-6}	NY	(8, NY, 8)	(16,NY,16)	(32,NY,32)
NY	ω_i	ω_i	ω_i		ω_i	ω_i	ω_i
32	0.155332	0.156024	0.156028	32	0.130842	0.130379	0.130380
64	0.155301	0.155275	0.155277	64	0.130305	0.129809	0.129806
128	0.155301	0.155300	0.155301	128	0.129795	0.129961	0.129961
				256	0.129930	0.129948	0.129948

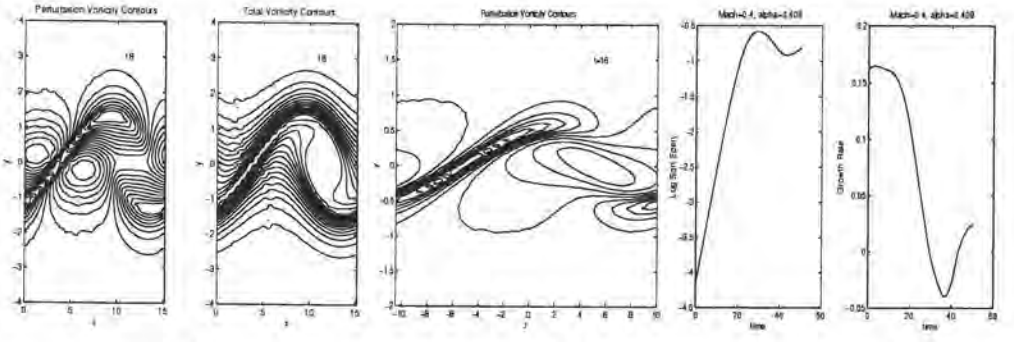

(a) (b) (c)

Figure 2: Nonlinear development of (a) 2D and (b) 3D unstable inviscid mode; (c) perturbation energy and growth rate evolution with time in the 2D simulation.

boundaries (Adams, 1992). The solution is obtained exclusively in real space, derivatives being calculated by straightforward matrix multiplication as opposed to the classic FFT; the former approach has been found to be of comparable efficiency to the latter for the grids and machine architecture utilised. Both the conservative form of the governing equations, as well as the pressure equation (Pruett *et al.*, 1995) have been solved with identical results obtained including the nonlinear stages.

The quality of the DNS solution in the linear regime is assessed by monitoring the reproduction of two- and three-dimensional linear growth rates. Such a comparison is presented in Table 1 as a function of the number of nodes NY utilised in the normal direction y. Both a two-dimensional ($\psi = tan^{-1}\left(\frac{\beta}{\alpha}\right) = 0$) and a three-dimensional linear perturbation are used to initialise the DNS. The former was used in order to monitor spurious growth of three-dimensionality in our code; the perturbation eigenvector was obtained on the same grid as that used for the DNS. By contrast, the three-dimensional mode was obtained on a grid different to that on which the DNS was performed and was transferred on the latter using piecewise cubic Hermite interpolation. The agreement between LST and DNS results for the 2D mode may be seen as typical of well-resolved DNS; no spurious three-dimensional growth was detected in this simulation. The interpolation procedure was proven to be responsible for the discrepancy between LST and DNS for the 3D mode; with the DNS performed on the grid on which the LST problem is solved agreement similar to that obtained for the 2D mode is achieved.

In Figs 2a and 2b the results of two simulations starting with the 2- and 3D modes as initial conditions, respectively, are presented. The nonlinear structures characterising the vortex roll-up at the late transitional stages may be seen. The wiggles present in both simulations are a result of attempting to solve the Euler equations without any form of artificial dissipation, and not of low resolution. In a corresponding Navier-Stokes calculation these wiggles disappear. Finally in Fig. 2c we present the evolution of a 2D mode through the linear stage

(growth rate obtained by the slope of the function $ln(E_{\rm pert})^{1/2}(t)$, $E_{\rm pert}$ being the perturbation energy) into nonlinear saturation at large t; at this time a well-resolved analogous three-dimensional calculation would have resulted into a turbulent state having been reached.

Conclusion

The theoretical difficulties in modelling secondary stability in the attachment line problem, combined with the lack of experimental support for a specific model of base flow and its primary stability, led us to design a DNS for the stagnation region. The numerical tools to be utilised have been validated on a compressible three-dimensional model problem, physically relevant to the flow at hand.

A simplified model has been proposed for secondary destabilisation of the corresponding incompressible flow; its results are currently being compared with recent experiments and, if validated, will be used to provide intuition in the parameter ranges to be monitored by DNS. Work in this area, as well as on the remaining issues regarding the STAR DNS described, namely buffer implementation as well as base flow and its LST is currently underway.

Acknowledgement

Part of this work was performed at the Dept. of Appl. Mathematics, Univ. of Twente, The Netherlands.

References

Adams, N. A. 1992 – An explicit temporal spectral/finite-difference method for the Direct Numerical Simulation of compressible flat plate boundary layer transition. *DLR IB 221-92 A 25.*

Arnal, D. 1993 – Boundary layer transition: Predictions based on linear theory. *AGARD Rep.793*, 2-1 – 2-63.

Bertolotti, F. P. 1991 – Linear and nonlinear stability of boundary layers with streamwise varying properties. Ph. D. Thesis, *The Ohio State University*, Columbus, Ohio.

Eissler, W. & Bestek, H. 1996 – Spatial numerical simulations of linear and weakly-nonlinear wave instabilities in supersonic boundary layers. *Theor. Comp. Fluid Dyn.* (to appear).

Herbert, Th. 1988 – Secondary instability of boundary layers. *Ann. Rev. Fluid Mech.*, **20**, 487-526.

Israeli, M. & Orszag, S. A. 1981 – Approximation of radiation boundary condition. *J. Comp. Physics* **41**, 115-135.

Kachanov, Yu., S. & Levchenko, V. Ya. 1984 – The resonant interaction of disturbances at laminar-turbulent transition in a boundary layer. *J. Fluid Mech.*, **138**, 209-247.

Mack, L. M. 1984 – Boundary layer linear stability theory. *AGARD Rep. 709*, 3-1 – 3-81.

Malik, M. R.& Beckwith, I. E. 1988 – Stability of a supersonic boundary layer along a swept leading edge. *AGARD CP-438*, 3-1 – 3-9.

Poll, D. I. A., Danks, M. & Yardley, M. R. 1996 – The effects of suction and blowing on stability and transition at a swept attachment line. See this volume.

Pruett, C. D., Zang, T. A., Chang, C.-L. & Carpenter, M., H. 1995 – Spatial Direct Numerical Simulation of high-speed boundary-layer flows. Part 1: Algorithmic considerations and validation. *Theor. Comp. Fluid Dyn.* **7**, 49-76.

Reed, H., L. & Saric, W. S. 1989 – Stability of three-dimensional boundary layers. *Ann. Rev. Fluid Mech.* **21**, 235-284.

Reshotko, E. & Beckwith, I. E. 1958 – Compressible laminar boundary layer over a yawed infinite cylinder with heat transfer and arbitrary Prandtl number. *NACA Rep. 1379.*

Spalart, P. R. 1988 – Direct numerical study of leading-edge contamination. *AGARD CP-438*, 5-1 – 5-13.

Stolte, A., Bertolotti, F. P., Hein, S., Simen, M. & Dallmann, U. 1995 – Nichtlokale und nichtlineare Instabilitäts- untersuchungen an kompressiblen Strömungen. *DLR IB 223-95 A54.*

Streett, C. L. & Macaraeg, M. G. 1989 – Spectral multi-domain for large-scale fluid dynamic simulations. *Appl. Num. Math.* **6**, 123-139.

Theofilis, V. & Poll, D. I. A. 1995 – Numerical and Experimental Investigation of Secondary Instability in Leading Edge Boundary Layer Flow. IUTAM *Laminar-Turbulent Transition Symposium* IV, Sendai, R. Kobayashi (ed.), Springer, pp. 429-435.

Theofilis, V. 1995 – Spatial stability of incompressible attachment-line flow. *Theor. Comput. Fluid Dyn.* **7**, 159-171.

Theofilis, V. 1996 – On the transition along the leading edge of swept wings: High Reynolds number secondary instability of leading edge boundary layer. *DLR IB 223-96 A 26.*

Wray, A. A. 1986 – Very low storage time-advancement schemes. *NASA Ames* Int. Rep.

Author's address

Deutsche Forschungsanstalt für Luft- und Raumfahrt e.V.
Bunsenstrasse 10
D-37073 Göttingen, Germany

Session 4:
Applied Transition Analysis

J.L. van Ingen

Some Introductory Remarks on Transition Prediction Methods Based on Linear Stability Theory

Abstract

Nearly 40 years ago the e^n method was introduced independently by A.M.O. Smith and the present author. Further developments have been made by many researchers, extending it to higher speeds, three-dimensional flows and including the effects of suction and heat transfer. Various papers at the present Colloquium will discuss these developments.

That the method is still being used is on the one hand due to the inherent difficulties of transition prediction from first principles. On the other hand, the e^n method contains enough physics to allow it to "predict" the distance to transition with only a simple experimental calibration. It was realized from the beginning that not enough physics was included to predict the process of transition itself.

The paper reviews the early developments of the method by the author and gives some comparisons with recent experimental verifications at the Low-Speed Aerodynamics Laboratory of the Faculty of Aerospace Engineering of Delft University of Technology.

The birth of the e^n method

In 1956 the e^n method for transition prediction in 2D incompressible flow, using linear stability theory, was introduced simultaneously and independently by Smith & Gamberoni (1956a) and the present author (Van Ingen, 1956a,b). From the end of the 19th century to about 1940 linear stability theory had been developed by a large number of mathematicians and theoretical aerodynamicists. Only through the famous experiments by Schubauer and Skramstadt (1948) it was shown that the theory was indeed applicable to real flows (the experiments were done in the period 1940-1945, but due to the war conditions the results became only widely known in 1948).

Although Pretsch (1941, 1942) had already done some amplification calculations, it was only in the fifties that it was realized that linear stability theory might be used to bridge the sometimes large distance between the point of first instability and real transition.

Liepmann (1945) had postulated that at transition the maximum eddy shear stress due to the laminar instability would be equal to the maximum laminar

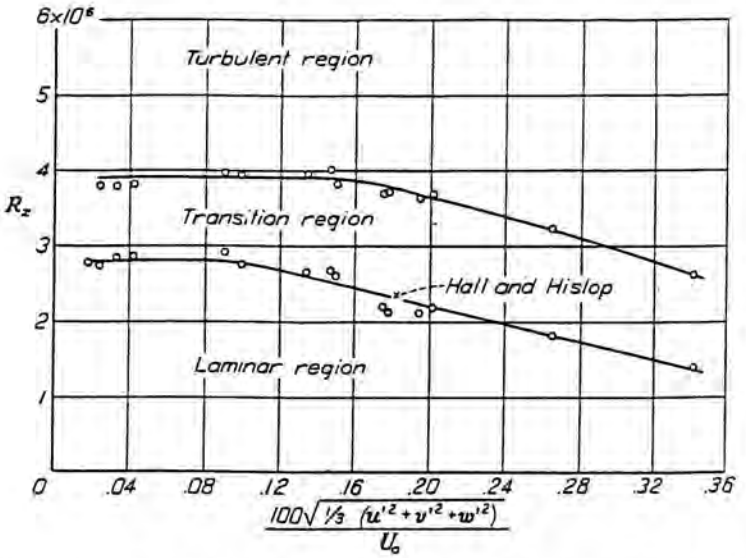

Figure 1: Transition Reynolds number for the flat plate according to Schubauer and Skramstadt (1948).

shear stress. This postulate was the starting point of the discussion by Smith and Gamberoni. Apparently Smith soon realized that it would be too ambitious to calculate the disturbance amplitude occurring in Liepmann's equation. Especially it was considered to be difficult - if not impossible - to specify the initial disturbances from which to start the amplification calculations. In fact up to the present time this remains a very difficult issue. How are disturbances generated inside the boundary layer? How are they related to outside disturbances like free stream turbulence, noise and vibration of the surface? At present this problem is denoted as "receptivity". Smith satisfied himself (and in fact had to be satisfied) with the calculation of the ratio between the amplitude of the most amplified disturbance according to linear theory at the experimental transition position and the original amplitude of this disturbance at its neutral position. From Smith's analysis it turned out that in many cases the same amplification ratio of about e^9 was found.

It is to be noted that under the many cases considered by Smith the Schubauer-Skramstadt flat plate experiment did not take a prominent place. The present author however started from this experiment (Fig. 1). At turbulence levels less than about 0.1% the transition region extends over a large distance, corresponding to Reynolds numbers Ux/ν from 2.8×10^6 to 3.9×10^6. In addition the present author considered some of his own transition experiments on an EC 1440 airfoil. Guided by the flat plate experiment this led to the conclusion that beginning and end of the transition region correspond to amplification ratios of $e^{7.8}$ and e^{10} respectively. On airfoils the transition region is in most cases only a few percent chord in length. Therefore it is not surprising that Smith, putting

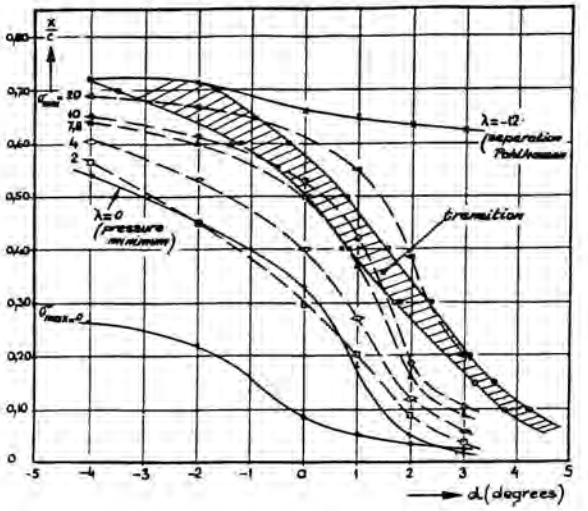

Figure 2: Calculated amplification factor and measured transition region for the EC 1440 airfoil section.

much emphasis on his results for airfoils, had concluded to a mean value of e^9. The exponent 9 was very close to the mean value indicated by van Ingen.

The present author, at that time not yet aware of Smith's results and not having access to as many transition experiments as Smith, had concluded that the prediction method looked promising but that more experiments would have to be evaluated. The reports by Smith and the present author were published only one month apart. A public paper on the method was given by Smith (1956b) in September 1956 at the 9th International Congress of Applied Mechanics at Brussels and by the present author (1956b) just one week later at the European Aeronautical Congress at Scheveningen.

It was at Scheveningen that Schlichting himself, having been present at both congresses, informed the present author about the presentation by Smith. Some of the results which the present author produced for the EC 1440 airfoil, making use of the Pretsch charts, are collected in Fig. 2. It should be noted that the factors 7.8 and 10 do not provide a very precise prediction of the transition region. This may have been caused by the fact that the laminar boundary layer was calculated by the Pohlhausen method which is known to be inaccurate near laminar separation. From Fig. 2 it follows that at the higher angles of attack transition occurs near or sometimes even downstream of laminar separation. Stability calculations were not available for separated flows (and hence Pretsch charts had to be extrapolated) and also the Pohlhausen method could not predict separated flows. It should also be realized that only later the possible existence of laminar separation bubbles was realized.

In 1956 both Smith and Van Ingen based their calculations on the temporal stability diagrams which had been calculated by Pretsch (1942) for some of the Falkner-Skan velocity profiles. Pretsch used an asymptotic method which

was only applicable at very high Reynolds numbers. Therefore he had been unable to calculate the (very low) critical Reynolds number for the Falkner-Skan separation profile. To the present author the Pretsch diagrams were only available on the small scale presented in Pretsch (1942). Smith apparently had already available some larger scale diagrams from Pretsch (1945). Both authors had to do some tedious cross plotting from these charts. It should be noted that Pretsch was already aware of the fact that there may be a large distance between the position of the first instability and the actual transition position and that the then customary idea that transition location would be somewhere between the positions of instability and laminar separation, was not sufficiently precise. He even suggested that amplification calculations might give some more insight.

Since the Pretsch charts had been calculated for the temporal mode, a propagation speed of the disturbances had to be selected to calculate the streamwise development. The present author used the phase velocity in his first version of the method. Although Smith had realized that the group velocity should be taken, he used for convenience also the phase velocity. It should be noted that only in the sixties the importance of the group velocity was emphasized by Lighthill (1965) and especially by Gaster (1962).

To emphasize that in 1956 the available numerical results of stability theory were not very consistent, Table 1 gives the critical Reynolds number based on displacement thickness for the Blasius profile as calculated by different authors. A number of neutral curves for the flat plate boundary layer is shown in Fig. 3.

$\left(\frac{U\delta^*}{\nu}\right)_{crit}$	author
321	Timman (1956)
420	Tollmien (1929)
420	Lin (1945, 1946)
575	Ulrich (1944)
645	Schlichting-Ulrich (1942)
680	Pretsch (1941, 1942)

Table 1: Critical Reynolds numbers for the flat plate as calculated by various authors before 1956.

Extension of the e^n method to suction (1965)

In his Ph.D. thesis, Van Ingen (1965) demonstrated that the e^9 method could also be used for the case of porous suction. An extensive series of wind tunnel measurements was done (using filtering paper as a porous surface). At that time larger scale stability diagrams were available to the present author (Pretsch, 1945). These charts had been reduced to a database containing about 100 numbers. In order to be able to analyse the suction experiments a two-parameter integral method for the calculation of the laminar boundary layer with suction was developed. Since in 1965 still only the Pretsch charts were available to the

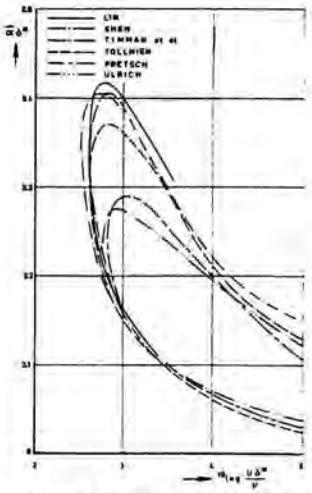

Figure 3: Neutral stability curves for the flat plate without suction from different sources.

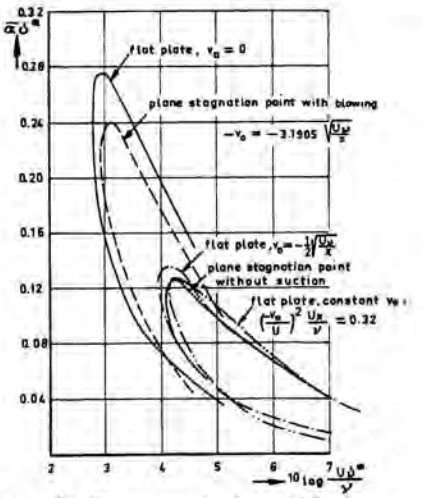

Figure 4: Some neutral stability curves for different boundary layers according to Ulrich.

present author, the database method mentioned above had to be made applicable to the suction case. This was done by assuming that:

- All possible stability diagrams form a one parameter family with the critical Reynolds number (based on momentum loss thickness) as the parameter;
- The critical Reynolds number for the velocity profiles used in the two-parameter method can be calculated from the approximate formula due to Lin (1955).

Fig. 4 gives a comparison of neutral curves for various flows with pressure gradient and/or suction or blowing. From such comparisons it was concluded in van Ingen (1965) that the above mentioned extension of the database method to the suction case, where the effect of suction is replaced by an equal effect of the pressure gradient on the critical Reynolds number, might be a workable proposition.

It should be emphasized that each time one of the components in the whole e^n method is changed (new boundary layer calculation method, new database for the stability diagrams, possibly improved stability diagrams, new experiments in the same or a different wind tunnel or flight tests) the whole method will have to be re-calibrated. In this way the present author had come up in 1965 with n factors of 9.2 and 11.2 for the beginning and end of the transition region for the same EC 1440 results as in Fig. 2 (see Fig. 5).

It cannot be overemphasized that the n factor is not a magic number. It is just a convenient way to correlate into one single number a series of factors which are known from experiment to influence transition. The success of the method is due to the fact that an appreciable fraction of the distance between the point of instability and transition is covered by linear theory.

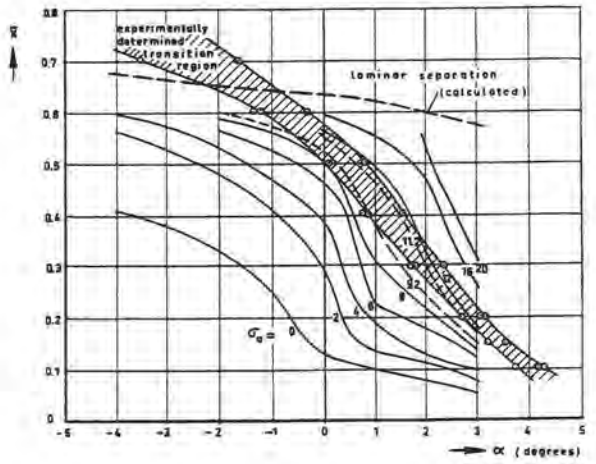

Figure 5: Calculated amplification factor and measured transition region for the EC 1440 airfoil section (Van Ingen, 1965).

Some results of the suction experiments and the stability calculations are shown in Fig. 6. It should be noted that also in the suction case separating laminar boundary layers were encountered for which neither the two-parameter integral method nor the Pretsch charts were applicable (some results have been obtained through extrapolation). In view of all the simplifications which had to be made, the conclusion at that time was that the e^n method could be applied with some confidence to the suction case.

Extension of the method to laminar separation bubbles

In 1966 the present author started to be involved in the design of airfoil sections for 2D incompressible flows. The foundation of this work was laid while spending a sabbatical year at the Lockheed Georgia Research Laboratory. The then available numerical methods for conformal transformation, laminar and turbulent boundary layer calculation and the e^n transition prediction method were used (Van Ingen, 1970). Later in Delft these design methods were continuously improved, based on comparisons between calculations and wind tunnel tests. A large number of airfoil designs were made (especially by Boermans *et al.* 1976, 1982, 1988, 1989, 1994) and applied in many different sailplanes. It was soon realized that at the chord Reynolds numbers applicable to sailplanes (and also wind turbines) the occurrence of laminar separation bubbles was very important and warranted extensive research.

The e^n method could be extended to separated flows because stability diagrams had been made available by Taghavi and Wazzan (1974) for the Stewartson reversed flow solutions of the Falkner-Skan equation. Moreover improved stability calculations for the Falkner-Skan velocity profiles had been published

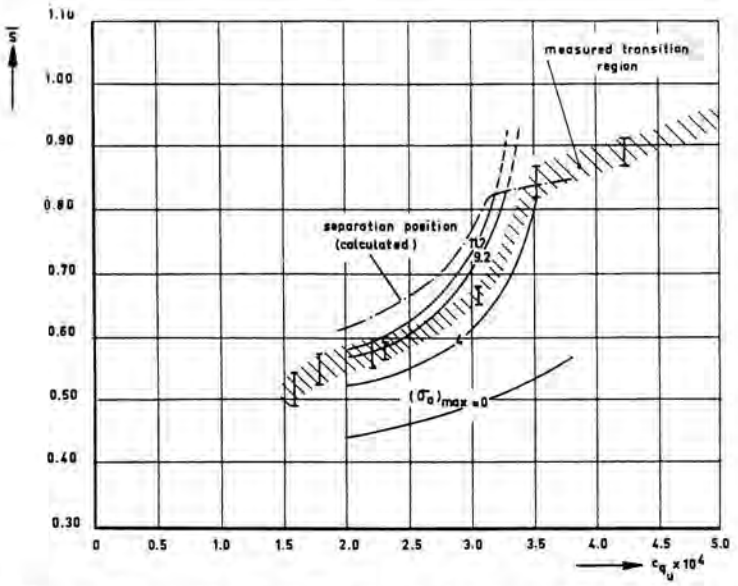

Figure 6: Measured transition region and calculated amplification factor for the upper surface of a suction airfoil.

by Wazzan, Okamura and Smith (1968) and by Kümmerer (1973). The present author had supplemented these results with solutions of the Rayleigh equation for the inviscid instability of the inflexional Falkner-Skan profiles for attached and reversed flow.

Using all the above mentioned results for the spatial mode, a new data base method was developed. The method is based on the observation that the stability diagrams show quite some similarity when as independent variable is used $^{10}\log(U\theta/\nu) - ^{10}\log(U\theta/\nu)_{crit}$ and the amplification rates are scaled with the maximum value for each diagram. The database consists of a table of about only 300 numbers. Fig. 7 gives an application of the e^n method to laminar separated flow on a Wortmann airfoil.

The influence of free stream turbulence on the n factor

At the time the above mentioned database was developed, it had been realized already for quite some time that a constant n factor could no longer be used. That for so long a constant n factor (with the value 9) had been useful, may have been due to the fact that most modern low speed, low turbulence wind tunnels had been built according to the same recipe, aiming at a turbulence level of just below 0.1% as had been suggested to be sufficiently low according to the Schubauer and Skramstad experiment. (Fig. 1). From this experiment it had been concluded that reducing the turbulence level Tu below 0.1% had no use because "transition would not be influenced by a reduction of Tu below

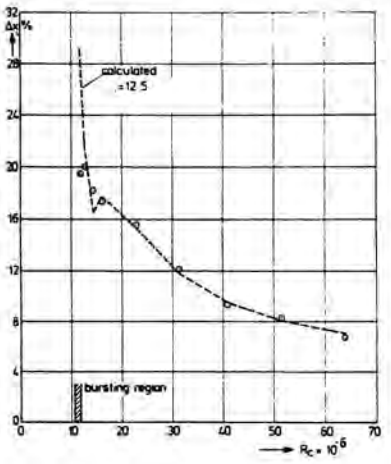

Figure 7: Distance between separation and transition on Wortmann airfoil in a small "noisy" wind tunnel.

0.1%". Since a further reduction of Tu requires a larger contraction ratio or more screens (and hence more money) most modern low speed wind tunnel designs have aimed at $Tu = 0.1\%$. The n factor needed to predict flat plate transition as a function of turbulence level Tu follows from an evaluation of various transition experiments on flat plates at various turbulence levels and from the calculation of the n factor as a function of Ux/ν (Fig. 8).

It was shown by Wells (1967) and by Spangler and Wells (1968) that transition Reynolds numbers larger than the Schubauer and Skramstadt values could be obtained by further reducing the turbulence level and the acoustic disturbances (apparently the acoustic disturbances rather than turbulence have caused transition in the Schubauer and Skramstadt experiments for $Tu < 0.1\%$). From Fig. 8. the present author concluded that beginning and end of transition could be predicted by n factors n_1 and n_2 respectively according to

$$n_1 = 2.13 - 6.18^{10}\log Tu$$

$$n_2 = 5 - 6.18^{10}\log Tu$$

(where Tu is the turbulence level in %). Mack (1975) has given independently a similar formula for n_1.

It should be clear that the free-stream turbulence level alone is not sufficient to describe the disturbance environment. Information about the distribution across the frequency spectrum should also be available and in addition to turbulence the acoustic disturbances are important. Of course the most important issue is "receptivity": how are the initial disturbances within the boundary layer related to the outside disturbances. Therefore we can only use Fig. 8 and the equations for n_1 and n_2 to specify the n factor if an "effective Tu" is known. This effective turbulence level can only be defined through a comparison of measured

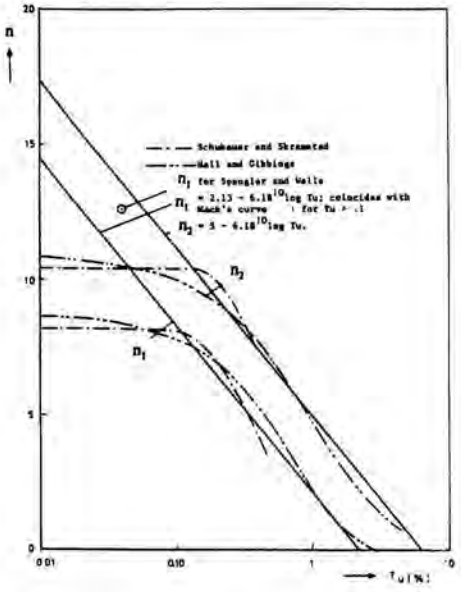

Figure 8: Relation between n_1, n_2 and Tu for the flat plate.

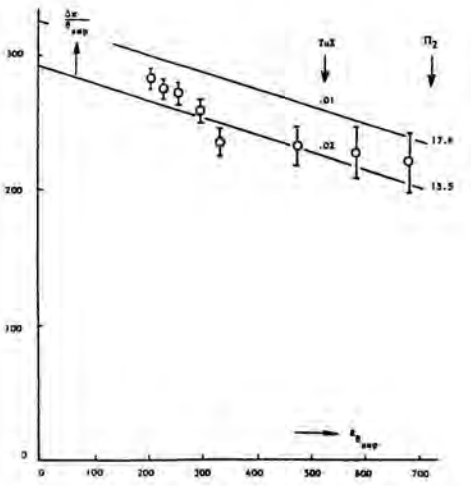

Figure 9: Length of the laminar part of the bubble on a Wortmann airfoil; bars indicate errors in Δx of + or −0.5% chord.

transition position with calculated amplification ratios. In fact it has become customary to define the quality of a wind tunnel by stating its "critical n factor".

Through a combination of the e^n method with calculation methods for separated flows it has become possible to develop a suitable prediction method for laminar separation bubbles (van Ingen, 1975). Some examples, are given in Figs 9 and 10. Brief explanations are given in the captions to the figures. In a simplified version of the method, the length of the laminar part of the bubble is correlated with the effective turbulence level (and hence with the n factor).

At one time the author tried to do some additional calibrations of the e^n method for separation bubbles by trying to shorten the bubble by means of additional turbulence due to grids. Not much happened due to the fact that apparently turbulence was added by the grid in the wrong frequency band.

Some applications of the Delft e^n method to airfoil designs

It should be realized by now that the e^n method does not automatically lead to useful results. The airfoil designer should be aware of its shortcomings and should make a judicious choice of the n factors to be used. In general we use at Delft the following n factors and "effective turbulence level" for various circumstances.

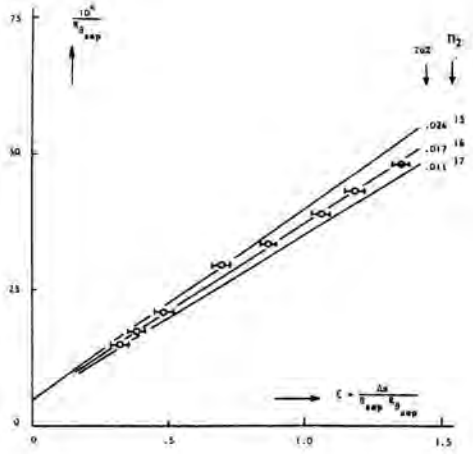

Figure 10: The same results as in Fig. 9, but plotted in an improved way.

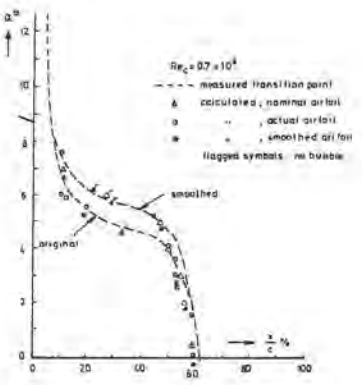

Figure 11: Position of transition on the upper surface of the M-300 airfoil (Boermans & Blom, 1976) according to viscous flow calculations and the stethoscope measurements.

environment	Tu %	n_1
NACA LTT	0.10	9.75
Delft Low Turbulence Tunnel	0.06	11.2
Free Flight of Gliders	0.014	15.0

In the author's group L.M.M. Boermans is the designer using the various calculation methods described above. He also has performed rather extensive wind tunnel measurements and has evaluated many flight tests. A number of examples can be found in the references to his work. As an example, Fig. 11, taken from Boermans & Blom (1976), shows results of computations with the e^n method for wavy and smooth versions of the same nominal airfoil. It follows that the e^n method is capable of predicting the shift in transition position due to waves in the surface. Fig. 12 gives the n factor for the beginning of transition on the airfoil DU89-122 tested in the low turbulence tunnel at Delft, using the infrared imaging technique (Boermans, private communication).

A possible explanation for the success of the e^n method for 2D incompressible flow at low Tu

In the past decades the e^n method has established itself as a useful method to predict the distance to transition in 2D incompressible flow. Apparently the linear stability theory has enough physics in it to account for the effects of

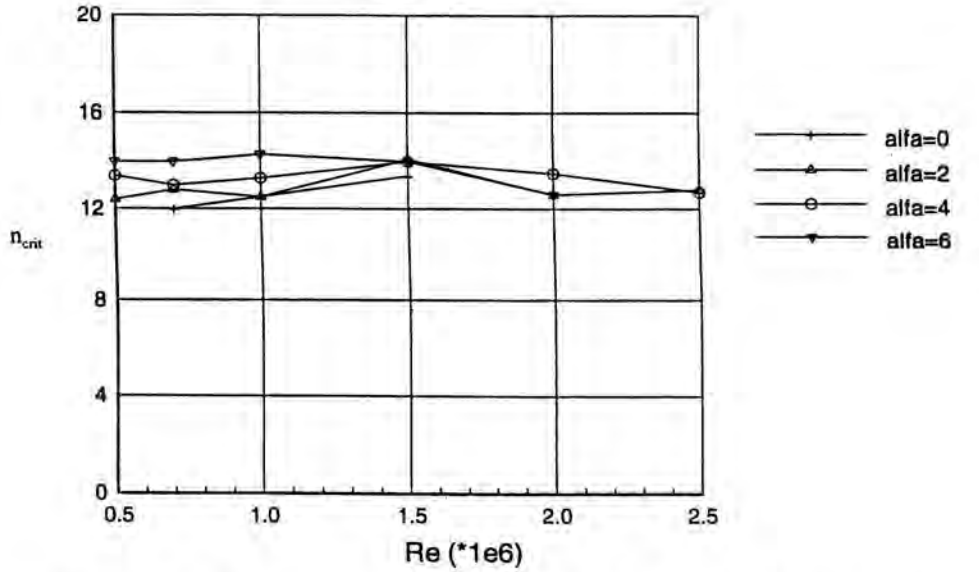

Figure 12: Critical n factors for the DU89-122 airfoil as a function of Reynolds number and angle of attack.

pressure gradient, suction, heating and cooling, etc. on transition. Hence it may be expected that under these circumstances the linear part of the amplification process covers a large percentage of the distance between first instability and transition. Obremski (1969) gives some background to this idea by quoting the following characteristic numbers.

In low speed, low turbulence wind tunnels (such as at Delft) the overall turbulence level at low speed is certainly less than 0.1%, even as low as 0.02%. Since only part of the spectrum contains the dangerous Tollmien-Schlichting frequencies, the amplitude of the neutral disturbances, being present inside the boundary layer and which somehow (through "receptivity") may be related to the external turbulence level, may be of the order of 0.001%. Linear theory is found to give a good description of the amplification process up till an amplitude of 1 to 1.5%. When transition is completed disturbance levels of the order of 10 to 20% are found. Hence the linear part extends to an n factor of 7. The nonlinear part only has to cover the range of n values between 7 and 10. Hence one should not be surprised about the relative success of the e^n method. A calibration by comparison with experiment should be adequate to "predict" the distance to transition. Of course the physical process of real transition is not described by linear theory.

An experimental illustration can be found in the work of Wubben *et al.* (1989). Transition experiments were done in a small boundary layer channel with a pressure distribution meant to represent a constant Hartree β-flow of -0.14 (Fig. 13). This tunnel has a rather large disturbance environment due to

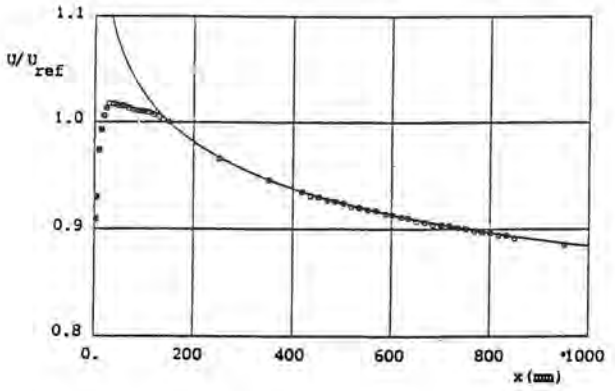

Figure 13: Experimental (⊙) and theoretical (-) velocity distribution, Hartree $\beta = -0.14$ ($U_{ref} = 10.96\ m/s$) (Wubben *et al.*, 1989).

turbulence, vibrations, blade passing frequency of the blower, etc. Therefore it is not easy to verify experimentally the initial amplification. Fig. 14 gives some velocity fluctuation spectra as measured with hot wires. To eliminate most of the noise and to determine the relative amplification the spectra at different x-values were compared to that at $x = 330$ mm by subtracting the latter from the others. Included in the figure is the amplification spectrum as calculated from our database method, also points calculated by the NLR version of the COSAL code are indicated.

Considering the various causes for inaccuracies it is seen that the linear calculations give a reasonable description of the amplification until $x = 616$ mm. Transition sets in at about $x = 790$ mm (to be concluded from the broadening of the spectrum). The relative n factor between $x = 330$ mm and $x = 518$ mm is equal to 4. As the calculated n factor at $x = 330$ mm equals 5, the results are comparable with the values mentioned by Obremski. A comparison between n factors obtained in flight and in the DNW low speed wind tunnel is given in Fig. 15 (Horstmann *et al.*, 1990).

Concluding remarks

In the present paper some of the history of the e^n method for 2D incompressible flow has been highlighted. A discussion of further developments by other researchers would have been appropriate but proved to be impossible due to lack of space. Other papers in this volume may be consulted to learn about extensions to 3D flows and higher speeds. Not in all cases the extension is straightforward. An important issue is to define the proper "integration strategy" for 3D flows. Also an extensive discussion of simpler methods which also have some relation to the e^n method such as Michel's (1953) and Granville's (1953) methods would have been relevant. The Granville method uses a correlation between the difference between $U\theta/\nu$ at transition and at the instability point and the mean

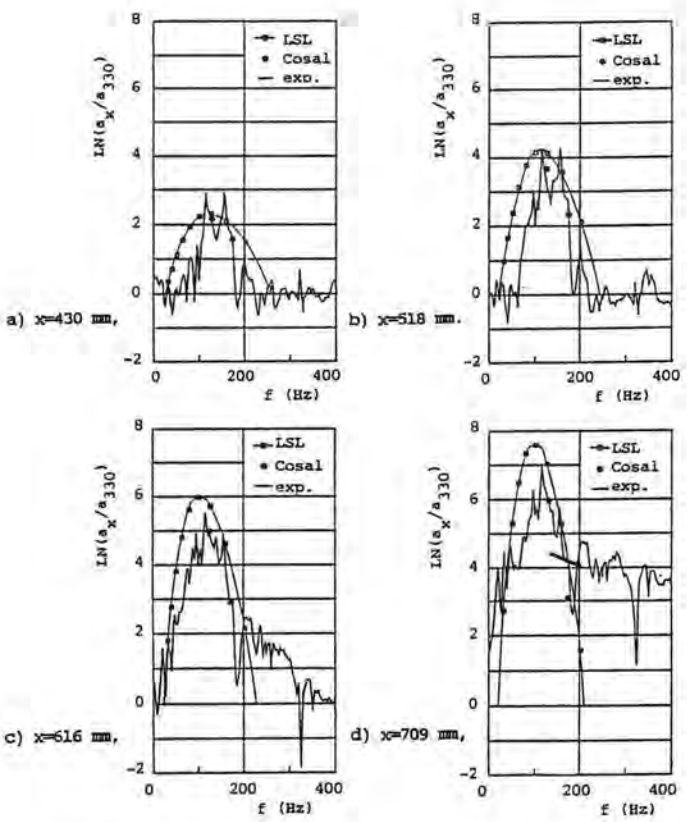

Figure 14: Amplification spectra. Amplification is with respect to the spectrum, measured at $x = 330$ mm; here a calculated 'n-factor' of 5 is found. Hence, figure 14b shows an n-factor of about 9.

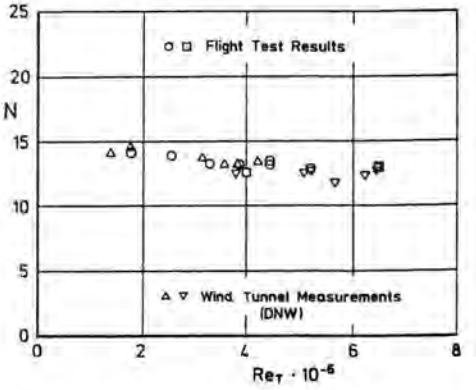

Figure 15: Calculated n-factors at transition based on flight and wind tunnel test (o Δ: 0 deg. flap; □ ∇: 3.5 deg. flap) (Horstmann *et al.*, 1990).

value of the pressure gradient parameter $K = \frac{\theta^2}{\nu}\frac{dU}{dx}$. Michel uses a correlation between $\frac{Ux}{\nu}$ and $\frac{U\theta}{\nu}$ at transition. It was shown by Smith that Michel's curve corresponds to the e^9 criterion for the similar Falkner-Skan boundary layers. The reader is referred to an extensive discussion of all these problems by Arnal (1993).

References

Arnal, D. 1993 – Boundary layer transition predictions based on linear theory. In: AGARD Rept. 793, Special course on progress in transition modelling.

Boermans, L.M.M. & Blom, J.J.H. 1976 – Low speed aerodynamic characteristics of an 18% thick airfoil section designed for the all-flying tailplane of the M-300 sailplane. Rept. LR-226, Delft University of Technology, Dept. Aerospace Eng.

Boermans, L.M.M., Donker Duyvis, F.J., Ingen, J.L. van, & Timmer, W.A. 1989 – Experimental aerodynamic characteristics of the airfoils LA5055 and DU 86-084/18 at low Reynolds numbers.In T.J. Mueller (ed.) Low Reynolds number aerodynamics, Proc. Conf. Notre Dame, 5-7 June 1989, pp. 115-130.

Boermans, L.M.M. & Garrel, A. van, 1994 – Design and windtunnel test results of a flapped laminar flow airfoil for high-performance sailplane applications. ICAS-94-5.4.3.

Boermans, L.M.M. & Selen, H.J.W. 1982 – Design and tests of airfoils for sailplanes with an application to the ASW-19B. ICAS-Paper 82-5.5.2.

Boermans, L.M.M. & Waibel, G. 1988 – Aerodynamic and structural design of the Standard Class sailplane ASW-24. ICAS-paper 88-2.7.2.

Gaster, M. 1962 – A note on the relation between temporally increasing and spatially increasing disturbances in hydrodynamic stability. *J. Fluid Mech.* **14**, 222-224.

Granville, P.S. 1953 – The calculation of viscous drag of bodies of revolution. David Taylor Model Basin, Rept 849.

Horstmann, K.H., Quast, A. & Redeker, G. 1990 – Flight and Wind-tunnel investigations on boundary layer transition. *J. Aircraft* **27**, 146-150.

Ingen, J.L. van, 1956a – A suggested semi-empirical method for the calculation of the boundary layer transition region. Rept. VTH74, Dept. Aeron. Eng., Delft (extended version in Dutch in Rept. VTH-71).

Ingen, J.L. van, 1956b – A suggested semi-empirical method for the calculation of the boundary layer transition region. Proc. Second European Aeronautical Congress, Scheveningen, pp. 37.1 - 37.16.

Ingen, J.L. van, 1965 – Theoretical and experimental investigation of incompressible laminar boundary layers with and without suction. Rept. VTH-124, Delft University of Technology, Dept. of Aerospace Engineering.

Ingen, J.L. van, 1970 – Advanced computer technology in aerodynamics: a program for airfoil section design utilizing computer graphics. AGARD Lecture Series 37. High Reynolds-number subsonic aerodynamics, pp. 8.1–8.33.

Ingen, J.L. van, 1975 – On the calculation of laminar separation bubbles in two-dimensional incompressible flow. AGARD DP-168 Flow Separation, Göttingen.

Kümmerer, H. 1973 – Numerische Untersuchungen zur Stabilität ebener laminarer Grenzschichtströmungen. Ph.D. Thesis, Univ. Stuttgart.

Liepmann, H.W. 1945 – Investigation of boundary layer transition on concave walls. NACA Wartime Rept. ACR-4J28.

Lighthill, M.J. 1965 – Group velocity. *J. Inst. Math. Applic.* **1**, 1-28.

Lin, C.C. 1945, 1946 – On the stability of two-dimensional parallel flows. *Quart. Appl. Math.* **3**, July 1945, pp. 117-142, Oct. 1945, pp. 218-234, Jan. 1946, pp. 277-301.

Lin, C.C. 1955 – The theory of hydrodynamic stability, Cambridge University Press.

Mack, L.M. 1975 – A numerical method for the prediction of high-speed boundary-layer transition using linear theory. Paper no. 4 in Aerodynamic analysis requiring advanced computers. NASA SP-347.

Michel, R. 1952 - Détermination du point de transition et calcul de la trainée des profils d'ailes en incompressible. ONERA rept. no. 58.

Obremski, H.J., Morkovin, M.V. & Landahl, M. 1969 – A portfolio of stability characteristics of incompressible boundary layers. AGARD, Agardograph 134.

Pretsch, J. 1941 – Die Stabilität einer ebenen Laminarströmung bei Druckgefälle und Druckanstieg. *Jahrbuch der Deutschen Luftfahrtforschung* **1**, 158-175.

Pretsch, J. 1942 – Die Anfachung instabiler Störungen in einer laminarer Reibungsschicht. *Jahrbuch der Deutschen Luftfahrtforschung*, 154-171.

Pretsch, J. 1945 – Berechnung der Stabilitätsgrenze von Grenzschichtprofilen und der Anfachung von Störungen. Göttingen Monograph, part. B.3.2.

Schlichting, H. & Ulrich, A. 1942 – Zur Berechnung des Umschlages laminar-turbulent. *Jahrbuch Deutschen Luftfahrtforschung* I, 8.

Schubauer, G.B. & Skramstadt, H.K. 1948 – Laminar boundary layer oscillations and transition on a flat plate. Report NACA 909.

Smith, A.M.O. & Gamberoni, N. 1956a – Transition, pressure gradient and stability theory, Report ES 26388, Douglas Aircraft Co.

Smith, A.M.O. 1956b – Transition, pressure gradient and stability theory. Proc. 9th Int. Congress Appl. Mech., Brussels **4**, 234-244.

Spangler, J.G. & Wells, C.S. 1968 – Effects of free stream disturbances on boundary layer transition. *AIAA J.* **6**, 543-545.

Taghavi, H. & Wazzan, A.R. 1974 – Spatial stability for some Falkner-Skan profiles with reversed flow. *Physics of Fluids* **17**, 2181-2183.

Timman, R., Zaat, J.A., & Burgerhout, Th.J. 1956 – Stability diagrams for laminar boundary layer flow. NLL Rept. F193.

Tollmien, W. 1929 – Über die Enstehung der Turbulenz 1. Mitteilung Nachr. Ges. Wiss. Göttingen, Math. Phys. Klasse 21-44 (also NACA TM 609, 1931).

Ulrich, A. 1944 – Theoretische Untersuchungen Über die Wider standsersparnis durch Laminar-haltung mit Absangung. Schr. Dtsch. Akad. Luftfahrt, 8B, no. 2 (also NACA TM 1121).

Wazzan, A.R., Okamura, T.T. & Smith, A.M.O. 1968 – Spatial and temporal stability charts for the Falkner-Skan boundary layer profiles. Rept. DAC-67086, McDonnell Douglas.

Wells. C.S., 1967 – Effects of free-stream disturbances on boundary layer transition. *AIAA J.* **5**, 172-174.

Wubben, F.J.M., Passchier, D.M. & Ingen, J.L. van 1989 – Experimental investigation of Tollmien Schlichting instability and transition in similar boundary layer flow in an adverse pressure gradient, In: Laminar-Turbulent transition, D. Arnal & R. Michel (eds), IUTAM Symposium, Toulouse, Springer, pp. 31-42.

Author's address

Faculty of Aerospace Engineering
Delft University of Technology
Kluyverweg 1, 2629 HS Delft, The Netherlands.

H.W. Stock ° & W. Haase ▷

Some Aspects of Linear Stability Calculations in Industrial Applications

Abstract

In the design of laminar airfoils, using coupled inviscid-viscous methods, the transition prediction by the e^n method represents a large computational and moreover user's effort.

In order to reduce these efforts, a data base method is developed. Hence, the iterative calculation of the inviscid and viscous flow together with the transition prediction is feasible at highly reduced costs.

For the production of the data base, artificial boundary layers are generated, which show self-similar velocity and temperature profiles. The amplification rates are computed via the linear stability theory, using the envelope approach. It will be shown, that for real boundary layer flows the comparison between the N-factors computed by the stability theory and the data base method is excellent. The flows include compressibility, suction and heat transfer effects.

Using Navier-Stokes methods for the design of laminar airfoils, transition prediction can also be done by the e^n method. The requirements will be described concerning the mesh generation and mesh adaption, to obtain meaningful results from Navier-Stokes and stability calculations. The quality of the Navier-Stokes results is validated by comparison to a boundary layer method using as input the pressure distribution obtained from the Navier-Stokes result. Finally, it will be demonstrated, that the coupling of the Navier-Stokes method with the data base method is feasible.

Introduction

One of the most challenging demands in aerodynamics of laminar airfoils and wings is the reliable computation of boundary layer transition. The range of existing transition prediction methods extends from simple empirical relationships via stability theories of different levels (parallel flow and linear; linear or nonlinear PSE-methods) to direct numerical simulations. The e^n method, based on linear stability theory and the parallel flow assumption, is used in aircraft industry for the design of laminar wings most frequently.

However, the application of the e^n method is time and cost consuming, regarding the computational and moreover the user's efforts. There is clearly a need for a rapid and inexpensive data base method for transition prediction, which can be used routinely. Such a method allows to run coupled methods for

the prediction of the flow around airfoils in an extended version by computing iteratively the inviscid and viscous flow together with the transition prediction.

Moreover, there exists also the possibility, to perform Navier-Stokes calculations in combination with the data base method in an iterative manner.

Description of the data base method

Arnal (1988) developed independently a data base method, using a different approach. In the actual case laminar velocity and temperature profiles are generated, using the similar solutions of the laminar boundary layer. For 13 shape parameters H_i, which cover the range from highly accelerated up to separating flows, artificial boundary layers are generated, which show identical velocity and temperature profiles. The growth of the boundary layer is simulated by varying the Reynolds number, based on the incompressible displacement thickness

$$Re_{\delta_i^*} = \frac{U_e \delta_i^*}{\nu_e} \ . \tag{1}$$

For each artificial boundary layer, stability computations are completed for a sufficient large range of excited frequencies. The results for the amplification rates α_i are stored in the data base, where

$$\alpha_i = \alpha_i[H_i,\ Re_{\delta_i^*},\ F] \ , \tag{2}$$

with F being the reduced frequency

$$F = 2\pi f \frac{\nu_e}{U_e^2} \ . \tag{3}$$

The stability computation for real boundary layers, using the data base method, is executed for a given frequency f in Hz in the following way: At each station the properties f, $Re_{\delta_i^*}$, H_i, U_e and ν_e are known. Evaluating F from eq. (3), α_i is obtained from eq. (2) via interpolation in the data base.

Data base method for incompressible flows (Stock & Degenhart, 1989)

The similarity solutions are produced, using the approach of Falkner & Skan (1930). The Sally code (Skrokowski *et al.*, 1979) is applied, using for that method the perturbation propagation direction Ψ=0, which is identical to the use of the envelope method at $M_e = 0$, except for large values of $Re_{\delta_i^*}$.

Data base method for incompressible flows with suction (Stock, 1990)

It is shown, that laminar boundary layer flows with pressure gradient and suction are almost identical to flows for a corresponding pressure gradient without

suction. Hence, the data base method can be applied to boundary layers with suction directly.

Data base method for compressible, adiabatic flows (Stock, unpublished)

The near-similarity solutions are produced using the approach of Horton (1994). The stability code of Schrauf (1988, 1993) is applied, using the envelope method. The calculations are done for 4 Mach number levels $M_e = 0,\ 0.5,\ 0.9$ and 1.4, such that the amplification rate α_i is expressed by

$$\alpha_i = \alpha_i[M_e,\ H_i,\ Re_{\delta_i^*},\ F] \ . \tag{4}$$

Data base method for compressible, adiabatic flows with suction (Stock, unpublished)

It is shown, that also compressible laminar boundary layer flows with pressure gradient and suction are almost identical to flows for a corresponding pressure gradient without suction. Consequently, the data base method can be applied to compressible boundary layers with suction directly.

Data base method for compressible flows with heat transfer (Stock, unpublished)

The near-similarity solutions including compressibility and heat transfer are produced, using the approach of Horton & Stock (unpublished), which is an extension of Horton (1994). The stability code of Schrauf (1988, 1993) is applied, using the envelope method. The calculations are done, in supplement to the 4 Mach number levels, for 5 different heat transfer parameter values $S_w = -0.2, -0.1, 0.0, 0.1$ and 0.2, where S_w is defined by

$$S_w = 1 - \frac{H_t}{H_{te}} \ , \tag{5}$$

with H_t being the total enthalpy. The amplification rate α_i is expressed by

$$\alpha_i = \alpha_i[S_w,\ M_e,\ H_i,\ Re_{\delta_i^*},\ F] \ . \tag{6}$$

Description of the Navier-Stokes Method (Haase, 1992)

The Navier-Stokes equations, describing two-dimensional, unsteady, compressible flows in conservation form, are solved by means of a finite volume approach using a Runge-Kutta time-stepping method with multigrid acceleration.

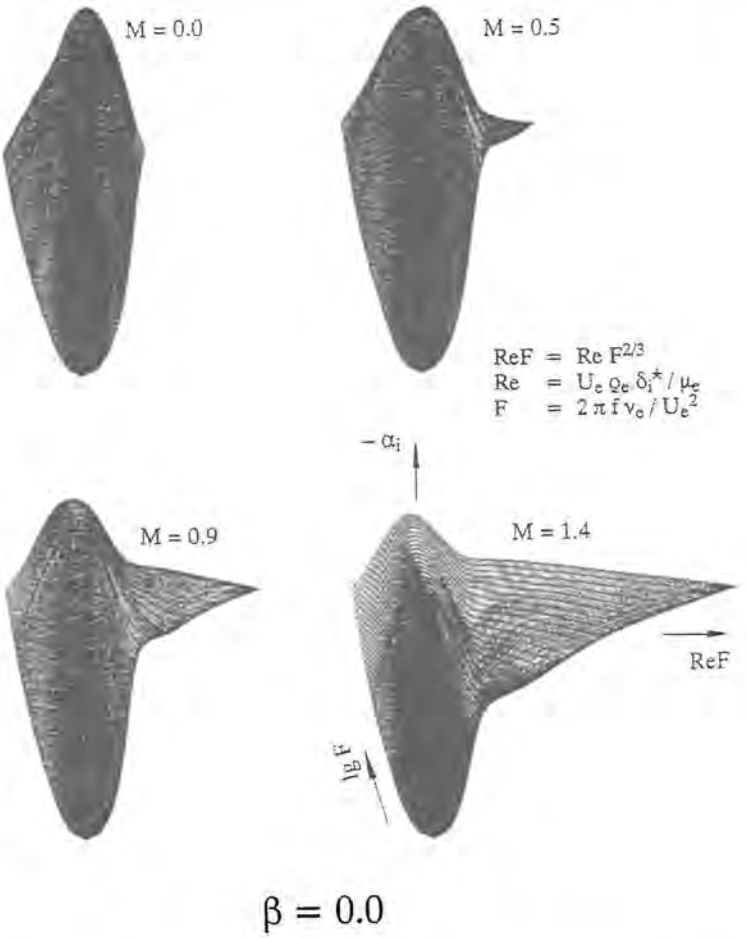

Figure 1: Spatial representation of the amplification rate α_i for flat plate flow and different Mach numbers M.

The Johnson-King turbulence model (1985) in its original form is used. For the turbulent length scale in the equilibrium outer layer eddy viscosity the formulation of Stock & Haase (1989) is applied.

The viscous length scales in the laminar and turbulent regime are determined by the diagnostic function

$$F = y^{\alpha}[\frac{dU}{dy}] \,, \tag{7}$$

the maximum of which gives the wall distance y_{max}, where $F = F_{max}$. The viscous layer thickness is evaluated from

$$\delta = \beta y_{max} \,. \tag{8}$$

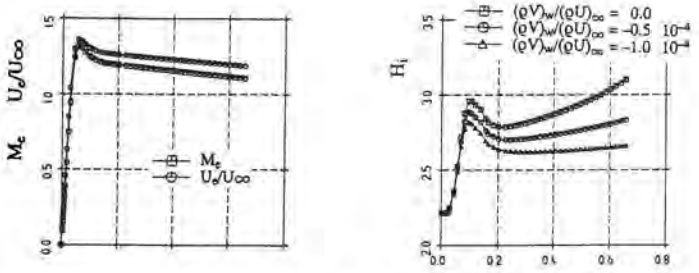

Figure 2: Boundary layer results for a linearly decelerated flow and and different suction rates $M = 0.9$ and $Re = 9.4 \times 10^6$.

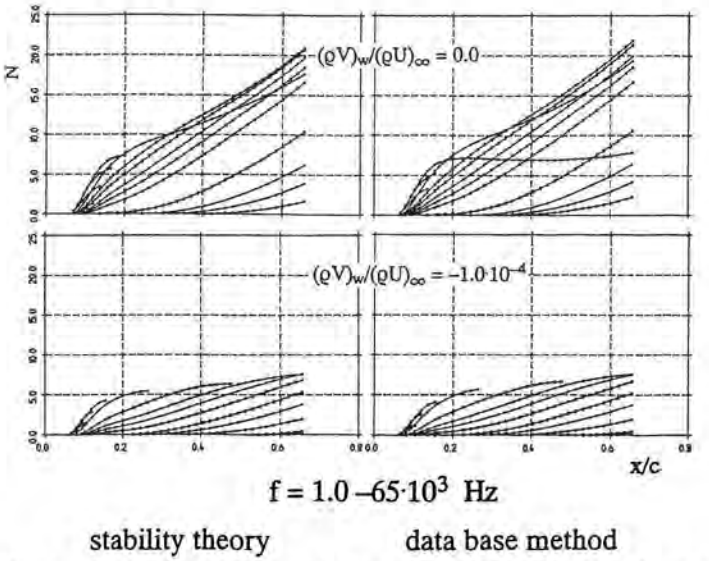

Figure 3: N-factor computed by the stability theory and the data base method using the envelope approach.

In the laminar regime the values are α=3.9 and β=1.423, Stock & Haase (unpublished) and in the turbulent regime α=1.0 and β=1.936, Stock & Haase (1989). In the transitional region the viscous layer thickness is given by

$$\delta = [1 - \gamma]\delta_{lam} + \gamma\delta_{turb} \ , \tag{9}$$

where γ is the intermittency function, given by Dhawan & Narashima (1958)

The extent of the transition region is expressed by the formulation of Chen & Thyson (1971), being based on the source density distribution of Emmons (1951).

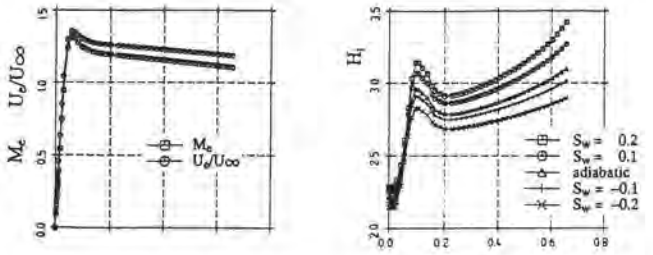

Figure 4: Boundary layer results for a linearly flow and different heating rates, $M = 0.9$ and $Re = 9.4 \times 10^6$.

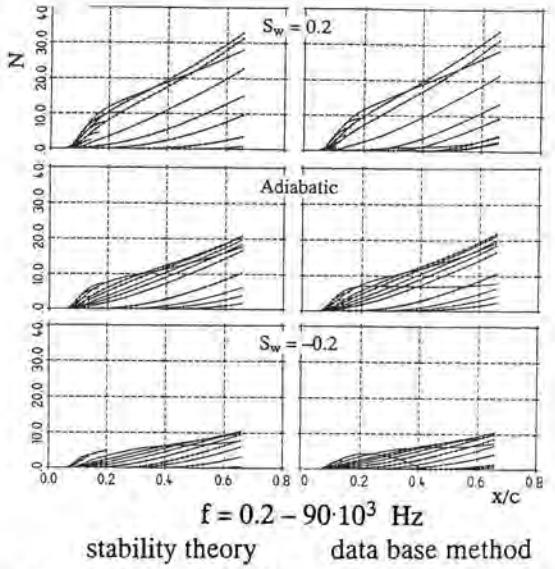

Figure 5: N-factor computed by the stability theory and the data base method using the envelope approach.

Results of the data base method

Compressible, adiabatic flows with suction

For the flat plate flow, Fig. 1 gives a spatial representation of the results for the data base, where F is the reduced frequency. For a strongly decelerated flow, the boundary layer is calculated for different suction rates, where the suction is applied from $x/c = 0$ on, see Fig. 2. The boundary layer calculations are performed using the method of Horton & Stock (1995). The corresponding N-factors are shown in Fig. 3. For the stability theory data the method of Schrauf (1988, 1993) is applied.

Compressible flows with heat transfer

For the flow conditions of Fig. 2, the boundary layer is calculated for different heating and cooling rates, where the heat transfer is applied from $x/c = 0$ on, see Fig. 4. The comparison of the N-factors, obtained from the stability theory and the data base method is seen to be excellent, see Fig. 5

Results of the Navier-Stokes method

The Doal3-airfoil is designed at Dornier and tested under free transition conditions in the transonic facility of the DLR-Braunschweig (Lück, 1987).

The meaningful application of the Navier-Stokes and the stability method requires a solution-dependent mesh, besides an adequate number of mesh points (512 x 128). The adapted mesh is arranged such, that a nearly constant number of mesh points (60-70 mesh points) is embedded in the viscous layer including the wake. The Navier-Stokes calculations are initially started by fixing the transition at the place of laminar separation. This choice seems plausible as the combination of the Navier-Stokes method with the stability theory is easiest, if during the iterations the transition location moves continuously upstream. All further results, except those in the last part of the paper, are produced with transition fixed at laminar separation.

Polar

The lift and drag coefficient as a function of the angle of attack α is depicted in Fig. 6. The computational results for the initial and adapted mesh are almost identical. The maximum lift and the minimum drag are well predicted. The overprediction of the extent of the laminar bucket is caused by fixing the transition at laminar separation. The discrepancy of the value of $dC_L/d\alpha$ is not well understood. Possible reasons are the absence of wind tunnel corrections and, may be, the presence of slotted walls in that Mach number range. All further computational efforts are concentrated on the upper surface of the airfoil and the flow condition at α=1.5°. This value of α is just outside the measured laminar bucket and well inside the computed one. The lower surface boundary layer flow is stable up to separation.

Mesh generation

For the initial and the adapted mesh inside the viscous layer (laminar, transitional and turbulent) 60-70 points are embedded. In order to render the mesh differences more understandable, the mesh lines y/c [i,j=const] are given in the upper part of Fig. 7. As seen the laminar separation and thereby the transition occurs at $x/c \approx 0.6$. The line y/c [i,j=65] is almost identical to the computed viscous layer thickness δ/c for the adapted mesh. The lower part of Fig. 7 clarifies

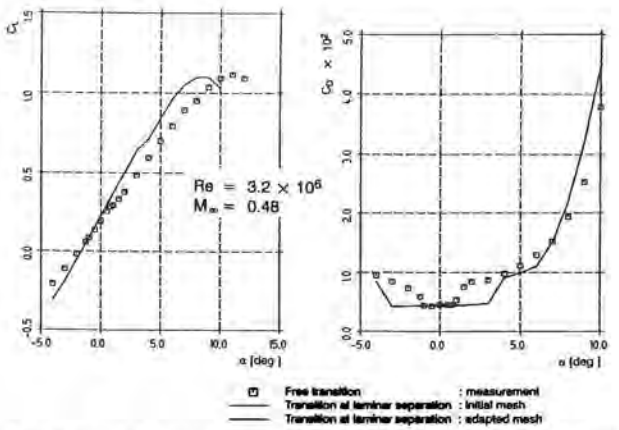

Figure 6: Lift and drag coefficient for the DOAL3 laminar airfoil as a function of the angle of attack.

the structure of the adapted mesh inside the viscous layer. The lines y [i,j=const] are non-dimensionalized by the value of the line y [i,j=70]. In the laminar regime a mild geometric stretching is performed, to come close to an equidistant mesh. In the turbulent layer region a larger stretching is used. Furthermore, the size of the first volume adjacent to the surface is evaluated solution-dependent, such that a value of $y^+ \approx 1$ is achieved. In the transitional region a meaningful junction between the laminar and turbulent structure is adopted.

Comparison of Navier-Stokes and boundary layer results

The pressure distributions for the initial and the adapted mesh are almost identical, except in the transition/separation region. This result supports the identity of the lift and drag coefficient in both meshes, see Fig. 6.

To quantify the Navier-Stokes results in the viscous layer region boundary layer results are obtained for comparison. The pressure distribution of the Navier-Stokes solution is used as input to the boundary layer method (Horton & Stock, 1995). The Navier-Stokes and the boundary layer data are presented for the initial mesh in the upper part of Fig. 8. As seen, the values of the shape parameter H_i are very different. The incompressible analysis of the Navier-Stokes and the boundary layer data for the initial mesh via the envelope approach of the stability method of Schrauf (1998, 1993) delivers the expected result, that the Navier-Stokes viscous layer is clearly more stable. The maximum value of N is 2.5 instead of 7.0.

The viscous layer data for the adapted mesh are given in the lower part of Fig. 8. The viscous layer results are in a good agreement and consequently the stability data, see Fig. 9. In the lower part of Fig. 9 results of the data base method are given too. In the damping region (decaying N-factor) the results deviate from those of the stability theory. The reason is, that only amplified data are computed for the data base, in regions of damping the stability data are evaluated simply by extrapolation.

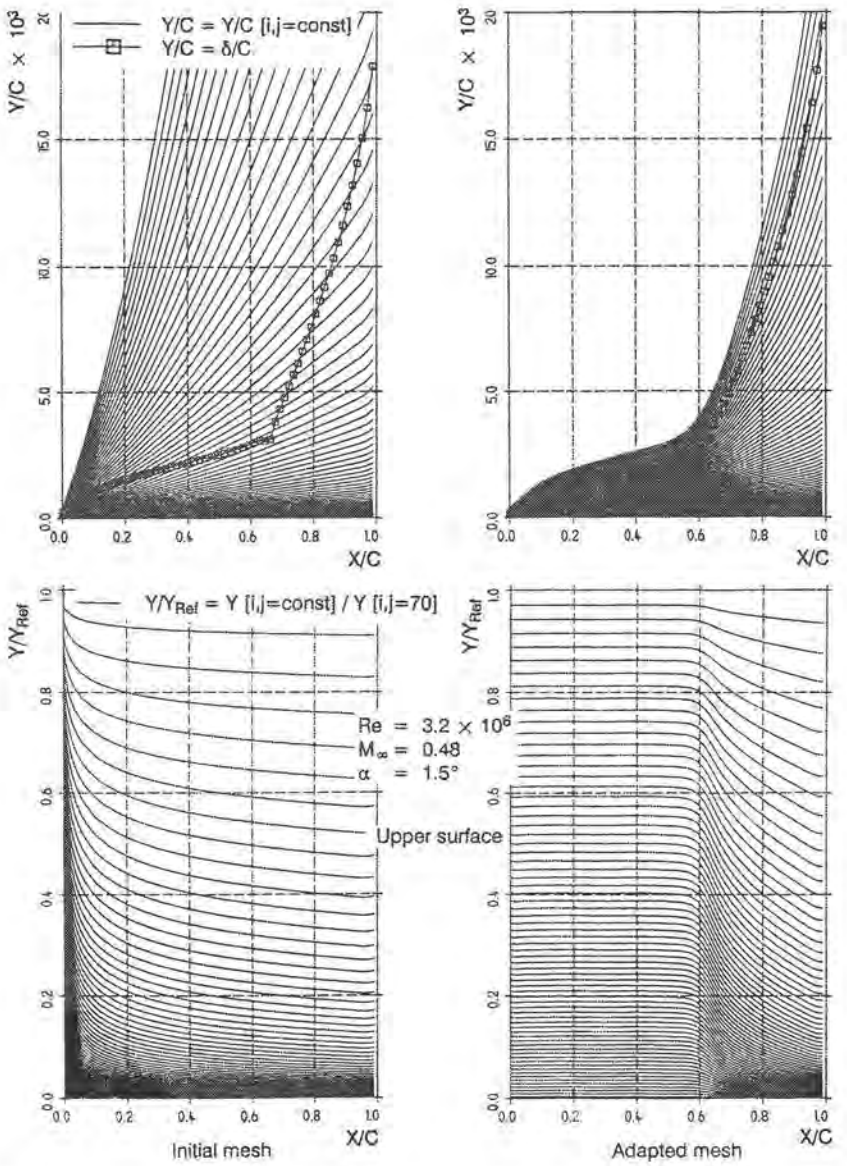

Figure 7: Mesh lines y $[i, j$ =const] in different presentation forms for the initial and the adapted mesh plotted versus x/c.

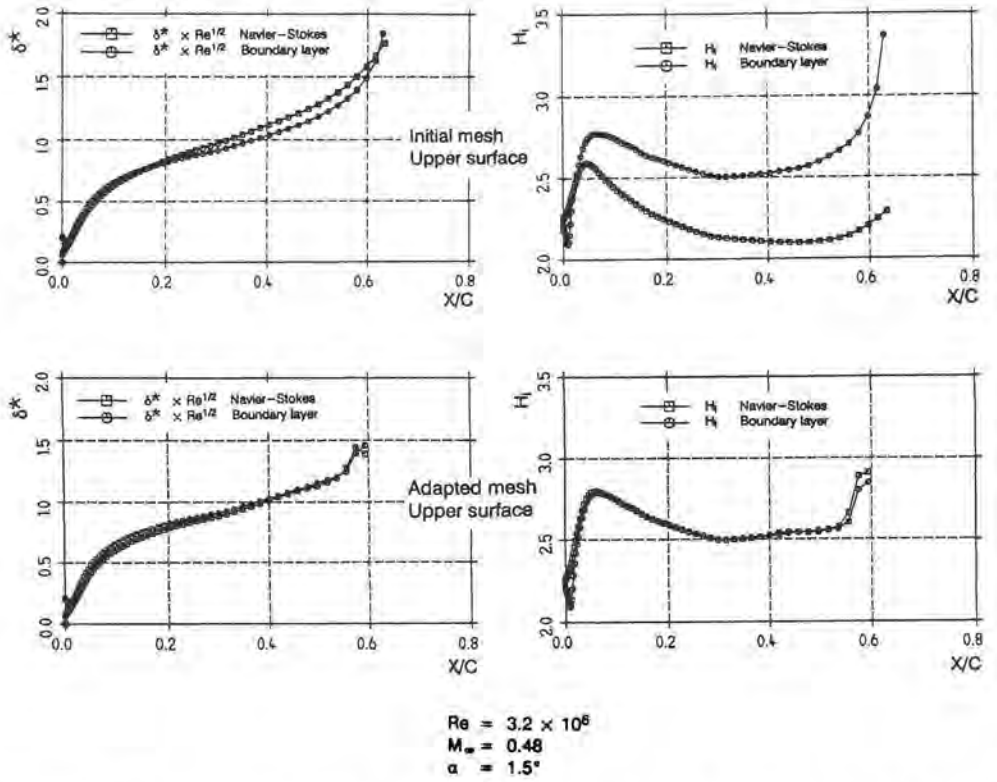

Figure 8: Comparison of the Navier-Stokes and the boundary layer results for the initial mesh and the adapted mesh.

N-factor calibration of the wind tunnel

Köster & Müller (1988) calibrated the N-factor for the TWB facility of the DLR-Braunschweig, using the e^n method for incompressible flow. The N-factor range, depending slightly on the Mach number but clearly on the Reynolds number, is from 5 to 7. Based on this information an N-factor of N=6 is used for the actual case, thus predicting transition at x/c= 0.17, see Fig. 9.

Prediction of the transition location in Navier-Stokes

Iterations are performed between the Navier-Stokes method and the stability method, moving by underrelaxation the transition location upstream. For the converged situation the transition location is found to be at x/c=0.11. The corresponding values of the lift and drag coefficient are shown in Fig. 10. The free transition measurements and the solutions in the adapted meshes, where the transition is fixed at the laminar separation location, are given for comparison. The lift coefficient for x_{tr}/c=0.11 is slightly smaller than for x_{tr}/c =0.6 due to

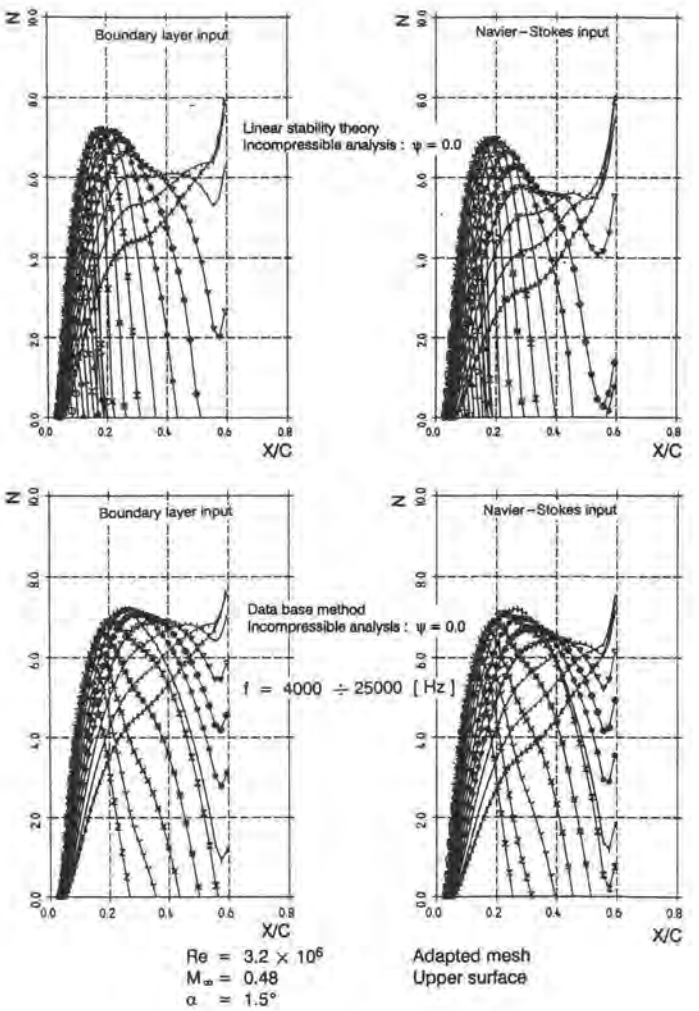

Figure 9: Stability theory results for the Navier-Stokes and the boundary layer input in the adapted mesh using the envelope approach.

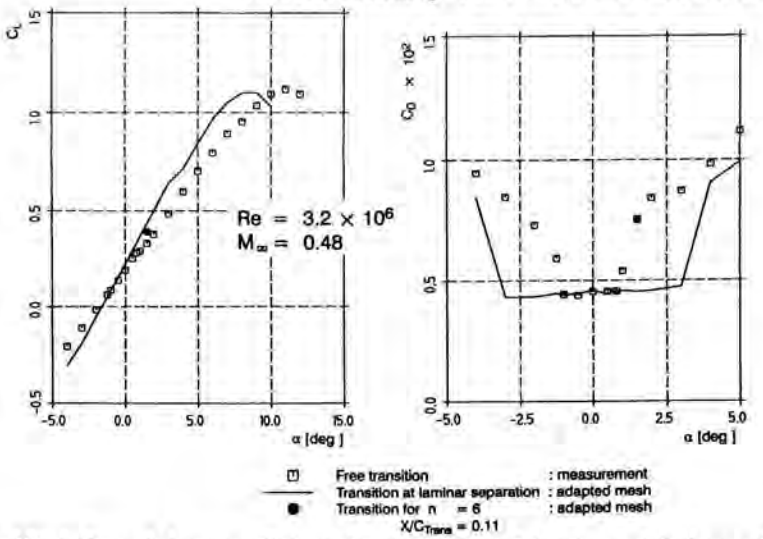

Figure 10: Lift and drag coefficient for the DOAL3 laminar airfoil as a function of the angle of attack with $x/c_{Trans} = 0.11$.

the enlarged viscous effects. The drag coefficient is nearly doubled and almost identical to the measurement.

Conclusion

The data base method delivers results of sufficient quality, when compared to results of the stability theory. This is shown for flows, including compressibility, suction and heat transfer effects. This simplified e^n method can easily be combined with coupled methods, to allow for joined iterations of the inviscid and viscous flow together with the transition prediction calculation.

It is at least shown, that in principal Navier-Stokes methods can be combined with the e^n method. So far only the feasibility of the jointedly used methods is demonstrated. For practical applications the computational and the user's costs should clearly to be reduced by automizing the described procedure of the computational sequences. Further studies have to be undertaken to augment the efficiency, i.e. at which convergence level and in which grid level the combined action of mesh adaption and new transition location prediction is optimum.

Acknowledgement

This research has been supported in part by the European Commission in the BRITE/EURAM programme ELFIN II.

References

Arnal, D. 1988 – Transition prediction in transonic flow. Symp. Transsonicum III Oertel and Zierep ed., Springer Verslag.

Chen, K.K. & N.A. Thyson 1971 – Extension of Emmons' spot theory to flows on blunt bodies. *AIAA J.***9**, 821-825.

Coles, D.E. 1956 – The law of the wake in the turbulent boundary layer. *J. Fluid Mech.* **1** 191-226.

Dhawan, S. & R. Narashima 1958 – Some properties of boundary layer flows during transition from laminar to turbulent motion. *J. Fluid Mech.* **3**, 418-436.

Emmons, H.W. 1951 – The laminar-turbulent transition in a boundary layer – part I. *J. Aerosp. Sci.* **18**, 235-246.

Falkner, V.M. & S.W. Skan 1930 – Some approximate solutions of the boundary layer equations. *ARC Rep.* 1314.

Haase, W. 1992 – EUROVAL – A European Initiative on Validation of CFD Codes. *Notes on Numerical Fluid Mechanics* **42**, 82-87, Vieweg Verlag.

Horton, H.P. 1994 – Near-similarity approximation for compressible, laminar boundary layers on adiabatic walls. *Queen Mary and Westfield College University of London,* Rep. No. QMW/EP/1093.

Horton, H.P. & H.W. Stock 1995 – Computation of compressible, laminar boundary layer on swept, tapered wings. *J. Aircraft* **32**, 1402-1405.

Johnson, D.A. & L.S. King, 1985 – A mathematical simple turbulence closure model for attached and separated turbulent boundary layers. *AIAA J.* **23**, 1684-1692.

Köster, K. & R. 1988 – Bestimmung des N-Faktors im Transsonischen Windkanal Braunschweig (TWB) anhand von Druckverteilungs- und Umschlagpunktmessungen und dem Sally-Verfahren, 6_{th} DGLR Fach-Symposium 8-9.11.1988. *DGLR-Bericht* 88-05.

Lück, H. 1987 – Windkanalmessung mit dem 2-D Profilmodell Doal3 bei der DFVLR-Braunschweig. *Dornier-Aktenvermerk* No. BF40-59/87.

Schrauf, G. 1988 – An efficient solver of the eigenvalue problem of the linear stability equations for three-dimensional, compressible boundary layer flows, 6^{th} DGLR Fach-S symposium 8-9.11.1988. *DGLR-Bericht*88-05.

Schrauf, G. 1993 – COAST2 – A compressible stability code – User's guide and tutorial. *DA-Bericht* EF1-1973.

Skrokowski, A.J.,S.A. Orszag, K. Kaups & T. Cebeci, 1979 – A fortran program to compute and integrate disturbance amplification rates on swept, tapered laminar flow control wings with suction. *Computer software management and information center*, The university of Georgia, Athens, USA.

Stock, H.W. 1980 – On laminar boundary layers with blowing and suction. *Z. Flugwiss. Weltraumforsch.* **4**, 93-100.

Stock, H.W. & E. Degenhart, 1989 – A simplified e^n method for transition prediction in two-dimensional, incompressible boundary layers. *Z. Flugwiss. Weltraumforsch.* **13**, 16-30.

Stock, H.W. & W. Haase 1989 – Determination of length scales in algebraic turbulence models for Navier-Stokes methods. *AIAA J.* **27**, 5-14.

Stock, H.W. 1990 – The stability and amplification rates of two-dimensional, incompressible, laminar boundary layers with suction. *Z. Flugwiss. Weltraumforsch.* **14**, 263-272.

Authors' addresses

°Daimler Benz Aerospace Dornier Luftfahrt
Dep. TE2, 82230 Weßling
P.O. Box 1103, Germany

▷Daimler Benz Aerospace LM
Dep. LME 12, 85073 Manching
P.O. Box 1149, Germany

Tuncer Cebeci, Hsun H. Chen & Eric Besnard

The Role of Zarf in Predicting Transition in Three-Dimensional Flows with the Saddle-Point Method

Abstract

The e^n-method used to predict the onset of transition location in two and three-dimensional flows requires the specification of dimensional frequencies to initiate the calculation of the amplification rates. This paper describes a convenient procedure based on the use of zarfs for calculating the frequencies needed in the e^n-method and discusses the role they have in predicting transition in three-dimensional flows.

Introduction

The e^n-method, first proposed independently by Smith and Gamberoni (1956) and van Ingen (1956), is the current state-of-the-art method for predicting the onset of transition in incompressible and compressible flows. It is based on the solutions of the linear stability equations obtained by using either temporal or spatial amplification theory. In the former case, the wave numbers α and β in the x- and z-directions are real but the radian frequency ω is complex ($\equiv \omega_r + i\omega_i$). In the spatial amplification theory α and β are complex ($\equiv \alpha_r + i\alpha_i$, $\beta_r + i\beta_i$) but ω is real. For three-dimensional flows, the solution procedure in either theory involves an eigenvalue problem with five scalars α, β, ω_r, ω_i and R in the temporal approach and six scalars α_r, α_i, β_r, β_i, ω and R in the spatial approach, and is considerably more difficult than its counterpart in two-dimensional flows because the requirements of a nontrivial solution of the stability equations provides only two relations connecting the eigenvalues α, β, ω and R. In the spatial amplification approach for transition prediction, ω and R are prescribed and so two new relations connecting α and β must be given before the solutions of the stability equations can be obtained.

The formulation of the relationship between α and β plays a crucial role in the eigenvalue problem since the onset of transition depends on the direction, magnitude and rate of the growth of the disturbances which propagate through the boundary layer and this information is represented by α and β which form a wave number vector, $\vec{k}$, at an angle ϕ to the flow direction. There are several formulations developed to provide this relationship. Mack's approach (1988) for an infinite swept wing, for example, employs spatial amplification theory and assumes that the spanwise wave number β is obtained from the irrotationally

condition applied to the complex wave number vector which, for an infinite swept wing, requires that the dimensional β is real and remains constant as the waves move downstream. With this assumption, the problem reduces to the calculation of the complex chordwise wave number α at each chordwise position for the specified dimensional values of β and ω. Arnal *et al.* (1989) used this formulation and showed that the calculated locations of the onset of transition agreed much better with experiment on an infinite swept wing when the amplification rates (α_i) were maximised at each chordwise position by varying β.

Malik's approach (1982) is based on temporal amplification theory in which the two wave numbers α and β are related through a disturbance angle ϕ which is not known initially and is obtained iteratively. With ω_r specified and β given by

$$\beta = \alpha \tan \phi \tag{1}$$

the eigenvalue problem is solved for α and ω_i. Upon convergence, calculations are performed for other values of ϕ in order to find the maximum value of ω_i.

The formulations of Cebeci and Stewartson (1980), and Nayfeh (1980) make use of the saddle-point method or the method of multiple scales in which the relationship between α and β is not assumed but computed from the requirement that $\partial\alpha/\partial\beta$ is real, as follows from concepts based on group velocity. According to this requirement, the wave orientation and growth direction of the disturbance are given by

$$\left(\frac{\partial \alpha}{\partial \beta}\right)_{\omega,\, R} = -\tan \phi \tag{2}$$

with spatial amplification theory. The amplification rate Γ

$$\Gamma = \alpha_i - \beta_i \left(\frac{\partial \alpha}{\partial \beta}\right)_{\omega,\, R} \tag{3}$$

is calculated with α and β determined with the constraints of Eq. (2), and further calculations for different values of $(\partial\alpha/\partial\beta)$ lead to new values of α and β and to the maximum value of Γ.

In the application of the e^n-method to two-dimensional flows, stability calculations often begin on the lower branch of the neutral stability curve where several dimensional frequencies needed in the amplification rate calculations are determined. It is plausible to assume that in the extension of the e^n-method to three-dimensional flows, the stability calculations should also begin on a neutral curve. Except for the work of Cebeci and Stewartson, however, precise definition or extension of a neutral stability curve for three-dimensional flows has not been formally discussed and used in the literature. As a result, all current e^n-methods, except that of Cebeci and Stewartson, assume the location and magnitude of these frequencies and calculate the amplification rates. The implications of this procedure are not clear and so far have not been studied.

In this paper we discuss the importance of calculating the location and magnitude of these frequencies. We use the definition of a neutral curve introduced in the saddle-point method of Cebeci and Stewartson for this purpose. This

curve, known as the zarf (lit. "envelope", Turk) is defined as one on which disturbances neither grow nor decay at a large distance from the origin of the flow in any direction. It has the following properties,

$$\alpha_i = \beta_i = 0, \quad \frac{\partial \alpha}{\partial \beta} = real. \tag{4}$$

The following section presents results obtained with the saddle-point method for three-dimensional incompressible and compressible flows with and without suction. It is followed by another section which shows the behaviour of zarfs used to perform the stability/transition calculations presented in the previous section. The paper concludes with a summary of the more important conclusions.

Application of the saddle-point method

The saddle-point method of Cebeci and Stewartson has been applied to several three-dimensional flows. A sample of results are presented in this section to demonstrate the accuracy of the method. Fig. 1 and 2 show the experimental setup and a comparison between calculated and experimental results for the data of Arnal and Juillen (1987) obtained in the F2 wind tunnel at LeFauga-Maujac Center, respectively. The model had an ONERA-D airfoil section, symmetric between $x/c = 0.20$ and $x/c = 1$ and equipped with a cambered leading edge (Fig. 1a), so that the pressure distributions differed from those observed on the classical ONERA-D profile. The chord normal to the leading edge was 300 mm and the span 900 mm with zero angle of sweep. The wing and the half-fuselage were mounted on a turntable (Fig. 1b). Three kinds of experiments were performed so that pressure distribution measurements, flow visualizations by sublimation technique, and hot-film measurements were obtained. Ten hot-films were glued on the model, from 2.5 to 86 percent of chord, and recorded simultaneously for more than one hundred combinations of the wind tunnel speed, angle of sweep, and angle of attack. The positions of the hot-films are indicated on Fig. 1b and were chosen to avoid interactions between probes. These results were verified by comparing the transition positions obtained by the hot-film records and by the flow visualization (in the absence of hot-films): the results were similar. Three angles of sweep (λ= 49, 55 and 61°) and four angles of attack (α = 0, −2, −4 and 8°) were studied.

The calculated results shown in Fig. 2 for $\lambda = 49°$ and $\alpha = -2°$ indicate very good agreement in the data. Similar agreement was also obtained for other sweep angles and angles of attack as discussed by Cebeci, Chen, Arnal and Huang (1991).

Fig. 3 shows calculated results for an Aérospatiale wing for which data was obtained by Séraudie *et al.*(1989) for compressible flows on a 15-degree swept tapered wing. The chord was 0.228 m at the root and 0.145 m at the tip. The wing had a span of 0.39 m with an AS409 cross-section and a trailing-edge sweep angle of three degrees. In order to avoid the need to perform fully three-dimensional stability/transition calculations, the measurements were carried out

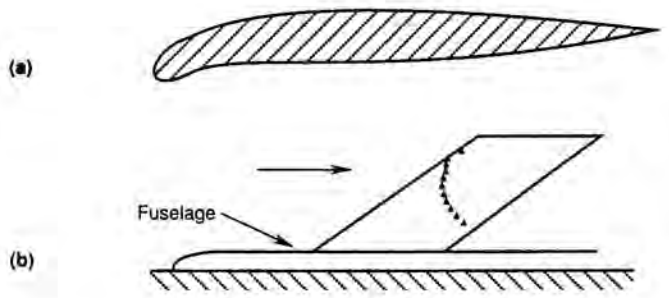

Figure 1: (a) ONERA-D airfoil with a cambered leading edge and (b) experimental setup.

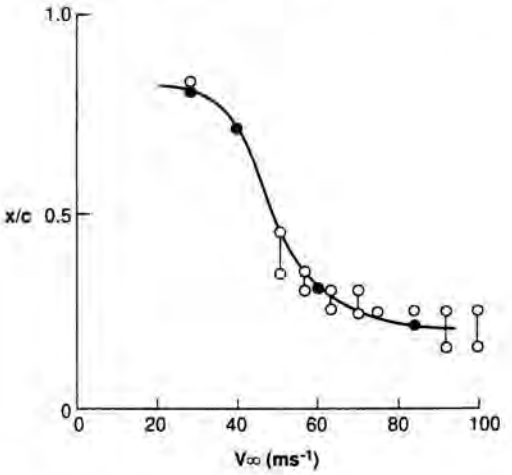

Figure 2: Comparison of calculated (closed symbols) and experimental (open symbols) transition locations. $\lambda = 49°$, $\alpha = -2°$.

under infinite swept wing conditions with the wing having a mean sweep angle of 12 degrees at an angle of attack of 0.3 degrees.

The results in Fig. 3 are for a freestream Mach number of 0.74 and Reynolds number of 14×10^6. The calculations were carried out by Cebeci, Chen, and Arnal (1994) for both adiabatic wall and specified wall temperature conditions. If we take the n value to 7.5 (a mid-n value of the expected n-value range for this wind tunnel) then transition occurs at $x/c \cong 0.46$ for adiabatic wall conditions and $x/c = 0.47$ for measured wall conditions. This compares well with the experimental transition location of $x/c = 0.47$.

Fig. 4 shows a comparison between the calculated and experimental results for the data of Meier and Kreplin (1981) obtained for a three-dimensional incompressible flow on a prolate spheroid at an incidence angle of 10°. The dashed line corresponds to the locus of transition location computed with the saddle-point

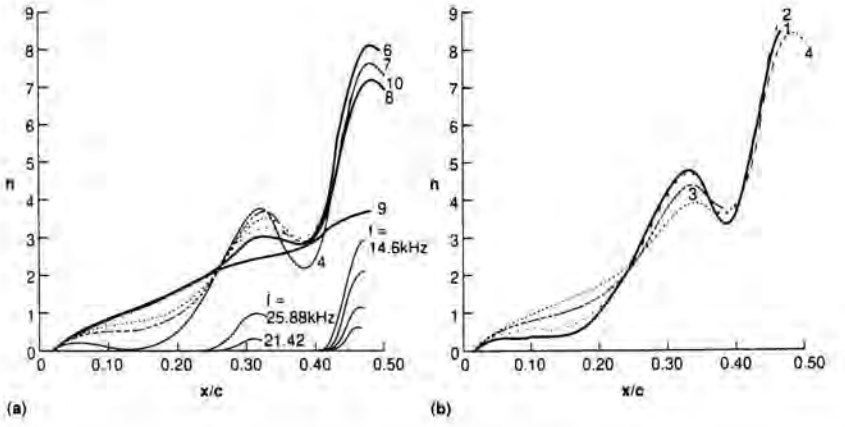

Figure 3: Calculated results for the Aérospatiale wing for (a) adiabatic and (b) measured wall temperature distributions.

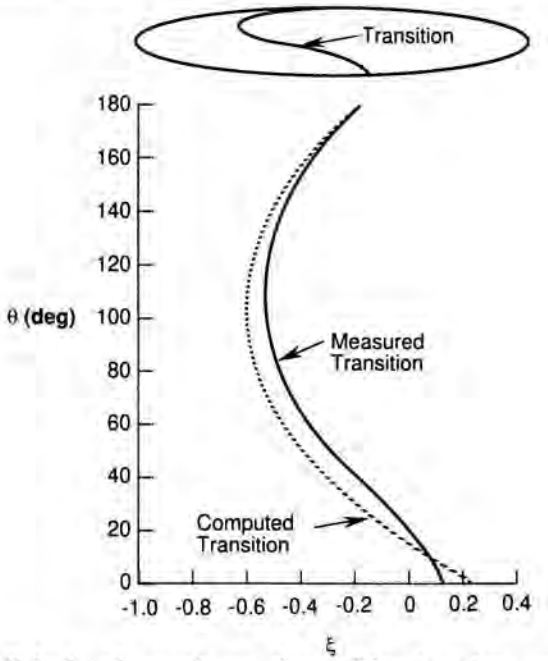

Figure 4: Calculated experimental transition locations on the prolate spheroid at $\alpha = 10°$.

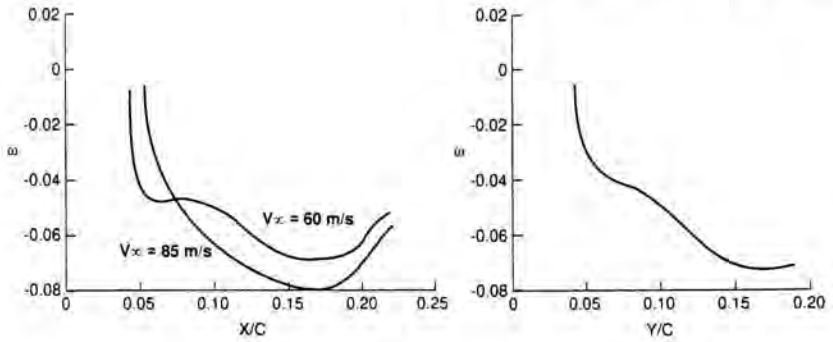

Figure 5: Variation of ω on zarf near the leading edge: (a) $\lambda = 49°$, $V_\infty = 60$ m/s, 85 m/s, $\alpha = 0°$; (b) $\lambda = 49°$, $V_\infty = 60$ m/s, $\alpha = -2°$.

method for $n = 10$. The experimental values denoted by the solid line are in good agreement with calculated values as reported by Cebeci, Chen, Arnal, and Huang (1991).

Zarfs for some three-dimensional flows

The calculated transition locations presented in the previous section utilized dimensional frequencies obtained from zarfs which have interesting and somewhat unusual behaviour in a very small region near the wing stagnation line.

Fig. 5 shows the variation of zarf near the leading edge of the wing for the data of Arnal and Juillen. As can be seen, the lower branch of the ω-zarf is negative with relatively flat values of ω away from the leading edge, whereas ω undergoes a very rapid variation near $x/c = 0.04$ and 0.05.

Figs. 6a and 6b show that ω becomes positive and increases rapidly around $x/c = 0.04$ for $\alpha = 0°$, $V_\infty = 60$ m/s, and around $x/c = 0.05$ for $\alpha = -2°$, $V_\infty = 85$ m/s. This behaviour of ω near the leading edge is very important since the e^n-method requires the calculation of the frequency that leads to the greatest amplification rate Γ. An accurate calculation of this frequency and its location is crucial to the accuracy of calculating the transition location.

Fig. 7 shows the zarfs used to obtain the n-factors presented in Fig. 3. As can be seen, the frequencies originate at nearly the same location (on a vertical line) and vary drastically from one another. Knowing the range of these frequencies and their location is an accurate and efficient way of computing n-factors.

Fig. 8 shows a sample of integrated amplification rates with disturbances originating at various circumferential locations (θ) of a prolate spheroid with frequencies determined on the zarf. As discussed in detail by Cebeci, Chen, Arnal and Huang (1991), the zarf shape at each θ-location is different.

Fig. 9 shows the location of the critical frequencies on the zarf used to obtain the n-factors in Fig. 4. We note from this curve that its behaviour approaching the leeward line of symmetry ($\theta = 180°$) begins to exhibit a difference for

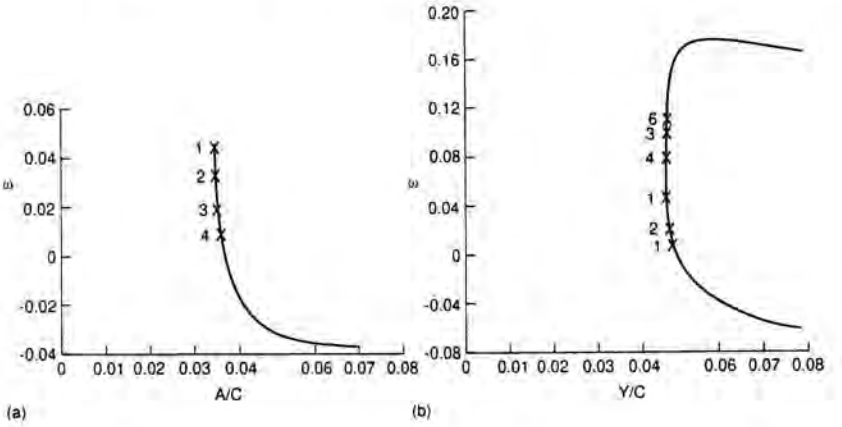

Figure 6: Variation of ω on zarf near the leading edge: (a) $\alpha = 0°$, $V_\infty = 60$ m/s; (b) $\alpha = -2°$, $V_\infty = 85$ m/s.

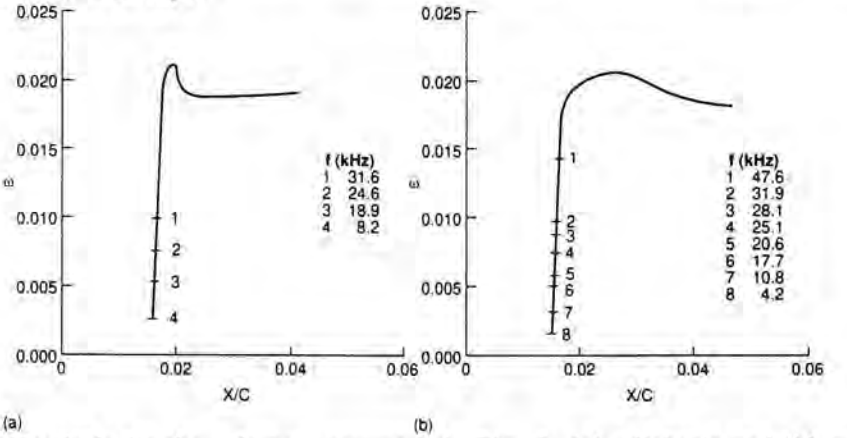

Figure 7: Zarfs for the n-factors presented in Fig. 3: (a) adiabatic and (b) measured wall temperature distributions.

$\theta \geq 160°$ from $\theta < 160°$. As discussed by Cebeci *et al.*, this difference is due to the effect of crossflow velocity profiles which exhibit significant changes as we approach the leeward line of symmetry. The calculated zarfs account for these changes in velocity profiles very well and are the main reason for obtaining the good agreement with the data, especially near the line of symmetries. Figs. 10 and 11 show the zarfs on a typical transport wing with and without suction, respectively, for transonic flow conditions. The results in Fig. 10a indicate that with increasing suction rates (C_q), the location of the zarfs moves downstream and the magnitude of the dimensional frequencies increases. The results in Fig. 10b show the effect the frequencies have on the computed n-factors. Fig. 11 shows a similar behaviour for the same transport wing, this time for a flow without suction. The figure also shows the procedure used to generate the zarf. The stability calculations begin first on the lower branch where the

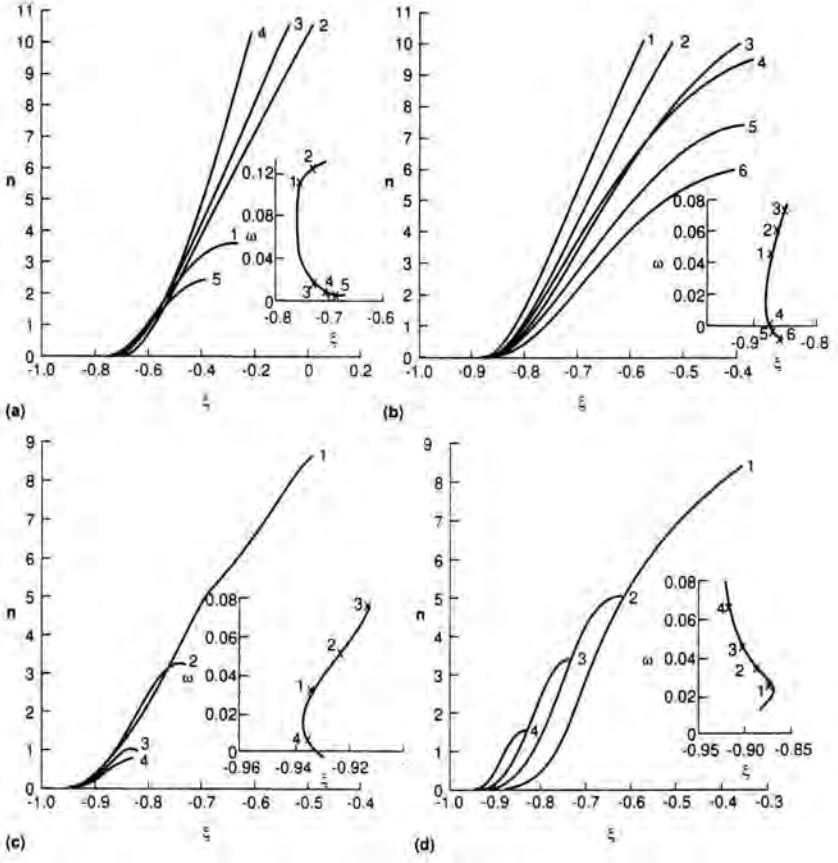

Figure 8: Variation of n-factors and zarfs at various θ-locations on the prolate spheroid of Meier and Kreplin. (a) $\theta = 20°$, (b) $\theta = 40°$, (c) $\theta = 120°$, (d) $\theta = 150°$.

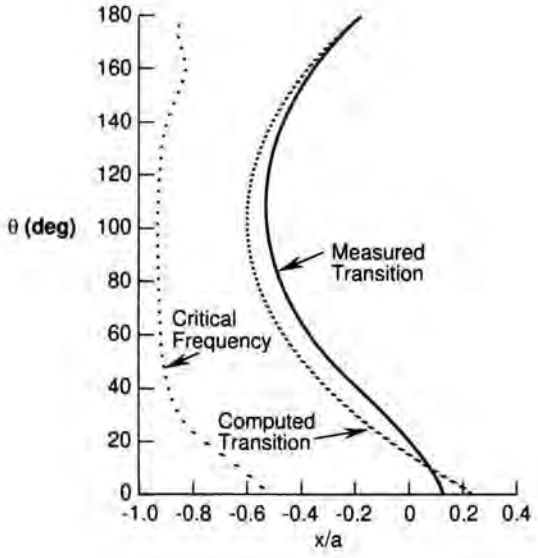

Figure 9: Critical frequencies, computed and measured transition locations on the prolate spheroid of Meier and Kreplin.

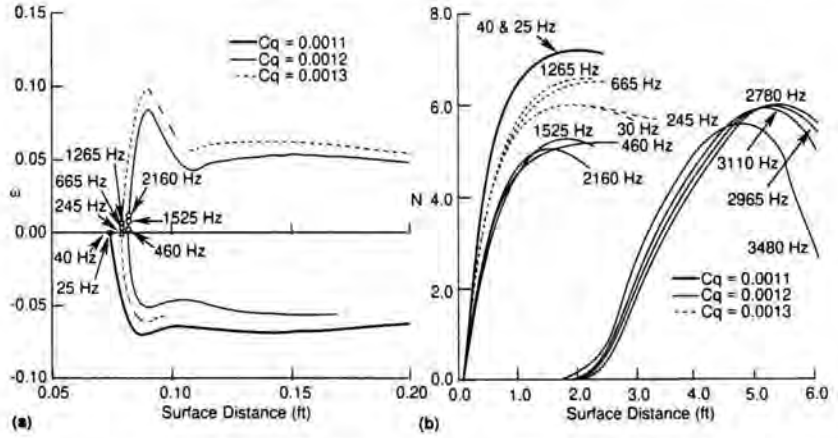

Figure 10: Behaviour of zarf on a typical transport wing with suction for transonic flow conditions (a) zarfs and (b) computed integrated amplification rates.

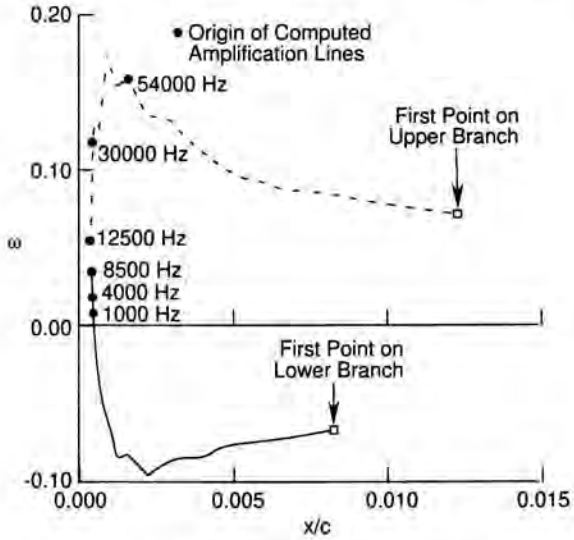

Figure 11: Behaviour of zarf on a typical transport wing without suction.

frequencies are negative and move upstream. In the region where the frequencies become positive, as in other zarfs, frequencies increase significantly in a very small x/c-interval near the wing leading edge. Our experience with the calculations indicate that only the frequencies near the most upstream part of the zarf lead to amplification rates that increase with increasing distance. Others, either on the lower or upper branches of the zarf do not continuously amplify. The integrated amplification rates first increase with increasing x but begin to decrease further downstream.

Conclusions

The studies conducted with the saddle-point method indicate that zarfs play a very useful role in the calculation of the location and the magnitude of the dimensional frequencies. The critical frequencies that lead to the highest amplification rates occur very close to the wing stagnation line and the use of zarf allows them to be located easily and accurately.

References

Arnal, D., Casalis, G. & Juillen, J.C. 1989 – Experimental and theoretical analysis of natural transition on infinite swept wings. In: IUTAM Symp. Toulouse, France, 1989: Laminar-Turbulent Transition (Eds. D. Arnal and R. Michel), pp. 311-326, Springer-Verlag, Berlin.

Arnal, D. & Juillen, J.C. 1987 – Three-dimensional transition studies at ONERA/CERT. AIAA Paper No. 87-1335.

Cebeci, T., Chen, H.H. & Arnal, D. 1994 – Natural transition in compressible flows on wings: spatial theory and experiment. AIAA Paper No. 94-0824.

Cebeci, T., Chen, H.H., Arnal, D. & Huang, T.T. 1991 – A three-dimensional linear stability approach to transition on wings and bodies of revolution at incidence. AIAA J., **29**, 2077.

Cebeci, T. & Stewartson, K. 1980 – Stability and transition in three-dimensional flows. AIAA J., **18**, 398.

Mack, L.M. 1988 – Stability of three-dimensional boundary layers on swept wings at transonic speeds. Presented at the IUTAM Symp., Transsonicum III, Göttingen, Germany.

Malik, M.R. 1982 – COSAL – A black-box compressible stability analysis code for transition prediction in three-dimensional boundary layers. Report NASA CR 165952.

Meier, H.U. & Kreplin, H.P. 1981 – Experimental investigation of the boundary layer transition on a body of revolution. Z. Flugwiss. Weltraumforsch., 4, 65.

Nayfeh, A.H. 1980 – Stability of three-dimensional boundary layers. AIAA J., **18**, 406.

Séraudie, A., Archambaud, J.P. & Payry, M.J. 1989 – Etude de la laminarité sur l'aile as409 jusqu'à des nombres de Reynolds de l'ordre de 14 millions dans la soufflerie T2. ONERA/CERT Internal Report No. 33/5006-19.

Smith, A.M.O. & Gamberoni, N. 1956 – Transition, Pressure gradient and stability theory. Douglas Aircraft Co. Report No. ES 26388.

Van Ingen, J.L. 1956 – A suggested semi-empirical method for the calculation of the boundary layer region. Report No. VTH71, VTH74, Delft, The Netherlands.

Authors' address

Aerospace Engineering Department
California State University, Long Beach
Long Beach, California 90840, USA

Th. Herbert

On the Status of Applied Transition Analysis

Abstract

The implementation of the compressible, nonlinear PSE in general curvilinear coordinates enables the analysis of transition in boundary-layer flows over objects of practical interest, such as swept and tapered wings or turbine blades. Our efforts to produce PSE results and to establish links to the traditional e^N method met with some success, but also with various obstacles that hamper reliable estimates of the transition location. We discuss our experience and offer suggestions for the improvement of analysis software, input data, N-factor computation, and basic knowledge. We illustrate the current capabilities to model the complete path from the external environment through receptivity, transient or unstable disturbances, and nonlinear mechanisms to the ultimate breakdown to determine the transition location. Nonlinear studies on swept wings demonstrate that the growth of crossflow vortices significantly exceeds the linear predictions and can cause transition at low N factors and unexpected locations.

Introduction

The desire to increase efficiency of fluid machinery often requires the designer to increase the area of laminar flow, because drag and heat transfer in laminar boundary layers are lower than in their turbulent counterparts. The transition from the laminar to the fully turbulent motion is an evolutionary process that may extend over a considerable streamwise distance. During this process the skin-friction coefficient C_f and Stanton number St increase, typically overshoot, and ultimately settle down to the values for fully turbulent flow. The length of the transition region may be further extended through the intermittent appearance of transition in space or time. For practical purpose, it is necessary to (i) estimate the location x_t of the onset of transition and (ii) evaluate the downstream evolution of drag and heat transfer in the transitional flow. Given the transition location, empirical relations for the production rate of turbulent spots and intermittency factors together with turbulence models have been exploited to solve the second problem with reasonable success. Other attempts to use the Reynolds-averaged equations and "adapted" turbulence models to describe the complete transition zone including its onset have met with limited success even in simple situations, as shown by the ERCOFTAC test case T3A (Savill, 1992). Because of the large discrepancy between the laminar and turbulent C_f values at the same location, a small shift in the transition point causes significant changes

in the resulting drag. Therefore the accurate prediction of the transition location along the chord of an aircraft wing or turbine blade has attracted intense efforts. However, the complexity of the transition process still leaves challenging questions open.

Since the discovery and experimental verification of TS waves, the transition process has been associated with the instability of boundary layers. Based on the linear stability theory (LST), various types of disturbances have been identified as capable of exponential growth, such as Görtler vortices on concave surfaces, cross-flow (CF) vortices in the three-dimensional boundary layers on swept wings, or Mack's higher modes at supersonic speeds. Numerous transition criteria have been developed (see e.g. the review by Arnal, 1984) involving characteristic parameters such as the Reynolds number formed with the momentum thickness and empirical corrections to account for the turbulence level, pressure gradients, and other conditions. While these criteria meet the demand for simplicity, their accuracy is unacceptable for all but rough estimates.

The shortcoming of the simple criteria as well as the methods based on averaged equations is their lack of accounting for the disturbance level, the detailed stability characteristics of the flow, and the resulting nonlinear processes that constitute transition. One of these obstacles was independently overcome by Van Ingen (1956) and Smith & Gamberoni (1956) who found that the transition locations in the 2D incompressible flow over airfoils correlated well with a constant value of the limiting N factor

$$N = \max_{\omega} n(x_t;\omega) \ , \quad n(x;\omega) = -\int_{x_0}^{x} \alpha_i(\omega) dx$$

in the range of 8 to 9, where ω is the frequency, $x_0(\omega)$ the onset location of instability, $-\alpha_i$ the spatial growth rate of the TS wave, and $n(x;\cdots)$ or $n(s;\cdots)$ describe the amplitude growth of the disturbance along the chord or arc of the airfoil. This observation is the basis of the e^N method, and links the transition location to a certain ratio of the disturbance amplitude A_t at transition to the amplitude A_0 before the onset of instability, $A_t/A_0 \approx e^N$.

Meanwhile, the e^N method has been extended to compressible and 3D boundary layers, and is extensively used in aerodynamic design for the low-disturbance environments found in wind tunnels and atmospheric flight. The widespread applications also have revealed some shortcomings of the method. Since the "strategies" for computing N vary, different values of N can be obtained for a given problem. In fully 3D boundary layers[1] the transition front does not correlate with a single value of N. The database of reliably measured transition locations for boundary layers at high supersonic speeds is too sparse to obtain N factors in a narrow range, and to validate the e^N method. The method also fails at the higher disturbance levels of flows in turbomachinery with turbulence levels above $Tu = 0.5\%$. In these flows, transition is attributed to a process that

[1]With the attribute *fully 3D* we distinguish flows that vary significantly in all three spatial directions from those that have three velocity components, but vary only in two spatial directions.

"bypasses" the linear instabilities and causes rapid transition, as in the ERCOFTAC test cases T3A and T3B with $Tu = 3\%$ and $Tu = 6\%$, respectively, at $x = 0$.

Clearly a method based only on the growth rate of linear instability modes is insufficient to find the transition location. While there is no strict definition of "transition", all operational definitions rely on the nonlinearity of this process. Changes in C_f or St are caused by changes of the mean flow, which necessarily result from the nonlinear interaction of finite-amplitude disturbances. Even if we disregard bypass transition, improved methods for estimating the transition location will need to account for nonlinearity and the disturbance level.

Direct numerical simulations (DNS) based on the Navier-Stokes equations, though successful in basic research, are still too limited and expensive for practical applications. The parabolized stability equations (PSE) (Herbert & Bertolotti, 1987) have reproduced microscopic experiments and DNS results for 2D boundary layers (Bertolotti, 1991) at a fraction of the cost of DNS and were suggested by Herbert (1991, 1994) as a new approach to transition analysis in engineering applications. While this approach is fully developed for quasi-3D boundary layers up to high supersonic speeds, our intense efforts to produce PSE results and to establish links to the traditional e^N method met not only with success, but also with various obstacles and questionable concepts that hamper reliable estimates of the transition location.

Needs in applications

The engineering practice poses a discouraging dilemma for any effort to improve transition estimates, both by the demands on the codes and by the input data provided. Engineering practice wants results at low cost, hence requires codes that run fast on lower-end computers, are robust, foolproof, and can be operated by engineers without special training in the intricate matter of transition[2]. Obviously these demands must be part of the nonfunctional requirements and user interface specifications for the software development. As functional requirements, however, speed and ease-of use should not compromise the underlying physics and jeopardize the usefulness of the results.

Before any comparison with linear PSE results, we evaluated various proprietary and nonproprietary e^N codes for a swept, untapered wing at supersonic speed, $Ma = 1.5$, using essentially the same input data. Some results for COSAL (Malik, 1982) are reported by Stuckert *et al.* (1993). Using virtually identical strategies, different codes, and in some cases different versions of the same code, provide different results. The codes vary widely in speed, depending on the order of the numerical method and the routines used to solve algebraic systems. The results depend on the numerical specifications which are left to trial-and-error by the user. Therefore, different users may obtain different results. Influential

[2]These requirements were also emphasized by the industry representatives at this colloquium.

options to suppress compressibility or curvature effects, or the chosen strategy are insufficiently documented in the results. The results of different strategies differ significantly. The envelope method – probably the fastest e^N strategy besides database methods – provides much higher amplitude growth than other strategies owing to the violation of physical constraints. In a larger variety of applications to wings and to compressor and turbine blades, one of the most cumbersome tasks is the search for unstable regions and the identification of unstable modes for the relevant types of instability. The codes show weaknesses in dealing with multiple regions of instability as they often appear on turbine blades. Input data, e.g. for the fluid properties, are often hard-coded and difficult to change. With respect to user interface, internal and external documentation, readability, and other quality requirements, the e^N codes we evaluated do not meet the minimum standards for up-to-date software. Unfortunately, this criticism applies to many CFD codes in current use.

The input of the basic flow for the LST or PSE based e^N codes can be given directly in the form of a large file with precomputed boundary-layer parameters and profiles at numerous stations x_n along the chord, or indirectly by separate data for fluid properties, geometry, freestream conditions, pressure distribution, and the distributions of wall suction, wall temperature, or wall-heat transfer. In the latter case, the boundary layer must be obtained by a separate code. Transition analysis requires an unusually high quality of the input data because the stability characteristics are sensitive to small changes of the basic flow.

The fluid properties – specified or hard-coded – may not be the same for the boundary-layer code and the e^N code. The independent use of values for the gas constant R, the specific heat c_p, and the ratio γ of specific heats for an ideal gas may be inconsistent with the relation $c_p = \gamma R/(\gamma - 1)$ exploited elsewhere. The geometry is usually specified by a number of coordinate pairs along the airfoil. If this number is too small, the profile may be too inaccurate to compute the boundary layer and evaluate the curvature correctly. Data sets used for numerical solutions of the Euler equations often have too many points of limited accuracy (number of digits) and introduce unacceptable round-off errors in the curvature and wiggles in the C_p distribution. Differences between the geometry specified for the numerical work and the actual geometry in wind-tunnel or flight tests can cause major discrepancies in the correlation of N factors.

The pressure distribution can be obtained by measurements or computations with panel, Euler, or Navier-Stokes codes. The difference between computed and wind-tunnel data for single wings is usually significant, and increases for the even more confined flow in turbine cascades. Various detailed experiments on transition in turbines provide insufficient information e.g. on side-wall boundary layers to configure the input for 3D computations, and the use of 2D approximations is questionable for the relatively short blades of contemporary turbines. In the past, the accuracy requirements for flow computations in turbines have not been as stringent as in external aerodynamics, and the use of stability-based transition analysis is relatively new. Our experience with some of the CFD codes for turbine design indicates the need for improvements, from the generation and

implementation of better grids in the passage of the cascade to the removal of heuristic factors that may accelerate the convergence to a less desirable solution.

CFD codes often provide C_p at points other than those defining the geometry. Linear interpolation of the geometry and pressure distribution is insufficient, while higher-order interpolation (e.g. by cubic splines) tends to overshoots, except for smooth data. Because the boundary-layer starts at the stagnation point, this point must be accurately specified in the pressure distribution. An incorrect starting point can have significant effects on the boundary-layer and the N factors by affecting the crossflow instability near the leading edge. Inappropriate C_p distributions in the neighbourhood of the stagnation point can, and should, be corrected.

We have found it necessary to perform detailed checks of the input data by computer, and to qualify geometry and C_p distribution by visual inspection of the data used in the computation of boundary-layer profiles and N factors. This inspection cannot be performed if the boundary-layer profiles are given directly to protect the proprietary geometry and/or pressure distribution.

Most boundary-layer codes have been developed to compute the skin friction in the laminar and turbulent region and provide the profiles of the streamwise and spanwise velocity components U and W and the temperature T as a byproduct. While these profiles look unsuspicious, the derivatives in the normal direction y which are needed in the stability equations are not necessarily accurate. The widely used modification WING of the Kaups-Cebeci code distributed with COSAL provides first and second derivatives that deviate from the correct values in the neighbourhood of the wall and critical layer for TS waves. The second derivatives do not appear in the stability equations but are introduced by some numerical methods such as the fourth-order compact method used in COSAL. Based on the work of Kaups & Cebeci (1977) for conical wings, we developed a new code CBL to obtain correct derivatives. This code was validated by comparison with results of LISW (Elsholz, 1988), which solves the boundary-layer equations for a locally infinite swept wing in surface-oriented coordinates. The neglect of the surface curvature in the boundary-layer computation with CBL has a minor effect on the N factors. However, the concept of a locally infinite swept wing offers more flexibility to relax the restrictions on the sweep angles of leading and trailing edge, and on the spanwise variation of the pressure distribution, thus benefitting the analysis of 2D as well as more general 3D boundary layers. Calculating 2D flows with a code for conical flows starts the boundary layer from the wrong profile at the stagnation point, no matter how small the sweep angles may be set.

The development of a new code was also necessary to obtain the small normal velocity profile V, the streamwise derivatives of U and W, and the surface curvature terms which appear in the PSE. Attempts to retrieve these small velocity terms from the output of traditional codes provided unsatisfactory results. For the rough pressure distributions measured in flight tests, the V component and streamwise derivatives often exhibit strong variations and oscillations from station to station that are visible in the growth rates obtained from the PSE.

We had some success using the Plot3D files produced by various Navier-Stokes codes to retrieve the boundary-layer profiles, derivatives, and metric information, although this procedure required pushing the grid resolution to the limits. Inconsistency between the grids of the CFD codes and those used for the transition analysis necessitates extensive 3D interpolation. In general, it is more efficient and more accurate to retrieve the geometry and pressure distribution for application of a boundary-layer code. For boundary layers on turbine blades, knowledge of the C_p distribution does not allow matching the boundary layer asymptotically with the inviscid flow which exhibits strong velocity gradients at the wall. Boundary-layer solutions miss characteristic features revealed by Euler and Navier-Stokes solutions.

To meet the needs of applications, improvements are necessary on both sides: code developers must improve the software quality for basic-flow and transition analysis, and the users of the software must improve the quality of the input data. This approach should permit largely unattended operation of the codes, and relieve the insistence on higher speed. Efficiency increases can be achieved with proper numerical methods but not beyond the limit set by the need to resolve our intricate physical problem.

N-factor computation

Traditional codes for N-factor computations rest on the LST for locally parallel flow. The parallel-flow assumption neglects the streamwise and spanwise variation of the basic flow and cuts the physical connection between the local solutions in different points on the surface. Different strategies can then be selected to reconnect these local solutions to provide amplitude-growth curves $n(s;\cdots)$ along the arclength or chordwise direction. Depending on the strategy, other options and approximations, and on the settings specific to the implemented numerical method, the results for $n(s;\cdots)$ vary widely, and so do the limiting N values obtained by correlation with known transition points. The numerical methods reach from spectral collocation methods (slow, but most accurate), seventh- or fourth-order Hermitean, Runge-Kutta shooting, fourth-order compact (needs higher derivatives of the basic flow), to second-order methods (fastest) on suitably stretched grids. Minimum specifications are the number of grid points and the parameters of the stretching function. Most codes use transformed temporal growth rates instead of the more accurate spatial growth rates. Options are provided to include or exclude compressibility and/or curvature effects. Leaving aside undetected omissions in the tedious stability equations and small coding errors as well as differences in the hard-coded thermal fluid properties, it takes hard work to obtain the same result for $n(s;\cdots)$ with identical input into two different codes.

The PSE provide different amplitude-growth curves $\tilde{n}(s;\omega,\beta)$ by accounting for the streamwise changes of U, W, and T, even if terms like V and $\partial U/\partial s$ are suppressed. Spanwise variations in fully 3D boundary layers are normally

neglected[3]. The effect of this approximation can be reduced or eliminated by proper choice of the general curvilinear coordinates implemented in our code COPS. By solving the parabolized equations with a marching method, the solution is automatically connected from point to point along the marching direction, without leaving the freedom of choice for strategies. Therefore, the PSE results are comparable only with certain results of LST-based codes that are obtained with fitting strategies.

Besides 2D flows, rigorous proof for the *correct strategy* can only be given for the quasi-3D boundary layers on infinite wings (Mack, 1977): the dimensional frequency ω^* and spanwise wavenumber β^* must be fixed, i.e. independent of s, during the evolution of a normal mode. This requirement is grossly violated by the envelope method which selects the mode with the largest growth rate at every station s_n. Some commercial airplane companies use the more sophisticated and computationally more demanding $N_{TS} - N_{CF}$ method. N_{CF} is computed for fixed $\omega^* = 0$ from the envelope of amplitude growth curves for various fixed β^*, and is consistent with the physical requirements. N_{TS} is obtained from the growth curves for various fixed frequencies ω^* while the wavenumber vector $\mathbf{k} = (\alpha_r^*, \beta^*)$ is aligned with the edge streamline. This procedure allows β^* to vary with s and ω^*, except in 2D flows where it is strictly justified. The deviation from the physics may be relatively small for wings where TS instability occurs in a region with small curvature of the edge streamline. Unsteady crossflow modes are ignored in the $N_{TS} - N_{CF}$ method, although their growth rates exceed those of steady CF vortices. The focus on steady modes appears justified for the low-disturbance environment in flight, where roughness is regarded as the dominant source of crossflow instability. The lower values of N_{CF} obtained from correlation with wind-tunnel data (as in the ATTAS tests, see Schrauf *et al.*, 1992) is likely caused by the increased levels of unsteady CF modes.

In fully 3D boundary layers where the flow field depends on all three spatial variables, we have no rigorous theoretical basis to judge the various procedures for computing N factors, nor are there accurate experimental or computational data for comparison of different strategies. Experience with 3D bodies (e.g. Schwoerke, 1993) has shown that the transition front is not associated with a single value of N. Also for wings, the e^N method deteriorates in regions of stronger spanwise variation of the boundary layer, e.g. near the engines. These spanwise variations are also neglected in the current PSE method. The attempt to retrieve lost physics by heuristic strategies is understandable, because the designer has to cope with these flows. However, there is a definitive need for improvements in this area. Such improvement requires first of all additional knowledge of the boundary layer: the spanwise variation, which can be obtained with a 3D boundary-layer code. Second, it is necessary to prescribe the initial disturbances along a line, not just in a single point. Tracking the evolution of this disturbance in the boundary layer is possible by solving the PSE appropriately in combination with the irrotationality condition (Mack, 1977). The computational demand, however, is obviously higher than for a single amplitude-growth curve.

[3] Fully 3D boundary layers can be correctly analyzed by a more elaborate PSE code.

Finally, there is the issue of "options". Compressibility has a minor effect on N_{CF} but reduces N_{TS} significantly for the Mach numbers of commercial flight. The N_{TS} calculation ignores the shift of the maximum amplification of TS waves to different wave angles that occurs at higher Ma. For the ATTAS flight tests, N_{TS} shows a clear decrease as the Mach number increases (Schrauf, 1994). There is no physical justification to prefer the N_{TS} factors for incompressible flow, because they are "more consistent" with the illusion of a convenient "universal N factor".

The proper account for curvature in N factor computations has stirred controversial discussions. Judging from the PSE analysis, only surface curvature has an effect, that hardly changes TS waves, but strongly stabilizes CF vortices on convex surfaces. The inherent streamwise changes in the boundary-layer flow over a convex surface partly compensate the effect of curvature alone. The use of LST with surface curvature does not permit accounting for the streamwise changes and provides unexpectedly low values of N_{CF} or may suppress CF instability completely.

We face here another opportunity to improve transition predictions from two sides: by research to clarify the fuzzy approach to fully 3D boundary layers and by adhering to the physically (most) justified methods to link disturbance growth to transition even if they are not as fast and convenient as one would like them to be.

Nonlinear PSE studies

All operational definitions of transition by changes in C_f or St, simultaneous growth of modes, spectral broadening, and others rely on the nonlinearity of this process. The PSE provide a relatively inexpensive means for tracking this nonlinear process, but require the specification of proper initial and boundary conditions - a difficult task.

The transition process is forced by environmental disturbances. These disturbances affect the flow through the boundaries of the computational domain either in the form of initial disturbances at the starting position of the marching procedure, or through the boundary conditions in the free stream and at the wall. The disturbances do not directly enter the boundary layer, but are filtered through the mechanisms of receptivity. In a given environment, these mechanisms in essence determine the streamwise and spanwise length scales, time scales, and amplitudes of internal disturbances which may harmlessly linger around or participate in the early or later stages of the transition process. Key to an efficient PSE analysis is the selection of a few "most dangerous" ingredients considering the disturbance environment and the selective mechanisms of receptivity, primary growth, and nonlinear secondary instability.

The environment is given at best by the turbulence level or average roughness, without the important spectral characteristics in the range of relevant scales. The atmospheric disturbance environment is largely unknown. The various receptivities, e.g. to free-stream turbulence, are still too incompletely known for deter-

mining the internal disturbances by quantitative analysis. To overcome these obstacles, we have resorted to "input models" for different transition scenarios. Most parameters of these models are derived from the primary and secondary stability characteristics of the specific flow, and few others such as the receptivity coefficients are fixed by correlation with experiments. The models provide the input into the relevant growth mechanisms, including both instabilities and transient growth (Butler & Farrel, 1992; Herbert & Lin, 1993).

Transition on a turbine blade

To explore the nonlinear modeling capabilities, we have studied transition in various flows where experimental data are available (Herbert *et al.*, 1993), including the flow over heated flat (Sohn & Reshotko, 1991) or curved plates (Wang *et al.*, 1985; Kim & Simon, 1991), and over the stator blade of a turbine (Dring *et al.*, 1986) at turbulence levels Tu between 0.5 and 2.4%. K-type transition is most likely at these turbulence levels. Strong secondary instability of TS waves with respect to low-frequency spanwise modulations appears at TS amplitudes in excess of 1%. Given the turbulence level and receptivity coefficient, and assuming equal receptivity in the band of relevant frequencies, this information is sufficient to select the TS frequency from the known amplitude growth curves as the highest frequency that achieves growth beyond the threshold. The spanwise modulation is provided by a steady Klebanoff mode or Görtler vortex of a fixed nondimensional wavenumber consistent with observations of Kendall (1991) and in the range of strong secondary instability. The initial amplitude of this vortex is lower than the TS amplitude A_0 at onset of instability and is less critical. The TS receptivity was estimated to provide $A_0 = 0.3\%$ at $Tu = 0.4\%$. After minor parameter changes, a test run for the conditions of Sohn & Reshotko at $Tu = 0.4\%$ showed the rise of St at the observed location, and hence confirmed the validity of this simple model. For fixed receptivity coefficients, all initial amplitudes increase linearly with the turbulence level. With the built-in decrease of the frequency, and earlier onset of instability at a higher initial amplitude, additional runs with the same input model provided results in good agreement with the observed transition locations (minimum of St) at turbulence levels up to $Tu = 2.4\%$. Similar agreement was found with the measurements on concave and convex heated plates at $Tu \approx 0.6\%$. Weak convex curvature stabilizes the longitudinal vortex and shifts x_t slightly downstream. Kim & Simon (1991) attributed the early rise of St on concave walls to bypass transition. The PSE results show instead that the concave curvature causes strong amplification of the longitudinal vortex by Görtler instability. The nonlinear Görtler vortex reaches high amplitudes and strongly affects the heat transfer without participation of the TS wave and before breakdown.

For the blade of the annular stator used by Dring *et al.* (1986), the basic flow at mid span was obtained sequentially with a 2D panel code and the boundary-layer code WING after extension to the heated-wall boundary conditions. After

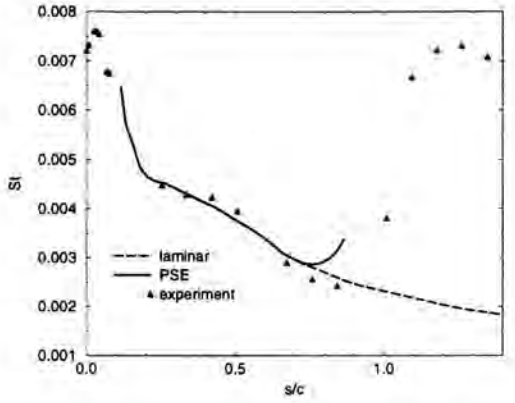

Figure 1: Variation of the Stanton number St with the arclength s/c along a turbine stator blade, where c is the chord length.

converting scales and performing a linear stability analysis of the flow, the input model of the previous cases was adapted using the established rules. The PSE results for the variation of the Stanton number along the arclength s/c on the suction side are shown in Fig. 1 together with the laminar values and experimental data.

The PSE run provides a minimum of St at $s/c = 0.764$, somewhat lower than the experimental value. We certainly can speculate on flaws of our input model, e.g. insufficient account for changes in the turbulence through the passage. However, we see the main reason in the deviation between computed and actual laminar flow in the experiments, which is caused by three-dimensionality and the use of the lowest boundary-layer approximation in the narrow passage. Similar calculations for the pressure side show the observed increase in St as a result of strong nonlinear Görtler vortices.

Transition on swept wings

Applications of the nonlinear PSE analysis to the 3D flows over swept wings have required extensive preparations to overcome the lack of knowledge on the variety of transition mechanisms and the disturbance environment in the absence of microscopic experiments and with restricted access to flight-test data. These efforts have focused on TS-dominated and CF-dominated transition as the most common types observed.

For TS-dominated cases, we can lean on the results for 2D flows, and track the known mechanisms for increasing sweep angles. In essence, all secondary instability mechanisms (Herbert, 1988) carry over to 3D boundary layers. Owing to the loss of symmetry across the edge streamline, the "left" and "right"

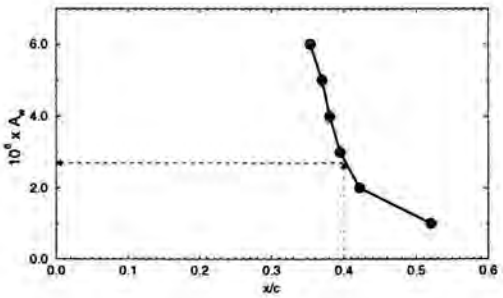

Figure 2: Variation of the transition location with the disturbance level A_w for subharmonic resonance in ATTAS test case B.

subharmonic waves initially show different characteristics, but synchronize and grow simultaneously as the growing TS wave strengthens the parametric instability. Combination resonance with weak detuning between left and right wave is slightly stronger than subharmonic resonance, but this small effect does not warrant introducing the additional detuning parameter for practical purpose. Fundamental, or K-type, resonance occurs primarily in combination with longitudinal vortices. As the sweep angle increases, the Klebanoff modes may be amplified by CF instability (Herbert & Lin, 1993). The amplification characteristics of the secondary instabilities are sufficiently similar to the 2D case to obtain rough estimates from results for 2D flows.

With the basic transition mechanisms known, we can construct input models for the PSE analysis. Receptivity coefficients are of little use without information on the flight environment. However, the initial amplitudes can be directly obtained through evaluation of flight tests. Using the database of the ATTAS flight tests (Schrauf *et al.*, 1992), we have performed systematic parametric studies of the TS-dominated mechanisms for test case A with moderate and case B with insignificant CF instability (Schrauf *et al.*, 1995) to identify the most dangerous parameter combinations. We assume that noise and free-stream turbulence cause a common disturbance level of amplitude A_w for all wave components of the input model, and surface roughness independently provides vortices at the common level A_v. From PSE runs with fixed A_v, we obtain the variation of the transition location with A_w shown in Fig. 2 for case B.

In-flight infrared photographs exhibit transition near 40% chord, which we attribute to an amplitude level A_w of $2 - 3 \cdot 10^{-6}$. Similar levels of A_w in the range of $1 - 3 \cdot 10^{-6}$ lead to K-type or subharmonic transition in case A, where transition is observed at 17% chord. The CF amplitude in the K-type model has been varied between $A_v = 10^{-8}$ and $A_v = 10^{-6}$, but causes only a small shift of less than 1% chord. Other test cases must be analyzed to extract the strength A_v of CF modes. It would also be desirable to evaluate independent flight-test data to cross-check the range of A_w. So far, we can only resort to the e^N method

to support the broader validity of our result: with $N_{TS} = 9$, we obtain transition when the TS wave reaches an amplitude of $2 \cdot 10^{-6} \cdot e^9$, or 1.6%, which is well in the proper range.

Our earlier work on CF-dominated transition mechanisms for canonical flows like swept Hiemenz flow has been supported by the experiments of Bippes and co-workers (e.g. Müller & Bippes, 1988). Flows over swept wings are different, though, since the significant growth of the boundary layer causes the range of unstable steady and unsteady CF modes to change from high wavenumbers near the leading edge to much lower wavenumbers downstream. The analysis of the CF-dominated ATTAS flight test C has not yet progressed beyond a catalogue of interesting nonlinear interactions (Herbert & Schrauf, 1996). Single low-wavenumber CF modes can nonlinearly grow to large, slowly varying saturation amplitudes similar to results for swept Hiemenz flow. The saturation amplitudes depend weakly on the initial amplitudes. Single modes of high wavenumbers decay after reaching a maximum amplitude, leaving behind a mean-flow distortion that slowly decays. Traveling CF modes grow stronger than steady modes, and at large amplitude exert damping on steady modes, as observed by Bippes. We also found that steady modes at large amplitudes exert damping on traveling modes. The mean-flow distortion receives the largest contribution from the mode with the largest amplitude, and is key to saturation as well as the modification of the growth rates of other modes, including TS waves.

The infrared photograph for case C shows the characteristic zig-zag front of transition in the range between 15% and 28% chord. The stationary wedges suggest that transition is associated with roughness-induced steady CF modes. Crouch (1994) finds that receptivity to distributed roughness introduces a broad band of steady CF modes. In contrast to the procedure for TS waves, it is impossible to select a single steady CF mode from the linear $n(x;\beta)$ diagram for the input model, because the nonlinear growth is significantly different. Already obvious for single modes, the differences increase by interactions of multiple modes.

Fig. 3 shows the development initiated by the steady modes $(0,m)$ of wavenumbers $\beta_m = m\beta$ with $\beta = 600$ m^{-1}, $m = 5,\cdots 12$, and $A_v = 2 \cdot 10^{-6}$. Clearly, none of the modes decay as predicted by linear analysis. Self-interaction of the modes creates a strong mean-flow distortion $(0,0)$ which governs the saturation process. Interaction of the high-wavenumber components forces the low-wavenumber components with $m = 1,\cdots,4$ at the difference of their wavenumbers. These modes grow unexpectedly strong because of nonlinear forcing in combination with instability further downstream. In turn, the low-wavenumber modes maintain the high-wavenumber modes as harmonics and forcing at the sum of their wavenumbers. At $x/c \approx 0.15$, the mode with $m = 3$ dominates, although its initial amplitude was zero. At the end of the run, the mode $(0,1)$ with wavenumber $\beta = 600$ m^{-1} has the largest amplitude although linear analysis indicates negligible growth, as shown by the dashed line in Fig. 3.

The deeper reason for the evolution of CF modes as in Fig. 3 is the shift of the unstable region toward lower wavenumbers in flows with strongly growing

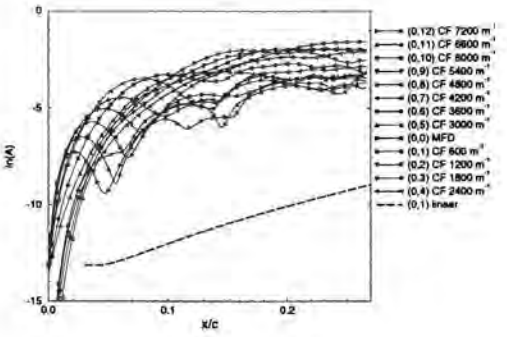

Figure 3: Interaction of steady CF vortices of different wavenumbers with $A_v = 2 \cdot 10^{-6}$. The linear growth of mode $(0, 1)$ is given by the dashed line.

boundary-layer thickness. The results suggest that the creation of strong CF vortices by the combination of nonlinear forcing with weak unstable growth can lead to CF-dominated transition at relatively small limiting N factors and at unexpected locations. For practical applications, it will be necessary to account for these nonlinear effects without repeating the tedious computation and interpretation of the results. With the insight and quantitative information we have gained through our studies, it appears possible to develop a relatively simple model to estimate saturation phenomena and nonlinear mode interactions on the basis of the known linear amplitude-growth curves. The development of this model, and the analysis of the high-frequency breakdown process will be the next steps in our studies of ATTAS test case C.

Conclusions

In our efforts to improve prediction methods for the transition location, we have found that various groups must be cooperatively involved. Researchers should provide a solid basis for the analysis of fully 3D boundary layers, the developers of CFD software should improve the quality of their codes, and practising engineers should improve the quality of the input data and favour the physically best justified approach. Transition is a synergetic process and requires care at every step of the analysis. Linear amplitude growth curves and N factors are an important ingredient of the transition process, but fail in some situations where nonlinearity causes significant effects. Progress in the understanding of receptivity and more detailed documentation of the disturbance environment will enhance the capabilities to trace the transition process from its beginnings without employing questionable concepts or requiring undue empiricism. It will be unavoidable, though, to apply intelligence and criticism to prevent failures, and to employ existing and future tools for transition analysis to fully benefit engineering design.

Acknowledgement

The development and evaluation of the PSE method has been supported by the Air Force Office of Scientific Research. The codes LISA and COPS for compressible PSE analysis in curvilinear coordinates have been developed in cooperation with G. K. Stuckert, N. Lin, S. Huang, and D. C. Hill. This work has been supported by Wright Laboratories, NASA Ames Research Center, and NASA Lewis Research Center. The ongoing analysis of the ATTAS flight tests is conducted in cooperation with G. Schrauf, Daimler-Benz Aerospace Airbus GmbH, and is supported by the technology program RaWiD.

References

Arnal, D. 1984 – Description and prediction of transition in two-dimensional, incompressible flow. In *Special Course on Stability and Transition of Laminar Flow*, pp. 2/1–71. AGARD Report 709.

Bertolotti, F.P. 1991 – *Linear and nonlinear stability of boundary layers with streamwise varying properties.* PhD thesis, The Ohio State University, Columbus, Ohio.

Butler, K.M. & Farrell, B.F. 1992 – Optimal perturbations and streak spacing in wall-bounded turbulent shear flow. *Phys. Fluids A*, **5**, 774–777.

Crouch, J.D. 1994 – Distributed excitation of cross-flow vortices in three-dimensional boundary layers. In Kobayashi, R., editor, *Laminar-Turbulent Transition*, pp. 499–506. Springer Verlag.

Dring, R.P., Blair, M.F., Joslyn, H.D., Power, G.D. & Verdon, J.M. 1986 – The effects of inlet turbulence and rotor/stator interactions on the aerodynamics and heat transfer of a large-scale rotating turbine model. NASA CR 4079.

Elsholz, E. 1988 – Ein inverses LISW-Grenzschicht-Verfahren. MBB-Report TE-1681.

Herbert, Th. 1988 – Secondary instability of boundary layers. *Ann. Rev. Fluid Mech.*, **20**, 487–526.

Herbert, Th. 1991 – Boundary-layer transition – analysis and prediction revisited. AIAA Paper 91-0737.

Herbert, Th. 1994 – Parabolized stability equations. In *Special Course on Progress in Transition Modelling*, pp. 4/1–34. AGARD Report 793.

Herbert, Th. & Bertolotti, F.P. 1987 – Stability analysis of nonparallel boundary layers. *Bull. Am. Phys. Soc.* **32**, 2079.

Herbert, Th. & Lin, N. 1993 – Studies on boundary-layer receptivity with parabolized stability equations. AIAA Paper 93-3053.

Herbert, Th. & Schrauf, G. 1996 – Crossflow-dominated transition in flight tests. AIAA Paper 96-0185. Submitted to *AIAA J.*

Herbert, Th., Stuckert, G.K. & Esfahanian, V. 1993 – Effects of free-stream turbulence on boundary-layer transition. AIAA Paper 93-0488.

Kaups, K. & Cebeci, T. 1977 – Compressible laminar boundary layers with suction on swept and tapered wings. *J. Aircraft* **14**, 661–667.

Kendall, J.M. 1991 – Studies on laminar boundary layer receptivity to freestream turbulence near a leading edge. In Reda, D. C., Reed, H. L., & Kobayashi, R., editors, *Boundary Layer Stability and Transition to Turbulence*, volume 114, pp. 23–30. ASME FED.

Kim, J. & Simon, T.W. 1991 – Free-stream turbulence and concave curvature effects on heated, transitional boundary layers. Technical report, NASA CR 187150.

Mack, L.M. 1977 – Transition prediction and linear stability theory. In *Laminar-Turbulent Transition*, pp. 1/1–22. AGARD CP 224.

Malik, M.R. 1982 – COSAL - A black box stability analysis code for transition prediction in three-dimensional boundary layers. NASA CR-165925.

Müller, B. & Bippes, H. 1988 – Experimental study of instability modes in a three-dimensional boundary layer. In *Fluid Dynamics of Three-Dimensional Turbulent Shear Flows*. AGARD CP 438.

Savill, A.M. 1992 – A synthesis of T3 test case predictions. In Pironneau, O., Rodi, W., Ryhmig, I.L., Savill, A.M., and Truong, T.V., editors, *Numerical Simulation of Unsteady Flows and Transition to Turbulence*, pp. 404–442. Cambridge University Press.

Schrauf, G. 1994 – Transition prediction using different linear stability analysis strategies. AIAA Paper 94-1848. Submitted to *AIAA J. Aircraft.*

Schrauf, G., Bieler, H. & Thiede, P. 1992 – Transition prediction – the Deutsche Airbus view. In *First European Forum on Laminar Flow Technology.* DGLR-Report 92-06.

Schrauf, G., Herbert, Th. & Stuckert, G.K. 1995 – Evaluation of transition in flight tests using nonlinear PSE analysis. AIAA Paper 95-1801. To appear in *AIAA J. Aircraft.*

Schwoerke, S. 1993 – Quiet tunnel results and analysis for various forebody shapes at Mach 3.5. Hypersonics Symposium, Wright-Patterson AFB.

Smith, A.M.O. & Gamberoni, A.H. 1956 – Transition, pressure gradient and stability theory. Report ES26388, Douglas Aircraft Co.

Sohn, K.H. & Reshotko, E. 1991 – Experimental study of boundary layer transition with elevated freestream turbulence on a heated flat plate. NASA TM 187068.

Stuckert, G., Herbert, Th. & Esfahanian, V. 1993 – Stability and transition on swept wings. AIAA Paper 93-0078.

Van Ingen, J.L. 1956 – A suggested semi-empirical method for the calculation of the boundary layer transition region. Report VTH 74, Dept. Aero. Eng., Delft University of Technology.

Wang, T., Simon, T.W. & Buddhavarapu, J. 1985 – An experimental investigation of curvature and freestream turbulence effects on heat transfer and fluid mechanics in transitional boundary layer flows. NASA Report NAG 3-286.

Author's address

DynaFlow, Inc.
3040 Riverside Dr.
Columbus, Ohio 43221, USA
herbert@dynaflow.com

and

The Ohio State University
Department of Mechanical Engineering
Columbus, OH 43210-1107, USA
tht@signac.eng.ohio-state.edu

Session 5:
Transition Modelling

P. R. Spalart

Topics in Industrial Viscous Flow Calculations

Abstract

Progress in Navier-Stokes methods, both in terms of accuracy and flow complexity, has made it unacceptable to ignore the presence of laminar regions in the boundary layers. After some examples we examine the behaviour of current turbulence models in three flow modules, such as a transitional separation bubble, that put laminar and turbulent regions in forced contact. This behaviour is found to be correct, but only qualitatively. The need for a robust "Turbulence Subsystem" that is insensitive to the type of grid, and functions with almost no user input or scrutiny, is shown to conflict with the desire to resolve the finer features of Transitional Boundary Layers in Aeronautics.

Introduction

Viscous flow calculations based on the Reynolds-Averaged Navier-Stokes (RANS) equations with simple turbulence models have matured and will, from now on, contribute at least to the high-speed shape of any new airliner. The impact of Computational Fluid Dynamics (CFD) on high-lift system design is much weaker, but aggressive ongoing efforts in grid generation and algorithms mean that those responsible for the "Turbulence Subsystem" of CFD must now foresee the requirements of three-dimensional (3D), viscous, high-lift CFD.

By far the easier use of a turbulence model, whether it is algebraic or based on transport equations, is to have the model active everywhere in the shear layers. On a conventional airliner in high-speed flight, the laminar regions are small and a "Fully Turbulent" (FT) treatment is justified. The only certain laminar patches are on the nose and the engine nacelle lips. The difference between a fully turbulent solution and one with correct laminar patches is only a few percent of the drag; more importantly, the difference is probably similar for different airplane models. At wind-tunnel Reynolds numbers the difference grows, especially if portions of attachment lines are laminar. The effect cannot be neglected, compared with typical drag guarantees. Airplanes with Laminar-Flow Control (LFC) of course require detailed control of the turbulence in CFD solutions. High-lift systems also allow numerous possible laminar patches, since many stagnation points are present, and small leading-edge radii on flap elements lower the attachment-line Reynolds numbers. The effect is weaker on skin friction than on lift and pressure drag, because of separation; a classical example is the "drag crisis" of a 2D circular cylinder.

For these reasons, the Turbulence Subsystem of any mature high-lift CFD code will have to recognize laminar patches. In this paper we do not discuss the prediction of transition internal to the boundary layer, such as caused by Tollmien-Schlichting or cross-flow instabilities. Our approach to RANS calculations is that a distinct subsystem predicts that type of transition, and then "instructs" the turbulence model to become active. We have studied how well the model responds to these instructions, as well as situations in which the model "over-rides" the instructions from the transition-prediction module. An example is a boundary layer which transitions because it is touched by an already turbulent shear layer flowing next to it.

Transition has long been incorporated to some extent in boundary-layer codes or Navier-Stokes codes with simple structured grids. Given a transition point (in 2D) or line (in 3D), an algebraic turbulence model is simply disabled on grid lines upstream of transition. Similar treatments have been made with transport-equation turbulence models, often by disabling the production terms. The method is zonal. Some codes incorporate "ramping up" of the eddy viscosity over a few streamwise grid stations. Two motivations for ramps are to avoid discontinuities (which benefits the numerics), and to improve the realism. Realism demands a gradual rise of the skin friction, and often an overshoot over the eventual turbulent value. Much of the research and implementation work on the transition zone has been of that nature, narrowly directed at boundary-layer codes, and not readily applicable to even structured-grid RANS codes, especially in 3D.

Zonal methods quickly become unmanageable when complex geometries such as high-lift systems are immersed in the now common multi-block or unstructured grids. Any logic that uses grid lines and blocks violates the physics when shear layers cross grid boundaries. As an example, high-lift airfoils depend on the interaction between the main-wing-element wake and the flap. It would be unacceptable to have the flap grid block "zero out" the turbulence in that wake just because the boundary layer on the flap has not achieved internal transition. This led us to constraining but clear policies for our viscous codes: no zonal information enters the turbulence model; the transition subsystem may instruct the model to transition to turbulence, but it may not disable the model. The result is that the turbulence model is left in control of phenomena that are transitional, although most would be termed "by-pass transition". Conversely, the model has no competence for internal transition in boundary layers below a quiet freestream (it has no sensitivity to pressure gradient, cross-flow, or even suction); by itself, it remains at zero in any attached boundary layer. We do expect the transition-prediction subsystem to remain zonal and "boundary-layer oriented"; there are compelling physical reasons for that, but the logistical difficulties are substantial in 3D.

Since the inception of the Spalart-Allmaras (S-A) one-equation turbulence model, we have explored several transitional phenomena through model problems or local analysis of solutions (Spalart & Allmaras, 1994, and Appendix). An example is the propagation of turbulence into freestream fluid, the "entrainment"

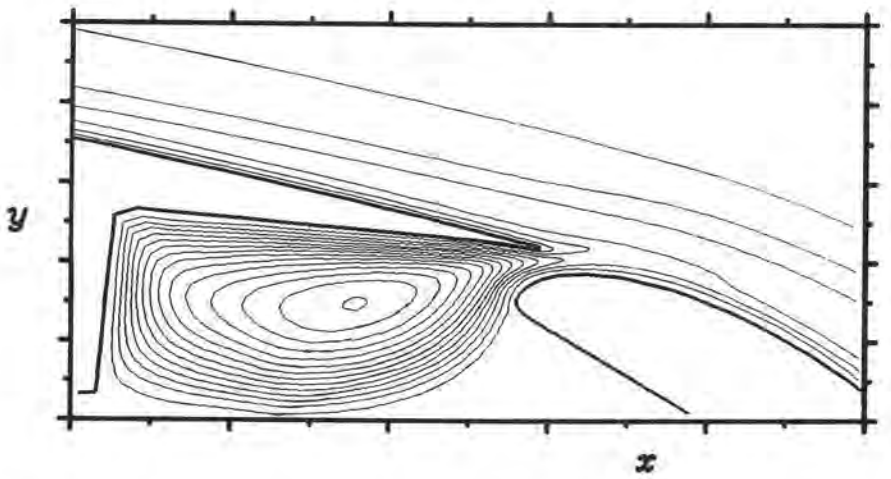

Figure 1: Eddy-viscosity contours in the cove and flap region of an airfoil.

problem (Cazalbou *et al.*, 1994). Another is the transition of a laminar boundary layer as it makes contact with an already turbulent shear layer. Fig. 1 was provided by Drs. Kusunose and Cao of Boeing (1994) and shows the flow details at the leading edge of a high-lift flap. The eddy viscosity on the upper surface of the flap rises away from zero, not due to the usual S-A "trip term", but because of diffusion from the turbulent region in the cove of the main airfoil (the lower flap boundary layer remains laminar). A more subtle effect the model would not reproduce is the accelerated transition caused by pressure fluctuations *without* contact of the vortical regions. Another issue is the extent of the transition region, the first of our three model problems.

Transition as simulated by the S-A model

Few transport turbulence models, particularly two-equation and more complex models, are equipped for transition control; many encounter problems with spurious "turbulence" outside the boundary layer, near the stagnation point. The S-A model may be the first designed with laminar regions in mind. A separate method predicts the transition line, and the "trip terms" activate the model at that line (upstream of the trip, the eddy viscosity is much smaller than the molecular viscosity, zero if possible).

We now examine transition in the S-A model, using results obtained for Boeing by Drs. Bassina, Shur, Strelets and Travin of the Russian Scientific Center "Applied Chemistry" in St. Petersburg (Shur *et al.*, 1995). A flat-plate boundary layer is calculated, and the standard S-A trip placed at a streamwise Reynolds number $R_x \equiv xU_\infty/\nu$ equal to 10^6 ($R_\theta = 664$). Here x is the streamwise coordinate, U_∞ the edge velocity, and ν the kinematic viscosity. Fig. 2 shows the flow

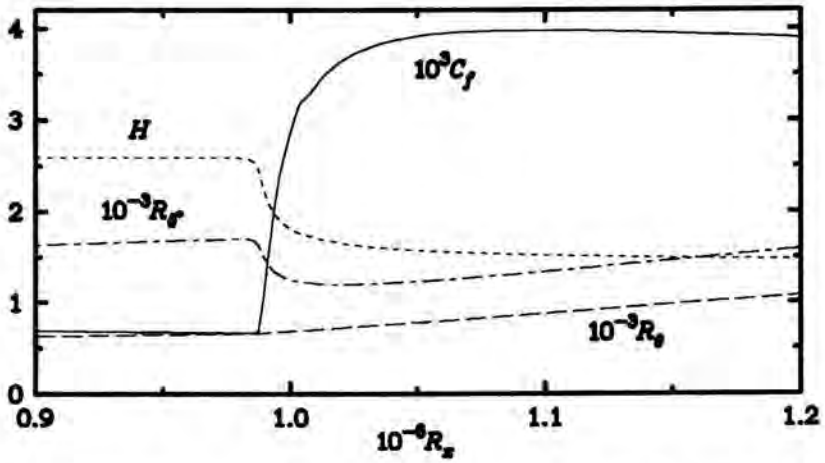

Figure 2: Boundary layer with S-A model "tripped" at $R_x = 10^6$. Note that $R_\delta \approx 5500$ at $R_x = 10^6$.

evolution in the streamwise direction. The grid was fine enough ($R_{\Delta x} = 2000$) for the results to be grid-independent. R_θ increases smoothly, whereas R_{δ^*} and H drop steeply at transition. The skin-friction coefficient C_f rises from 0.441 10^{-3} to 4. 10^{-3} starting near $R_x = 0.98\ 10^6$, which is about 4 boundary-layer thicknesses upstream of the trip "point". This anticipation is controlled by the constant c_{t2}, which is not critical. Nevertheless, users may want to shift the trip downstream by 4δ if they want to accurately locate the beginning of the C_f rise. Almost all the rise has occurred by $R_x = 1.02\ 10^6$, therefore, it takes about 8δ. Transition is complete roughly at $R_x = 1.1\ 10^6$.

Fig. 3 shows velocity and eddy-viscosity profiles at three x stations. At $R_x = 0.965\ 10^6$, the trip term has slightly raised the eddy viscosity $\tilde{\nu}$, but the velocity profile is unaffected. At $R_x = 1.045\ 10^6$ the eddy-viscosity profile is full and the velocity profile turbulent. The usual law of the wall $U^+(y^+)$ is also rapidly established, from the wall up (not shown).

Calculations were conducted with larger grid spacings Δx, up to $R_{\Delta x} = 80,000$, more typical of Navier-Stokes practice. They yield values of g_t as low as 0.01 (g_t is an auxiliary function in the S-A model, and its value with a fine grid is 0.1), and are not grid-independent. They produce a more extended transition region but no numerical difficulties, and little effect on the virtual origin of the turbulent layer. The trip system is quite robust.

Completing transition within 8 boundary-layer thicknesses is not typical of natural transition in zero pressure gradient. The normal extent is about 80δ (Narasimha, 1985). Thus, the model behaves much like a physically tripped flow, or one with strong adverse pressure gradient. The shape of the C_f is also inaccurate in that it has a steep initial rise, and does not overshoot the turbulent C_f curve. This is not as important as the transition-zone length. We now show that these behaviours will not be controlled simply by altering the trip term.

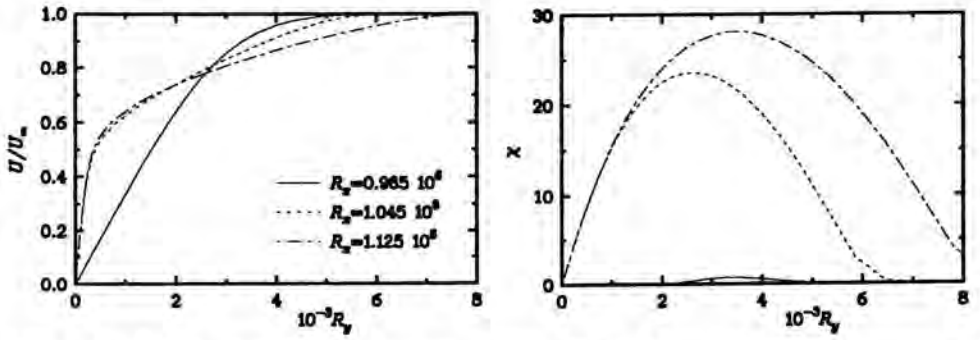

Figure 3: Profiles in a boundary layer "tripped" at $R_x = 10^6$. Left, velocity; right, eddy viscosity. $R_y \equiv yU_\infty/\nu$ and $\chi \equiv \tilde{\nu}/\nu$.

When the S-A eddy viscosity $\tilde{\nu}$ is small compared with $U_\infty\delta$, it obeys the linearized S-A equation $D\tilde{\nu}/Dt = c_{b1}S\tilde{\nu}$ where S is the shear rate. In a Blasius boundary layer at $y = \delta/3$ this leads to exponential growth in x at a rate of roughly $0.3/\delta$ (recall that $c_{b1} = 0.1355$). As a result, in a distance of 8δ the amplitude ratio is over 10, and transition ends as the nonlinear terms come into play. Reducing the "trip constant" c_{t1} by a factor of 100 delays transition, but only by about 10δ, and makes the solutions more vulnerable to numerical errors. We expect other models, such as the ν_{t92} model of Secundov (Shur *et al.*, 1995), to face similar conflicts.

Elaborate "transition-zone models" are found in the literature. However, they use the distance from the leading edge, or the boundary-layer thickness, and of course the flow direction. The thickness cannot be reliably calculated in general grids, and its use is against the locality requirements we placed on the S-A model. The flow direction may also change across the shear layer. For these reasons, we have been unable to incorporate these models.

In summary the transition-control feature of the S-A model (with a separate prediction method) is used routinely in 2D (Kusunose & Cao, 1994) and will be in 3D, especially if its cost can be reduced (the cost is currently $O(N^4)$ operations, in a grid with N^3 points). Similar devices will probably be a standard feature of widely-used models for thorough studies of viscous flows. However, there was no attempt to obtain the correct length for the transition region; it is regarded as a "higher-order" effect.

Lateral propagation of turbulence in a boundary layer

With a transport-equation model, "turbulence" follows streamlines, where "turbulence" means eddy viscosity and associated variables such as k, ϵ, or ω. For example, if the root region of a swept wing is turbulent, turbulence propagates along the attachment line and the whole wing is turbulent without any further tripping. This is qualitatively correct.

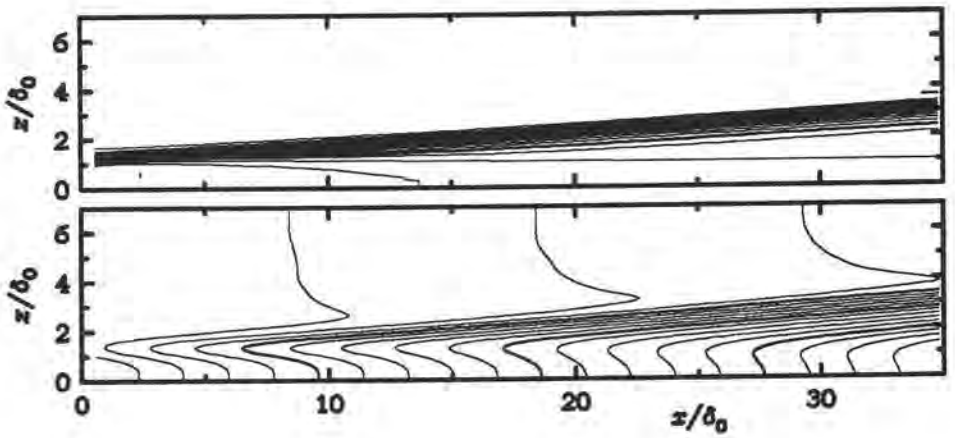

Figure 4: Plan view of a turbulent wedge in a boundary layer. Upper graph: skin-friction coefficient C_f; lower graph: momentum thickness θ.

Here we address a weaker type of propagation than directly along streamlines. When a laminar and a turbulent boundary layer are side by side, the turbulence propagates laterally. A typical situation is an LFC wing, on which turbulence can be injected locally by the fuselage boundary layer, or by the engine strut, creating a "turbulent wedge". We wish to know the wedge angle relative to the streamlines, and the eddy viscosity pattern at the laminar-turbulent interface. We understand the propagation of simple models into shear-free regions (Cazalbou *et al.*, 1994), but the propagation into a boundary layer should be different. All the calculations and supporting studies were performed for Boeing under Dr. A.N. Secundov at the Central Institute of Aviation Motors in Moscow, by Drs. V.Ye. Kozlov and D.A. Lubimov.

Calculations were conducted at several levels of complexity, regarding the slender-flow approximations. They gave close answers; the figures are taken from a solution of the 3D parabolized Navier-Stokes equations, in which the spanwise velocity and pressure variations were not suppressed. Several turbulence models were also applied. Grid-refinement studies demonstrated grid convergence. The flow had no mean pressure gradient, and the inflow Reynolds number was $R_\theta = 550$. The S-A model is used in the figures.

Fig. 4 shows plan views of the flow. The skin-friction coefficient C_f is much higher in the lower region, which is turbulent. There the momentum thickness θ grows much more rapidly, and the shape factor H (not shown) drops from 2.6 to 1.5, as expected. On the other hand the wedge angle is only about 3.6° compared with at least 8° in experiments. It appears that the model fails to reproduce the "growth by destabilization" described by Gad-el-Hak *et al.* (1981). The lateral propagation is faster than the vertical propagation, which makes an angle of only about 1°. Thus, lateral propagation is enhanced by the shear, which enters the production term, but remains far below the actual destabilization effect. The

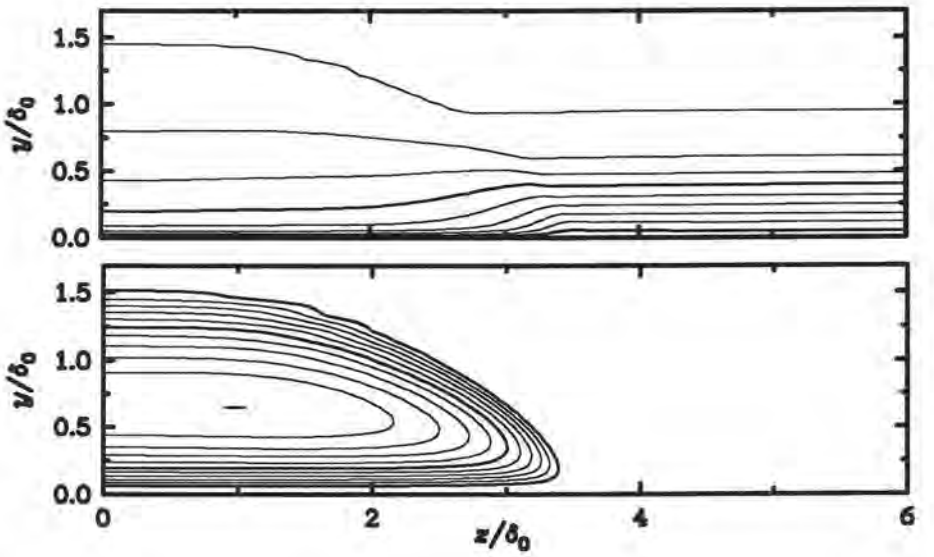

Figure 5: Contours at the edge of a turbulent wedge. Upper graph, velocity, levels $U/U_\infty = 0.095$ to 0.995 by 0.09; lower graph, eddy viscosity.

wedge angle in the model (3.6°) is somewhat larger than the thermal wedge angle (2°), which Gad-el-Hak *et al.* used to estimate pure diffusion effects. We believe the calculated wedge angle would also fail to respond to pressure gradients, because the model has little sensitivity to the second derivative of the velocity profile.

Fig. 5 shows contours of streamwise velocity and eddy viscosity in a transverse plane at the outflow boundary, $x/\delta_0 = 35$. The turbulent velocity reflects the transfer of momentum from the upper part to the lower part of the layer, as in Fig. 3. The eddy viscosity is biased towards the wall, where the shear rate is higher, leading to higher production. In practice, at higher Reynolds numbers, the ratio of turbulent to laminar thickness is larger than it is here; calculations with such ratios produced marginally lower wedge angles.

The ν_{t92} (Shur *et al.*, 1995) and SST (Menter, 1994) turbulence models produced wedge angles marginally lower than the S-A model. This suggests that simple models constrained to give about the same rate of diffusion normal to the wall end up giving about the same rate of lateral propagation. We may have to be content with angles well below 4°; unfortunately this is not a conservative prediction (the skin friction on a wing is slightly under-predicted). Also note that grids used in industrial practice are much too coarse in the spanwise direction to resolve the structure shown in Fig. 4. As a result, the lateral propagation may well be suppressed further; indeed, we found that calculations on coarser grids produced slightly smaller wedge angles.

Unsteady calculations past a circular cylinder

The group of Drs. Strelets, Shur and Travin, in St. Petersburg, is exercising turbulence models in separated flows under Boeing contract. The unsteady solutions we report on here are preliminary, because the grid-refinement study is still under way. A complete analysis will be presented elsewhere (Shur *et al.*, 1996). Steady solutions were considered for backward- and forward-facing steps and rather successful especially for the SST model (Shur *et al.*, 1995). In contrast, for the circular cylinder and other bluff bodies, time-dependent solutions with vortex shedding are appealing and have been claimed to be vastly more accurate than steady RANS solutions (Franke & Rodi, 1991; Johansson, Davidson & Olsson, 1993; Durbin, 1995). Predictably, they are much less sensitive to the turbulence model. At first sight this appears to be a costly but well-defined step forward. In reality, even before considering transition (all three studies concerned bodies with sharp corners) the situation is far from simple, as many different computing policies could be justified.

First, it is legitimate to produce a steady (possibly unstable) symmetric solution; the "perfect" turbulence model would give the perfect average answer. With little or no separation, this steady solution is probably the only one, but we cannot predict at which amount of separation it loses stability (Franke & Rodi even obtained stable steady solutions around a square cylinder, but then only with wall functions). Second, one could produce symmetric but time-accurate solutions; these could be unsteady in a "varicose" mode. In our opinion they have little physical value, but they may well show up if researchers rely on symmetry alone (as opposed to more obscure means such as long time steps) to obtain steadiness. Third, we have 2D shedding solutions as found in the literature. Fourth, if one argues that Reynolds-averaging in time is naive, then so is Reynolds-averaging in the spanwise direction. Three-dimensional cells can well alter the flow (Najjar & Vanka, 1995). Much work remains to be done.

If separation occurs from a smooth wall, transition becomes important and a turbulence model such as S-A can be exercised in at least four modes. The most convenient (although not mentioned in the original paper) is to set the inflow eddy viscosity $\tilde{\nu}$ to a value such as 5ν. Then the turbulence model rapidly "lights up" in the boundary layers (but *not* in the irrotational region), leading to a fully turbulent (FT) solution. The two modes of operation prescribed in the original paper have near-zero inflow values, and trips at the wall. In one mode the trips are fixed, either because physical trips exist or because good predictions of natural transition cannot be made. In the other mode the trips follow the (time-dependent) transition location predicted by a separate method (Kusunose & Cao, 1994). This is the most appealing mode, but it can be sensitive to exactly where transition is triggered, relative to separation.

The fourth mode, conceived in St. Petersburg, is to establish some turbulence in the initial condition, but then to remove any trip or nonzero inflow value. We describe it as "trip-less" (TL). In an attached flow, all eddy viscosity would be convected out of the domain, and a laminar solution would result (unless numerical errors sustained the non-zero eddy viscosity). For the cylinder, turbulence

is swept out of the boundary layers on the windward side, but survives in the separated region. It is convected back towards the separation point. We expect the same qualitative behaviour in three-dimensional "separation". In our experience, it is not sensitive to grid density. This mode of operation avoids transition prediction and plausibly addresses the Reynolds-number range in which separation from the cylinder is laminar, and Kelvin-Helmholtz transition rapidly takes place in the separated shear layer. We consider a diameter Reynolds number $Re = 50,000$, which is well within that range. The TL mode is of course not sufficient at high Reynolds numbers, or for aerodynamic flows.

It appears that even in a 2D symmetric geometry at a single Reynolds number, a model could potentially give sixteen different answers (by changing the steadiness, the symmetry, the three-dimensionality, and the tripping mode). The industrial community is not well prepared to deal with this non-uniqueness, which we predict will show up as more massively separated flows are calculated. It is of considerable interest whether loss of stability of the steady CFD solutions correlates with large-scale unsteadiness in the experiment. A less palatable but equally urgent subject is the relationship between convergence failure of a steady-state CFD code, and limit-cycle behaviour of a good time-accurate CFD solution of the same flow. In real situations, neither 2D not symmetric, the only issue besides transition is time-dependence (although 3D cells could still be silently suppressed by a coarse spanwise grid spacing) and "only" eight modes would exist. We now review which modes actually lead to appreciable differences in the results, for the cylinder.

We do not consider symmetric time-dependent cases, and we leave 3D calculations for future work. Thus in terms of time- and spanwise-dependence we only consider steady cases (S), and 2D unsteady cases (U). In terms of transition control, we do not present cases with natural transition. We also found that cases with non-zero upstream eddy viscosity and cases with trips well upstream of separation gave very close results. Thus, we only have these "FT" cases and the "TL" cases. This leads to a two-by-two matrix of cases.

Steady laminar solutions could not be obtained at $Re = 50,000$. This illustrates our incomplete control over steady solutions: their availability depends on numerical features of the method, such as its tolerance of large time steps. The unsteady laminar solution was noisy and suspect in terms of grid convergence and time sample, and we elected not to use it.

Fig. 6 shows the four solutions of the S-A model, and the experimental results of Achenbach (1968) at $Re = 10^5$ for laminar separation, and Roshko (1961) at $Re = 8.5\ 10^6$ for turbulent separation. The best agreement is between the U-FT solution and the turbulent-separation experiment. This is physically logical and encouraging. None of the other three solutions agree very well with either experiment. The steady solutions give much longer recirculation bubbles, much higher eddy viscosity, and lower drag than the unsteady ones. This is consistent with published results on sharp-edged bluff bodies. On the other hand, the agreement between the U-TL solution and the laminar-separation experiment is disappointing; the back pressure and drag are quite good, but the pressure is

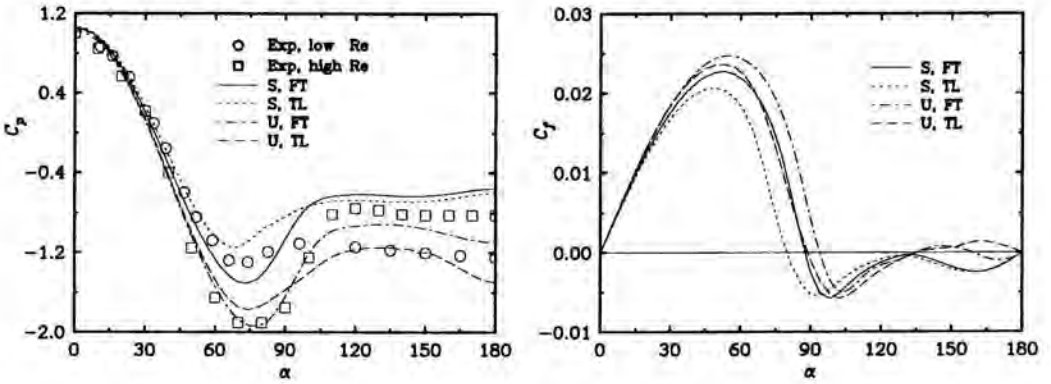

Figure 6: Pressure (left) and skin friction (right) on circular cylinder. U, unsteady; S, steady; FT, fully turbulent; TL, trip-less.

inaccurate near the crest ($60° \leq \alpha \leq 120°$). The TL flow is less resistant to separation than the FT flow, as expected, but still more resistant than a laminar boundary layer.

Fig. 6b shows the separation location, which for some cases is curiously inconsistent with the pressure; for instance for the U-TL case the pressure would suggest about 120°, but the skin friction crosses zero near 90°. We also note that the peak skin-friction coefficient (near $\alpha = 60°$) is not much lower when the flow is laminar (TL cases) than when it is turbulent. With this Reynolds number and this pressure gradient, turbulence is not dominant.

Fig. 7 displays the U-TL solution, at a particular phase of the shedding cycle. x and y are normalized by the cylinder diameter. The eddy viscosity is zero upstream of separation, and then rises due to the reversed flow and diffusion. The separating streamline (using a definition that is loose in an unsteady flow), line of peak vorticity, and line of peak eddy viscosity almost coincide for $x \geq 0.05$; we attribute this to the facts that vorticity is convected, and that the production term of eddy viscosity is proportional to vorticity. The propagation of eddy viscosity upwards across streamlines appears unexpectedly rapid, compared with that of vorticity. This is largely an illusion due to the fact that the peak vorticity is decreasing, while the peak eddy viscosity is increasing.

To conclude, transitional separation bubbles are produced in a free-standing and qualitatively correct manner by one-equation models in trip-less mode (we have not attempted TL solutions with two-equation models). However, separation occurs somewhere between the locations of laminar and turbulent separation in experiments. This is probably controlled by the diffusion mechanisms of the model, which were of course adjusted in other flows. In practice, this effect could be powerful for high-lift configurations, which are sometimes dependent on transitional bubbles.

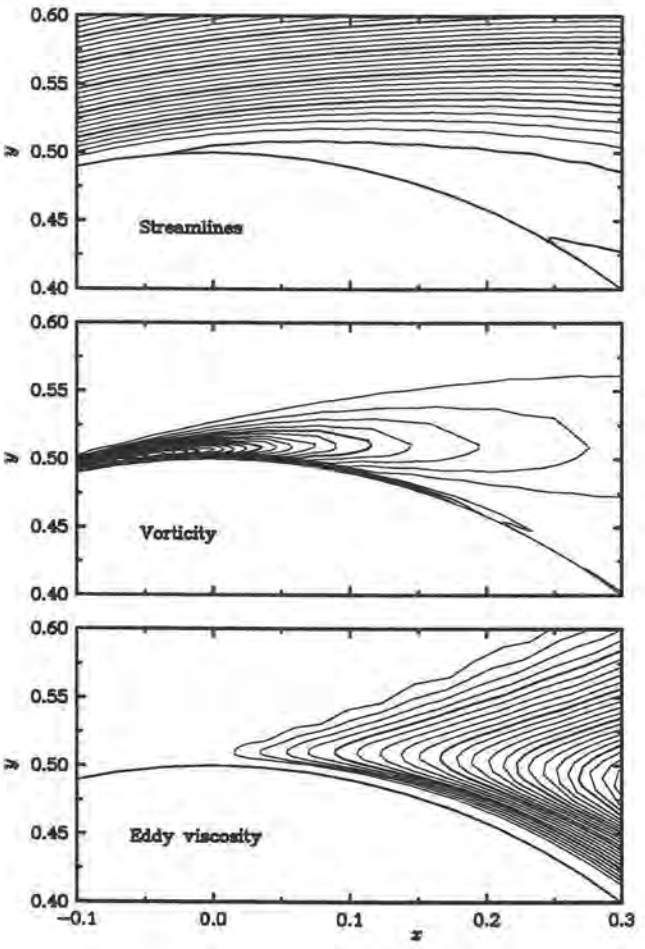

Figure 7: Trip-less solution on circular cylinder. Flow from left to right.

Summary

The studies presented here are a reminder that perfection is not expected from turbulence models, particularly when dealing with transition. In that, they respond to the Scientific Committee's wish for the aircraft industry to make their "problems and wishes" known! On the other hand, our attempts reflect the firm ambition to treat a wide variety of flow phenomena with a single model. In addition, the models are about the simplest that can be formulated in complex grids and geometries. Such models will long be favoured to solve complex problems. Subtle aspects of transition are given a rather low priority. The ultimate objective is a full high-lift configuration. There is no lack of challenges as CFD further

pervades the Aerospace design activity; those facing the Turbulence Subsystem include the need to accurately and economically represent the effect of vortex generators, and to obtain relaminarization due to favourable pressure gradients or streamline divergence without zonal devices.

Appendix: Spalart-Allmaras turbulence model

The Reynolds stresses are given by $-\overline{u_i u_j} = 2\nu_t S_{ij}$, S_{ij} the strain tensor. The eddy viscosity ν_t is given by

$$\nu_t = \tilde{\nu}\, f_{v1}, \qquad f_{v1} = \frac{\chi^3}{\chi^3 + c_{v1}^3}, \qquad \chi \equiv \frac{\tilde{\nu}}{\nu}. \tag{A1}$$

ν is the molecular viscosity. $\tilde{\nu}$ obeys the transport equation

$$\frac{D\tilde{\nu}}{Dt} = c_{b1}\,[1 - f_{t2}]\;\tilde{S}\;\tilde{\nu} + \frac{1}{\sigma}\left[\nabla.((\nu + \tilde{\nu})\nabla\tilde{\nu}) + c_{b2}\,(\nabla\tilde{\nu})^2\right]$$

$$- \left[c_{w1} f_w - \frac{c_{b1}}{\kappa^2} f_{t2}\right]\left[\frac{\tilde{\nu}}{d}\right]^2 + f_{t1}\;\Delta U^2. \tag{A2}$$

Here

$$\tilde{S} \equiv S + \frac{\tilde{\nu}}{\kappa^2 d^2} f_{v2}, \qquad f_{v2} = 1 - \frac{\chi}{1 + \chi f_{v1}}, \tag{A3}$$

where S is the magnitude of the vorticity, and d is the distance to the closest wall. The function f_w is

$$f_w = g\left[\frac{1 + c_{w3}^6}{g^6 + c_{w3}^6}\right]^{1/6}, \qquad g = r + c_{w2}\,(r^6 - r), \qquad r \equiv \frac{\tilde{\nu}}{\tilde{S}\kappa^2 d^2}. \tag{A4}$$

The wall boundary condition is $\tilde{\nu} = 0$. In the freestream and as initial condition 0 is best, and values below $\nu/10$ are acceptable. The f_{t2} function is $f_{t2} = c_{t3}\,\exp(-c_{t4}\,\chi^2)$. The trip function f_{t1} is as follows: d_t is the distance from the field point to the trip, which is on a wall, ω_t is the wall vorticity at the trip, and ΔU is the difference between the velocity at the field point and that at the trip. Then $g_t \equiv \min(0.1, \Delta U/\omega_t \Delta x_t)$ where Δx_t is the grid spacing along the wall at the trip, and

$$f_{t1} = c_{t1}\; g_t\; \exp\left(-c_{t2}\,\frac{\omega_t^2}{\Delta U^2}\left[d^2 + g_t^2 d_t^2\right]\right). \tag{A5}$$

Finally $c_{b1} = 0.1355$, $\sigma = 2/3$, $c_{b2} = 0.622$, $\kappa = 0.41$, $c_{w1} = c_{b1}/\kappa^2 + (1 + c_{b2})/\sigma$, $c_{w2} = 0.3$, $c_{w3} = 2$, $c_{v1} = 7.1$, $c_{t1} = 1$, $c_{t2} = 2$, $c_{t3} = 1.2$, $c_{t4} = 0.5$.

Acknowledgements

We had many discussions with Drs. J. Crouch and S. Allmaras of Boeing.

References

Achenbach, E. 1968 – Distribution of local pressure and skin friction around a circular cylinder in cross-flow up to $Re = 5\ 10^6$. *J. Fluid Mech.* **34** , 625-639.

Cazalbou, J. B., Spalart, P. R. & Bradshaw, P. 1994 – On the behavior of two-equation models at the edge of a turbulent region. *Phys. Fluids A* **6**, 1797-1804.

Durbin, P. A. 1995 – Separated flow computations using the $k - \epsilon - v^2$ model. *AIAA J.* **33**, 659-664.

Franke, R. & Rodi, W. 1991 – Calculation of vortex shedding past a square cylinder with various turbulence models. 8th Turbulent Shear Flow Symp., Munich.

Gad-el-Hak, M., Blackwelder, R. F. & Riley, R. R. 1981 – On the growth of turbulent regions in laminar boundary layers. *J. Fluid Mech.* **110**, 73-95.

Johansson, S., Davidson, L. & Olsson, E. 1993 – Numerical simulation of the vortex shedding past triangular cylinders at high Reynolds number using a $k - \epsilon$ turbulence model. *Int. J. Num. Meth. in Fluids* **16**, 859-878.

Kusunose, K. & Cao, H. V. 1994 – Prediction of transition location for a 2-D Navier-Stokes solver for multi-element airfoil configurations. *AIAA-94-2376.*

Menter, F. R. 1994 – Two-equation eddy-viscosity turbulence models for engineering applications. *AIAA J.* **32**, 1598-1605.

Najjar, F. M. & Vanka, S. P. 1995 – Effects of intrinsic three-dimensionality on the drag characteristics of a normal flat plate. *Phys. Fluids A* **7** , 2516-2523.

Narasimha, R. 1985 – The laminar-turbulent transition zone in the boundary layer. *Prog. Aerospace Sci.* **22**, 29-80.

Roshko, A. 1961 – Experiments on the flow past a circular cylinder at very high Reynolds numbers. *J. Fluid Mech.* **10**, 345-356.

Shur, M., Strelets, M., Zaikov, L., Gulyaev, A., Kozlov, V. & Secundov, A. 1995 – Comparative numerical testing of one- and two-equation turbulence models for flows with separation and reattachment. *AIAA-95-0863.*

Shur, M., Spalart, P. R., Strelets, M. & Travin, A. 1996 – Navier-Stokes simulation of shedding turbulent flow past a circular cylinder and a cylinder with backward splitter plate. 3rd European CFD Conf., Sept. 9-13, 1996, Paris, France.

Spalart, P. R. & Allmaras, S. R. 1994 – A one-equation turbulence model for aerodynamic flows. *La Recherche Aérospatiale* **1**, 5-21.

Author's address

Boeing Commercial Airplane Group
P.O. Box 3707
Seattle, WA 98124-2207, USA.

K. Hanjalić & I. Hadžić

Modelling the Transition Phenomena with Statistical Turbulence Closure Models

Abstract

The paper discusses some issues related to modelling the laminar-to-turbulent and reverse transitions with single-point closure models. It is argued that an important prerequisite for modelling by-pass transition or revival of inactive ("background") turbulence in a laminar-like flow is to model separately the effects of viscosity and those associated with non-viscous, directionally biased wall-blockage effects. A second-moment closure model with low-*Re*-number and non-viscous wall effects in invariant form has been applied to the prediction of several cases of transitional flows including by-pass transition at plane and curved surfaces and at different pressure gradients, relaminarization of strongly accelerating flows, as well as a sequence of forward and reverse transitions in periodic and oscillating flows at transitional *Re* numbers.

Introduction

Reynolds averaging, which serves as a basis for most single-point turbulence closure models, conceals by its virtue the dynamics of flow disturbances, the incipience, development and amplification of local instabilities and the actual mechanism of natural laminar-to-turbulent transition. For that reason the statistical single-point closure models have been regarded as inappropriate tools for dealing with the problem of transition. However, because an alternative to single-point closures for computation of industrial flows is still not in the offing, there has been much activity in accommodating statistical models to handle at least some forms of transition phenomena, such as by-pass transition caused by the diffusion of free stream turbulence into the boundary layer. It is generally accepted that the turbulence closures offer more flexibility and better prospects for predicting real complex flows with transitions then any classical linear stability theory. The ability to predict a *change-over* from one regime to another (not necessarily the actual transition mechanism) at appropriate location and under appropriate conditions, and consequent modifications of mean flow parameters - without having to introduce any artificial triggering - will often serve the purpose of computing complex industrial flows involving transition.

Successful reproductions of the reverse transition (laminarization) have been reported already in early seventies even with simple two-equation models, modified to account for "low-*Re*-number effects" (Jones and Launder, 1972). Since then a substantial progress has been made in the development of turbulence models, expanding gradually their applicability to a wider range of flows including

some forms of transition. Progress reports on the activity of the ERCOFTAC Transition Special Interest Group (SIG), (Savill, 1993) provide a good overview of the current achievements of single-point closures in modeling the diffusion-controlled by-pass transition. In spite of substantial efforts the outcome seems to be inconclusive. Particularly disappointing is the evidence that higher model complexity brought only marginal improvements, and only in some cases. Nevertheless, some conclusions did emerge. The models which use the invariant turbulence parameters such as the turbulence Re number, perform better than those which use the local wall distance. Satisfying the correct wall limits of the shear stress and of energy dissipation rate was also found to be important for a successful reproduction of the transition. Finally, few contributions with the Reynolds-stress models (RSM) with low-Re-number modifications seemed all to perform better than two-equation models, particularly for low free stream turbulence e.g. $\mathcal{O}(1\%)$. Major advantages of the RSM were located in the provision to account for anisotropy of the free stream- and of the near-wall stress field, particularly in the ability to reproduce the normal-to-the-wall velocity fluctuations. Another merit is in the exact treatment of the turbulence production and of effects of streamline curvature. These features help also in handling other forms of non-equilibrium phenomena frequently encountered jointly with different forms of transition and present authors believe that a general model for complex flows should be sought within a low-Re-number RSM framework.

This paper discusses some issues related to modelling transition with the low-Re-number single-point closures. It attempts to identify minimum constraints which a model should meet, and discusses possible reasons for unsatisfactory performances of some models. The fulfillment of limiting and asymptotic turbulence states (two-component turbulence, vanishing turbulence Reynolds number), identified as important prerequisites for modelling transition, will also be discussed. A version of the second-moment (RSM) closure model with low-Re-number and wall proximity modifications was used, which was validated earlier in a series of non-equilibrium attached and separated wall flows, some involving strong low-Re-number effects (Hanjalić *et al.*, 1996). In this paper we consider four flows with by-pass transition with different levels of free stream turbulence above 3% and a case of low-Re-number oscillating boundary layer in which the flow undergoes a sequential change of forward and reverse transition within a single cycle. The by-pass transition cases were selected from the ERCOFTAC Transition SIG database, known under the code names T3A, T3B, T3C and T3L4. The specification of the flows will be given together with the discussion of the results later in the text.

Some basic model requirements

Current statistical models can be expected to reproduce transition only when either a continuous source of turbulence exists somewhere in the flow or at its edge from where the turbulence will diffuse (be entrained) into the rest of the non-turbulent flow. Alternatively, the laminar flow must contain some background

turbulence, sufficiently weak not to influence laminar-like mean flow properties, but sufficient to amplify itself when the flow deformation or other disturbance is imposed or reaches a sufficient strength to interact with the background turbulence. Such is the case of re-transition, e.g. in an oscillating turbulent boundary layer at low Re numbers, or in a laminar-like or laminarizing boundary layers subjected to a strong adverse pressure gradient e.g. in a compressor cascades. The ability to predict the first type (by-pass) transition depends on the model of turbulent diffusion, particularly away from the wall, which essentially controls the boundary layer turbulization. In contrast to that, the prediction of laminarization and of a subsequent re-transition depends on the model ability to reproduce accurately the process of turbulence decay and production at a low turbulence Re number in a strongly anisotropic field in the near wall region.

Low-Re-number modifications have been proposed at different modeling levels, but in most cases they were tailored to achieve overall damping of turbulence as the wall approaches in equilibrium wall flows. In most cases no distinction is made between the pure viscosity effects, which are of scalar nature, and non-viscous, directionally biased wall blockage and a consequent pressure reflection. Unlike the viscosity which damps evenly the turbulence fluctuations in all directions, a solid wall imposes a selective damping of the normal-to-the-wall velocity fluctuations and a consequent eddy splatting, resulting in increased turbulence anisotropy approaching the two-component state very close to the wall. Most low-Re-number models treat both effects jointly and often relating the overall damping to the local wall distance. While such a practice can reproduce near wall behaviour in near-equilibrium steady flows similar to those in which the model was tuned, it fails in most cases with complex wall topography, or with a significant departure from equilibrium conditions. In view of the fact that most transitional phenomena are provoked, enhanced or otherwise controlled by sudden changes in boundary or external conditions, it is obvious that such models can not reproduce a broader variety of transition phenomena.

A second-moment closure

The present model is a variant of the low-Re-number second-moment closure, based on the standard high-Re-number $\overline{u_i u_j} - \varepsilon$ model with linear pressure strain terms, which serves as the high-Re-number asymptote. The novelty is in modeling separately the viscous and wall-proximity effects by a set of functions, which are all expressed in terms of invariant turbulence properties. The viscous effect is introduced through the turbulence Reynolds number $Re_t = k^2/(\nu\varepsilon)$, which is both physically justifiable and numerically convenient. The non-viscous wall blockage effects and pressure reflection depend indeed on the distance from a wall and its topography. However, the use of the wall distance and the unit normal vector (representing the local wall orientation), as practiced in most near-wall turbulence models, is inconvenient for flows domains with irregular boundaries. A solid wall damps primarily the turbulent fluctuations in the normal direction, causing a strong anisotropy of the turbulence field. Hence the parameters characterizing the anisotropy can be used to represent the wall blockage effects. In

the model described here we model the non-viscous wall effects in terms of the invariants of the turbulent stress tensor $A_2 = a_{ij}a_{ij}$, $A_3 = a_{ij}a_{jk}a_{ki}$ and of the dissipation rate tensor $E_2 = e_{ij}e_{ij}$, $E_3 = e_{ij}e_{jk}e_{ki}$, where $a_{ij} = \overline{u_iu_j}/k - 2/3\delta_{ij}$ and $e_{ij} = \varepsilon_{ij}/\varepsilon - 2/3\delta_{ij}$. In contrast to early models which assumed a proportionality of these invariants, recent direct numerical simulation (DNS) of simple wall flows showed a substantial difference in the anisotropy of the stress- and dissipation rate fields even in equilibrium conditions. This is particularly evident in the behaviour of the "flatness" parameters $E = 1 - 9/8(E_2 - E_3)$, $A = 1 - 9/8(A_2 - A_3)$ which characterize a departure from two-dimensionality of the small- and large scale turbulence, respectively: both parameters become zero in two-dimensional turbulence and unity in isotropic turbulence. The DNS results for low-*Re*-number wall flows clearly illustrate that E reaches a value close to 1 at much closer distance from the wall than A indicating a higher degree of isotropy in the small scale motion over most part of the flow (Hanjalić *et al.*, 1996). This notable difference in the behavior of A and E, particularly close to the wall, gives a justification for using both parameters for modeling separately the wall effects on large and small scale turbulence fields. The low-*Re*-number dissipation equation is used with the additional term $-C_{\varepsilon 4}f_4k\Omega_k\Omega_k$ introduced earlier (Hanjalić and Launder, 1982) with the purpose of differentiating the effects of irrotational and rotational straining on the energy transfer process (production of ε). Here $\Omega_k = \epsilon_{ijk}(\partial U_i/\partial x_j)$ is the mean vorticity vector. This term has proved to be essential in modeling the flows with strong linear straining particularly because it accounts for the sign of the linear strain rate, producing a desired effects on the dissipation rate dynamics both in strongly accelerating and strongly decelerating flows. The modelled transport equations for the turbulent stress and energy dissipation rate are:

$$\frac{D\overline{u_iu_j}}{Dt} = \frac{\partial}{\partial x_k}\left[\left(\nu\delta_{kl} + C_s\frac{k}{\varepsilon}\overline{u_ku_l}\right)\frac{\partial\overline{u_iu_j}}{\partial x_l}\right] - \left(\overline{u_iu_k}\frac{\partial U_j}{\partial x_k} + \overline{u_ju_k}\frac{\partial U_i}{\partial x_k}\right) + \Phi_{ij} - \varepsilon_{ij}, \quad (1)$$

$$\begin{aligned}\frac{D\varepsilon}{Dt} &= \frac{\partial}{\partial x_k}\left[\left(\nu\delta_{kl} + C_\epsilon\frac{k}{\varepsilon}\overline{u_ku_l}\right)\frac{\partial\varepsilon}{\partial x_l}\right] - C_{\varepsilon_1}\frac{\varepsilon}{k}\overline{u_iu_j}\frac{\partial U_i}{\partial x_j} - C_{\varepsilon_2}f_\varepsilon\frac{\varepsilon\tilde{\varepsilon}}{k} \\ &\quad + C_{\varepsilon_3}\nu\frac{k}{\varepsilon}\overline{u_ju_k}\frac{\partial^2U_i}{\partial x_j\partial x_l}\cdot\frac{\partial^2U_i}{\partial x_k\partial x_l} - C_{\varepsilon 4}f_4k\Omega_k\Omega_k. \quad (2)\end{aligned}$$

Model of the pressure strain:

$$\Phi_{ij,1} = -C_1\varepsilon a_{ij}, \qquad \Phi_{ij,2} = -C_2\left(P_{ij} - \frac{2}{3}P_k\delta_{ij}\right),$$

$$\Phi^w_{ij,1} = C^w_1 f_w\frac{\varepsilon}{k}\left(\overline{u_ku_m}n_kn_m\delta_{ij} - \frac{3}{2}\overline{u_iu_k}n_kn_j - \frac{3}{2}\overline{u_ku_j}n_kn_i\right),$$

$$\Phi^w_{ij,2} = C^w_2 f_w\left(\Phi_{km,2}n_kn_m\delta_{ij} - \frac{3}{2}\Phi_{ik,2}n_kn_j - \frac{3}{2}\Phi_{kj,2}n_kn_i\right),$$

$$C_1 = C + \sqrt{A}E^2, \quad C = 2.5AF^{1/4}f, \quad F = \min\{0.6; A_2\},$$

$$f = \min\left\{\left(\frac{Re_t}{150}\right)^{3/2}; 1\right\}, \quad f_w = \min\left[\frac{k^{3/2}}{2.5\varepsilon x_n}; 1.4\right],$$

$$C_2 = 0.8A^{1/2}, \quad C_1^w = \max(1-0.7C; 0.3), \quad C_2^w = \min(A; 0.3),$$

$$A = 1 - \frac{9}{8}(A_2 - A_3), \quad A_2 = a_{ij}a_{ji}, \quad A_3 = a_{ij}a_{jk}a_{ki}, \quad a_{ij} = \frac{\overline{u_iu_j}}{k} - \frac{2}{3}\delta_{ij},$$

$$E = 1 - \frac{9}{8}(E_2 - E_3), \quad E_2 = e_{ij}e_{ji}, \quad E_3 = e_{ij}e_{jk}e_{ki}, \quad e_{ij} = \frac{\varepsilon_{ij}}{\varepsilon} - \frac{2}{3}\delta_{ij}.$$

The model of the stress dissipation rate:

$$\varepsilon_{ij} = f_s\varepsilon^*_{ij} + (1-f_s)\frac{2}{3}\delta_{ij}\varepsilon, \quad \varepsilon^*_{ij} = \frac{\varepsilon}{k}\frac{[\overline{u_iu_j} + (\overline{u_iu_k}n_jn_k + \overline{u_ju_k}n_in_k + \overline{u_ku_l}n_kn_ln_in_j)f_d]}{1 + \frac{3}{2}\frac{\overline{u_pu_q}}{k}n_pn_qf_d},$$

$$f_s = 1 - \sqrt{A}E^2, \quad f_d = (1 + 0.1Re_t)^{-1}, \quad f_\varepsilon = 1 - \frac{C_{\varepsilon_2} - 1.4}{C_{\varepsilon_2}}\exp\left[-\left(\frac{Re_t}{6}\right)^2\right].$$

The term $-C_{\varepsilon 4}f_4k\Omega_k\Omega_k$ in the dissipation equation was used in a simplified form which emerges from the near-wall equilibrium constraint, $C^*_{\varepsilon 4}(\overline{u_2^2} - \overline{u_1^2})(\partial U_1/\partial x_1)\varepsilon/k$. This form eliminates the need to use the function f_4 and is computationally more convenient. In this case $C_{\varepsilon 1}$ remains unchanged (i.e. $C_{\varepsilon 1} = 1.44$) and so does C_{ε_2}=1.92, while the corresponding value of $C^*_{\varepsilon 4}$ is 1.16. The remaining coefficients take the following values:

$$C_s = 0.22, \quad C_\varepsilon = 0.18, \quad C_{\varepsilon_3} = 0.25.$$

Numerical method

Computations of the by-pass transition on a flat plate (cases T3A, T3B and T3C, see bellow) as well as the oscillating boundary layer, were performed with a parabolized Navier-Stokes numerical code using the control-volume approach with typically 100 nodes across the flow in a collocated variable arrangement. The corresponding pressure gradient was specified explicitly and the V-component of the mean velocity evaluated from the continuity equation. The parabolic computations started at the leading edge with uniform profiles of all quantities equal to the streamline values supplied by experiments. Some modifications of the dissipation scales were made in some cases as discussed later. A partial validation of the parabolic approach was performed by computing the case T3B by the full (elliptic) Navier-Stokes solver, over a computational domain starting at the leading edge and extending sufficiently downstream to capture in full the transition region. Admittedly, this was not sufficient since the elliptic effect of the leading edge could be detected only by starting the computation ahead of the edge and

accounting for the real shape and thickness of the plate. These were ignored in this case, but studied in details in the case of a symmetric round-edged plate.

The flow over the finite thickness plate with round leading edge (case T3L4) test case has been computed with a finite volume 2-dimensional Navier-Stokes code with block-structured, body-fitted mesh with local refinement, Cartesian vector and tensor components, and collocated variable arrangement, developed by Perić (1993). In this code several high- and low-Re-number eddy-viscosity and Reynolds-stress turbulence models are implemented. The results are obtained on a numerical grid with two blocks the inner with 308×60 and the outer with 184×15 control volumes (CV). Quadratic upwind interpolation (QUICK) is used for connective terms in the momentum equations and the upwind differencing scheme (UDS) for turbulence properties.

Some illustrations

As an illustration of the ability of the model described above to predict transitional flows, we consider four cases of by-pass transition and a case of periodic re-transition. The by-pass transition flows were selected from the ERCOFTAC benchmark library. The performance of the model is illustrated by comparison with experimental and/or DNS data. It should be noted that the same model with the same values of all coefficients was earlier tested in several classes of equilibrium and non-equilibrium attached and separating wall flows covering a broad range of Re numbers (Hanjalić *et al.* 1996). Comparison with a variety of experimental and DNS results supplied independently over the years by different authors gave in most cases very good agreement for all mean flow properties and in most cases also for the second moments.

The first two cases, denoted as T3A and T3B, are the by-pass transition in an initially laminar boundary layer at a flat plate at constant pressure with free stream turbulence intensities $(\tilde{u}_\infty/U_\infty) \approx 3\%$ and 6% and corresponding free stream velocities of 5.2 and 9.6 m/s, respectively. The experimental data originate from Rolls-Royce Appl. Science Lab. (P.E. Roach *et al.* and J. Coupland).

Fig. 1 shows the comparison of the computed friction factors and shape parameters for the two cases considered. The results for 6% were obtained using the initial data fully in accord with the experiments. Except for a more gradual inception of transition, than found experimentally, the agreement is remarkably good, particularly in the later stage, when the model reproduces in full both the friction- and the shape factors. The case with 3% appeared to be more sensitive to the initial conditions. Using the suggested initial value produced a milder transition, though its commencement was predicted well (dotted line in Fig. 1). An increase in the initial dissipation length scale moves the line closer to experimental data, though achieving a satisfactory agreement required a substantial increase (almost by factor of 10), as shown in Fig. 1. Contrary to the 6% case, the agreement is better in the initial than in the later stage.
Further illustration of the model ability is illustrated in Fig. 2, where the profiles of mean velocity and of turbulence stresses are shown for the 6% case (T3B) at

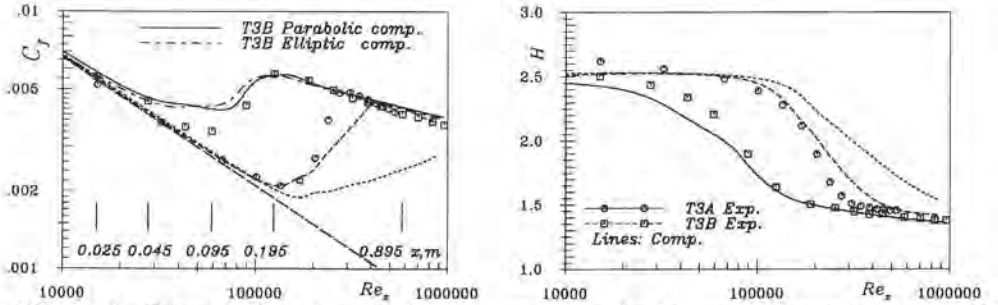

Figure 1: Friction factor and shape parameter for by-pass transition cases T3A and T3B. Symbols: Experiments Rolls–Royce ASL. Lines: Computation.

several locations starting at $x = 25$ mm downstream from the leading edge. Mean velocity is reproduced very well at all stations and so are the components of the normal stresses, particularly the u-component. However, the computed shear stress exceeds substantially the experimental data at all locations. This finding is strange in view of excellent prediction of the mean velocity.

The third case (T3C) involves variable pressure starting with favourable pressure gradient and reverting to adverse pressure gradient further downstream. We present the results of the case T3C1, which corresponds to 8% free stream turbulence. Strong acceleration in the initial region makes this flow very sensitive to the initial condition. This sensitivity is illustrated by three computed lines corresponding to three slightly different initial dissipation length scales. The chain line obtained with $L_{\varepsilon_{\infty i}} = 5.0$ mm shows no transition: the boundary layer remains laminar throughout the considered flow domain. A small increase to 5.5 mm reproduced the transition reasonably well (full line), though its incipience started somewhat earlier than found by experiments. Further increase in $L_{\varepsilon_{\infty i}}$ moves the transition location back towards the leading edge, but the effect is not very pronounced, as shown by dotted line. It should be noted that an accurate reproduction of the pressure gradient from the experimental data for the free stream velocity variation is difficult and a small changes can make a noticeable effect on the prediction outcome.

The fourth case (T3L4) is the transition in a laminar boundary layer developing over a finite thickness plate with round leading edge of 5 mm and free stream turbulence of 5.5%. Experiments indicated that the transition is preceded and enhanced by a thin laminar separation bubble. Predicting the correct shape and size of the separation region, which is crucial for predicting correctly the transition, was found to be a major challenge in which most conventional low-Re-number models failed (Chien *et al.*, 1994). Since at the leading edge the flow is still laminar, the major problem is of a numerical nature: accurate numerical resolution of the thin boundary layer at the round leading edge and later in the separation bubble is an essential prerequisite for predicting the transition evolution. For that reason we applied the block-structured numerical mesh, clustered towards the wall, with local refinement in the domain of 5 plate half-thickness around the plate, as shown in Fig. 4. Fig. 4c shows the streamline pattern ob-

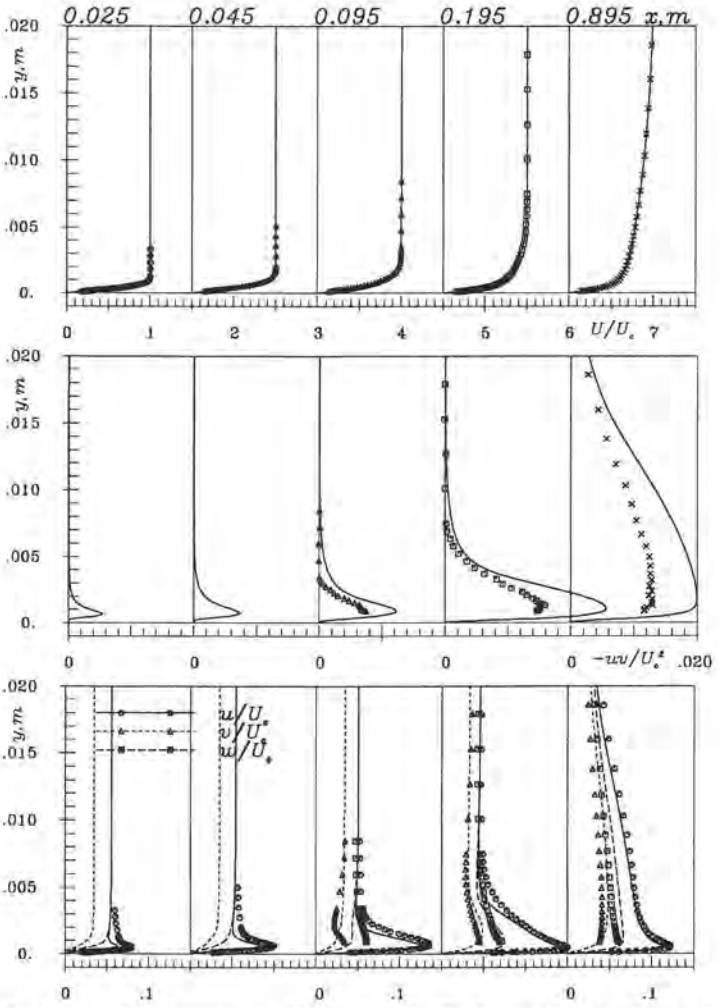

Figure 2: Velocity and stresses profiles, case T3B (locations indicated in figure 1). Symbols: Experiments Rolls–Royce ASL. Lines: Computation.

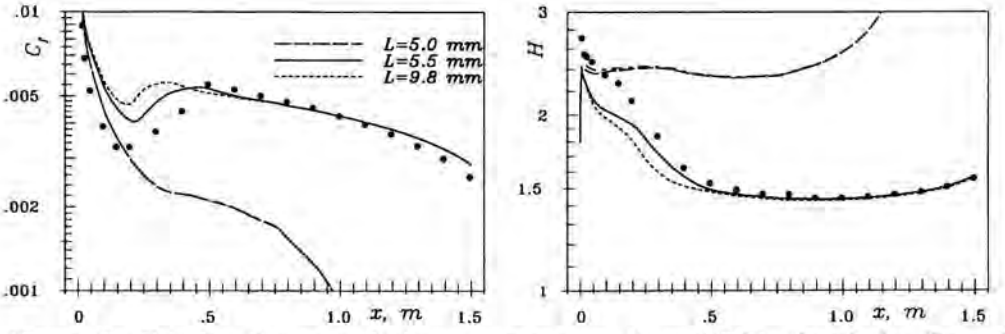

Figure 3: Friction factor and shape parameter. Case T3C1. Symbols: Experiments Rolls–Royce ASL. Lines: Computation.

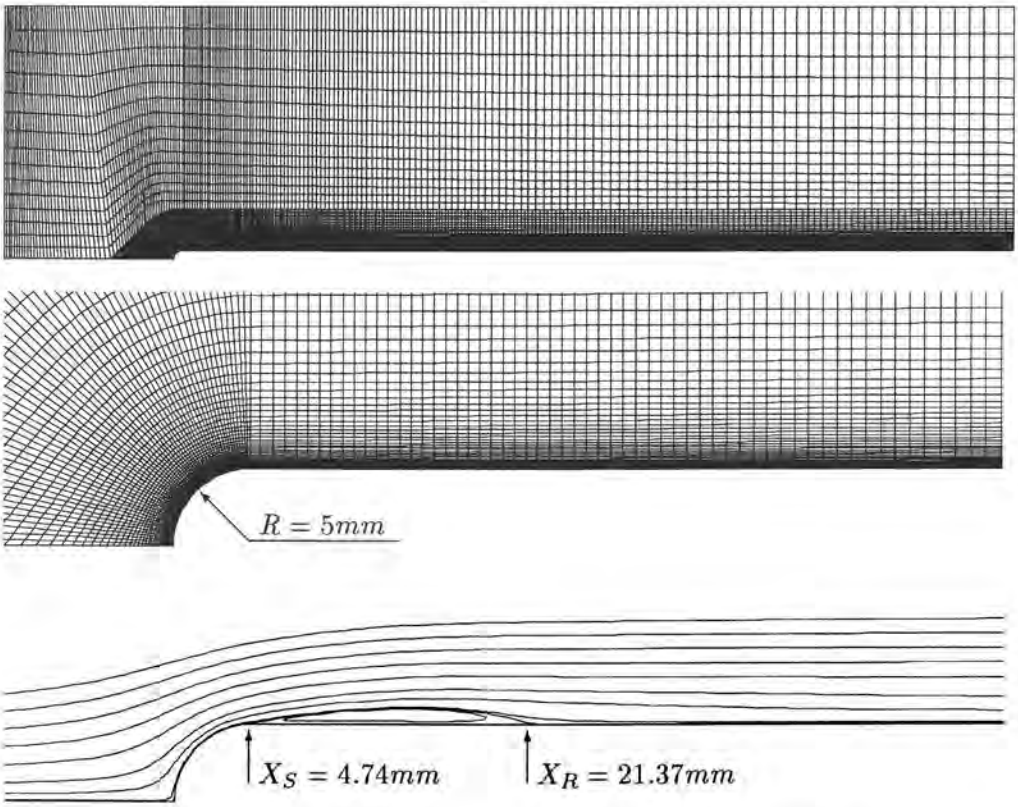

Figure 4: Numerical grid (full and blow–up of the near–wall region) and the computed streamlines. Case T3L4.

tained with the QUICK scheme, which is in close agreement with experiments. Further illustration is provided in Fig. 5 where the profiles of mean velocity and of the streamline fluctuation is shown for several locations at x = 6, 15, 26, 75 and 300 mm downstream from the leading edge. The first two locations fall within the recirculation bubble. The agreement for all stations can be regarded as fully satisfactory, particularly in view of high demands for numerical resolution.

The last case considered is a boundary layer on a flat plate oscillating around the zero mean with a different transition mechanism. In the range of Reynolds numbers Re_{δ_S} (defined with the Stokes-layer thickness $\delta_S = \sqrt{2\nu/\omega}$) between 600 and about 2000 the flow undergoes a sequential change of strong damping (acceleration phase) and revival of turbulence (onset of deceleration) within a single cycle. Although the turbulence does not fully disappear, the damping is sufficient to produce laminarization effect in the mean flow. The turbulence revival at the phase angle when the flow deformation becomes sufficiently high is a form of forward transition, although the mechanism is different both from the natural and by-pass transition. This flow has been reported in more details in (Hanjalić *et al.*, 1995) and here we will only illustrate some results. Fig. 6a shows the friction factor (based on the maximum wall shear stress in a cycle) for

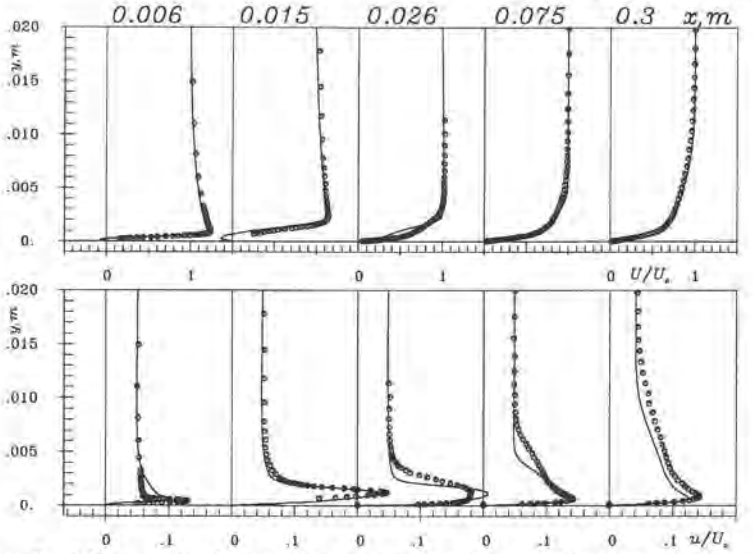

Figure 5: Mean velocity and streamwise fluctuation profiles in the case T3L4. Symbols: Experiments Rolls–Royce ASL. Lines: Computation.

a range of Re numbers. Compared are the computations with the present model and several sets of experimental and DNS data. Fig. 6b presents the phase lead of the maximum wall shear stress ahead of the maximum free stream velocity for Re numbers corresponding to those in Fig. 6a. The agreement with most data is very good over the whole rage considered.

Fig. 7 presents the variation of maxima of all non-zero turbulent stresses, illustrating the extent of turbulence damping and amplification during a cycle for the case for $Re_{\delta_S} = 1000$, compared with the DNS data of Spalart and Baldwin (1987). In addition to excellent agreement with the DNS results, diagram shows that despite substantial variation, the shear stress still retains a non-negligible value ($[\overline{uv}/U_\infty^2]_{max} \approx 0.0005$). It should be noted that the distance of the positions of the stress maxima from the wall varies along the flow and it increases during the acceleration, thickening the viscous sublayer and producing the laminarizing effects on the mean flow. This is better seen in Fig. 8, where a blow up of the phase-evolution of the turbulence Re-number is shown. As seen, Re_t decreases below 100 up to $y/\delta_S \approx 1$ over much of the acceleration phase ($\phi = 110 - 130^0$) leading to typically laminar mean flow velocity distribution and wall shear stress, in spite of the fact that a substantial turbulence is still present in the outer region.

Conclusions

The ability of second-moment closures to handle the laminar-to-turbulent and reverse transition has been examined by applying a model, developed by the authors, to transition caused either by entrainment of outer free-stream turbulence, or by revival of the damped turbulence after laminarization. The considered bypass transition cases are all well reproduced for higher free stream turbulence, even with a parabolic solver, starting the computation at the leading edge. The

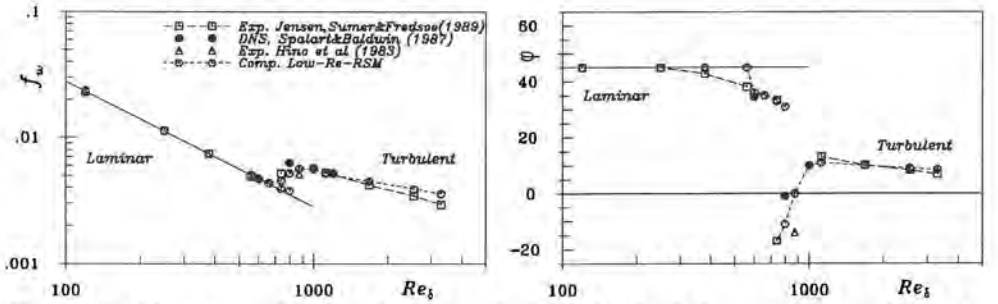

Figure 6: Maximum friction factor and phase lead of the maximum shear stress in regard to maximum free stream velocity.

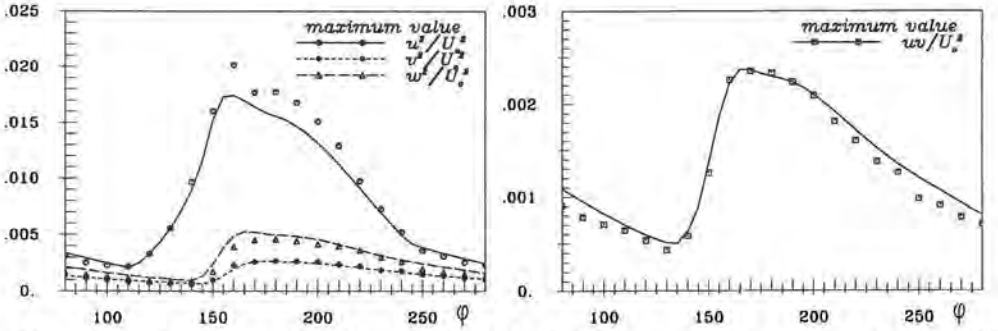

Figure 7: Evolution of maximum turbulent stresses over a cycle. $Re_{\delta_S} = 1000$. Symbols: DNS Spalart and Baldwin (1987). Lines: Computations.

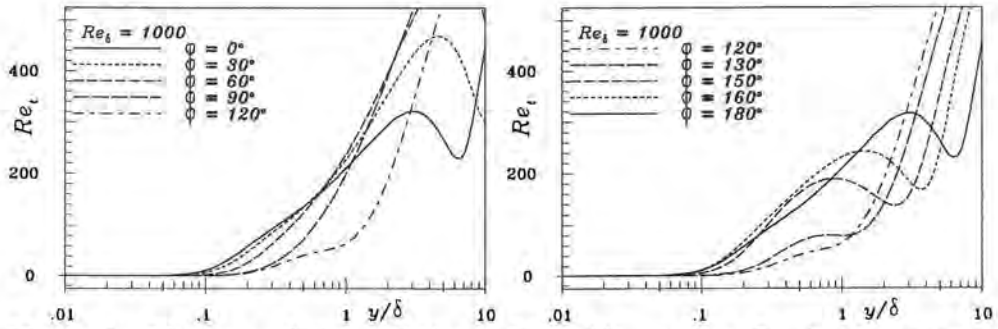

Figure 8: Blow-up of the turbulence Reynolds number Re_t in the near-wall region at different phase angles. $Re_{\delta_S} = 1000$.

lower turbulence intensity (3% and bellow) poses a problem: better agreement can be achieved by decreasing the initial dissipation level as compared with experimental data. The application of the elliptic solver with the computational domain starting at the leading edge produced only marginal effects. The uncertainty in the inlet flow dissipation is expected to have a smaller influence if the elliptic solutions were carried out ahead of the leading edge. The leading-edge effect was investigated in more details in flow around a finite-thickness round-edge flat plate, which was solved by full-Navier-Stokes solver with block-structured locally refined numerical mesh. The results show a good agreement with experiments. The predictions of the oscillating transition flows were reproduced in excellent agreement with the DNS and experiments, indicating that the revival of laminarized turbulence, particularly in cases which are independent of the inlet flow conditions, can be successfully handled with the present model.

References

Chen, W.L., Lien, F.S. and Leschziner, M.A. 1994 – Computational modelling of turbulent flows in turbomachine passage with low-*Re* two-equation models. *Computational Fluid Dynamics '94*, pp. 517–524.

Coupland, J. 1995 – Private communication.

Hanjalić, K., Jakirlić, S. and Hadžić, I. 1995 – Computation of oscillating turbulent flows at transitional *Re*-numbers. *Turbulent Shear Flows* Vol 9, (Eds F. Durst *et al.*), pp. 323–342, Springer.

Hanjalić, K., Jakirlic, S. and Hadžić, I. 1996 – Expanding the limits of "equilibrium" second-moment turbulence closures. *Fluid Dynamics Research*, (in press).

Hanjalić, K. and Launder, B.E. 1982 – Sensitizing the dissipation equation to irrotational strains. *ASME J. Fluids Eng.* **102**, 34–40.

Jones, W.P. and Launder, B.E. 1972 – The prediction of laminarisation with a two-equation model of turbulence. *Int. J. Heat Mass Transfer* **15**, 301–314.

Perić, M. 1993 – Private communication.

Roach, P.E. and Brierley, D.H. 1990 – The influence of a turbulent free stream on zero pressure gradient transitional boundary layer development. Part 1: testcases T3A and T3B. *Numerical simulation of unsteady flows and transition to turbulence*, (Eds O. Pironneau *et al.*), pp. 319–347.

Savill, A.M. 1993 – Some recent progress in the turbulence modelling of bypass transition. *Near-Wall Turbulent Flows*, (Eds R.M.C. So *et al.*), pp. 829–848.

Spalart, P.R. and Baldwin, B.S. 1987 – Direct simulation of a turbulent oscillating boundary layer. *Turbulent Shear Flows* Vol. 6, (Eds J.C. Andre *et al.*), pp. 417–440, Springer.

Authors' address

Faculty of Applied Physics, Delft University of Technology,
Lorentzweg 1, 2628 CJ Delft, The Netherlands.

R. Narasimha

Some Recent Developments in the Linear Combination Model

Abstract

Progress in the parameterisation of turbulent spot formation and propagation, which is at the heart of linear-combination (l.c.) models, is reviewed. Recent experimental data demonstrate the strong influence of pressure gradient on both spot generation and growth; on the other hand flow divergence, while changing spot shape and direction of propagation, appears to have no other strong effect. A detailed study shows that the use of non-parallel stability theory is generally unlikely to make significant changes to the prediction of transition onset as obtained with e^n methods. The range of flow conditions over which l.c. models can make reasonable predictions is increasing, and now covers pressure gradients, compressibility and divergence, but a thorough exploration of flows in severe and varying pressure gradients, including possible subtransitions within the transition zone, is necessary to gain greater confidence in predictions for aeronautical applications.

Introduction

There has been increasing interest in recent years in developing satisfactory models for the transition zone in a boundary layer, the zone being defined as one within which the flow changes from a laminar (but possibly disturbed) state at its upstream end to fully developed turbulence towards the dowstream end; more specifically, the intermittency γ (i.e. the fraction of time that flow is turbulent) varies from zero (0+) to near-unity (1-). This interest is driven in part by technological applications where the design either forces operation in or seeks to utilize the benefits of extensive regions of laminar *or* transitional flow (e.g., laminar-flow aircraft, turbomachinery blades), or is governed by peak heat transfer rates such as occur in the transition zone (e.g. turbomachinery, space shuttle, aerospace plane). A second reason for the interest in the transition zone is that a proper accounting of it could automatically provide the natural initial conditions for the computation of fully turbulent flow downstream. In turbomachinery applications, the flow may experience a succession of events that include laminar separation, transition, reattachment, relaminarization etc., generally both three-dimensional and unsteady (the latter because of periodic tripping by upstream rotor stages: see e.g. Mayle, 1991). No current model can handle satisfactorily the whole range of phenomena thus encountered, although understanding of

various elements in this chain is increasing. Indeed, even the two-dimensional steady case still poses certain problems.

A remarkable feature of the current research scene is a sharp division of labour between workers studying the pre-onset ($\gamma = 0$) stage of the flow and those studying the post-onset stage ($\gamma > 0$). Few experimental investigations cover extensively both sides of onset (an exception being Arnal *et al.*, 1977). From the analysis in Narasimha (1985), it appears that the effective location of transition onset, as defined in the transition zone models we shall describe below, is very close to the well-known appearance of sharp spikes in the velocity signal in K-type breakdown. However, whether the environment is relatively quiet or not, and whether the linearly unstable Tollmien-Schlichting regime is apparent or not, the transition zone is almost always intermittent in the same way (Narasimha, 1994).

Approaches to modelling

The earliest models (e.g., Goldstein, 1938) assumed transition to occur abruptly at some station $x = X$ (say), the fully turbulent flow at $x > X$ being so determined that the momentum thickness θ is continuous at X. Such abrupt-transition models are still frequently used in engineering design. However, they yield unrealistically high values of peak wall stress and heat transfer.

More sophisticated models for the transition zone can be classified broadly into three categories (Narasimha, 1985): algebraic, differential and linear-combination. In algebraic models (e.g. Cebeci & Smith, 1974), the molecular viscosity ν_m is enhanced by an intermittency-weighted eddy viscosity, the effective total viscosity being taken as

$$\nu = \nu_m + \gamma \nu_T. \tag{1}$$

Differential models tackle directly the Reynolds-averaged equations of motion, usually with one- or two-equation turbulence closures. In these models, some initial disturbance has to be specified; Wilcox (1981) uses the linear stability solutions at the e^4 amplification point to provide initial profiles of turbulent energy and dissipation. More recently, Wilcox (1994) has proposed a numerical trip on a K-ω model. Vancoillie (1984) formulates equations for conditional averages, introducing the intermittency explicitly in the K-ϵ approach. Steelant & Dick (1995) have pursued the 'K-ϵ-γ' model further. Most other differential models do not explicitly use intermittency, and a recent assessment (Narasimha, 1994) concluded that, at that time at least, they needed considerably more development before they could be effectively used.

The linear-combination model has been extensively used by the author and his co-workers (Dey & Narasimha, 1988, 1990a), as well as by other groups. Here the laminar and turbulent boundary layers (the latter originating at a specified or predicted onset location x_t) are separately calculated, and then combined in the proportion $(1 - \gamma)$:γ to obtain the transitional boundary layer. As the method gets to be used more widely, it may be worthwhile to begin by saying what it is

not. It is *not* necessarily an effective eddy viscosity method (although Warren *et al.*, 1995 so imply), but the fully turbulent flow that is one element of the linear combination could be computed on that basis. It is also *not* (in general) a momentum integral method, for the momentum integral equation may not be obeyed. This might at first sight seem disturbing, but it must be noted that for laminar flow computations the DN model uses the method of Thwaites (1949), or a refinement of it (Dey & Narasimha, 1990b); neither of these satisfies the momentum integral either. Indeed the spirit of the Thwaites method is that there are relations between integral parameters that are more robust than those that might be derived by using momemtum integral conservation (invariably based on velocity profiles that do *not* conserve momentum). Nevertheless, as the linear-combination method has a more general foundation than the Thwaites method, a version of it that conserves integral momentum may also be devised (Dey & Narasimha, to be published). Finally, we should note that the conditionally averaged velocity profiles in the transition zone are close to but do not strictly match the 2D laminar or turbulent profiles, as assumed by the method.

In spite of these limitations, we know of no other transition-zone model which has been validated against so many test cases with such generally satisfactory results.

We will confine ourselves here to developments beyond those surveyed by Narasimha & Dey (1989) and Narasimha (1991a). It will be recalled that the overall structure of the DN model is modular, the different modules computing, respectively, laminar flow parameters and velocity profiles, turbulent flow parameters and velocity profiles, onset location and extent of the transition zone. The objective of this paper is to describe certain recent developments pertaining to the model, especially in the last two modules (which are critical to its success), and to review the status regarding its applications.

Onset prediction

With recent developments in treating the stability of non-parallel flows (e.g. Bertolotti *et al.*, 1992), a question that arises is how important it is in practice to take into account the effects of non-parallelism in onset prediction using the classical Smith-van Ingen e^n methods. This question has been analysed in detail by Govindarajan & Narasimha (1995). They first provide a rational analysis of the 2D non-parallel linear stability problem to $O(R^{-1})$, where R is a local Reynolds number based on boundary layer thickness. The key to their analysis is the use of a transformation of the independent variables that is an extension of the well-known Falkner-Skan approach. Arbitrary pressure gradients are treated by a locally similar or a weakly non-similar approach. Fig. 1 shows a typical example of their analysis. Their general conclusion is that non-parallelism is significant only in strong adverse pressure gradients, and for tracking the growth of high-frequency disturbances at relatively low Reynolds numbers. For example, they find that for the Falkner-Skan flow with $m = -0.06$, disturbances with a frequency parameter $F = 2.52 \times 10^{-4}$ (where $F = \omega\nu/U^2$, ω is the frequency, ν

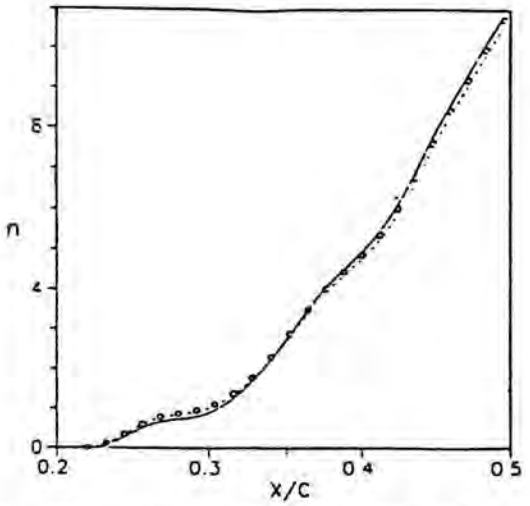

Figure 1: Effect of non-parallelism in estimation of n-factor on a Wortmann FX-63-137 aerofoil, at zero angle of attack, chord Reynolds number = 2×10^6. Parallel flow: – – –. Non-parallel flow: o o (local similarity), — (weakly non-similar). From Govindarajan (1994).

the kinematic viscosity and U the local free-stream velocity), the log amplification ratio is respectively 20% and 40% higher at the inner and outer maximum of the eigenfunction.

Another interesting conclusion from this work is that a reduced Orr-Sommerfeld equation already contains the major lowest-order effects of non-parallelism in the flow. It should be noted that inclusion of all effects of $O(R^{-1})$ is unjustified unless the mean flow is known to that order, which demands the use of higher order boundary layer theory. For flow past a flat plate, if $f(\eta)$ is the well-known Blasius solution, the reduced Orr-Sommerfeld equation can be written as

$$(f' - c)(\phi'' - \alpha^2\phi) - f'''\phi = (\alpha R)^{-1}(\phi'''' - 2\alpha^2\phi''), \tag{2}$$

where dashes denote differentiation in the Blasius variable η and ϕ is the eigenfunction of stability theory. Equation (2) has the same form as that considered by Smith *et al.* (1984), but the variables are different: the independent variable is η, ϕ is scaled according to *local* free-stream velocity and boundary layer thickness and α is a local wavenumber (being the streamwise derivative of an appropriate phase function). Realizing that R is a function of the streamwise coordinate x, it will be seen that the solution ϕ of (2) depends on both η and x. Govindarajan & Narasimha (1995) show that it contains considerable information about the effects of non-parallelism; e.g. the dependence of the critical Reynolds number on distance from the wall, characteristic of non-parallel theories, is predicted to great accuracy by (2). To be asymptotically correct, however, some additional terms need to be included (Govindarajan & Narasimha, to be published).

The conclusion is that a non-parallel analysis is required, if at all, for accurate computations of amplitude ratios only in high disturbance environments (implying low amplification factors n_t at transition) and significant adverse pressure gradients (where transition Reynolds numbers tend to be low). In general the non-parallel theory predicts slightly higher amplitude ratios (perhaps raising the n factor by up to 0.5); however for such results to be accepted as rational, higher order effects on the mean flow in the boundary layer, due to curvature, displacement effect etc, would need to be taken into account. At the present state of development of e^n methodology, it appears that Orr-Sommerfeld computations (with or without the $\alpha^4\phi$ term) should be adequate.

Turbulent spot propagation characteristics

Spot parameterization is a key component of l.c. models. There is beginning to be useful data on spot behaviour in pressure gradients, but a consistent picture has not yet emerged. Katz *et al.* (1990) report that, in a favourable Falkner-Skan pressure gradient with β-parameter of 0.12, spot growth is inhibited (spread angle reduced to half its constant pressure value), and that spot propagation velocities tend to remain constant (instead of increasing in proportion to free-stream velocity). Narasimha *et al.* (1984a), using varying favourable gradients, find that spread rates can change downstream, tending relatively abruptly to constant-pressure values as soon as pressure gradients are relaxed. They suggest stability as a possible explanation: in a varying pressure gradient the stability-critical Reynolds number, as determined say from the Orr-Sommerfeld equation, can exhibit dramatic variations downstream, so the flow may change back and forth between subcritical and super-critical states as it develops. Data on the suction surface of a blade tripped periodically by the moving wake of rods upstream, simulating rotor blades in a turbine stage (Dong & Cumpsty, 1990), show abrupt changes in velocity of propagation of the resulting turbulent "slab" as it moves downstream along the blade.

On the other hand, Clark *et al.* (1994), studying spots in natural transition in constant favourable pressure gradients, report that leading edge velocities remain a constant fraction of local free-stream velocity, but trailing edge velocities tend to higher fractions than in constant pressure flows. (Incidentally their data are not inconsistent with a sudden change in the latter (at $x = 55$ mm, their Fig. 14).)

Gostelow *et al.* (1995) have recently studied spots in adverse pressure gradients, and report that spread rates can be doubled over values in zero pressure gradient. A spot in divergent constant-pressure flow has been investigated by Jahanmiri *et al.* (1995); they find that the divergence changes spot shape substantially, and that, while the angle of the envelope of spot positions with the local streamline can vary considerably (3^o to 13^o), the spread rate remains at the standard 2-D value of about 10^o. These results are consistent with the explanation that divergence produces chiefly a *geometric* distortion of the coherent structure in the spot, but not any significant *dynamic* modification.

These investigations show, as suggested by Narasimha (1985), that gross changes in spot propagation characteristics can occur under certain flow conditions. Recent work has begun to address these problems, but much still remains to be done to provide a rational framework for understanding the observed effects.

Intermittency distributions

Emmons (1951) showed how the intermittency $\gamma(x)$ could be related to a source function giving the rate at which turbulent spots are formed over the surface. The assumptions underlying this formulation appear to be sufficiently realistic that the resulting expression provides an effective means for analyzing transition-zone data. The additional hypothesis of concentrated breakdown (Narasimha, 1957) leads to the result, in 2D constant-pressure flow with linear spot propagation,

$$\begin{aligned} \gamma &= 0, \quad x < x_t \\ \gamma &= 1 - \exp\left[-\tfrac{(x-x_t)^2 \overline{n}\sigma}{U}\right] = 1 - \exp(-0.41\xi^2), \quad x_t < x \end{aligned} \tag{3}$$

where

$$\xi = (x - x_t)/\lambda \tag{4}$$

is a non-dimensional variable using the distance λ between the stations where γ=0.25 and 0.75 to characterize the extent of the transition zone, $\overline{n}$ is the mean rate of spot formation and σ is the spot propagation parameter defined by Emmons (1951). The hypothesis of concentrated breakdown has received some direct support from the recent work of Shaikh & Gaster (1993).

The validity of eq. (3) has been confirmed by a variety of measurements, the more recent ones including Fraser *et al.* (1988) and Gostelow & Walker (1990) in weak pressure gradients, Ramesh *et al.* (1996) in constant-pressure divergent flow (consistently with the spot data cited above), and Schmisseur *et al.* (1996) in supersonic flow. Other curves have also been suggested for the distribution, and a critical discussion will be found in Narasimha (1991b). With suitable fitting procedures any of several expressions provide reasonable approximations to the data, (3) being perhaps the most satisfactory (Fraser *et al.*, 1988; cf. their Figs 3, 4 and 5). The real advantage of (3), however, is its direct relation to spot theory, and the natural way in which extensions can be derived for more complex situations based on information on spot behaviour. (See Narasimha (1985) for examples, using a generalized intermittency distribution.)

In using (3), it is necessary to take some care in determining both λ and x_t, especially as small departures from (3) are sometimes noticed near x_t. A good procedure to follow (Narasimha, 1957, 1985) is to plot $F(\gamma) = [-\ln(1-\gamma)]^{1/2}$ vs. x, and extrapolate from the best linear fit for $F(\gamma)$ in the middle of the transition zone to the point $\gamma = 0$. Failure to analyze results on this "$F(\gamma)$, t basis", as Walker & Gostelow (1989) call it, has sometimes been responsible for

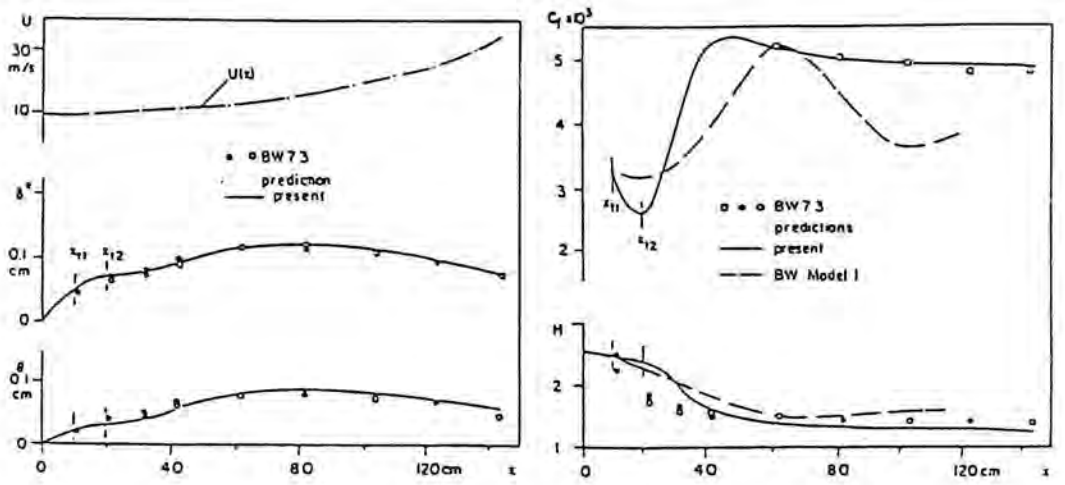

Figure 2: Comparison of DN predictions with flow BW73 from Blair & Werle (1981). Note the thinning of the boundary layer in the favourable gradient. Onset at x_{t_1}, subtransition at x_{t_2}; other notation is standard.

unjustified conclusions (as demonstrated by Dey & Narasimha, 1988; Gostelow & Walker 1990).

We now consider the effect of pressure gradient on the intermittency distribution. Abu-Ghannam & Shaw (1980) find no effect in their experiments; in the earlier work of Gostelow & Walker (1990) also, the intermittency distribution followed the expression (3). On the other hand the extensive data of Narasimha *et al.* (1984b) found significant effects, especially when the pressure gradients vary appreciably within the zone. It is now clear that weak pressure gradients do not affect the distribution; in favourable gradients, Dey & Narasimha (1990) suggest the limit in terms of the Thwaites pressure gradient parameter as

$$L \equiv \frac{dU}{dx}\,\frac{\theta^2}{\nu} < 0.06. \tag{5}$$

The Chen-Thyson (1971) model, also based on the hypothesis of concentrated breakdown, seeks to take account of pressure gradients and flow divergence based on two further assumptions: (i) the spot propagation velocities are proportional to the local free-stream velocity $U(x)$; and (ii) the spot spreads across the local streamlines at a (universal) angle. These assumptions are contradicted by some of the spot studies cited earlier.

Under strong and varying pressure gradients, the flow can behave in strange ways, as demonstrated by the experiments of Blair & Werle (1981; see in particular the flows called BW72, BW73 in Dey & Narasimha (1990), and Fig. 2). Indeed, it is possible to conceive of a situation in which, following onset, transition is aborted midway by a strong laminarizing favourable pressure gradient; an instance of this might be the 10^o swept wing data shown in Narasimha

(1985) (Fig. 33). In these and other cases, it seems necessary to recognize that the intermittency distribution can best be seen as involving "subtransitions" (Narasimha, 1984), which are characterised by a kink in the dependence of $F(\gamma)$ on x. Now $F(\gamma)$ is proportional to the square root of the dependence area at x (Narasimha, 1985), and so *mirrors* spot growth in some sense. The kink can therefore be marking a rapid change in spot propagation characteristics of the kind noted above. The existence of a subtransition in some of the flows studied by Blair & Werle (1981) was suspected by Dey & Narasimha (1988) on the basis of the observed mean-flow parameters; this has since been confirmed by Blair (1992) through direct measurements of the intermittency. Early experiments, quoted in Narasimha *et al.* (1984b), show that a favourable pressure gradient in the beginning of the transition zone has a marked effect on the intermittency distribution, and results in a subtransition, whereas a similar gradient in the downstream half of the transition zone has little effect. An obvious explanation is that the gradient is stabilizing in the first case, but in the second, where the flow is turbulent for a substantial part of the time, the response would be weaker. This suggests that the effect of pressure gradient cannot be seen in terms only of its magnitude in laminar flow scales (Eq. (5)), but must be coupled with the intermittency levels at which the pressure gradient is imposed. It therefore appears doubtful whether a simple prescription of spot formation rate as a function of L (see discussion below) would be able to describe the situation, unless the pressure gradient is low and the flow is always supercritical.

There are other kinds of subtransition as well. For example there are many interesting situations where there is a "subtransition" from the 2-D to the 1-D law in the same flow. (The 2-D law is given by Eq. (3), and the so-called "1-D law" is applicable to situations where one dimension of the spot is fixed, as for example happens in a pipe; see Narasimha, 1984.) This is easily understood on an axisymmetric body (Rao, 1974) that becomes, downstream of the nose, a circular cylinder with axis aligned to the flow: if x_t is in the nose region, a 2-D law near x_t changes to a 1-D law sufficiently far downstream (Narasimha, 1984). A similar situation occurs in the study of the phenomenon of wake-induced transition, currently of great interest in turbomachinery (where the wakes of passing rotor blades create a 1-D "slab" of turbulence (Narasimha, 1991b)): Mayle & Dullenkopf (1990) have provided an appropriate combination of 2D and 1D laws relevant to the problem.

While it cannot be doubted that such subtransitions can occur because of relatively abrupt changes in spot characteristics, distributed breakdown could contribute to the observed effect. Gaussian distributions of the spot formation rate were already considered by Dhawan & Narasimha (1958), and have been revived recently by Mayle (1991) as a possible explanation for the observed departure of $F(\gamma)$ from linearity near x_t in pressure-gradient flows. Further work is required to determine the relative importance of these mechanisms.

Current status

The code TRANZ 2, used in Dey & Narasimha (1988, 1990a), has been updated in several ways, and should result before long in a new version, to be called TRANZ 3. The modifications to TRANZ 2 consist of the following.

(i) Onset prediction
Govindarajan & Narasimha (1991) showed that, at very low free stream turbulence levels q, it is necessary to take account of residual disturbance levels in the facility or application situation (e.g. turbomachinery), as free-stream turbulence ceases to be the driving force in such a situation. They introduced an additional parameter q_0 to characterize the residual disturbance, and correlated results with the total disturbance

$$q_t = (q^2 + q_0^2)^{1/2}. \tag{6}$$

By a proper choice of q_0, they could find a single correlation that agreed with all available data. What values of q_0 would be appropriate for flight conditions still needs to be investigated.

As e^n methods have the advantage of providing an indication of the sensitivity of transition location to pressure gradients and can be of great use in design (e.g. of aerofoils), Govindarajan (1992) has sought to express the n-factor for transition in terms of disturbance level and pressure gradient. For zero or adverse pressure gradients, she suggests

$$n_t = 0.87e^{-97L}(1 + 3/q_t)(1 + 6Le^{-q^2}) - 1.85e^{-16L}. \tag{7}$$

The situation in favourable gradients is more complicated, as transition can often occur at sub-critical Reynolds numbers even at relatively modest disturbance levels (as is evident in the data of Abu-Ghannam & Shaw (1980)). It appears essential here to estimate transient sub-critical growth of disturbances, along the lines of Reddy & Henningson (1993).

(ii) Extent:
This is specified through the parameter $N = \overline{n}\sigma\theta_t^3/\nu$ (Narasimha & Dey, 1986). For severe favourable pressure gradients, Dey & Narasimha (1991) propose a relation for N normalized at the *subtransition* point. For low pressure gradients, new correlations have been proposed by Fraser (1994) and Gostelow *et al.* (1995), showing a continuous variation of N with $L_t \equiv L(x_t)$ and q. It must incidentally be pointed out that the "Narasimha-Dey" curves presented in Gostelow *et al.* (1995) are *not* predictions given by us, as they are not based on our model for subtransitions (for which the reader is referred to Fig. 7 of Dey & Narasimha, 1990a). When a subtransition does occur, the prediction of its location still remains a major problem.

Commentary on applications

Gostelow *et al.* (1994) have computed ERCOFTAC cases T3AM, T3A and T3C, and find generally good agreement with predictions made by the DN method. They find however that the predictions depend quite strongly on the initial conditions for integrating the equations for the turbulent boundary layer. They also find that the extent of the transition zone, but not the onset location, is given reasonably well by Abu-Ghannam & Shaw's correlation, and suggest that the effect of high free-stream turbulence on the *laminar* layer can not be neglected.

More recently, Solomon *et al.* (1995) have made comparisons with experimental data in pressure gradients, chiefly those obtained by Narasimha *et al.* (1984b), Sharma *et al.* (1982) and ERCOFTAC case T3C2. Using new correlations for N as a function of pressure gradient and free-stream turbulence level, Solomon *et al.* report good agreement in several cases. It would also be interesting to find out how well the abrupt increase in the Reynolds number R_θ sometimes noted at the subtransition point (e.g. in flow DFU3) would be predicted by this method, and also in such rapidly varying pressure gradients as in the flows DFD1, NFD1 and NFU1 of Narasimha *et al.* (1984b).

Swaminathan & Balu (1995) have applied the DN method to incompressible 3D boundary layer flows. Comparison with the experiments of Meier & Kreplin (1980) on a 1:6 spheroid shows that, while DN is doing rather better than other methods, it predicts a shorter transition zone than is observed, especially at an angle of attack of 5°. However, a slightly downstream choice of x_t should appreciably reduce the discrepancy, and a slightly lower value of N should further improve the agreement.

Bishnoi & Nandanan (1995) find that, in their analysis of a supercritical natural laminar flow aerofoil, the transition onset correlations of Govindarajan & Narasimha (1991) play a useful role; in particular they are helpful in design, as they can pinpoint those parts of the aerofoil (more precisely the pressure distribution) which are particularly vulnerable to transition, as in such areas the predicted $R_{\theta t}$ may be very close to (although higher than) the R_θ computed for the laminar flow on the aerofoil.

The linear-combination method is being applied in supersonic flows as well. McKeel *et al.* (1995) do this on three test cases: cone at Mach 6, compression ramp at Mach 10.08 and flared cone at Mach 7.93, respectively representing zero, adverse and favourable pressure gradients. The agreement was considered good in the first and third cases and excellent in the second, but in the first two the values of N that gave best agreement were somewhat lower than those recommended by Narasimha & Dey (1986) for *zero* pressure gradient (based largely on indirect evidence): it would not be surprising if they need some revision in the light of more elaborate modelling, especially when the pressure gradient is not zero.

Warren *et al.* (1995) report that they do not get good agreement on recovery factors measured on a cone and a flat plate at Mach 3.36, but the experimental data are puzzling as they show a slow and continuous fall with increasing Reynolds number and do not tend to standard turbulent values far downstream.

A linear-combination (or, indeed, any other) model cannot of course do well if the behaviour of the fully turbulent flow is anomalous.

Future work

Further progress in transition zone modelling requires several careful experimental programmes. First of all, the behaviour of turbulent spots when subjected to such influences as pressure gradient, distortion, curvature, three-dimensionality, compressibility etc., needs to be investigated more extensively. Parameters of interest will include shape, velocities of propagation, conditional statistics, and flow structure. Further experiments are also needed in two-dimensional flows with pressure gradient, both favourable and adverse, with a disturbance environment that is well understood and carefully controlled; the conditions under which subtransitions occur need to be investigated more thoroughly. Data on flows with separation bubbles are badly needed in turbomachinery applications. Little has been done on three-dimensional transition zones. Significantly better models are unlikely to emerge without the benefit of all this experimental work, although certain improvements can be envisaged on current models and will undoubtedly appear as a result of work on hand. Predicting onset remains of course a major problem, but we also need better ways of estimating the spot formation rate parameter N.

Acknowledgement

This work has been supported in part by ONR contract no. N00014-94-1-1133. I am indebted to Dr J Dey and Prof. A Prabhu (Indian Institute of Science, Bangalore), and Dr R Govindarajan (National Aerospace Laboratories, Bangalore) for long years of collaboration and shared insight and experience; and to Dr M Y Hussaini for a short visit to ICASE in 1990, which resulted in a report (ICASE 90-90) that has provided a basis for this present substantial update.

The paper is dedicated to Prof Satish Dhawan on his 75th birthday, in warm gratitude for launching me 40 years ago on the trail pursued in this paper.

References

Abu-Ghannam, B.J. & Shaw, R. 1980 – Natural transition of boundary layers – the effects of turbulence, pressure gradient, and flow history. *J. Mech. Engng Sci.* **22**, 213-228.

Arnal, D., Juillen, J.C. & Michel, R. 1977 – Analyse experimentale et calcul de l'appartition et du developpement de la transition de la couche limite. ONERA T.P. 1977-54.

Bertolotti, F.P., Herbert, T. & Spalart, P.R. 1992 – Linear and nonlinear stability of the Blasius boundary layer. *J. Fluid Mech.* **242**, 441-474.

Bishnoi, P.K. & Nandanan, M. 1996 – Prediction of transition on a supercritical natural laminar flow airfoil. To be published.

Blair, M.F. & Werle, M.J. 1981 – Combined influence of free-stream turbulence and favourable pressure gradients on boundary layer transition and heat transfer. Report R81-914388-17, United Technologies Research Center, Connecticut.

Blair, M.F. 1992 – Boundary-layer transition in accelerating flows with intense freestream turbulence: Part 2 – The zone of intermittent turbulence. Trans. ASME, *J. Fluids Engng* **114**, 322-332.

Cebeci, T. & Smith, A.M.O. 1974 – *Analysis of turbulent boundary layers.* Academic Press, New York. pp. 234-239.

Chen, K.K. & Thyson, N.A. 1971 – Extension of Emmons' spot theory to flows on blunt bodies. *AIAA J.* **5**, 821-825.

Clark, J.P., Jones, T.V. & La Graff, J.E. 1994 – On the propagation of naturally-occurring turbulent spots. *J. Engng Maths.* **28**, 1-19.

Dey, J. & Narasimha, R. 1988 – An integral method for the calculation of 2-D transitional boundary layers. IISc Report 88 FM 7, Dept. Aero. Engg.

Dey, J. & Narasimha, R. 1990a – Integral method for the calculation of incompressible two-dimensional transitional boundary layers. *J. Aircraft* **27**, 859-865.

Dey, J. & Narasimha, R. 1990b – An extension of Thwaites's method for calculation of incompressible laminar boundary layers. *J. I.I.Sc* **70**, 1-24.

Dey, J. & Narasimha, R. 1991 – Effect of favorable pressure gradient on transitional spot formation rate. *Exptl. Thermal & Fl. Sci.* **4**, 192-197.

Dhawan, S. & Narasimha, R. 1958 – Some properties of boundary layer flow during the transition from laminar to turbulent motion. *J. Fluid Mech.* **3**, 418-437.

Dong, Y. & Cumpsty, N.A. 1990b – Compressor blade boundary layers. Part 2 – Measurements with no incident wakes, *J. Turbomachinery,* Trans ASME **112**, 231-240.

Emmons, H.W. 1951 – The laminar turbulent transition in a boundary layer – Part I. *J. Aeronaut Sci.* **18**, 490-498.

Fraser, C.J., Milne, J.S. & Gardiner, I.D. 1988 – The effect of pressure gradient and freestream turbulence intensity on the length of transitional boundary layers. *Proc. Inst. Mech. Eng.* **202**, 195-203.

Fraser, C.J. 1994 – Transition models for engineering calculations. *Proc. Symp. End-Stage Transition*, Syracuse Univ.

Goldstein, S. 1938 – *Modern developments in fluid dynamics.* Oxford.

Gostelow, J.P. 1989 – Adverse pressure gradient effects on boundary layer transition in a turbulent free stream. *Proc. 9th Intl. Symp. Air-Breathing Engines*, Athens.

Gostelow, J.P. & Walker, G.J. 1990 – Similarity behaviour in transitional boundary layers over a range of adverse pressure gradients and turbulence levels. *ASME Gas Turbine Conference*, Brussels.

Gostelow, J.P., Hong, G., Walker, G.J. & Dey, J. 1994 – Modelling of boundary layer transition in turbulent flows by linear combination integral method. *ASME Paper* 94-GT-358.

Gostelow, J.P., Melwani, N. & Walker, G.J. 1995 – Effects of a streamwise pressure gradient on turbulent spot development. *ASME Paper* 95-GT-303.

Govindarajan, R. & Narasimha, R. 1991 – The role of residual nonturbulent disturbances on transition onset in two-dimensional boundary layers. *J. Fluids Engng* **113**, 147-149.

Govindarajan, R. 1992 – Transition prediction from linear stability computations. *Proj. Doc.* PD CF 9218, Natl. Aerosp. Labs., Bangalore.

Govindarajan, R. 1994 – Stability of spatially developing boundary layers in pressure gradients. Ph.D. Thesis, Dept. Aero. Engg., I.I.Sc., Bangalore.

Govindarajan, R. & Narasimha, R. 1995 – Stability of spatially developing boundary layers in pressure gradients. *J. Fluid Mech.* **300**, 117-147.

Jahanmiri, M., Prabhu, A. & Narasimha, R. 1995 – Turbulent spot in 3-D constant pressure flow. *Laminar - Turbulent Transition* (Proc. IUTAM Symp., ed. R. Kobayashi), pp. 279-286. Springer.

Katz, Y., Seifert, A. & Wygnanski, I. 1990 – On the evolution of the turbulent spot in a laminar boundary layer with a favourable pressure gradient *J. Fluid Mech.* **221**, 1-22.

Mayle, R.E. & Dullenkopf, 1989 – A theory of wake-induced transition. *J. Turbomachinery* **112**, 188-195.

Mayle, R.E. 1991 – The role of laminar-turbulent transition in gas turbine engines. *J. Turbomachinery* **113**, 509-537.

McKeel, S.A., Walters, R.W. & Chadwick, K.M. 1995 – Investigation into transition modelling. *AIAA Paper* 95-1746-CP.

Meier, H.V. & Kreplin, H.P. 1980 – Experimental investigation of the boundary layer transition and separation on a body of revolution. *Z. Flugwiss. Weltraumforsch.* **4**, 65-71.

Narasimha, R. 1957 – On the distribution of intermittency in the transition region of a boundary layer. *J. Aero. Sci.* **24**, 711-712.

Narasimha, R. 1984 – Subtransitions in the transition zone. In: *Laminar-Turbulent Transition* (Proc. IUTAM Symp., Novosibirsk, ed. V.V. Kozlov), pp.141-151. Springer-Verlag, New York.

Narasimha, R., Subramanian, C. & Badrinarayanan, M.A. 1984a – Turbulent spot growth in favorable pressure gradients. *AIAA J.* **22**, 837-839.

Narasimha, R., Devasia, K.J., Gururani, G. & Badrinarayanan, M.A. 1984b – Transitional intermittency in boundary layers subjected to pressure gradient. *Exp. Fluids* **2**, 171-176.

Narasimha, R. 1985 – The laminar-turbulent transition zone in the boundary layer. *Prog. Aerosp. Sci.* **22**, 29-80.

Narasimha, R. & Dey, J. 1986 – Transitional spot formation rate in two-dimensional boundary layers. In: *Numerical and Physical Aspects of Aerodynamic Flows,* III (ed. T. Cebeci), pp. 57-74. Springer-Verlag, New York.

Narasimha, R. & Dey, J. 1989 – Transition zone models for 2-D boundary layers. *Sādhanā* **14**, 93-120.

Narasimha, R. 1991a – In: *Boundary layers in turbomachines.* VKI Lecture Series 1991-06.

Narasimha, R. 1991b – Recent advances in the dynamics of the transition zone. In: *Proc. 10th Intl. Symp. Air-Breathing Engines,* Nottingham, UK, pp. 71-79.

Narasimha, R. 1994 – A report on the workshop on end-stage transition. *Current Science* **67**, 6-9.

Ramesh, O.N., Dey, J. & Prabhu, A. 1996 – Transitional intermittency distribution in the 3-D constant pressure diverging flow. To be published.

Rao, G.N.V. 1974 – Mechanics of transition in axisymmetric boundary layer on a circular cylinder. *ZAMP* **25**, 63-75.

Reddy, S.C. & Henningson, D.S. 1993 – Energy growth in viscous channel flows. *J. Fluid Mech.* **252**, 209-238.

Schmisseur, J.D., Young, J.O., & Schneider, S.P. 1996 – Measurement of boundary-layer transition on the flat sidewall of a rectangular Mach 4 quiet-flow nozzle. *AIAA Paper* 96-0852.

Shaikh, F.N. & Gaster, M. 1993 – Investigation of transition to turbulence using white noise equation. *Nonlinear instability of non-parallel flows* (Proc. IUTAM Symp., Potsdam, NY), pp. 147-159. Springer-Verlag, New York.

Sharma, O.P., Wells, R.A., Schlinker, R.A. & Bailey, D.A. 1982 – Boundary layer development on turbine airfoil suction surfaces. ASME *J. Eng. Power* **104**, 698-706.

Smith, F.T., Papageorgiou, D. & Elliott, J.W. 1984 – An alternative approach to linear and nonlinear stability calculations at finite Reynolds numbers. *J. Fluid Mech.* **146**, 313-330.

Solomon, W.J., Walker, G.J. & Gostelow, J.P. 1995 – Transition length prediction for flows with rapidly changing pressure gradients. *ASME Paper* 95-GT-241.

Steelant, J. & Dick, E. 1995 – Conditioned Navier-Stokes equations combined with the k_ϵ model for by-pass transitional flows. *Lecture Notes in Physics 453* (Proc. 14th Intl. Conf. on Numerical Methods in Fluid Dynamics, Bangalore, eds. S. M. Deshpande, S. S. Desai, R. Narasimha), pp. 353-357. Springer, Berlin.

Swaminathan, R. & Balu, R. 1995 – Some studies on 3-D boundary layer flows. *Tech. Report* TR:373:95, VSSC Trivandrum.

Thwaites, B. 1949 – Approximate calculation of the laminar boundary layer. *Aeronaut Q.* **1**, 245-280.

Vancoillie, G. 1985 – A turbulence model for the numerical simulation of transitional boundary layers. *Laminar-turbulent transition* (ed. V.V. Kozlov), pp. 87-92. Springer.

Walker, G.J. & Gostelow, J.P. 1990 – Effects of adverse pressure gradients on the nature and length of boundary layer transition. *J. Turbomachinery* **112**, 196-205.

Warren, E.S., Harris, J.E. & Hassan, H.A. 1995 – Transition model for high-speed flow. *AIAA J.* **33**, 1391-1397.

Wilcox, D.C. 1981 – Alternative to the e^9 procedure for predicting boundary layer transition. *AIAA J.* **19**, 56-64.

Wilcox, D.C. 1994 – Simulation of transition with a two-equation turbulence model. *AIAA J.* **32**, 247-255.

Author's address

Department of Aerospace Engineering and
Jawaharlal Nehru Centre for Advanced Scientific Research
Indian Institute of Science, Bangalore 560 012, India

A.M. Savill

Transition Prediction with Turbulence Models

Abstract

The prediction of transition location (onset and length) is of vital importance in many internal and external aerodynamic flow applications. For aeroengine flows it may be regarded as the pacing item controlling the move from traditional (largely empirical) to future CFD design methods. Over the last five years the European Research Community on Flow Turbulence and Combustion (ERCOFTAC) Transition Special Interest Group (SIG) has made considerable progress in evaluating and refining intermittency descriptions and turbulence modelling approaches for predicting by-pass transition in turbomachinery. The present paper considers how the results may be relevant also to some external aerodynamic flow situations and discusses the possibility of extending the same predictive capability to natural transition under very low free-stream turbulence.

Introduction

Even today most industrial design methods use 'point transition' at an assumed transition location and force a switch between laminar and turbulent computations at that point, or make use of empirical correlations to estimate the 'start' of transition and then scale up the eddy viscosity by a further empirical transition function until fully turbulent conditions are attained at the 'end' of transition so that the transition length is again determined by a correlation. These two approaches are generally used in conjunction with so-called zero equation mixing length models or even simpler integral methods.

However, as early as 1972 it was demonstrated that the Jones-Launder two-equation low-Re $k-\varepsilon$ model could predict a range of relaminarising flows and shortly afterwards also shown that this type of transport equation approach could be used to predict by-pass transitional flows as well – see Savill (1996).

This and other early work on the application of low-Re turbulence models to such transitional flows led to the first extensive evaluations of transition predictions for simple and turbine blade test cases, using the Lam & Bremhorst low-Re $k-\varepsilon$ model. For free-stream turbulence (fst) intensities above 0.5% it was found this model could quite accurately predict the observed by-pass transition provided the initial conditions were carefully controlled. This remains the lowest level of fst for which low-Re turbulence models can provide results.

The first real inter-comparison of the full range of different closure models for predicting by-pass transition, from the simplest correlation methods to

Direct Numerical Simulations (DNS), was conducted as part of the 1st European Research Community on Flow Turbulence and Combustion (ERCOFTAC) Workshop held at the EPF Lausanne in 1990 – see Pironneau *et al.* (1992). Two sharp leading-edge test cases were considered for transition in zero pressure gradient under the influence of isotropic 3% (T3A Case) and 6% (T3B) fst.

The results showed that specific turbulence models and DNS could predict flow development through transition more accurately than standard industrial correlation methods and led to the setting up of the ERCOFTAC Transition Special Interest Group (SIG) – see Savill (1992) – with the aim of evaluating and refining turbulence models for predicting transition; initially for turbomachinery applications. Work carried out over the last 5 years has established the optimum approaches at each level of model closure, in terms of potential for predictive ability and and widest ranging applicability, by reference to progressively more complex test cases – see Table 1 and Savill (1996).

At the same time similar projects to assess turbulence models for predicting transition in natural convection flows and pipes, as well as relaminarising flows have been undertaken by other researchers. In addition NASA are coordinating a very similar evaluation exercise for by-pass transition models amongst USA research groups. All of these projects have reached similar conclusions, at least regarding the optimum low-Re $k-\varepsilon$ approach for predicting all these flows. The present paper concentrates on the ERCOFTAC Project results because model validation within this has been strictly controlled by insisting that test case computations are initially done 'blind'; using only specified initial/boundary conditions, and then compared with detailed experimental data complimented by DNS (with the industrial input to ensure relevance of comparisons).

Recent developments in the prediction of by-pass transition

In order to use (high-Re) turbulence models to predict transition one must introduce additional (low-Re) model approximations to handle the turbulence development through transition. For this approach to be successful there has to be some initial source of turbulence activity within or outside the initial (pseudo-laminar) shear layer, and one has to make the inherent assumption that the transition is 'diffusion-controlled' in the sense that it is triggered by diffusion of free-stream turbulence into the flow. Such 'by-pass transition' only occurs for free-stream turbulence intensity levels 1%. It was given this name by Morkovin because most of the development stages in natural transition are then by-passed and transition to turbulence then occurs at a point where breakdown of free-stream-turbulence-induced streaks and secondary instability produces (in 2D) a line of turbulent spots across the span of the flow.

Alternatively one can adopt an intermittency description and adopt the premise that the transition process can be modelled as a superposition of laminar and turbulent flow in changing proportions γ – taking γ times a turbulent solution and (1-γ) times laminar – where γ is an intermittency factor varying from 0 at the start of transition to 1 at the end of transition.

Table 1: ERCOFTAC SIG Test Cases

T3A$^-$	zero pressure gradient, 1% isotropic fst (theoretical or experimental initial conditions)
T3A	zero pressure gradient, 3% isotropic fst (theoretical or experimental initial conditions)
T3A$^+$	zero pressure gradient, 3% isotropic fst, but variable length scale (theoretical or experimental initial conditions)
T3B	zero pressure gradient, 6% isotropic fst (theoretical or expt. initial conditions)
T3B$_{LES}$	zero pressure gradient, 4.5% weakly anisotropic fst (simulated initial conditions)
T3B$^+$	zero pressure gradient, 10% weakly anisotropic fst (experimental initial conditions)
T3C	pressure gradient representative of aft-loaded turbine blade (expt. initial conditions; various Re): C1 (6% fst) & C2 (3% fst, same design Re); C3 & C4 (3% fst , lower Re without/with laminar sepn.); C5 (3% fst, higher Re)
T3D1-3	zero pressure gradient, 0.1% isotropic fst, following laminar separation (expt. conditions; various Re)
T3E	strong favourable/adverse pressure gradient, 0.01% fst, relaminarisation/retransition (expt. initial conditions)
T3L	semi-circular leading edge, 0.2 – 6% fst (expt. initial conditions; various Re, fst, etc)
T3K	Low-Speed (HP Rotor) Turbine Cascade, 4% free-stream turbulence (expt. initial conditions)

It has to be stressed however that neither approach considers many of the individual mechanisms and stages of transition. The low-Re modelling approach takes no specific account of receptivity, algebraic growth, secondary instability, or turbulent spots. Instead the modelling implicitly assumes that the diffusion of (generally isotropic) free-stream-turbulence into an initial pseudo-laminar (essentially Blasius profile) boundary layer leads to a build-up of weakly correlated turbulence activity and transition is initiated once the local production of turbulence energy sufficiently exceeds the local dissipation. All low-Re models are rather insensitive to the actual turbulent (spot) structure.

Intermittency methods do attempt to account for spot formation and growth rates, with varying degrees of sophistication based on an ever expanding experimental database, but only a few of these make any allowance for receptivity and algebraic growth, and even those that do lump these together with secondary instability effects in 'so-called' sub-transition corrections.

It is also important to note that the the division between natural and bypass transition regimes is not as clear as Morkovin suggested. There is ample evidence in the literature to show that the 'T-S mechanism' can co-exist with other 'strongly amplifying mechanisms' over a wide range of fst intensities from well below to well above 1%. Indeed the Large Eddy Simulations performed for

3 & 6% fst test cases revealed the existence of TS wave-like behaviour as well as free-stream-turbulence-induced streaks and isolated spots in the wall layer upstream of transition onset (characterised by minimum C_f).

Turbulence modelling

It must be emphasised that all current low-Re models were originally developed to handle low-Re near-wall regions of turbulent flows, by introducing appropriate damping factors in order to extend the modelling right though the buffer layer where high-Re models resort to wall functions, and that no models have so far been proposed primarily to model low-Re transition regions instead or even as well. For the purposes of the present paper it is sufficient to note that each model version introduces different low-Re extensions to the standard high-Re turbulence model equations for turbulence energy and dissipation (length scale), and that the damping factors are always functions of on of the following flow Reynolds numbers:

$$R_y = \frac{k^{1/2}y}{\nu} \quad , \quad y^+ = \frac{u_\tau y}{\nu} \, ,$$

$$R_\varepsilon = \frac{y}{(\nu^3/\varepsilon)^{1/4}} = \frac{y}{\eta} \quad , \quad R_t = \frac{k^2}{\varepsilon\nu} = \frac{\nu_t}{C_\mu \nu} \, ,$$

$$R_L = \frac{k^{3/2}}{\varepsilon\eta} = \frac{l\varepsilon}{\eta} \, .$$

A very large number of low-Re one and two-equation models ($k-l$, $k-\varepsilon$, $k-\tau$ & $k-\omega$) have now been evaluated for their ability to predict by-pass transition flows; including most, if not all, of the best known variants - see Savill (1993).

The results obtained for zero pressure gradient, but variable fst, T3A & B series of test cases have confirmed earlier findings that the Launder-Sharma low-Re $k-\varepsilon$ model variant is the best simple eddy-viscosity approach for predicting such by-pass transition. This is partly because it employs R_t dependent damping factors which allow a more general response to low-Re effects than alternative factors incorporating a specific wall dependence. However it must be regarded as at least partly fortuitous that the Launder-Sharma functions damping of uv with y happens to give roughly the correct functional change in uv with x through transition (particularly in the light of Direct and Large Eddy Simulations (LES) for by-pass transition by Yang & Voke - see Pironneau (1992) & Savill (1994) - since other R_t-based models including the Jones-Launder scheme predict very different transition locations.

The Launder-Sharma model also correctly predicted a delay in transition onset with acceleration, but failed to capture the correct degree of sensitivity to pressure gradient variations representative of an aft-loaded turbine blade operating at its design condition. In fact this is a general problem with eddy-viscosity models. Correction factors need to be introduced to sensitise them to applied

strain rates in transitional and turbulent flows and to improve their sensitivity to the irrotational straining encountered in stagnation regions.

This is one of the two major advantages in moving up to the RST level of closure to predict by-pass transition flows, and indeed many more complex turbulent flows: stress transport models automatically capture the main effects of applied strain rates in both irrotational and curved flows. They can account for effects of (free-stream) turbulence anisotropy and correctly model the production of uv in the transitional boundary layer due to the product of an imposed (external) v^2 with the initial (Blasius) mean flow velocity gradient.

One model in particular, the Savill-Launder-Younis (SLY) low-Re RST scheme has proved particularly successful in predicting a wide range of transitional flows. This model again uses only R_t damping factors, based on an extension of the Launder-Sharma low-Re treatment to the RST level of closure.

The basic SLY model can accurately predict the onset of transition under nominally zero pressure gradient conditions for levels of free-stream turbulence in the range 1-10%, exhibits almost exactly the correct sensitivity to pressure gradient and Re for both on-design and off-design aft-loaded turbine blade test cases, and the correct trends with imposed curvature and large variations in the anisotropy of the free-stream turbulence. It has also has been found to correctly predict the effect on transition onset of a three-fold variation in free-stream length scale, and therefore represents a considerable advance over the simpler low-Re $k-\varepsilon$ scheme of Launder-Sharma.

There is of course no *a priori* reason why one should expect to successfully predict low-Re transitional flows with any of the current low-Re models since, as stated above, these have all been developed to model only the low-Re near-wall regions of fully turbulent flows. Fortunately it would seem that the turbulence Reynolds number is a sufficiently general property of low-Re flows that one can in fact obtain reasonable predictions, at least for integral properties, with such a gross assumption. Such R_t-dependent models also have the advantages that they can easily be applied to non-planar wall geometries and incorporated into unstructured codes and these provide powerful reasons for concentrating on such modelling for practical flow computations.

Intermittency modelling

Intermittency weighting for transitional flows has until recently only been employed in simple closure models, at least for design purposes. In particular a number of different integral/correlation methods have been developed and used to some effect. The first moderately successful model was that of Dhawan & Narasimha, which determined the onset of transition (at Re_{xs}) by extrapolating Narasimha's own assumed universal intermittency distribution as a function of x, and proposed a correlation for the length of transition in terms of Re_{xs} itself.

Within the ERCOFTAC SIG it has been found that a new new correlation for Re_{xs}, based on a wide range of University of Technology Sydney (UTS) data, provides better Cf & H prediction for the zero pressure gradient 3% fst test case,

and a better transition length prediction for the higher 6% fst case than that of Narasimha & Dey's model, while a modified version of the UTS integral method has been shown to produce good predictions for the lower (1%) fst and turbine blade pressure gradient test cases as well – see Savill (1996).

In principle the intermittency approach could be applied to any type of transition, but until now it has always required some empirical input regarding the location of transition onset and the precise streamwise variation of γ.

Prospects for extending predictions to natural transition

Combined intermittency/turbulence modelling approaches

The transition length prediction deficiencies of the best turbulence model approaches, may be rectified by introducing a Production Transition Modification (PTM), whereby the Production of turbulence energy is limited by an empirical function through transition. However the same results may be achieved by introducing intermittency scaling.

In fact intermittency-weighting is still most often used to improve point transition methods by including an allowance for the 'length-of-transition' over which γ varies from 0 to 1, but it has now also been utilised in a wide range of (high-Re) turbulence models. Both intermittency function/correlation methods and more empirical transition weighting factors have been incorporated in the well-known Baldwin-Lomax & Cebeci-Smith mixing length models and used to produce reasonable results for a range of simple by-pass transition test cases, with variable adverse pressure gradient and concave stream-line curvature.

The equally well-known Fish & MacDonald integrated one-equation model, which is used in many other industrial design methods, also utilises a transition weighting factor which produces quite good predictions for transition onset, at least at fst levels of 0.25, 0.5 & 1.0%.

The Dhawan & Narasimha intermittency description has also been successfully introduced into other one-equation and Algebraic Stress Model (ASM) schemes. In both cases the mean flow was separated into turbulent and non-turbulent components conditionalised by γ and the only turbulence model modification was to introduce a similar type of linear-combination allowance for the influence of T-S waves on the mixing-length scale. Good agreement was obtained for the case of natural transition. Although allowance for T-S waves had little effect on the Cf predictions, the predicted turbulence intensity profiles were considerably improved when this was included.

It would be expected that low-Re models which contain damping factors that are only a function of wall-proximity, and thus provide much poorer predictions for transitional flows than they do for turbulent ones, could also be by introducing additional x-dependent damping functions.

There have been two recent attempts to improve the transition prediction performance of low-Re $k-\varepsilon$ models utilising y-dependent damping-function

by introducing an additional x-dependent intermittency functions – see Savill (1993). In both cases excellent predictions were produced for 3 & 6% fst test cases – better even than those obtained with the Launder-Sharma model.

However, although the linear-combination concept inherent in the use of intermittency functions appears to work well in practise, experimental data indicate that transitional profiles are not a simple combinations of purely laminar and fully turbulent forms. Therefore, in order to take better account of intermittency, zonal conditional averaging of the mean and turbulent equations is required. Several earlier theoretical analyses by Libby, Dopazo and Chevray & Tutu – see Savill (1995) – have laid the foundation for developing models based on such conditional equations.

This is the approach generally adopted within the SIG – see Savill (1994) – following exactly the original work of Libby to derive separate equations for laminar and turbulent zone mean velocities, as well as equations for k and (simply by analogy) ε, which contain additional source terms relating to crossings of the turbulent/non-turbulent interface. Simplifying assumptions are then introduced in order to model these; primarily by considering only an idealised purely 2D turbulent spot geometry. The resulting conditionally zone-averaged $k-\varepsilon$ model approach with prescribed Dhawan & Narasinmha intermittency predicts transition fairly accurately, under zero pressure gradient conditions, for 3 & 6 % fst, but too early for the lower (1%) fst and too late for the higher (10%) fst test cases. An alternative version, which employs an ODE for γ, is now being developed and has already produced better predictions.

The use of prescribed intermittency variations is thus clearly well established for transition prediction, but as noted above, even the best low-Re models tends to underpredict transition length. This is particularly so for the 1% fst test case, which is not surprising since this is on the boundary between by-pass and natural transition conditions and so one might expect a strong influence of intermittency effects associated with spot generation. An attempt has therefore recently been made to introduce an additional allowance for intermittency transport into the SLY low-Re RST model. There have been few attempts thus far to develop equations to predict the intermittency variation through transition, but a transport equation for intermittency has in fact already been proposed and included in both conditionally-averaged $k-\varepsilon$ and RST models – see Savill (1995) – in order to model inhomogeneous turbulent free-shear flows and boundary layers. More recently an RST-γ model has been applied to adverse pressure gradient boundary layers, while an alternative transport equation for γ has been into a conventional high-Re Reynolds-averaged $k-\varepsilon$ scheme in which the eddy viscosity is conditionalised by γ, but the k and ε equations are not (although an extra intermittency source term is included in the latter) – again see Savill (1995). This latter model has been applied successfully to a range of turbulent free shear flows and is now being extended to low-Re to predict first turbulent and later transitional wall flows.

In order to keep the most general formulation all the terms from both models have been retained in the final SLY version with the sign of the source terms

altered to reflect the differences in modelling a pseudo-laminar flow with a turbulent free-stream instead of a turbulent flow with an inviscid free-stream. In coupling this equation to the SLY RST equations the production terms are conditionalised by the maximum value of $(\gamma, 1-\gamma)$.

Following limited optimisation the resulting SLY-γ model has been found to predict growth of maximum intermittency under 1 and 3% fst quite accurately, although the γ profile development is not so well predicted.

Simulations, PSE & e^n methods

In addition to establishing an LES database for the by-pass transition, a number of coarser mesh LES have been performed for the ERCOFTAC T3A, T3B & T3C1 by-pass transition test cases and the T3D2 & T3L test cases involving transition following laminar separation under very low, background fst conditions – see Table 1. Each of these simulations appears to capture the essential features of the development of the mean flow and turbulence fields, including in the last case the detailed features of the laminar separation region, and a second fine resolution data base is now being created for this.

At the same time a series of LES numerical experiments for variations on the $\mathrm{T3B}_{LES}$ case have been carried out in order to investigate further the mechanisms of transition and the effect of varying degrees of fst anisotropy.

Separate zero pressure gradient transition DNS have also been performed at NASA Ames (for 2.5% fst), which have generally produced results similar to those of Yang & Voke for the 3 & 6 % fst test cases, and other groups are already performing simulations of natural transition flows.

At the same time interest is now developing in possible extensions of e^n and particularly Parabolised Stability Equation (PSE) approaches to variable fst by-pass transition cases, because there is already some evidence from the NASA Transition Project and elsewhere that both methods can be used successfully to predict the onset of transition for non-zero fst.

Concluding remarks

It should be clear from the above discussion that there are considerable prospects for extending the use of intermittency methods and low-Re turbulence modelling, particularly in combination, to the prediction of low free-stream turbulence transitional, relaminarising, and retransitional flows encountered in external aerodynamic applications. At Cambridge work is now beginning on the refinement of the low-Re RST/intermittency transport scheme and its extension to the prediction of by-pass transition on riblet surfaces and natural transition on smooth surfaces. The possible advantages, particularly in terms of mesh resolution requirements, of integrating intermittency transport with high-Re $k-\varepsilon$ and simpler Johnson & King models also need to be investigated.

Future research must focus on developing methods less demanding of cpu/-store, but offering greater predictive abilities and applicability. The combination

of PSE with intermittency transport modelling may thus offer a novel route towards this goal.

References

Pironneau, O., Rodi,W., Ryhming, I.L., Savill, A.M. & Truong, T.V. 1992 – *Numerical simulation of unsteady flows & transition to turbulence (CUP).*

Savill, A.M. 1992 – Evaluating turbulence model predictions of transition – an ERCOFTAC SIG Project. *Applied Scientific Research* **51**, 555.

Savill, A.M. 1993 – Some recent progress in the turbulence modelling of by-pass transition. In: *Near-Wall Turbulent Flows* (Elsevier B.V.), pp. 829-848.

Savill, A.M. 1994 – Transition modelling for turbomachinery III. *Summary Proceedings of 1st ERCOFTAC Transition SIG Workshop of the BRITE-EURAM AERO-CT92-0052 Project on Transition in Turbomachinery*, VUB.

Savill, A.M. 1995 – The SLY RST intermittency model for predicting transition. *ERCOFTAC Bulletin* **24**, 37-39.

Savill, A.M. 1996 – One-point closures applied to transition. Chapter 6 In: *Turbulence and Transition Modelling* Kluwer Academic Publishers.

Author's addresses

Senior Research Associate
Engineering Department
University of Cambridge
Cambridge CB2 1PZ

Visiting Research Fellow
Mechanical Engineering Department
UMIST Manchester, England UK

W.J. Solomon° G.J. Walker° & J.P. Gostelow▷

Transition Zone Predictions for Rapidly Varying Flows

Abstract

A new transitional flow model incorporating recent experimental data for the influence of free-stream pressure gradient on both the inception rate of turbulent spots and their subsequent spreading rate is reviewed. It gives good estimates of transition length for steady flows with marked spatial variations in free-stream conditions, and successfully predicts departures from the standard Narasimha intermittency distribution (or 'subtransitions') accompanying sudden changes in streamwise pressure gradient. A quasi-steady application of the new transition model is used in a preliminary attempt to describe the periodically unsteady boundary layer development during wake-induced transition on an axial compressor blade. Experimental observations show the relaxation of non-turbulent flow behind a wake-induced turbulent strip to be an important factor in turbomachine blade design; data for the length of relaxing flow from three independent transition experiments are compared.

Introduction

This paper is concerned with the prediction of transitional flow in cases where the boundary conditions change rapidly in space and/or time. The problem of rapid spatial variations is first examined. A new model making due allowance for the influence of pressure gradient on spot inception rate, and assuming spot spreading rate to be controlled by the local pressure gradient, is shown to give reasonable estimates of transition length under such varying conditions and to predict a priori the departures from Narasimha's standard intermittency distribution (or 'subtransitions') accompanying sudden changes in streamwise pressure gradient.

Transitional flow behaviour in the presence of rapid temporal variations is then examined with particular reference to the problem of periodic wake-induced transition observed on turbomachine blades. Some observations of wake-induced turbulent spot development on axial compressor blades are compared with wind tunnel measurements of triggered turbulent spots in a self-similar decelerating flow. An initial attempt to model the periodic flow on the compressor blade is made by applying the new model for spatially varying flow in a quasi-steady manner. The paper concludes by suggesting future directions for research.

Spatial variations – the influence of changing pressure gradient

Previous work

A comprehensive review of basic work on laminar-turbulent transition has been given by Narasimha (1985). The problem of modelling boundary layer development through the transition zone is examined in detail by Dey & Narasimha (1988), who also discuss the experimental data on transition published prior to that date. The early experimental surveys generally suffer from a lower level of accuracy and a lack of consistency in defining the extent of the transition zone.

The more recent survey by Gostelow *et al.* (1994), covering a wide range of pressure gradients and free-stream turbulence levels, has overcome this problem by fitting the universal distribution of Narasimha to measurements of intermittency γ within the transition zone. The fitted curve is then extrapolated to $\gamma = 0$ and $\gamma = 1$ to define the onset and completion of transition, respectively. This procedure has resulted in more reliable correlations for transition length, in terms of the boundary layer conditions at transition onset, which are presented in various forms by Gostelow *et al.* (1994).

It should be noted, however, that such simple correlations are only valid for cases in which the pressure gradient is slowly changing and conditions remain approximately similar through the transition zone. They may break down in cases such as the suction surface of an aft-loaded aerofoil, where transition may commence in a region of accelerating flow and end in a region of strong deceleration. As observed also by Narasimha *et al.* (1984), such sudden changes in the magnitude and sign of pressure gradient may cause marked deviations from the universal intermittency distribution (termed 'subtransitions').

Intermittency models for spatially varying flow

Narasimha *et al.* (1984) noted that a logarithmic plot of the intermittency distribution often exhibited a piecewise linear behaviour when subtransitions occurred. However, this does not provide a method of predicting the intermittency distribution a priori for flows with arbitrary pressure distributions.

The intermittency model of Chen & Thyson (1971), based on the turbulent spot theory of Emmons (1951), purports to describe the influence of changes in pressure gradient through the transition zone. However, as noted by Walker (1989) it only allows for the changes in turbulent spot convection rates with local changes in free-stream velocity. The more important effects of changing breakdown physics and spot spreading rates with streamwise pressure gradient variations are not accounted for.

Solomon *et al.* (1995) extended the Chen-Thyson model to incorporate the latter effects, using data of Gostelow *et al.* (1994) for the dimensionless spot breakdown rate $N = n\sigma\theta_i^3/\nu$ and data compiled by Gostelow *et al.* (1995) for the spot spreading half-angle α and spot propagation parameter σ, as shown in Fig. 1. A slight modification adopted here is that the spot breakdown rates for

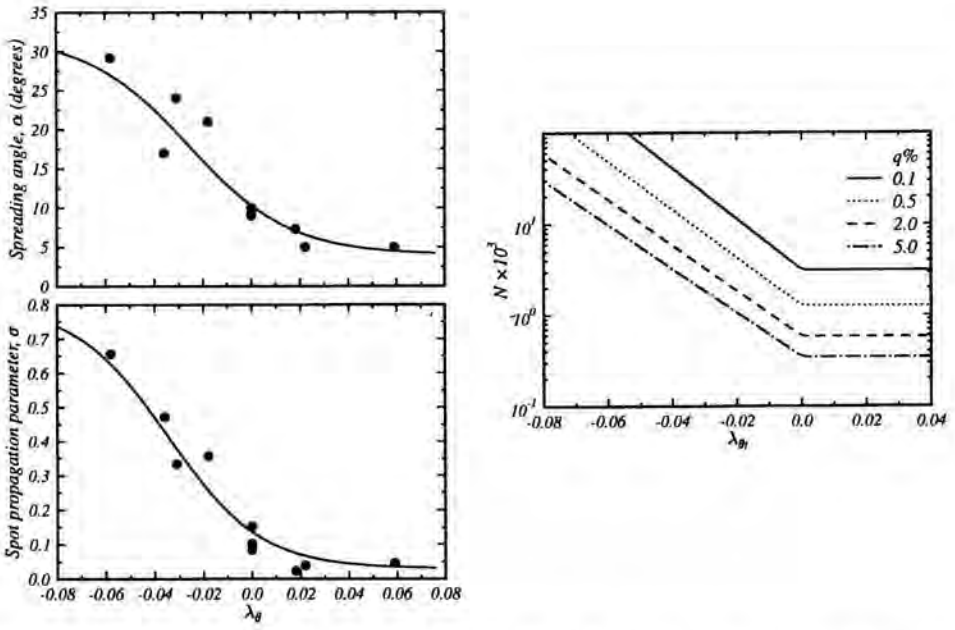

Figure 1: Correlations for spot spreading half angle α, spot propagation rate σ and generation rate N. Experimental data from various sources compiled by Gostelow *et al.* (1995).

negative pressure gradients have been assumed constant at their zero pressure gradient values. The latter change was made because the small amount of data available for accelerating flow made extrapolation dubious.

These data correlations are expressed analytically as

$$\sigma = 0.03 + (0.37/(0.48 + 3.0\exp(52.9\lambda_\theta))) \tag{1}$$

$$\alpha = 4 + (22.14/(0.79 + 2.72\exp(47.63\lambda_\theta))) \tag{2}$$

$$N = \begin{cases} 0.86 \times 10^{-3}\exp(2.134\lambda_\theta \ln(q) - 59.23\lambda_\theta - 0.564\ln(q)) & \text{if } \lambda_\theta \leq 0 \\ 0.86 \times 10^{-3}\exp(-0.564\ln(q)) & \text{if } \lambda_\theta > 0 \end{cases} \tag{3}$$

where λ_θ and q are respectively the the local Pohlhausen pressure gradient parameter and free-stream turbulence intensity values.

The intermittency distribution from the new model is given by

$$\gamma = 1 - \exp\left[-n\int_{x_t}^{x_i} \frac{\sigma}{\tan(\alpha)}\left(\frac{dx}{U}\right)\int_{x_t}^{x_i} \tan\alpha \; dx\right] \tag{4}$$

where n is the spot generation rate ($m^{-1}s^{-1}$) and $U(x)$ is the free-stream velocity distribution. Assuming the turbulent spots are triangular in planform, with

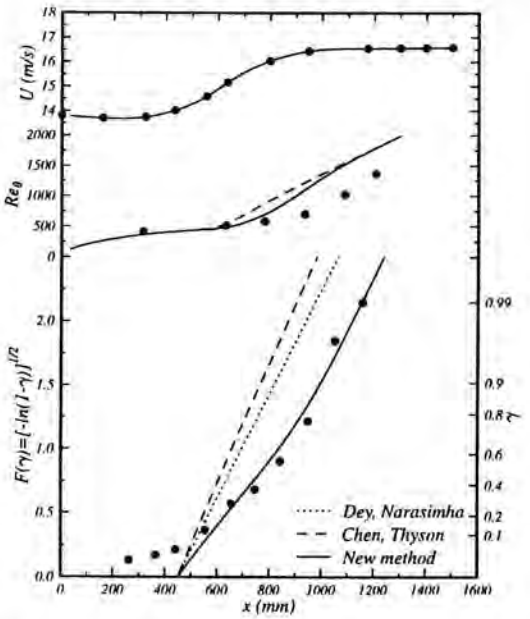

Figure 2: Calculation of transition in flow with a changing pressure gradient. Experimental data from Narasimha *et al.* (1984) – case DFU1.

leading and trailing edge celerities of aU and bU respectively, the propagation parameter is given by $\sigma = \tan\alpha(b^{-1} - a^{-1})$.

The model retains Narasimha's concentrated breakdown hypothesis, with the spot generation rate being determined by the boundary layer parameters and streamwise pressure gradient at transition onset. As seen from Fig. 1, the application of positive pressure gradient may alter the generation rate by an order of magnitude. The spot spreading angle and propagation parameter are assumed to vary continuously through the transition zone, according to the local value of λ_θ obtained from a purely laminar boundary layer calculation.

Fig. 2 shows the results of the new model for the flow DFU1 reported by Narasimha *et al.* (1984). Case DFU1 involves an increasing acceleration over the forward part of the transition region; this is subsequently relaxed to near zero pressure gradient at the end of transition. The new model successfully describes the the observed intermittency distribution; in particular, it predicts the marked kink or 'subtransition' in the logarithmic intermittency plot of $F(\gamma)$ around $x = 900$ mm. The comparative predictions by the methods of Dey & Narasimha (1988) and Chen & Thyson (1971) exhibit a linear variation in $F(\gamma)$ over the whole transition region, with slope approximating the observed behaviour in near zero pressure gradient conditions over the rearward part of the transition zone; the marked reduction in growth rate of intermittency in accelerating flow over the forward part of the transition zone is not predicted.

The predicted boundary layer growth through the transition zone is too rapid

despite the intermittency distribution being reasonably well estimated. This indicates that there are deficiencies in modelling of the emerging turbulent boundary layer which remain to be addressed.

Temporal variations - periodically unsteady flows

Triggered turbulent spots

Fig. 3 shows the development of transition in a strongly decelerating laminar boundary layer subjected to periodic perturbations from triggered turbulent spots generated at a fixed position by blowing through a hole in the surface. The time-space $(t - x)$ diagram uses shading to indicate ensemble-averaged values of RMS disturbance level integrated over the boundary layer height; the contours indicate ensemble-averaged values of velocity profile shape factor H (displacement thickness/momentum thickness).

The development of the triggered spot is evident from the band of increasing disturbance level which appears at the upstream limit of the figure at times between 25 and 30 ms. This is accompanied by a sudden reduction in shape factor H at the leading edge of the spot. Prior to the spot passage the unperturbed laminar layer undergoes a natural transition with a characteristic fall in shape factor and the RMS disturbance level peaking around the centre of the transition zone.

Behind the spot is the familiar relaxation zone (or calmed region) which is characterised by a low disturbance level and a slow return of H to the unperturbed laminar value. The energyzing of the surface layer associated with the passage of a turbulent spot has the very important practical implication that laminar separation will be temporarily delayed in this region. Another important consequence is the stabilisation of flow associated with the lower shape factor values in the relaxation zone; this significantly delays the natural transition process behind the spot, as evidenced by the tongue of low disturbance level extending beyond $x = 500$ mm.

Wake-induced transition

Fig. 4 shows a similar time-space contour plot for the process of transition on the suction surface of a C4 section blade in an axial compressor stator. t^* is time normalised by the rotor wake passing period; s^* is surface distance normalised by the blade chord. The shading indicates ensemble-averaged intermittency obtained from a chordwise array of surface hot-film sensors; it changes from white to black as γ increases from 0 (fully laminar) to 1 (fully turbulent).

The dark wedges commencing around $s^* = 0.1$ at intervals of $t^* = 1$ correspond to transitional and turbulent flow wedges induced by passing free-stream disturbances from the wakes of upstream rotor blades. These are interspersed with laminar or transitional flow regions extending rearward to around $s^* = 0.9$.

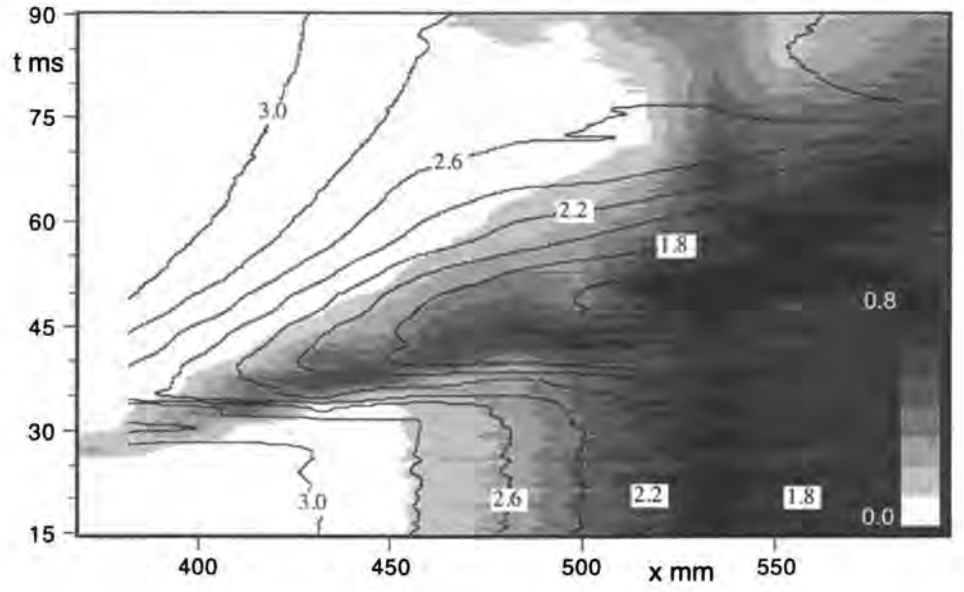

Figure 3: $t - x$ diagram for a triggered spot in an adverse pressure gradient. Shading indicates RMS disturbance level integrated over the boundary layer height. Contours give the shape factor H.

The turbulent strip which should have originated around $t^* = 2$ is missing because the corresponding rotor blade was removed to investigate the influence of changing wake frequency on the unsteady flow behaviour. In the absence of this strip, the turbulent onset following the passage of the preceding strip moves forward to around $s^* = 0.5$ when the following wake-induced transitional strip arrives. The inter-wake turbulent onset would probably asymptote to a fixed streamwise location, given a sufficiently long time interval between successive rotor wake passages (possibly around $s^* = 0.4$ where laminar boundary layer separation is predicted by a steady flow boundary layer calculation).

These results mirror those of the triggered spot observations, and clearly indicate the existence of marked flow stabilisation caused by a preceding wake-induced turbulent strip. The altered boundary layer profile behind the wake-induced turbulent strip is able to maintain laminar flow regions over the majority of the blade surface, whilst preventing intermittent laminar separation provided that the rotor wake passing frequency is sufficiently high. Full optimisation of axial turbomachine blade design clearly requires a detailed understanding of these unsteady phenomena and an ability to incorporate them in engineering design calculations.

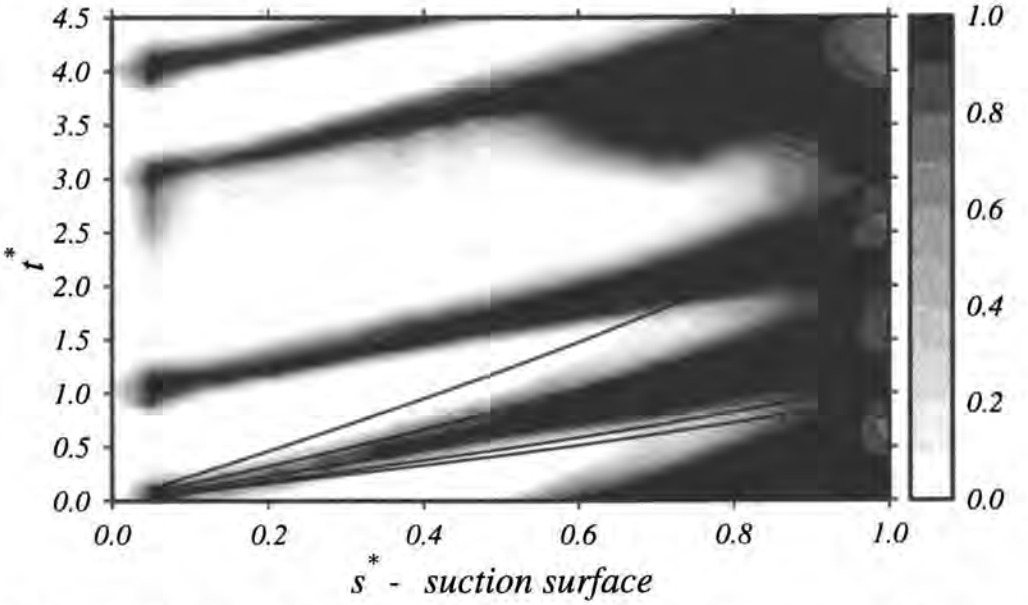

Figure 4: Wake-induced turbulent spots developing on an axial compressor blade. $t-s$ diagram of ensemble averaged intermittency. Wake induced turbulent strip at $t^* = 2$ eliminated by removal of a single upstream rotor blade. Particle trajectories for $1.0U$, $0.88U$, $0.7U$, $0.5U$, $0.35U$ overlaid.

Detailed observations of wake-induced transition have also been reported by Halstead *et al.* (1995) for blade surfaces in multi-stage axial compressors and turbines. Unsteady hot-wire measurements of boundary layer development were used to complement surface film data in these studies. Fig. 5, reproduced from Halstead *et al.* (1995), illustrates the morphology of boundary layer development on the suction surface of a stator blade in an embedded compressor stage. The behaviour is closely similar to that observed in the present study, but the existence of an alternative mode of transition in regions of the $t-x$ plane between successive wake-induced turbulent strips is more clearly evident.

Quasi-steady calculations for wake-induced transition

The transition model for spatially varying flow described above has been applied in a quasi-steady manner as a first attempt at modelling the periodically unsteady flow associated with wake-induced transition. The results are compared with experimental data of Halstead *et al.* (1995) for the boundary layer development on the suction surface of an axial compressor stator (Test Point 2B), shown in Fig. 6.

Fig. 6 presents data for three separate cases:

1. Long-term time-average values of boundary layer parameters.

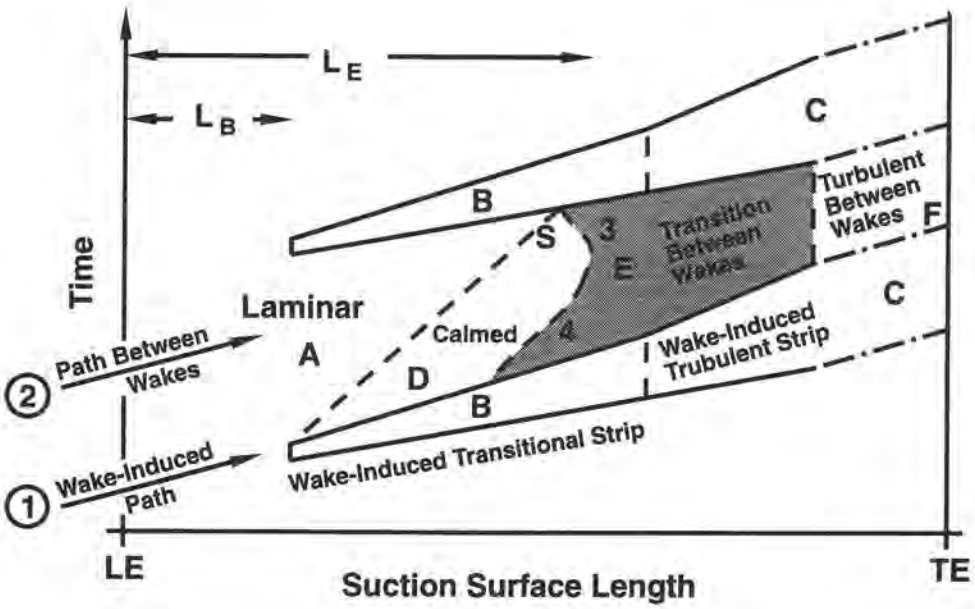

Figure 5: Unsteady boundary layer development on an axial compressor blade Halstead *et al.* (1995) - Test Point 2B.

2. Ensemble-average values along a wake-induced transition path in the $t - x$ plane (Path 1 shown in Fig. 5).

3. Ensemble-average values along a path between successive wake passages in the $t - x$ plane (Path 2 shown in Fig. 5).

The ensemble-average values fluctuate quite significantly during the wake passing cycle, the values for the wake path being around twice those for the long-term time-mean.

The boundary layer calculations have all been implemented with the time-mean surface pressure distribution reported by Halstead *et al.* (1995). The linear combination integral method of Dey & Narasimha (1988) was employed with the following modifications:

1. Calculation of the laminar component was progressed beyond separation by the artificial device of maintaining the shape factor H and skin friction coefficient C_f at their separation values of 3.70 and 0.0 respectively.

2. The initial momentum thickness for the turbulent component at transition onset was assumed equal to that of the laminar component, and the power law model for starting the turbulent calculation was limited to one streamwise step.

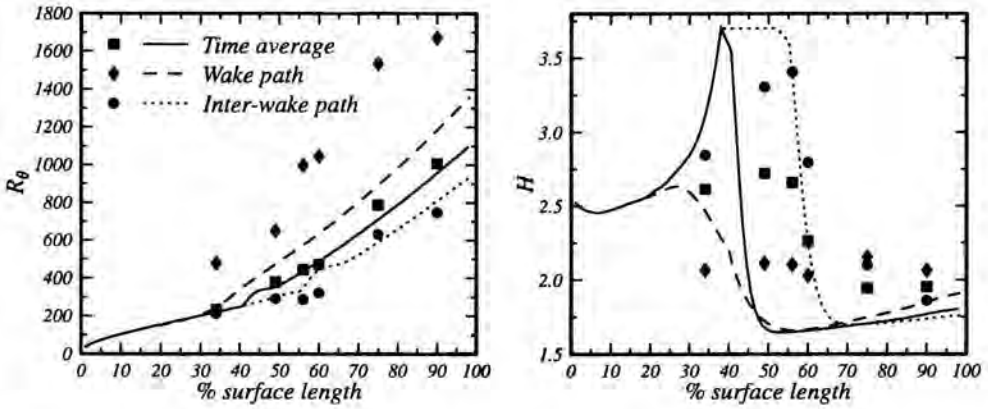

Figure 6: Quasi-steady calculation of the boundary layer development in the unsteady flow on the suction surface of a compressor blade. Symbols are experimental data of Halstead *et al.* (1995) - Test Point 2B.

The transition onset was variously computed or prescribed from experimental data, as described below. The intermittency variation through the transition zone was computed from the model for spatially varying flow described above.

The time-mean boundary layer calculation was implemented with transition onset at 38% suction surface length (SSL) as calculated from the method of Ghannam & Shaw (1980). The free-stream turbulence level of 2.2% at transition onset was estimated from measurements upstream of the blade row, with due allowance for variation in free-stream velocity up to the onset point. The predicted variation in boundary layer thickness, as indicated by the momentum thickness Reynolds number R_θ, is in surprisingly good agreement with experiment. However, this is somewhat deceptive in view of the significant fluctuations in ensemble-average values mentioned earlier and the less satisfactory predictions of velocity profile shape factor H through the transition zone.

The wake path calculation uses the experimentally observed transition onset of 19% SSL, with a corresponding free-stream turbulence level of 4.4%. The computed end of transition ($\gamma = 0.99$) at 60% SSL compares very well with the experimentally observed value of 62% SSL, indicating that the intermittency model is performing quite reasonably in this situation. However, the values of R_θ indicate that the boundary layer growth along the wake path is markedly underpredicted. This is thought to be largely due to deviations from two-dimensionality associated with relative flows normal to the blade surface in the passing rotor wakes: similar calculations for a turbine blade suction surface, where the direction of rotor wake relative flow is reversed, show an overprediction of boundary layer thickness along the wake path. There nevertheless remain significant turbulence modelling problems, as can be seen from a comparison of the shape factor data.

The inter-wake path calculation uses the experimental onset position of 52% SSL with corresponding free-stream turbulence level of 1.5%. This computation

is likely to be the least reliable, as it completely ignores the marked flow relaxation effects following the passage of the preceding wake-induced transitional strip. Transition occurs somewhat too rapidly, with the predicted end of transition at 70% SSL compared with 84% SSL from experiment. The boundary layer thickness is in fair agreement, but the shape factor development again shows significant discrepancies.

There is a general trend in all three computations for the shape factor to be overestimated immediately prior to transition onset and in the forward part of the transition zone. This probably results from the combined effects of:

1. The influence of free-stream turbulence in reducing the laminar boundary layer shape factor prior to transition.

2. The neglecting of relaxation effects producing a higher than normal shape factor value for the laminar boundary layer component in the transition zone.

The shape factor falls too rapidly through the transition zone, and only slowly recovers towards experimental values in the region of fully turbulent flow further downstream. This indicates significant problems with modelling of the emerging turbulent boundary layer.

Modelling of the relaxation zone

For differential types of boundary layer calculations the extent of the relaxation zone following a turbulent spot should be predicted directly provided that an appropriate variation of intermittency is prescribed. For integral calculation methods, and for general engineering design purposes, it is necessary to provide some estimate of the relaxation time T_r needed for the laminar flow to approach its unperturbed state.

Table 1 gives data for dimensionless relaxation time $T_r = t_r U/\delta_L$ for the zero pressure gradient experiment of Schubauer & Klebanoff (1955), the triggered spot in adverse pressure gradient of Gostelow *et al.* (1995) and the wake-induced transition observations of Solomon & Walker (1995). δ_L is the total thickness of the unperturbed laminar layer surrounding a turbulent spot. There is some scatter in the individual experiments, but the values of T_r are all of order 100.

Concluding remarks

A new model for the intermittency variation in flows with rapid spatial variations has been applied in a quasi-steady manner to periodic flows involving wake-induced transition on axial turbomachine blades. The predictions of intermittency for this case are encouraging, but some significant deficiencies in modelling the boundary layer development through the transition zone remain to be addressed.

Table 1: Comparison of relaxation times $T_r = \frac{t_r U}{\delta_L}$ observed in different flows. q is local free-stream turbulence level.

Flow	T_r	q
Schubauer & Klebanoff (1955), flat plate, zero pressure gradient	100-220	0.03%
Gostelow *et al.* (1995), flat plate, adverse pressure gradient	90	0.3%
Solomon & Walker (1995), compressor blade	50-150	2.2%

One of the most important challenges is the modelling of flow relaxation following the passage of a turbulent spot. The increased shear stress within the relaxing non-turbulent flow region has the important consequences of delaying laminar separation and locally stabilising the flow. Some typical values of dimensionless relaxation time have been presented as a first step in the modelling process.

Other areas of uncertainty which remain for future investigation include improvement of the spot growth rate correlations with more experimental data and development of a correlation for the spot generation rate which is independent of the spot growth parameters and valid in favourable pressure gradients. The effects of free-stream turbulence on all of these parameters also needs to be clarified. The model could be refined to allow for changes in spot shape around separation and possibly to predict transition in the separated shear layer. Transition onset correlations or prediction methods need to be improved as does the modelling of the emerging turbulent boundary layer.

Acknowledgements

The authors gratefully acknowledge financial support from the Australian Research Council and Rolls-Royce plc.

References

Abu-Ghannam, B.J. & Shaw, R. 1980 – Natural transition of boundary layers – the effects of pressure gradient and flow history. *J. of Mech. Eng. Sc.* **22**, 213-228.

Chen, K.K. & Thyson, N.A. 1971 – Extension of Emmons' spot theory to flows on blunt bodies. *AIAA Journal* **9**, 821-825.

Dey, J. & Narasimha, R. 1988 – An integral method for the calculation of 2-D transitional boundary layers. Fluid Mechanics Report 88 FM 7, Indian Institute of Science, Bangalore.

Emmons, H.W. 1951 – The laminar-turbulent transition in a boundary layer – part I. *J. of Aerosp. Sc.* **18**, 490-498.

Gostelow, J.P., Blunden, A.R. & Walker, G.J. 1994 – Effects of free-stream turbulenc and adverse pressure gradients on boundary layer transition. *ASME J. of Turbomachinery* **116**, 392-404.

Gostelow, J.P., Melwani, N. & Walker, G.J. 1995 – Effects of a streamwise pressure gradient on turbulent spot development. ASME Paper 95-GT-303, International Gas Turbine Congress, Houston.

Halstead, D.E., Wisler, D.C., Okiishi, T.H., Walker, G.J., Hodson, H. P. & Shin, H. 1995 – Boundary layer development in axial compressors and turbines: Parts 1-4. ASME Papers 95-GT-461-464.

Narasimha, R. 1985 – The laminar-turbulent transition zone in the boundary layer. *Progress in Aerospace Science* **22**, 29-80.

Narasimha, R., Devasia, K.J., Gururani, G. & Narayanan, M. A.B. 1984 – Transitional intermittency in boundary layers subjected to pressure gradient. *Experiments in Fluids* **2**, 171-176.

Schubauer, G.B. & Klebanoff, P.S. 1955 – Contributions on the mechanics of boundary layer transition. NACA TN 3489.

Solomon, W.J. & Walker, G.J. 1995 – Incidence effects on wake-induced transition on an axial compressor blade. Proc. 12th Int. Symposium on Air Breathing Engines **2**, pp. 954-964, Melbourne, Australia.

Solomon, W.J., Walker, G.J. & Gostelow, J.P. 1995 – Transition length prediction for flows with rapidly changing pressure gradients. ASME Paper 95-GT-241 (Accepted for publication in the Transactions of the ASME).

Walker, G.J. 1989 – Transitional flow on axial turbomachine blading. *AIAA J.* **27**, 595-602.

Authors' addresses

°Department of Civil and Mechanical Engineering
University of Tasmania
Hobart, Tasmania, Australia

▷Department of Engineering
University of Leicester
Leicester, England

Session 6:
Asymptotic Analysis

F.T. Smith

Combining Theory and Computations for Transition

Abstract

A combination of theory and computation seems needed, with physical understanding, to improve computational capabilities especially at high Reynolds numbers, where numerous paths occur in deep transition (the later stages of transition). This contribution shows recent developments. Certain aspects of the combination have been followed through mostly in 2D for the TS path alone: e.g. composite approaches followed by parabolized stability approaches. The theory is being extended into deep transition. A challenge is to obtain a theory-computation duet for 3D at large Reynolds numbers and capture most relevant paths. Parts of the 3D theory are in place and include encouraging agreements with experiments, on the first spike, on the Klebanoff and Nishioka paths, on transitional spot characteristics, on other transition paths; and the theory is now being developed further; but the repercussions for computations have still to be followed through.

Introduction (item 1)

To be specific we concentrate on spikes and nonlinear spots in transition, mostly for incompressible boundary layers. The emphasis is towards strong nonlinearity. Starting with spikes, the theory used herein is that of 2D or 3D interacting boundary layers (IBL), capturing nonlinear TS waves or following a vortex-wave interaction. Finite-time break-up produces shortened scales, yielding agreement with computations and experiments on the first spike in transition, with subsequent spot formation. After the break-up normal pressure gradients and vortex wind-up become significant locally. Also discussed herein are initial-value problems for spots containing a wide band of 3D nonlinear disturbances. The theory points to successive nonlinear stages starting at the wing tips near the spot trailing edge but gradually entering the middle as the amplitudes increase, downstream. This effect combined with shortening scales produces a spread angle near 11°, close to experimental observations. Viscosity enters later as for the spikes above originating near the surface or through a novel interaction influencing the global spot. This research on spikes, spots and their reproductions is directed towards greater understanding of deep transition. The theoretical understanding, e.g. of scales, should help Direct Numerical Simulations by determining which terms in the Navier-Stokes equations matter in any zone of flow and/or by interpreting results and/or by suggesting improved simulation methods, as well as providing

parameterization and comparisons with experiments. Here, through addressing spikes and spots, we highlight three main nonlinear theories, vortex/wave interaction theory, pressure-displacement IBL theory, high-frequency cum Euler-scale theory, corresponding basically to increasing amplitudes. These nonlinear interactions can completely alter the mean-flow profiles. Their major assumption is that the global Reynolds number Re is large, in line with practical interest: eg. see comparisons herein at both subcritical and supercritical Re values.

First, item 2 below on *spikes*, e.g. in forced transition, considers nonlinear TS or IBL interactions, controlled by the unsteady IBL equations. Emphasis is given to nonlinear finite-time breakups, detailed comparisons with computations and experiments, and the repercussions. This breakup involves the scaled pressure gradient and skin friction becoming unbounded locally. A change of scales is therefore induced. The repercussions are concerned principally with sublayer eruption and vortex formation.

Second, numerous aspects of turbulent *spots* have been studied experimentally, e.g. the main arrowhead-shaped spot, its tail, its notional speed, and spreading rate. From reviews by Clark *et al.* (1994), Henningson *et al.* (1994), Seifert *et al.* (1994), Shaikh & Gaster (1994), Smith *et al.* (1994), much of the spot dynamics resembles that in a fully turbulent boundary layer; a spot develops fast from localized disturbances with large initial amplitude; growth and spreading perhaps take place in a domino-like manner, via successive production of hairpin vortices, or by other mechanisms; spanwise growth greatly exceeds normal growth; the leading edge and side edges are sharp, with side-interaction with trailing wave packets. Again computations have been performed; see reviews above. Much extra physical understanding has still to be provided, nevertheless. Systematic tracking of increasing amplitudes remains absent, experimentally and computationally. Few if any systematic theoretical studies had been made until recently. The research below appears the only effort towards strongly nonlinear theory, for spot evolutions as initial-value problems. Much of the experimental findings can be described by the theory, even though many complex phenomena arise during spot evolution. The Euler stage examined corresponds to disturbance wavenumbers α, β, frequencies ω, propagation speeds c and amplitudes (e.g. pressure p', velocity $\underline{u}'$) all of $0(1)$, based on the boundary-layer thickness and local freestream speed, thus representing a wider range than conventional linear-type TS disturbances which have $\alpha, \beta, \omega, c, |p'|, |\underline{u}'|$ all smaller. In consequence, it seems not unreasonable to proceed first by means of the Euler-stage approach, but as a nonlinear 3D initial-value problem for a localized input disturbance. This is the concern of much of item 3.

Item 3 splits the *spot* dynamics into global (mainly inviscid) and internal (viscous-inviscid) properties, and concentrates on the former. Nevertheless, a new long/short-scale global interaction is identified linking the 3D boundary-layer equations and unsteady Euler equations via Reynolds-stress forces, far downstream. Moreover, internal properties, flow structures and interactions with global dynamics are mentioned, having been addressed in item 2. The viscous sublayer, its eruptions and ensuing vortex formations can become important in

practice. They introduce shorter length and time scales, and hence even higher frequency and wavenumber content, and they play a key part in the domino process. Item 3 is aimed at relatively high-amplitude nonlinear responses, as opposed to gradual transition. Further comments are in item 4.

IBL transitions and breakup: spikes (item 2)

The velocities $(\bar{u}, \bar{v}, \bar{w})$ in Cartesian coordinates $(\bar{x}, \bar{y}, \bar{z})$ (streamwise, normal, spanwise), pressure $\bar{p}$ and time $\bar{t}$ are nondimensionalized globally, with respect to (say) airfoil chord and freestream speed, and then scaled. So, near the typical 0(1) station $\bar{x} = \bar{x}_0$, $\bar{z} = \bar{z}_0$, the sublayer flow problem reduces to the unsteady nonlinear IBL one:

$$\frac{\partial \bar{u}}{\partial \bar{x}} + \frac{\partial \bar{v}}{\partial \bar{y}} + \frac{\partial \bar{w}}{\partial \bar{z}} = 0 \,, \tag{1}$$

$$\left(\frac{\partial}{\partial \bar{t}} + \bar{u}\frac{\partial}{\partial \bar{x}} + \bar{v}\frac{\partial}{\partial \bar{y}} + \bar{w}\frac{\partial}{\partial \bar{z}}\right)(\bar{u}, \bar{w}) = -\left(\frac{\partial \bar{p}}{\partial \bar{x}}, \frac{\partial \bar{p}}{\partial \bar{z}}\right) + Re^{-1}\frac{\partial^2(\bar{u}, \bar{w})}{\partial \bar{y}^2} \,, \tag{2}$$

$$\bar{u} = \bar{v} = \bar{w} = 0 \ \text{ at } \ \bar{y} = 0 \ \text{ (no slip)}, \tag{3}$$

$$\bar{u} \sim \bar{y} + A(\bar{x}, \bar{z}, \bar{t}) \ \ \bar{w} \to 0 \quad \text{as } \ \bar{y} \to \infty \ \text{ (unknown displacement)}, \tag{4}$$

$$\bar{p}(\bar{x}, \bar{z}, \bar{t}) = -\frac{1}{2\pi}\int_{-\infty}^{\infty}\int_{-\infty}^{\infty} \frac{\partial^2 A/\partial \chi^2(\chi, \phi, T)\, d\chi d\phi}{[(\bar{x} - \chi)^2 + (\bar{z} - \phi)^2]^{1/2}} \ \text{ (interaction law)}. \tag{5}$$

Here (5) applies for subsonic flow. Two alternatives to the above are Direct Numerical Simulations and IBL/related versions at finite Re. Both require numerical treatments. In general, the former is hindered by grid-resolution difficulties, among others. IBL and similar methods, which are zonal treatments involving sensible interpretations of (1)-(5) at finite Re, have been developed a little for unsteady flows (Smith *et al.* 1984, our Fig. 1, Peridier *et al.* 1991). These link with, and incidentally show the ellipticity implicit in, the parabolized stability equations (Bertolotti *et al.* 1992, Dr. M.R. Malik 1990's) developed successfully recently.

For strongly nonlinear amplitudes, the unsteady IBL system (1)-(5) yields localized finite-time breakups (Smith, 1988). These breakups have, in 2D, $\bar{x} - \bar{x}_s = c(\bar{t} - \bar{t}_s) + (\bar{t}_s - \bar{t})^N \xi$,

$$\frac{\partial \bar{p}}{\partial \bar{x}} \sim (\bar{t}_s - \bar{t})^{-1} p_1'(\xi), \ \ \bar{u} \to u_0(\bar{y}) \tag{6}$$

near the breakup position $\bar{x}_s$ and time $\bar{t}_s$. The local profile u_0 is smooth, $u_0 = c$ at the inflection point, ξ is 0(1), and the phase speed c is 0(1). The power $N = 3/2$ is the most likely. Approaching the breakup an inviscid Burgers equation

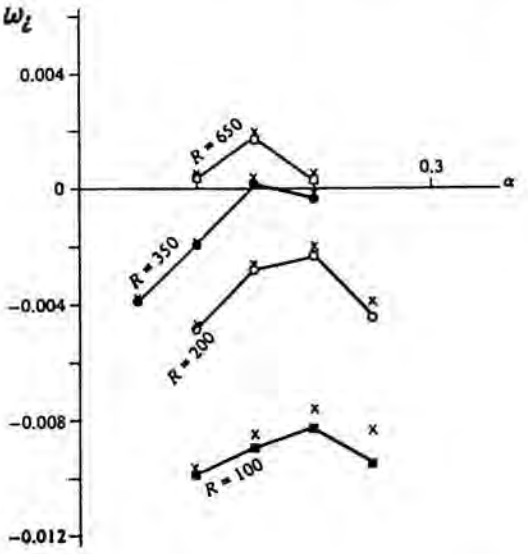

Figure 1: Comparison between IBL-related results (×) and Orr-Sommerfeld results for linear growth rates in Blasius flow, at subcritical and supercritical Reynolds numbers $R \sim Re^{1/2}$, from Smith *et al.* (1984).

governs $p_1(\xi)$, from integration in $\bar{y}$, provided the integral constraint (8) below on u_0 is satisfied. This gives $p_1(\xi)$, with $|p_1| \propto |\xi|^{1/3}$ at large $|\xi|$, so that

$$\bar{p} - p_0 \propto |\bar{x} - \bar{x}_s|^{1/3} \quad \text{as} \quad \bar{x} \to \bar{x}_s \pm \tag{7}$$

where $p_0 \equiv \bar{p}(\bar{x}_s)$ is constant. Hence a singularity in pressure gradient is predicted at the breakup time $\bar{t} = \bar{t}_s$, as well as increasingly large wall-shear responses. IBL computations support (6), (7) as do some direct simulations, whereas experimental comparisons are described just below. The breakup applies to most unsteady interactive flows. Detailed quantitative comparisons between computations and theory in (6), (7) by Peridier *et al.* (1991) show good agreement.

New physical effects then come into play as normal pressure gradients become significant on shorter length scales. An appropriate computational approach in principle then is in Smith *et al.* (1984), Smith (1991). The new faster stage is discussed by Hoyle *et al.* (1991), He *et al.* (1996) where an extended *KdV* equation holds for the pressure, subject to matching with (6), (7). Beyond that, in still faster time scales a strong vortex formation takes place (Bowles *et al.*, 1996). This is associated with initiation and eruption of a vortex. Intuition suggests that this breakup process, repeated, is connected with intermittency. Smith and Bowles (1992) compare (see our Fig. 2) the breakup criterion (Smith,

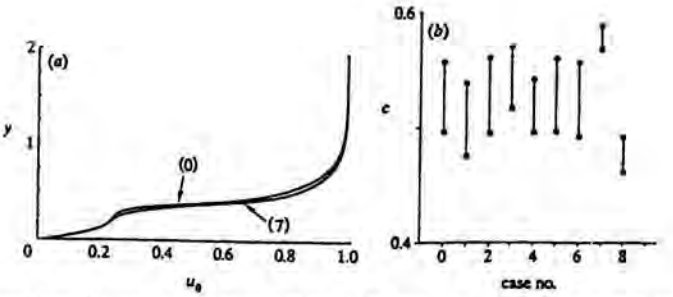

Figure 2: Comparisons between theory (Smith & Bowles, 1992) and experiment (Nishioka *et al.*, 1979), concerning the nonlinear criterion (8) and the first transitional spike. All the cases (0)-(8) studied are close to the two representative cases (0), (7) for the local experimental profile shown in (a). In (b), effectively the circles denote theoretical results and the squares experimental results. Note that the complete range of possible c values is between 0 and 1, and that the variation with case number in (b) indicates sensitivity with respect to the velocity-profile measurement.

1988) for (6), (7), namely

$$\int_0^\infty [u_0(\bar{y}) - c]^{-2} d\bar{y} = 0 \,, \tag{8}$$

with Nishioka *et al.*'s (1979) experiments concerning *the first spike*. The agreement is relatively close, given that Re is subcritical in the experiments.

There are many related or follow-on aspects. First, high-frequency theory applied to (1)-(5) yields an alternative view of spikes, associated more with still larger disturbances as discussed in item 3(e) below. In the same regime Kachanov *et al.* (1993) compare 2D nonlinear theory and experiments showing other apparent spikes, finding good agreement as shown in Fig. 3(a); while at suitably reduced amplitudes upper-branch features and critical layers tend to arise further downstream of the lower-branch regime (1)-(5). Second there is recent work by Vickers & Smith (1994) on break-up of separating flows; see also Savenkov (1993). Next, Hoyle & Smith (1994) consider the extension of (6)-(8) to 3D, where (8) again applies and

$$\bar{z} - \bar{z}_s \sim (\bar{t}_s - \bar{t})^{5/4} \tag{9}$$

gives a crucial spanwise scale. Likewise in 3D, Smith & Walton (1989), Stewart & Smith (1992) and Smith & Bowles (1992) imply that vortex/wave interactions based on (1)-(5) for example can act at low input amplitudes as precursors to the strong-amplitude finite-time break-up above. The latter two yield good agreement with boundary-layer and channel flow experiments (Figs 3b,c), in addition to that above. Other vortex/wave interactions are studied in the series by Hall & Smith (1988, 1989, 1990, 1991), with related works by Benney & Chow (1989), Wu (1993), Churilov & Shukhman (1987, 1988), Walton & Smith (1992), Timoshin & Smith (1995), Walton, Bowles & Smith (1994), Smith, Brown &

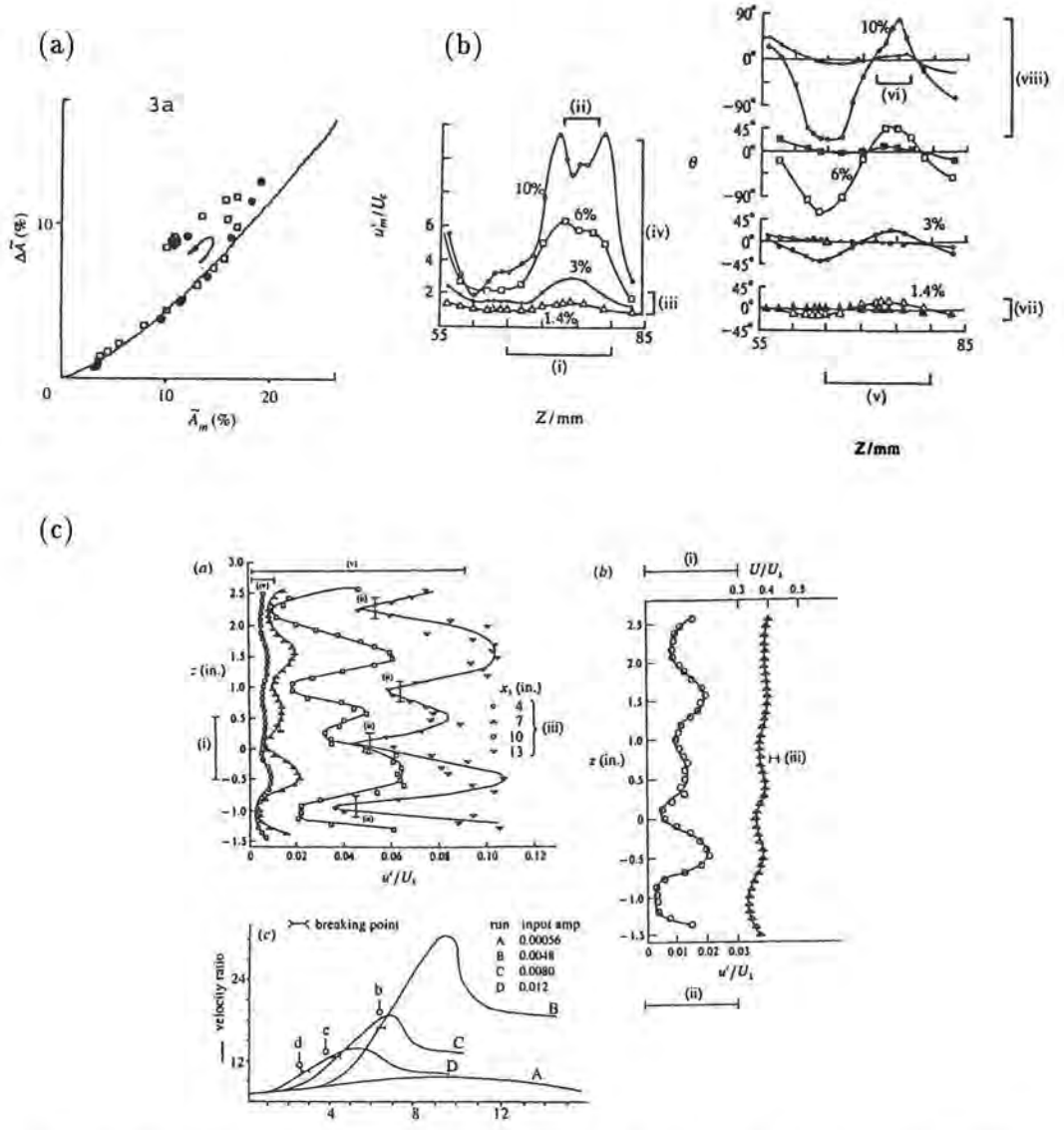

Figure 3: Further comparisons with experiments. (a) From Kachanov *et al.* (1993), in mostly quasi-2D transition. (b) From Smith & Bowles (1992), in the channel-flow 3D transition of Nishioka *et al.* (1979). Theoretical results are shown as bars (i) - (viii). (c) From Stewart & Smith (1992), in the boundary-layer 3D transition of Klebanoff & Tidstrom (1959). Theoretical predictions are indicated by bars (i) - (v) in the left-hand diagram, (i) - (iii) in the middle, and b,c,d (compared with experimental breaking points) in the right-hand diagram.

Brown (1993), in various weakly or strongly nonlinear settings with TS or inflectional disturbances. Hall & Smith (1988-1991) in particular emphasize the ability of vortex/wave interactions to provoke strongly nonlinear effects even for quite tiny 3D input disturbances. Vortex effects are clearly very powerful, both theoretically and in practice. Finally here, further work following on directly from (6)-(8) is mentioned later.

The transitional spot (item 3)

For free spots (cf. forced spots arising in item 2) the Euler stage has, throughout the boundary layer,

$$\overline{u}_x + \overline{v}_y + \overline{w}_z = 0\,, \tag{10}$$

$$(\partial_t + \underline{\bar{u}}.\underline{\nabla})\underline{\bar{u}} = -\underline{\nabla}\bar{p}. \tag{11}$$

The coordinates, with an origin shift, are scaled on the thickness $0(Re^{-1/2})$ and similarly for t, while

$$(\overline{u},\overline{v},\overline{w},\overline{p}) \to (u_B(y),0,w_B(y),0) \quad \text{as} \quad x^2+z^2 \to \infty, \tag{12}$$

$$(\overline{u},\overline{v},\overline{w},\overline{p}) \to (u_e,0,w_e,0) \quad \text{as}\, y \to \infty, \tag{13}$$

$$\overline{v} = 0 \quad \text{at} \quad y = 0, \tag{14}$$

with the undisturbed profile $u_B(y)$ holding far from the initial disturbance. For the present $u_e \equiv 1$, $w_e = w_B(y) \equiv 0$, but compare (d) below. The profile $u_B(y)$ is monotonic, inflexion-free, and $u_B(\infty) = 1$, $u_B'(0) = \lambda_B > 0$, and the initial disturbance itself has $(\overline{u},\overline{v},\overline{w},\overline{p})$ prescribed for all x,y,z at $t = 0$. The problem (10)-(14) is a computational one usually.

Smith *et al.* (1994) consider properties at large times, especially far downstream. Two major scales arise in the plan-view at distances $0(t^{1/2})$ and $0(t)$. See Fig. 4. In the $0(t^{1/2})$ zone, the solution takes on a three-layer form, the 'lowest' layer having

$$(\overline{u},\overline{v},\overline{w},\overline{p}) \sim \left[t^{-1}U,\ t^{-3/2}V,\ t^{-1/2}W,\ t^{-1}P\right],\ y = t^{-1/2}\overline{Y}\,, \tag{15}$$

and similarly for the 'middle' and 'uppermost' layers. The unknown surface pressure $P(\overline{X},\overline{Z})$ and negative displacement $A(\overline{X},\overline{Z})$ depend on $(\overline{X},\overline{Z})$ defined by

$$(x,z) = t^{1/2}(\overline{X},\overline{Z}). \tag{16}$$

From (10)-(14) a nonlinear similarity inviscid-boundary-layer-like system then holds. (a) - (c) below are concerned with the spot "trailing edge", where $(\overline{X},\overline{Z})$ are large, between the $0(t^{1/2})$ and $0(t)$ zones, the latter being discussed in (d), (e).

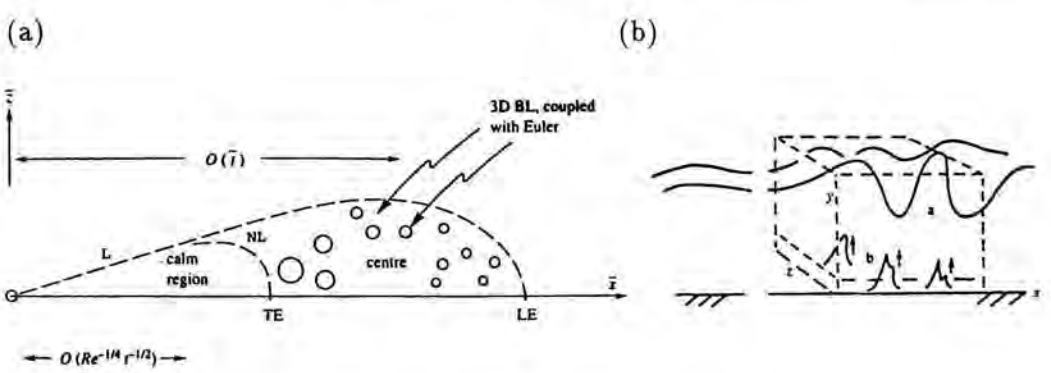

Figure 4: (a) Plan view of the theoretical spot structure in item 3, with symmetry about the $\bar{x}$-axis. In item 3(a-c) $Re^{-1/2} << \bar{t} << 1$, whereas when time $\bar{t}$ becomes 0(1), in item 3(d,e), coupling occurs between the global (3DBL) and local (Euler, see (b)) properties as indicated. $\mathcal{L}, \mathcal{NL}$ denote linear and nonlinear regions in turn, the former envisaged as bounding the calm region observed in experiments, while LE,TE denote the leading and trailing edges respectively. (b) The local 3D Euler structure *a* and subsequent sublayer eruptions *b*, leading to spots within spots: see item 2, item 3(e).

(a) *Amplitude level I*

At comparatively large distances $\overline{X} >> 1$ downstream, in the edge layer near $\overline{Z} \approx \mu\overline{X}$ (Fig. 4),

$$P = \overline{X}^{2/3}(Ep_0 + c.c.) + ... + \overline{X}^{-2/3}p_m + ..., \tag{17}$$

where $\mu = 8^{-1/2}$, $\overline{Z} - \mu\overline{X} = \overline{X}^{-1/3}\eta$, and the dominant fluctuating part (subscript zero) has $E = \exp\left[i(b_1\overline{X}^2 + \lambda\overline{X}^{2/3}\eta)\right], b_1 = 3^{3/2}/16, \lambda = (3/8)^{1/2}, \eta \sim 1$. The subscript m refers to the real mean-flow, and c.c. denotes the complex conjugate. The nonlinear interaction is dominated by the fluctuations $E^{\pm 1}$ and the mean-flow correction E^0,due physically to the relative slowness of the mean-flow variations; similarly in (b).

The governing equations (Smith *et al.*, 1994) stem from the outer interaction law and the relation $p_m \propto -|p_0|^2$ due to the mean components of momentum coupled with modulation by the mean-flow (vortex) correction. Sample solutions are presented in the last reference.

(b) *Amplitude level II*

Significant changes occur first when the amplitudes increase slightly and $\overline{Z} - \mu\overline{X} = \hat{\eta}$ becomes 0(1). Now

$$P = \overline{X}^{3/4}(\hat{E}\hat{p}_0 + c.c.) + ... + \overline{X}^{-1/2}\hat{p}_m + ... \tag{18}$$

The fluctuation with unknown $\hat{f}(\hat{\eta})$, because of enhanced phase variations, is $\widehat{E} = \exp\left[i(b_1\overline{X}^2 + \lambda\overline{X}\hat{\eta} + \overline{X}^{1/2}\hat{f}(\hat{\eta}))\right]$. New contributions come from extra momentum in the mean-flow, preserving the dominance of the long/short interaction between fluctuations and mean flow. Solutions are presented by Dodia *et al.* (1995). For enhanced amplitudes II there is a diminution of the mean-flow effect produced by the external motion. A new stage occurs when the whole trailing-edge region becomes affected by strong nonlinearity, as $\overline{Z} - \mu\overline{X}$ rises to $0(\overline{X})$. Then the mean-flow correction becomes comparable with the basic mean flow.

(c) *Amplitude level III affecting the entire trailing edge*

Here the amplitude of fluctuations and mean-flow parts is raised to $0(\overline{X})$, in U, W, with corresponding increases in V, P (Fig. 4). The interactions become *strongly nonlinear* and higher harmonic fluctuations are significant. In polars r, θ, where $(\overline{X}, \overline{Z}) = r(\cos\theta, \sin\theta), \theta$ is $0(1)$, with r being large, the flowfield solution has

$$\overline{U} = r(\overline{U}_m + \overline{U}_f) + \ldots\,, \quad \overline{W} = r(\overline{W}_m + \overline{W}_f) + \ldots\,, \quad P = r^2\overline{P}_f + (\overline{P}_m + P_f) + \ldots\,, \tag{19}$$

where $\overline{U}, \overline{W}$ are the r-, θ-velocities. The subscript f refers to fluctuations, having zero mean. The *total* mean flow, e.g. $\overline{U}_m$, is unknown now but varies slowly, being dependent on $\overline{Y}, \theta$, whereas unknown fluctuations, e.g. $\overline{U}_f$, also depend on the rapid variable $F \equiv b(\theta)r^2$. Smith *et al.* (1994) show that a closed nonlinear system is produced controlling the dominant fluctuations, the total mean flow, and the phase $b(\theta)$.

(d) *The spot centre*

Here, at larger distances $x \sim t$ downstream, the full Euler equations (10), (11) re-apply. The three-layer structure collapses into one and the x, z scale falls to $0(1)$ for fluctuations. (c) points to strong nonlinearity persisting here. The unsteady $3D$ Euler system holding implies a large numerical task. But also there is interplay between those fluctuations and the slow total mean flow. So extra length scales operate, x, z of $0(t)$ in addition to $0(1)$, associated with slender-flow equations for the mean, and they play an equally important role, linking the main short- and long-scale behaviour similarly to (c).

Moreover, as the spot continues downstream, to x, z of order $Re^{1/2}$ i.e. global distances of $0(1)$, the interacting short- and long-length scales become $0(Re^{-1/2})$ and $0(1)$ respectively, in the global coordinates $\bar{x}$, $\bar{z}$, with the normal coordinate staying $0(Re^{-1/2})$. These scalings are physically sensible. Viscous forces now affect the mean-flow through the 3D boundary-layer equations

$$\bar{u}_{\bar{x}} + \bar{v}_y + \bar{w}_{\bar{z}} = 0\,, \tag{20}$$

$$\bar{u}_{\bar{t}} + \bar{u}\bar{u}_{\bar{x}} + \bar{v}\bar{u}_y + \bar{w}\bar{u}_{\bar{z}} = \bar{s}_1 - \bar{p}_{\bar{x}} + \bar{u}_{yy} \,, \tag{21}$$

$$\bar{w}_{\bar{t}} + \bar{u}\bar{w}_{\bar{x}} + \bar{v}\bar{w}_y + \bar{w}\bar{w}_{\bar{z}} = \bar{s}_2 - \bar{p}_{\bar{z}} + \bar{w}_{yy} \,, \tag{22}$$

for the mean-flow $(\bar{u}, \bar{v}, \bar{w})(\bar{x}, y, \bar{z}, \bar{t})$, where $\bar{t} \equiv Re^{-1/2}t$ denotes global time. Here $\bar{p}(\bar{x}, \bar{z}, \bar{t})$ is the external-stream pressure, whereas $\bar{s}_1, \bar{s}_2$ are the unknown Reynolds-stress terms comprising nonlinear effects from the fluctuating velocity components governed by (10)-(14). The full interaction between (20)-(22) and (10)-(14) also involves the mean profile $\bar{u} = u_B$ in (13), which is now dependent on $\bar{x}, y, \bar{z}, \bar{t}$ and unknown, as is the corresponding nonzero $\bar{w} = w_B$ in general. It is intriguing that, according to the above argument, the flow properties on those two length scales remain fully interactive, with the viscous $3D$ boundary-layer system (20)-(22) and the inviscid $3D$ Euler system (10)-(14) being coupled together via the Reynolds stresses in (21), (22) and the profiles in (13). See Smith *et al.*'s (1994) Fig. 4 and our Fig. 4.

(e) *Internal dynamics and viscous effects*

The major element missing so far in item 3 is viscosity, governing the finer-scale dynamics and the connection with larger scales, apart from the global-scale effect in (20)-(22) etc.. Although our concern in the majority of item 3 is with global features, internal features are considered briefly in Smith (1995), more details and description being given in item 2 and in references cited.

Further comments (item 4)

There is still much to be explained. Further work is needed to understand the impact of the eruptive sublayer (item 2) on the larger-scale evolution in item 3, and the generation of faster time and length scales.

Yet the global spot theory tentatively is in line with the experimental findings summarized in item 1 in a qualitative or quantitative sense. Bowles & Smith (1995) point to important short-scaled effects combining with nonlinearity above to give a theoretical spread angle (Fig. 5) of approximately 11°, close to the experimental observations, for zero pressure gradient. On compressibility effects, Clark *et al.*'s (1994) results demonstrate experimental agreement with the theory over a range of Mach numbers (Fig. 6). On internal features quantitative agreement with computations and experiments has been noted in item 2 and is shown in Figs 2 and 3; in particular the breaking point in Fig. 3(b) signals the onset of turbulent spots in the forced flow there, linking with the free type of spot considered in item 3. Comparisons of the integral criterion (8) with direct simulations have been attempted, in addition to those with experiments in Fig. 2 which we repeat are at *subcritical* Reynolds numbers, indicating wide application of the theory (see also Fig. 1).

The same criterion (8) applies to the onset of transition in 3D over surface roughnesses and similar flows (FTS with D.J. Savin). Other 3D theory is developing, e.g. vortex/wave interactions. The repercussions for 3D computation

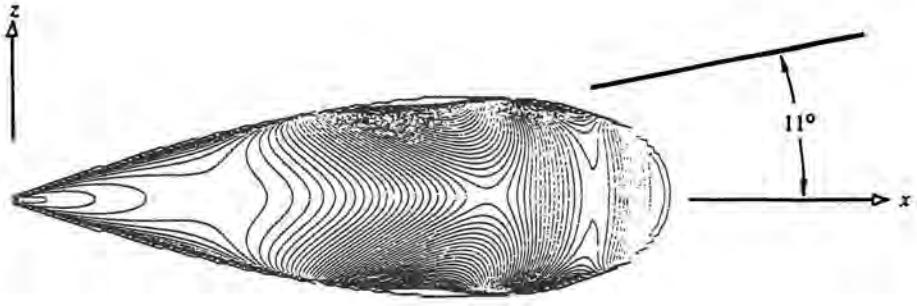

Figure 5: Theoretical spot solution from Bowles & Smith (1995) incorporating short-scale effects, and comparison with the typical 11° spread angle found experimentally.

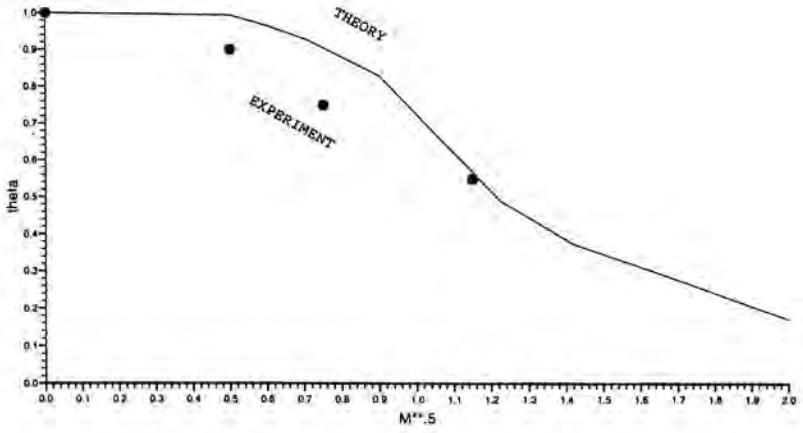

Figure 6: Spot spreading angle vs. Mach number, for compressible boundary layers, from Clark *et al.*'s experiments (1994) and theory by Dr. R.G.A. Bowles with FTS (1995), following on from Bowles & Smith (1995).

are fairly clear, given the resolution difficulties of direct simulations at large Re. Item 2 implies that an IBL-type system is needed but supplemented by Euler terms, because of normal pressure gradient effects (item 2, end) along with item 3 and Bowles & Smith's (1995) results. The composite system of Smith *et al.* (1984), Smith (1991b) has these in unsteady 2D flows (Fig. 1), while 3D steady computations (Smith 1991a) indicate accuracy and efficiency. Work is in progress on the 3D unsteady extension but it needs more attention.

References

Benney, D.J. & Chow, C. 1989 – *Studies in Appl. Math.* **80**, 37-62.

Bertolotti, F.P., Herbert, Th. & Spalart, P.R. 1992 – Linear and nonlinear stability of the Blasius Boundary layer, *J. Fluid Mech.* **242**, 442-474.

Bowles, R.G.A. & Smith, F.T. 1995 – Short-scale effects on model boundary-layer spots, *J. Fluid Mech.* **295**, 395-407.

Bowles, R.I., Smith, F.T. & Walker, J.D.A. 1996 – to be submitted.

Churilov, S.M. & Shukman, I.G. 1987 – Nonlinear stability of a stratified shear flow: a viscous critical layer, *J. Fluid Mech.* **180**, 1-20.

Churilov, S.M. & Shukman, I.G. 1988 – Nonlinear stability of a stratified shear flow in the regime with an unsteady critical layer, *J. Fluid Mech.* **194**, 187-216.

Clark, J.P., Jones, T.V. & LeGraff, J.E. 1994 – On the propagation of naturally-occurring turbulent spots, *J. Eng. Math.* **28**, 1-19.

Dodia, B.T., Bowles, R.G.A. & Smith, F.T. 1995 – Tto appear in *J. Eng. Math.*.

Hall, P. & Smith, F.T. 1988 – The nonlinear interaction of Tollmien-Schlichting waves and Taylor-Görtler vortices in curved channel flows, *Proc. Roy. Soc.* **A417**, 255-282.

Hall, P. & Smith, F.T. 1989 – Nonlinear Tollmien-Schlichting/vortex interaction in boundary layers, *Europ. J. Mechs* **B8**, 179-205.

Hall, P. & Smith, F.T. 1990 – Near-planar TS waves and longitudinal vortices in channel flow: nonlinear interaction and focussing. In Instability and Transition II, eds. Hussaini, M.Y. and Voigt, R.G., Springer.

Hall, P. & Smith, F.T. 1991 – On strongly nonlinear vortex-wave interactions in boundary layer transition, *J. Fluid Mech.* **227**, 641-666; also 1989, Institute for Computer Appl. in Sc. & Eng., Rept. 89-92.

He, J., Walker, J.D.A., Bowles, R.I. & Smith, F.T. 1996 – To be submitted.

Henningson, D.S., Johansson, A.V. & Alfredson, P.H. 1994 – Turbulent spots in channel flows, *J. Eng. Maths.* **28**, 21-42.

Hoyle, J.M., Smith, F.T. & Walker, J.D.A. 1991 – On sublayer eruption and vortex formation, *Comp. Phys. Comms* **65**, 151-157; also Hoyle, J.M., 1992, Ph.D. Thesis, London Univ., London.

Hoyle, J.M. & Smith, F.T. 1994 – On finite-time break-up in three-dimensional unsteady interacting boundary layers, *Proc. Roy. Soc.* **A 447**, 467-492.

Kachanov, Y.S., Ryzhov, O.S. & Smith, F.T. 1993 – Formation of solitons in transitional boundary layers: theory and experiment, *J. Fluid Mech.* **251**, 273-297.

Klebanoff, P.S. & Tidstrom, K.D. 1959 – The evolution of amplified waves leading to transition in a boundary layer with zero pressure gradient, Tech. Notes Nat. Aero. Space Admin., Wash., D-195 (see in 1963, Stuart, J.T., Ch. IX of Laminar Boundary Layers, ed. Rosenhead, L.)

Nishioka, M., Asai, M. & Iida, S. 1979 – An experimental investigation of the secondary instability, in Laminar-Turbulent Transition, Springer-Verlag.

Peridier, V.J., Smith, F.T. & Walker, J.D.A. 1991 – Vortex -induced boundary-layer separation. Part 2. Unsteady interacting boundary layer theory, *J. Fluid Mech.* **232**, 132-165.

Savenkov, I.V. 1993 – Wave packets, resonant interactions and soliton formation in inlet pipe flow, *J. Fluid Mech.* **252**, 1-30.

Seifert, A., Zilberman, M. & Wygnanski, I. 1994 – On the simultaneous measurements of two velocity components in the turbulent spot, *J. Eng. Maths* **28**, 43-54.

Shaikh, F.N. & Gaster, M. 1994 – The non-linear evolution of modulated waves in a boundary layer, *J. Eng. Math.* **28**, 55-71.

Smith, C.R., Walker, J.D.A., Haidari, A.H. & Sobrun, U. 1991 – On the dynamics of near-wall turbulence, *Phil. Trans. R. Soc.* **A336**, 131-175.

Smith, F.T., Papageorgiou, D.T. & Elliott, J.W. 1984 – An alternative approach to linear and nonlinear stability calculations at finite Reynolds numbers, *J. Fluid Mech.* **146**, 313-330.

Smith, F.T. 1988 – Finite-time break-up can occur in any unsteady interacting boundary layer, *Mathematika* **35**, 256-273.

Smith, F.T. & Walton, A.G. 1989 – Nonlinear interaction of near-planar TS waves and longitudinal vortices in boundary-layer transition, *Mathematika* **36**, 262-289.

Smith, F.T. 1991a, Steady and unsteady 3-D interactive boundary layers, *Comp. & Fluids* **20**, 243-168. (Also given as a presentation at the R.T. Davis Memorial Symp., Cincinnati, U.S.A. (1987).)

Smith, F.T. 1991b – Composite, Navier-Stokes and Euler unsteady-flow computations in boundary layers, Utd. Tech. Res. Cent. Rept. UTRC91-2, Hartford, CT; Composite, Navier-Stokes and Euler unsteady-flow computations in boundary layers, *J. Eng. Maths*, in press (1996).

Smith, F.T. & Bowles, R.I. 1992 – Transition theory and experimental comparisons on (I) amplification into streets and (II) a strongly nonlinear break-up criterion, *Proc. Roy. Soc.* **A439**, 163-175.

Smith, F.T., Dodia, B.T. & Bowles, R.G.A. 1994 – On global and internal dynamics of spots: a theoretical approach, *J. Eng. Math.* **28**, 73-91.

Smith, F.T., Brown, P.G. & Brown, S.N. 1993 – Initiation of three-dimensional nonlinear transition paths from an inflexional profile, *Europ. J. Mech.* **12**, 447-473.

Smith, F.T. 1995 – On spikes and spots: Strongly nonlinear theory and experimental comparisons, *Phil. Trans. Roy. Soc.* **A352**, 405-424.

Stewart, P.A. & Smith, F.T. 1992 – Three-dimensional nonlinear blow-up from a nearly planar initial disturbance, in boundary-layer transition: theory and experimental comparisons, *J. Fluid Mech.* **244**, 79-100.

Timoshin, S.N. & Smith, F.T. 1995 – Vortex/inflectional-wave interactions with weakly three-dimensional input. Parts I, II, *J. Fluid Mech.*, submitted.

Vickers, I.P. & Smith, F.T. 1994 – Theory and computations for breakup of unsteady subsonic or supersonic separating flows, *J. Fluid Mech.* **268**, 147-173.

Walton, A.G. & Smith, F.T. 1992 – Properties of strongly nonlinear vortex/Tollmien-Schlichting waves interactions, *J. Fluid Mech.* **244**, 649-676.

Walton, A.G., Bowles, R.I. & Smith, F.T. 1994 – Vortex/wave interaction in separating flows, *Europ. J. Mechs.* **B13**, 629-655.

Wu, X. 1993, Nonlinear temporal-spatial modulation of near-planar Rayleigh waves in shear flows: formation of streamwise vortices, *J. Fluid Mech.* **256**, 685-719.

Author's address

University College London
Department of Mathematics
Gower Street, London WC1E 6BT, UK

Peter W. Duck

Solutions of the Inviscid Triple-Deck Equations

Abstract

The three-dimensional triple-deck equations are derived and considered in some detail. Expressions for linearised solutions (valid for small levels of imposed disturbance) are described, and details of a numerical scheme appropriate for the nonlinear problem, based on a spectral approach are also given. In the case of two-dimensional disturbances, the solutions obtained appear to exist for all times, whilst in the case of nonlinear, three-dimensional disturbances, finite-time singularities appear to occur.

Introduction

One of the most notable successes of triple-deck theory has been its ability to describe the lower branch of the neutral-stability curve of Blasius-like boundary layers in the (important) limit of large Reynolds numbers. This connection was firmly established by Smith (1979a), and formed the basis of a number of studies, including Smith (1979b), Duck (1985), Smith & Burggraf (1985). These later studies also strongly suggested that the earlier stages of transition are also captured by (non-linear) triple-deck theory.

Of particular interest is the appearance, quite frequently, of finite-time singularities that seem to occur in numerical solutions of these equations. Found by Duck (1985, 1987), singularities of this type have also been investigated by Brotherton-Radcliffe & Smith (1987), Smith (1988) and Peridier *et al.* (1991). The conclusion seems to be that these 'breakdowns' are predominantly inviscid in nature, related in some way to an important physical (transitional) process, such as (conceivably) a burst of vorticity into the main body of the boundary layer.

The work of Smith & Burggraf (1985) (effectively a high-frequency limit), led to the Benjamin-Ono equation. More recently this and related aspects have been the subject of further investigations. Kachanov, Ryzhov & Smith (1993) attempted a comparison between results from this equation, and experimental data, whilst Bogdanova-Ryzhova & Ryzhov (1995) have mounted a thorough investigation into solutions of the forced Benjamin-Ono type, and found a number of diverse, interesting features, including bifurcation phenomena, nearly limit cycle type oscillations and irregular pulsations with erratic sequences of amplitude and temporal behaviour.

This previous work has focused on two-dimensional situations, and more specifically still for particular transverse distributions of velocity. All this work

stems from the so-called inviscid triple-deck equations (Smith & Burggraf, 1985, Goldstein & Lee, 1992). Indeed these equations appear quite generic in nature. The aims of this paper are (i) to present results for two-dimensional cases, *without* the previous restriction on transverse solution variation, and (ii) to extend the ideas to three dimensions.

Formulation

The initial formulation of the problem follows that of the full triple-deck problem, as described by Duck (1981, 1987, 1990). We suppose that we have a laminar incompressible flow over a flat plate. At a distance L^* downstream of the leading edge of the plate, some form of disturbance is introduced into the flow. This could either be a surface disturbance, or alternatively some disturbance in the freestream - for our point of view the specifics here are not important. The origin of the coordinate system is taken close to the disturbance, the coordinates being (L^*x, L^*y, L^*z) relative to the streamwise, transverse and crossflow directions, respectively.

The flow far from the plate has a constant kinematic viscosity v and density ρ, and a constant freestream velocity $U_\infty(u,v,w) = U_\infty(1,0,0)$. The dimensional pressure is written as $\rho U_\infty^2 p$, and the Reynolds number R and associated small parameter ϵ are defined as $R = \epsilon^{-8} = U_\infty L^*/\nu$. We assume $R >> 1$ (and consequently $\epsilon << 1$) throughout. We take the typical timescale of the disturbance to be T, and this then enables us to define a second dimensionless parameter, namely $\Omega_0 = L^*/(U_\infty T)$, with dimensional time written as Tt. If unsteadiness plays a leading-order role in the problem, then we require $\Omega_0 = \epsilon^{-2}\Omega$, where $\Omega = O(1)$ (generally, although this condition will be relaxed later). We further suppose (again, at least initially) that the disturbance has dimensions $O(\epsilon^3 L^*)$, $O(\epsilon^3 L^*)$, $O(\epsilon^5 L^*)$ in the streamwise, crossflow and transverse directions respectively.

This class of disturbance leads to a triple-deck structure, the key problem being in the lower deck, wherein $x = \epsilon^3 X$, $y = \epsilon^5 Y$, $z = \epsilon^3 Z$ and $\mathbf{u} = (\epsilon U, \epsilon^3 V, \epsilon W)$ and $p = \epsilon P(X,Z)$. The following system then results:

$$\Omega U_t + UU_X + VU_Y + WU_Z = U_{YY} - P_X, \tag{1}$$

$$\Omega W_t + UW_X + VW_Y + WW_Z = W_{YY} - P_Z, \tag{2}$$

$$U_X + V_Y + W_Z = 0, \tag{3}$$

with

$$U = V = W = 0 \text{ on } Y = 0, \tag{4}$$

and as $Y \to \infty$:

$$W \to 0, U \to Y + hF(X,Z,t) + A(X,Z,t), \tag{5}$$

and

$$U \to Y, W \to 0 \text{ as } X \to -\infty. \tag{6}$$

Here $A(X,Z,t)$ denotes a displacement function, which is unknown *a priori*, but may be related to the pressure by consideration of the upper layers (Smith *et al.*, 1987) which for the three-dimensional, incompressible case may be written

$$P(X,Z,t) = -\frac{1}{2\pi}\int_{-\infty}^{\infty}\int_{-\infty}^{\infty}\frac{A_{\xi\xi}d\xi d\zeta}{[(X-\xi)^2+(Z-\zeta)^2]^{\frac{1}{2}}}. \tag{7}$$

The forcing function $F(X,Z,t)$ is some prescribed function. As pointed out above, we shall not concern ourselves with the particular details (i.e. origin) of this term. The parameter h is an amplitude parameter, which is useful when we consider diminishingly small flow disturbances (in the following section).

The full system above has been treated before by Duck (1987, 1990), specifically in the form of an initial value problem. However, here, we consider an important limit of the above system.

We suppose that $\Omega >> 1$ (corresponding to increasingly first time variations). Without any further rescaling, the high frequency problem of Duck (1981) results; however here, instead, we allow the following scalings to also occur

$$\begin{gathered} U = \Omega^{\frac{1}{2}}\hat{U}(\hat{X},\hat{Z},\hat{Y},t)+\ldots, V = \Omega^{\frac{3}{2}}\hat{V}(\hat{X},\hat{Z},\hat{Y},t)+\ldots, \\ W = \Omega^{\frac{1}{2}}\hat{W}(\hat{X},\hat{Z},\hat{Y},t)+\ldots, X = \Omega^{-\frac{1}{2}}\hat{X}, Y = \Omega^{\frac{1}{2}}\hat{Y}, Z = \Omega^{-\frac{1}{2}}\hat{Z}, \\ P = \Omega\hat{P}(\hat{X},\hat{Z},t)+\ldots, A = \Omega^{\frac{1}{2}}\hat{A}(\hat{X},\hat{Z},t)+\ldots, F = \Omega^{\frac{1}{2}}\hat{F}(\hat{X},\hat{Z},t). \end{gathered} \tag{8}$$

This is equivalent to the procedure adopted by Bogdanova-Ryzhova & Ryzhov (1995) in a two-dimensional context. The resulting system (with "hats" dropped) is then

$$U_t + UU_X + VU_Y + WU_Z = -P_X, \tag{9}$$

$$W_t + UW_X + VW_Y + WW_Z = -P_Z, \tag{10}$$

$$U_X + V_Y + W_Z = 0. \tag{11}$$

The appropriate boundary conditions are that $V(Y = 0) = 0$, whilst as $Y \to \infty$:

$$U \to Y + A(X,Z,t) + hF(X,Z,t), \quad W \to 0, \tag{12}$$

and to close the problem, (7) is appropriate.

The above system does of course violate the no-slip condition on $Y = 0$. This may be remedied by a scaling of the transverse variable, involving $Y = O(\Omega^{-\frac{1}{2}})$. Although notionally passive (as in Bogdanova-Ryzhova & Ryzhov, 1995), this aspect could be crucial, and is discussed later in the paper.

In the following section we consider linearised solutions of the problem above, corresponding to $h \to 0$. Details of a full numerical treatment are given later.

Linearised solution

Here we consider linearised solutions of the system (7), (9)-(12), in the limit as $h \to 0$, i.e. diminishingly small disturbance amplitudes. Just as in the linearised solutions of the full triple-deck equations, by so doing, we are able to gain much physical and mathematical insight into the solution of the nonlinear problem.

Specifically, as $h \to 0$, we expect the flow to comprise a uniform shear in the X direction, plus some small perturbation, and so we write

$$U = Y + h\tilde{U} + \ldots, \qquad V = h\tilde{V} + \ldots, \qquad W = h\tilde{W} + \ldots,$$

$$P = h\tilde{P} + \ldots, \qquad A = h\tilde{A} + \ldots. \tag{13}$$

We find it useful to introduce the double Fourier transform in X and Z, defined as follows (for example)

$$U^*(Y,t) = \int_{-\infty}^{\infty}\int_{-\infty}^{\infty} \tilde{U}(X,Y,Z,t)e^{ikX+i\ell Z}dX\,dZ, \tag{14}$$

(and similarly for all other flow variables).

Considering the $O(h)$ terms in (9)-(11) leads to

$$U_t^* + ikYU^* + V^* = -ikP^*, \tag{15}$$
$$W_t^* + ikYW^* = -i\ell P^*, \tag{16}$$
$$ikU^* + i\ell W^* + V_Y^* = 0. \tag{17}$$

Differentiating (15) with respect to Y, and adding to this $\dfrac{\ell}{k}$ times the derivative of (16) with respect to Y, leads to the following, very simple equation

$$\sigma_t^* + ikY\sigma^* = 0, \tag{18}$$

where $\sigma^* = U_Y^* + \frac{\ell}{k}W_Y^*$. Since there is no forcing term to this equation, supposing $\sigma^*(t = 0) = 0$, then $\sigma^* \equiv 0$, (an alternative scenario is considered later in this section).

Integrating σ^* leads to the conclusion

$$U^*(Y,t) + \frac{\ell}{k}W^*(Y,t) = A^* + F^*. \tag{19}$$

Conditions on $Y = 0$ imply

$$U_t^*(Y = 0,t) = -ikP^*, \tag{20}$$
$$W_t^*(Y = 0,t) = -i\ell P^*, \tag{21}$$

and the pressure/displacement relationship (7) transforms to

$$P^* = \frac{k^2}{(k^2+\ell^2)^{\frac{1}{2}}} A^*, \tag{22}$$

(see Duck & Burggraf 1986).

Combining the equations above leads to the result

$$A_t^* + F_t^* + ik(k^2+\ell^2)^{\frac{1}{2}} A^* = 0. \tag{23}$$

If we confine our attention to forcing functions of the form

$$\begin{aligned} F^* &= 0, \quad t \leq 0 \\ F^* &= F_0^*(k,\ell)[e^{i\omega t} - e^{-t}], \quad \text{for} \quad t > 0 \end{aligned} \tag{24}$$

then

$$P^* = \frac{-\omega k^2 F_0^*[e^{i\omega t} - e^{-ikt(k^2+\ell^2)^{\frac{1}{2}}}]}{(k^2+\ell^2)^{\frac{1}{2}}[\omega + k(k^2+\ell^2)^{\frac{1}{2}}]} - \frac{k^2 F_0^*[e^{-t} - e^{-ikt(k^2+\ell^2)^{\frac{1}{2}}}]}{(k^2+\ell^2)^{\frac{1}{2}}[ik(k^2+\ell^2)^{\frac{1}{2}} - 1]}, \tag{25}$$

$$\begin{aligned} W^* &= \frac{\ell\omega k^2 F_0^*[e^{i\omega t} - e^{-ikYt}]}{(k^2+\ell^2)^{\frac{1}{2}}(\omega + kY)[\omega + k(k^2+\ell^2)^{\frac{1}{2}}]} \\ &+ \frac{\ell\omega k^2 F_0^*[e^{-ikY} - e^{-ikt(k^2+\ell^2)^{\frac{1}{2}}}]}{(k^2+\ell^2)^{\frac{1}{2}}[\omega + k(k^2+\ell^2)^{\frac{1}{2}}][kY - (k^2+\ell^2)^{\frac{1}{2}}k]} \\ &+ \frac{i\ell k^2 F_0^*[e^{-t} - e^{-ikYt}]}{(k^2+\ell^2)^{\frac{1}{2}}[ik(k^2+\ell^2)^{\frac{1}{2}} - 1][ikY - 1]} \\ &- \frac{\ell k F_0^*[e^{-ikt(k^2+\ell^2)^{\frac{1}{2}}} - e^{-ikYt})}{(k^2+\ell^2)^{\frac{1}{2}}[ik(k^2+\ell^2)^{\frac{1}{2}} - 1][Y - (k^2+\ell^2)^{\frac{1}{2}}]}. \end{aligned} \tag{26}$$

U^* may be determined by (19).

An alternative scenario to the above is the situation when $\sigma^*(t=0) \neq 0$, $A^*(t=0) \neq 0$, but $F^* \equiv 0$, corresponding to some initial disturbance to the flowfield, but without any forcing.

The solution procedure is similar to the above, and leads to the following result

$$\sigma^* = \sigma^*(t=0,Y)e^{-ikYt}. \tag{27}$$

The following equation determines A^*:

$$A_t^* + ik(k^2+\ell^2)^{\frac{1}{2}} A^* = -\int_0^\infty ikY\sigma^*(t=0,Y)e^{-ikYt}dY. \tag{28}$$

The solution of this may then be written

$$A^* = A^*(t=0) - e^{-ik(k^2+\ell^2)^{\frac{1}{2}}t} \int_0^t e^{ik(k^2+\ell^2)^{\frac{1}{2}}t} \int_0^\infty ikY\sigma^*(t=0,Y)e^{-ikYt}dY\,dt. \tag{29}$$

P^* then follows from (22), W^* from (16) and U^* from (19).

Before considering any numerical results of the above, we consider a numerical scheme to treat the full nonlinear ($h = O(1)$) system, using a method based to a large extent on the above.

Numerical procedure

The linearised solution as described in the previous section is seen to be solved conveniently using the double Fourier transform approach in X and t. In the light of this, and also in the spirit of Burggraf & Duck (1981) and Duck & Burggraf (1985), we adopt an analogous technique when considering the nonlinear problem (9)-(12).

In this case we write

$$U = Y + \tilde{U}, V = \tilde{V}, W = \tilde{W}, P = \tilde{P}, A = \tilde{A}, \tag{30}$$

where tilde quantities are not necessarily small, and then (9)-(11) may be written as

$$\tilde{U}_t + Y\tilde{U}_X + \tilde{V} + \tilde{P}_X = -\tilde{U}\tilde{U}_X - \tilde{V}\tilde{U}_Y - \tilde{W}\tilde{U}_Z = R_1, \tag{31}$$

$$\tilde{W}_t + Y\tilde{W}_X + \tilde{P}_Z = -\tilde{U}\tilde{W}_X - \tilde{V}\tilde{W}_Y - \tilde{W}\tilde{W}_Z = R_2, \tag{32}$$

$$\tilde{U}_X + \tilde{V}_Y + \tilde{W}_Z = 0. \tag{33}$$

Taking the double Fourier transform of the above (see (14)), then differentiating the transform of (31) with respect to Y, and adding to this $\frac{\ell}{k}$ times the Y derivative of the transform of (32) yields

$$\sigma_t^* + ikY\sigma^* = R_{1Y}^* + \frac{\ell}{k}R_{2Y}^*. \tag{34}$$

The following equation determines A^*:

$$\int_0^{\eta\infty} \sigma_t^* dY = A_t^* + F_t^* - R_1^*(Y=0) - \frac{\ell}{k}R_2^*(Y=0) + ik(k^2+\ell^2)^{\frac{1}{2}}A^*, \tag{35}$$

P^* is determined from (22), and W^* from the transform of (32), U^* from (19), and V^* from continuity.

The Y coordinate was mapped to a transform coordinate and discretisation was applied in all four independent variables; Crank-Nicolson differencing was implemented temporally. We generally took, at $t = 0$:

$$U^* = V^* = W^* = P^* = A^* = 0. \tag{36}$$

At the first time step ($t = \Delta t$, say), initially we set $R_1^* = R_2^* = 0$, thus mimicking the linear system (indeed, the computer code was written to operate in either nonlinear or linear mode). To evaluate the right-hand-side terms R_1^* and R_2^*, although it is possible to write these in terms of convolution-type integrals, it is best (Burggraf & Duck 1981) to use the fast Fourier transform method to transform variables to physical (X, Z) space from transform (k, ℓ) space. Then, the nonlinear terms are evaluated to yield $R_1(X, Y, Z, t)$ and $R_2(X, Y, Z, t)$. Next these quantities are fast-Fourier-transformed back to transform (k, ℓ) space; this has considerable computational advantages over the more direct convolution techniques. With the newly evaluated R_1^* and R_2^*, the process is repeated, until the change in the values of all the physical quantities was sufficiently small; the process was then moved forward to the next timestep ($t = 2\Delta t$) and repeated.

Results and Conclusions

Two-dimensional disturbances

The two-dimensional analogue of the system (31)-(33) does admit solutions of the form

$$U = Y + A(X,t) + hF(X,t), \qquad V = -YA_X - YhF_X, \tag{37}$$

where the displacement function $A(X, t)$ satisfies the forced Benjamin-Ono equation, namely

$$A_t + hF_t + (A + hF)(A_X + hF_X) = \frac{1}{\pi}\int_{-\infty}^{\infty} \frac{A_{\xi\xi}}{X - \xi} d\xi. \tag{38}$$

This class of problem is clearly simplified because of the removal of the $Y-$dependency, and has been considered by Bogdananova-Ryzhova & Ryzhov (1995) and was shown to exhibit some very interesting features. For the purposes of this paper we consider, instead, two-dimensional solutions which do not fall into this category. Here we take initial disturbances of the form

$$U(X, Y, t = 0) = Y + G(X)H(Y), \quad P(X, t = 0) = A(X, t = 0) = 0, \tag{39}$$
$$F(X, t) = 0 \quad \forall t.$$

Note that in the *linear* solution of problems of this type, $\tau = U_Y(Y = 0)$ is predicted to be independent of time, a property confirmed by our numerical calculations. Here we present nonlinear results for the case

$$G(X) = \frac{1}{2\sqrt{\pi}} e^{-\frac{X^2}{4}}, \qquad H(Y) = e^{-Y}. \tag{40}$$

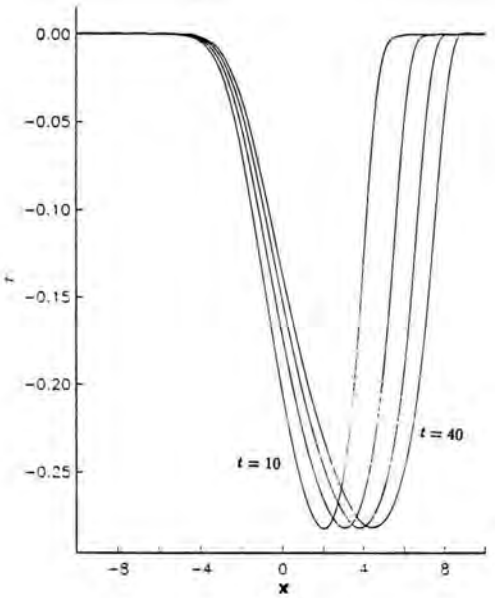

Figure 1: τ at $t = 10,\ 20,\ 30,\ 40$

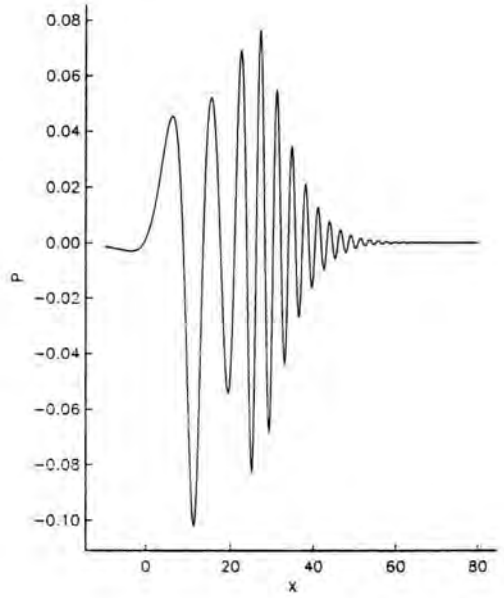

Figure 2: a) $P(t = 10)$

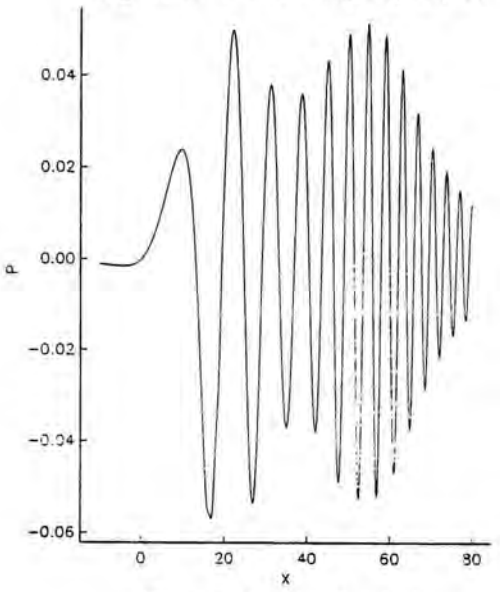

Figure 2: b) $P(t = 20)$

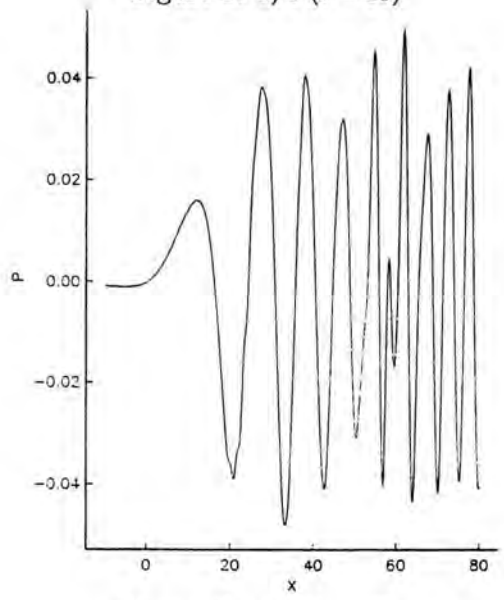

Figure 2: c) $P(t = 30)$

Fig. 1 shows results for τ at $t = 10, 20, 30, 40$. This indicates a gradual drift/movement of this distribution downstream with time (a feature of the non-linearity of the problem). Figs 2a-c show the corresponding pressure distributions and present a very different (oscillatory) picture, the oscillations becoming increasingly predominant as t increases. There was no real evidence of any solution breakdown; there was a fairly slow growth in the magnitudes of the higher wavenumbers of the (spectral) solution, but solution integrity could be controlled (up to and somewhat beyond) the time period shown, with a relatively modest numerical grid (2048 modes, with a spacing of 0.005, and 161 η points, together with a timestep of 0.05).

One important factor not incorporated into the above analysis is the role of viscous sub-layers that must inevitably occur, as alluded to earlier in this paper, of thickness $O(\Omega^{-\frac{1}{2}})$ relative to the original lower deck scale. These layers will be of the classical, unsteady boundary-layer type, in so far as the pressure gradient (and consequently the outer streamwise velocity) will be prescribed *a priori*, (as determined from the calculations above). On account of the highly oscillatory nature of the imposed pressure gradients, it therefore seems possible that these boundary layers themselves may exhibit finite-time singularities of the Van Dommelen & Shen (1981) type, leading to an eruption of this sublayer into the main body of the boundary layer.

Three-dimensional disturbances

Here we restrict our attention to zero initial disturbances by taking undisturbed initial conditions corresponding to (36). the forcing to the problem provided by a forcing function of the form

$$F(X, Z, t) = \frac{1}{4\pi}(1 - e^{-t})e^{-\frac{(X^2+Z^2)}{4}}, \tag{41}$$

corresponding to an initially undisturbed flow, with a forcing that grows in amplitude, but ultimately becomes a steady forcing. Here we present results for the particular case $h = -5$. Careful monitoring of the spectral solution revealed that shortly after $t = 1.75$, a rapid growth in the high-wavenumber solution occured (reminiscent of that observed in many full triple-deck problems, indicating a finite-time breakdown).

Figs 3a, b show contours for the streamwise slip velocity, i.e. $U(Y = 0)$ at $t = 1.0$ and 1.75 respectively. These figures indicate also gradual solution development. Figs 4a, b show the corresponding contours of the (perturbation) streamwise velocity component along the centreline (i.e. $\tilde{U}(Z = 0)$), and these indicate rather more dramatic solution development as time progresses. Taken together, these results point to a finite-time breakdown of the solution not observed in any of our 2D calculations. This indicates a clear distinction between

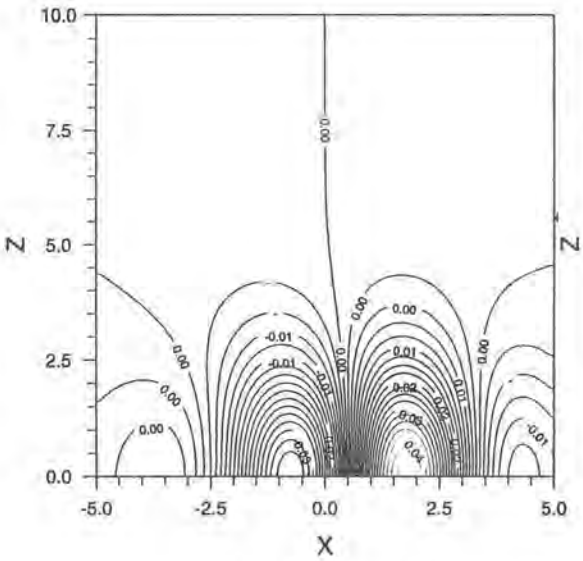

Figure 3: a) $U(X, Y = 0, Z, t = 1.0)$ contours

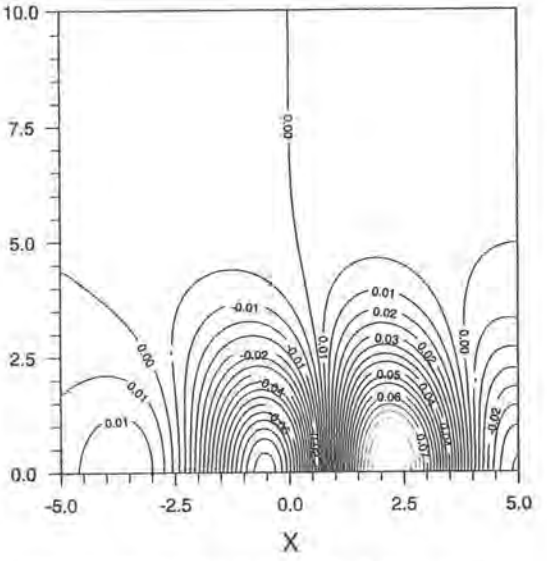

Figure 3: b) $U(X, Y = 0, Z, t = 1.75)$ contours

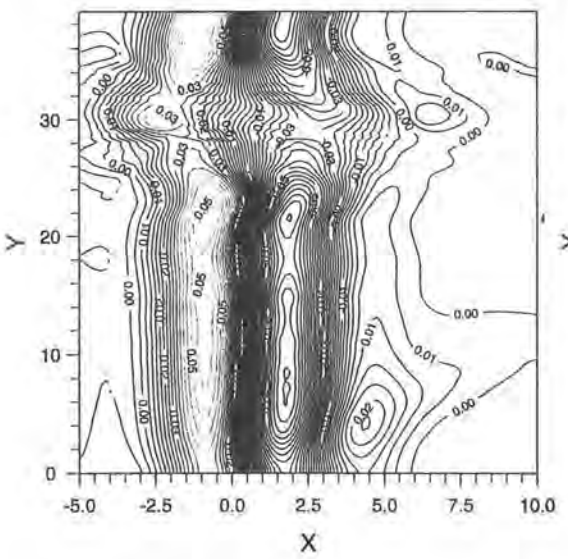

Figure 4: a) $U(X, Y, Z = 0, t = 1.0)$ contours

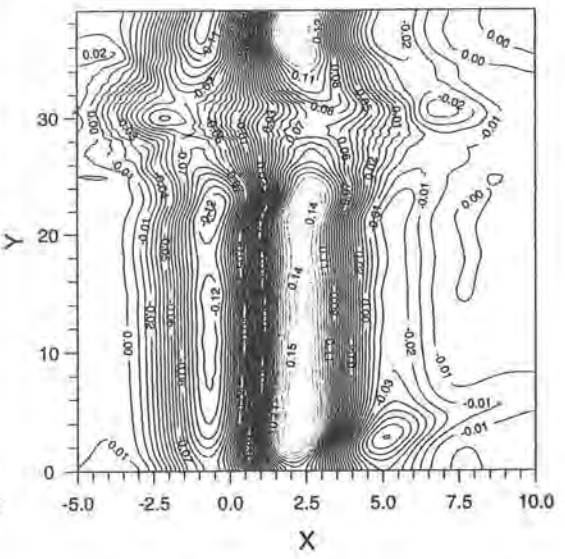

Figure 4: b) $U(X, Y, Z = 0, t = 1.75)$ contours

2D and 3D computations of this type, and will be the subject of further investigation. Indeed, the 3D case appears much more complex; in the 2D case the vorticity is frozen, whilst this can not be the case in 3D (Kachanov *et al.*, 1993).

References

Bogdanova-Ryzhova, E.V. & Ryzhov, O.S. 1995 – Solitary-like waves in boundary-layer flows and their randomization, *Phil. Trans. Roy. Soc.* **352** , 389.

Brotherton-Radcliffe, R.V. & Smith, F.T. 1987 – Complete breakdown of an unsteady interactive boundary layer (over a surface distortion or in a liquid layer), *Mathematika* **34**, 86.

Burggraf, O.R. & Duck, P.W. 1982 – Spectral computation of triple-deck flows. *Proc. Symposium on Numerical Physical Aspects of Aerodynamic flows*, Springer, 145.

Duck, P.W. 1981 – Laminar flow over a small unsteady three-dimensional hump. *ZAMP* **32**, 62.

Duck, P.W. 1987 – Unsteady triple-deck flows leading to instabilities. *Proc. IUTAM Sym. on boundary layer separation,* Springer, p. 297.

Duck, P.W. 1990 – Triple-deck flow over unsteady surface disturbances: the three-dimensional development of Tollmien Schlichting waves. *Computers and Fluids* **18**, 1.

Duck, P.W. & Burggraf, O.R. 1986 – Spectral solutions for three-dimensional triple-deck flow over surface topography. *J. Fluid Mech.* **162**, 1.

Goldstein, M.E. & Lee, S.S. 1992 – Fully coupled resonant-trial interaction in an adverse-pressure-gradient boundary layer. *J. Fluid Mech.* **245**, 523.

Kachanov, Y.S., Ryzhov, O.S. & Smith, F.T. 1993 – Formation of solitons in transitional boundary layers: theory and experiment, *J. Fluid Mech.* **251**, 273.

Peridier, V.J., Smith, F.T., & J.D.A. Walker 1991 – Vortex induced boundary-layer separation, Part 2, unsteady interacting boundary-layer theory. *J. Fluid Mech.* **232**, 133.

Smith, F.T. 1979a – On the non-parallel flow stability of the Blasius boundary layer. *Proc. Roy. Soc.* **A366**, 91.

Smith, F.T. 1979b – Nonlinear stability of boundary layers for disturbances of various sizes. *Proc. Roy. Soc.* **A368**, 573.

Smith, F.T. 1988 – Finite-time breakup can occur in any unsteady interacting boundary layer. *Mathematika* **35**, 256.

Smith, F.T. & Burggraf, O.R. 1985 – On the development of large-sized short-scaled disturbances in boundary layers. *Proc. Roy. Soc.* **A399**, 25.

Van Dommelen, L.L. & Shen, S.F. 1981 – The spontaneous generation of the singularity in a separating boundary layer. *J. Comp. Phys.* **38**, 125.

Author's address

Department of Mathematics
University of Manchester
Manchester, England

V.A. Kazakov

On the Formation of Spikes in the Growing Waves for a Laminar Boundary Layer

Abstract

The formation and evolution of a wave packet in a two-dimensional laminar boundary layer on a flat plate in incompressible fluid is studied numerically. The flow perturbation is generated by a local distortion of the plate surface. The analysis is carried out within the framework of triple-deck theory. A nonlinear initial-boundary value problem is formulated and solved by the strongly implicit procedure. To increase the accuracy of the finite-difference scheme, a nonsymmetric compact approximation is used. At a nonlinear stage, vortical separated bubbles are generated on the plate surface. Spikes peculiar to the K-type transition appear on the waves crests, and, as a result of their rapid growing, the flow breaks down. Their appearance may be considered to be a two-dimensional phenomenon.

Introduction

Since the pioneering observations of the K-type transition (Klebanoff, Tidstrom & Sargent, 1962), the appearance of spikes (high-frequency oscillations in hot-wire traces) with the following breakdown to turbulence has remained the subject of investigations and speculation (e.g. Kachanov, 1987 and references therein). This way of transition (in contrast to the subharmonic transition) is characterized by a rather large amplitude of growing waves traveling downstream, which makes the disturbed region more susceptible to secondary instabilities.

In the present paper, computational experiments have been performed to study two-dimensional instability waves with emphasis on the nonlinear stage. In the computations, the waves are not sustained by a continuously vibrating ribbon but are generated by initial disturbances of the flow from a small hump rising at some moment on the plate with subsequent formation of a wave packet (see Duck, 1985, 1987; Kazakov, 1986). A formulation of the problem within the framework of a triple-deck model of asymptotic theory (Stewartson, 1974; Ryzhov & Terent'ev, 1977) allows to somewhat simplify the study (see e.g. computations by Fasel, 1984).

Governing equations

We consider a two-dimensional unsteady flow of viscous incompressible fluid, which develops in a laminar boundary layer on a flat plate as a result of a small

hump rising on its surface at a distance L from the leading edge. Let U_∞ be the velocity of the undisturbed flow ahead of the plate and ν the kinematic viscosity, then $Re = UL/\nu$ is the Reynolds number, which is assumed to be large and $\varepsilon = Re^{-1/8} << 1$. The height of the surface disturbance is assumed to be of the order $O(L\varepsilon^5)$, its length $O(L\varepsilon^3)$, the characteristic time $O(L/U_\infty\varepsilon^2)$.

We locate the origin of the Cartesian coordinate system at the centre of a surface disturbance with the x axis directed downstream along the plate and y normal to the plate. In accordance with triple-deck asymptotic theory in the wall region of a boundary layer with streamwise dimension $O(L\varepsilon^3)$ and normal dimension $O(L\varepsilon^5)$, the flow is described by Prandtl's equations (standard triple-deck nondimensional variables are used):

$$u_t + uu_x + vu_y = -p_x + u_{yy}\,, \tag{1}$$

$$u_x + v_y = 0\,, \qquad p_y = 0\,.$$

At the outer boundary, as $y \to \infty$, matching with the external inviscid flow gives an interaction condition which links the unknown pressure with the boundary-layer thickness function $A(t,x)$ determined by the velocity field in the wall layer.

At the outer boundary, as $y \to \infty$, matching with the external inviscid flow gives an interaction condition which links the unknown pressure with the boundary-layer thickness function $A(t,x)$ determined by the velocity field in the wall layer:

$$p(t,x) = \frac{1}{\pi}\int_{-\infty}^{\infty} \frac{\partial A/\partial s}{x-s} ds\,. \tag{2}$$

The solution is subjected to the boundary conditions:

$$u = v = 0 \quad at \quad y = 0\,,$$

$$u \to y, \quad v \to 0, \quad p \to 0 \quad as \quad x \to -\infty\,, \tag{3}$$

$$u - y \to A(t,x) + f(t,x) \;\; as \;\; y \to \infty\,.$$

The function $f(t,x)$ describes the shape of the disturbed surface. In the numerical method, the boundary conditions are prescribed at finite, sufficiently remote distances.

Numerical method

The governing equations are approximated by finite-difference relationships on a grid $(x_i, y_j), i = 0, ..., N, j = 0, ..., K$. The temporal derivative in the momentum equation (1) is approximated by a usual three-point back second-order accuracy formula. The nonlinear terms in this equation are quasi-linearized also to the

second order, $O(\Delta t^2)$. The derivative of u is calculated according to the flow direction. To increase the accuracy of the numerical scheme we approximate u by non-symmetric compact differences of third-order accuracy on a three-point stencil (x_{i-1}, x_i, x_{i+1}) (Tolstykh, 1973).

We introduce the operators $D^{\pm}$ of a one-sided two-point approximation to the derivative u_x at a point x_i :

$$D^- u_i = \frac{u_i - u_{i-1}}{\Delta x} = \frac{1}{\Delta x}\int_{x_{i-1}}^{x_i} u_x dx \ , \quad D^+ u_i = \frac{u_{i+1} - u_i}{\Delta x} = \frac{1}{\Delta x}\int_{x_i}^{x_{i+1}} u_x dx \ .$$

The integrals on the right-hand sides for an arbitrary function $f(x)$ can be approximately calculated by interpolating $f(x)$ over the segment $[x_{i-1}, x_{i+1}]$ by a quadratic parabola. Define the operators $A^{\pm}$ as

$$A^- f_i = \frac{1}{12}(5f_{i-1} + 8f_i - f_{i+1}) \approx \frac{1}{\Delta x}\int_{x_{i-1}}^{x_i} f(x)dx \ ,$$

$$A^+ f_i = \frac{1}{12}(5f_{i+1} + 8f_i - f_{i-1}) \approx \frac{1}{\Delta x}\int_{x_i}^{x_{i+1}} f(x)dx \ ,$$

It is easy to show that $A^{\pm}(f) - D^{\pm} f = O(\Delta x^3)$. Thus, in the momentum equation (1), the derivative u_x is treated as a new variable for which we have an additional equation

$$A^{\pm}(u_x)_i - D^{\pm} u_i = 0,$$

with

$$A^{\pm}(u_x)_{ij} = (\frac{1}{6} + \frac{s}{4})(u_x)_{i-1,j} + \frac{2}{3}(u_x)_{ij} + (\frac{1}{6} - \frac{s}{4})(u_x)_{i+1,j} \ ,$$

$$D^{\pm} u_{ij} = \frac{1}{2\Delta x}[-(1+s)u_{i-1,j} + 2su_{ij} + (1-s)u_{i+1,j}] \ .$$

If $u_{ij} > 0$ then $s = 1$ and the operators with the sign "$-$" are taken; else, if $u_{ij} < 0$ then $s = -1$ and the operators with "$+$" are taken. The other derivatives p_x u_y, u_{yy} in the momentum equation are approximated by ordinary central differences of the second order.

The continuity equation is approached to second-order accuracy at points $(x_i, y_{j-1/2})$ by central differences $\delta_x u_i = (u_{i+1} - u_{i-1})/2\Delta x$:

$$\frac{1}{2}(\delta_x u_{ij} + \delta_x u_{ij-1}) + \frac{1}{\Delta y}(v_{ij} - v_{ij-1}) = 0 \ .$$

Equation $p_y = 0$ in (1) is represented as $p_{ij+1} - p_{ij} = 0$.

Before the discretization the governing equations were written in new variables x, h obtained as a result of exponential stretching of the variable $x = x(\xi)$ (in both directions from the coordinate origin) and $y = y(\eta)$.

The interaction integral (2) used as a boundary condition at $y = y_K$ is calculated as a sum of integrals over segments $[a_m, a_{m+1}]$, $a_m = (x_{m-1} + x_m)/2$. In each segment, the derivative u_x in the integral is linearly approximated by means of derivatives $(u_x)_{mK}$ and $(u_{xx})_{mK}$ which are replaced by central differences for a nonuniform mesh.

The resulting system with respect to vectors $F_{ij} = [u_{ij}, (u)_{ij}, v_{ij}, p_{ij}]^T$, is solved by the strongly implicit procedure (Stone, 1968). In the first step, at each point (i, j), auxiliary matrix coefficients are calculated by recurrent formulas (Kazakov 1985) using values of these coefficients already found at points $(i, j-1)$ and $(i-1, j)$. In the second step, increments at an iteration, $\Delta\Phi_{ij}$, and new iterative values $\Phi_{ij}^{s+1} = \Phi_{ij}^{s} + \Delta\Phi_{ij}$ are determined. As a result of convergence of iterations, the solution Φ_{ij} at a new time level is obtained.

Numerical analysis

The distortion of the plate was prescribed by the function $f(t, x) = H(t)/ch(4x)$, noticeably different from zero in the interval $(-1, 1)$, $H(t)$ being the height of the hump. Initially, the hump of this kind rose linearly in time during the interval $0 < t < 0.1$ up to its maximum height h and then disappeared in the same way. Computations were performed on nonuniform grids: with 270×30 cells in the domain $-12 < x < 24$, $0 < y < 15$ with the zero point, $x_{i_0} = 0$, at $i_0 = 90$ and minimum values $\Delta x_{i_0} = 0.1$, $\Delta y_0 = 0.2$; on grid 360×50, $i_0 = 120$, $-15 < x < 30$, $0 < y < 30$, $\Delta x_{i_0} = 0.05, 0.1$, $\Delta y_0 = 0.1$; and on a finer grid 540×50, $i_0 = 240$, $-20 < x < 35$, $0 < y < 30$, $\Delta x_{i_0} = 0.025$, $\Delta y_0 = 0.1$. The time steps were taken to be equal to $\Delta t = 0.02$, 0.01 and 0.005 depending on the value of the minimum grid step Δx_{i_0}.

The developing wave packet travels rather far downstream, so, to follow its evolution including a nonlinear stage, the computational domain is also transferred downstream in a certain time. Flows from disturbances of different height, with $h = 0.001, 0.1, 1$ and 2, have been computed.

The formation and development of a wave packet from a hump, with $h = 0.001$, are traced in Fig. 1 (the results of computations on the finest mesh are presented). At the initial linear stage the waves amplitude grows exponentially, with the increment of 0.26, as was obtained by linear theory (Ryzhov & Terent'ev, 1986). With the beginning of a nonlinear stage, the places of higher pressure are moving faster, the front parts of the waves become steeper (Fig. 1, $t = 8, 8.5$), and a tendency to waves tilting manifests itself. For increasing pressure gradients and waves distortion, intensive local shear layers with large positive peaks of the skin-friction $\tau = \partial u/\partial y$ develop. These layers separate from the plate under the effect of unfavourable pressure growth, and regions of negative skin-friction appear on the surface within the packet, which corresponds to the formation of vortices (separated bubbles with a reverse flow). This is clearly seen in Fig. 2 where the flow patterns (streamlines) at different times are shown. As the packet continues develop other vortices arise. Thus at time $t = 8$, we see three small regions of reverse flow, at $t = 8.5$ four, at $t = 8.8$ six. Such regions of

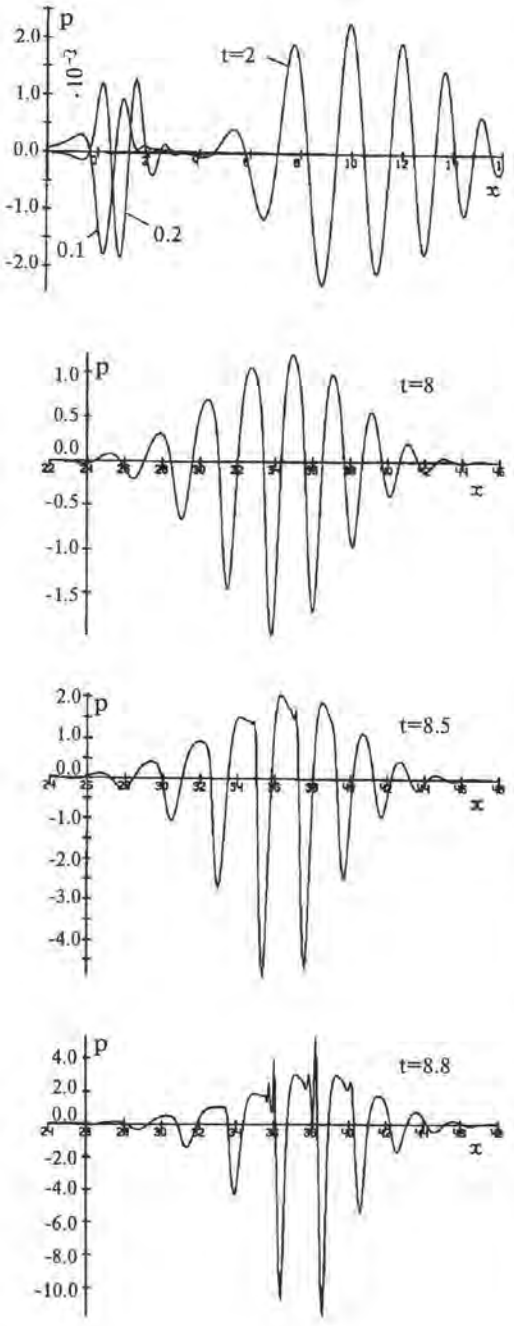

Figure 1: Wave packet formation and evolution. p = presure; τ= skin-friction.

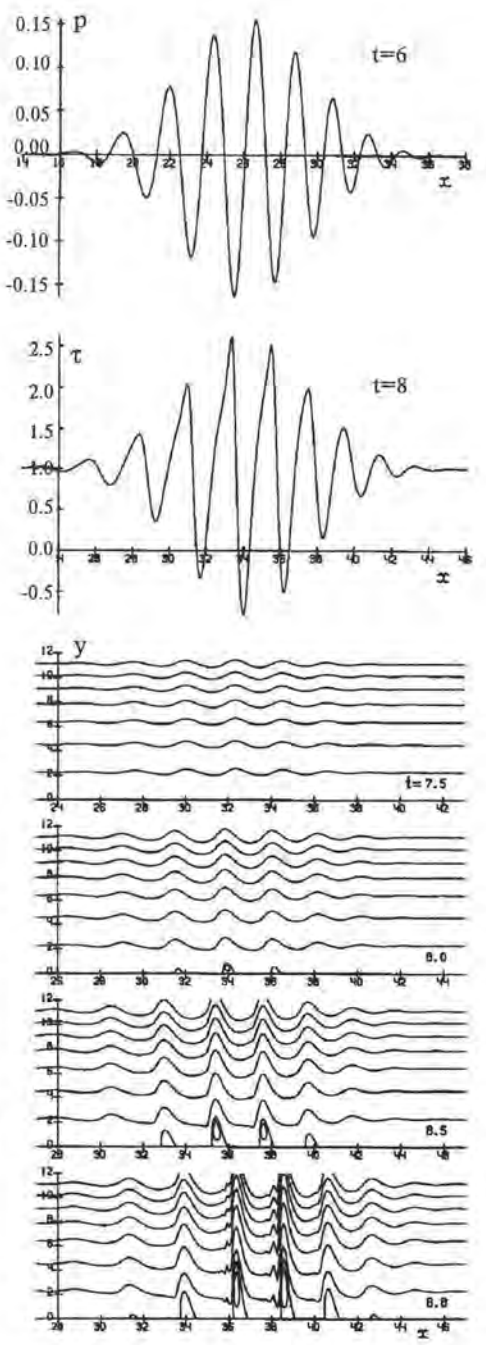

Figure 2: Flow patterns (streamlines) in the region of the wave packet at different times.

reverse flow within Tollmien-Schlichting waves in a boundary layer were recorded experimentally by Kosorygin (1994). An adverse pressure gradient imposed on the flow he studied made the appearance of separated bubbles earlier and easier.

For increasing amplitude of the oscillations and pressure gradients in the packet, the intensity of the vortices grows, and they extend from the plate surface into the main body of the fluid. At this stage, a new phenomenon is observed: small-scale fluctuations with still further increasing amplitudes, "spikes", appear. First one, then two, and finally three (Fig. 1). The spikes are growing very fast and, as a result, the flow breaks down. The streamlines at the places where the spikes develop also exhibit oscillations (Fig. 2). Their largest amplitude is reached at some elevation above the plate, which increases when the packet goes downstream. The distributions of the streamwise velocity component $u' = u - y$ on the lines of constant y near the plate surface are qualitatively the same as that of the skin-friction, with the spikes growing generally in the direction of positive values, which is related to the vortical structure of the flow near the plate. At time $t = 8.8$, the spikes in the u' distribution are the largest at $y = 0.7 - 0.8$. Farther from the surface, their amplitude diminishes (Fig. 3), and the wave-like flow within the packet is less distorted. As one can see, the spikes arise at the end of the accelerating section of decreasing pressure and considerably increasing skin-friction on the plate, at the place where the flow is slowing down before a local separation. Thus, their appearance is linked with the formation of an unstable instantaneous inflectional velocity profile, which is recorded in experiments.

The evolution of the wave packet from the point of view of its spectral characteristics is followed in Fig. 4, where the square of the absolute value of the pressure Fourier transform versus wavenumber is depicted.

As followed from calculations on different grids the wavelength of the forming spikes are dependent on the grid cells size in accordance with Tutty & Cowly (1986) who showed that the unsteady interaction model included the mechanism for Rayleigh inviscid instability. In the case of marginal separated regions these short-scale instabilities lead to splitting the separation region into small eddies which start growing and destroy the flow very fast (Kazakov, 1985; Henkes & Veldman, 1987). Extensive studies of the latter phenomenon (so called finite time singularity) were made by F.T. Smith and some others (Bodonyi & Smith, 1987 and works later on). In the present case the separated bubbles forming within the wave packet are initially small and short-scale instabilities are first displayed on the waves crests in front of the bubbles. A short time later the bubbles are destroyed too and the flow breaks down.

Although a turbulent flow is essentially three-dimensional, the numerical solution evidences that the beginning of its formation, in the form of small-scale fluctuations on the crests of the carrying primary two-dimensional wave of instability, can be displayed already at the stage of the development of wave disturbances in a two-dimensional flow. As the conditions of their appearance, we find the following characteristics: fairly large pressure amplitudes and gradients; the increasing steepness of the waves fronts in the packet (a process of waves

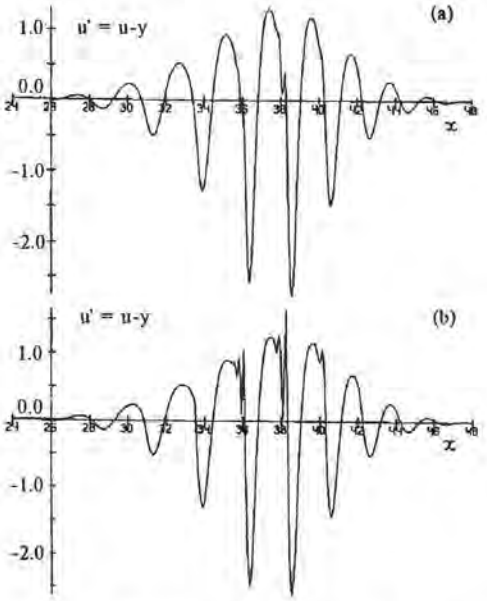

Figure 3: Streamwise velocity diturbance at two levels above the plate; (a) $y = 5.56$; (b) $y = 1.9$.

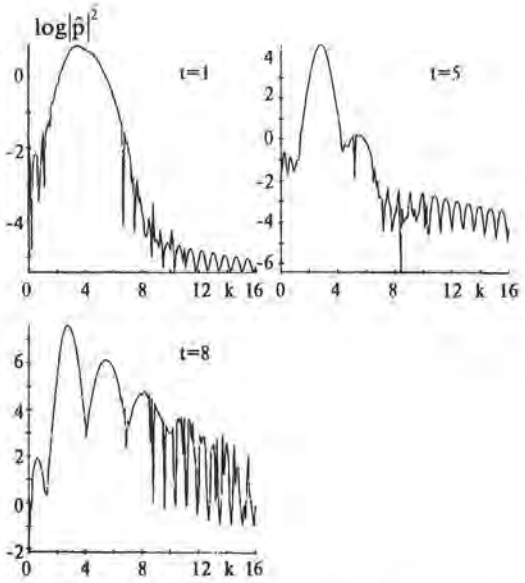

Figure 4: Spectral density of pressure amplitude.

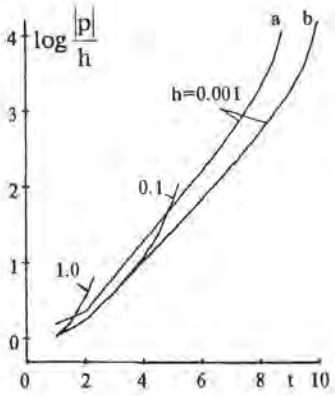

Figure 5: Growth of pressure amplitude of the wave packet computed on different grids: (a) 540 × 50; (b) 360 × 50.

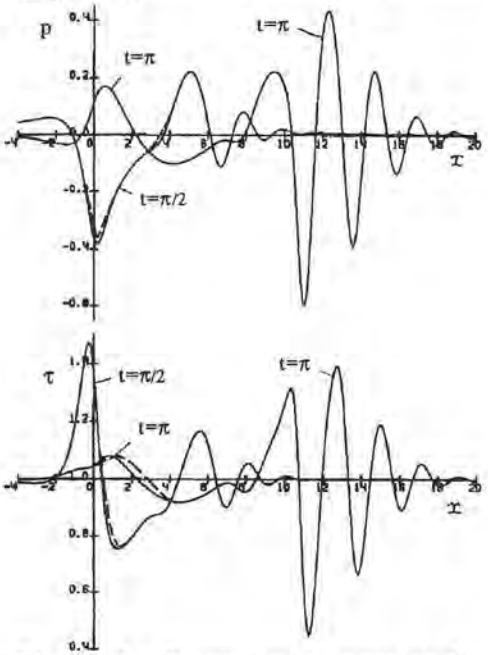

Figure 6: Formation of wave packet from oscillating hump, $H(t) = h \sin t$, h=1; —— present; – – – Duck (1985), $|x| < 5$.

tilting), which is accompanied by the appearance of new short-wave harmonics in the spectrum of disturbances at a nonlinear stage; the formation of unstable shear layers with inflectional velocity profiles. These features make the flow prone to Rayleigh type instability. The role of three-dimensionality of the flow in the formation of short-scale fluctuations at the initial stage of transition is actually reduced only to localization of the places with sufficiently large amplitudes and gradients of the flow.

Validation of the numerical method used is presented in Figs 5 and 6. Some results for Duck's (1985) oscillating hump are depicted in Fig.6. Present computations were carried out in the domain $-15 < x < 32$, $0 < y < 30$ on a 400×50 grid, $i = 100$ with $\Delta x_{i_0} = 0.05$, $\Delta y_0 = 0.1$ and $\Delta t = 0.01$. Duck solved the problem by the spectral method. Both methods give close results within the section $-5 < x < 5$, for which Duck's data are presented.

References

Bodonyi, R.J. & Smith F.T. 1987 – On short-scale inviscid instabilities in the flow past surface-mounted obstacles. In: *Stability of time-dependent and spatially varying flows.* N.Y. pp. 148-163.

Duck, P.W. 1985 – Laminar flow over unsteady humps: the formation of waves. *J. Fluid Mech.* **160**, 465-498.

Duck, P.W. 1987 – Unsteady triple-deck flows leading to instabilities. In: *Boundary-layer Separation.* Springer, Berlin, pp. 297-312.

Fasel, H. 1984 – Numerical simulation of nonlinear growth of wave packets in a laminar boundary layer. In: *Turbulence and chaotic phenomena in fluids,* North-Holland, Amsterdam, pp. 31-37.

Henkes, R.A.W.M. & Veldman, A.E.P. 1987 – On the breakdown of the steady and unsteady interacting boundary-layer description. *J. Fluid Mech.* **179**, 513-529.

Kachanov, Yu.S. 1987 – On the resonant nature of the breakdown of a laminar boundary layer. *J. Fluid Mech.* **184**, 43-74.

Kazakov, V.A. 1985 – Strongly implicit alternately-triangular procedure for the solution to the problems of asymptotic theory of a boundary layer (in Russian). *Zhurnal vychisl. matem. i matem. fiz.* **25**, 1382-1390.

Kazakov, V.A. 1986 – On spreading disturbances and generation of vortices in a laminar boundary layer (in Russian). In: *VI All-Union Congress on Theor. and Appl. Mech., Abstracts.* Tashkent, p. 320.

Klebanoff, P.S., Tidstrom, K.D. & Sargent, L.M. 1962 – The three-dimensional nature of boundary-layer instability. *J. Fluid Mech.* **12**, 1-34.

Kosorygin, V.S. 1994 – Stability and transition to turbulence in 2-D boundary layer under the influence of adverse pressure gradients. In: *Nonlinear Instability of Nonparallel Flows,* Springer, Berlin, pp. 86-91.

Ryzhov, O.S. & Terent'ev, E.D. 1977 – On the nonstationary boundary layer with self-induced pressure (in Russian), *Prikl. matem. i mekh.* **41** , 1007-1023.

Ryzhov, O.S. & Terent'ev, E.D. 1986 – On the transitional regime characterizing the start-up of a vibrator in a subsonic boundary layer on a plate (in Russian). *Prikl. matem. i mekh.* **50**, 974-986.

Stewartson, K. 1974 – Multistructured boundary layers on flat plates and related bodies. *Advances in Appl. Mech.* **14**, 145-239.

Stone, H.L. 1968 – Iterative solution of implicit approximations of multidimensional partial equations. *SIAM J. Numer. Analys.* **5**, 530-558.

Tutty,O.R. & Cowly S.J. 1986 – On the stability and the numerical solution of the unsteady interactive boundary-layer equation. *J. Fluid Mech.* **168**, 431-456.

Tolstykh, A.I. 1973 – On a method of numerical solution of the Navier-Stokes equations for compressible fluid in a wide range of the Reynolds numbers (in Russian), *Dokl. AN SSSR*, **210**, 48-51.

Author's address

Central Aero-Hydrodynamic Institute Zhukovsky
Moscow region 140160, Russia

Session 7:
Disturbance Sources and Receptivity

P. H. Alfredsson & M. Matsubara

Streaky Structures in Transition

Abstract

There is an increasing amount of evidence that streaky streamwise-oriented structures confined in the laminar boundary layer are the embryo for so called "bypass" transition in many flows of engineering interest. This paper mainly focuses on boundary layer development under the influence of moderate levels of free stream turbulence. Experiments show that free stream turbulence gives rise to very long streamwise structures, which grow in amplitude as they move downstream. These structures may lead to rms disturbance levels as high as 10% inside the boundary layer before turbulence is observed. Flow visualisation suggests that turbulent spots originate from an instability of a "strong" streak, probably due to a secondary instability of (spanwise) inflectional type. Artificial introduction of temporal disturbances drastically enhances breakdown in the disturbed boundary layer.

Introduction

Consider a wind tunnel experiment where a laminar boundary layer develops along a flat surface. At some distance downstream the leading edge a short pulse disturbance is introduced through a small hole in the wall. The development of this disturbance depends on several parameters; the two most important are the amplitude of the pulse and the Reynolds number at which it is generated. Several different scenarios may follow (see Fig. 1); if the disturbance is small and the Reynolds number above a critical value a wave packet may form and grow; if the disturbance is large enough it may result almost immediately in a turbulent spot even for Reynolds numbers below the critical value, i.e. the Reynolds number for which linear waves are amplified. For disturbances of an intermediate strength the result may be a narrow (in the spanwise direction) elongated structure. The initial development of the wave packet can be described by linear theory (Gaster, 1975) and both propagation velocity, spreading and amplification are well predicted (although non-parallel effects become increasingly important with increasing wave angle, see e.g. Kachanov & Michalke, 1994). In case of a turbulent spot it spreads with a half-spreading angle of typically 10° and its rear propagates with about 50% of the free stream velocity (see Elder, 1962). The disturbance of intermediate strength is however quite different: its spanwise spreading is almost negligible and the maximum streamwise velocity perturbation is found in the middle of the boundary layer. Grek, Kozlov & Ramazanov (1985) found this type of disturbance in a laminar boundary layer and gave it the name 'puff'. Similar disturbances were also found experimentally in channel

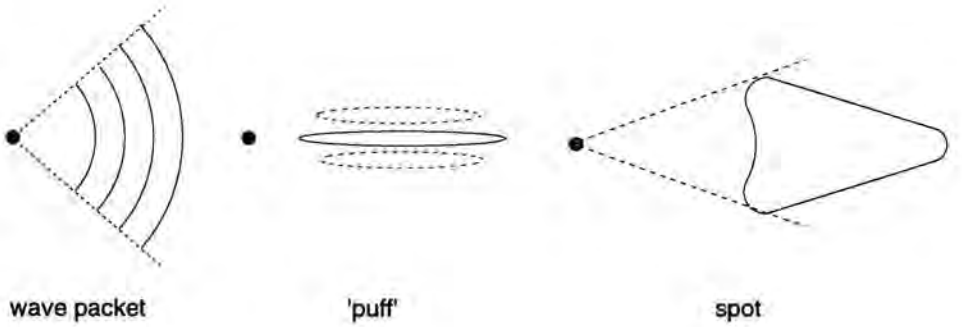

Figure 1: Three different types of propagating disturbances originating from a localized disturbance of different strength inside the boundary layer, a) wave packet, b) streaky structure, 'puff', c) turbulent spot.

flow by Klingmann (1992), who also showed that there are many similarities between the growth of such a disturbance and the development known as algebraic or transient growth (Landahl 1980, Gustavsson, 1991, Reddy & Henningson, 1993).

Similar streaky structures are induced into a laminar boundary layer which is subjected to moderate levels of free stream turbulence. This paper describes in some detail the work done at KTH on such structures. However also other types of boundary layer flows for which growth of streaky structures dominates the first stages of the transition process are described. The flows that will be discussed are *i*) a Blasius boundary layer subjected to free stream turbulence, *ii*) a Blasius boundary layer subjected to a deterministic free stream vortex, *iii*) a plane channel flow for which interaction of oblique TS-waves gives rise to streaky structures and *iv*) a rotating channel flow where the Coriolis force gives rise to a primary instability of streamwise oriented roll cells. All these flows may break down to turbulence through a process of a secondary instability of wave type and possible connections between transition to turbulence in the different cases will be discussed. It is concluded that a combination of longitudinal streaks and continuous forcing by temporal disturbances plays an important role in many types of natural transition.

An example of algebraic growth

A simple example of the algebraic growth mechanism can be obtained by studying the equation for the normal vorticity ($\eta = \frac{\partial u}{\partial z} - \frac{\partial w}{\partial x}$) in the inviscid limit.[1] If this equation is Fourier transformed, with α and β denoting the wave numbers in the streamwise and spanwise directions, respectively, it can be written as

[1] u, v and w are the disturbance velocity components in the streamwise (x), normal (y) and spanwise (z) directions, respectively whereas U is the mean velocity in the x-direction.

$$(\frac{\partial}{\partial t} + i\alpha U)\hat{\eta} = -i\beta U'\hat{v},$$

with the initial conditions $\hat{\eta}(t=0)=\hat{\eta}_0$. This equation can be directly integrated to become

$$\hat{\eta} = \hat{\eta}_0 e^{-i\alpha U t} - i\beta U' e^{-i\alpha U t} \int_0^t \hat{v}(\tau) e^{i\alpha U \tau} d\tau.$$

In the case of structures of long streamwise extent, i.e. $\alpha \to 0$, and assuming that the normal velocity is constant, i.e. $\hat{v} = \hat{v}_0$, we obtain the following expression for the normal vorticity

$$\hat{\eta} = \hat{\eta}_0 - i\beta U' \hat{v}_0 t.$$

This shows that the normal vorticity will grow algebraically with time. If the streamwise velocity was measured one would see an amplitude growth of streaks of alternating high and low streamwise velocity.

A laminar boundary layer subjected to free stream turbulence

Free stream turbulence (FST) has a strong influence on the onset of transition and this was recognized already by Schubauer & Skramstad (1947) who took, at that time, unprecedented efforts to reduce the free stream turbulence level in their wind tunnel in order to be able to detect Tollmien-Schlichting waves. However FST influence transition also in many engineering situations, as for instance in turbomachinery applications.

Attempts have been made to establish empirical correlations between the free stream turbulence and the transition Reynolds number. At FST levels above 5-10%, transition occurs at the minimum Reynolds number where self-sustained boundary layer turbulence can exist, i.e. at $R \approx 500$ where R denotes the Reynolds number based on the displacement thickness. At lower levels of FST, however, different experiments disagree widely for the location and extent of the transition region. There seems to be no strong correlation between the level of FST and the location of transition onset.[2] Neither can the transition Reynolds number be found by merely taking into account the fluctuations inside the boundary layer. Transition may also be sensitive to a large number of other parameters, including not only the overall level of FST but also spatial scales, conditions at the leading edge of the model, presence of pressure gradients, etc., each of which requires special attention. Depending on these conditions, FST-induced transition may be caused by different types of boundary layer instabilities. At low ambient disturbance levels TS-waves (or rather wave packets) may still be of importance, but at higher levels different types of interaction are at hand, and the results of such mechanisms will be described in the following.

[2]Some success has been made through an empirical relation for the N-factor used in the e^N-method and the turbulence level. However from the physical point of view TS-waves have very little to do with the processes leading to transition in these cases.

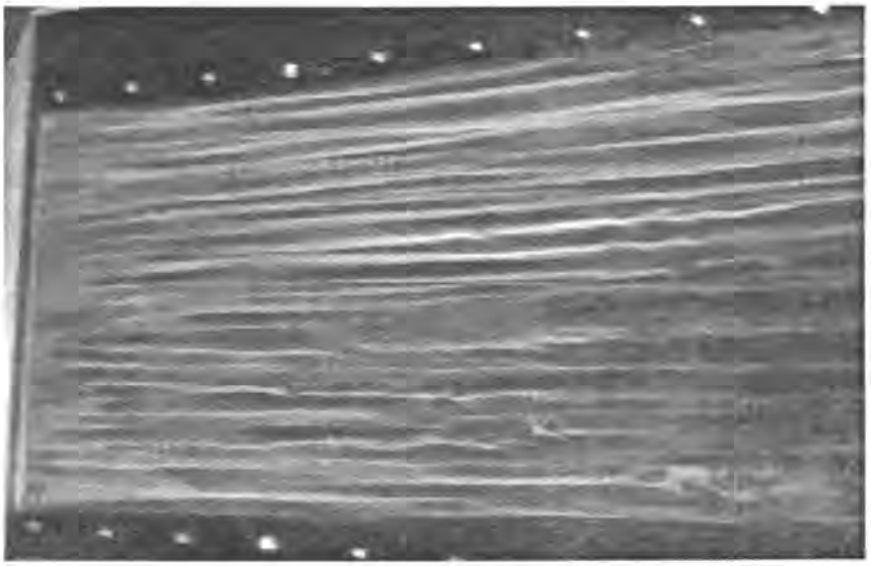

Figure 2: Streaky structures, observed through smoke visualization, in a laminar boundary layer at U_∞ =2 m/s subjected to 6 % free stream turbulence. Flow is from left to right. White markers are 10 cm apart. Note the sign of streak oscillations and breakdown at the downstream end of the photograph.

Flow visualization

Flow visualisation experiments in the MTL-wind tunnel at KTH (Matsubara & Alfredsson, 1995) have shown that during the initial receptivity and evolution phases FST induces longitudinal streaks with a spanwise, fairly periodic regularity inside the boundary layer. These structures grow downstream both in length and amplitude and their streamwise scale is much larger than typical longitudinal scales in the free stream (see Fig. 2). The spanwise scale of the boundary layer perturbations is comparable to the transverse scales in the free stream, however, no direct relation can be established from available data.

Flow visualisation shows that breakdown to turbulent spots occurs where the smoke visualisation shows intensive streaks. The breakdown of streaks often occurs after a wavy motion of the streak has been observed and results in the appearance of turbulent spots which grow in number and size downstream, until the boundary layer becomes fully turbulent.

Mean velocity and fluctuating disturbances

Fig. 3 shows an illuminating comparison between time traces of the velocity outside and inside a laminar boundary layer. It is clear that the high frequencies in the free stream are effectively damped and that low frequencies are amplified inside the boundary layer. These low frequency fluctuations are probably related

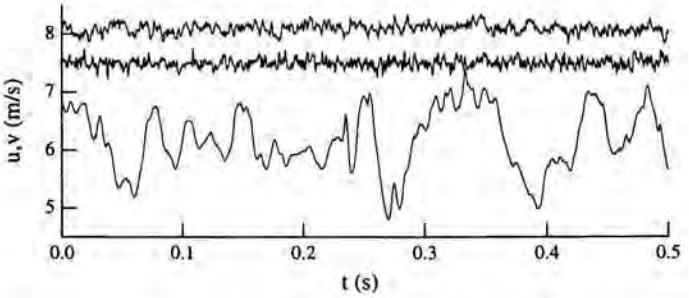

Figure 3: Comparison between velocity signals inside and outside a 'laminar' boundary layer (U_∞ =8.1 m/s). The upper two traces are u and v measured in the free stream, whereas the lower trace is u measured at y/δ^*=1.5.

to meandering long structures of low and high velocity. The existence of streaky structures is also illustrated through spanwise correlation measurements of the streamwise velocity which show a distinct negative minimum corresponding to the average distance between high and low velocity streaks (Westin *et al.*, 1994).

Although the u_{rms} levels inside the boundary layer may reach 10% or more before transition to turbulence occurs, the mean flow boundary layer profile is only slightly changed as compared to the undisturbed flow. The presence of FST gives profiles with larger mean velocity close to the wall, whereas there is a velocity deficit in the outer part of the boundary layer, i.e. a systematic development towards a fuller profile, whereas the boundary layer thickness is only slightly affected. If the difference between the measured and Blasius profiles is plotted it is found that the shape is fairly self similar at all measured stations. The modification gives an increase in the wall shear stress and a decreasing shape factor in the downstream direction. The rms-profiles for both u and v for a case with 1.5% FST are shown in Fig. 4 for four different downstream positions. It is clearly shown how the intensity increases in the downstream direction and that u_{rms} has a maximum in the centre of the boundary layer. This position is further out in the boundary layer compared to the position of the maximum amplitude of the TS-wave. It is also found that the maximum of u_{rms}/U_∞ grows at a rate which is proportional to R. The level of v_{rms} starts to decrease from its free stream value towards the wall already several boundary layer thicknesses from the wall. This is due to that the wall limits motion normal to its surface on a scale typical of the FST rather than the boundary layer thickness. Within the boundary layer there is a local maximum in v_{rms}, which possibly occurs through production of u^2 within the boundary layer which is redistributed into v^2 and w^2 or from the continuous forcing from the FST.

High frequency disturbances and breakdown

It is not clear to what extent the development of the streaks and their eventual breakdown inside the boundary layer are due to the internal dynamics or

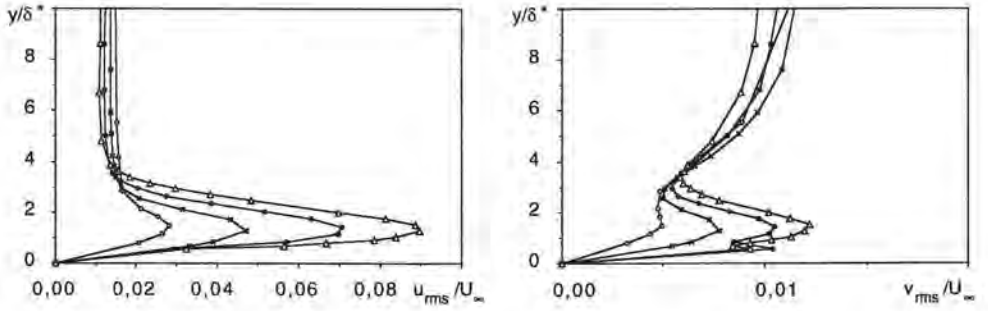

Figure 4: u_{rms} and v_{rms}-profiles for four different downstream positions in a Blasius boundary layer at U_∞ = 8 m/s affected by 1.5 % free stream turbulence (at the plate leading edge). Note different scale on u_{rms} and v_{rms}-axis. o: x =100 mm, ×: x =250 mm, •: x =500 mm, △: x =800 mm

whether they are a result of the continuous forcing from the free stream turbulence along the boundary layer edge. Boiko *et al.* (1994) showed that the streaks were sensitive to TS-waves, and by forcing them with small amplitude waves at frequencies in the range F=100-300 ($F = 2\pi f\nu/U_\infty^2 \cdot 10^6$) breakdown occurred much earlier than without forcing.

A localized free stream disturbance

There are many difficulties associated with experiments at high FST-levels if one wants to look into the details of the generation and growth of disturbances due to their random appearance in space and time. To separate and study details in the transitional structures is therefore an intricate task. Assuming that transition at high and moderate levels of FST is the result of the evolution of localized, transient disturbances caused by free stream vortices impinging onto the boundary layer, Bakchinov *et al.* (1995) tried to simulate this in a controlled manner. They introduced a deterministic disturbance into the free stream from a small pipe located upstream of the leading edge of a flat plate. The free stream eddy gave rise to a surprisingly simple disturbance inside the boundary layer. It consisted of three longitudinal streaks, with the maximum perturbation amplitude approximately in the middle of the boundary layer. However in this case the amplitude decayed downstream, despite a rather high amplitude of the deterministic vortex when it impinged the plate leading edge. In Fig. 5c, the spanwise distribution shows a positive u-disturbance on the centreline, surrounded by two negative regions. The peak values of the perturbation (positive and negative) are located approximately in the middle of the boundary layer (Fig. 5a,b). The localized character of the disturbance should also be emphasized. The downstream development of the structure shows a slowly decaying amplitude whereas the disturbance itself is elongated, though without any dramatic changes in its

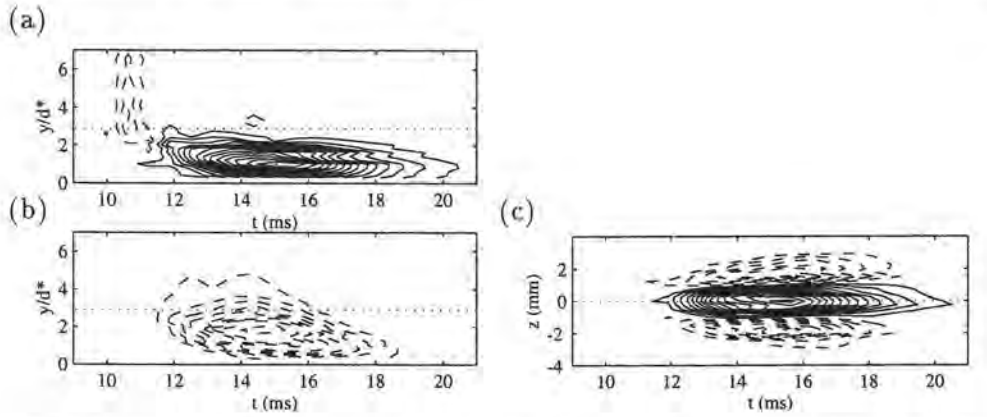

Figure 5: Localized disturbance at $R = 125$. Contour increments are 1% of U_∞. Negative increments are shown as dashed lines. a) yt-plane at $z = 0$, b) yt-plane at $z \approx -1.75$ mm c) zt-plane at $y/\delta^* \approx 1$. Dotted lines in a) and b) mark the boundary layer edge. (See Bakchinov *et al.*, 1995)

structure. The front of the disturbance is convected with approximately $0.9U_\infty$, and the rear part with $0.5U_\infty$.

When comparing the characteristics of this controlled disturbance with results for boundary layers subjected to free stream turbulence, it is striking that the maximum perturbation amplitude is found approximately in the middle of the boundary layer in both cases. However, the localized disturbance amplitude is always decaying downstream, in contrast to the growing u_{rms} in the FST-case. It is possible that the downstream development of u_{rms} depends to a large extent on the continuous forcing from the FST above the boundary layer, and is not only confined to the leading edge receptivity.

An interesting comparison can be made between this structure and the optimal disturbances discussed by Butler & Farell (1992). They found that a streamwise vortex has the largest growth for short times in the Blasius boundary layer. After the initial growth, the amplitude of the disturbance starts to decay, which is first observable in the v-component. The streamwise perturbation also starts to decay, but damping is smaller and low- and high-velocity streaks can be observed for long times.

Interaction with high frequency wave disturbances

The localized disturbance described above was also subjected to controlled TS-waves to investigate whether interaction took place. The frequency was chosen to obtain the largest possible interaction for a specified forcing amplitude. This was realized for a non-dimensional frequency F of about 460.

In order to study and distinguish non-linearly induced disturbances, three separate measurements were carried out at each position in space: a) Generation of localized disturbance (puff), b) Generation of TS-wave, c) Generation of

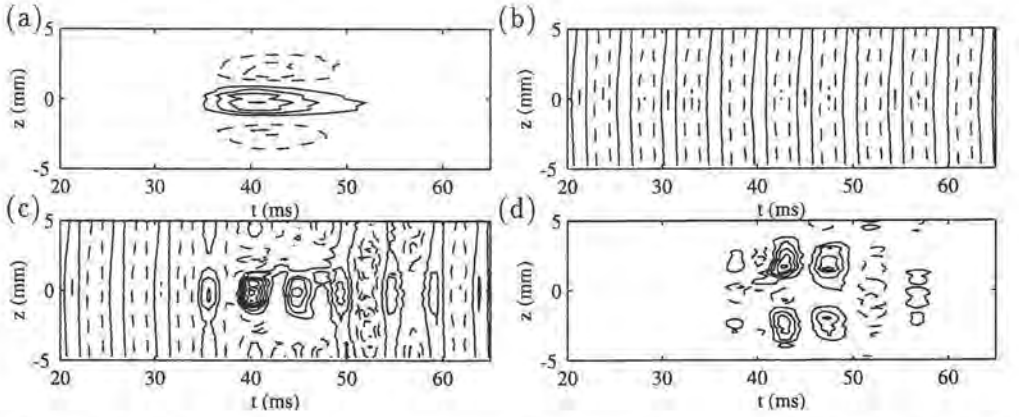

Figure 6: Non-linear interaction between 'puff' and TS-wave, a) 'puff', b) TS-waves, c) combined structure, d) non-linear interaction part. Contour levels are 1% of U_∞. (See Bakchinov *et al.*, 1995).

localized disturbance and TS-wave simultaneously. The three sets of data were collected sequentially which gives the possibility to subtract the generated disturbances (puff and TS-wave), giving only the perturbation that is non-linearly induced (Fig. 6d).

It was found that both the puff and the TS-wave show a downstream decay of the amplitude when they were generated separately. However, when generated simultaneously, a strong amplification could be observed. At this stage the total disturbance is almost entirely dominated by the effects of the interaction, which gives its largest contributions inside the high and low speed streaks. At a later stage oblique waves were formed and a new streaky structure was generated.

An example of streak instability

A flow visualization experiment of a similar situation was made in the MTL wind tunnel in which a small roughness element was placed near the leading edge of the plate creating a laminar wake (low velocity streak) inside the flat plate boundary layer. When introducing TS-waves from a slot downstream of the roughness element it was clearly observed how breakdown occurred in the wake of the roughness element. The sensitivity to breakdown was largest for high frequency disturbances, which were highly damped waves.

Oblique transition

For incompressible flow three-dimensional TS-waves were for long considered to be of little importance, since Squire's theorem showed that such waves always are more stable than their 2D counterpart. However, non-linear interaction of small but finite amplitude oblique waves has recently been investigated numerically

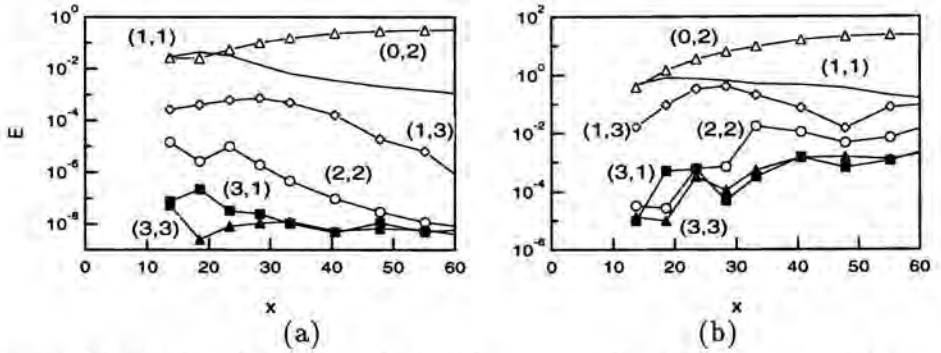

Figure 7: Evolution of various modes in oblique transition. E is the energy of the various modes and x is the downstream distance from the vibrating ribbon normalized with half channel width. a) low initial amplitude, b) high initial amplitude (from Elofsson & Alfredsson, 1995)

and experimentally and was found to give rise to rapid transition also in flows subcritical to linear disturbances. The transition scenario consists of the formation and transient growth of streamwise streaks of high and low velocity and the subsequent rapid growth of high frequency disturbances leading to breakdown.

Formation of streaky structures

Consider an initial disturbance consisting of two finite amplitude, oblique waves, which interact non-linearly to form longitudinal streaks. The TS-waves can be specified through their frequency and spanwise wave numbers $(\omega, \pm\beta)$ where ω is the angular frequency and $\pm\beta$ are the spanwise wave numbers. For non-linear interaction between the two waves, i.e. $(\omega, +\beta)$ and $(\omega, -\beta)$, the first interaction may result in the components (0,0), $(2\omega,0)$, $(2\omega, \pm 2\beta)$ and $(0, \pm 2\beta)$. The first corresponds to a mean flow distortion, the second to a travelling two-dimensional wave with the double frequency, the third corresponds to higher harmonic oblique travelling waves, whereas finally the fourth corresponds to a stationary, spanwise periodic disturbance. It was found by Schmid & Henningson (1992) that the highest energy growth was obtained in the $(0, \pm 2\beta)$ mode which corresponds to a streaky structure in the streamwise velocity. This was also found by Berlin, Lundbladh & Henningson (1994) in a numerical simulation of oblique interaction in a Blasius boundary layer.

In the experiments by Elofsson & Alfredsson (1995) with two oblique waves generated in a plane Poiseuille flow at a sub-critical Reynolds number it was shown that both low and high TS-wave amplitudes gave rise to a spanwise mean velocity structure of large amplitude. In the low amplitude case this structure is sustained far downstream of the ribbons despite a decay in the fundamental wave, and for the high amplitude both the mean velocity structure and the fundamental is growing downstream until a turbulent-like state is reached. Also,

in spectra obtained for the high amplitude a strong growth in higher harmonics can be observed which further downstream leads to a smooth distribution of the amplitude spectrum except for a peak at the fundamental frequency. Fig. 7 displays the streamwise evolution of energy in different (ω, β)-modes at $Re = U_{CL}h/\nu = 2000$ (where h is the half channel height) and with a wave angle of 45° at $y = 0.75$ for a low and high amplitude case (y is normalized with h and $y = 0$ is at the channel centreline). For the high amplitude case breakdown was observed but the behaviour of the $(0,2)$-mode was similar to the low amplitude case. The main difference was that also other modes were growing. Initially the $(0,2)$ and $(1,3)$ modes experienced the largest growth but further downstream the modes that were multiples of the fundamental frequency grew the most. In Fig. 7b the strong growth of the $(2,2)$, $(3,1)$ and $(3,3)$ modes can be observed but also higher modes have a large growth.

Streaky structures in flows affected by body forces

An interesting class of stability problems has its origin in body forces. Two types of body forces, common in engineering situations, are due to either streamline curvature (centrifugal forces) or system rotation (Coriolis forces). Such effects may be of importance in flows along curved surfaces and/or in rotating machinery. The primary instability in such flows is of a completely different character as compared to TS-waves, since for the primary disturbance the principle of "exchange of stabilities" is valid and the instability takes the form of stationary streamwise aligned roll cells.

A centrifugal instability will occur if there is an unbalance between the centrifugal force acting on fluid elements and the pressure gradient whereas a Coriolis instability occurs when there is an unbalance between the Coriolis force and the pressure gradient. For rotating channel flow two parameters are needed to characterise the stability of the flow, namely the Reynolds number and the rotation number ($Ro = 3\Omega h/U_{CL}$, where Ω is the system angular velocity). The linear stability theory gives, for $Ro = 0.5$, a critical Reynolds number which is almost two orders of magnitude smaller than that for which Tollmien-Schlichting waves become unstable.

Secondary instability of roll cells

For low enough Re it is found both experimentally and from numerical simulations that the primary instability saturates (usually after a slight overshoot in amplitude, see Bottaro *et al.*, 1991). The typical maximum amplitude of the streamwise disturbance velocity is around 50% of the undisturbed centreline velocity. For high Re, however, a secondary instability in the form of travelling wave disturbances develops which was first observed in flow visualization experiments by Alfredsson & Persson (1989). At least two different kinds of such secondary instabilities have been observed in experiments and simulations, one

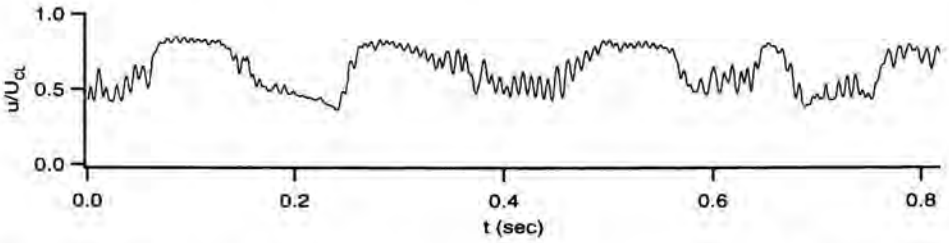

Figure 8: Naturally occuring secondary instability in curved channel flow. Re=4.4Re_{cr}. (Data from Matsson & Alfredsson, 1992)

with short (order of the channel width) and one with long (an order of magnitude larger than the channel width) streamwise wave length (see Fig. 8). Another instability which can be stationary or time dependent is merging and splitting of vortices. The occurrence of this latter instability is not restricted to high Re but depends on the initial wavelength of the primary instability.

It is clear that a primary instability induced by body forces is of quite different origin than the type of instabilities causing streaky structures in the cases discussed above. However the resulting streamwise velocity distribution has some similarities, as in both cases neighbouring regions of high and low velocity are dominating.

Matsubara & Alfredsson (1995) described experiments in a rotating channel and investigated wave type secondary instabilities where the secondary disturbance was introduced through two small holes, one at each side of a low velocity region. The forcing was either in phase or out of phase. It was clearly observed that the out of phase disturbance was the dominating one and that the disturbance maxima were in the regions of large spanwise gradients of the streamwise velocity (Fig. 9). The maximum amplification occurred at quite high frequencies and stability calculations based on the spanwise velocity distribution could fairly well depict the frequency of the instability as well as its phase velocity.

Breakdown of streaky structure - a unified scenario?

The examples of wall bounded shear flows described in this paper have all in common that streaky structures occur in the near wall region although they are formed in various ways. They are initially stable, but have in common that they can and often spontaneously will go through a wavy-type of secondary instability before breakdown to turbulence occurs. For boundary layers the possibility of transient growth seems to give a mechanism for subcritical growth, which favours the development of streaky structures. It is interesting to note that the deterministic free stream eddy did not increase in amplitude as it moved downstream, but in fact decayed. However this is not true for the disturbance energy: through its elongation there was initial growth before it started to decay. The

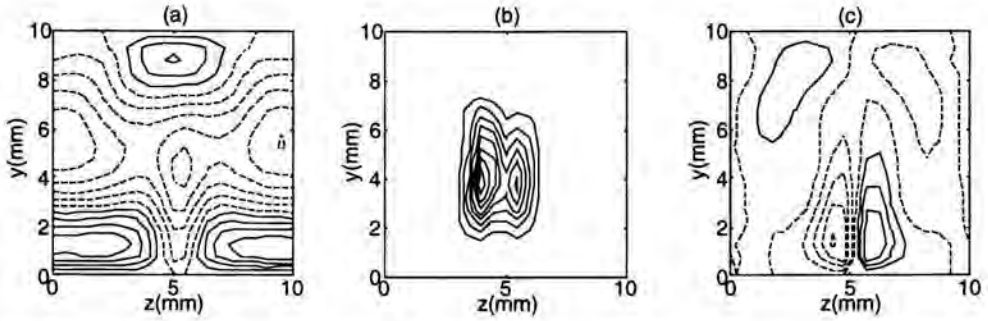

Figure 9: Secondary instability in rotating channel flow at Ro =0.026 and Re/Re_{cr} =2.4. a) mean streamwise velocity field, b) distribution of the fundamental disturbance (note that the two peaks are 180° out of phase), c) distribution of spanwise velocity gradient (see Matsubara & Alfredsson, 1995)

energy associated with the streaks stayed however at a constant level. Although a growth of the rms-amplitude is observed in the boundary layer with FST the mechanism for streak generation may still be the same. In the FST case the collective behaviour among streaks formed by different free stream eddies, can give rise to a meandering of the streaks which may result in an increasing rms-amplitude. For the FST case one should also remember that there is a continuous forcing by the free stream eddies. This forcing may also be the forcing required to trigger the secondary instability. In the case of interacting oblique waves the importance of algebraic growth is amply demonstrated, however breakdown is still through a mechanism related to high frequency secondary instability. Finally in the rotating channel case there is an exponential instability which gives rise to the streaky structures and the resulting flow field is again that of low and high velocity streaks (the streamwise vorticity is small) which is susceptible to secondary instabilities.

It has been suggested for flows with body forces that the instability is of inflectional type (Le Cunf & Bottaro, 1993). However, some experimental results presented above seem to indicate a similar instability also in other cases. For instance the effect of high frequency TS-waves on the 'puff', on the wake behind a small roughness element and on the breakdown in oblique transition all indicate that inflectional instabilities play a role. For the FST case a hypothesis is that FST causes the streaks in the boundary layer whereafter it acts as a forcing for the initiation of secondary instability on the streaks.

Acknowledgement

The experimental results described in this paper has been obtained over a period of several years in co-operation with Andrey Bakchinov, Andrey Boiko, Per Elofsson, Barbro Klingmann, Viktor Kozlov, John Matsson and Johan Westin. The enlightening numerical simulations as well as stimulating discussions with Stellan Berlin, Alessandro Bottaro and Dan Henningson are also acknowledged. The

support from The Swedish National Board for Industrial and Technical Development (NUTEK) and The Swedish Research Council for the Engineering Sciences (TFR) for various parts of this work as well as from The Göran Gustafsson Foundation, The Royal Swedish Academy of Sciences (KVA) and The Swedish Institute (SI) for support of visiting scientist is gratefully acknowledged.

References

Alfredsson, P.H. & Persson, H. 1989 – Instabilities in channel flow with system rotation. *J. Fluid Mech.* **202**, 543-557.

Bakchinov, A.A., Westin, K.J.A., Kozlov, V.V. & Alfredsson, P.H. 1995 – On the receptivity of a flat plate boundary layer to localized free stream disturbances. In *Laminar-Turbulent Transition* (ed. R. Kobayashi), pp. 341-348, Springer.

Berlin, S., Lundbladh, A. & Henningson, D.S. 1994 – Spatial simulations of oblique transition. *Phys. Fluids* **6**, 1949-1951.

Boiko, A.V., Westin, K.J.A., Klingmann, B.G.B., Kozlov. V.V. & Alfredsson, P.H. 1994 – Experiments in a boundary layer subjected to free stream turbulence. Part II: The role of TS-waves in the transition process. *J. Fluid Mech.* **281**, 219-245.

Bottaro, A., Matsson, O.J.E. & Alfredsson, P.H. 1991 – Numerical and experimental results for developing curved channel flow. *Phys. Fluids* A **3**, 1473-1476.

Butler, K.M. & Farrell, B.F. 1992 – Three-dimensional optimal perturbations in viscous shear flow. *Phys. Fluids* A **4**, 1637-1650.

Elder, J.W. 1962 – An experimental investigation of turbulent spots and breakdown to turbulence. *J. Fluid Mech.* **9**, 235-246.

Elofsson, P.A. & Alfredsson, P.H. 1995 – Experiments on nonlinear interaction between oblique Tollmien-Schlichting waves. In *Laminar-Turbulent Transition* (ed. R. Kobayashi), pp. 465-472, Springer.

Gaster, M. 1975 – A theoretical model of a wave packet in the boundary layer on a flat plate. *Proc. Roy. Soc. Lond.* A **347**, 271-289.

Grek, H.R., Kozlov, V.V. & Ramazanov, M.P. 1985 – Three types of disturbances from the point source in the boundary layer. In *Laminar-Turbulent Transition 2* (ed. V.V. Kozlov), pp. 267-272, Springer.

Gustavsson, L.H. 1991 – Energy growth of three-dimensional disturbances in plane Poiseuille flow. *J. Fluid Mech.* **224**, 241-260.

Le Cunff, C. & Bottaro, A. 1993 – Linear stability of shear profiles and relation to the secondary instability of the Dean flow. *Phys. Fluids* A **5**, 2161-2171.

Kachanov, Y.S. & Michalke, A. 1994 – Three-dimensional instability of flat-plate boundary layers: Theory and experiment. *Eur. J. Mech., B/Fluids* **13**, 401-422.

Klingmann, B.G.B. 1992 – On transition due to three-dimensional disturbances in plane Poiseuille flow. *J. Fluid Mech.* **240**, 167-195.

Landahl, M.T. 1980 – A note on algebraic instability of inviscid parallel shear flows. *J. Fluid Mech.* **98**, 243-251.

Matsson, O.J.E. & Alfredsson, P.H. 1992 – Experiments on instabilities in curved channel flow. *Phys. Fluids* A **4**, 1666-1676.

Matsubara, M. & Alfredsson, P.H. 1995 – Experiments on secondary instability of channel flow with body forces. In *Laminar-Turbulent Transition* (ed. R. Kobayashi), pp. 229-236, Springer.

Matsubara, M. & Alfredsson, P.H. 1995 – Free stream turbulence induced boundary layer transition. *APS-Bulletin* **40**, 12, 1956.

Reddy, S.C. & Henningson, D.S. 1993 – Energy growth in viscous channel flows. *J. Fluid Mech.* **252**, 209-238.

Schmid, P.J. & Henningson, D.S. 1992 – A new mechanism for rapid transition involving a pair of oblique waves. *Phys. Fluids* A **4**, 1986-1989.

Schubauer, G.B. & Skramstadt, H.F. 1947 – Laminar boundary layer oscillations and the stability of laminar flow. *J. Aero. Sci.* **14**, 69-78.

Westin, K.J.A., Boiko, A.V., Klingmann, B.G.B., Kozlov. V.V. & Alfredsson, P.H. 1994 – Experiments in a boundary layer subjected to free stream turbulence. Part I: Boundary layer structure and receptivity. *J. Fluid Mech.* **281**, 193-218.

Authors' address

Department of Mechanics
Royal Institute of Technology
S-100 44 Stockholm, Sweden

V.V. Kozlov & G.R. Grek

Effect of Riblets on Flow Structures at Laminar-Turbulent Transition

Abstract

This paper presents the results of an experimental study on the influence of riblets on various structures of the laminar-turbulent transition in the Blasius boundary layer in subsonic flow such as two-dimensional Tollmien-Schlichting waves and longitudinal vortex structures of the Görtler-like or cross flow-like vortices, Λ-vortices and vortices excited in the wake behind a roughness. It is shown that triangular riblet profiles mounted in the direction of the flow result in an unfavourable influence on the development of two-dimensional Tollmien-Schlichting waves. On the other hand, riblets were also found to significantly affect the development of nonlinear wave packets (Λ-vortices) giving a slower growth of their intensity and delaying their transformation into the turbulent spots. The effect of riblets on the development of a crossflow-like single vortex and Görtler-like vortices lead up to reduction of their intensity, resulting in slow damping of the secondary travelling waves and the flow remains laminar throughout the studied region. The riblets inhibit the transition to turbulence in the wake behind a roughness.

Introduction

So far many studies on riblets were carried out in the turbulent boundary layer, where riblets can cause drag reduction. Some of the earliest and more important results were obtained by Walsh (1979, 1983, 1984). He showed that drag reduction could be obtained when the height of the riblet structure expressed in wall units $s^+ = su^*/\nu$ is below 30; the maximum reduction of 7-8% occurred when s^+ is about 15. One of the possible concepts for the drag reduction mechanism by means of riblets is that it is due to changes in the near-wall coherent structures as presented, particularly, by Bacher & Smith (1985), Bechert *et al.* (1989) and Choi (1989). These studies demonstrated the importance of preventing cross-flow by using longitudinal ribs, leading to drag reduction. The coherent structures of the turbulent boundary layer are similar to the vortex-structures of the transition region and an experimental study in a laminar boundary layer by Smith *et al.* (1989) showed that this method is very promising for understanding the influence of riblets on coherent structures in the turbulent boundary layer.

Studies on the influence of riblets on laminar-turbulent transition were presented only in a few papers and the conclusions are sufficiently contradictory to justify a more detailed investigation. Belov *et al.* (1990) did not find a

favourable influence of the riblets on the laminar-turbulent transition independent of whether the riblets were located along or across the main flow. It should be noted that riblets in this case were placed on the entire surface of the flat plate, where the transition takes place. The work by Kozlov *et al.* (1990) demonstrated that longitudinal grooves on a test plate surface result in a positive or negative influence on by-pass transition due to high free stream turbulence ($Tu = 1.5-3\%$) depending on the pressure gradient or leading edge shape of their test plate. In experimental investigations carried out by Neumann & Dinkelacker (1991) it was found that riblets delay the development of initial turbulent structures in the transitional zone of flow on the body of revolution. Numerical simulations by Chu *et al.* (1992) showed, that in comparison with the smooth surface in the transitional regime there is drag reduction by means of riblets. The basic conclusions of the calculations by Luchini (1993) are that grooving has a destabilizing effect upon Tollmien-Schlichting instability but a stabilizing effect on the Taylor-Görtler instability. The contradictory nature of these studies seems to be connected with paying too little attention to the type of disturbances and to the different stages leading to the so-called "natural" laminar-turbulent transition. Thus, the main purpose of this paper is to study the influence of riblets on the development of Tollmien-Schlichting (TS) waves at linear (*i.e.* two-dimensional TS waves) and nonlinear (i.e. Λ-structures) stages of transition. The effect of riblets on the disturbances of other types of transition such as Görtler-like or cross flow-like flows and flow in the wake behind a roughness were also studied.

The experiments were performed in the low turbulence ($Tu \leq 0.04\%$) wind tunnel on a flat plate and swept wing at free-stream velocities (U_∞) from 5.4 to 9 m/s, depending on the type of experiment. The disturbances were artificially excited and hence, measurements were carried out under controlled conditions. The rubber or steel disk with 160 mm diameter (riblet plate number 1) and the plastic riblet plate, being 285 mm long and 285 mm wide (riblet plate number 2) were mounted on the surface and used in the experiments for the flat plate. Riblet plate 1 (rubber disk) was used also in the experiment on the swept wing. A symmetrical triangular shape of the riblets was chosen. The riblet height and spacing were optimized in preliminary investigations by Grek, Kozlov & Titarenko (1996) with respect to the influence of these sizes on the development of the Λ-vortex. The height and spacing were varied from 0.3 mm to 3 mm and from 0.5 mm to 3 mm for plates 1 and 2 respectively, but the favourable influence on the Λ-vortex behaviour was found only for the height ranging from 0.7 mm to 1.2 mm and for the spacing ranging from 1.0 mm to 1.5 mm. The riblet lateral spacing was normalized by "outer" (δ^*) and "inner" (ν and u^*) variables. Here δ^* is the displacement thickness and ν is kinematic viscosity. The non-dimensional lateral spacing is $s^+ = su^*/\nu$, where $u^* = \sqrt{\nu\,|\partial u/\partial y|_{y=0}}$ is the laminar friction velocity and $|\partial u/\partial y|_{y=0} = 0.332U_\infty/\delta$ is the mean velocity gradient on the wall , where $\delta \sim \sqrt{\nu X/U_\infty}$. In the range of Re_x considered, the non-dimensional lateral spacing and height normalized by "inner" variables are $26 \geq s_1^+ \sim h_1^+ \geq 17$ ($17 \geq s_2^+ \sim h_2^+ \geq 11$) and normalized by "outer" variables (s/δ^* and h/δ^*) are $1.4 \geq (s/\delta^*)_1 \sim (h/\delta^*)_1 \geq 0.8$ ($1.0 \geq (s/\delta^*)_2 \sim (h/\delta^*)_2 \geq$

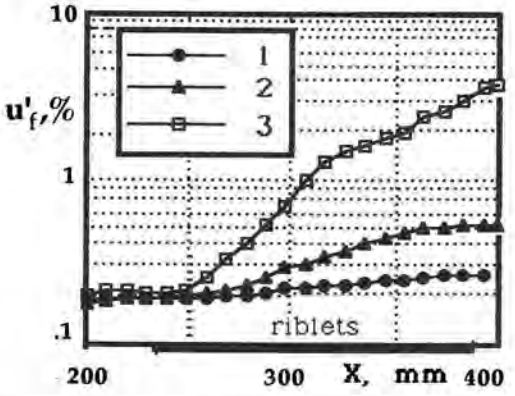

Figure 1: Amplification curves of the T-S waves on the smooth surface (1), riblets located across (2) and along (3) the main flow, $Y = Y(u'_{max})$, $Z = 0$ mm.

0.5) for riblet plates number 1 and 2, respectively. Hot wire anemometry of constant temperature was used to measure the longitudinal components of the mean velocity ($\bar{u}$) and the fluctuations (u') with respect to the axes X, Y, Z, which denote the streamwise, normal and the spanwise directions, respectively. Note that R.M.S.-values u'_f of the velocity fluctuations are measured for the narrow frequency band ($\Delta f = 4$ Hz) of the fundamental TS wave frequency ($F = 102$ Hz). The values for u' (summarized for all velocity fluctuations) are measured for the broad-band frequency.

Effects on the linear development of forced Tollmien-Schlichting waves

Riblet plate 1 ($s^+ \sim h^+ = 17-26$; $h/\delta^* = 0.8-1.4$) was used in this experiment. It is seen from Fig. 1 that locating the riblets in the main flow direction leads to a considerable amplification rates of the TS waves in comparison with their development at the smooth surface. Locating the riblets perpendicular to the main flow lead to smaller amplification rate of the TS waves in comparison with their development if the riblets are located in the main flow direction. Observations by Dinkelacker *et al.* (1987) showed that some sharks have smooth scales close to the stagnation lines where the flow can be expected to be laminar or transitional and ribbed scales elsewhere. This fact is in excellent agreement with the present findings.

Effect on the development of Λ-vortices on ribbed surfaces

The behaviour of the Λ-vortices measured at the plane of symmetry at $X = 370$ mm on the smooth and riblet surfaces is presented in Fig. 2. The ensemble averaged 20 events amplitude spectra show a favourable influence of the riblet located along the flow and an unfavourable influence of the riblet located across the flow.

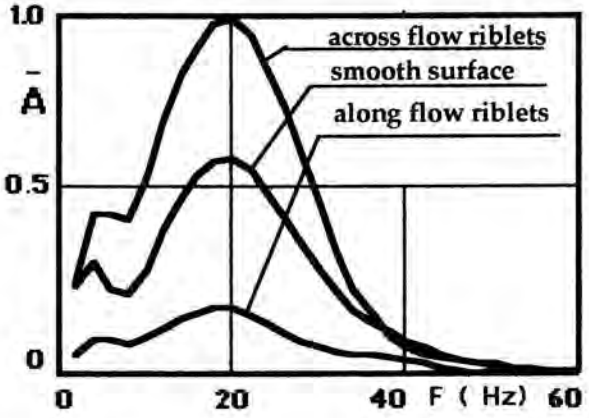

Figure 2: The ensemble averaged amplitudes spectra measured in the plane of symmetry of the Λ-vortices at $X = 370$ mm, $Y = Y(u'_{\max})$.

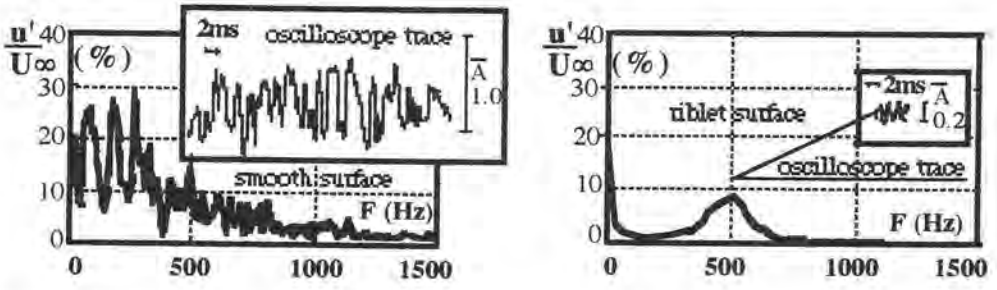

Figure 3: Power spectra and oscilloscope traces of the disturbance development measured in the plane of symmetry of the vortex street behind a single roughness element on both the smooth and ribbed surfaces at $X = 420$ mm, $Y = 0.5$ mm.

The detailed measurements of the Λ-vortex characteristics performed by Grek *et al.* (1995) showed that the behaviour of the disturbances on the riblet surface remains deterministic, while the disturbances on the smooth surface include the high frequency fluctuations of the beginning turbulent spot. The height of the Λ-vortex above the riblet surface is almost twice as small as that found above the smooth surface.

Effect of riblets on the vortices in a wake behind a single roughness element

The experimental results of the effect of riblets on the vortex development in the wake behind a single roughness element (a small cylinder) in the laminar boundary layer on a flat plate are presented in the work by Grek, Kozlov & Titarenko (1996). This investigation showed that the riblet can substantially affect the way in which vortices develop in the wake behind a single roughness element (so

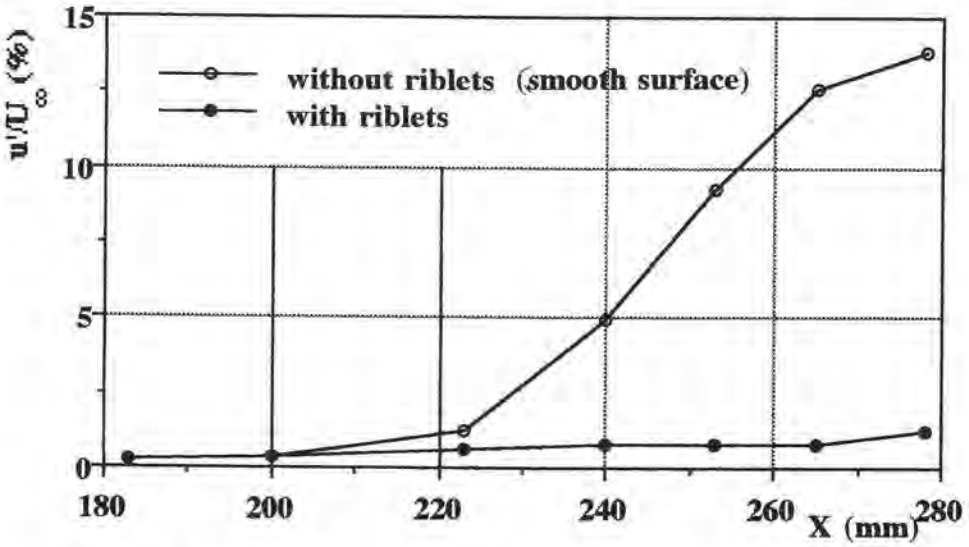

Figure 4: Influence of riblets on the amplification of disturbances.

called "vortex-street"). A triangular riblet located in the flow direction approximately halved the height and span of the vortex street compared to the smooth surface of the flat plate. Furthermore, the riblet made the flow inside the vortex street more steady, resulting in delay of the turbulence, see Fig. 3. According to the hot-wire measurements, this large influence of riblets on the vortex street was related to changes in the inner vortex structure.

Influence of riblets on a swept wing boundary layer with embedded cross flow-like vortex

The influence of riblets on the transition in a single stationary, artificially generated, vortex in a swept wing boundary layer was investigated by Boiko *et al.* (1995). It was found that placing the riblets directed along the vortex results in a significant prolongation of the laminar regime. The comparison is presented in Fig. 4. Beginning from $x = 223$ mm the disturbances on the smooth surface grow rapidly leading to turbulence whereas on the riblets surface their amplitude level is almost unchanged and the flow is laminar.

Influence of riblets on a boundary layer with embedded streamwise Görtler-like vortices

Laminar-turbulent transition in boundary layers is in many instances caused by the breakdown of longitudinal streak or vortex structures, such as Görtler vortices, crossflow vortices, or vortices caused by roughness elements or free stream disturbances. An important factor which promotes this mechanism is the

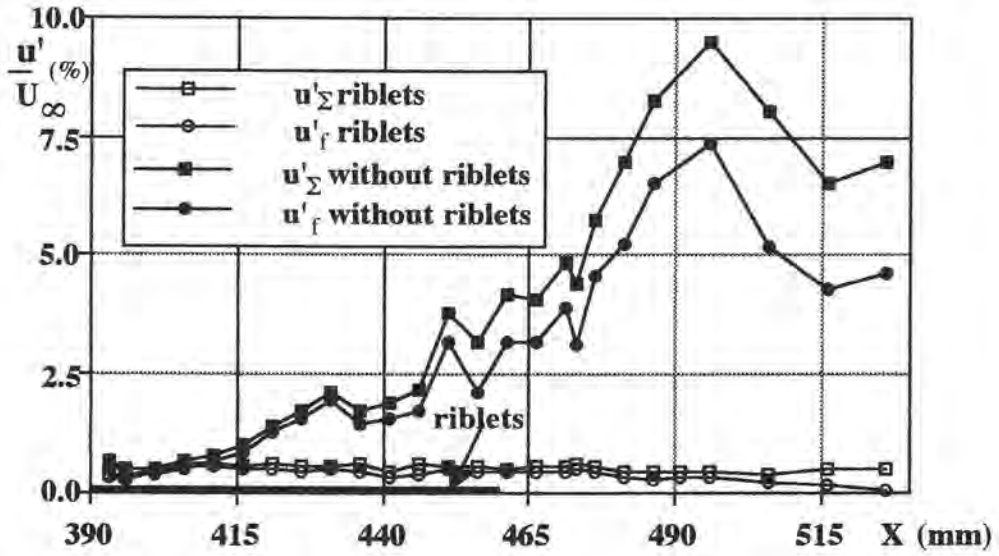

Figure 5: Downstream development of the disturbances of streamwise vortices, measured both in the narrow (u'_f) and in the broad (u'_Σ) frequency bands, at $Z = 17$ mm, $Y = Y(u'_{max})$.

strength of the spanwise mean velocity in the boundary layer, *i.e.* the normal vorticity. A recent experimental study by Bakchinov *et al.* (1995) shows that such flows are unstable with respect to high frequency travelling waves, which can cause rapid transition. Available experimental results on this subject are reviewed in their paper. The study described by Grek *et al.* (1996), shows hat surface manipulation makes it possible to suppress longitudinal vortex structures in a boundary layer, and thereby stabilize it with respect to high frequency travelling waves, and delay the transition to turbulence (see Fig. 5). The results can be of interest for the control of transition in crossflow and Görtler flow.

Conclusion

The present study has shown that the effect of riblets mounted in the direction of the flow is the suppression of longitudinal vortex structures in a boundary layer, such as Λ-vortices in the nonlinear stage of transition, vortices caused by roughness elements and Görtler-like or cross flow-like vortices. On the other hand, the same riblets promote the growth of the two-dimensional T-S waves and the effect is that the boundary layer flow is destabilized. Hence when transition is initiated by TS waves, riblets can be used as means of control for only the later stages of transition.

Acknowledgements

The present work has been supported by the Russian Basic Science Foundation under Grants No. 93-01-17359 and No. 96-01-01892.

References

Bacher, E.V. & Smith, C.R. 1985 – A combined visualization-anemometry study of the turbulent drag reduction mechanisms of triangular micro-groove surface modification. *AIAA* Paper 85-0548.

Bechert, D.W., Bartenwerfer M. & Hoppe, G. 1989 – The viscous flow on surfaces with longitudinal ribs. *J. Fluid Mech.* **206**, 105-129.

Bakchinov, A.A., Grek, G.R., Klingmann, B.G.B. & Kozlov, V.V. 1995 – Transition experiments in a boundary layer with embedded streamwise vortices. *Phys. Fluids.* **7** , 820-832.

Belov, I.A., Enutin G.V. & Litvinov V.N. 1990 – Influence of a plate streamwise and spanwise ribbed surface on the laminar-turbulent transition. *Uch. Zap. TsAGI* **17**, 10. 7-111 (In Russian; English translation in: Fluid Mechanics - Soviet Research).

Boiko, A.V., Kozlov, V.V., Syzrantsev, V.V. & Scherbakov, V.A. 1995 – Experimental study of secondary instability and breakdown in a swept wing boundary layer. IUTAM Symposium, Sendai/Japan (Ed. R. Kobayashi), pp. 289-295, Springer- Verlag Berlin Heidelberg

Choi, K.-S. 1989 – Drag reduction mechanisms and near-wall turbulence structure with riblets. IUTAM Symposium, Zurich (Ed. A.Gyr), pp. 553-560, Springer Berlin Heidelberg

Chu D., Henderson, R. & Karniad kis, G.E. 1992 – Parallel spectral- element-Fourier Simulation of turbulent flow over riblet-mounted surfaces. *Theoret. Comput. Fluid Dynamics* **3**, 219-229.

Dinkelacker, A., Nitschke-Kowsky, P. & Reif W.-E. 1987 – On the possibility of drag reduction with the help of longitudinal ridges in the walls. IUTAM Symposium, Bangalore (Eds. H.W. Liepmann & R. Narasimha), pp. 109-120, Springer-Verlag Berlin, Heidelberg

Grek, G.R., Kozlov, V.V., Klingmann, B.G.B. & Titarenko, S.V. 1995 – The influence of riblets on boundary layer with embedded streamwise vortices. *Phys. Fluids* **7**, Brief Communications, 2504-2506.

Grek, G.R., Kozlov, V.V. & Titarenko, S.V., 1996 – Effects of riblets on vortex development in the wake behind a single roughness element in the laminar boundary layer on a flat plate. La Recherche Aerospatiale.

Grek, G.R., Kozlov, V.V. & Titarenko, S.V. 1996 – An experimental study on the influence of riblets on transition. To appear in *J. Fluid Mech.*

Kozlov, V.F., Kusnetsov V.R., Mineev B.I. & Secundov, A.N. 1990 – The influence of free stream turbulence and surface ribbing on the characteristics of a transitional boundary layer. Proc. Int. Sem. Ser. Near Wall Turbulence, Dubrovnik.

Luchini, P. 1993 – Effects of riblets upon transition. Abstract at 8th Drag Reduction Meeting, September 23-24, 1993. Lausanne.

Neumann, D. & Dinkelacker, A. 1991 – Drag measurements on V-grooved surfaces on a body of revolution in axial flow. *Appl. Sci. Res.* **48**, 105-114.

Smith, C.R., Walker, J.D., Haidary A.H. & Taylor, B.K. 1989 – Hairpin vortices in a turbulent boundary layer: the implication for reducing surface drag. IUTAM symposium, Zurich (Ed. A. Gyr), pp. 51-58, Springer-Verlag Berlin, Heidelberg.

Walsh, M.S. 1979 – Drag characteristics of V-groove and transverse curvature riblets. In "Viscous flow and drag reduction", Progress in Astronautics and Aeronautics, (Ed. G.R. Hough), Volume 72, presented at the AIAA Symposium on Viscous Drag Reduction, Dallas, Texas, November.

Walsh, M. S. 1983 – Riblets as a viscous drag reduction technique, *AIAA J.* **21**, 485.

Walsh, M.S. & Linderman, A.M. 1984 – Optimization and application of riblets for turbulent drag reduction , AIAA Paper 84-0347, presented at the 22nd AIAA Aerospace Science Meeting, Reno, Nevada, January.

Authors' address

Russian Academy of Sciences, Siberian Branch,
Inst. Theoretical and Applied Mechanics
630090, Novosibirsk, Russia

E. Laurien

Direct Simulation of the Development of a Local Finite Amplitude Disturbance in a Compressible Boundary Layer

Abstract

The development of a local disturbance consisting of two pairs of counter-rotating vortices within a boundary layer is investigated numerically. As a model problem parallel flow along a flat surface with prescribed velocity and temperature profiles is studied. After a transient phase the disturbance is damped when the initial amplitude is small and amplified when the initial amplitude is finite. In the amplified case the initially large vortices move closer to each other, become smaller, and form a compact structure with larger gradients as compared to the damped case. The vortices are stretched in downstream direction and wind around each other. These mechanisms are interpreted in the context of the first stages of a possible bypass transition mechanism.

Introduction

The understanding and modelling of laminar-turbulent transition initiated by local finite amplitude disturbances (bypass transition) in compressible boundary layers is essential for the development of improved transition prediction methods, e.g. for boundary layers on turbomachine blades, where bypass-transition is dominant (Mayle, 1991). Within this framework the present research is concerned with the direct numerical simulation of the development of a generic disturbance present in a model boundary layer in order to predict amplitude-dependent (i.e. nonlinear) amplification for any given base flow and disturbance. Our method could later be combined with empirical or theoretical models of boundary-layer receptivity to study and maybe even predict bypass transition in boundary layers for a given disturbance environment.

Because a finite disturbance amplitude is necessary to initiate turbulent spot formation, we focus our interest on the comparison of two simulations with the same physical parameters and disturbance shapes but different initial amplitudes. In the first case the amplitude is low and the nonlinear amplification may be absent. In the second case the initial amplitude is large, as in a boundary layer with high free-stream turbulence level. Nonlinear amplification is expected to occur in the second case, eventually leading to a turbulent spot. In the present paper the ability of our numerical simulation method, which is similar to that of Henningson *et al.* (1993) but for compressible flow, to describe nonlinear amplification

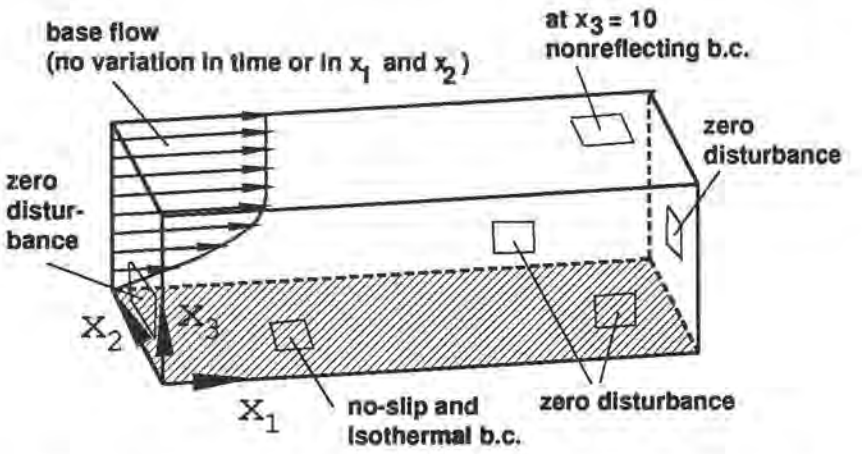

Figure 1: Integration domain, coordinate system and boundary conditions.

is investigated. A possible physical mechanism leading to amplitude-dependent amplification is identified.

Integration domain and numerical method

In the simulation, the blade surface having very little curvature in the transition zone, is approximated as plane. Furthermore the parallel flow assumption is employed, neglecting the effects of the boundary-layer growth. The nondimensional coordinates x_1, x_2, and x_3, see Fig. 1, have been normalized with the local boundary-layer thickness $\delta \approx 0.01\,c$, with c being the chord length.

Beginning with an initial flow field, which consists of a given boundary-layer profile (base flow) and a superposed disturbance, the three-dimensional compressible Navier-Stokes equations are integrated in time. At the surface $x_3 = 0$ no slip and isothermal boundary conditions and at $x_3 = 10$ non-reflecting characteristic boundary conditions are employed for the disturbances. The lateral boundary conditions are imposed by periodicity.

A spectral-finite-difference method (Laurien & Delfs, 1994), based on Fourier expansions in x_1- and x_2-directions and on sixth order compact differences in x_3-direction, is used. All flow quantities are required to vanish at one streamwise and one spanwise station (preferably but not necessarily at $x_1 = 0, L_1$ and $x_2 = 0, L_2$). With $L_1 = 10$ and $L_2 = 5$ the domain is large enough to satisfy this boundary condition in an approximative manner up to the particular stage of development considered here. In order to keep the base flow stationary any unrealistic temporal development of the flow averaged in both horizontal directions over the entire integration domain (base flow, mode 0,0) is suppressed. The temporally averaged flow (mean flow) may change due to nonlinear interactions.

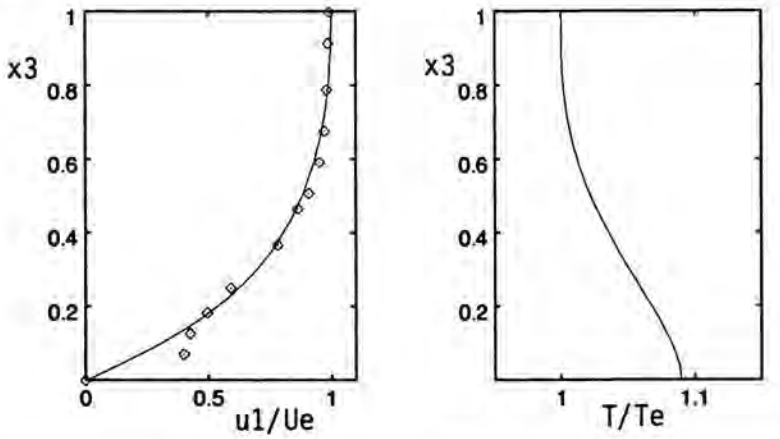

Figure 2: Velocity and temperature profiles of the base flow : measured data of Hoheisel 1990 (◇) and curve fit used in the simulation (—).

Base flow and initial disturbance

As the base flow, see Fig. 2, the velocity profile of an accelerated boundary layer with adiabatic wall is considered. Although it is not intended to make any comparison of simulation results with experiments in this paper, we have derived the base flow from experimental data using curve fits. This is done in order to ensure, that the nonlinear amplification mechanisms to be investigated is present in this flow. We chose an experimental test case relevant for subsonic turbine cascades (Hoheisel, 1990) at a chordwise position $x/c = 0.65$ and a free-stream turbulence level $Tu_1 = 7.1\%$ (Tu has an influence on the velocity profile at $x/c = 0.65$). This position is close to transition onset as determined from the measured boundary layer shape factors (2.2 here). With the reference quantities δ, U_e and T_e (velocity and temperature at the boundary layer edge), the Reynolds number is $Re_\delta = 5800$ and the Mach number is $M_e = 0.65$.

The initial disturbance is chosen similarly to a distribution used by Henningson *et al.* (1993). This disturbance has been chosen in order to establish a reference case for later investigation of other initial disturbances. All quantities are multiplied by a free amplitude parameter A. The disturbance centre is located at $x_1 = 0.15\,L_1$ and $x_2 = 0.5\,L_2$; see the areas of upward or downward motion in Fig. 3. The disturbance consists of two pairs of counter-rotating vortices, see Fig. 4.

Simulation results

The low amplitude case $A = 0.005$ has been simulated using a numerical resolution of $32^2 \times 76$ points and a time step width of $\Delta t = 0.25$ (nondimensionalized by u_e and δ). In the large amplitude case the initial disturbance is chosen two

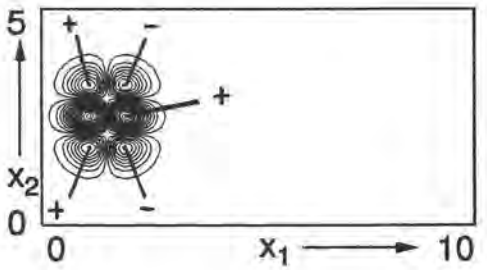

Figure 3: Initial disturbance, contour lines of the normal velocity u_3 in a plane $x_3 \approx 0.4$, line spacing is $A/20$.

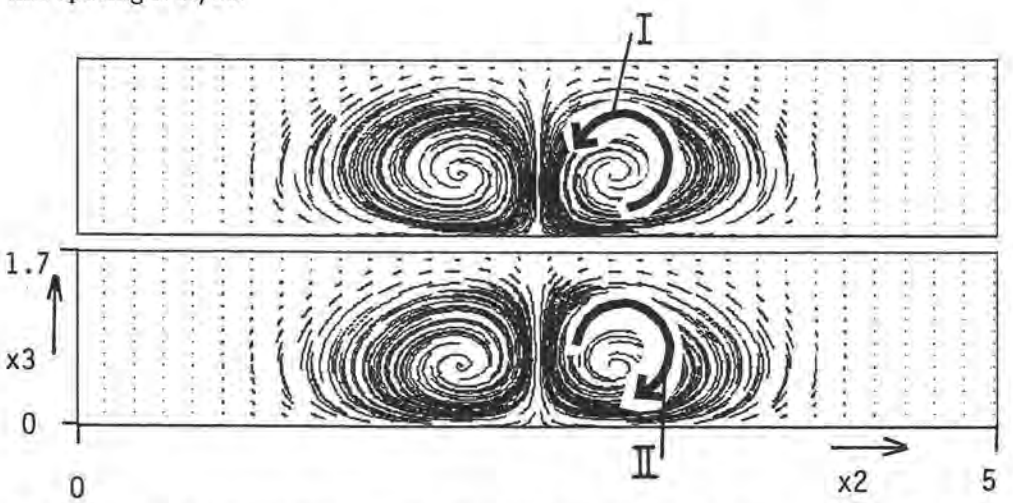

Figure 4: Initial disturbance, projections of streamlines on the x_2-x_3-plane at $x_1 = 1$ (top) and $x_1 = 2$ (bottom). The disturbance is three-dimensional.

orders of magnitude larger, namely $A = 0.5$ and the resolution is $32 \times 64 \times 76$, $\Delta t = 0.125$. The development of the maximum normal velocity u_3/A in the integration domain is compared in the following table:

A	$t = 0$	1	2	3	4	5	6	7	8
0.005	.180	.129	.123	.106	.086	.071	.056	.048	.038
0.5	.180	.132	.129	.112	.099	.091	.104	.138	.176

The low amplitude case is damped up to $t = 8$, whereas the large amplitude case becomes amplified for $t > 5$. The development for $t < 5$ may be interpreted as an initial transient.

The normal velocity distributions in a wall-parallel plane, see Figs 5 and 7, indicate, that the flow structures are stretched in streamwise direction while travelling downstream. In the low amplitude case, Fig. 5, the distribution is very smooth with small gradients; the structure spreads out and seems to be

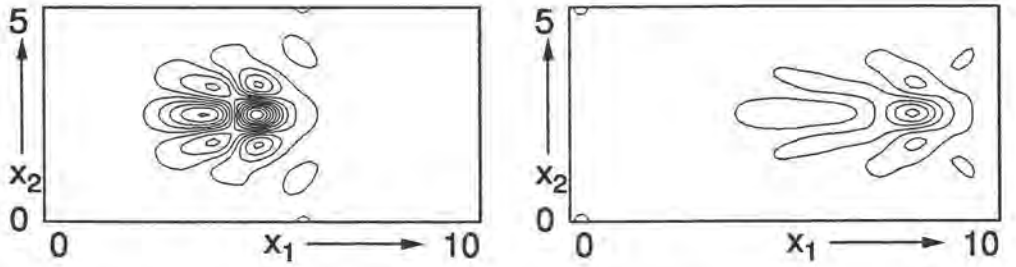

Figure 5: Low amplitude case: contour lines of the normal velocity in a plane $x_3 \approx 0.4$ at $t = 4$ (left) and $t = 8$ (right), line spacing is 2.5×10^{-4}.

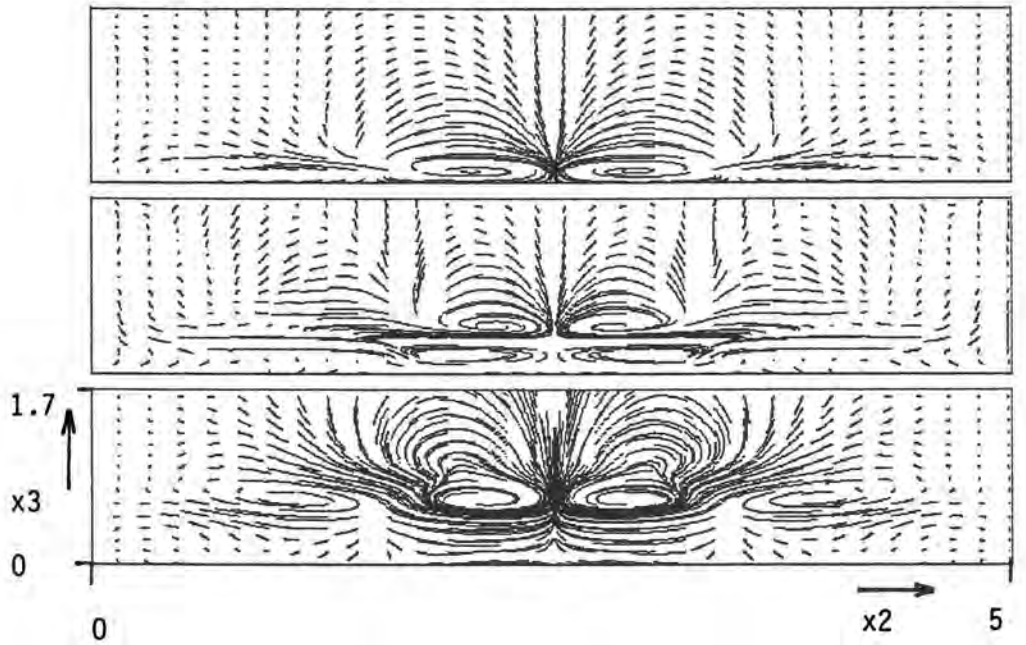

Figure 6: Low amplitude case: projections of streamlines on x_2-x_3-plane at $x_1 = 4, 6, 8$ (top to bottom).

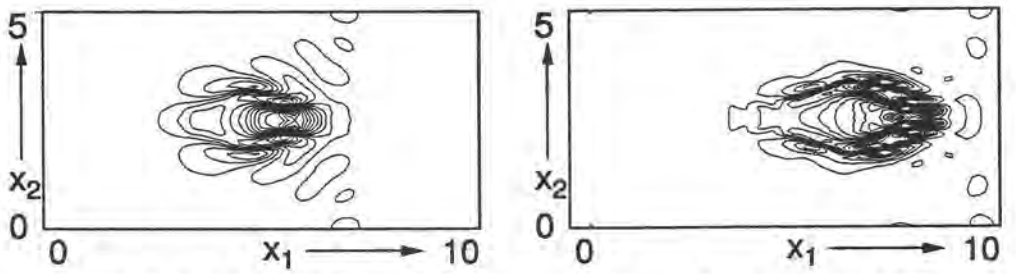

Figure 7: Same as Fig. 5 for the finite amplitude case, line spacing is 0.025.

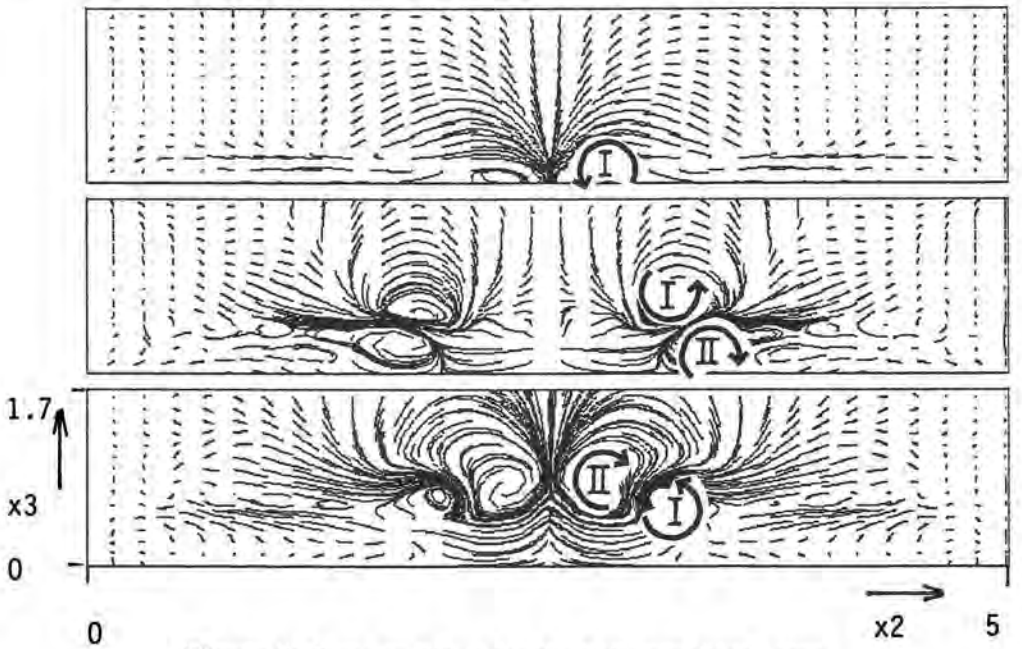

Figure 8: Same as Fig. 6 for the finite amplitude case.

dissipated. In contrast to this, in the large amplitude case, Fig. 7, steep gradients in x_2-direction develop and the spreading is much less pronounced. Since the amplitude A is the only parameter different in the two cases this development must be due to the nonlinearity of the governing equations.

The instantaneous velocity field represented by streamlines starting and projected on planes $x_1 = const.$ at $t = 8$ is shown in Figs 6 and 8 for the two cases. The visualization technique used is helpful to understand the structure of the velocity field by identification of the vortex centres (we are aware that the centre positions depend on the choice of the projection plane, the term vortex is used here for the particular structure observed). In the nonlinear case the vortices are smaller with their centres closer together than in the linear case. A detailed investigation of the position of two vortices I and II suggests that the nonlinear structure consists of a system of two counter-rotating vortices winding around each other. There seems to be little difference between our observation and the corresponding mechanism in incompressible flow as described by Henningson *et al.* (1993). When the simulation is continued with much higher numerical resolution it is expected, that the disturbance will finally lead to a turbulent spot.

Conclusion

Our numerical method is able to describe amplitude-dependent amplification or damping as expected. It has been shown, that the physical mechanisms observed in the development of the streamwise stretched disturbance can be described

with nonlinear vortex interaction. These mechanisms, previously described by Henningson *et al.* (1993) for incompressible channel and boundary layer flows, seem to be relevant in compressible boundary layers as well. Our visualizations give further insight into the velocity field of the developing flow structures.

This investigation considers a model problem and must be regarded as a strong simplification of the real problem (transition in turbo-engines). It should not be interpreted as a practical transition prediction method in its earliest stage.

References

Henningson, D.S., Lundbladh, A. & Johansson, A.V. 1993 – A mechanism for bypass transition in wall-bounded shear flows, *J. Fluid Mech.* **250**, 169-207.

Hoheisel, H. 1990 – V.6 Test case E/CA-6, subsonic turbine cascade, in: L. Fottner (ed.):*Test cases for computation of internal flows in aero-engine components*, AGARD-AR-275, 112-123.

Laurien, E. & Delfs, J. 1994 – Direct simulation of turbulence phenomena in compressible boundary layers, in: R. Voke, L. Kleiser & J.P. Chollet (eds.): *Direct and Large-Eddy Simulation I*, Kluwer Academic Publishers, 347-358.

Mayle, R.E. 1991 – The role of laminar-turbulent transition in gas turbine engines, *J. of Turbomachinery* **113**, 509-537.

Author's address

Institute for Fluid Mechanics
Technical University of Braunschweig
Bienroder Weg 3
D-38106 Braunschweig, Germany

Thomas C. Corke° & Osamah M. Haddad▷

Receptivity to Sound on a Parabolic Leading Edge

Abstract

The receptivity of the boundary layer over slender parabolic bodies subject to a free-stream sound disturbance is investigated. For this study, the full incompressible Navier-Stokes (N-S) equations, in stream function and vorticity variables, were solved numerically. A novel formulation was used which allowed the unsteady N-S equations to be converted into two steady systems of equations describing the basic flow and its disturbance field. The solutions for the two flow fields agreed well with those found in the literature. The leading-edge receptivity was found to increase as the leading edge nose radius decreased, reaching a maximum for the infinitely thin flat plate.

Introduction

The term "receptivity" was first introduced by Morkovin (1969) to characterize the relation between disturbances outside the steady laminar boundary layer, and the internalized disturbances that may be amplified according to stability theory. Our knowledge of the physics of this process is important because it represents the first stage in the development of growing disturbances which lead to turbulence. Our understanding of the receptivity process has largely come from asymptotic theories. The earliest of these were by Goldstein (1983, 1985). Although these set the framework, they referred to infinite flat plates without a leading edge.

Murdock (1980, 1981) used a numerical approach to study the receptivity over an infinitely thin flat plate and parabolic cylinders. For both cases, Murdock modeled the receptivity by the parabolized form of the N-S equations. More recently Hammerton & Kerschen (1992) have considered an asymptotic approach for a parabolic leading edge. Presently, there are no other analytical solutions or physical experiments to which these results can be checked.

One of the earliest physical experiments on leading-edge receptivity was for a sharp flat plate by Shapiro (1977). More recently an elliptic leading edge joined to a flat plate was used in the experiments by Saric & Rasmussen (1992) and Saric, Wei & Rasmussen (1994). Lin, Reed & Saric (1990) performed a full Navier-Stokes calculation to model those elliptic leading edge experiments. Their numerical results are not complete from the point that it is difficult to distinguish between receptivity produced by the leading edge, or produced at the

joint between the ellipse and flat plate. Also, it is impossible in their geometry to separate the effects of curvature and pressure gradient on receptivity.

The parabolic geometry has the advantage of having a constant curvature. For a zero angle of attack, the pressure gradient is everywhere favourable. The pressure gradient however can be changed by placing the body at an angle of attack. In terms of the basic flow, at 0° angle of attack, Davis (1972) has already formulated the numerical method. In this, he introduced a change in variables which removes the singularity in the vorticity that occurs in the limit as the body approaches a sharp infinitely thin plate. We follow a similar approach here in terms of both the basic flow and perturbation solutions.

Physical problem

Here, we consider the 2-D laminar incompressible flow of a constant-property fluid over a parabolic body. The equation of the surface of the parabolic-body is given by

$$x(y) = \frac{1}{2R}(y^2 - R^2), \tag{1}$$

where R is recognized as the nose radius of curvature of the parabola[1].

Governing equations

The governing equations are the 2-D N-S equations in stream function (ψ) and vorticity (ω) form. These are made dimensionless and converted into parabolic coordinates (ξ, η). In order to be able to solve for the flow over a flat plate (which is equivalent to the flow over a parabola in the limit as the nose radius of curvature goes to zero) including the leading-edge, it is necessary to remove the singularity at the leading-edge. To do so, we follow Davis (1972) and introduce the new variables f and g which are related to ψ and ω by

$$\psi = \xi f(\xi, \eta, t) \qquad \omega = -\frac{\xi}{(\xi^2 + \eta^2)} g(\xi, \eta, t). \tag{2}$$

The new dependent variables are then governed by the equations,

$$f_{\eta\eta} - g + f_{\xi\xi} + \frac{2}{\xi} f_\xi = 0 \tag{3}$$

$$g_{\eta\eta} + \left(f + \xi f_\xi - \frac{4\eta}{\xi^2 + \eta^2}\right) g_\eta + \left(\frac{\xi^2 - \eta^2}{\xi^2 + \eta^2} f_\eta - \frac{2\eta}{\xi^2 + \eta^2}(f + \xi f_\xi)\right) g -$$

[1] note that R in the dimensional form is the nose radius of curvature, but when nondimensionalized, it is the Reynolds number based on the nose radius.

$$\xi g_\xi \left(f_\eta + \frac{4}{\xi^2 + \eta^2} \right) - \left(\xi^2 + \eta^2 \right) g_t + g_{\xi\xi} + \frac{2}{\xi} g_\xi = 0. \tag{4}$$

This is the final form of the governing equations. We note that they are coupled and non-linear.

To investigate the leading-edge receptivity to freestream sound waves, we consider the freestream to be composed of the uniform flow in x-direction with a superposed uniform small oscillation of temporal frequency σ and amplitude ϵ,

$$\psi_\infty = \left(1 + \epsilon e^{i\sigma t} \right) \xi\eta, \tag{5}$$

where ϵ is sufficiently small for linearization. We then decompose the unsteady flow field into a steady basic state plus unsteady perturbation (in normal mode form), according to

$$f(\xi, \eta, t) = F(\xi, \eta) + \epsilon e^{i\sigma t} \tilde{f}(\xi, \eta) \tag{6}$$

$$g(\xi, \eta, t) = G(\xi, \eta) + \epsilon e^{i\sigma t} \tilde{g}(\xi, \eta). \tag{7}$$

Substituting the above equations (6 & 7) back into the governing equations (3 & 4) as well as the boundary conditions and then equating terms of equal powers in ϵ on both sides of each equation leads us to the governing equations of both the basic and perturbation flow fields.

The basic flow (zero-order terms in ϵ) is governed by the following equations,

$$F_{\eta\eta} - G + F_{\xi\xi} + \frac{2}{\xi} F_\xi = 0 \tag{8}$$

$$G_{\eta\eta} + \left[F + \xi F_\xi - \frac{4\eta}{\xi^2 + \eta^2} \right] G_\eta + \left[\frac{\xi^2 - \eta^2}{\xi^2 + \eta^2} F_\eta - \frac{2\eta}{\xi^2 + \eta^2} F - \frac{2\xi\eta}{\xi^2 + \eta^2} F_\xi \right] G - \left[\xi F_\eta + \frac{4\xi}{\xi^2 + \eta^2} \right] G_\xi + G_{\xi\xi} + \frac{2}{\xi} G_\xi = 0. \tag{9}$$

The boundary conditions consist of no-slip, no-penetration at the wall, and uniform vortex-free flow in the free stream. This yields:

$$\text{as} \quad \eta = R^{1/2} \quad : \quad F = 0\,, \qquad F_\eta = 0 \quad \text{and} \quad G = F_{\eta\eta} \tag{10}$$

$$\text{as} \quad \eta \to \infty \quad : \quad \frac{\partial F}{\partial \eta} \to 1 \quad \text{and} \quad G \to 0 \tag{11}$$

These equations which govern the basic flow are steady, coupled and non-linear in the real variables F and G.

After linearizing in ϵ, the perturbation field (first-order terms in ϵ) is governed by

$$\tilde{f}_{\eta\eta} - \tilde{g} + \tilde{f}_{\xi\xi} + \frac{2}{\xi} \tilde{f}_\xi = 0 \tag{12}$$

$$\tilde{g}_{\eta\eta} + [F + \xi F_\xi - \frac{4\eta}{\xi^2+\eta^2}]\tilde{g}_\eta - [\xi F_\eta + \frac{4\xi}{\xi^2+\eta^2}]\tilde{g}_\xi + [\frac{\xi^2-\eta^2}{\xi^2+\eta^2}F_\eta - \frac{2\eta}{\xi^2+\eta^2}F - \frac{2\xi\eta}{\xi^2+\eta^2}F_\xi]\tilde{g} + [\frac{\xi^2-\eta^2}{\xi^2+\eta^2}G - \xi G_\xi]\tilde{f}_\eta + [\xi G_\eta - \frac{2\xi\eta}{\xi^2+\eta^2}G]\tilde{f}_\xi + [G_\eta - \frac{2\eta}{\xi^2+\eta^2}G]\tilde{f} - i\sigma\left(\xi^2+\eta^2\right)\tilde{g} + \tilde{g}_{\xi\xi} + \frac{2}{\xi}\tilde{g}_\xi = 0, \quad (13)$$

with the boundary conditions,

$$\text{as} \quad \eta = R^{1/2} \quad : \quad \tilde{f} = 0\,, \quad \tilde{f}_\eta = 0 \quad \text{and} \quad \tilde{g} = \tilde{f}_{\eta\eta} \quad (14)$$

$$\text{as} \quad \eta \to \infty \quad : \quad \tilde{f}_\eta \to 1 \quad \text{and} \quad \tilde{g} \to 0. \quad (15)$$

These equations governing the perturbation field are steady, coupled and linear in the complex variables $\tilde{f}$ and $\tilde{g}$. The disturbance frequency, σ, appears explicitly in the perturbation equations, therefore, the solution will depend on the frequency. The formulation of the two sets of equations developed here was first proposed by Herbert (1991).

Method of solution

The general method of solution was to formulate a set of simultaneous algebraic equations using 2nd order differencing forms. The details of the numerical solution are given by Haddad (1995). The computational grid was nonuniform in both directions due to the use of Robert's stretching to cluster more points near the body surface and near the leading edge. In order to calculate the flow for the body at angles of attack, the computational grid extends over the whole body. No assumptions about symmetry between the upper and lower halves of the body were made in the boundary conditions for the zero angle of attack case.

Central differencing was used whenever possible, otherwise, forward or backward differencing was used as applicable. The finite-difference scheme was second-order accurate throughout the grid. At the surface of the body ($\eta = R^{1/2}$), there existed two conditions on the stream function (f in Eq. 14). To implement both of these conditions, the condition $f_\eta = 0$ was finite differenced first and the resulting equation was solved for one of the unknown variables. This was then substituted into the difference equation of the condition $g = f_{\eta\eta}$, thus allowing us to implement all the boundary conditions at the wall.

At the outflow boundaries, a so-called "non-reflecting" boundary condition was used. To implement this condition, a "buffer-zone" was used to gradually zero the elliptic terms in the governing equations. This was done using a 'tanh' weighting function which was multiplied by the elliptic terms. The streamwise

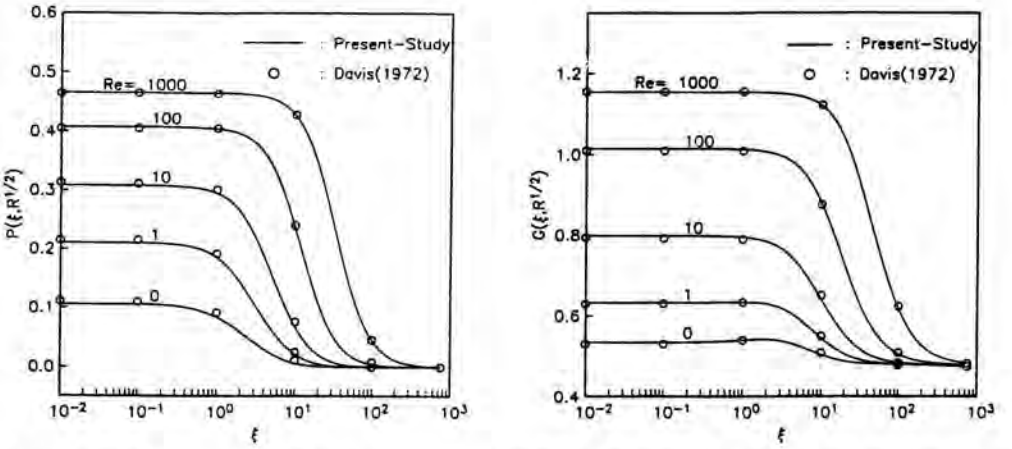

Figure 1: Comparison of surface pressure (left) and skin friction (right) distributions along parabolic body to those of Davis (1972).

extent of the buffer zone was set to be at least four wavelengths of the instability waves expected in the perturbation solution.

For the basic flow, the governing equations were linearized using a Newton's Method. The set of equations was solved using a standard banded matrix solver.

Sample results

The sample results are all for cases with a zero mean angle of attack. Two of the basic flow quantities consisting of the streamwise distributions of the surface pressure and skin friction are shown in Fig. 1. These are compared to the calculations by Davis (1972) for a range of nose Reynolds numbers, $0 \leq Re \leq 1000$. The symbols correspond to Davis' results and the solid curves represent the results from the present study. The agreement is excellent. We observe that far from the leading edge, the values of both quantities converge to constant (asymptotic) values. We have checked these against the asymptotic solution for the basic flow in the paper by Davis (1972), and again found excellent agreement.

The results for the perturbation flow have been compared to those of Murdock (1981) and Ackerberg and Phillips (1972). The agreement was excellent (Haddad, 1995). Samples of the perturbation solution are shown in Fig. 2. All the results are for $Re = 10$ and dimensionless frequency $F = 2.3 \times 10^{-4}$. In these cases, the u-component of the unsteady Stokes flow has been subtracted from the total perturbation flow. This was done by solving the original equations (12 & 13), less the inertial terms, on the same computational grid and subtracting that solution from that of the full governing equations. The left part of Fig. 2 has amplitude scales which capture the large peak in u at the leading edge. The scales of the plots in the right part of Fig. 2 have been magnified to better show the fluctuations in the linear amplified region.

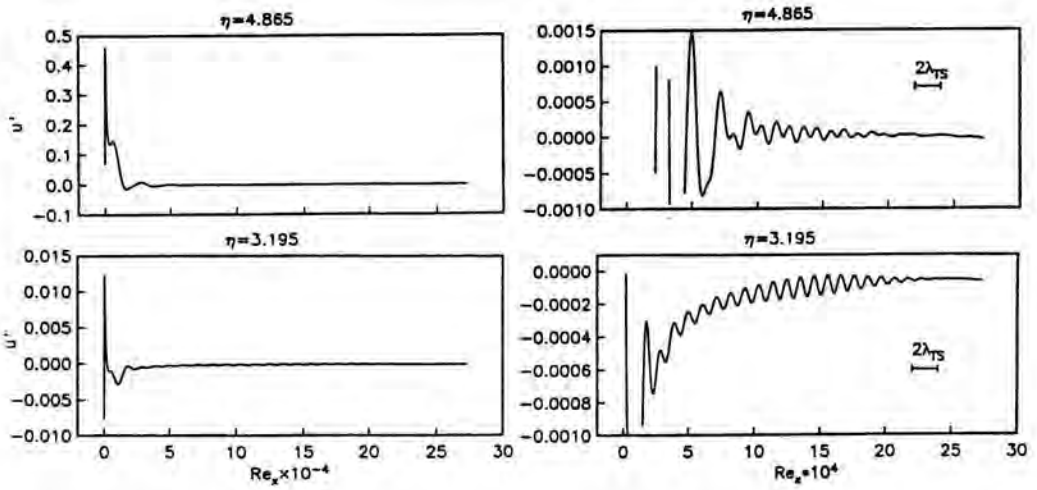

Figure 2: Streamwise velocity perturbation amplitude distributions along parabolic body just above the wall (bottom) and at the amplitude maximum (top). Right set of graphs have magnified scale.

Fig. 3 shows wall-normal amplitude profiles of the streamwise perturbation velocity at consecutive downstream positions, starting from the leading edge. These show that slightly downstream of the leading edge, the amplitude distribution has a T-S eigenfunction shape. This however decays rapidly. By the position where $R_x^{1/2} \approx 55$, the upper lobe is lost. This location is still far upstream of the linear stability Branch I.

Starting from the leading edge, we can expect that the fluctuations in the boundary layer will be made up of a combination of forced (non Orr-Sommerfeld (O-S)) modes, and O-S modes of both discrete and continuous spectrum types. Recall that we have already removed the unsteady Stokes flow. The O-S modes will initially decay exponentially until they reach Branch I. Past that point they are expected to grow until they reach Branch II. Beyond Branch II, they again decay.

Murdock (1980) found that near Branch I, the amplitude of the discrete O-S mode was overwhelmed by modes which he believed were part of the O-S continuous spectrum. These were especially evident away from the wall, near the location of the O-S discrete-mode maximum. He believed that these were part of the continuous spectrum because at a fixed frequency, their longer wavelengths gave them a dimensionless phase speed close to 1. The appearance of longer wavelength modes were also observed by Gatski & Grosch (1987) in numerical simulations for the flow over an infinitely thin flat plate.

Focusing again on Fig. 2 in the top-right plot, we can see evidence of a longer wavelength modulation of the streamwise velocity fluctuations. As with Murdock (1980, 1981), when we viewed the u-fluctuations close to the wall (bottom, Fig. 2)

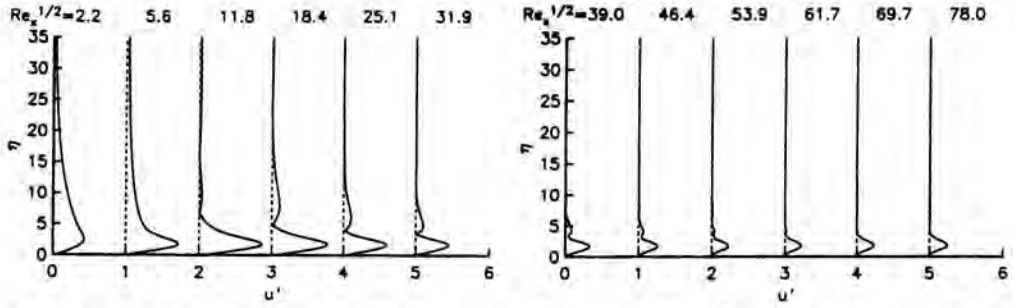

Figure 3: Wall-normal amplitude profiles at consecutive downstream positions, close to the leading edge (Stokes wave has been subtracted).

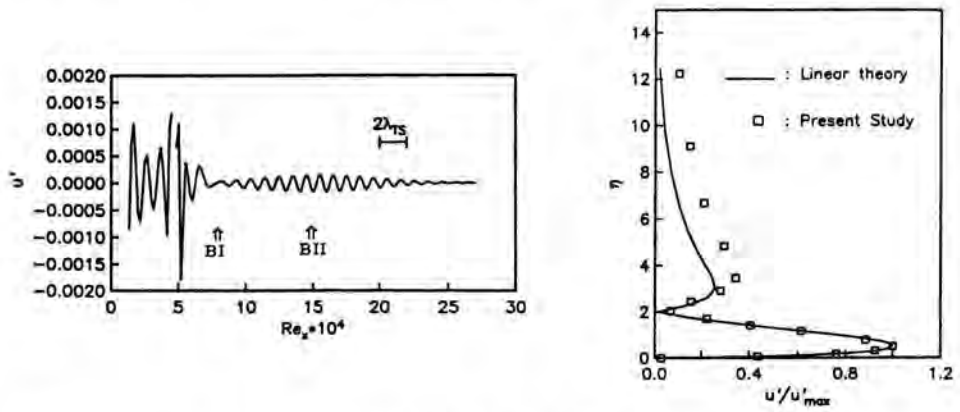

Figure 4: u-amplitude distribution along body (left) at the height of the maximum amplitude, and wall-normal distribution at Branch II location (right), after filtering long wave-length fluctuations.

we can better differentiate a single fluctuation which has the proper wavelength for a discrete O-S mode at the freestream oscillation frequency. In order to separate out this mode from the total fluctuations, we used a spectral high-pass filter. The filter was designed to remove fluctuations with wavelengths less than that of the expected theoretical discrete T-S mode. The result is shown in the left part of Fig. 4. The magnified view clearly shows u-fluctuations which decay, grow and decay. We have marked the theoretical locations of the linear-theory neutral growth Branches I & II, as well as the theoretical wavelength. Similar filtered results at different heights above the surface were taken to construct the wall-normal distribution shown in the right part of Fig. 4. The T-S eigenfunction based on linear theory for a Blasius boundary layer is shown as the solid curve. The agreement between it and the computed amplitude distribution is quite good.

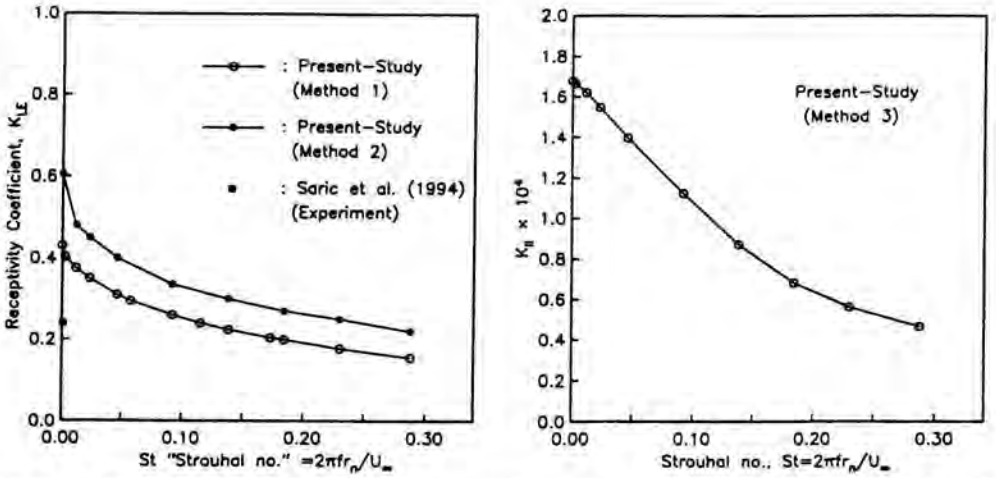

Figure 5: Dependence of leading edge receptivity on nose radius of curvature, r_n, based on different methods. The left plot corresponds to methods 1 and 2. The right plot corresponds to the amplitude at Branch II, referred to as K_{II}.

Fig. 5 documents the effect of nose radius on the leading edge receptivity coefficient, $K_{LE} = |u'_{TS_{LE}}|/|u'_\infty|$. Following Hammerton & Kerschen (1992), we have represented the nose radius in terms of a Strouhal number, $St = 2\pi f r_n/U_\infty$. The amplitude at the leading edge $u'_{TS_{LE}}$ was determined by three different methods. The first followed that of Murdock (1980). It involved fitting an exponential function to the envelope of amplitude fluctuations between the leading edge and the first neutral growth region. This method makes no discrimination about the origin of the fluctuations, namely if they are forced or O-S modes. The second method attempts to address this. It is based on an exponential extrapolation to the leading edge of the maximum amplitude at streamwise locations where amplitude distributions had a T-S-like eigenfunction shape (e.g. Fig. 3 at $Re_x^{1/2} = 18.4$). The third method used the maximum amplitude of the filtered fluctuation profiles (e.g. Fig. 4) at Branch II. The result of this method is shown at the right plot of Fig. 5. These could be projected back to the leading edge based on the integrated amplitude ratio based on linear theory. The results show that the leading edge receptivity coefficient is maximum for the infinitely sharp flat plate, and decreases with increasing nose radius. The difference in the first two methods only results in a shift between their respective distributions. The result from the third method corresponds to the amplitude at Branch II, which we refer to as K_{II}. Using the amplitude ratio, based on linear theory for a Blasius layer (which is relevant except very close to the leading edge), these amplitudes will be $\mathcal{O}(1)$ at the leading edge.

The dependence of the leading edge receptivity coefficient on nose radius is in good qualitative agreement with the analysis of Hammerton & Kerschen (1992), which shows a decrease in K_{LE} with increasing Strouhal number. We can make a quantitative comparison to the experiment of Saric *et al.* (1994). Their value

of the leading edge receptivity coefficient is shown as the filled square in the left plot of Fig. 5. We find that the experimental value falls between that predicted by the two methods, and within 4% of that predicted by method 1.

Conclusions

The spatial formulation used in this problem was successful in predicting the evolution of instability waves induced by acoustic freestream disturbances. We found that the leading edge receptivity coefficient depended on the nose radius of curvature, with the largest receptivity occurring for the infinitely sharp leading edge. This agreed with the numerical results of Murdock (1980) and the asymptotic analysis of Hammerton & Kerschen (1992). We also found excellent agreement with the experiment of Saric *et al.* (1994).

Acknowledgement

This problem was first introduced to the first author by Thorwald Herbert while the author was on sabbatical and working at Ohio State University and DynaFlow, Inc. The author is indebted to him for suggesting the problem and for the frequent suggestions as it evolved.

References

Ackerberg, R. C. & Phillips, J. H. 1972 – The unsteady laminar boundary layer on a semi-infinite flat plate due to small fluctuations in the magnitude of the free-stream velocity. *J. Fluid Mech.* **51**, 137-157.

Davis, R. T. 1972 – Numerical solution of the Navier-Stokes equations for symmetric laminar incompressible flow past a parabola. *J. Fluid Mech.* **51**, 417-433.

Gatski, T. & Grosch, C. 1987 – Numerical experiments in boundary layer receptivity. Proc. Symp. on Stability of Time Dependent and Spatially Varying Flows, Springer-Verlag, pp. 82-96.

Goldstein, M. E. 1983 – The evolution of Tollmien-Schlichting waves near a leading edge. *J. Fluid Mech.* **127**, 59-81.

Goldstein, M. E. 1985 – Scattering of acoustic waves into Tollmien-Schlichting waves by streamwise variations in surface geometry. *J. Fluid Mech.* **154**, 509-530.

Haddad, O. M. 1995 – Numerical study of leading edge receptivity over parabolic bodies. Ph. D. Thesis, Illinois Institute of Technology.

Hammerton, P. W. & Kerschen, E. J. 1992 – Effect of nose bluntness on leading-edge receptivity. *Stability, Transition and Turbulence*, eds. M. Y. Hussaini, A. Kumar, C. L. Streett, Springer-verlag, New York.

Herbert, Th. 1991 – Numerical study of leading-edge receptivity. Internal report, Ohio State University, Columbus OH.

Lin, N. Reed, H. L. & Saric, W. S., 1990 – Leading edge receptivity to sound: Navier-Stokes computations. *Appl. Mech. Rev.* **43**, 175.

Morkovin, M. V., 1969 – On the many faces of transition. *Viscous Drag Reduction*, ed. C. S. Wells, Plenum.

Murdock, J. W., 1980 – The generation of a Tollmien-Schlichting wave by a sound wave. *Proc. R. Soc. Lond. A* **372**, 517-534.

Saric, W. S. & Rasmussen, B. K. 1992 – Boundary layer receptivity: Freestream sound on an elliptical leading edge. *Bull. Am. Phys. Soc.* **37**, 1720.

Saric, W. S., Wei, W. & Rasmussen, B. K. 1994 – Effect of leading edge on sound receptivity. *Laminar-Turbulent Transition*, **Vol IV**, Ed. R. Kobayashi, Proc. IUTAM Symp; Sendai, Japan.

Shapiro, P. J. 1977 – The influence of sound upon laminar boundary layer instability. *MIT Acoust. Vib. Lab. Rep. 83485-83560-1.*

Authors' addresses

[a]Fluid Dynamics Research Center
Mechanical and Aerospace Engineering Department
Illinois Institute of Technology
Chicago, Il 60616

[b]Jordan University of Science and Technology
Mechanical Engineering Department
Jordan, Irbed, P.O. Box 3030

N.V. Semionov, A.D. Kosinov & A.A. Maslov

Experimental Investigation of Supersonic Boundary-Layer Receptivity

Abstract

The leading-edge receptivity of a supersonic boundary layer on a flat plate to controlled acoustic disturbances is experimentally studied. It is found that external disturbances spreading upstream with negative phase velocities do not cause a response in the boundary layer. The acoustic disturbances with positive phase velocities generate oscillations in the boundary layer. The receptivity coefficients were obtained for the latter case.

Introduction

At present it is generally recognized that transition is connected with the loss of stability of the initial laminar flow and with the receptivity of boundary layers. By receptivity we mean the process in which external disturbances generate unstable waves inside boundary layers (Morkovin, 1957). The majority of theoretical and experimental investigations on receptivity were carried out for subsonic flow. Mack (1975) theoretically studied the interaction of acoustic waves and a supersonic boundary layer for the first time. He found that eigen oscillations can exceed the amplitude of acoustic waves a few times. Recently other theoretical studies of leading-edge receptivity of supersonic boundary layers to external acoustic waves have appeared (Duck 1990, Fedorov & Khokhlov 1992, Gaponov 1995).

Fedorov & Khokhlov (1992) examined the case of arbitrary incidence angle of the external wave falling on the leading edge, and invented two mechanisms of generation. The first is connected with sound diffraction, the second with diffusion of acoustic waves on the leading edge. They found that the generation of unstable waves in the boundary layer depends on the incidence angle of the acoustic wave and on whether the sound source is located above or below the model. Gaponov studied the generation of boundary-layer oscillations by a longitudinal sound field and found that the intensities of the disturbances in the boundary layer depend on the spatial orientation of the external acoustic wave.

The receptivity problem of supersonic boundary layers has almost not been investigated experimentally. One of the few examples is Kendall (1975), who measured the receptivity coefficient between free-stream pulsations and the disturbances in the boundary layer at Mach numbers in the range 1.6 to 8.5. The receptivity problem can be solved with the help of external controlled disturbances, which generate eigen oscillations in the boundary layer. Using an external disturbance source Maslov & Semionov (1986) could experimentally establish

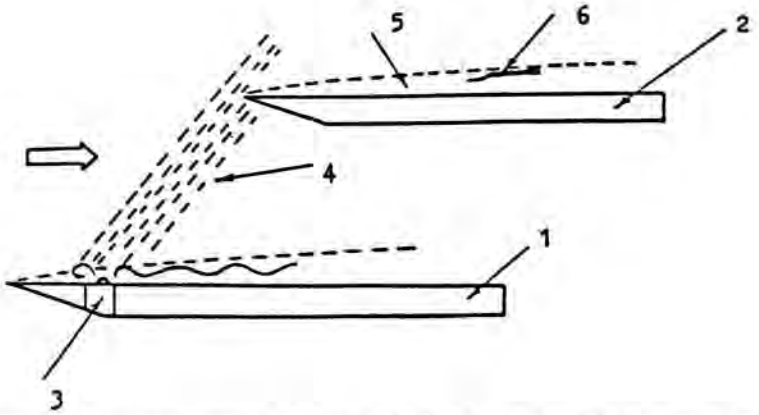

Figure 1: Scheme of the experiment: plates (1 & 2); discharge (3); acoustic radiation (4); measured boundary layer (5); hot-wire probe (6).

the regions of maximum boundary-layer receptivity on a flat plate to acoustic disturbances. These regions are: a) the leading edge of the plate; b) the area corresponding to the acoustic branch of the neutral curve; and c) the area corresponding to the lower branch of the neutral stability curve. Maslov & Semionov (1989) studied the wave structure of disturbances in the boundary layer when the maximum of the sound radiation fell on the leading edge of the flat plate. These data were compared with the wave structure of disturbances generated by a point source in the boundary layer (Kosinov *et al.*, 1990a). These results show the complex process of the transformation of an acoustic wave to unstable waves within the supersonic boundary layer.

Experimental conditions

The experiments were performed in the supersonic wind tunnel T-325 of the Institute of Theoretical and Applied Mechanics of the Russian Academy of Sciences with the test section dimensions $600 \times 200 \times 200$ mm^3, at Mach number $M = 2$, unit Reynolds number $Re_1 = 6.6 \times 10^6$ m^{-1}. The model is presented in Fig. 1. It consists of two flat plates, mounted at zero angle to the flow. Vortical and acoustic disturbances were generated by using a surface discharge with frequency $f = 20$ kHz as described by Maslov & Semionov (1987) and Kosinov *et al.* (1994). Plate 1 contains the surface discharge and can be moved in normal direction. Plate 1 was placed below plate 2. In this case generation of disturbances in the boundary layer by the controlled external acoustic field takes place near the leading edge of plate 2. Disturbances were registered by a constant temperature hot-wire anemometer; a probe with a tungsten wire of 5 μm diameter and 1.2 mm length was used. The probe could be moved along three coordinates with the help of a traversing device with an accuracy of 0.1 mm for the longitudinal and spanwise coordinates (x and z, respectively), and 0.01 mm for the normal coordinate y. The hot-wire signal was processed by a

computer with a 10 bit 1 MHz A/D converter. Synchronous summation of the signal up to 200 points was carried out in the experiments for improvement of the signal-to-noise ratio. Amplitudes $A(f,x,z)$ and phases $\Phi(f,x,z)$ of the initial acoustic disturbances and oscillations in the boundary layer of plate 2 were measured. The discrete Fourier transformation was used to define the complex wave-number spectra (Kosinov *et al.*, 1990b). After transformation, the data were presented as $A_f(\chi)$, $\Phi_f(\chi)$ - distributions of the amplitude and phase of disturbances at f =const over the wave inclination angles defined by

$$\chi = \mathrm{arctg}(\beta/\alpha_r), \tag{1}$$

where α_r, β - wave numbers are in x- and z-direction respectively. Wave numbers $4\alpha_r$, β were defined from the relation

$$A_f(\alpha_r,\beta)\exp(i\Phi(\alpha_r,\beta)) = \frac{1}{T}\sum E(x_i,z_j,t_k)\,\exp(-i(\alpha_r x_i + \beta z_j - 2\pi f t_k)), \tag{2}$$

where $E(x_i,z_j,t_k)$ denotes the oscillations as obtained from the hot wire, and T denotes the realization time. To define the ratio between the disturbances generated in the boundary layer and the amplitude of the acoustic waves falling on the leading edge, a receptivity coefficient K was calculated from the relation

$$K(\chi) = \frac{A_f(\chi)_{x=x_i^*}}{A_f(\chi)_{x=x_0}} \tag{3}$$

Results

To define the initial amplitude of the fluctuations in the free stream, the disturbance field was measured in the plane of plate 2 (while plate 2 itself was temporarily removed). Fig. 2 shows the amplitude and phase distributions $A_0(x)$, $\Phi_0(x)$. Here the coordinate x was measured downstream from the border of radiation. To analyze the obtained data it is useful to present a simplified physical model of the disturbances source. An electric arc was drawn on the surface of plate 1. We propose that the vortices are generated with distinct directions of rotation in the yx plane in front of and behind the arc. Besides the disturbances T-S waves appear in the boundary layer of plate 1 and propagate downstream. This process is accompanied by the sound radiation into the external flow. Using this physical model and distributions of $A_0(x)$ and $\Phi_0(x)$ we can choose the characteristic zones, corresponding to the different types of external disturbances. The zone $1.5 < x < 5$ mm approximately corresponds to vortex radiation in front of the discharge, while the zone $9 < x < 13$ mm corresponds to vortex radiation behind the discharge and the zone of radiation of travelling waves is $x > 14$ mm.

Fig. 3 shows the distribution of A_0 over α_r, obtained after processing the data presented in Fig. 2. The amplitude is normalized by its maximum. The

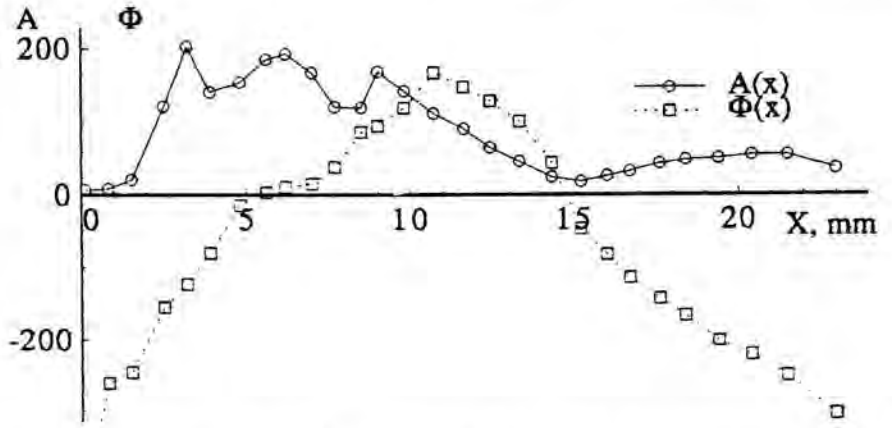

Figure 2: Dependence $A_0(x)$, $\Phi_0(x)$ of controlled initial disturbances at the plane of plate 2 (while plate 2 was removed).

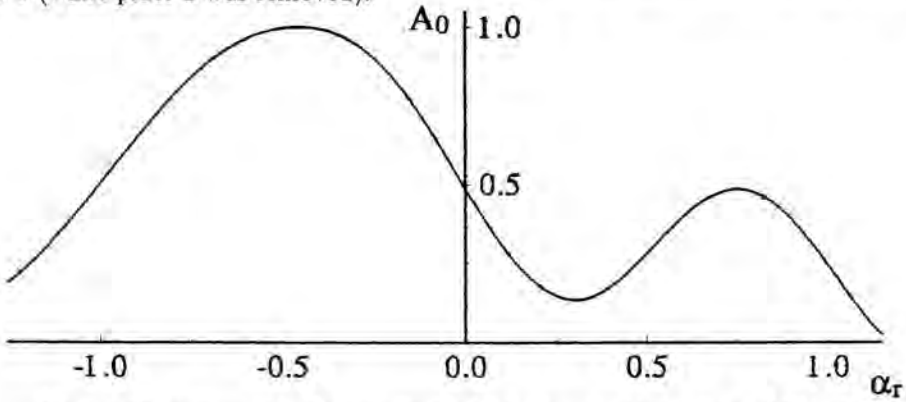

Figure 3: α_r-spectra of controlled initial disturbances (data of Fig. 2).

distribution $A_0(\alpha_r)$ has two peaks with $\alpha_r = -0.45$ and $\alpha_r = 0.75$ rad/mm. The first peak corresponds to radiation of the vortex in front of the discharge, and the second peak corresponds to the radiation of the other zones. Values of α_r were used for the computation of the disturbance phase velocity in x-direction by

$$C = \frac{2\pi f}{\alpha_r U}. \tag{4}$$

Here U is free stream velocity. $C = -0.54$ was obtained for the first zone of radiation. The negative C corresponds to upstream spreading disturbances. For the other zones the phase velocity is $C \approx 0.33$ (acoustic disturbances).

To define β-spectra the initial distributions $A_0(z)$ and $\Phi_0(z)$ were measured at x equal to 3.5, 11 and 23 mm, corresponding to different zones of radiation. The leading edge of plate 2 was installed at these three locations, where external disturbances were measured. The distributions $A(z)$, $\Phi(z)$ of disturbances

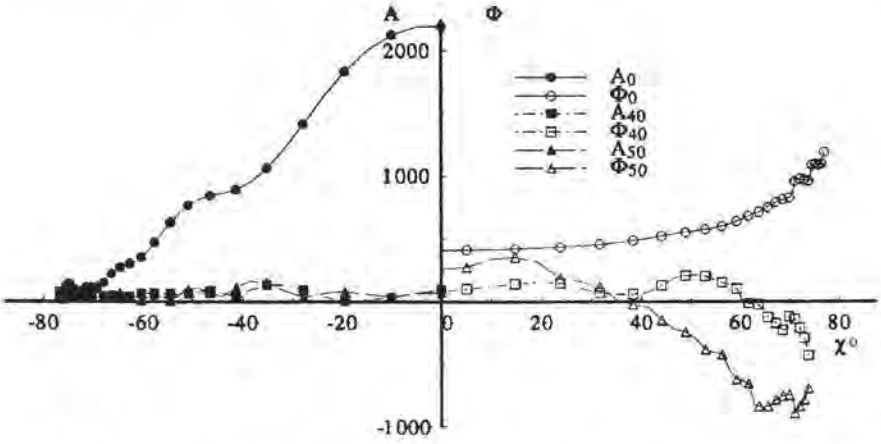

Figure 4: Amplitudes and phases of initial disturbances and oscillations in the boundary layer for leading-edge coordinate $x = 3.5$ mm.

were measured in the boundary layer of the plate 2 at x^* equal to 40 and 50 mm (here x^* is the distance from the leading edge). The amplitude β-spectra were calculated. In this way the structure of the external disturbances and the waves generated by them in the boundary layer were defined. The measurements allow to make a quantitative estimation of the transfer function between initial and eigen oscillations. Fig. 4 shows amplitude and phase spectra over χ of the external disturbances and oscillations excited by them in the boundary layer at $x = 3.5$ mm. Obviously, the amplitude of excited oscillations is close to zero. Consequently the receptivity coefficients are close to zero for the excited oscillations by the upstream spreading disturbances. Hence, external disturbances with negative C do almost give no response in the supersonic boundary layer.

Let us consider the analogous results for other zones. Fig. 5 shows the distributions of $A_f(\chi)$ and $\Phi_f(\chi)$ of the external disturbances and the oscillations excited by them in the boundary layer at $x = 11$ mm. It should be noted that the distributions of $A_f(\beta)$ and $\Phi_f(\beta)$ are similar (Kosinov *et al.*, 1994) in the free stream and in the boundary layer, but the difference of phase velocities leads to the non-coincidence in magnitudes of χ. Amplitudes of inclination waves with $\chi \approx 10^o$ and $\chi \approx 30^o$ become maximum in the radiation of the second zone, and disturbances with $\chi \approx 30^o$ are mainly generated in the boundary layer.

Fig. 6 shows the distributions of $A_f(\chi)$ and $\Phi_f(\chi)$ of external disturbances and the oscillations excited by them in the boundary layer at $x = 23$ mm. Here the distributions of $A_f(\chi)$ and $\Phi_f(\chi)$ are similar in the external flow and in the boundary layer. The main amplitude peaks are observed at $\chi = 0$, which is in good agreement with results of Maslov & Semionov (1987), where the radiation from travelling waves was studied. The oblique waves have smaller amplitude, but for $\chi \geq 35^o$ the amplitude of oscillation in the boundary layer is larger than the amplitude of external disturbances. It may be noted that the distributions of $A(z)$ and $\Phi(z)$ are coinciding qualitatively with the results of Maslov & Semionov

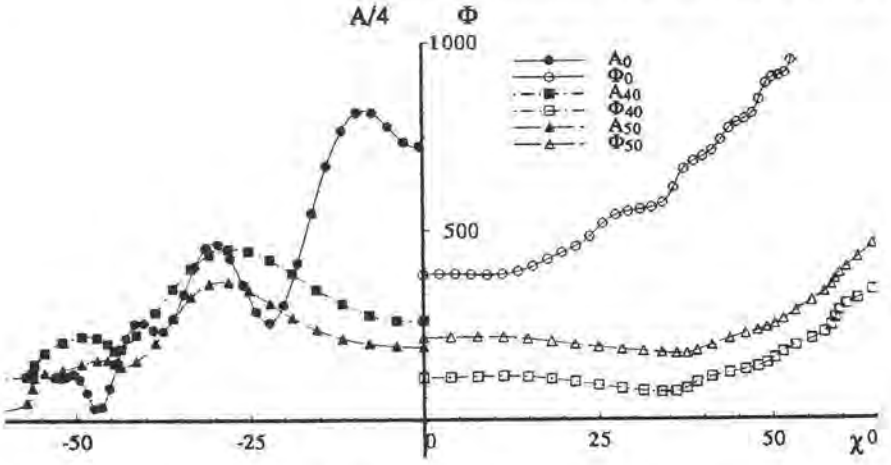

Figure 5: Amplitudes and phases of initial disturbances and oscillations in the boundary layer for leading-edge coordinate $x = 11$ mm.

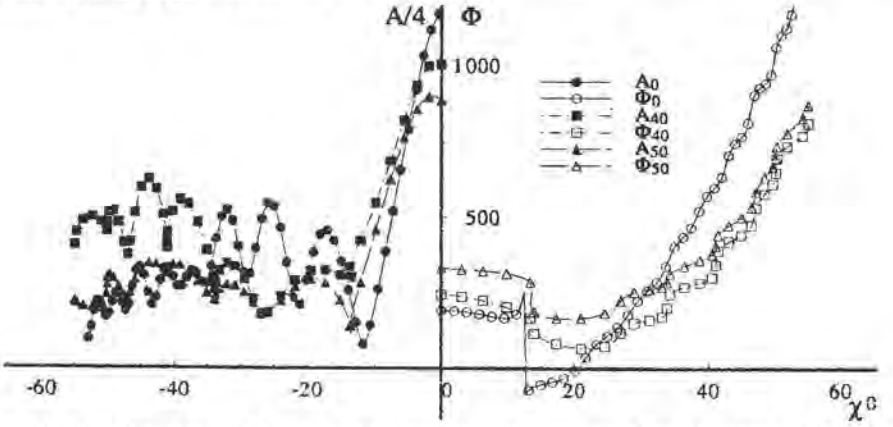

Figure 6: Amplitudes and phases of initial disturbances and oscillations in the boundary layer for leading-edge coordinate $x = 23$ mm.

(1989), where the disturbances in the boundary layer were excited by sound falling from above on the plate leading edge. The modulations in $A(x, z)$ were observed in both experiments, which points to the existence of several types of disturbances in the boundary ayer.

Fig. 7 shows the receptivity coefficients $K(\chi)$ for the second and third zone. For the second zone two characteristic regions of amplified disturbances over χ are selected. The first region is within 10^o, where the receptivity coefficients are minimum, and the second region is $\pm(20^o - 40^o)$, where the coefficients are maximum. The data are presented for a disturbance amplitude that is above one third of the maximum amplitude. This is the reason that the receptivity coefficients for the third zone are presented the $-6^o \leq \chi \leq 6^o$ too. There is a difference in the receptivity coefficients for various zones in corresponding c. One of the reasons may be the distinct nature of external waves: radiation of

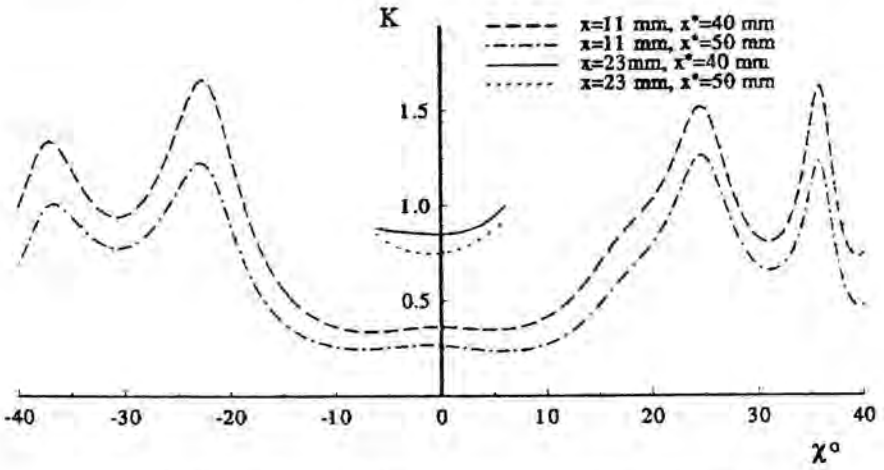

Figure 7: Dependence of the receptivity coefficient K on χ.

the second zone is due to the stationary sources and radiation of the third zone is due to travelling waves. These results correspond with theoretical conclusions (Fedorov & Khokhlov 1992, Gaponov 1995). The experiments also show that oblique waves are more amplified than the waves at $\chi \approx 0$. This experimental result with theoretical results obtained by Gaponov (1995).

Conclusions

Experimental data for the leading-edge receptivity in a supersonic boundary layer at Mach number 2 were obtained. Using controlled acoustic disturbances, the receptivity coefficients for different inclination waves were determined. It was found that the linear excitation of unstable waves in the supersonic boundary layer depends on the initial phase velocities and wave inclination of the external disturbances. The maximum receptivity coefficient corresponds to oblique waves with χ angles from 20 to 40 degrees.

Acknowledgements

This research has been supported by NASA, Cooperative Agreement NCCW-74.

References

Duck, P.W. 1990 – The response of a laminar boundary layer in supersonic flow to small amplitude progressive waves. *J. Fluid Mech.* **219**, 423-448.

Fedorov, A.V., Khohlov, A.P. 1992 – Supersonic boundary layer receptivity to the acoustic disturbances. *Izv. Akad. Sci. USSR. Zh. Mech. Zhid. G.* **1**, 40-47. (in Russian).

Gaponov, S.A. 1995 – On the interaction of a supersonic boundary layer with acoustic waves. *J. Thermophysics & Aeromechanics* **3**, 181-189.

Kendall, J.M. 1975 – Wind tunnel experiments relating to supersonic and hypersonic boundary-layer transition. *AIAA J.* **3**, 290-299.

Kosinov, A.D., Maslov, A.A., Semionov, N.V. 1994 – Methods of controlled disturbances generation for experimental investigation of supersonic boundary layer receptivity. in: Proceedings of ICMAR-7, Part 1 (A.M.Kharitonov ed.). Russia, Novosibirsk, 138-144.

Kosinov, A.D., Maslov, A.A., Semionov, N.V., Shevel'kov, S.G. 1990a – Wave structure of artificial disturbances in a supersonic boundary layer on a flat plate *J. AMTP* **31**, 250-252.

Kosinov, A.D., Maslov, A.A., Shevelkov, S.G. 1990b - Experiments on the stability of supersonic laminar boundary layers. *J. Fluid Mech.* **219**, 621-633.

Mack, L.M. 1975 – Linear stability theory and the problem of supersonic boundary layer transition. *AIAA J.* **3**, 423-448.

Maslov, A.A., Semionov, N.V. 1986 – Excitation of eigen boundary layer oscillation by external acoustic field. *Izv. Akad. Sci. USSR. Zh. Mech. Zhid. G.* **3**, 74-78. (in Russian).

Maslov, A.A., Semionov, N.V. 1987 – Radiation of acoustic oscillations from the supersonic boundary layer. *Izv. SO AN SSSR. Seria tech. nauk.* **2**, 58-63. (in Russian).

Maslov, A.A., Semionov, N.V. 1989 – Structure of artificial disturbances, caused by the external acoustic field, in the supersonic boundary layer. *Izv. Akad. Sci. USSR. Zh. Mech. Zhid. G.* **3**, 113-117. (in Russian).

Morkovin, M.V. 1957 – On transition experiments at moderate supersonic speeds. *J. Aeronaut. Sci.* **7**, 480-486.

Authors' address

Institute of Theoretical and Applied Mechanics
630090, Novosibirsk, Institutskaya 4/1, Russia

Session 8:
High-Speed Flows

Arild Bertelrud° & Sharon Graves▷

Transition in Flight at Supersonic and Hypersonic Mach Numbers

Abstract

Features of a planned hypersonic transition experiment designed to validate stability codes are described, along with instrumentation and data handling techniques developed. A flight experiment concerning transition on a flat plate with elliptical nose section mounted underneath an F-15 flying at speeds up to Mach 2 was performed to verify the instrumentation and the data acquisition techniques. Results from the transition sensors (surface hot films and microphones) are exemplified.

Introduction

Over the past decades the use of computational tools for transition prediction has become increasingly important. This also means that it is essential to verify the correctness of the codes and explore their reliability for different flow situations. The present paper concerns code validation experiments in flight at high Mach numbers.

Two of the important issues in experiments of this type are:

1. The experiment design has to be tailored to the code it is intended to validate; input parameters to the code and corresponding output results should be measured. For example, validation of a simple empirical formula valid for incompressible flows where Reynolds number at transition, pressure gradient and turbulence intensity are correlated, can be limited to the measurement of these three quantities. To validate linear stability codes, the type of transition needs to be documented, and the most unstable frequencies, their wavelengths and directions should be measured. If possible mean velocity profiles should be measured along with the pressure distributions. However, the free stream disturbance level is not part of the input and enters the validation only indirectly through the N-factor chosen to identify the transition, if the e^N method is used. For PSE codes, the disturbance level and characteristics such as free stream turbulence, noise, vibration and roughness may be used as input for the code and hence should be measured.

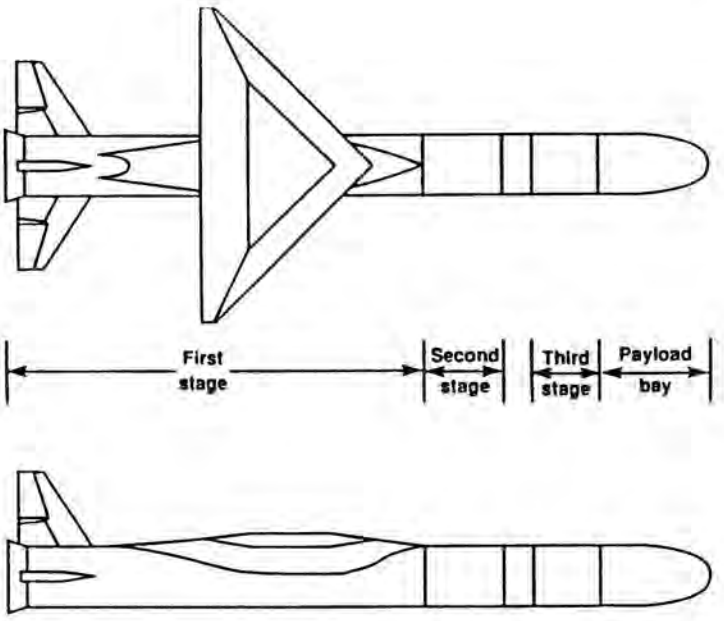

Figure 1: The Pegasus launch vehicle. Length approximately 15 meters and wing span 6.7 meters. The glove will be mounted on the starboard wing.

2. Flight transition conditions are almost always 'reality'. In particular for supersonic and hypersonic ground facilities where the disturbance levels are very high, transition measurements may be useless in many cases, since a different type of transition (most often bypass) occurs in wind tunnel than in flight. While ground experiments can provide uncoupled parameter variations, a flight test will in general mean that a combination of parameters is changing, and it may be necessary to perform combinations of experiments to extract the effects of each parameter. A simple example is acceleration and retardation through the same Mach/Reynolds number range where the noise and vibration levels can be monitored.

A hypersonic transition experiment

A hypersonic flight experiment (Bertelrud, Graves, Young & Anderson, 1995) is in preparation to validate stability codes at Mach 6 to 8 and Reynolds numbers of interest for single-stage-to-orbit vehicles. A smooth, metallic 'glove' has been designed to be mounted on the delta wing of the first stage booster of the Pegasus launch vehicle (Mendenhall *et al.*, 1991), as illustrated in Fig. 1. The main portion of the data is obtained at 120,000 to 180,000 ft (36 to 55 km) altitude while the vehicle is accelerating at close to zero angle-of-attack with a Mach number above 6.

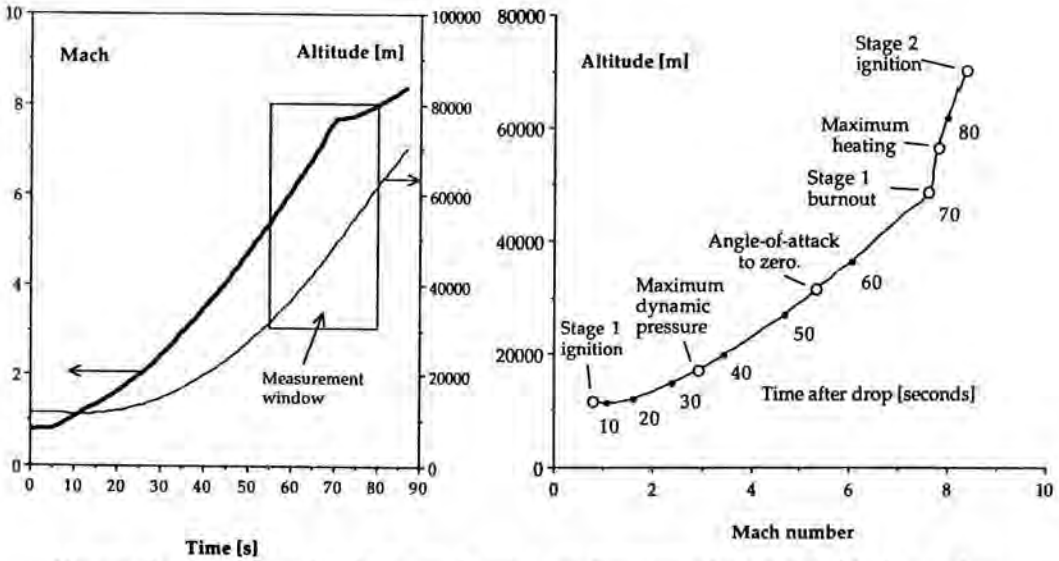

Figure 2: Trajectory for Pegasus, Stage 1, as function of time and Mach number.

The glove shape was designed using linear stability codes, enhancing the crossflow instability and reducing the probability of TS-type transition. Several steps were taken to avoid bypass transition:

- the leading edge radius was minimized to avoid attachment line contamination.
- vibration effects were evaluated using another launch to obtain acceleration levels and spectra up to high frequencies.
- surface roughness was minimized through use of a metallic, smooth glove.
- waviness was minimized through choice of a developable, single-radius profile.

Fig. 2 illustrates the trajectory of the Pegasus vehicle for the time period of interest for the crossflow transition experiment. During the launch, the predictions of attachment line transition indicate a laminar leading edge flow above Mach 5 to 5.5 (depending on the amount of leading edge contamination from the fuselage). Transition is assumed to move back as the vehicle accelerates and the Reynolds number is reduced due to the increasing altitude, moving past the glove trailing edge of the glove before reaching Mach 8.

Instrumentation

The instrumentation includes flush pressure taps for verification of pressure distribution, thermocouples for temperature and transition location. A pressure

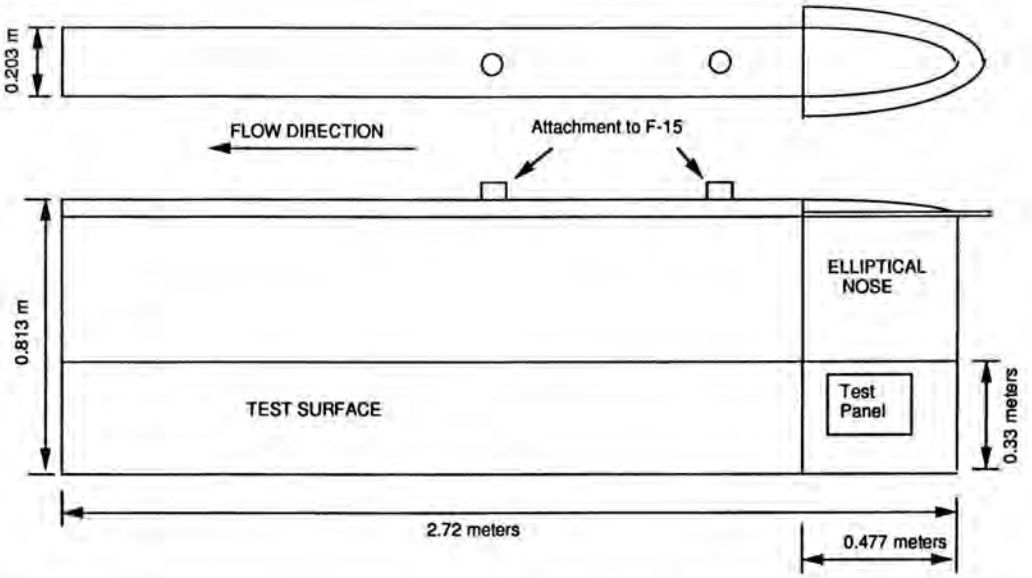

Figure 3: Layout and dimensions of FTF (Flight Text Fixture), flown underneath the F-15.

rake, Preston tubes and Stanton tubes are used to document time-averaged properties of the boundary layer.

Dynamic data will be obtained using recently developed dual surface hot films capable of high-frequency response at high temperatures along with fast pressure transducers mounted in an array to attempt space-time correlation.

Since the Stage 1 of the Pegasus is non-recoverable and telemetry links do not permit transmission of high-frequency data at the rate needed for turbulence measurements, it is necessary to acquire the data, analyze it and compress it real-time. A 4-channel Data Acquisition and Processing System (DAPS, Graves *et al.*, 1994) was developed using 100 kHz sampling per channel with digital processing and compression of the dynamic signals was developed.

A flight experiment in supersonic flow

Characteristics of the experiment

To verify the instrumentation and data acquisition techniques required for the hypersonic experiment, a flight experiment was performed on a flat plate with elliptical nose mounted underneath an F-15, the Flight Test Fixture (FTF) (See Fig. 3) (Richwine & del Frate, 1994), and flown at Mach numbers up to 2, with the main region of interest for transition characterization being at flight Mach numbers 0.8 to 1.4.

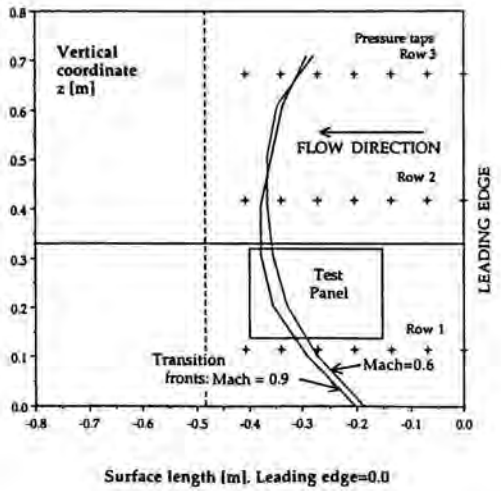

Figure 4: An interpretation of the transition pattern found for two Mach numbers. Elliptical nose region shown with the location of the test panel and static pressure taps.

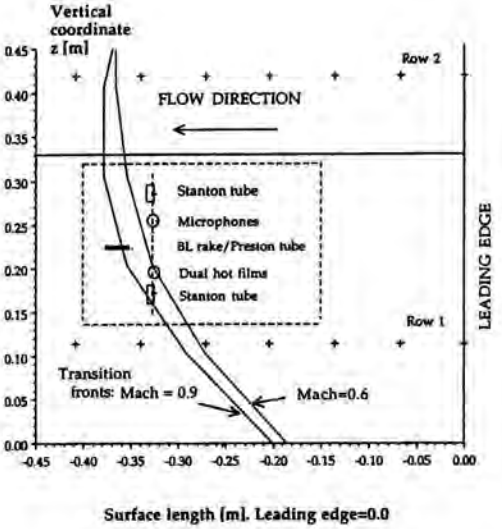

Figure 5: Removable panel with instrumentation used for transition characterization.

From initial flight tests, where temperature-sensitive paint was used, it was known that transition would take place over the elliptical nose region. Fig. 4 is an interpretation of the transition pattern found, for two Mach numbers. Despite the small aspect ratio of the FTF, transition appears to be fairly uniform and 'quasi' two-dimensional, with a transition 'front' curving forward in the upper and lower edges of the test surface.

Reference data defining the inflow conditions to the experiment was obtained from a boom mounted in the lower upstream corner of the FTF. Pressure distributions were measured along the surface at three spanwise locations. The instrumentation used for flow characterization (surface hot films, microphones, a pressure rake and Stanton tubes) was located on a removable panel, as shown in Fig. 5.

Limited computations indicated that T-S instabilities existed only up to approximately 7 - 8 kHz, and the 25 kHz frequency response of the Pegasus instrumentation was considered suitable.

Results

With the layout of the transition sensors in a spanwise row, but no streamwise simultaneous information obtained, the analysis of the results is done in two distinct parts.

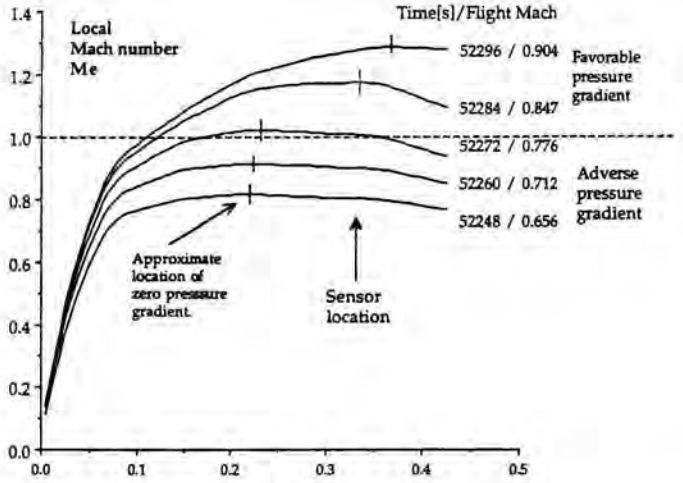

Figure 6: Velocity distributions as function of time/flight Mach number.

1. When a sensor indicates a change, either in terms of level (DC or rms), or the DAPS output indicates a change in signal characteristics, it is possible to identify the transition onset or transition end as it happens at the sensor. At any other time instance, the transition is either ahead of or behind the sensor, and the data is usable for qualitative estimates but not as quantitative measurements.

2. For the identified transition passage it is possible to use the coincident information of flight conditions, Mach number distributions, vibration levels etc. to assess the data and compare it with computational codes.

   A time segment with an acceleration followed by a deceleration at constant altitude of 30,000 ft (9 km) is used as an example. Fig. 6 illustrates the flight Mach number as function of time along with the local Mach number at the sensor location. Already at a flight Mach number of 0.75 the flow contains a local supersonic region. As illustrated by Fig. 6, the local pressure gradient initially is weakly adverse at the sensor location, but for flight Mach numbers above 0.85-0.9 the local gradient is favourable. Based on the measured velocity distributions, the boundary layer as function of time was predicted, using Mann & Whitten's integral method (White 1974), and simple (incompressible) formulas such as e.g. Michel's or van Driest & Blumer's techniques were used to indicate where transition is expected to occur. The trend of estimated transition locations is in general agreement with the experimentally observed trends.

Low-frequency information

Figs 7a through 7c show the time series output from some of the transition sensors. The Preston tube and Stanton tube outputs in Fig. 7a indicates very

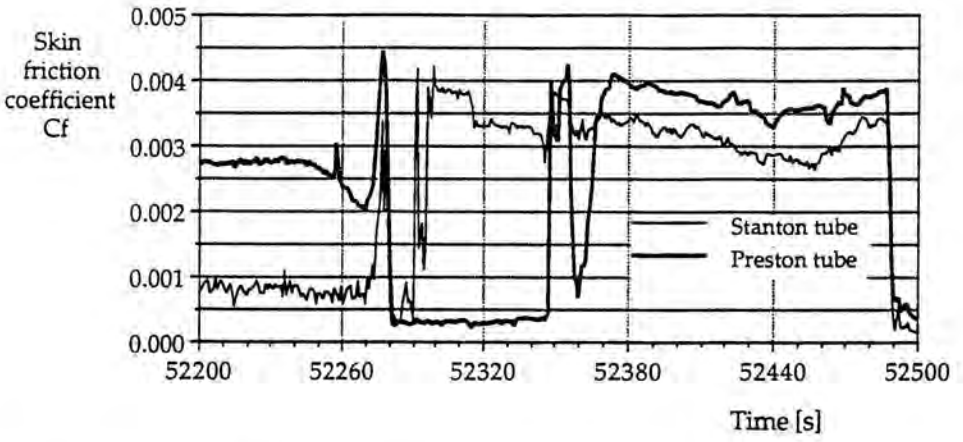

Figure 7: a) Local skin friction coefficient from Preston tube and Stanton tube.

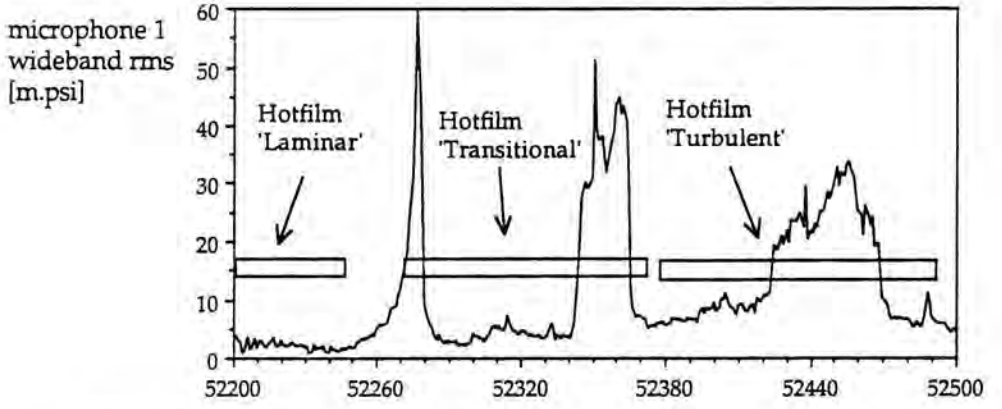

Figure 7: b) Wideband RMS output from microphone as function of time.

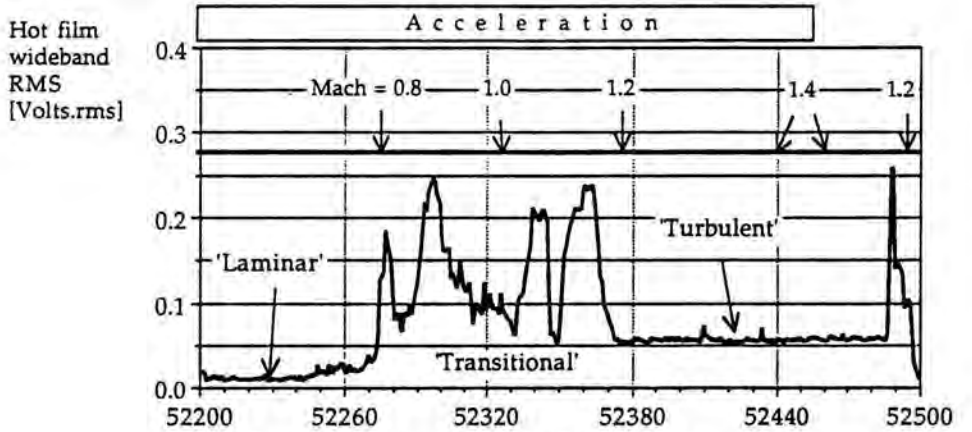

Figure 7: c) Hot film wideband RMS output versus time.

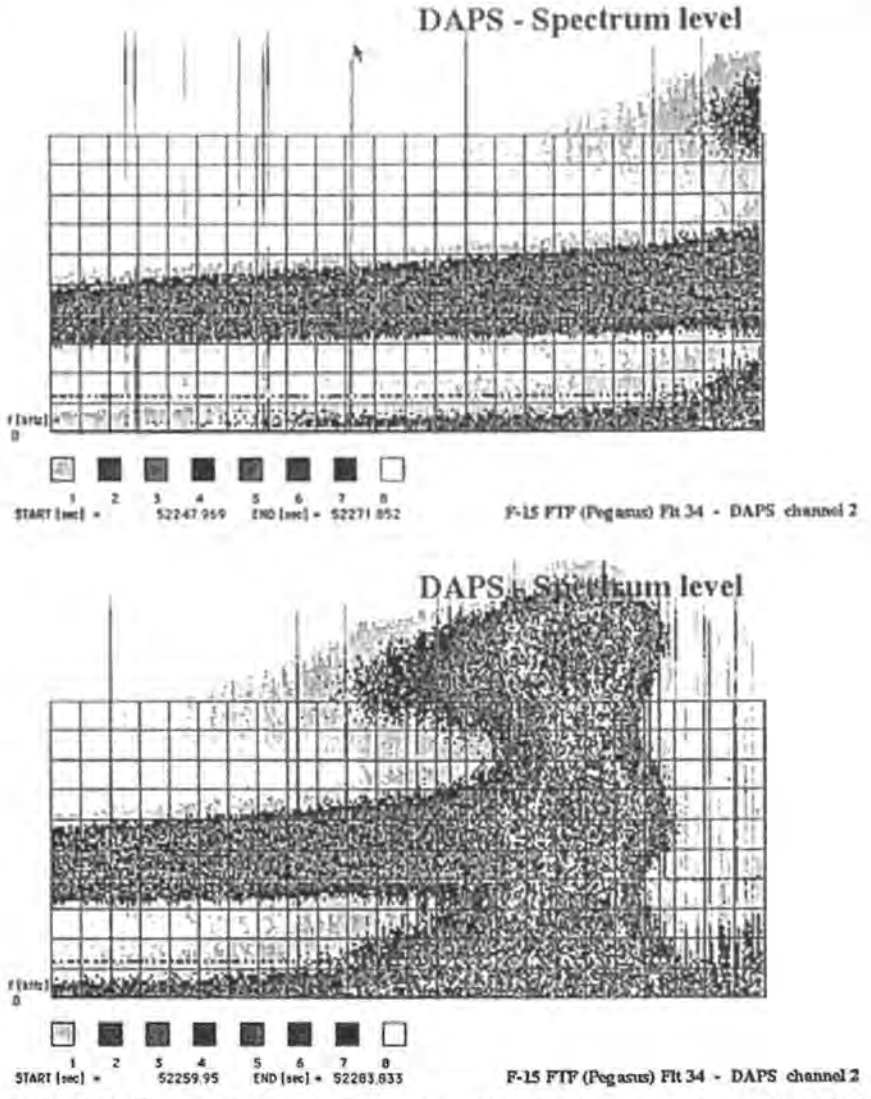

Figure 8: Hot film spectra. Time on horizontal axis, frequency on vertical (grid covers 0 to 0 kHz, with grid lines every 2 kHz). Time axis has a grid line per second. The level of spectral content is determined by grey coding. The graph shows the development of one frequency around 8 kHz, widening of the spectral content and shift to higher frequencies, then a second harmonic, transition to turbulent flow with subsequent laminar and transitional time sequence.

distinct changes in skin friction levels, that can be used for documentation of transition 'front' passage. The different sensors indicate changes of laminar/transitional/turbulent flows at slightly different times, as can be expected due to the spanwise physical separation of the sensors (Fig. 5). While local flow is laminar, the wideband RMS from a microphone can be used to indicate the turbulence level associated with the experiment (Fig. 7b). Increases in the noise level is associated with changes in external noise level (e.g. engine/thrust) or transitional/turbulent flow. Fig. 7c shows the output from one of the surface hot films. It indicates clear regions of laminar and turbulent flow, but in the example there is a time segment where the flow is transitional and seems to change in character continuously.

High-frequency information

In the preceding section, the information could be used to estimate if transition has occurred at a certain time. However, it does not give any indication of the reason for transition - for this it is necessary to examine the characteristics of the dynamic signals, which more closely can be compared with predictions.

Fig. 8 shows time-series of spectra from the hot film in Fig. 7c. It can be seen how oscillations occur at a frequency slightly below 7 kHz. As the aircraft is accelerating (and the pressure distribution along the elliptical nose of the FTF changes), the disturbance frequency increases slowly, and at one point a higher harmonic shows up. As the Mach number (and Reynolds number) increase further, the intensity increase further until the spectra are filled out. Then after a few seconds, the flow suddenly loses the high frequency content; as can be seen in Fig. 6 this correspond to the pressure gradient turning favourable (i.e. damping disturbances) at the sensor location.

The next segment shows the low frequencies increasing in amplitude and spreading in frequency, and the segments of intermittent and turbulent flow can be clearly distinguished. In this case, the vibration levels are increasing as the aircraft it accelerating up to Mach 1.4.

Conclusions

An account of plans for a hypersonic experiment to document crossflow transition has been given, along with a description of and results from a quasi-two-dimensional experiment up to flight Mach numbers of 2. An example of how to extract data for use as a validation experiment has been described. However, it is clear that a proper comparison with linear stability codes or PSE codes involves a large amount of computations to explore the experimental database for the parametric effects that exist in the flight data.

References

Bertelrud, A., Graves, S., Young, R. & Anderson, B. 1995 – Documentation of crossflow transition in flight at hypersonic Mach numbers. *AIAA* Paper 95-6060, AIAA 6th International Aerospace Planes and Hypersonics Technologies Conference, April 3-7, 1995, Chattanooga, TN.

Bertolotti, F.P. 1991 – Compressible boundary layer stability analyzed with the PSE equations. *AIAA* Paper 91-1637, presented at the AIAA 22nd Fluid Dynamics, Plasma Dynamics & Lasers Conference, June 1991, Honolulu, Hawaii.

Graves, S., Bertelrud, A., Diamond, J.K. & Nagurny, W. 1994 – High frequency data acquisition using digital signal processing. *AIAA* Paper 94-2134, 7th Biennial AIAA Flight Test Conference, Colorado Springs, Colorado, June 1994.

Mendenhall, M.R., Lesieutre, D.J., Caruso, S.C., Dillenius, M.F.E. & Kuhn, G.D. 1991 – Aerodynamic design of Pegasus. Concept to flight with CFD. *AIAA* Paper 91-0190, 29th Aerospace Sciences Meeting, Reno, Nevada, January 7-10, 1991.

Richwine, D.M. & Del Frate, J.H. 1994 – Development of a low-aspect ratio fin for flight research experiments. *AIAA* Paper 94-2133, presented at the 7th Biennial AIAA Flight Test Conference, Colorado Springs, Colorado, June 1994.

White, F.M. 1974 Viscous fluid flow, McGraw-Hill, New York.

Authors' addresses

°Analytical Services & Materials
Hampton VA, USA

▷Lockheed Eng. and Sciences Corp.
Hampton VA, USA

M.A. Zanchetta & R. Hillier

Blunt Cone Transition at Hypersonic Speeds: The Transition Reversal Regime

Abstract

This paper reports on an experimental investigation of transitional hypersonic boundary layers. The test geometry is a five-degree semi-angle cone. Experiments are performed in the Mach 9 Imperial College gun tunnel. Time-resolved heat-transfer rates are obtained for laminar, transitional and turbulent boundary layers, for cases in the pre-reversal and transition reversal regimes.

Introduction

Of the many problems encountered in hypersonic aerodynamics, boundary-layer transition from laminar to turbulent motion remains an elusive area, of extreme interest to the scientist and also the designer/engineer. Severe thermal loads are encountered in hypersonic flight, and vehicles often present nose blunting to attenuate the kinetic heating. The blunt-body flowfield contains sub-, tran-, super- and hypersonic regions, in which many mechanisms (Mack modes, entropy layer instabilities, nonlinear by-pass, etc.) can promote transition.

The nose-based Reynolds number Re_n is defined as the product of the unit Reynolds number $Re_\infty(\mathrm{m}^{-1})$ and the nose radius r_n. Transition studies have shown that increasing Re_n initially delays the location of transition onset and increases the length to transition, as illustrated in Fig 1. Above a certain Re_n, the transition front becomes highly three dimensional and may move upstream to the sphere-cone junction. This change in transition trend is denoted transition reversal and the range of Re_n in which it occurs is named the transition reversal regime. In this paper examples of hypersonic transition in both the pre- and reversal regime will be given.

Facility

The Imperial College number 2 gun tunnel is an intermittent facility with a 4 ms steady run window, capable of testing slender models up to 0.8 m in length. Three fully calibrated operating conditions exist, with the following nozzle exit plane conditions:

	M_∞	Re_∞ (m^{-1})	p_∞ ($\mathrm{N/m}^2$)	$T_{0,\infty}$ (K)	T_∞ (K)
low	8.89	7.51×10^6	441	1060	63.07
medium	8.93	12.62×10^6	760	1090	64.31
high	9.01	47.35×10^6	2815	1105	64.11

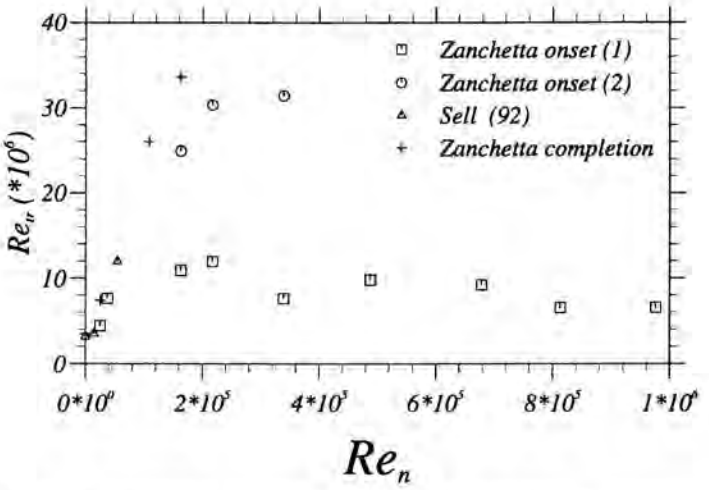

Figure 1: Transition Reynolds number versus nose Reynolds number.

Model

The basic model geometry is a five-degree semi-angle cone. A selection of interchangeable hemi-spherically blunted noses is used to obtain Re_n from 0 (nominally sharp) to 1 million. The model is equipped with 65 thin film gauges aligned along a generatrix of the cone. Prior to and during the run, the temperature evolution is sampled and stored digitally at 125 kHz and successively convoluted to obtain the time-resolved heat-transfer rate using the expression of Cook & Felderman (1966).

Transition in the pre-reversal regime

To illustrate the pre-reversal transition process, a test case with $Re_n = 2.4 \times 10^4$ has been selected. Time-resolved heat-transfer rates at five different streamwise locations in the laminar, transitional and turbulent regions are given in Fig. 2.

Gauge 02, located at the most upstream station, shows the typical laminar signal. The fluctuations arise mainly from digitisation and convolution noise. The boundary-layer edge properties at this location, as predicted by CFD, are given below:

s	δ	δ^*	θ	Re_{edge} (m^{-1})	M_e
0.361 m	2 mm	1.34 mm	0.07 mm	19.2 $\times 10^6$	7.69

At station 24, the appearance of transition events can be seen. Inspection of other time histories (which are not presented in Fig. 2) indicate that the first station at which the transition events are witnessed is gauge 06, (s = 0.385 m) giving Re_{tr}=4.73 $\times 10^6$. The high-frequency intermittent nature of the transition

process can be observed at gauge 34. Station 46 shows that the transition process is almost complete (other experiments show "stubborn regions" of laminar flow still persisting here). At the most downstream location (station 65) the boundary layer is believed to be fully developed turbulent. Again, inspection of time traces not included in Fig. 2, indicate that transition completion occurs at about gauge 60, $s = 0.69$ m, $Re_s = 8.47 \times 10^6$). In Fig. 3, the variation of time-averaged heat-transfer rate versus gauge location is given, together with the laminar CFD prediction. The mean heat-transfer rates can be seen to depart dramatically from the laminar trend given by the computation once the transition process begins, showing a local maximum (at $s = 0.6$ m) upstream of transition completion. Also of interest is the signal RMS, shown in Fig. 4. Although the inherent system noise has not been removed, the increase of signal RMS due to the onset of transition is obvious. The RMS reaches a certain peak value at a location corresponding to the steepest gradient in mean heat-transfer rate, thereafter decreasing to a turbulent RMS value greater than the laminar level. The intermittency distribution for this case, obtained using a threshold-type criterion, can be found in Fig. 5. The universal distribution based on the hypothesis of concentrated breakdown of Narasimha (1957) is also included in this plot. It is seen that it shows close agreement with the experimental data, except at the low levels of intermittency activity, where the experimental intermittency criterion is most prone to error. In Fig. 6, the PDF for selected gauges is given. The PDF for the "laminar" gauge (02) and the "turbulent" gauge (65) show a quasi Gaussian distribution, centred around the respective mean heating levels. The transitional gauges 24, 34 and 45 show the progressive re-arrangement of the PDFs with the advancement of the transition process.

Transition in the reversal regime

Visualisation experiments indicate that the reversal regime is characterised by sensitivity to roughness transition mechanisms. Experiments conducted with $Re_n = 1.08 \times 10^6$, illustrate the role of roughness in the hemispherical nose region. In Figs 7a and 7b, two liquid crystal visualisations are presented. In Fig. 7a, the nose region is polished to create a smooth surface and the boundary layer remains laminar over the entire model length ($Re_s > 3 \times 10^7$). In Fig. 7b, 50 μm mean diameter roughness elements are distributed uniformly over the nose region. Streak-like wake structures appear downstream of the sphere cone junction and undergo transition by $Re_s = 4 \times 10^6$. Heat-transfer measurements indicate that the turbulent events occurring in the reversal regime are characterised by a low-intermittency frequency (< 1 kHz).

The division between the pre-reversal and reversal regime is not distinct, and there exists a range of Re_n in which both mechanisms occur concurrently and "compete" to produce transition. In Fig. 8, the heat-transfer time trace for a "transitional gauge" can be seen. The nose Reynolds number is 1.26×10^5. Two types of transition events can be seen. The first are reversal regime events, marked X in Fig. 8, and originating in the nose and near nose region (x_{tb} in

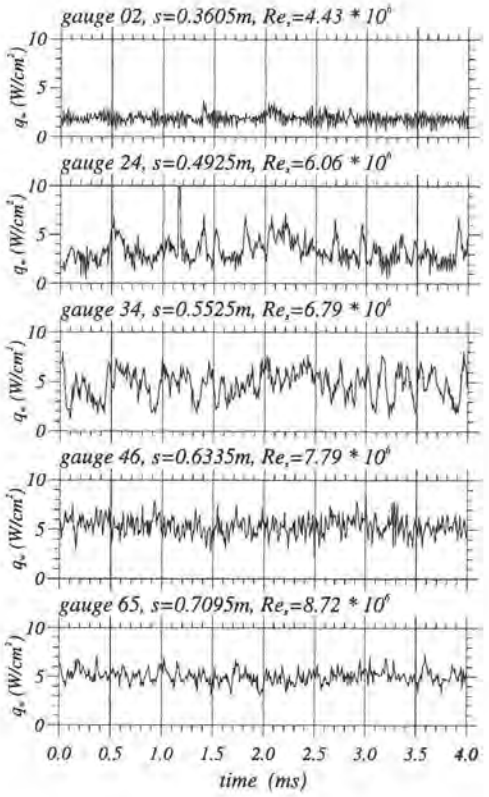

Figure 2: Time-resolved heat-transfer rates for five selected gauges, $Re_n = 2.4 \times 10^4$.

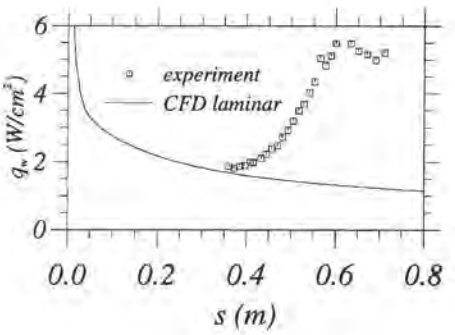

Figure 3: Time-average heat-transfer rate versus wetted distance, $Re_n = 2.4 \times 10^4$.

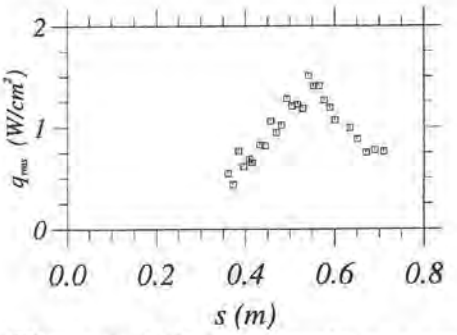

Figure 4: RMS heat-transfer rate versus wetted distance, $Re_n = 2.4 \times 10^4$.

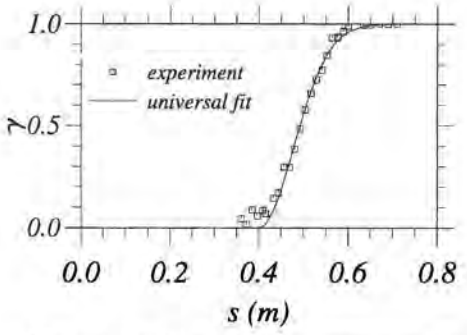

Figure 5: Intermittency versus wetted distance, $Re_n = 2.4 \times 10^4$.

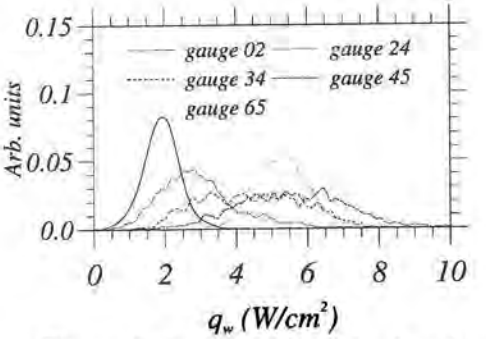

Figure 6: Probability density function, $Re_n = 2.4 \times 10^4$.

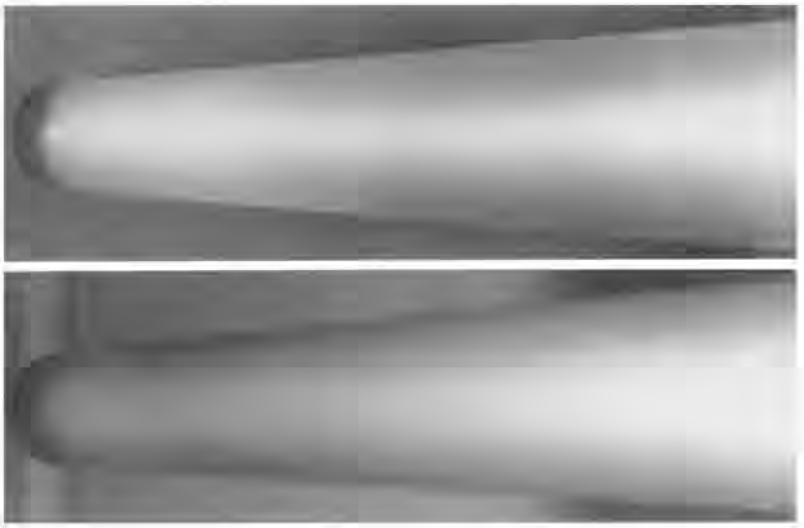

Figure 7: Liquid crystal visualisation, $Re_n = 1.08 \times 10^6$; (a) smooth nose, (b) rough nose.

Fig. 9). The second are transition spikes caused by the pre-reversal transition mechanism starting at x_{ts}. In this particular case, after the onset of the pre-reversal mode, (s = 0.4 m Re_s =16.8 $\times 10^6$; found by inspection of the time histories not presented here), transition occurs rapidly. The occurrence of this transition mode is also highlighted by an abrupt rise in the transition event passage frequency, Fig. 10, reaching a maximum in excess of 5 kHz at s = 0.52 m which is found to be the 50% intermittency location.

Reversal regime transition events

The reversal regime transition event with its characteristic low frequency (< 1 kHz) and large spatial scales (> 100 mm) is reasonably well resolved by the sensors and A/D equipment. For the Re_n=1.26$\times 10^5$ test case, the leading and trailing edge passage times for events have been tracked, using the time-history data, at 5 stations upstream of s = 0.4 m ($Re_s = 1.68 \times 10^7$). These are depicted in Fig. 11, and indicate for the leading and trailing edges speeds of 94% and 63% of the boundary layer edge velocity respectively. This information is included in the illustration of Fig. 12. Estimates for the mean-event convection speeds, evaluated using the cross-spectral density function and the correlation functions, are of 71% and 82% of the edge velocity respectively.

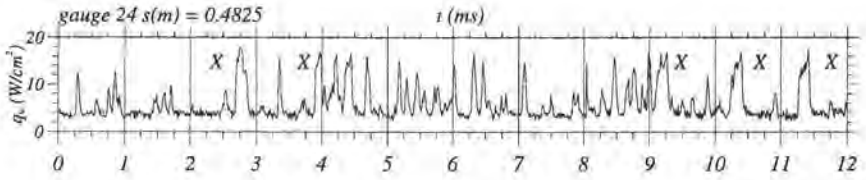

Figure 8: Time-resolved heat-transfer rates, gauge 24, $Re_n = 126,000$. X indicates reversal regime transition events.

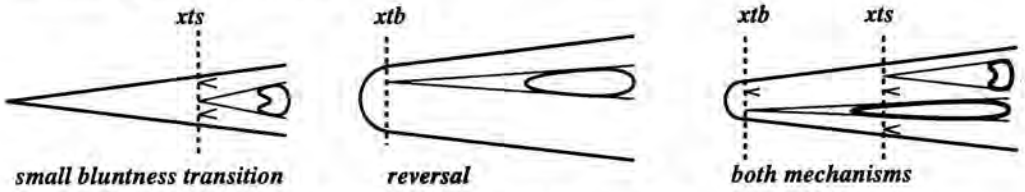

Figure 9: Schematics of transition dynamics.

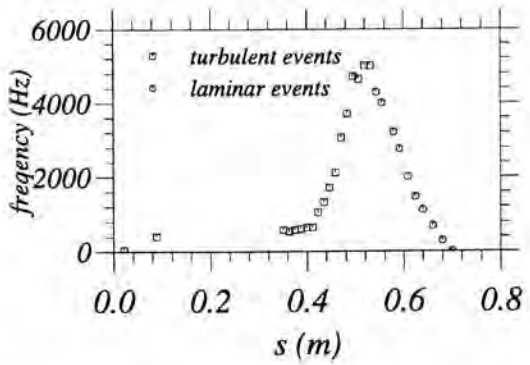

Figure 10: Turbulent event passage frequency versus wetted distance for $Re_n = 1.26 \times 10^5$.

Conclusion

In this paper, pre- and transition reversal regimes have been explored. The experiments indicate that transition in the pre-reversal is characterised by the breakdown of the laminar boundary layer at some streamwise location. Transition completion occurs by a high-frequency formation and subsequent growth of turbulent events. Increasing Re_n moves the point of breakdown further downstream. In the reversal regime, low-frequency turbulent events are formed in the nose and near nose region. The formation rate (spatial and temporal) is dependent on the severity of the roughness environment in the hemispherical nose region. The "reversal" event has a streamwise length in excess of 100δ and leading and trailing edge speeds of 94% and 63% of the edge velocity respectively.

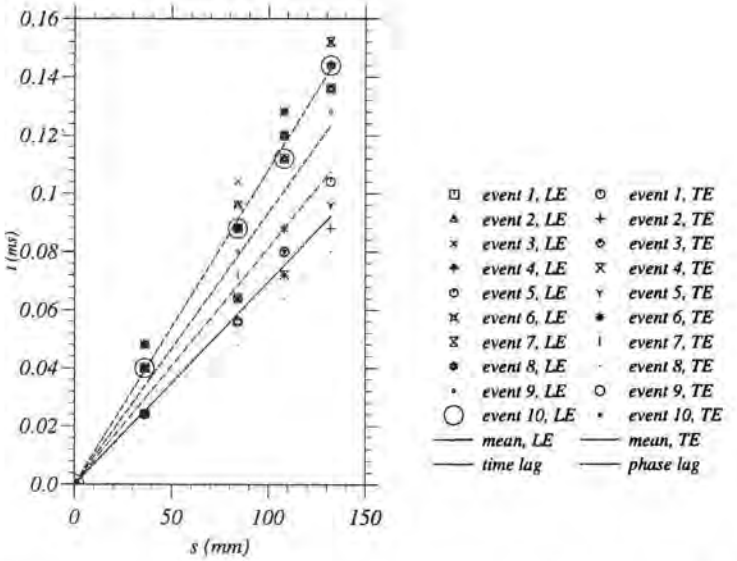

Figure 11: Transition event trajectories. Data obtained at five stations for the $Re_n = 1.26 \times 10^5$ test case.

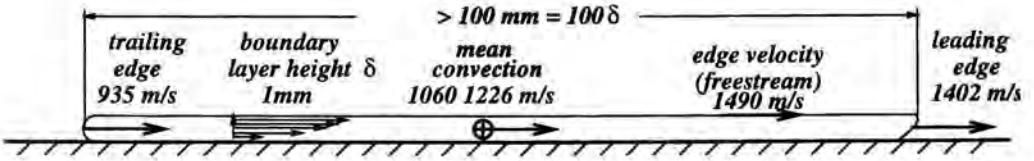

Figure 12: Quasi one dimensional illustration of a turbulent event.

Acknowledgements

This work was funded by the Defence Research Agency. The authors wish to thank Mr. S. Johnson and Mr. R. Hutchins of Imperial College and acknowledge the support and guidance of Dr. T. Caine, Dr. M. Collyer, Dr. M. Gilmore and Dr. I. Wrisdale of DRA Farnborough.

References

Cook, W.J. & Felderman, E.J. 1966 – Reduction of data from thin film heat transfer gauges. A concise numerical technique. *AIAA* 4, 561-562.

Narasimha, R. 1957 – On the distribution of intermittency in the transition region of a boundary layer. *J. Aer. Sci.* bf 24, 711-712.

Sell, M. 1992 – Hypersonic blunt cone aerodynamics. *Ph.D. thesis University of London.*

Authors' address

Department of Aeronautics, Imperial College of Science,
Technology and Medicine. SW7 2BY, London, U.K.

V. Wendt

Experimental Investigation of Instabilities in Hypersonic Laminar Boundary-Layer Flow

Abstract

Hot-wire measurements are made in the laminar boundary layer of a flat plate and a cone at Mach 5. These measurements do not show the expected dominance of high-frequency second-mode instabilities, predicted by linear stability theory and found in other experiments. The growth of natural disturbances within a broad frequency band up to 50 kHz on the flat plate and up to 200 kHz on the cone can be observed.

Introduction

To develop an understanding of the physical processes involved in laminar-turbulent transition in hypersonic boundary-layer flows it is necessary to perform detailed boundary-layer stability experiments, rather than obtaining only the transition location.

The most detailed hypersonic boundary-layer stability experiments are conducted by Stetson *et al.* (1992) on a cone at a free-stream Mach number of 8. These investigations show a distinct dominance of second-mode instabilities. The measured amplification rates of second-mode instabilities are in good agreement with theoretical results recently obtained by e.g. Simen (1993) and Simen, Kufner & Dallmann (1993) using Thin Layer Navier Stokes solutions for the basic flow and local stability analysis with conical metric for the instability analysis. In contrast, measurements in the laminar boundary layer of a flat plate by Kendall (1975) and Wendt, Simen & Hanifi (1995) and for a hollow cylinder by Stetson *et al.* (1991) do not show the expected dominance of high-frequency second-mode instabilities. However, the growth of natural disturbances with rather low frequencies, partly growing in a frequency band that was predicted to be stable by linear stability theory, can be observed. It has to be determined whether the discrepancy between linear stability theory and planar boundary-layer instability experiments is a feature of the planar boundary layer or whether other effects (e.g. a noisy wind-tunnel characteristic) are responsible for the differences mentioned above.

Figure 1: Experimental setup showing the flat plate and the cone both with mounted hot-wire probes in the Ludwieg tube.

Experimental apparatus

Wind tunnel

The experiments are conducted in the Ludwieg-tube wind tunnel of DLR Göttingen. The range of possible test Mach numbers is $M_\infty \approx 3$ to $M_\infty \approx 12$, and the Reynolds number can vary between $Re_\infty/l \approx 1.5 \times 10^6$ m^{-1} and $Re_\infty/l \approx 80 \times 10^6$ m^{-1}. A detailed description of the facility and its operational characteristics is given by Ludwieg *et al.* (1969).

Models

For the boundary-layer investigations a flat plate and a cone are used. The aluminum flat plate is 300 mm long and 10 mm thick, and it spans the full test section width of 500 mm. The sharp leading edge has a bevel angle of 11.6°. The cone is 500 mm long with a half angle of 7° and a sharp tip. The cone is made of steel and has a wall thickness of 5 mm. The nose is exchangeable, and the frustum can be divided in two parts allowing further instrumentation inside the cone. Fig. 1 shows the experimental setup of the flat plate and the cone with mounted hot-wire probes in the Ludwieg tube.

Test conditions

The Mach number for all the experiments presented here is $M_\infty \approx 5$. For the boundary-layer measurements on the flat plate and on the cone almost constant charge conditions of $p_{t,0} \approx 5$ bar and $T_{t,0} \approx 110$ °C are used, which results in a unit Reynolds number of $Re_\infty/l \approx 7.5 \times 10^6$ m^{-1}. In the case of the cone the Reynolds number at the boundary-layer edge is $Re_{\infty,e}/l \approx 9.3 \times 10^6$ m^{-1}.

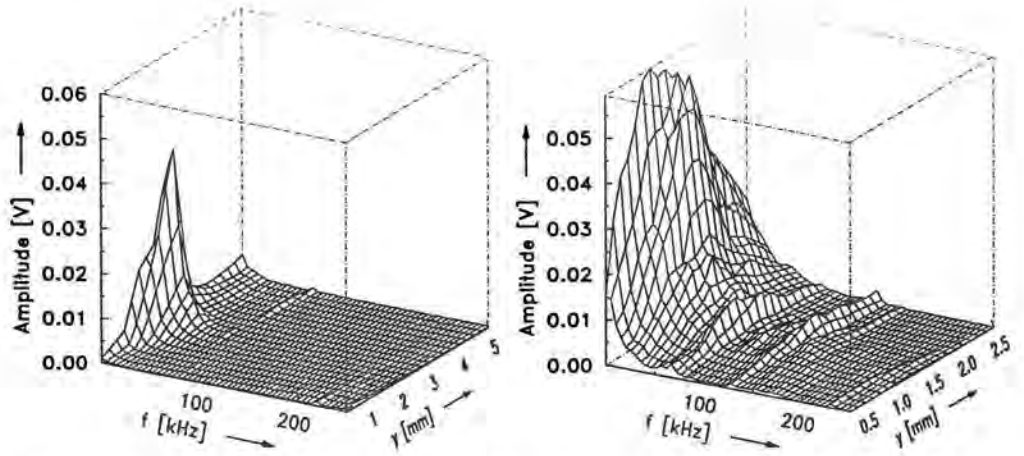

Figure 2: Disturbance amplitude spectra for the flat plate (left, R=995) and the cone (right, R=1950) as a function of the wall distance.

Hot-wire anemometry

For the measurements a single wire probe with a tungsten wire of 1.25 mm length and 5 μm diameter is operated by a constant temperature anemometer. In all the experiments the wire is operated at a high overheat ratio to assure that the wire is mainly sensitive to mass-flow fluctuations (Kovásznay, 1950; Morkovin, 1956). This is proved by a wire calibration in the free stream of the Ludwieg tube at different stagnation temperatures, while keeping the stagnation pressure constant. This calibration cannot be used for the boundary-layer measurements, since the different temperatures and mass flows -according to the boundary-layer profiles- cannot be resolved by a single-wire probe.

Results

The unit Reynolds number in the flat plate experiments is $Re_\infty/l = 7.5 \times 10^6$ m^{-1}, which results in local Reynolds numbers ranging from $Re_x \approx 0.4 \times 10^6$ ($R \approx 650$) to $Re_x \approx 1.7 \times 10^6$ ($R \approx 1300$). In the cone experiments the unit Reynolds number is $Re_\infty/l \approx 9.3 \times 10^6$ m^{-1}, which results in local Reynolds numbers from $Re_x \approx 0.7 \times 10^6$ ($R \approx 840$) to $Re_x \approx 4.4 \times 10^6$ ($R \approx 2100$). At a fixed unit Reynolds number the range of the local Reynolds number is only dependent on the range of possible probe locations. Here R is the Reynolds number based on the local Blasius length, $R = \sqrt{Re_x}$.

The measurement of profiles in the laminar boundary layer of the flat plate and the cone reveals disturbance-amplitude profiles with a strong peak at approximately 75 % of the boundary-layer thickness. This peak is typical for an unstable laminar boundary layer. The boundary-layer profiles also show growing maximum disturbance amplitudes with increasing distance from the leading

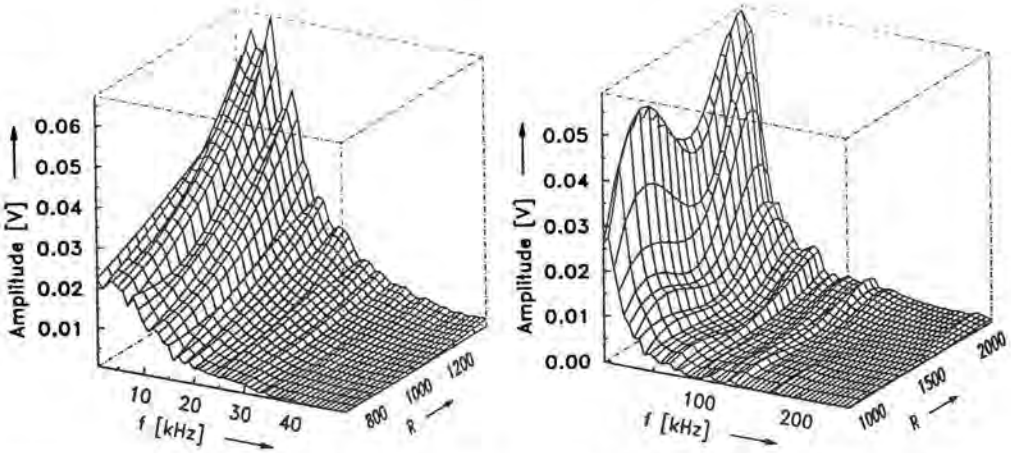

Figure 3: Maximum disturbance-amplitude spectra for the flat plate (left) and the cone (right) as a function of the nondimensional streamwise position.

edge of the flat plate and the tip of the cone, respectively. To obtain information about the frequencies contributing to the maximum disturbance amplitudes in the laminar boundary layer, fluctuation spectra are calculated and plotted against the distance normal to the wall, as shown in Fig. 2.

A broad frequency band up to an upper frequency limit of 50 kHz contributes to the peak of the disturbance amplitude for the flat-plate case. The region above 50 kHz, especially above 100 kHz, where linear stability theory predicts second-mode disturbances, does not contribute to the disturbance level significantly. In the case of the cone a broad frequency band up to an upper frequency limit of 200 kHz -what is in the first- and second-mode frequency range- contributes to the peak of the disturbance amplitude. In both cases the upper frequency limit slightly increases with increasing Reynolds number, but the difference between the flat plate and the cone case cannot only be explained by a Reynolds-number effect.

The fluctuation spectra at the peak positions of the disturbance amplitudes in the laminar boundary layer are calculated at different streamwise positions. These disturbance spectra are plotted against the dimensionless free-stream position R in Fig. 3.

For the flat-plate case one can clearly observe a growth of disturbance amplitudes with increasing streamwise position R in the significant frequency range. For the cone the behaviour of the disturbance amplitudes is a little different: After a first increase of the maximum disturbance amplitude with increasing streamwise position it slightly decreases in the region between $R \approx 1200$ and $R \approx 1500$ to increase again further downstream. This slight decrease of the maximum disturbance amplitude cannot yet be explained. One possible cause might be measurement uncertainties. Another possible cause might be nonlinear instability effects. Calculations with nonlinear stability theory (which is not yet

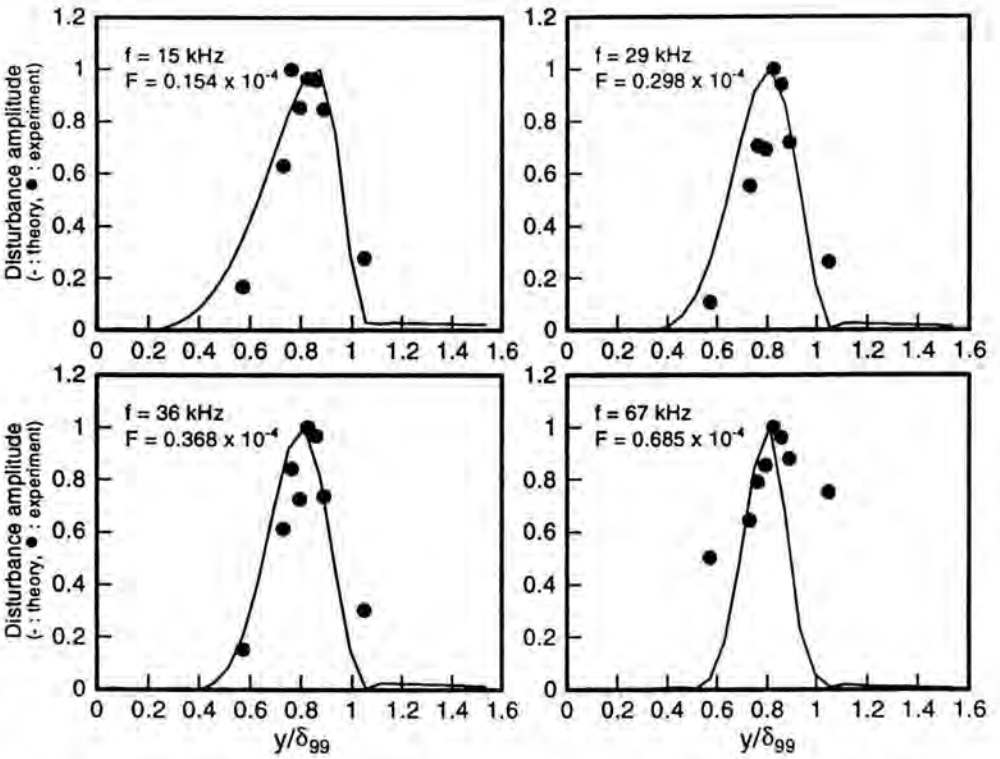

Figure 4: Profiles of experimental and theoretical, band-limited, disturbance amplitudes for various frequencies ($\Delta f = 500$ Hz, $R = 1050$, flat-plate case).

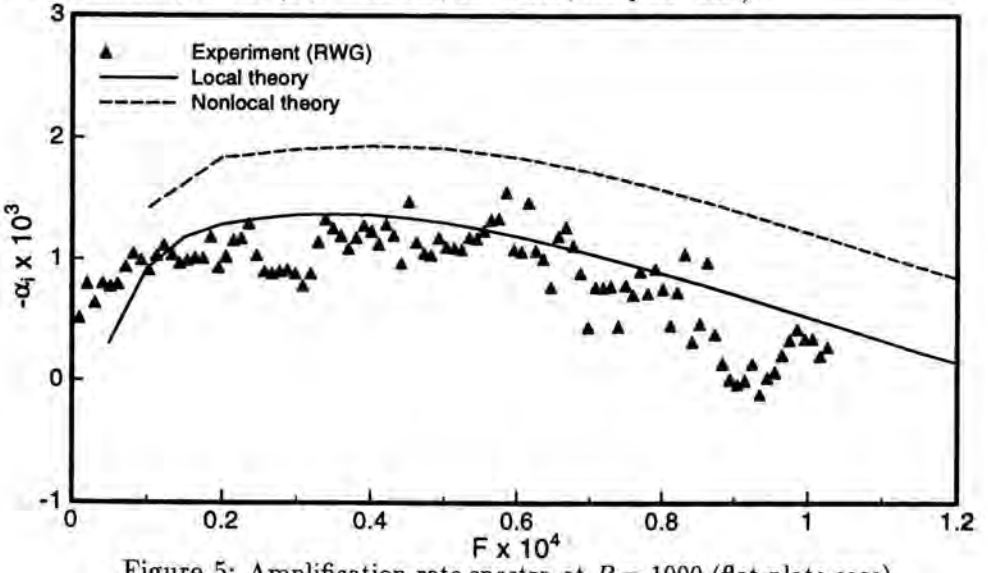

Figure 5: Amplification-rate spectra at $R = 1000$ (flat-plate case).

available) might give an answer regarding whether this is a reasonable explanation.

Finally, some results of further data analyses are presented for the flat-plate case only.

At the local Reynolds number $R = 1050$ the band-limited ($\Delta f \approx 500$ Hz) disturbance amplitudes are computed and compared with theoretical results obtained by Simen & Hanifi (1994, private communication). They carry out a nonlocal linear instability analysis based on maximum amplified mass flow fluctuations and obtain amplitude profiles for four different frequencies. In Fig. 4 results of this comparison are shown.

The location of the maximum values is in close agreement for all frequencies, although the boundary-layer thickness in the experiment can only be determined within an uncertainty of $\Delta y/\delta = \pm 0.05$. The shapes of the disturbance-amplitude profiles, i.e. the form of a sharp peak near the boundary-layer edge, also closely agree. Only for $f = 67$ kHz the experimentally determined profile is significantly wider than the theoretical one. As already mentioned, in the frequency range above 50 kHz the maximum values in the spectra of the anemometer voltage are in the range of the free-stream disturbance amplitudes. Hence the boundary-layer mass-flow fluctuation profiles may be contaminated by free-stream noise, which would explain the deviation from theory.

The comparison of experimental and theoretical results in Fig. 5 shows good agreement of amplification-rate spectra from the experiment and local instability analysis for a Reynolds number of $R \approx 1000$. Since the theoretical data represent the amplification of oblique first-mode instability waves, the experimentally observed disturbance growth can be regarded as an amplification of oblique first-mode instabilities.

It is surprising that the nonlocal instability analysis, which additionally takes into account the variation of the basic and disturbance flow in the direction of the spatial amplification, and thus models the experimental conditions more completely than the local analysis, consistently yields higher amplification rates than the experiment. On the theoretical side this might be explained by the use of similarity profiles for the modeling of the basic flow. Thus the effect of interaction of the viscous boundary-layer flow with the inviscid free-stream is not taken into account. With this effect included, the theoretical amplification rates are reduced, as the interaction yields a negative pressure gradient in free-stream direction, which is known to stabilize first-mode waves (see Simen, 1993).

Conclusions

Hot-wire measurements inside of the laminar boundary layer on a flat plate and a sharp cone show disturbance amplitude profiles with a maximum at approximately 75 % of the boundary-layer thickness. This type of disturbance-amplitude profiles is typical for unstable hypersonic boundary layers. But the expected dominance of a high-frequency disturbance growth, as predicted by linear stability theory, cannot be confirmed. Only streamwise growth of natural disturbances

within a broad frequency band up to 50 kHz and 200 kHz for the flat plate and the cone respectively, can be observed. Hence, lower frequency disturbances seem to dominate the transition process of the hypersonic flat-plate boundary-layer flow in the Ludwieg tube.

A main result of the comparison between fluctuation measurements within the hypersonic flat-plate boundary-layer flow and a local or nonlocal instability analysis is that the experimentally observed disturbance growth can be regarded as an amplification of oblique first-mode instability waves.

Amplified disturbances can be identified for the cone in the unstable first and second mode frequency range, but no dominance of amplified high-frequency second-mode disturbances is found in the experiments.

References

Kendall, J. M. 1975 – Wind tunnel experiments relating to supersonic and hypersonic boundary-layer transition, *AIAA J.* **13**, 290-299.

Kovásznay, L. S. G. 1950 – The hot-wire anemometer in supersonic flow, *J. Aeronautical Sciences* **17**, 565-572.

Ludwieg, H., Grauer-Carstensen, H. & Hottner, Th. 1969 – Der Rohrwindkanal der Aerodynamischen Versuchsanstalt Göttingen, Jahrbuch 1969 der DGLR, 52-58.

Morkovin, M. V. 1956 – Fluctuations and hot-wire anemometry in compressible flows, AGARDograph 24.

Stetson, K. F., Thompson, E. R., Donaldson, J. C. & Siler, L. G. 1991 – A comparison of planar and conical boundary-layer stability and transition at a Mach number of 8, AIAA Paper, 91-1639.

Stetson, K. F. & Kimmel, R. L. 1992 – On hypersonic boundary-layer stability, AIAA Paper, 92-0737.

Simen, M. 1993 – Lokale und nichtlokale Instabilität hypersonischer Grenzschichtströmungen, DLR FB 93-31.

Simen, M., Kufner, E. & Dallmann, U. 1993 – *Effects on transition of hypersonic flows based on local and nonlocal instability analysis*, AIAA Paper 93-5143.

Wendt, V., Simen, M. & Hanifi, A. 1995 – An experimental and theoretical investigation of instabilities in hypersonic flat plate boundary layer flow, *Phys. Fluids* **7**, 877 - 887.

Author's address

DLR, Institut of Fluid Mechanics,
Bunsenstrasse 10, 37073 Göttingen, Germany

A.D. Kosinov, N.V. Semionov & Yu.G. Yermolaev

Laminar-Turbulent Transition of a Supersonic Boundary Layer on a Flat Plate

Abstract

Experimental data are presented for the nonlinear development of 3-D artificial disturbances in a supersonic boundary layer on a flat plate at Mach numbers 2 and 3. The excitation of high frequency disturbances is observed.

Introduction

Nonlinear stability experiments in hypersonic and supersonic boundary layers were recently started. Kendall & Kimmel (1990) examined the development of natural disturbances in a hypersonic boundary layer and found nonlinear interacting fluctuations. Studying the development of artificial disturbances Kosinov *et al.* (1994a) have shown that subharmonic resonance takes place in supersonic boundary layers. Up to now experiments and nonlinear theory have developed quite independently. Recently a theoretical model of subharmonic resonance relevant to experiments (Kosinov *et al.*, 1994a) was developed by Tumin (see Kosinov & Tumin, 1995). Theoretical work by Chang & Malik (1994) reveals the growth of a streamwise vortex, but this was not yet tested experimentally. Gaponov *et al.* (1995) found a new experimental feature for the nonlinear stability of the supersonic boundary layers: the transformation of wave spectra from three- to two-dimensional disturbances occurs for increasing Reynolds number. Parametric generation of sound waves at $M = 2$ was indicated by Ermolaev *et al.* (1995). The main goal of the present paper is a discussion of nonlinear excitation of high frequency disturbances in the supersonic boundary layer.

Experimental equipment

The experiments were performed in the supersonic wind tunnel T-325 of the Institute of Theoretical and Applied Mechanics of the Siberian Division of the Russian Academy of Sciences. The test section dimensions are $200 \times 200 \times 600$ mm^3. Measurements were carried out in the boundary layer of a flat plate at Mach numbers 2 and 3. The model was 10 mm in thickness, 450 mm in length and 200 mm in width. The leading edge had an angle of 14.5° and its thickness was $b = 0.02$ mm. The flat plate was mounted at zero angle of attack. Artificial disturbances in the boundary layer were generated by a localized periodic source using an electrical discharge technique, as described by Kosinov *et al.*

(1994a) and Gaponov *et al.* (1995). The disturbances from the discharge chamber penetrated into the flow through a small hole in the plate surface. The diameter of the hole was 0.42 mm. The coordinates of the disturbance source were $x = 38$ mm, $z = 0$ mm, where x is the flow direction and z is the transversal direction. The perturbation is described by Kosinov *et al.* (1994b). The disturbances in the flow were registered with a constant-temperature anemometer. The probes were constructed from tungsten wires of 5 μm in diameter and 0.7 or 1.2 mm in length. To measure the dominant fluctuations in the mass flow, we gave the wire an overheating equal to 0.8. As the diagram for the amplitude of the disturbances is linear in the boundary layer, the following relation, based on Kovasznay's method, was used to estimate the fluctuations in the mass flow:

$$\rho u' = \frac{e}{E} K_{exp}, \tag{1}$$

where e is a measured fluctuation signal and E is a mean voltage of the hot-wire bridge. To calculate $K_{\exp}$ an approximation $< \rho u >' / < T_0 >' = const.$ for $Re_1 = const.$ was used. Here $< T_0 >'$ is the total r.m.s. value of the temperature fluctuation in the boundary layer. In this case we can define the mass flow fluctuations as it was indicated above. Using a traversing gear, the probe was moved in x, y, and z directions (where y is the coordinate normal to the flat plate). The coordinates of the hot-wire were measured in steps of 0.1 mm for x and z and 0.01 mm for y. Signals from the hot wire were recorded by a 10 bit, 1 MHz A/D converter. To improve the signal-to-noise ratio in the experiments, we used a synchronous summation of 500 digital diagrams on 400 points for $M = 2$ and 200 points for $M = 3$. The measurements of the wave train development were performed at $y/\delta \approx 0.5$ for $M = 2$, where the fluctuations reached a maximum. To define the disturbance spectra, the discrete Fourier transformation was used (see *e.g.* Ermolaev *et al.*, 1995). To measure the transition location, we used the hot-wire technique.

Results

Below we present data for the transition measured for $M = 2$ and discuss the initial development of the wave trains close to the source hole at $M = 3$. Fig. 1 shows the measured transition for $M = 2$. Here $Re = Ux/\nu$ is the Reynolds number. The measurements have been performed in the boundary layer at $y = 0.2$ mm, $z = 0$ and for different unit Reynolds numbers, (1) $Re_1 = 6.7 \times 10^6$, (2) 11.6×10^6 and (3) 18.6×10^6 m^{-1} (where $Re_1 = U/\nu$). These measurements were performed at different noise levels in the test section. The noise level was about 0.1% of the fluctuations in the mass flow for $Re_1 = 6.7 \times 10^6$ m^{-1}, about 0.07% for $Re_1 = 11.6 \times 10^6$ m^{-1} and about 0.09% for $Re_1 = 18.6 \times 10^6$ m^{-1}. (The noise level includes electronic noise of the hot-wire anemometer.) The transition data correlate with the changing noise level in the test section of the wind tunnel. To study the wave train development we have used conditions where the initial amplitude of the artificial disturbances was sufficiently small to

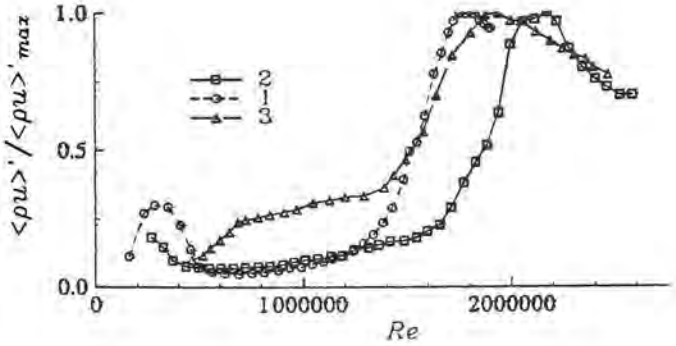

Figure 1: Transition data on a flat plate at $M = 2$. Here $< \rho u >'$ is the total r.m.s. of the mass flow fluctuations.

have the transition region close to the natural disturbance case at $Re_1 = 6.7 \times 10^6$ m^{-1} and $M = 2$ (Ermolaev *et al.*, 1995).

On disturbance excitation close to the localized source at M=3

The background of this experiment were data obtained by Balakumar & Malik (1992). Figs 2 and 3 show the results of measurements of the disturbance magnitude near to the source at $Re_1 = 11.2 \times 10^6$ m^{-1}. The measurements were performed with a variable x step from 0.5 to 3 mm. Fig. 2 presents the three-dimensional surface of the averaged fluctuations in the mass flow, $\rho u'(t)$ in x-direction at $z = 0$. These data show the evolution of excited disturbances for $x > 29$ mm. Note that the measurements were carried out at $y/\delta = const$ for $x > 38$ mm (that corresponds to the maximum fluctuation in the boundary layer) and at $y = const$ for $x < 38$ mm. Artificial disturbances propagate downstream from the source (with the coordinate of the source at $x \approx 38$ mm). This can be seen in Fig. 3 where $\rho u'(t)$ is shown for different x. Curve 1 and 2 correspond to positions upstream from the source ($x = 29$ and 33 mm), and 3 and 4 to positions downstream from the source at $x = 38.9$ and 41 mm. The disturbances are very small at $x = 29$ mm only. The results confirm the data obtained by Kosinov *et al.* (1992) on the upstream spread of disturbances from the localized source in the supersonic boundary layer. Similar results were observed in the free stream as described by Semionov *et al.* (1996).

On nonlinear excitation of high frequency disturbances in a supersonic boundary-layer at M = 2

It is well known that high-frequency disturbances appear at the laminar-turbulent transition in boundary layers (Morkovin, 1991; Kachanov, 1994). In our previous experiments we did not obtain data that indicate the existence of high-frequency fluctuations because the Reynolds numbers were too low. In this paper we

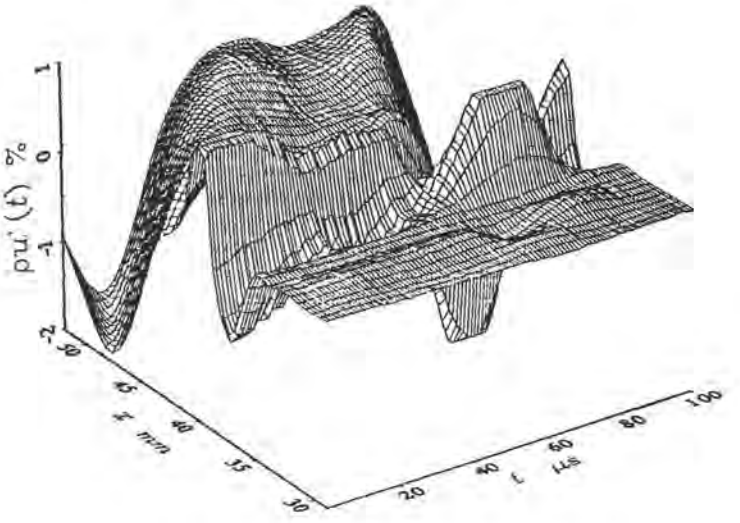

Figure 2: Fluctuations close to localized source; $M = 3$, $Re_1 = 11.2 \times 10^6$ m^{-1}.

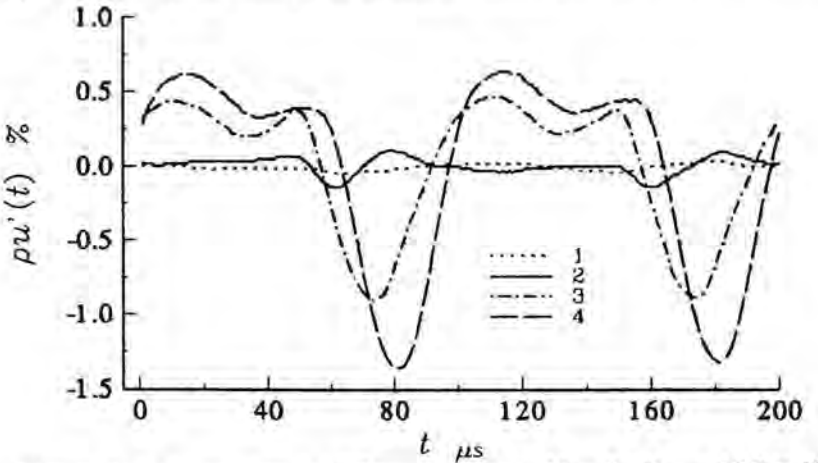

Figure 3: Fluctuations at different stations; $M = 3$, $Re_1 = 11.2 \times 10^6$ m^{-1}.

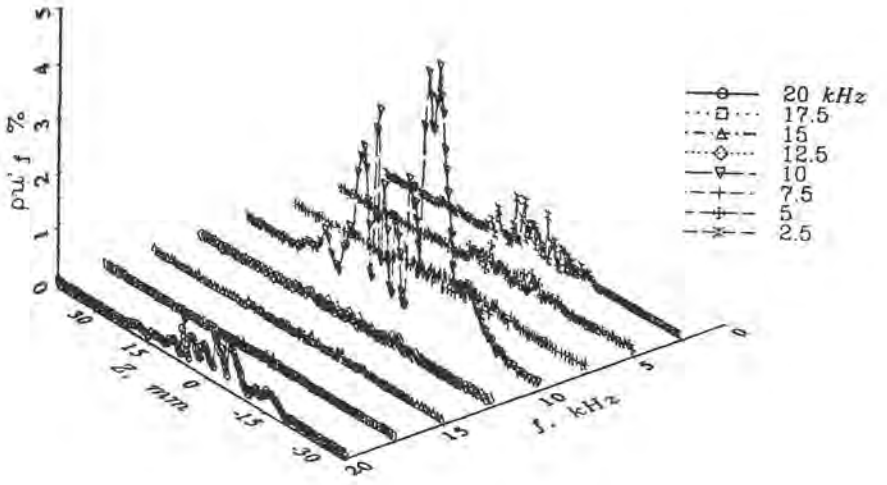

Figure 4: Amplitude distributions at $x = 179$ mm, $f = \text{const}$, $M = 2$.

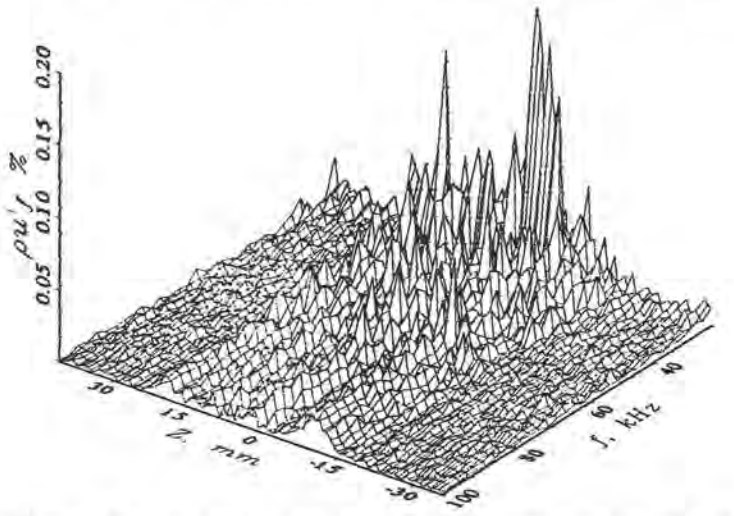

Figure 5: Amplitude distributions at $x = 179$ mm for $M = 2$.

present data on the excitation of high-frequency and low-frequency, nonlinear disturbances in the supersonic boundary layer at increasing Reynolds number. The experiment was made at $M = 2$ and $Re_1 = 6.71 \times 10^6\ m^{-1}$ and had the same set up as in Kosinov *et al.* (1994a). Figs 4 and 5 show the amplitude spectra of the mass-flow fluctuations induced by artificial disturbances over z at $x = 179$ mm. Fig. 4 shows the low-frequency part and Fig. 5 shows the high-frequency part of the spectra. Subharmonic disturbances of $f = 10$ kHz predominate as described in Gaponov *et al.* (1995), but disturbances from 2.5 kHz to 100 kHz with step 2.5 kHz are observed too. The used averaging method can only detect fluctuations that are correlated with the disturbances in the experiments. The excitation of the low-frequency disturbances at $f = 2.5$, 5, 7.5 kHz may be due to a secondary subharmonic amplification as the primary fundamental disturbances ($f = 20$ kHz) decrease according to the linear stability theory and the primary subharmonic amplification probably is insufficiently strong. However the primary subharmonic disturbances ($f = 10$ kHz) may put on the secondary subharmonic amplification, which could then explain the excitation of low-frequency fluctuations. It is difficult to explain the excitation of high-frequency fluctuations. Perhaps their appearance is caused by a nonlinear mechanism or by interaction of Mach waves in the boundary layer. Those Mach waves may be excited at the leading-edge angle of the flat plate through reflections on the wind tunnel walls. Figs 6 and 7 show wave spectra over β. Fig. 6 presents the low-frequency part of the f, β-spectra and Fig. 7 shows the high-frequency part. We have found a phase synchronism of the disturbances at $-0.8 < \beta < 0.8$ rad/mm and for $f > 30$ kHz. A more detailed processing of the fluctuations in future research may explain this behaviour because the transient wave packets are clearly observed at each period in the diagrams (with the period almost equal to the period of the subharmonic disturbances), whereas there are also low-frequency modulations in the realizations.

Conclusions

Our experiments in the supersonic boundary layer show the development of wave trains including: linear growth, subharmonic amplification, subharmonic sound radiation, secondary subharmonic amplification, and high-frequency harmonic excitation. One of the main aims of studying laminar-turbulent transition in conventional supersonic wind tunnels is to find the influence of sound waves on the initiation of waves and transition within the boundary layer. The nonlinear interaction of sound waves radiated by the turbulent boundary layers on the wind tunnel walls and the development of nonlinear wave trains in the supersonic boundary layer will be investigated in future experiments. It might be that the parametric resonance interaction of sound waves and nonlinear vortex waves in the supersonic boundary layer is the main cause of early laminar-turbulent transition in conventional wind tunnels.

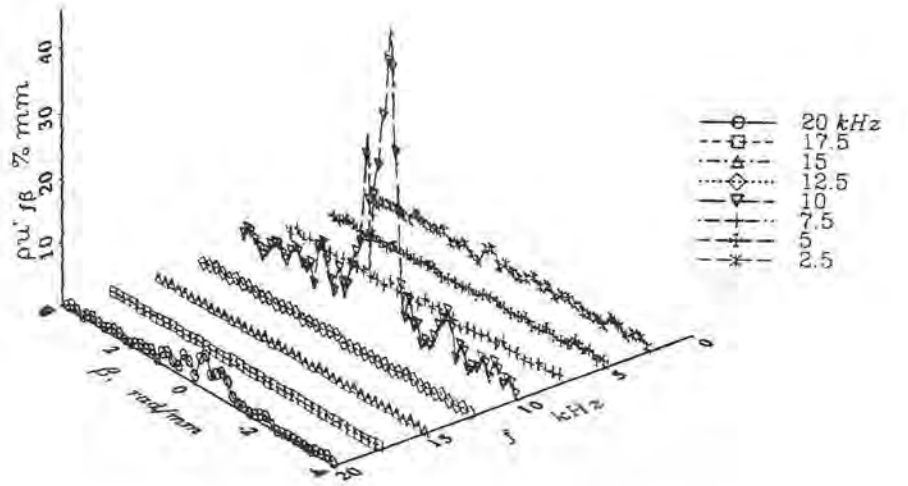

Figure 6: Amplitude of the β-spectra at $x = 179$ mm, $f = \text{const}$, $M = 2$ and $Re_1 = 6.71 \times 10^6$ m^{-1}.

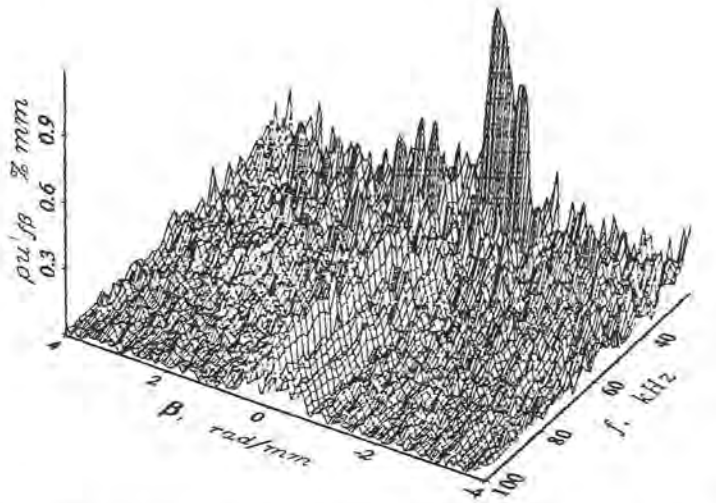

Figure 7: Amplitude of the β-spectra at $x = 179$ mm, $M = 2$ and $Re_1 = 6.71 \times 10^6$ m^{-1}.

Acknowledgements

This work has been supported in part by the International Science Foundation grants NQZ000, NQZ300 and the Russian Fundamental Research Foundation grants 94-01-00052-a, NQZ300.

References

Balakumar, P. & Malik, M.R. 1992 – Discrete modes and continuous spectra in supersonic boundary layers. *J. Fluid Mech.* **239**, 631-656.

Chang, C.L. & Malik, M.R. 1994 – Nonlinear stability of a Mach 1.6 flat plate boundary layer. In: Nonlinear Instability of Nonparallel Flows (S.P. Lin, W.R.C. Phillips and D.T. Valentine eds). Springer-Verlag, Berlin, pp. 232-241.

Ermolaev, Yu.G., Kosinov, A.D. & Semionov, N.V. 1995 – Experimental investigation of laminar-turbulent transition process in supersonic boundary layer using controlled disturbances. In: Nonlinear Instability and Transition in 3D Boundary Layers (to be published in Proceedings IUTAM Symposium, Manchester, UK, 1995).

Gaponov, S.A., Kosinov, A.D., Maslennikova, I.I., Semionov, N.V. & Shevelkov, S.G. 1995 – Nonlinear development of waves in the supersonic boundary layer. In Laminar-Turbulent Transition (R. Kobayashi ed.). Springer-Verlag, Berlin, pp. 181-188.

Kachanov, Yu.S. 1994 – Physical mechanisms of laminar-boundary-layer transition. *Ann. Rev. Fluid Mech.* **26**, 411-482.

Kendall, J.M. & Kimmel, R.L. 1991 – Nonlinear disturbances in hypersonic laminar boundary layer. *AIAA* Paper. 91-0320.

Kosinov, A.D., Semionov, N.V. & Shevelkov, S.G. 1992 – Special features of generation and development of a harmonical wave in supersonic boundary layer. In: Recent Advances in Experimental Fluid Mechanics (F.G. Zhuang ed.). IAP, Beijing, pp. 53-58.

Kosinov, A.D., Semionov, N.V., Shevelkov, S.G. & Zinin, O.I. 1994a – Experiments of the nonlinear instability of supersonic boundary layers. In: Nonlinear Instability of Nonparallel Flows (S.P. Lin, W.R.C. Phillips and D.T. Valentine eds). Springer-Verlag, Berlin, pp. 196-205.

Kosinov, A.D., Semionov, N.V. & Shevelkov, S.G. 1994b – Investigation of supersonic boundary layer stability and transition using controlled disturbances. In: Proceedings of ICMAR-7, Part 2 (A.M. Kharitonov ed.). Russia, Novosibirsk, pp. 159-166.

Kosinov, A.D. & Tumin, A. 1995 – Resonance interaction of spatial wave packets in a supersonic boundary layer. In: Nonlinear Instability and Transition in 3D Boundary Layers. (to be published in Proceedings IUTAM Symposium, Manchester, UK, 1995).

Morkovin, M.V. 1991 – Panoramic view of changes in vorticity distribution in transition instabilities and turbulence. In: Boundary Layer Stability and Transition to Turbulence (D.C. Reda, H.L. Reed and R. Kobayashi eds). Vol. 114, Fluids Engineering Division, American Society of Mechanical Engineers, New York, pp. 1-12.

Semionov, N.V., Kosinov, A.D. & Maslov, A.A. 1996 – Experimental investigation of supersonic boundary layer receptivity. In: Transitional Boundary Layers in Aeronautics. See this volume.

Authors' address

Institute of Theoretical and Applied Mechanics
630090, Novosibirsk
Institutskaya 4/1, Russia

W. Eißler & H. Bestek

Wall-Temperature Effects on Transition in Supersonic Boundary Layers Investigated by Direct Numerical Simulations

Abstract

The effects of different wall-temperature conditions on laminar-turbulent transition in Mach 4.8 flat-plate boundary layers at flight conditions are investigated using spatial direct numerical simulations. Using radiation adiabatic wall temperature conditions, the simulations allow, for the first time, to calculate the realistic increase of the wall temperature caused by the fundamental-type transition process.

Introduction

Heat loads resulting from friction and compression of air represent a key problem of hypersonic flight. The wall temperature is determined by the heat balance between heat transfer to the surface due to aerothermal loads, heat radiated from the surface, and heat conducted within and stored in the vehicle structure. For the design of hypersonic vehicles, a good estimate of the resulting aerothermal loads and wall temperatures is of vital importance, which requires the accurate prediction of boundary-layer transition and turbulence. However, the existing transition prediction methods and turbulence models needed for this task still contain an unknown degree of uncertainty as detailed experiments do not exist for such flow conditions.

Transition to turbulence in supersonic and hypersonic boundary layers is still a poorly understood problem. While the first initial stage of the transition process, i.e. the growth of linear disturbances is adequately described by compressible linear stability theory (Mack, 1969; Mack, 1984), the subsequent nonlinear stages are widely unknown, as there is no guidance from experiments. Transition experiments in high-speed boundary layers are very difficult to perform. Therefore, linear stability theory is widely used to determine the important parameters affecting transition and their trends, that is, whether and how much a change of some parameter is stabilizing or destabilizing. In recent years, direct numerical simulations have shown their capability to be used as a new tool in high-speed transition research, as they can be applied in situations where experiments seem impossible to perform. This is demonstrated in the present paper for transition at flight conditions.

In the past several years many efforts have been made experimentally, theoretically, and numerically in order to gain a better understanding of supersonic

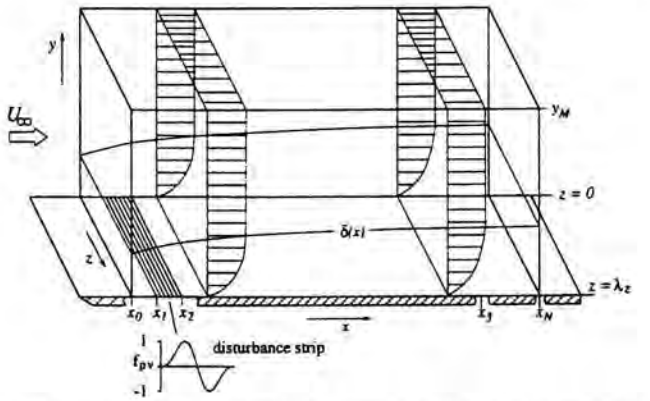

Figure 1: Sketch of the integration domain and the disturbance input.

transition, which is indispensable for the development of reliable transition prediction methods and turbulence models for compressible boundary layer flows. However, most of these studies were concerned with transition at wind-tunnel temperature conditions, aiming to understand and model the phenomena observed in a few detailed experiments. The effect of high temperatures on transition, as encountered by a hypersonic vehicle in the atmosphere, are still completely unknown.

In this paper, we present results from several simulations to study the effect of different wall-temperature conditions on transition in Mach 4.8 flat-plate boundary layers at flight conditions. The flat-plate is a representative model for the boundary-layer flow on a hypersonic aerospace plane at flight conditions at 25 km altitude. Using radiation adiabatic wall-temperature conditions the simulations allow, for the first time, to calculate the realistic streamwise increase of the wall temperature caused by the transition process.

Numerical model

Laminar-turbulent transition phenomena in a supersonic boundary-layer flow over a flat plate are investigated by spatial direct numerical simulations based on the complete, three-dimensional Navier-Stokes equations, the continuity equation, the energy equation, and the thermodynamic equation of state for a compressible perfect gas in equilibrium. The equations are used in conservative form for the variables $\rho, \rho u, \rho v, \rho w$ and ρe (Eißler & Bestek, 1995). The integration domain shown in Fig. 1 extends from $x = x_0$ to $x = x_N$ in the streamwise x-direction, with x_0 being the downstream distance from the leading edge of the flat plate. In the wall-normal y-direction, the integration domain extends from $y = 0$ to $y = y_M$ and typically covers several boundary-layer thicknesses. In the spanwise z-direction, the flow is assumed to be periodic with the domain extending from $z = 0$ to $z = \lambda_z$, where λ_z is a fundamental spanwise wavelength which can be chosen arbitrarily.

The governing equations are normalized with the freestream values of the velocity, the temperature, and the density. Furthermore the global Reynolds number $Re = \frac{\rho^\star_\infty u^\star_\infty L}{\mu^\star_\infty} = 10^5$ is used, where the superscript $\star$ denotes the dimensional quantities, and thus the local Reynolds number is defined as $Re_x = \frac{\rho^\star_\infty u^\star_\infty x^\star}{\mu^\star_\infty} = x \cdot Re$. The thermodynamic properties are approximated as a calorically perfect gas with a constant Prandtl number $Pr = 0.71$, a constant ratio of the specific heats $\kappa = 1.4$, and Sutherland's law for the dynamic viscosity μ. For all simulations discussed in this paper the freestream Mach number is $Ma = 4.8$.

Numerical method

The numerical method is based on an explicit Runge-Kutta scheme of fourth-order accuracy in time. In x- and y-direction finite-difference approximations of fourth-order accuracy are used, and in the spanwise z-direction, a spectral (Fourier) approximation is employed. The grid is equally spaced in the x- and y-directions.

The numerical procedure is decomposed into two steps: the calculation of a steady, two-dimensional, laminar boundary layer by solving the two-dimensional form of the governing equations (Eißler & Bestek, 1995), and the calculation of the evolution of two- and three-dimensional disturbances which are introduced into the laminar boundary layer by localized periodic blowing and suction through a narrow disturbance strip at the plate surface (see Fig. 1). The reaction of the boundary layer to this periodic forcing, i.e. the spatial downstream development of the disturbance waves, is then simulated numerically.

Similar to the linear stability theory (LST) and the PSE-method, the flow is decomposed into the steady, laminar base flow Φ_B and the disturbance flow Φ', which consists of steady and unsteady disturbances. This procedure allows for the calculation of two- and three-dimensional harmonic waves as well as for a steady mean-flow distortion, which represents the transitional mean deviation from the laminar boundary layer.

Boundary conditions

Boundary conditions have to be defined for the steady, laminar two-dimensional base flow as well as for the three-dimensional disturbance flow. For the disturbance flow, the boundary conditions have to be valid for high-frequency harmonics as well as for the steady mean-flow distortion.

At the *inflow boundary* $x = x_0$ an undisturbed steady base flow, as obtained from the solution of the compressible boundary-layer equations, is assumed. No disturbances are allowed here. At the *outflow boundary* $x = x_N$ the second derivatives with respect to x are set to zero for the base flow. For the disturbance flow, a procedure similar to the "relaminarization technique" developed by (Kloker, Konzelmann & Fasel, 1993) is used (Eißler & Bestek, 1995). At

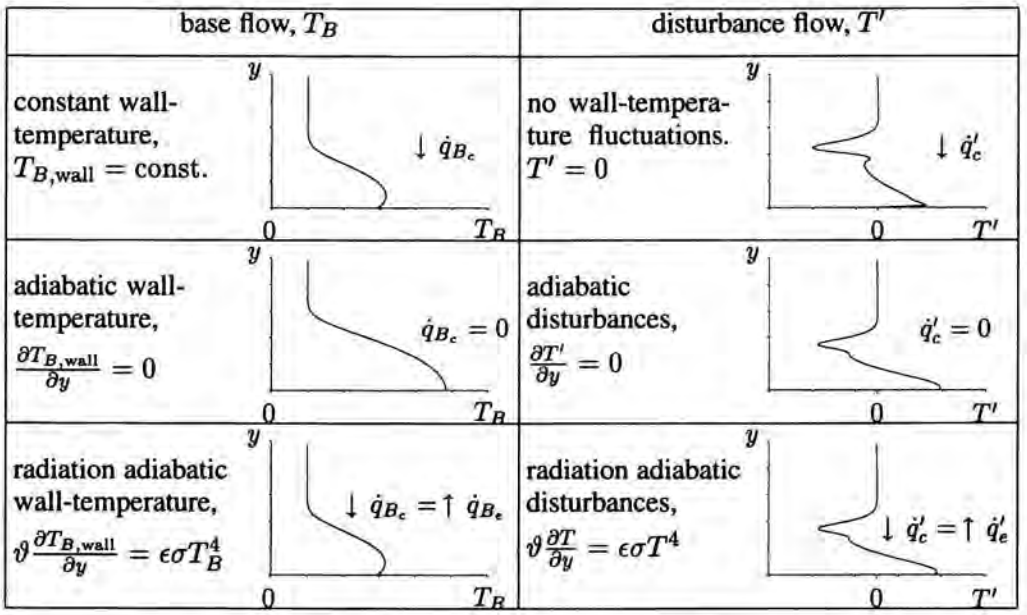

Figure 2: Shape of the temperature distribution for different wall temperature conditions for the base flow (left side) and for the disturbance flow (right side).

the *lateral boundaries* $z = 0$ and $z = \lambda_z$ the disturbances are assumed to be periodic with the spanwise wavenumber β. At the *freestream boundary* $y = y_M$ an inviscid flow is assumed. For the base flow as well as for the disturbance flow, non-reflecting characteristic conditions are used. At the *wall* $y = 0$ all velocity components are zero, the pressure is calculated from the y-momentum equation, density is determined from the equation of state, and internal energy is calculated from its definition.

No unique condition can be defined for the wall temperature, as we do not solve the Poisson heat equation within the wall, neither for the steady base-flow nor for the disturbance flow. Therefore, it is useful to know the temperature range that can occur principally. The conditions for the base flow and the disturbance flow are discussed separately, and are sketched in Fig. 2.

Without artificial heating, the maximum base-flow temperature is the recovery temperature of an adiabatic wall. For wind-tunnel experiments, the adiabatic-wall condition is often used. For a flight vehicle moving at Mach 5 in the atmosphere, the adiabatic wall temperature can reach some 1000 K. Of course, in reality wall heat conduction and radiation will lead to a cooled wall. These kinds of cooling can be approximated in the simulation by a constant wall temperature, or a radiation adiabatic wall, respectively.

For the disturbance flow, the situation becomes more difficult, as the wall-

temperature condition must be valid for the mean-flow distortion and the high-frequency disturbances. The condition almost always used, is the assumption of zero temperature disturbances at the wall. This condition seems to be reasonable as it is hardly conceivable that the wall temperature may fluctuate with frequencies in the order of 100 kHz. However, when applying this condition, the (mean) wall-temperature remains on its steady laminar value, even at the late stages of transition in DNS. This condition implies the largest temperature gradient that can be obtained at the wall and therefore the largest wall heat flux. In reality, this behaviour could be achieved by a wall with an infinite specific heat, where any heat flux does not affect the wall temperature. The opposite can be obtained using adiabatic temperature disturbances. Now, no heat flux penetrates into the wall but the temperature fluctuations are maximum. This would be true, if the the specific heat of the wall was zero. As a consequence, it is obvious that in reality the temperature condition must be somewhere between these two extremes, as neither the temperature fluctuations nor the heat flux should be zero at the wall.

A condition that contains both, temperature fluctuations and heat flux, is the radiation adiabatic wall. Here, the convective heat flux penetrating into the wall is equal to the radiative heat flux from the wall, and we get $\vartheta^\star \dfrac{\partial(T_B^\star + T^{\star\prime})}{\partial y^\star} = \epsilon\,\sigma\,(T_B^\star + T^{\star\prime})^4$, with the Stefan-Boltzmann constant σ, the emissivity constant ϵ of the surface and the thermal conductivity coefficient ϑ. The typical shapes of the temperature distributions in y-direction for the base flow and the disturbance flow, respectively, are plotted in Fig. 2 for the six boundary conditions discussed before.

Results

Effects of wall-temperature conditions

To investigate the effects of the wall temperature on transition, simulations were performed for four cases using different boundary conditions. In all cases, the freestream temperature was assumed to be $T^\star_{B,\infty} = 220$ K, corresponding to atmospheric conditions at 25 km altitude. The frequency of the forced disturbances was $F = 10 \cdot 10^{-5}$ and the integration domain was located inside the second-mode unstable region for that frequency. At the disturbance strip, a two-dimensional wave (mode (1,0)) and a pair of three-dimensional waves (mode (1,1)) were forced with the same frequency, in order to initiate the fundamental-type transition process. Here, the two- and three-dimensional disturbance components are denoted as modes (h, k), where h stands for the frequency in integer multiples of the fundamental frequency and k denotes multiples of the spanwise wave number. The resolution of the simulations was chosen to be sufficient for the initial nonlinear disturbance development. In agreement with a previous study (Eißler & Bestek, 1995), where we considered simulations $\mathcal{A}$ to $\mathcal{D}$, the four cases were denoted by $\mathcal{B}$,$\mathcal{C}$,$\mathcal{E}$, and $\mathcal{F}$. The parameters of the four simulations are given in Fig. 3.

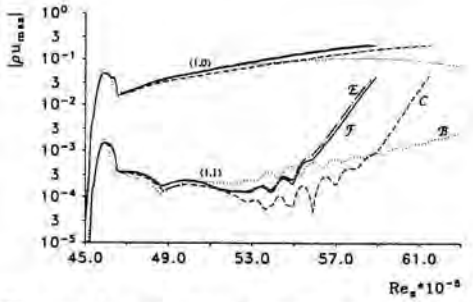

	$\mathcal{B}$	$\mathcal{C}$	$\mathcal{E}$	$\mathcal{F}$
T^*_∞ [K]	220			
T^*_w [K]	1065	650		647-633
T'_w	0		adiab.	rad. ad.
$F_{1,0}$	$10 \cdot 10^{-5}$			
$F_{1,1}$	$10 \cdot 10^{-5}$			
Trans. mech.	fundamental breakdown			

Figure 3: Amplitude maxima $|(\rho u)'_{h,k}|$, and simulation parameters of the four simulations for fundamental resonance at atmospheric conditions. (····· $\mathcal{B}$, – – – – $\mathcal{C}$, – · – · – $\mathcal{E}$, ——— $\mathcal{F}$)

In simulation $\mathcal{B}$, the base flow was assumed to be adiabatic ($T^*_{B,\text{wall}} = 1065$ K) and the temperature disturbances were set to zero at the wall. This is traditionally assumed in LST. The effect of a cooled boundary layer can be studied with simulation $\mathcal{C}$, were a constant wall temperature ($T^*_{B,\text{wall}} = 650$ K) was used. Again, the temperature disturbances were set to zero. The effect of adiabatic and radiation adiabatic disturbances can be studied with simulations $\mathcal{E}$ and $\mathcal{F}$, respectively. In simulation $\mathcal{E}$ the base-flow wall temperature was held constant ($T^*_{B,\text{wall}} = 650$ K), and adiabatic conditions were used for the temperature disturbances. In simulation $\mathcal{F}$ radiation adiabatic conditions were used for the base flow ($T^*_{B,\text{wall}}$ between 647 and 633 K), and for the disturbance flow.

It is well known from LST Mack, 1984) that wall cooling destabilizes second mode disturbances. Therefore, it is obvious that the amplitude of the two-dimensional, fundamental disturbance $(\rho u)_{1,0}$ of case $\mathcal{C}$ increases faster than the corresponding amplitude of case $\mathcal{B}$, as can be seen in Fig. 3. When the wall temperature disturbances are adiabatic or radiation adiabatic ($\mathcal{E}$,$\mathcal{F}$) instead of being zero ($\mathcal{C}$), the two-dimensional amplitudes $(\rho u)_{1,0}$ grow even faster. Thus, the onset of resonance in simulations $\mathcal{E}$ and $\mathcal{F}$ occurs upstream compared to simulation $\mathcal{C}$. In simulation $\mathcal{B}$, the two-dimensional disturbance reaches a maximum and decays further downstream. Consequently, the secondary amplification of the three-dimensional, fundamental disturbance $(\rho u)_{1,1}$ for case $\mathcal{B}$ is weak compared to the simulations $\mathcal{C}$,$\mathcal{E}$, and $\mathcal{F}$.

Comparing simulations $\mathcal{C}$ and $\mathcal{E}$, where minimum and maximum wall temperature fluctuations were assumed, it becomes clear, that transition predictions based on stability results using the traditional non-fluctuating conditions are too optimistic.

Fundamental transition for a radiation adiabatic wall

To investigate the effect of the most realistic radiation adiabatic wall-temperature condition in a transitional flow, simulation $\mathcal{F}$ was repeated with a better resolution in time and space. The streamwise amplitude developments of the 3-D

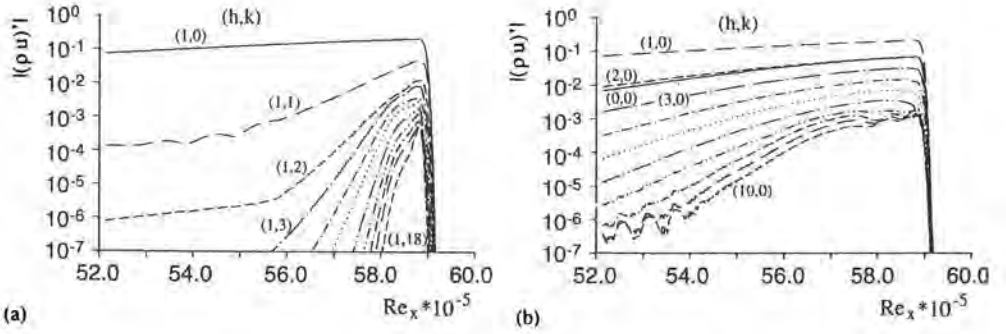

Figure 4: Amplitude development of $|(\rho u)'|$ for (a) 3-D disturbances with fundamental frequency (modes (1,k)), and for (b) 2-D disturbances (modes (h,0)).

disturbances with fundamental frequency $|(\rho u)_{1,k}|$, and the 2-D disturbances $|(\rho u)_{h,0}|$ are shown in Fig. 4. The fundamental 2-D disturbance (mode (1,0)) increases continuously caused by the primary instability. At $Re_x \approx 55.5 \cdot 10^5$ a secondary growth of the 3-D disturbances starts, and the growth rate increases for larger spanwise wave numbers. Here is the onset of fundamental resonance is found. At $Re_x \approx 58.5 \cdot 10^5$, where the resolution of the numerical simulation begins to be insufficient, the amplitudes of the leading 2-D disturbances are still higher than the 3-D disturbances. Thus, the initial transitional stages are dominated by 2-D disturbances, the effects of 3-D disturbances become important only in the late transitional stages, and the transitional region is small compared to the unstable region, which begins at $Re_x \approx 46 \cdot 10^5$.

In Fig. 5, the corresponding streamwise evolution of the boundary-layer thickness δ, the displacement thickness δ_1, the momentum thickness δ_2, the shape factor H_{12}, and the skin friction coefficient c_f are plotted. The location and the effect of the numerical damping zone near the outflow can be clearly identified for $Re_x > 59 \cdot 10^5$, where the boundary layer parameters are ramped down to their laminar values. At $Re_x \approx 57 \cdot 10^5$ the shape factor begins to deviate remarkably from its laminar value, and the skin friction starts to increase faster. Here the onset of the boundary-layer transition of this simulation occurs.

The radiation adiabatic wall-temperature condition was developed to study the effect of transition on the mean heat flux and the mean temperature development at the wall. In Fig. 6, isolines of the mean temperature gradient $\partial T/\partial y$ (which is proportional to the mean heat flux), and the mean wall-temperature distribution at the plate surface are shown. The spanwise distributions of both parameters are almost two-dimensional, and almost constant up to $Re_x \approx 57.5 \cdot 10^5$. Further downstream both parameters increase rapidly, and a three-dimensional deformation can be observed, which has a similar shape for both parameters. The fastest growth is observed in the plane $\lambda_z = 0.5$, which is the well known "Peak Plane" of fundamental transition in incompressible boundary layers (Kachanov *et al.*, 1985). These results demonstrate the capability of

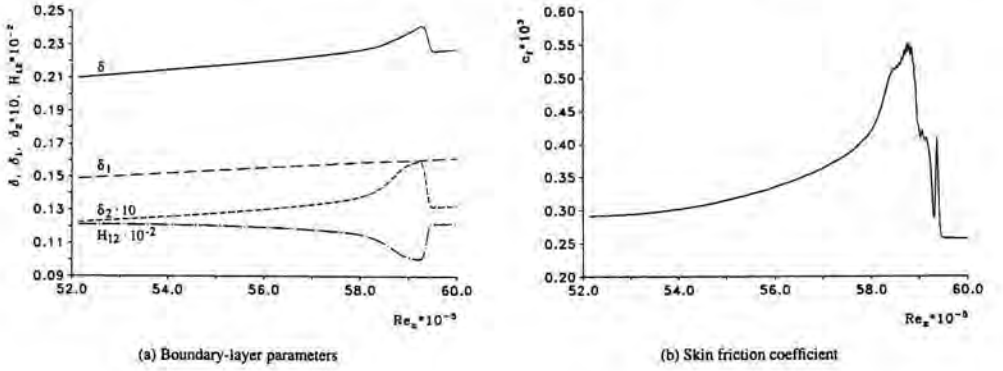

(a) Boundary-layer parameters (b) Skin friction coefficient

Figure 5: Streamwise evolution of the mean boundary-layer parameters δ, δ_1, δ_2 and H_{12}, and the mean skin-friction coefficient c_f.

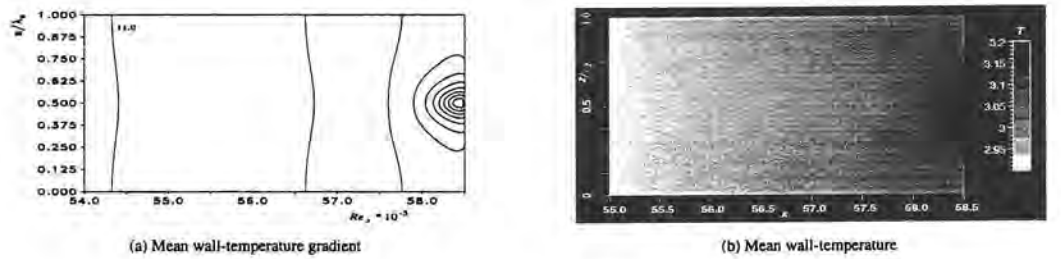

(a) Mean wall-temperature gradient (b) Mean wall-temperature

Figure 6: Distribution of the mean wall-temperature gradient ($\Delta\partial\langle T\rangle/\partial y = 1.0$), and of the mean wall-temperature.

the newly developed radiation-adiabatic wall-temperature condition for the disturbances to calculate the increase of the mean wall temperature in the late stages of transition, combined with a similar increase of the mean heat flux at the wall. This was not achieved in earlier DNS.

Conclusions

In the present paper, three different boundary conditions for the wall temperature to be used in spatial direct numerical simulations were discussed. The conditions were applied to the mean, laminar base flow and to the disturbance flow in a supersonic boundary layer. It was shown that the classic non-fluctuating wall-temperature disturbance condition produces the largest possible heat flux at the wall but the mean wall temperature does not change its laminar value, even

in the late stages of transition. The opposite boundary condition was demonstrated to be the assumption of adiabatic disturbances, where the temperature disturbances are maximum but the heat flux diminishes to zero. This condition led to a significantly lower transition Reynolds number than the non-fluctuating temperature condition for the investigated second-mode disturbances. A more realistic condition, the radiation adiabatic wall, was developed and applied. The resulting increase of the mean wall temperature and the mean heat flux at the wall using this condition was shown for fundamental transition in a flat-plate boundary layer at Mach 4.8 at flight conditions.

Acknowledgement

This work was supported by the Deutsche Forschungsgemeinschaft (DFG) Bonn-Bad Godesberg, FRG, as part of SFB 259.

References

Eißler, W. & Bestek, H. 1995 – Numerical simulations of initial transition in Mach 4.8 boundary layers at wind-tunnel and flight conditions. *Z. Flugwiss. Weltraumforsch.* **19**, 228–235.

Kachanov, Y., Kozlov, V., Levchenko, V. & Ramazanov, M. 1985 – On nature of K-Breakdown of a laminar boundary layer. New experimental data, *In* V. Kozlov, ed., Laminar-Turbulent Transition, Springer-Verlag, Berlin, pp. 61–73.

Kloker, M., Konzelmann, U. & Fasel, H. 1993 – Outflow boundary conditions for spatial Navier-Stokes simulations of transition boundary layers. *AIAA J.* **31**, 620–628.

Mack, L. 1969 – Boundary layer stability theory, Technical Report 900-277, Rev. A, Jet Propulsion Laboratory, Pasadena, CA.

Mack, L. 1984 – Boundary-layer linear stability theory, *In* R. Michel, ed., 'Special Course on Stability and Transition of Laminar Flow', AGARD-Report-709, pp. 3.1–3.81.

Authors' address

Institut für Aerodynamik und Gasdynamik,
Universität Stuttgart,
D-70550 Stuttgart, Germany.

Author Index